UNIVERSITAT DE BARCELONA

# From the Precision Era towards the Accuracy Era of Cosmology with DESI

Samuel Brieden

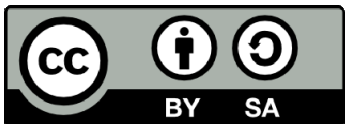

# FROM THE PRECISION ERA TOWARDS THE ACCURACY ERA OF COSMOLOGY WITH DESI

SAMUEL BRIEDEN

DIRECTORS:
Dr. Héctor Gil-Marín
Prof. Licia Verde


UNIVERSITAT DE BARCELONA

Departament de Física Quàntica i Astrofísica
Facultat de Física
Universitat de Barcelona

Samuel Brieden
*From the Precision Era towards the Accuracy Era of Cosmology with DESI*
PhD Thesis
Barcelona, Spain
July 12, 2022

# From the Precision Era towards the Accuracy Era of Cosmology with DESI

Memòria presentada per optar al grau de doctor per la

Universitat de Barcelona

Programa de doctorat en Física


Autor:
Samuel Brieden

Directors:
Dr. Héctor Gil-Marín
Prof. Licia Verde

Tutor:
Prof. Alberto Manrique Oliva


Barcelona, Espanya
12 de juliol de 2022


UNIVERSITAT DE BARCELONA

# DECLARATION

This thesis is presented following the regulations of the University of Barcelona (Aprovada pel CdG en sessió del 16 de març de 2012 i modificada pel CdG de data 9 de maig i 19 de juliol de 2012, 29 de maig i 3 d'octubre de 2013, 17 de juliol de 2014, 16 de juliol de 2015, 15 de juny i 21 de novembre de 2016, 5 de desembre de 2017, 4 de maig de 2018, 15 de maig de 2019 i 22 de juliol de 2019, 6 de marçde 2020 i 22 d'abril 2020). The listed regulations allow for the presentation of a PhD thesis as a "compendia of published articles". According to the regulations, the thesis must contain a minimum of three published or accepted articles. This thesis contains the published version of four articles, which is sufficient to allow its presentation. It also contains one additional article, submitted but not yet accepted for publication at the moment of thesis presentation.

*Barcelona, Spain, July 12, 2022*

S. Brieden

Samuel Brieden


UNIVERSITAT DE BARCELONA

IEEC

Institut d'Estudis Espacials de Catalunya

*...to my beloved infinite star.*

# ACKNOWLEDGMENTS

Words cannot express my gratitude to my thesis advisors, Héctor Gil Marín and Licia Verde for their enormous support during the last four years. Without their teachings, guidance, patience and their granted freedom for developing my own scientific personality, this achievement would not have been possible. Thank you so much for all the motivating meetings full of sparkling ideas and unforgettable moments in conferences on the other side of the globe. Thank you for making this PhD journey an experience I would never want to miss.

I would not have started this endeavor without my previous supervisors in Aachen, Alessandro Cuoco, Thejs Brinckmann, Maria Archidiacono and especially Julien Lesgourgues. Thank you for transmitting to me the curiosity and passion for cosmology.

I am deeply indebted to my collaborators José Luis Bernal Mera, Alexander Mead and Nils Schöneberg for the exchange of knowledge. Many thanks also to all the members of the Barcelona physical cosmology group for all the nice moments and stimulating discussions we had. Thank you Raúl, Ilia, Benedict, Davide B., Davide G., Benjamin, David, Katie, Sergi, Emanuele and special thanks to Nicola and Ali for helping me with paperwork in the early and late stages of the PhD respectively. I would like to extend my sincere thanks to all Master students Alba, David, Lorenzo and visiting scholars Axel, Viviana and Yacine for enriching my experience.

I am grateful to all my friends and colleagues from the "7th floor oasis" and beyond: Alfred, Ana, Arnau, Carlos, Dani, Dani-Marin, Edgar, Elina, Estef, Friedrich, Hamish, Helena, Ignasi, Josep, Joao, Jordi, Juan, Julien, Laia, Lluís, Mar, Marcel, Núria, Oscar, Pau, Paul, Quim, Roger, Stefano, Toni and Xiying. Thanks for all the joint adventures and fresh-air balcony moments! I also acknowledge the support of the FQA and ICC for solving my bureaucratic and technical problems. Thank you JR, Miriam, Esther, Kayla, Gabi, Jordi, Joan and Dani.

Mein herzlichster Dank geht an meine Familie, an meine Geschwister, Eltern, Großeltern, an alle Kochs, Limpergs, Briedens, Trillings mitsamt Linnenbergs und Elombats y también a los Chavez-Padilla y Dumitra. Danke, dass ihr mich in all meinen Schritten unterstützt und mir einen sicheren Hafen bietet. Ihr seid die Besten! Ein besonderer Dank geht an Gerd, der die Saat für meine Vorliebe in Physik setzte, die von Kreiseln bishin zu rotierenden Galaxien wuchs.

Zu guter Letzt, möchte ich meinen größten Dank meinem Liebling, Anita, aussprechen für ihre tatkräftige Unterstützung, Munterkeit und Liebe, die mich erdet und beflügelt. Danke, dass du mich auf dem Weg des Lebens begleitest!

## ABSTRACT

Observations of the cosmic microwave background and the large scale structure of the universe have established the concordance flat ΛCDM model, predicting an accelerated expansion of the universe via Einstein's cosmological constant Λ and structure formation dominated by "Cold Dark Matter" (CDM), a low-velocity fluid interacting gravitationally only.

Despite the successes of that model and having entered the "Precision Era of Cosmology" there are still open questions. The principal model ingredients, Λ+CDM, contribute to $\sim 95\%$ of the total energy density of the universe, but their underlying nature is still completely unknown. This lack of understanding is the main science driver behind many experimental and observational missions as well as theoretical efforts within the field of fundamental physics. Furthermore, different cosmological observations favor different parameter values, where the most famous discrepancy is the up to (depending on the considered dataset) $\sim 5\sigma$ "tension" between model-dependent early-time and direct late-time measurements of the Hubble constant $H_0$.

The Dark Energy Spectroscopic Instrument (DESI) survey is one of these campaigns. As the name indicates, it was launched to unravel the mystery of dark energy by measuring millions of distant galaxy and quasar spectra to create the largest, three-dimensional map of the large scale structure of the universe ever obtained. From that map, the DESI collaboration aims to extract both the expansion history and the growth rate of structures history throughout cosmic time. The expansion history is obtained via the so-called *standard ruler* technique: distances (in function of redshift) are measured in units of a characteristic scale, the standard ruler, which is an imprint of the gravity-pressure waves in early universe leading to the so-called *baryon acoustic oscillations* (BAO). The growth rate of structures is traced by the measurement of the anisotropy of galaxy clustering along and across the line-of-sight, which is induced by the peculiar velocities of galaxies impacting the redshift measurements from their spectra. As a consequence, distances inferred from these redshifts are distorted, hence this effect is called *redshift-space distortions* (RSD). Both the BAO and RSD observables deliver a pristine probe of the late-time dynamics of the universe.

In the first part of this thesis we present a method to blind the galaxy catalogs to mimic different BAO and RSD signals. Upcoming DESI data will benefit from blinding in order to remove the impact of confirmation bias on cosmological results. We explore two blinding shifts at the catalog level, perturbing individual galaxy positions

within the galaxy clustering catalog along the line of sight. The first one is a purely geometrical shift based on a different expansion law. In the second one redshifts are shifted depending on the galaxy density field mimicking RSD with a modified growth rate. We test both blinding shifts by performing BAO and full shape RSD analyses on original and blinded galaxy mocks.

In the second part, we elevate the established way how BAO and RSD analyses are performed towards including another observable, the *shape* of the clustering signal as function of galaxy separations. While the BAO and RSD incorporate the horizontal and vertical information respectively in the clustering signal, the *shape* capures the "diagonal" information. We find that this technique called *ShapeFit* is sufficient to obtain cosmological constraints as tight as direct model fits to galaxy two-point statistics while preserving the advantages of model-independence of the standard BAO and RSD analyses.

Both parts of this thesis stress the importance of model-agnosticism in the context of large surveys and cosmological tensions. They play a crucial role for the DESI survey cosmological analysis providing a road to transition from the "Precision Era" to the "Accuracy Era" of cosmology.

# RESUMEN EN ESPAÑOL

Las observaciones del fondo cósmico de microondas y de la estructura a gran escala del universo han establecido la concordancia del modelo plano $\Lambda$CDM, que predice una expansión acelerada del universo a través de la constante cosmológica de Einstein $\Lambda$ y una formación de estructuras dominada por la "materia oscura fría" (CDM), un fluido de baja velocidad que interactúa sólo gravitatoriamente.

A pesar de los éxitos de ese modelo y de haber entrado en la "Era de la precisión de la cosmología", todavía hay preguntas abiertas. Los principales ingredientes del modelo, $\Lambda$+CDM, contribuyen al $\sim 95\%$ de la densidad de energía total del universo, pero su naturaleza subyacente sigue siendo completamente desconocida. Esta falta de conocimiento es el principal motor científico de muchas misiones experimentales y observacionales tanto como avances teoricos en el campo de la física fundamental. Además, diferentes observaciones cosmológicas favorecen diferentes valores de los parámetros, con la discrepancia más famosa siendo la "tensión" de hasta (dependiendo del conjunto de datos considerado) $\sim 5\sigma$ entre las mediciones en tiempo temprano dependientes del modelo y sus mediciones directas en tiempo tardío de la constante de Hubble $H_0$.

El cartografiado del Instrumento Espectroscópico de Energía Oscura (DESI) es una de estas campañas. Como su nombre indica, se puso en marcha para desentrañar el misterio de la energía oscura midiendo millones de espectros de galaxias y cuásares distantes para crear el mayor mapa tridimensional de la estructura a gran escala del universo jamás obtenido. A partir de ese mapa, la colaboración DESI pretende extraer tanto la historia de la expansión como la tasa de crecimiento de las estructuras a lo largo del tiempo cósmico. La historia de la expansión se obtiene mediante la técnica denominada *regla estándar*: las distancias (en función del corrimiento al rojo) se miden en unidades de una escala característica, la regla estándar, que es una huella de las ondas de gravedad-presión en el universo primitivo que da lugar a las llamadas *oscilaciones acústicas de bariones* (BAO). La tasa de crecimiento de las estructuras se obtiene mediante la medición de la anisotropía de la agrupación de galaxias a lo largo y a través de la línea de visión, que es inducida por las velocidades peculiares de las galaxias que impactan en las mediciones de corrimiento al rojo de sus espectros. Como consecuencia, las distancias inferidas a partir de estos corrimientos al rojo están distorsionadas, por lo que este efecto se denomina *distorsiones del espacio de corrimiento al rojo* (RSD). Tanto los observables de BAO como los de RSD proporcionan una señal prístina de la dinámica del universo en sus épocas tardías.

En la primera parte de esta tesis presentamos un método de cegado en los catálogos de galaxias que enmascara la señal real de BAO y RSD. Los futuros datos de DESI se beneficiarán de este cegado para eliminar el impacto del sesgo de confirmación en los resultados cosmológicos. Exploramos dos tipos de desplazamientos para este cegado a nivel de catálogo, perturbando las posiciones individuales de las galaxias a lo largo de la línea de visión. El primero es un desplazamiento puramente geométrico basado en una ley de expansión diferente. En el segundo, los corrimientos al rojo se desplazan en función del campo de densidad de las galaxias imitando una señal de RSD con una tasa de crecimiento modificada. Demostramos que ambos desplazamientos distorsionan las señales de forma coherente al realizar analisis de BAO y RSD en los catalogos originales y ciegos.

En la segunda parte, mejoramos el estado del arte en que se realizan los análisis BAO y RSD incluyendo un nuevo observable, la *forma* de la señal de agrupamiento en función de las separaciones de las galaxias. Mientras que las señales de BAO y el RSD incorporan la información horizontal y vertical respectivamente en la señal de agrupamiento, la *forma* capta la información "diagonal". Encontramos que esta técnica llamada *ShapeFit* es suficiente para obtener mediciones cosmológicas tan precisas como los ajustes directos del modelo a las estadísticas de dos puntos de las galaxias, preservando al mismo tiempo las ventajas de la independencia del modelo de los análisis estándar BAO y RSD.

Ambas partes de esta tesis subrayan la importancia del agnosticismo hacia el modelo en el contexto de los grandes sondeos y las tensiones cosmológicas. Estas, despeñan un papel crucial para el análisis cosmológico del sondeo DESI, y proporcionan un camino para la transición entre la "Era de la Precisión" a la "Era de la Exactitud" de la cosmología.

# PUBLICATIONS

Complete list of publications at the moment of thesis deposit.

**Published articles included in this thesis**

- **S. Brieden**, H. Gil-Marín and L. Verde, *PT challenge: Validation of ShapeFit on large-volume, high-resolution mocks*, *JCAP* **2022** (Jun., 2022) 005, [2201.08400].
- **S. Brieden**, H. Gil-Marín and L. Verde, *Model-independent vs. model-dependent interpretation of the SDSS-III BOSS power spectrum: bridging the divide*, *Phys. Rev. D* **104** (Dec., 2021) L121301, [2106.11931].
- **S. Brieden**, H. Gil-Marín and L. Verde, *ShapeFit: extracting the power spectrum shape information in galaxy surveys beyond BAO and RSD*, *JCAP* **2021** (Dec., 2021) 054, [2106.07641].
- **S. Brieden**, H. Gil-Marín, L. Verde and J. L. Bernal, *Blind Observers of the Sky*, *JCAP* **2020** (Sept., 2020) 052, [2006.10857].

**Other published articles (not included in this thesis)**

- A. J. Mead, **S. Brieden**, T. Tröster and C. Heymans, *HMCODE-2020: improved modelling of non-linear cosmological power spectra with baryonic feedback*, *MNRAS* **502** (Mar., 2021) 1401–1422, [2009.01858].
- A. Spurio Mancini, F. Köhlinger, B. Joachimi, V. Pettorino, B. M. Schäfer, R. Reischke et al. (incl. **S. Brieden**), *KiDS + GAMA: constraints on horndeski gravity from combined large-scale structure probes*, *MNRAS* **490** (Dec., 2019) 2155–2177, [1901.03686].
- H. Hildebrandt, F. Köhlinger, J. L. van den Busch, B. Joachimi, C. Heymans, A. Kannawadi et al. (incl. **S. Brieden**), *KiDS+VIKING-450: Cosmic shear tomography with optical and infrared data*, *A&A* **633** (Jan., 2020) A69, [1812.06076].

**Submitted articles included in this thesis**

- **S. Brieden**, H. Gil-Marín and L. Verde, *Model-agnostic interpretation of 10 billion years of cosmic evolution traced by BOSS and eBOSS data*, [2204.11868]. Under review.

**Other submitted articles (not included in this thesis)**

- B. Abareshi et al. (incl. **S. Brieden**), *Overview of the Instrumentation for the Dark Energy Spectroscopic Instrument*, [2205.10939]; Under review.

# CONTENTS

# 1 INTRODUCTION

Cosmology is the study of the origin and evolution of our universe, from its birth until today and beyond. Since time immemorial, humankind have concerned themselves with the fundamental cosmological questions such as "Where do we come from?", "What gave rise to our existence?" and "What is the origin of the world we live in?". But only at this particular moment and for the first time in human history, thanks to the overwhelming technical, observational and theoretical advancements during the past century, we understand -on a rigorous scientific basis- how our universe evolved and how it looks like on the very large scales.

In this chapter we will review how these recent advancements culminate into the current cosmological paradigm and portray the challenges and open questions modern cosmology is facing at the moment. We will introduce the basic theoretical and observational concepts necessary to understand the original publications presented in chapters 2 and 3 and motivate the objectives of this thesis within the scope of addressing these challenges. In particular, part of this thesis and the publications [1–5] included in it, emerged from work for the Dark Energy Spectroscopic Instrument (DESI) collaboration. This instrument [6], which will set the new standard in large scale structure (LSS) observations for the next decade, will be introduced in this chapter as well.

## 1.1 ΛCDM- THE STANDARD COSMOLOGICAL MODEL

The theoretical basis of cosmology was laid out by Einstein in 1907 in his work *The Foundation of the General Theory of Relativity* [7]. While the previous notion of evolution of matter within space and time based on Newton's *Principia* [8] viewed space and time as absolute, like a rigid stage on which matter acts upon freely, Einstein introduced the concept of General Relativity (GR) where geometry and matter are directly intertwined. The matter distribution defines the curvature of spacetime, while the curvature of spacetime itself defines the trajectory of each body within that matter distribution. This notion paved the way for our current understanding of the universe, where not only its constituents, but also spacetime itself is evolving throughout cosmic time.

The first observational evidence for a dynamic spacetime geometry was delivered by Edwin Hubble in 1929 [9], who measured the recession velocity of distant galaxies with respect to us. He found a linear

relation between the velocity $v_{\rm gal}$ and the distance $D_{\rm gal}$ of galaxies hinting towards an expansion of the universe at the so-called "Hubble rate today" defined as

$$H_0 = \frac{dv_{\rm gal}}{dD_{\rm gal}} = 100\,h\frac{\rm km/s}{\rm Mpc}\,, \tag{1.1}$$

where the exact numerical value of the unitless parameter $h$ is still of primary interest for modern cosmology.

This observation led to the conclusion that spacetime itself is expanding, which implied that at earlier times the universe was more squeezed, hence denser and hotter than before. Ultimately, this gave rise to the theory of the "Big Bang", in which the universe emerged from an initial singularity.

The general formalism can be summarized as follows. Assuming the universe to be homogenous and isotropic at any time $t$, its geometry can be described by the Friedmann-Lemaître-Robertson-Walker (FLRW) metric, that relates the line element $ds^2$ to the spacetime coordinates (time $t$, radius $r$, solid angle $\Omega$) as

$$ds^2 = -c^2dt^2 + a^2(t)\left(\frac{dr^2}{1-kr^2} + r^2d\Omega^2\right)\,. \tag{1.2}$$

This metric allows for a global curvature of spacetime parameterised by $k$ and scales all distances with a time-dependent scale factor $a(t)$, normalised to $a_0 = a(t_0) = 1$ today. Going back in time, the scale factor decreases and reaches zero $a_{\rm ini} = a(t_{\rm ini}) = 0$ at the time $t_{\rm ini} = 0$ of the initial singularity, when the universe (and spacetime itself) was born. Cosmology does not (and cannot) probe the origin of that singularity nor describe the status at the precise time of the singularity. It rather deals with the evolution of the universe just after the singularity. For example, the determination of the age of the universe $t_0$ is of enormous interest in modern cosmology and closely related to determining $h$, as the age of the universe can be inferred from the expansion rate $H(t)$.

According to Einstein's GR, the expansion rate and the curvature of spacetime is directly linked to the energy content of the universe. Combining homogeneity and isotropy, i.e., eq. (1.2) with GR results in the Friedmann equation

$$H(t)^2 = \left(\frac{\dot a(t)}{a(t)}\right)^2 = \frac{8\pi G}{3}\rho(t) - \frac{k}{a^2} + \frac{\Lambda}{3}\,, \tag{1.3}$$

where the dot ($\dot{}$) denotes the derivative with respect to time $t$ and $\Lambda$ is the cosmological constant featuring a constant expansion rate, hence accelerated expansion. This new definition of the Hubble expansion rate after the first equal sign is equivalent to eq. (1.1) considering that the galaxies' recession velocities within the Hubble flow are a direct consequence of the time evolution of the scale factor.

So, what are the constituents of the universe contributing to the energy density $\rho(t)$ in eq. (1.3)? This question has been subject to active research in cosmology during the past century, with beneficial input from the ongoing advancements in particle physics and astronomy. To date, we know that the universe consists of the following stable elementary particle species $\{i\}$

- photons ($i = \gamma$),
- neutrinos ($i = \nu$),
- 'baryonic' matter consisting of electrons, protons, neutrons and combinations of these, i.e., elements such as hydrogen, helium, etc. ($i = \mathrm{b}$),
- cold dark matter ($i = \mathrm{cdm}$),

where cold dark matter (CDM) is a set of particles/objects only interacting gravitationally, whose underlying nature is still unknown. However, next to the cosmological evidence we will review later, there is a plethora of astrophysical evidence pointing to its existence, such as galaxy cluster dynamics [10], galaxy rotation curves [11] and the displacement of the mass centers of collided galaxy clusters with respect to their electromagnetic counterpart [12], to mention a few.

It is useful to define the relative density parameter $\Omega_i$ for each specie $i$ as

$$\Omega_i = \frac{\rho_i}{\rho_{\mathrm{crit}}} , \qquad \text{with} \quad \rho_{crit} = \frac{3H_0^2}{8\pi G} , \tag{1.4}$$

where $\rho_{\mathrm{crit}}$ is the critical density today and $G$ the gravitational constant. By interpreting also the curvature and cosmological constant terms in eq. (1.3) in terms of energy density

$$\Omega_k = -\frac{k}{a_0^2 H_0^2} , \qquad \Omega_\Lambda = \frac{\Lambda}{3H_0^2} , \tag{1.5}$$

and grouping each specie $i$ into relativistic radiation $\mathrm{r} = \{\gamma, \nu\}$ and non-relativistic matter $\mathrm{m} = \{\mathrm{cdm}, \mathrm{b}\}$, we can write (1.3) in the convenient form

$$\left(\frac{H(z)}{H_0}\right)^2 = \Omega_\mathrm{r}(1+z)^4 + \Omega_\mathrm{m}(1+z)^3 + \Omega_k(1+z)^2 + \Omega_\Lambda \tag{1.6}$$

fulfilling by construction the so-called budget equation

$$1 = \Omega_\mathrm{r} + \Omega_\mathrm{m} + \Omega_k + \Omega_\Lambda . \tag{1.7}$$

Since it is more closely related to actual observations, we have replaced the time $t$ and scale factor $a$ variables by the redshift $z$, which describes the relative stretching of a photon's wavelength $\lambda$ due to the

universe expansion between the time of emission $t$ and the time $t_0$ of its absorption in a telescope

$$z(t) = \frac{\Delta\lambda(t_0, t)}{\lambda(t)} = \frac{\lambda(t_0) - \lambda(t)}{\lambda(t)} = \frac{a_0}{a(t)} - 1 \,. \tag{1.8}$$

In eq. (1.6) we make use of the fact that the energy density of matter dilutes as $a^{-3}$ due to the scaling with volume while radiation dilutes as $a^{-4}$ due to the additional stretching of wavelength. Also, we assume that neutrinos are a relativistic specie, which is not strictly true due to their non-zero mass evidenced by neutrino oscillations [13–15].

The description of the universe's homogeneous background expansion by eq. (1.6) is of fundamental importance for cosmology. First, it sets the distances within the universe. In particular, throughout this work we will constantly use the comoving distance $D_C$ and comoving angular diameter distance $D_M$ of objects with respect to us defined as

$$D_C(z) = \int_0^z dz' \, \frac{c}{H(z')} \qquad D_M(z) = \frac{c}{H_0} S_k\left(\frac{D_C(z)}{c/H_0}\right)$$

with

$$S_k(x) = \begin{cases} \sin\left(\sqrt{-\Omega_k}x\right)/\sqrt{-\Omega_k} & \Omega_k < 0, \\ x & \Omega_k = 0, \\ \sinh\left(\sqrt{\Omega_k}x\right)/\sqrt{\Omega_k} & \Omega_k > 0 \,, \end{cases} \tag{1.9}$$

where $D_M(z) = D_C(z)$ in case of zero curvature $\Omega_k = 0$.

Moreover, eq. (1.6) implies that throughout its evolution the universe went through a certain hierarchy of different epochs. At very early times, the dominant energy contribution arises from radiation, which is surpassed by the contribution of matter at the redshift of equality between matter and radiation $z_{\text{eq}}$. In case of non-flatnesss, there is another phase of curvature domination until, at the latest times, the universe eventually becomes "dark energy" (or cosmological constant) dominated.

The current picture of the thermal history of our universe as supported by observations is as follows.

During a split second after the Big Bang, the universe is in a state of accelerated expansion called inflation. This mechanism introduced by [16–19] ensures causal connection between different patches of the sky, flatness, and generates the initial condition of small perturbations from homogeneity. These perturbations of order 0.001% are sourced by initial quantum fluctuations becoming macroscopic due to inflation. The spectrum of these primordial fluctuations $\mathcal{P}_\mathcal{R}(k)$ as function of wavenumber $k$ is predicted to be nearly scale-invariant, with scalar amplitude $A_s$ and primordial tilt (deviation from scale-invariance) $n_s$

$$\mathcal{P}_\mathcal{R}(k) = A_s \left(\frac{k}{0.05\,\text{Mpc}^{-1}}\right)^{n_s - 1} \,. \tag{1.10}$$

After the first standard model elementary particles form in a process called reheating, the strong force groups quarks into protons and neutrons, which form heavier ions within the next minute leading to the element abundances seen today by observing spectra of very distant systems [20] and can be predicted using "Big Bang Nucleosynthesis" (BBN) codes such as [21].

The universe is now a hot soup made of a tightly coupled photon-baryon pasma, in which the initial perturbations propagate as sound waves, driven by the gravitational and pressure forces. Until the temperature drops well below the binding energy between electrons and protons which consequently, driven by the electromagnetic force, recombine into neutral atoms. This phase transition called recombination takes place 380,000 years after the Big Bang, or in terms of redshift at $z_{\rm rec} = 1090$ shortly after the time of equality between matter and radiation at $z_{\rm eq} = 3400$. From that moment on, photons can travel freely and we can still observe the correspondent relic radiation called cosmic microwave background (CMB) radiation. The most precise measurement of the CMB monopole temperature today

$$T_0^\gamma = 2.72548 \pm 0.00057 \tag{1.11}$$

comes from the Cosmic Background Explorer (COBE) mission [22, 23] and its perturbations were measured in subsequent satellite missions of the Wilkinson Microwave Anisotropy Probe WMAP [24] and Planck [25]. The latter experiments also measured the polarisation spectra of the CMB, which are also probed independently by the earth-based Atacama Cosmology Telescope (ACT) [26] and the South Pole Telescope (SPT) [27], providing additional constraining power on cosmological parameters.

The theoretical prediction for the temperature and polarisation anisotropies is obtained by solving the perturbed Boltzmann equations numerically using Boltzmann codes such as CAMB [28] or CLASS [29]. All these efforts provide remarkable evidence for the Hot Big Bang model and exquisite measurements of the energy composition of the universe through the balance between pressure and gravity and the strength $A_s$ and tilt $n_s$ of primordial fluctuations.

After recombination, the universe enters the "dark ages", during which the gravitational force progressively groups the gas of neutral hydrogen, helium and metals into denser and denser clouds until they form the first galaxies and stars at the so-called redshift of reionisation $z_{\rm reio} \sim 10$. During that process the underlying CDM is key for the gas cooling and star formation mechanisms. Hence, from that moment on, structures emerged that we can observe with our telescope to map the expansion history of the universe. There is a wealth of different tracers of the universe's late-time dynamics. Here we point to three different methods that have become pivotal in establishing the current ΛCDM paradigm, where the latter two are of particular relevance for this thesis.

*The standard candle method.* The absolute luminosity of Type Ia Supernovae explosions is known theoretically (and can be calibrated using near supernovae) and is assumed to be the same independently of their distance to us. Hence, by measuring the apparent luminosity of distant supernovae one can infer the redshift-distance relation. With the launch of the Hubble Deep Field satellite mission [30] this method led to the observational evidence, that the universe is in a state of accelerating expansion [31, 32], hence cosmological constant or dark energy dominated today.

*The standard ruler method.* As mentioned before, the initial perturbations propagate as sound waves and become frozen once the baryon-photon fluid decouples at recombination, or more precisely, at the time of baryon drag $z_\mathrm{d} \approx 1060$. At this time, baryons do not feel the photon pressure anymore and it occurs a bit later than recombination, since the number of photons is much larger than the number of baryons. The comoving distance the pressure waves have propagated is

$$r_\mathrm{d} = \int_{z_\mathrm{d}}^{\infty} d\tilde{z}\, \frac{c_s(\tilde{z})}{H(\tilde{z})}\,, \qquad c_s^2(z) = \left[3\left(1 + \frac{4\Omega_\mathrm{b}(z)}{3\Omega_\gamma(z)}\right)\right]^{-1}\,, \tag{1.12}$$

where $c_s(z)$ is the sound speed of the photon-baryon fluid as a function of redshift. This process leaves a unique imprint known as the baryon acoustic oscillations (BAO) on the large scale clustering of, galaxies and other CDM tracers during late times. Measuring the angle under which this scale appears at different redshifts delivers another independent probe of the expansion rate of the universe. This method, first applied to data in [33, 34], has contributed to our current understanding that the universe is flat and the most recent BAO analyses from the Baryon Oscillation Spectroscopic Survey (BOSS) [35] and its extended campaign (eBOSS) [36] deliver the most precise and robust standard ruler based distance measurements to date.

*The redshift-space distortions method.* Finally, spectroscopic surveys do not only measure the expansion history through BAO, but also the structure formation history via redshift-space distortions (RSD). These distortions arise from the fact that the galaxies we observe have peculiar velocities that introduce an additional red- (or blue-) shift component on top of the redshift related to the Hubble flow. Crucially, this component is not random, since the galaxy peculiar velocity field is correlated with the real-space galaxy overdensity field, because of the gravitational attraction towards overdense regions. Indeed, it is easy to show within linear perturbation theory [37], that the bulk motion of galaxies on large scales depends on the so-called velocity fluctuation amplitude $f\sigma_8$, where $\sigma_8$ is the matter fluctuation

amplitude filtered on scales of $8h^{-1}$Mpc and $f$ the logarithmic growth rate of structures defined as

$$\begin{aligned} \sigma_8^2(z) &= \int_0^\infty \mathrm{d}(\ln k)\, k^3 P_\mathrm{m}(k,z) W_\mathrm{TH}^2(k \cdot 8h^{-1}\mathrm{Mpc}) \,, \\ f &= -\frac{1+z}{z}\frac{d\ln D(z)}{d\ln z} \,, \quad \text{with} \quad D(z) = \frac{\sigma_8^2(z)}{\sigma_8^2(0)} \end{aligned} \tag{1.13}$$

where $P_\mathrm{m}$ is the matter power spectrum, $W_\mathrm{TH}$ the spherical tophat window function, that smoothes the fluctuations on scales of $8h^{-1}$Mpc, and $D(z)$ the linear growth factor. The matter power spectrum can be seen as the evolved form of eq. (1.10), where the evolution of perturbations from the initial random seed until the redshift $z$ has been consistently taken into account by solving the Bolzmann equations. The large scale RSD lead to an apparent squashing of structures, also known as "Kaiser-effect" [37]. On small scales comparable to individual dark matter halo sizes however, the measurement of $f\sigma_8$ becomes obscured by non-linear redshift space distortions arising from virialised objects. This almost random motion leads to a suppression in power and elongation of structures, also known as the "Finger-of-God" (FoG) effect [38].

In conclusion, the ability to model and measure the temperature and polarization anisotropies of the CMB enabled us to enter the so-called "precision era of cosmology", in which the composition of the universe can be pinned down to percent precision, given a model. In combination with the direct probes of the late-universe mentioned above, this effort has nowadays established the so-called standard flat ΛCDM model together with the inflationary paradigm, with free parameters $\mathbf{\Omega}$ (other choices are possible)

$$\mathbf{\Omega} = \{\Omega_\mathrm{b}, \Omega_\mathrm{cdm}, h, A_s, n_s, z_\mathrm{reio}\} \,, \tag{1.14}$$

where the energy contribution from radiation $\Omega_\mathrm{r}$ is fixed by the measurement of the CMB photon temperature in eq. (1.11) and by assuming three standard neutrino species.

## 1.2 CURRENT CHALLENGES IN COSMOLOGY

Despite the remarkable success of the ΛCDM model in fitting all observations astonishingly well with only six parameters, it exhibits some severe shortcomings.

First of all, it is a purely *parametric* model and its most important ingredients, the cosmological constant or dark energy part ("Λ") and the cold dark matter part ("CDM"), still lack physical explanation. While the cosmological constant is a natural ingredient of GR, its microscopic origin is completely unknown and commonly dubbed

"dark energy" representing a fluid with equation of state $w$ (ratio between fluid pressure $p_{\rm de}$ and density $\rho_{\rm de}$)

$$w(z) = \frac{p_{\rm de}(z)}{\rho_{\rm de}(z)} < -\frac{1}{3} \tag{1.15}$$

leading to accelerated expansion, where $w(z) = -1$ is equivalent to a cosmological constant. Finding a deviation $w(z) \neq -1$ would therefore hint towards a different origin for accelerated expansion than through $\Lambda$, where the nature of the corresponding dark energy fluid would still need to be determined. For the other ingredient, CDM, many physical explanations of its fundamental nature have been proposed, from elementary particle candidates such as axions [39] or WIMPs [40] to astrophysical objects such as primordial black holes (PBH) [41], but none of them has yet been proven, neither in observations nor in laboratories. But the search for CDM candidates is one of the main drivers of active, multidisciplinary research of fundamental physics.

Also, the current model of inflation is completely *parametric* and lacks of physical microscopic explanation. Similar to the accelerated expansion observed today, inflation requires the presence of a fluid with negative pressure, or a constant scalar field slowly decaying during accelerated expansion until reaching the "ordinary" decelerated expansion of radiation domination. While inflation is capable to solve the flatness and causal horizon problems in an elegant way, the underlying nature of such an initial scalar field is still unknown and unfortunately very hard to probe, since there is no way to reproduce the energy scales present at the time of inflation. Nevertheless, the study of primordial non-Gaussianities, primordial B-modes in the CMB polarization [42], or the gravitational wave background with the Laser Interferometer Space Antenna (LISA) [43] could reveal more details about the nature of inflation.

Then, there is a huge redshift range between $z_{\rm reio} < z < z_{\rm rec}$ still completely unexplored, hence also referred as "dark ages". Fortunately, there is ongoing effort to map the universe during this gap in cosmic history using line intensity mapping (LIM) [44] arising from transitions between quantum states of the early gas.

Finally, the standard flat $\Lambda$CDM model exhibits some *tensions* when comparing early-time versus late-time probes. In particular, the $\Lambda$CDM interpretation of the CMB anisotropies [25] results in a Hubble parameter of

$$h_{\rm CMB} = 0.6736 \pm 0.0054 \,, \tag{1.16}$$

while the latest direct measurements of the local Hubble rate $H_0$ using supernovae [45] favor

$$h_{\rm SN} = 0.7304 \pm 0.0104 \,. \tag{1.17}$$

These values are in $5\sigma$ tension with each other and both early time or late time modifications to the standard model still fail to significantly

reduce this tension [46–48]. Assuming that this tension does neither originate from systematic nor statistical errors, finding hints for new physics to bring late and early times in concordance is of primary interest for modern cosmology.

Similarly, there is a mild tension between early-time and late-time measurements in the fluctuation amplitude of perturbations. While at time of recombination perturbations are of order $\mathcal{O}(10^{-5})$ deeply within the linear regime, they keep growing due to the gravitational potential reaching $\mathcal{O}(1)$ leading to non-linear dynamics today. Direct measurements of the matter overdensity field $\sigma_8$ via weak lensing [49], i.e., the distortion of galaxy shapes due to the matter field in between acting as gravitational lenses, prefer values of $\sigma_8$ slightly lower than the $\Lambda$CDM model prediction of $\sigma_8$ given the Planck bestfit parameters [25]. On the other hand, the BOSS+eBOSS galaxy clustering measurement of $\sigma_8$ is in good agreement with the Planck prediction [36].

As already indicated, all these shortcomings lead to a plethora of active research topics, not only in cosmology but also spanning several disciplines in fundamental physics, from experimental accelerator and detector physics to string theory model building. These shortcomings are also the main science drivers for upcoming LSS surveys such as Rubin [50], Euclid [51] and the ongoing DESI survey [52, 53], for which the methods presented in this thesis were developed in particular.

## 1.3 MAPPING THE UNIVERSE WITH DESI

The primary goal of the Dark Energy Spectroscopic Instrument [52] is to improve our understanding of the underlying nature of dark energy, which drives the accelerated expansion of the universe, by creating enormous galaxy and quasar maps with unprecedented speed and precision. DESI is located at the Mayall 4-meter telescope at Kitt Peak National Observatory, Arizona (USA), an overview of its intrumentation can be found in [6]. One of the main improvements of the instrument with respect to its antecessors BOSS and eBOSS is the focal plane: it is comprised of 5000 individually controlled robots, that can quickly position each fiber within their patrol radius, while for previous intruments holes needed to be drilled mechanically into aluminium plates to position the spectrographs for each night. Together with a substantially reduced exposure time, this allows DESI to observe over 40 million spectra of extragalactic objects over a wide angle and redshift range during its 5 year program. Similar to the BOSS and eBOSS campaigns, this galaxy map will be used to apply the BAO standard ruler technique, in order to provide a precise distance redshift relation and hence measure the dark energy equation of state. Furthermore, DESI will use the full shape (FS) or (BAO+RSD) technique to measure the growth history of structures $f\sigma_8(z)$, and hence probe the fundamental assumptions of GR.

To achieve this, the DESI collaboration distributed the work to be done for the Year 1 (Y1) analysis into several key projects (KP). The first, KP1, is the "Data Release of the Survey Validation Data Assembly" for which the first part, the DESI Overview is already done [6] and the validation of the scientific program and the early data release of *unblinded*[1] data is in progress. The second, KP2, is the "Data Release of the Y1 data" will release the spectra and catalogs of all DESI tracers, the BGS (bright galaxy survey, $0.1 < z < 0.5$) , LRG (luminous red galaxies, $0.4 < z < 1.1$), ELG (emission line galaxies, $0.8 < z < 1.6$), QSO (quasi-stellar objects or simply: quasars, $0.8 < z < 3.5$) and Lya (Lyman-alpha, $2 < z < 5$) . KP3 takes care of the "LSS catalogs and 2-point measurements", which are analysed by the KP4, KP5 and KP6 groups to extract the "galaxy BAO", "galaxy Full Shape" (FS, where FS = BAO+RSD), and "Lya BAO". Finally, KP7 is responsable for the "Likelihoods" necessary to carry out the cosmological analysis.

In order to extract cosmological information from a map of each galaxy tracer (KP4, KP5, and KP6), we need to compress the information into the summary statistics of choice. Here, we choose the galaxy power spectrum $P_g(k, \mu, z)$ suitably binned in wavevector $k$, projection of angle $\theta$ with respect to the line of sight $\mu = \cos(\theta)$, and redshift $z$. But this compression on its own is, already, a non-trivial process and topic of active research within KP3. Here we will summarize the most important concepts necessary for qualitative understanding, but for a full review see [54, 55].

Ideally, we would like to infer directly from the map the galaxy overdensity field $\delta_g(\mathbf{r})$ defined as

$$\delta_g(\mathbf{r}) = \frac{\rho_g(\mathbf{r}) - \langle \rho_g(\mathbf{r}) \rangle}{\langle \rho_g(\mathbf{r}) \rangle} \tag{1.18}$$

with observed galaxy density $\rho_g(\mathbf{r})$ and averaged (over all angles) density $\langle \rho_g(\mathbf{r}) \rangle$. However, the latter function is unknown *a priori*, the selection function of galaxies (i.e., their angle-averaged number density) as function of redshift $n_g(z)$ is obtained from the data, and hence does not necessarily represent the underlying "true" selection function. This is usually taken into account by imposing the so-called integral constraint, that the fluctuations in the limit towards the largest observable scale corresponding to the survey size should become zero [56].

Furthermore, the selection function usually contains "holes" in regions that are not observable due to the telescope position, the galactic center, bright stars, etc. It is therefore impossible to evaluate eq. (1.18), since the denominator becomes zero in those regions. To circumvent

1 The development of a blinding method and its validation for DESI is one of the projects carried out in this thesis and will be introduced later in chapter 2. It will be used for the Y1 analysis, whereas the early data release will contain only unblinded data obtained during survey validation prior to the start of the main survey.

this, as pioneered by [57], the denominator of eq. (1.18) is replaced by a constant and, instead, the denominator (also called window function) is multiplied or convolved (in case of operating in Fourier space) with the theory model. Usually, the window function is obtained from a synthetic catalog of random points, matching the selection function of the data, but with significantly more objects and without clustering signal. During that process, however, one has to be careful to define the window function and power spectrum normalisation consistently, otherwise the fluctuation amplitude will be biased [56, 58, 59].

Another real-world complication arises from the fact that observations might become contaminated by poor observing conditions (clouds, seeing, skylines, etc), instrument limitations (fiber collisions), and peculiarities of the observed region (redshift failures, trends in magnitude-color), which need to be carefully taken into account via systematic weights [60]. Also note that, [57] introduced the so-called FKP weights to minimize the variance at those scales important for BAO analysis. All these weights are not specified here for conciseness.

Last but not least, the measured redshifts and angles need to be converted to distances, in order to compute the density field. This conversion is usually done with the help of a fiducial cosmological model. But since the "true" underlying redshift-distance relation is unknown *a priori*, the distance scaling is allowed to vary at the model fitting step (explained below) in a generic way representing all possible changes in expansion history one can think of.

Once the galaxy overdensity field is obtained, i.e., eq. (1.18) including the corrections mentioned before, we can write the galaxy power spectrum as Fourier transforms of the real-space overdensity fields given a galaxy pair $\mathbf{r_1}, \mathbf{r_2}$ within one redshift bin

$$P_{\rm g}(\mathbf{k}) = \int d\mathbf{r_1} \int d\mathbf{r_2}\, \delta_{\rm g}(\mathbf{r_1})\delta_{\rm g}(\mathbf{r_2}) e^{i\mathbf{k}\cdot(\mathbf{r_1}-\mathbf{r_2})} \,, \tag{1.19}$$

and compute the power spectrum multipoles for $\ell = 0, 2, 4$ using the Legendre polynomial base composition $L^\ell$

$$P^\ell_{\rm g}(k) = \frac{2\ell+1}{2} \int_{-1}^{+1} d\mu\, P_{\rm g}(k,\mu) L^\ell(\mu) \,. \tag{1.20}$$

There is a subtle point hidden in eqs. (1.19) and (1.20), related to the definition of $\mu$. Ideally, $\mu$ corresponds to the cosine of the angle between $\mathbf{k}$ and the LOS position of the galaxy pair. However, the latter is ill-defined in case of large angular separations. A convenient choice for the LOS is to define it with respect to one of the galaxies within that pair, e.g. towards $\mathbf{r_2}$. In that case, eq. (1.19) can be written as a product of two separate integrals and inserted into eq. (1.20) defining the so-called Yamamoto estimator, which has been shown to deliver good enough precision, even for wide angles [61, 62]. Indeed, it is shown in [63] that wide angle effects only contribute to 5% of the systematic error in the even multipoles, while they dominate the

error in the odd multipoles. Correcting for wide-angle effects is hence important for studying primordial non-Gaussianities (affecting low-$k$ modes) and GR effects affecting the odd multipoles. This is, however, beyond the scope of this thesis.

Again, the discussion presented here is purely qualitative, with the purpose to emphasize the complications arising when dealing with real data. The full relevant equations can be found in section 2 of the published article within chapter 2, in particular see eqs. (2.4-2.6) therein. But note, that those equations are valid for BOSS+eBOSS dataproducts only and the exact implementation for DESI is still in development.

Once the power spectra and their covariance (obtained from the power spectra of mock catalogs) are measured successfully, the next step in the spectroscopic survey pipeline is the model fitting. This step is the principal research topic of all publications presented in this thesis. Again, we refer to the original publications for the detailed implementation and provide here only a brief overview of the issue at hand.

As mentioned before, with DESI we pursue measurements of the BAO (KP4) and FS (KP5) signals of each tracer independently in a model-independent way, such that, subsequentely, these signals can be interpreted in light of a cosmological model of choice (KP7). This follows closely the strategy of BOSS and eBOSS, where the different tracers [64–67] have been analysed individually both in Fourier space [58, 68, 69] and configuration space [70–72].

Generally, these individual model fits to the measured two-point statistics are performed using a fixed template of the power spectrum (or correlation function), in most cases (but not necessarily) consistent with the Planck cosmology. Hence, these types of fit are also referred as *fixed-template fit*. The fiducial template is allowed to vary in a controlled way, determined by a set of physical parameters $\boldsymbol{\Theta}$.[2] In the case of BAO analyses, the physical parameters $\boldsymbol{\Theta} = \{\alpha_\parallel(z), \alpha_\perp(z)\}$ defined as

$$\alpha_\perp(z) = \frac{D_M(z)/r_\mathrm{d}}{D_M^\mathrm{fid}(z)/r_\mathrm{d}^\mathrm{fid}} \qquad \alpha_\parallel(z) = \frac{H^\mathrm{fid}(z) r_\mathrm{d}^\mathrm{fid}}{H(z) r_\mathrm{d}} \,, \tag{1.21}$$

represent the distance scaling along and across the LOS in units of the sound horizon $r_\mathrm{d}$ from eq. (1.12). In case of FS (or BAO+RSD) analysis the growth rate of structures $f$ is introduced as an additional free parameter, $\boldsymbol{\Theta} = \{\alpha_\parallel(z), \alpha_\perp(z), f(z)\}$, representing the amount of anisotropy due to RSD in units of the fixed fiducial template amplitude $\sigma_8^\mathrm{fid}(z)$ from eq. (1.13).

2 The symbol $\boldsymbol{\Theta}$ is also used in the published articles of this thesis, see for instance eq. (3.1) of chapter 2, and the discussion in section 2 of chapter 6.

The reasoning behind fixed-template fits is that once the template-dependent parameters $\mathbf{\Theta}$ are fitted to the data, they can be easily converted into the template-independent quantities $\mathbf{\Theta}'$

$$\mathbf{\Theta} \rightarrow \mathbf{\Theta}' = \{D_M(z)/r_\mathrm{d}, H(z)r_\mathrm{d}, f\sigma_8(z)\} \tag{1.22}$$

by multiplying with the corresponding fiducial values. Of course, there is a residual template dependence which is carefully considered and quantified in each analysis [58, 68–72]. In general, the robustness of these measurement in terms of model-independence is very high as demonstrated by [73, 74] for BAO analyses and [58] for BAO+RSD analyses. We will see later that the works presented in chapter 3 open an additional window for increasing the robustness and template-independence of BAO+RSD analyses.

Finally, the set of model-independent, compressed, physical parameters can be compared to the cosmological models of choice as in [35, 36] and the article presented in chapter 6 of this thesis, which serves as a blueprint for the cosmological analysis envisioned for DESI.

## 1.4 OBJECTIVES AND STRUCTURE OF THE THESIS

With cosmological experiments gaining more and more precision, and with existing tensions between various probes, demonstrating the robustness of the observations and their analysis is crucial. The principal aim of the work provided in this thesis is to maximize the robustness of galaxy clustering measurements while at the same time extracting as much information as possible from the galaxy maps. This balancing act is represented by the two main research pillars provided in this thesis, "Blinding" (part i) and "ShapeFit" (part ii).

The first pillar, "Blinding", is the development of a catalog-level blinding scheme applicable for any spectroscopic survey in [1] as a key requirement for the DESI survey in particular. Carrying out blinded analyses is of major importance in order to reduce human confirmation bias. The idea behind this blinding scheme is to modify the galaxy redshifts in such a way that they mimick a different underlying expansion rate and growth rate of sructures, such that the physical parameters obtained from the blinded catalog are modified. In the article [1] which is included in chapter 2 we validate this method on mock galaxy catalogs and demonstrate that the signal imprinted into the catalogs indeed behaves as requested at the level of compressed variables.

The second pillar, "ShapeFit", is an extension of the standard template-fits extracting additional cosmological information beyond BAO and RSD from the galaxy power spectrum measurements. This information, captured in terms of a new physical *shape* parameter $m$ fulfills two purposes. First, it can be used to further reduce the residual fiducial template dependence on parameters $\mathbf{\Theta}'$. Second, when interpreted

in light of a cosmological model, it delivers additional constraining power, in bulk matching the "maximal achievable constraining power" of direct model fits.

Direct model fits, or "Full Modeling (FM) Fits" as called in the publications of this thesis, are not based on a fixed template, but rather fit the cosmological model parameters directly to the galaxy power spectrum multipoles, omitting the step of data compression into physical variables. FM fits have already been used in the early SDSS analyses [75–77], but were discontinued in subsequent data releases for several reasons. First, the late time galaxy density fluctuations of order $\mathcal{O}(1)$ (non-linear) are much harder to model than the CMB fluctuations of order $\mathcal{O}(10^{-5})$ (completely linear), which are routinely analysed using the FM technique. Second, there are further complications in the measurement step summarized in section 1.3 making a cosmological interpretation, especially on large scales, difficult. Finally, the compressed parameters have been shown to capture the information that is most synergetic with CMB data and completely suffice to break degeneracies. However, during the recent years FM fits have regained attention due to the works by [78–80]. This effort has been possible mainly due to recent advancements in fast perturbation theory calculations based on FFTLog [81, 82]. But their gain in constraining power comes at the cost of missing transparency to where that constraining power actually comes from and to what degree it depends on the prior assumptions.

The goal of this thesis is to augment the standard fixed template approach, such that even upon entering the precision era with DESI we maintain the ability to remain as model-agnostic as possible. For that purpose, we demonstrate explicitely on mocks [2] (chapter 3) and data [3] (chapter 4), that ShapeFit enables to match the constraining power of FM works while retaining the advantages (robust, fast, modular) of the fixed template compression. In our fourth published article [4] (chapter 5) we validate the ShapeFit accuracy by carrying out a blind analysis on the large volume, high precision PT challenge mocks provided by [83]. Last but not least, chapter 6 includes the submitted article [5], where we apply ShapeFit to the final BOSS+eBOSS legacy.

We finish the thesis with a summary of the results and future prospects with DESI in chapter 7.

# Part I

# BLINDING

# 2

# BLIND OBSERVERS OF THE SKY

The implementation of an appropriate blinding strategy is a key scientific requirement for the DESI cosmological analysis. The concept of blinding data has been recognized as a priority for modern cosmological surveys on the path towards preventing confirmation bias. Catalog level blinding has already been applied to photometric surveys for the weak lensing Kilo-Degree Survey (KiDS) both for ellipticities [84] and redshifts [85]. On the other hand, the Dark Energy Survey (DES), another photometric weak lensing survey, blinded their dataset at the level of summary statistics [86]. Another blinding method operating at the covariance and hence likelihood level is proposed in [87].

Within this thesis, the first (and only) catalog level blinding strategy for spectroscopic redshift surveys is developed. While it is targeted towards DESI, the procedure is generic for any galaxy redshift survey. It is applied as a proof of concept to BOSS but it could be implemented for other datasets as well. In the attached publication "Blind observers of the sky" [1] we present and validate this simple, yet efficient, blinding method: it introduces a shift in galaxy redshifts mimicking both a different expansion history of the universe (hence blinding the BAO position) and a different structure growth history (hence blinding the RSD signal).

The structure of [1] is as follows. After introducing the basics of BAO and RSD analyses in section 2, the exact blinding scheme is developed in section 3. It is tested on mocks and applied o real data in sections 4 and 5 respectively. Finally it concludes in section 6, featuring a summary of the blinding scheme in figure 17.

This blinding method is highly practical for several reasons. It directly blinds the observables spectroscopic galaxies are sensitive to, and by operating at the catalog level by construction it is coherent for any summary statistic of choice. Hence, it is well suited for the BAO and RSD analyses of DESI. An overview of how it is being implemented in DESI is shown in figure 1.

Journal of Cosmology and Astroparticle Physics
An IOP and SISSA journal

# Blind Observers of the Sky

**Samuel Brieden,**[a,b] **Héctor Gil-Marín,**[a] **Licia Verde**[a,c] **and José Luis Bernal**[a,b,d]

[a]ICC, University of Barcelona, IEEC-UB,
Martí i Franquès, 1, E-08028 Barcelona, Spain
[b]Dept. de Física Quàntica i Astrofísica, Universitat de Barcelona,
Martí i Franquès 1, E-08028 Barcelona, Spain
[c]ICREA,
Pg. Lluis Companys 23, Barcelona, E-08010, Spain
[d]Department of Physics and Astronomy, Johns Hopkins University,
3400 North Charles Street, Baltimore, Maryland 21218, U.S.A.
E-mail: sbrieden@icc.ub.edu, hectorgil@icc.ub.edu, liciaverde@gmail.com, jbernal2@jhu.edu

Received June 29, 2020
Accepted August 18, 2020
Published September 29, 2020

**Abstract.** The concept of *blind analysis*, a key procedure to remove the human-based systematic error called *confirmation bias*, has long been an integral part of data analysis in many research areas. In cosmology, *blind analysis* is recently making its entrance, as the field progresses into a fully fledged high-precision science. The credibility, reliability and robustness of results from future sky-surveys will dramatically increase if the effect of confirmation bias is kept under control by using an appropriate blinding procedure. Here, we present a catalog-level blinding scheme for galaxy clustering data apt to be used in future spectroscopic galaxy surveys. We shift the individual galaxy positions along the line of sight based on 1) a geometric shift mimicking the Alcock-Paczynski effect and 2) a perturbative shift akin to redshift-space distortions. This procedure has several advantages. After combining the two steps above, it is almost impossible to accidentally unblind. The procedure induces a shift in cosmological parameters without changing the galaxies' angular positions, hence without interfering with the effects of angular systematics. Since the method is applied at catalog level, there is no need to adopt several blinding schemes tuned to different summary statistics, likelihood choices or types of analyses. By testing the method on mock catalogs and the BOSS DR12 catalog we demonstrate its performance in blinding galaxy clustering data for relevant cosmological parameters sensitive to the background expansion rate and the growth rate of structures. We publicly release our data products at https://github.com/SamuelBrieden/BlindingCatalogs.

**Keywords:** baryon acoustic oscillations, cosmological parameters from LSS, galaxy surveys, redshift surveys

**ArXiv ePrint:** 2006.10857


https://doi.org/10.1088/1475-7516/2020/09/052

JCAP09(2020)052

## Contents



JCAP09(2020)052

## 1 Introduction

Thanks to a coordinated observational and theoretical effort over the past two decades, cosmology has entered the precision era. Precision cosmology rests on the extremely successful standard model of cosmology, the flat ΛCDM model, which provides a coherent and precise description of a suite of observations ranging from the early to the late Universe. Two main components of the model, dark energy with an equation of state parameter $w = -1$ equivalent to a cosmological constant Λ, and cold dark matter (CDM), are poorly understood and may be considered as effective descriptions for the true model's ingredients, which are yet to be found.

The goal to shed light on these components and their nature, as well as exploring other fundamental physics, is the main driver for forthcoming, observational efforts, especially for large-scale structure surveys as e.g. DESI [1], Euclid [2], LSST [3] and SKA [4]. Especially the LSS experiments listed above have the potential to induce a paradigm change in cosmology, since they will be sensitive to the cosmological parameters at nearly the same precision level as current CMB experiments as Planck [5].

Unaccounted systematic errors may be interpreted as signs of new physics. This is a risk that should be mitigated at all costs. Conversely however, signs of new physics may appear

as unexpected results, which the experimenter might attribute to systematic errors. It is therefore imperative to have an exquisite control on the systematic errors, which is ideally achieved by fulfilling the following conditions:

1. All potential sources of systematic errors need to be identified.

2. Each systematic needs to be modeled appropriately.

3. Their effect on the posterior distribution needs to be explored and correctly included in the systematic error budget of the final result.

While this is well known and a significant effort of the community is devoted to these aims with important successes, a basic question remains to be answered: at which point the search for further systematics may stop? This is the aspect more prone to confirmation bias: we, as scientists and human beings, unconsciously tend to accept results faster if they are in agreement with previous findings, than if they disagree.

One promising way of avoiding experimenter's bias is to carry out blind data analyses, where the original data vector is transformed as to hide the true signal in a controlled way before running the analysis pipeline. If suitably implemented, this allows for studying the degeneracies of systematic effects with theoretical models while being blind to the underlying values of the model parameters.[1] Once the analysis of the blinded data is finalised, i.e. the three conditions mentioned above are fulfilled, the analysis pipeline is frozen and either applied to the original data, or the results are unblinded.

The concept of blinding has already entered several fields of natural sciences. For the first time it was used in experimental particle physics in the 90's for the detection of the rare $K^0 \to \mu e$ decay [6]. They made use of the *hidden signal box* technique, that excludes the parameter space from the analysis, where the signal is expected. The "hidden box" is opened after the free parameters related to the experiment are fixed. There are various blinding techniques used for different problems in particle physics, which are reviewed in [7]. An alternative is adding fake signals. This method called "salting" was used by the LIGO-Virgo collaboration to test whether the claimed sensitivity to detect a gravitational wave event was accurate [8].

In cosmology we usually do not measure signals or events that can be separated from a background. Instead, we observe light from the sky, compute statistical quantities from its distribution and use these to infer the underlying cosmological model. Thus different blinding techniques need to be developed for cosmology. In general, there are three different levels, at which cosmological data can be blinded:

- Level 1: at the catalog level.

- Level 2: at the level of summary statistics.

- Level 3: at the level of cosmological parameter inference.

[1] In what follows we refer to the values of the model parameters preferred by the data as model's parameters *underlying* values. We prefer this nomenclature to *true* values which is often used, because, for example, the model adopted could in principle be incorrect or because of sample variance the values preferred by the data might differ from the true ones. When dealing with mock data or when neglecting this possibility, there is a common trend to loosely identify *underlying* values with *true* values.



JCAP09(2020)052

Level 3 blinding operates at the latest stage of the analysis. When fitting cosmological parameters to the model, an unknown offset is added to the parameters, so that the underlying values remain unknown until unblinding. This has the advantage that the step of unblinding can be done very fast. On the other hand, this means that it is also very easy to accidentally unblind. This approach has been used in the analyses of distant supernovae [9, 10], as well as in the DES Y1 analysis [11]. Level 2 blinding operates at an earlier stage; it shifts the summary statistics by the difference vector between two different cosmologies. This blinding strategy is adopted for DES Y3 [12], since it is feasible for a multi-probe survey (e.g., weak lensing + galaxy clustering). Another approach for blinding astronomical data has been presented recently [13], that operates at the level of the covariance matrix and is well suited for weak lensing analyses. Catalog-level or level 1 blinding operates at the earliest stage of the analysis which may be preferable in some cases. It has been used in the KiDS-450 weak lensing survey [14], where the ellipticities of galaxies were systematically modified, as well as in the KiDS-450+Viking analysis [15], where the redshift distribution was shifted by a constant factor.

Independently of the level at which it operates, it is desirable that a blinding scheme meets the following criteria:

- it should modify the data in such a way that the effect on observables and best-fit parameters can be predicted easily.
- it should make it difficult to unblind accidentally.
- it should not interfere too much with delicate and key aspects of the analysis such as systematic weights.
- it should not change significantly the shape of the posterior distribution.
- it should not be too numerically intensive.
- ideally it should be easy to infer (to a sufficiently good approximation) unblind parameter constraints without the need to rerun the analysis pipeline again. This is a"nice-to-have" but not a necessary condition.[2]

Inspired by these criteria, in this work we introduce a novel method of catalog-level blinding targeted to spectroscopic galaxy surveys. The method might be interesting for clustering measurements from photometric surveys (as discussed in [16, 17]) as well, especially if the photometric errors are small enough. Most of the cosmological signal that a galaxy redshift survey carries is enclosed in two main physical effects: background metric evolution and growth of structures. The background evolution is usually tracked via the purely geometrical Alcock-Paczynski (AP) effect [18], which is most visible on the baryon acoustic oscillation (BAO) feature. The most promising window into the growth of structures signal comes from the redshift-space distortions (RSD) effect (pioneered by [19] and also [20, 21]). The proposed blinding scheme affects both these signals.

A flowchart indicating how we envision the blinding scheme to be embedded into a galaxy clustering pipeline is shown in figure 1. All the systematic tests are done on the catalog before

[2]The pipeline should be frozen before unblinding and can be re-run on the un-blinded data, but knowing approximately the expected results makes the process more transparent and easier to interpret. Another advantage is the possibility to finalize introduction sections and sketching results and conclusions sections of the associated scientific papers even before the final runs on unblinded papers have finished.



JCAP09(2020)052

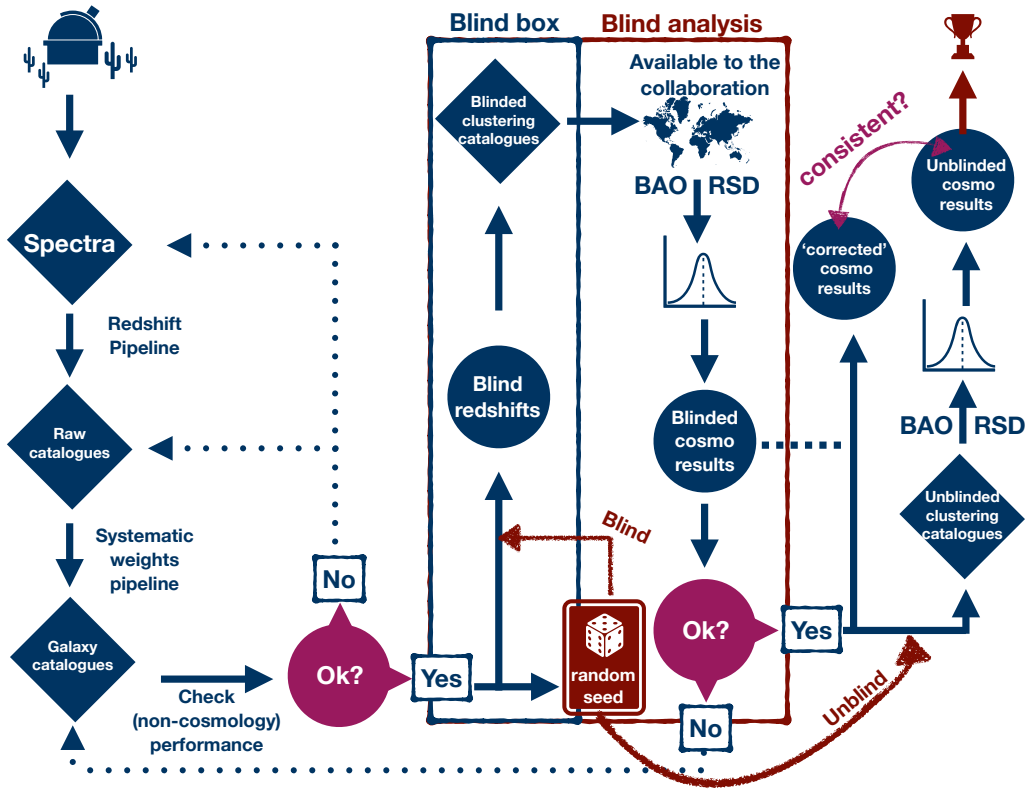


**Figure 1**. Flowchart of how the blinding fits in the generic workflow of a galaxy redshift survey analysis. See text for details. In this paper we introduce a scheme for the "blind box", carry out multiple "blind analyses" on mock and real catalogs and check the consistency between the results on the original catalog and the analytical prediction (fast unblinding).

JCAP09(2020)052

blinding, but no comparison with theory or cosmological inference can be done at this stage. Once the catalog is ready for cosmological analysis it goes through blinding (the "blind box") according to the procedure presented in this paper. The blinded catalog is released to the collaboration for cosmological analyses (the "blind analysis" box). This procedure may be reiterated whenever the methodology for systematic tests or cosmological analysis is changed. Once the analysis is complete, all pre-determined sanity checks are satisfied and the blinded results are obtained, the pipeline should be frozen and unblinding may be done. We propose to unblind in two parallel steps:

1) The posterior constraints can be shifted according to analytical expectations, as derived in sections 3.2 and 3.3. We call this process "fast unblinding".

2) The pipeline can now be re-run on the original catalog for obtaining precise numbers and results.

The paper is organised as follows: in section 2 we summarise the basics of BAO and RSD analyses and introduce the nomenclature and conventions that are used in the following sections. We present our blinding scheme in section 3 and discuss how blinding at the catalog

level is expected to change the cosmological parameter results ("blind box" in figure 1). In section 4 we compare this expectation to the results obtained from standard BAO+RSD analyses of unblinded and blinded mocks ("blind analysis" box in figure 1). The robustness of our results is tested in further detail in appendices A, B where we check for the impact of several changes to our fiducial setup. Results from the application to the BOSS data and a summary of our proposed blinding procedure are presented in section 5. In particular we are interested in whether the consistency between the two parallel unblinding steps explained before holds. We conclude with section 6.

## 2 Basics of BAO and RSD analyses

We start by reviewing the basic background of BAO and RSD analyses from the catalog to cosmological parameter inference. The methods and variables presented in the following paragraphs will be used repeatedly throughout the rest of this work, so this section serves also to introduce and define the key quantities used.

**The galaxy catalog.** We start with the galaxy catalog, that contains at least three quantities representing the 3D observational position $\mathbf{r}_i = (\mathrm{RA}_i, \mathrm{dec}_i, z_i)$ of each galaxy, parameterised by its right ascension, declination and redshift. These three numbers do not suffice to provide a distance measure though. A reference cosmology is needed to have a unique mapping from redshifts to distances (see next paragraph). Additionally, the catalog may also include relevant quantities such as the average galaxy density $\bar{n}(z)$ and correction weights; for example it is customary to have weights for angular systematics $w_{\mathrm{sys}}$, fiber collisions $w_{\mathrm{fc}}$ and redshift failures $w_{\mathrm{rf}}$ as used for the Baryon Oscillation Spectroscopic Survey[3] (BOSS) and also in the extended Baryon Oscillation Spectroscopic Survey[4] (eBOSS) in [22, 23] and [24].

**Reference cosmology.** As in most of BOSS and eBOSS analyses, we follow the fixed template-fitting approach, where the cosmology is not varied during posterior exploration, but a reference cosmology $\mathbf{\Omega}^{\mathrm{ref}}$ is chosen for two different purposes:

1. to convert the catalog redshifts to radial distances $z_i \to r_i$
2. to generate a power spectrum template.

In principle, the reference cosmologies for points 1 and 2 do not need to be the same. Here, (both for simplicity and because it is widespread) we use the same reference for both points. We assume a spatially flat model with parameters set

$$\mathbf{\Omega}^{\mathrm{ref}} = \{\Omega_{\mathrm{m}}^{\mathrm{ref}}, \Omega_{\mathrm{b}}^{\mathrm{ref}}, H_0^{\mathrm{ref}}, \sigma_8^{\mathrm{ref}}, n_s{}^{\mathrm{ref}}, M_\nu{}^{\mathrm{ref}}, w{}^{\mathrm{ref}}, \gamma{}^{\mathrm{ref}}\}\,, \tag{2.1}$$

where the total matter and baryon densities $\Omega_{\mathrm{m}}$ and $\Omega_{\mathrm{b}}$ at present, the Hubble rate evaluated today $H_0$, the (linear) density fluctuation amplitude $\sigma_8$ (smoothed on spheres of radius $8\,h^{-1}\,\mathrm{Mpc}$, with $h = H_0/100\,\mathrm{km/s/Mpc}$) and the primordial scalar tilt $n_s$ represent the standard ΛCDM parameter-basis. In addition, we consider the neutrino mass sum $M_\nu$, the dark energy equation of state parameter $w$ and the growth rate exponent $\gamma$.

[3] https://www.sdss.org/surveys/boss/.
[4] https://www.sdss.org/surveys/eboss/.



JCAP09(2020)052

For the conversion mentioned in point 1 we need to compute the angular comoving distance $D_M$ as a function of galaxy redshift $z_i$ and reference cosmology $\mathbf{\Omega}^{\rm ref}$

$$r_i = D_M(z_i, \mathbf{\Omega}^{\rm ref}) = \int_0^{z_i} dz \, \frac{c}{H(z, \mathbf{\Omega}^{\rm ref})} \,, \tag{2.2}$$

where $c$ is the speed of light and $H(z, \mathbf{\Omega}^{\rm ref})$ is the Hubble expansion rate at a redshift $z$, that in the assumed model is given by

$$H(z, \mathbf{\Omega}^{\rm ref}) = H_0^{\rm ref} \sqrt{\Omega_m{}^{\rm ref}(1+z)^3 + (1-\Omega_m{}^{\rm ref})(1+z)^{3(1+w{}^{\rm ref})}} \,. \tag{2.3}$$

The case $w{}^{\rm ref} = -1$ corresponds to the standard ΛCDM model. We call the distance obtained by eq. (2.2) the reference distance, which may differ from the underlying one. This fact must be included in the modeling (see paragraph Alcock-Paczynski effect and scaling parameters).

The computation of the template of the power spectrum requires to run a Boltzmann code like `CAMB` [25] or `CLASS` [26] with the reference cosmological parameters as input. The output linear power spectrum is used in the modelling as explained in paragraph BAO anisotropic power spectrum model et seq.

**Power spectrum estimator.** The next step is to compute the summary statistics of choice, which can be 2-point statistics (power spectrum and 2-point correlation function), 3-point statistics (bispectrum, 3-point correlation function), and even higher-order statistics if needed. As throughout this work we will operate in Fourier space, we introduce the FKP power spectrum estimator [27], which relies on computing the field

$$F(\mathbf{r}) = \frac{w_{\rm FKP}(\mathbf{r})}{I_2^{1/2}} \left[ w_{\rm c}(\mathbf{r}) n(\mathbf{r}) - \alpha_{\rm ran} n_{\rm ran}(\mathbf{r}) \right] \,, \tag{2.4}$$

where $n(\mathbf{r})$ and $n_{\rm ran}(\mathbf{r})$ are the number densities of the galaxies and Poisson-sampled randoms, respectively, $\alpha_{\rm ran}$ is the ratio between the sum of weighted data galaxies and the sum of random galaxies, and $w_{\rm c}$ denotes the (combined) weight. The standard FKP weight $w_{\rm FKP}(r)$ [27] is used to minimise the variance of the power spectrum at the BAO scale. The combined weight, $w_{\rm c}$, depends on survey characteristic corrections such as redshift failures, fiber collisions and angular systematics. The normalisation constant $I_2$ is given as

$$I_2 = \int d^3\mathbf{r} \, w_{\rm FKP}(\mathbf{r}) \, \langle n w_{\rm c}(\mathbf{r}) \rangle^2 \,. \tag{2.5}$$

The function defined in eq. (2.4) is used to build the power spectrum multipoles; for a varying line of sight (LOS), chosen towards one of the galaxies of each pair we follow the Yamamoto approximation to define the power spectrum estimator

$$P^{(\ell)}_{\rm meas}(k) = \frac{(2\ell+1)}{2} \int \frac{d\Omega}{4\pi} \left[ \int d\mathbf{r}_1 \, F(\mathbf{r}_1) e^{i\mathbf{k}\cdot\mathbf{r}_1} \int d\mathbf{r}_2 \, F(\mathbf{r}_2) e^{-i\mathbf{k}\cdot\mathbf{r}_2} \mathcal{L}_\ell(\hat{\mathbf{k}}\cdot\hat{\mathbf{r}}_2) \right] - P^{(\ell)}_{\rm sn} \,, \tag{2.6}$$

where $\mathcal{L}_\ell(x)$ is the Legendre Polynomial of order $\ell$ and $P^{(\ell)}_{\rm sn}$ is the Poisson shot noise term. Higher order multipoles $\ell > 0$ quantify the anisotropic clustering with respect to the LOS. There are two main sources for such an anisotropy, the AP effect and RSD.



JCAP09(2020)052

**Alcock-Paczynski effect and scaling parameters.** The deviation of the reference cosmology ($\mathbf{\Omega}^{\rm ref}$) from the underlying cosmology ($\mathbf{\Omega}$) leads to an anisotropic clustering signal known as Alcock-Paczynski effect [18]. This and the variation of the acoustic scale with respect to the fiducial template are usually accounted through scaling the wave-vector across ($\perp$) and along ($\parallel$) the LOS:

$$k_\perp \longrightarrow \widetilde{k}_\perp = k_\perp/\alpha_\perp\,, \quad k_\parallel \longrightarrow \widetilde{k}_\parallel = k_\parallel/\alpha_\parallel\,, \tag{2.7}$$

where the scaling parameters are defined as

$$\alpha_\perp(z_*) = \frac{D_M(z_*)\, r_{\rm d}^{\rm ref}}{D_M^{\rm ref}(z_*)\, r_{\rm d}}\,, \qquad \alpha_\parallel(z_*) = \frac{H^{\rm ref}(z_*)\, r_{\rm d}^{\rm ref}}{H(z_*)\, r_{\rm d}}\,, \tag{2.8}$$

where $r_{\rm d}$ is the sound horizon at radiation drag. Here, we introduced $D_M$ and $D_M^{\rm ref}$ as shorthand notation for $D_M(\mathbf{\Omega})$ and $D_M(\mathbf{\Omega}^{\rm ref})$ (and same for the Hubble distance $c/H$ and $r_{\rm d}$). The argument $z_*$ is the effective redshift of the galaxy sample in a given redshift bin. The ratios between the underlying and reference distances perpendicular ($D_M$) and parallel ($1/H$) with respect to the LOS scale the reference mapping from redshifts to distances towards the"correct" one. The ratio of $r_{\rm d}$ to $r_{\rm d}^{\rm ref}$ accounts for the different BAO peak position in the reference power spectrum template with respect to the one in the measured power spectrum.

**Redshift-space distortions and reconstruction.** Driven by dark matter over-densities, peculiar velocities of galaxies induce redshift-space distortions in galaxy clustering. The measured redshift of a galaxy comes from a superposition of its Hubble flow recession velocity $\mathbf{v}_{\rm r}$ and its peculiar velocity $\mathbf{v}_{\rm p}$. Hence, the measured redshift-space position $\mathbf{r}$ (found by transforming the observed galaxy redshift to a distance using the reference cosmology) is displaced from the real-space position $\mathbf{x}$ by its peculiar velocity projected on the LOS ($\mathbf{v}_{\rm p}\cdot\hat{\mathbf{x}}$), where $\hat{\mathbf{x}}$ is the unit vector in LOS direction. In general, the mapping from $\mathbf{x}$ to $\mathbf{r}$ is given by

$$\mathbf{r}(\mathbf{x}) = \mathbf{x} + \frac{(\mathbf{v}_{\rm p}(\mathbf{x})\cdot\hat{\mathbf{x}})\hat{\mathbf{x}}}{aH(a)} \tag{2.9}$$

with scale factor $a$. In the framework of Lagrangian perturbation theory the real-space (Eulerian) position $\mathbf{x}$ of a particle is written as the sum of its initial (Lagrangian) position $\mathbf{q}$ and a displacement vector $\mathbf{\Psi}$

$$\mathbf{x}(\mathbf{q},t) = \mathbf{q} + \mathbf{\Psi}(\mathbf{q},t)\,. \tag{2.10}$$

At first order, the peculiar velocity field is related to the Lagrangian displacement field by

$$\mathbf{v}_{\rm p}(\mathbf{x}(\mathbf{q},t)) = aHf\mathbf{\Psi}(\mathbf{q},t)\,, \tag{2.11}$$

where

$$f \equiv \frac{d\ln D(a)}{d\ln a} = (\Omega_{\rm m}(a))^\gamma \tag{2.12}$$

is the logarithmic growth rate, which depends on the scale-independent linear growth factor $D(a)$, and can be expressed as function of the matter density corresponding to a scale factor $a$ and the growth rate exponent $\gamma$, which for general relativity and $w=-1$ is $\gamma = 0.55$ to a very good approximation [28]. Combining eqs. (2.9), (2.10) and (2.11), and using the fact that $\hat{\mathbf{x}} = \hat{\mathbf{r}}$ yields

$$\mathbf{q}(\mathbf{r}) = \mathbf{r} - \mathbf{\Psi} - f(\mathbf{\Psi}\cdot\hat{\mathbf{r}})\hat{\mathbf{r}}\,. \tag{2.13}$$



JCAP09(2020)052

Using this equation together with the fact that the number of galaxies is conserved when transforming between real and redshift space, the displacement field is related to the smoothed redshift-space galaxy over-density field $\delta_g^{\rm red}$ as [29]

$$\nabla \cdot \mathbf{\Psi} + \frac{f}{b} \nabla(\mathbf{\Psi} \cdot \hat{\mathbf{r}})\, \hat{\mathbf{r}} = -\frac{\delta_g^{\rm red}}{b}\,, \tag{2.14}$$

where $b$ is the scale independent linear galaxy bias relating matter and galaxy over-densities, $\delta_m = b\delta_g$. This is at the basis of the so-called density-field reconstruction procedure, whereby eq. (2.14) is used to estimate the displacement field $\mathbf{\Psi}$ given $\delta_g^{\rm red}$ and reference values of $b$ and $f$. Galaxies, interpreted as test particles for the velocity field, can then be moved back to their initial Lagrangian positions $\mathbf{q}$ given in eq. (2.13) removing non-linear effects, which sharpens the BAO feature and increases its detection significance (see [30], [31] and [32] for reference).

**BAO anisotropic power spectrum model.** This model is used to describe the BAO scale in the power spectrum multipoles via template fitting: a linear power spectrum $P_{\rm lin}^{\rm ref}(k)$ computed at the reference cosmology is used to build a template that is fitted to the oscillatory pattern in the data by varying the scaling factors $\{\alpha_\parallel, \alpha_\perp\}$. The reference template is divided into a smooth part $P_{\rm lin,sm}$ and an oscillating part $\mathcal{O}_{\rm lin} = P_{\rm lin}/P_{\rm lin,sm}$ in order to separate the BAO information from the broadband, which is marginalised over.

Following [33] we model the anisotropic galaxy power spectrum including the non-linear damping of the BAO with two damping scales $\Sigma_\perp, \Sigma_\parallel$ as

$$P_{\rm aniso}(k,\mu) = P_{\rm aniso,sm}(k,\mu)\left[1 + (\mathcal{O}_{\rm lin}(k) - 1)\, e^{-\frac{1}{2}\left(\mu^2 k^2 \Sigma_\parallel^2 + (1-\mu^2) k^2 \Sigma_\perp^2\right)}\right], \tag{2.15}$$

with the smooth component given by

$$P_{\rm aniso,sm}(k,\mu) = B^2 (1 + \beta\mu^2 R)^2 P_{\rm lin,sm}(k)\,, \tag{2.16}$$

where $B$ is a free amplitude parameter and $\beta$ is a nuisance parameter effectively accounting for linear RSD and galaxy bias. We use the factor $R = 1$ before density-field reconstruction and $R = 1 - \exp\left(-k^2\Sigma_{\rm sm}^2/2\right)$ after reconstruction with smoothing scale $\Sigma_{\rm sm}$ as in [33] and [34]. The coordinates used here are defined as

$$k = |\mathbf{k}|\,, \quad \mu = \frac{\mathbf{k}\cdot\mathbf{r}}{kr} \tag{2.17}$$

where $\mathbf{k}$ is the Fourier mode and $\mu$ is the cosine of the angle between the Fourier mode and the LOS distance vector $\mathbf{r}$. The components of $\mathbf{k}$ across and along the LOS can be expressed as

$$k_\perp = k\sqrt{1-\mu^2}\,, \quad k_\parallel = \mu k\,. \tag{2.18}$$

To include the AP effect, we rescale the wave-vector components as in eq. (2.7) to scale the observed modes from the reference cosmology to the underlying cosmology. Combining eqs. (2.7) and (2.17) we find the transformation

$$k \longrightarrow \widetilde{k} = \frac{k}{\alpha_\perp}\left[1 + \mu^2\left(\frac{\alpha_\perp^2}{\alpha_\parallel^2} - 1\right)\right]^{1/2}, \quad \mu \longrightarrow \widetilde{\mu} = \mu\frac{\alpha_\perp}{\alpha_\parallel}\left[1 + \mu^2\left(\frac{\alpha_\perp^2}{\alpha_\parallel^2} - 1\right)\right]^{-1/2}. \tag{2.19}$$



JCAP09(2020)052

We write the anisotropic power spectrum as a function of the transformed parameters $(\widetilde{k}, \widetilde{\mu})$ and obtain its multipoles using angle-dependent Legendre polynomials. Also, we add a polynomial expansion in terms of $k$ accounting for nonlinear broadband effects and potential differences between the underlying broadband and the template, that have not been included in the modeling so far:

$$P_{\rm aniso}^{(\ell)}(k) = \left(\frac{r_{\rm d}^{\rm ref}}{r_{\rm d}}\right)^3 \frac{(2\ell+1)}{2\alpha_\perp^2\alpha_\parallel} \int_{-1}^{1} P_{\rm aniso}(\widetilde{k}(k,\mu),\widetilde{\mu}(\mu))\mathcal{L}_\ell(\mu)\, d\mu + \sum_{i=1}^{N_i} A_i^{(\ell)} k^{2-i}\,. \tag{2.20}$$

The extra normalisation factor in front of the integral accounts for the isotropic dilation induced by the change in volume between reference and modelled cosmology. The ratio between the sound horizons is reabsorbed into the overall amplitude parameter $B$. This means that the model consists of the physical parameters $\{\alpha_\parallel, \alpha_\perp\}$ and the nuisance parameters $\{\beta, B_j, A_{i,j}^{(\ell)}\}$ fitted to each redshift bin. The total number of nuisance parameters depends on the order of the polynomial expansion and the number of disconnected patches indexed by $j$ of the sky observed. The dispersion scales $\Sigma_\parallel$ and $\Sigma_\perp$ can either be varied and marginalised over, inferred from theoretical approaches or fitted to mock survey catalogs and then fixed in the data analysis. In this paper we follow the latter approach.

**Full shape power spectrum model.** While the BAO anisotropic model is tuned towards detecting the BAO pattern only, the full shape model also extracts information from the broadband and is not only sensitive to BAO, but to RSD and non-linear structure formation, too. Again, we use a template-fitting procedure, but instead of the linear matter power spectrum we use the 2-loop renormalisation perturbation theory extension described in [35] to compute the auto- and cross- density and velocity potential power spectra $P_{\delta\delta}$, $P_{\delta\theta}$ and $P_{\theta\theta}$ of the matter field. To go from the matter to the galaxy field we need to assume a galaxy bias model. Here, we use the model proposed by [36], consisting of four bias parameters $\{b_1, b_2, b_{s^2}, b_{3_{\rm nl}}\}$. The linear galaxy bias $b_1$ and the non-linear galaxy bias $b_2$ are treated as free nuisance parameters, while the other two are functions of $b_1$, given in [37] and [38]. We adopt the exact expressions from appendix B of [39] for the galaxy density-density, density-velocity potential and velocity potential-velocity potential power spectra given as

$$\begin{aligned}
P_{g,\delta\delta}(k) &= b_1^2 P_{m,\delta\delta}(k) + 2b_2 b_1 P_{m,b2\delta}(k) + 2b_{s2} b_1 P_{bs2,\delta}(k) + b_2^2 P_{m,b22}(k) + \\
&\quad 2b_2 b_{s2} P_{m,b2s2}(k) + b_{s2}^2 P_{bs22}(k) + 2b_1 b_{3nl}\sigma_3^2(k) P_{\rm lin}(k) \\
P_{g,\delta\theta}(k) &= b_1 P_{m,\delta\theta}(k) + b_2 P_{m,b2\theta}(k) + b_{s2} P_{m,bs2\theta}(k) + b_{3nl}\sigma_3^2(k) P_{\rm m,lin}(k) \\
P_{g,\theta\theta}(k) &= P_{\theta\theta}\,.
\end{aligned} \tag{2.21}$$

To include the effect of RSD explained in paragraph Redshift-space distortions and reconstruction we follow the approach of [40] writing the full shape power spectrum as

$$\begin{aligned}
P_{\rm FS}(k,\mu) = e^{-\frac{1}{2}[k\mu\sigma_P]^2} \big[\, & P_{g,\delta\delta}(k) + 2f\mu^2 P_{g,\delta\theta}(k) + f^2\mu^4 P_{g,\theta\theta}(k) + \\
& b_1^3 A^{\rm TNS}(k,\mu,f/b_1) + b_1^4 B^{\rm TNS}(k,\mu,f/b_1)\big]\,,
\end{aligned} \tag{2.22}$$

where the functions $A^{\rm TNS}$ and $B^{\rm TNS}$ are defined in [40]. The exponential damping term for scales smaller than $\sigma_P$ accounts for the so-called Fingers-of-God (FoG) effect [20]. This effect appears at small scales, where highly non-linear velocities smear out the density field in redshift space, such that the structures appear elongated along the line of sight and the



JCAP09(2020)052

power spectrum is damped. Finally, the full shape power spectrum multipoles are given as in eq. (2.20) but without the polynomial term

$$P_{\rm FS}^{(\ell)}(k) = \frac{(2\ell+1)}{2\alpha_\perp^2\alpha_\parallel}\int_{-1}^{1} P_{\rm FS}(\widetilde{k}(k,\mu),\widetilde{\mu}(\mu))\mathcal{L}_\ell(\mu)\,d\mu\,. \tag{2.23}$$

The AP effect is included via the same transformation as in eq. (2.19). This means that there are in total 3 cosmological parameters $\{\alpha_\parallel, \alpha_\perp, f\sigma_8\}$ per redshift bin and 4 nuisance parameters $\{b_1, b_2, \sigma_P, A_{\rm noise}\}$ per redshift bin and per observed patch of the sky. The last nuisance parameter $A_{\rm noise}$ is used to model deviations from Poissonian shot noise in the monopole. Note that we measure the growth rate $f$ for a fixed value of $\sigma_8$ of the template. This is why we are only sensitive to the product $f\sigma_8$, which is a template-independent quantity in the wave-vector range of interest (e.g. up to $k = 0.2\ h\,{\rm Mpc}^{-1}$, see [41] for reference).

**The survey geometry.** In order to compare the model power spectra to the data, we need to take into account the selection function of the survey. This can be achieved by convolving the model power spectrum $P_{\rm model}(\mathbf{k})$ with the survey window function $W(\mathbf{k})$ to obtain the "windowed" power spectrum $P_{\rm win,model}(\mathbf{k})$

$$P_{\rm win,model}(\mathbf{k}) = \int \frac{{\rm d}\mathbf{k}'}{(2\pi)^3}\,P_{\rm model}(\mathbf{k}')\,|W(\mathbf{k}-\mathbf{k}')|^2\,. \tag{2.24}$$

To avoid the computation of the expensive 3-dimensional Fourier transform, we follow the framework of [42] extended by [43] where the window function is obtained as a pair count in configuration space. This is more efficient, because the convolution in Fourier space becomes a multiplication in configuration space. The "windowed" power spectrum multipoles are then the 1-dimensional Hankel transform of the "windowed" correlation function multipoles.

The effects of this transformation of the model power spectrum are purely observational, hence it is not particularly interesting for blinding. But, we have to accept, we can only observe the galaxy density fluctuation through a window, which is why this is an important ingredient in BAO and RSD analyses.

## 3 Blinding scheme

### 3.1 General considerations

In this section we introduce the general idea of our blinding scheme and we derive analytic formulae describing its effects. Without introducing blinding, the standard procedure for BAO and RSD analyses is as follows. The galaxy catalog, in terms of angular positions, redshifts and weights, forms the raw data $\mathbf{d}$, the redshifts of which are transformed into distances using a reference cosmology. Subsequently, the power spectrum of this galaxy distribution is measured. Afterwards, a template for the power spectrum is computed at the same reference cosmology to build the models described in section 2. Finally, the model parameters that distort the template and are constrained with the data are

$$\mathbf{\Theta}(\mathbf{d},\mathbf{\Omega}^{\rm ref}) = \{\alpha_\parallel(z_{*1}),\ldots,\alpha_\parallel(z_{*n}),\ \alpha_\perp(z_{*1}),\ldots,\alpha_\perp(z_{*n}),\ f\sigma_8(z_{*1}),\ldots,f\sigma_8(z_{*n_{\rm bins}})\}\,, \tag{3.1}$$

where $n_{\rm bins}$ is the number of tomographic redshift bins analysed and $z_{*,i}$ denotes the effective redshift of each of them. These are *physical parameters* (two scaling parameters and one



JCAP09(2020)052

growth rate) which capture where the bulk of cosmological information is contained in the data and can be interpreted in a transparent and largely model-independent way. These parameters can also be easily interpreted and modelled within the adopted theory and/or specific cosmological model.

Next, the constraints on the physical parameters $\boldsymbol{\Theta}$ are used to infer the underlying cosmological model $\boldsymbol{\Omega}$, which is robust to the choice of reference cosmology (especially for BAO-only analyses, see e.g., [44, 45]), it only depends on the data:

$$\boldsymbol{\Omega} = \boldsymbol{\Omega}(\boldsymbol{\Theta}(\mathbf{d}, \boldsymbol{\Omega}^{\rm ref})) = \boldsymbol{\Omega}(\mathbf{d})\,. \tag{3.2}$$

In the standard approach to BAO and RSD the derivation of $\boldsymbol{\Theta}$ can be seen as a necessary intermediate step to compress and extract the signal. This makes possible to connect, via a model-independent set of physical parameters, the galaxy catalog to one (or several) cosmological models in a transparent way.

Since a change in the physical parameters has a very direct and transparent effect on the commonly used summary statistics (e.g., power spectra), it is much easier to understand the effect of the proposed blinding procedure, by working with these parameters.

For the purpose of blinding we aim to find a transformation of the raw data

$$\mathbf{d} \to \mathbf{d}' = \mathbf{d} + \Delta\mathbf{d}\,(\mathbf{d}, \boldsymbol{\Omega}, \boldsymbol{\Omega}') \tag{3.3}$$

fulfilling the condition that the modified raw data $\mathbf{d}'$ represents a Universe whose cosmological model is $\boldsymbol{\Omega}'$. $\boldsymbol{\Omega}'$ is the target blind cosmology, that we aim for. In what follows we will denote all quantities related to the blinded catalog with a prime in contrast to quantities referring to the original catalog, which are written without superscript. However, it is impossible to find an exact expression for $\Delta\mathbf{d}\,(\mathbf{d}, \boldsymbol{\Omega}, \boldsymbol{\Omega}')$, as by definition we are *blind* towards $\boldsymbol{\Omega}$. Hence, in the following we use the reference cosmology $\boldsymbol{\Omega}^{\rm ref}$ presented in section 2 as a starting point and introduce a shifted cosmology $\boldsymbol{\Omega}^{\rm shift}$ which depends on the same parameter set, but allowing for a variation $\Delta\boldsymbol{\Omega}$ with respect to the reference:

$$\boldsymbol{\Omega}^{\rm shift} = \boldsymbol{\Omega}^{\rm ref} + \Delta\boldsymbol{\Omega}\,, \tag{3.4}$$

with

$$\Delta\boldsymbol{\Omega} = \{\Delta\Omega_{\rm m}, \Delta\Omega_{\rm b}, \Delta H_0, \Delta\sigma_8, \Delta n_s, \Delta M_\nu, \Delta w, \Delta\gamma\}\,. \tag{3.5}$$

Then we can write eq. (3.3) in terms of the reference and shifted cosmologies:

$$\mathbf{d} \to \mathbf{d}' = \mathbf{d} + \Delta\mathbf{d}\,(\mathbf{d}, \boldsymbol{\Omega}^{\rm ref}, \boldsymbol{\Omega}^{\rm shift})\,. \tag{3.6}$$

Note that the shifted cosmology is just a tool to generate the perturbation in the data, so that the results of the analysis correspond to $\boldsymbol{\Omega}'$ instead of $\boldsymbol{\Omega}$. Finally, using $\boldsymbol{\Omega}^{\rm ref}$ and $\boldsymbol{\Omega}^{\rm shift}$, we aim to find a relation between $\boldsymbol{\Theta}'$ and $\boldsymbol{\Theta}$.

Here, we propose to shift the position $\mathbf{r}_i$ of galaxies along the LOS in a redshift- and density-dependent way. We avoid changing the angular positions because in current spectroscopic survey strategies target galaxies are selected based on the photometric surveys. Therefore, perturbing angular positions might add unnecessary complications into e.g. fiber collision corrections and other angular systematics. Hence, we only shift the individual galaxy redshifts, so we can express eq. (3.6) as

$$z_i' = z_i + \Delta z_i(z_i, \rho(\mathbf{r_i}), \boldsymbol{\Omega}^{\rm ref}, \boldsymbol{\Omega}^{\rm shift})\,, \tag{3.7}$$



JCAP09(2020)052

where $\rho(\mathbf{r_i})$ denotes the galaxy density in the position of the $i$-th galaxy. From the parameter basis given in eq. (2.1) here we choose to blind only for parameters that govern the late-time evolution of the Universe, such that eq. (3.5) becomes

$$\Delta\boldsymbol{\Omega} = \{\Delta\Omega_{\rm m},\, 0,\, 0,\, 0,\, 0,\, 0,\, \Delta w,\, \Delta\gamma\}\,. \tag{3.8}$$

Here, we choose not to blind for $H_0$, as its value is absorbed into the unit via the factor $h$. Therefore it has no impact on the galaxy catalog, only on the power spectrum template. More general blinding, including the effects of other parameters such as $H_0$, $\sigma_8$, $M_\nu$ and $f_{\rm nl}$, will be presented in a follow up paper [46].

The blinding scheme consists of two types of shifts to galaxies' redshifts:

- A homogeneous shift according to a modified redshift-distance relation (see section 3.2). It induces an anisotropy between radial and angular distances equivalent to the AP effect and blinds the cosmological background evolution. We refer to it as AP-like shift, $\Delta^{\rm AP}z$.
- A shift based on the gradient of the reconstructed galaxy density field along the LOS (see section 3.3). This perturbative shift is designed to imitate RSD and blind the growth of structures, hence we refer to it as RSD-shift, $\Delta^{\rm RSD}z$.

In summary $\Delta z_i$ of eq. (3.7) is given by the combination of $\Delta^{\rm AP}z_i$ and $\Delta^{\rm RSD}z_i$. In the following subsections we describe both shifts in more detail and discuss their effect on the physical parameters:

$$\boldsymbol{\Theta} \rightarrow\ \boldsymbol{\Theta}' = \boldsymbol{\Theta}(\mathbf{d}', \boldsymbol{\Omega}^{\rm ref}, \boldsymbol{\Omega}^{\rm shift}) \tag{3.9}$$

### 3.2 AP-like shift

We set off to find the redshift dependence of $\Delta z_i$ in eq. (3.7), such that it mimics the background expansion of a cosmology different from both the reference and the underlying ones. In practice, this affects the distances inferred from redshifts using the reference cosmologies, which affects to the measured clustering at all scales modifying the $\alpha_\parallel$ and $\alpha_\perp$ values.

The shift is obtained by converting the observed redshifts $z_i$ into comoving distances $D_{\rm M}(z_i, \boldsymbol{\Omega}^{\rm shift})$ using the shifted cosmology and inverting them back to blinded redshifts $z_i'$ using the reference cosmology as shown in the following sketch:[5]

$$z_i\,(\boldsymbol{\Omega}) \xrightarrow{\boldsymbol{\Omega}^{\rm shift}} D_{\rm M}(z_i, \boldsymbol{\Omega}^{\rm shift}) = D_{\rm M}(z_i', \boldsymbol{\Omega}^{\rm ref}) \xrightarrow{\boldsymbol{\Omega}^{\rm ref}} z_i'\,(\boldsymbol{\Omega}')\,. \tag{3.10}$$

In this way we can derive the shift numerically using

$$\Delta^{\rm AP}z(z_i, \boldsymbol{\Omega}^{\rm ref}, \boldsymbol{\Omega}^{\rm shift}) = z_i'(\boldsymbol{\Omega}') - z_i(\boldsymbol{\Omega}), \tag{3.11}$$

as illustrated in figure 2. This equation yields one of the two contributions to the $\Delta z$ to be applied in eq. (3.7). The blinded redshifts $z_i'$ appear to originate from a blinded or "fake" cosmology $\boldsymbol{\Omega}'$. Any geometric measurement of the background expansion is affected by this shift. Although only the radial dimension is affected, and not angles between objects, any measurement of a transversal distance on a patch of the sky will also be affected, because the distance to the objects is changed by the shift.

[5] The $z_i$ are observed redshifts so they do not have an explicit dependence on the parameters $\boldsymbol{\Omega}$, which are unknown and we can't change. However, in eq. (3.10) we leave the $\boldsymbol{\Omega}$ dependence in the argument of $z_i$ to stress that the observed redshifts are drawn from an (unknown) model parameterised by the (unknown) values of the model parameters.



JCAP09(2020)052

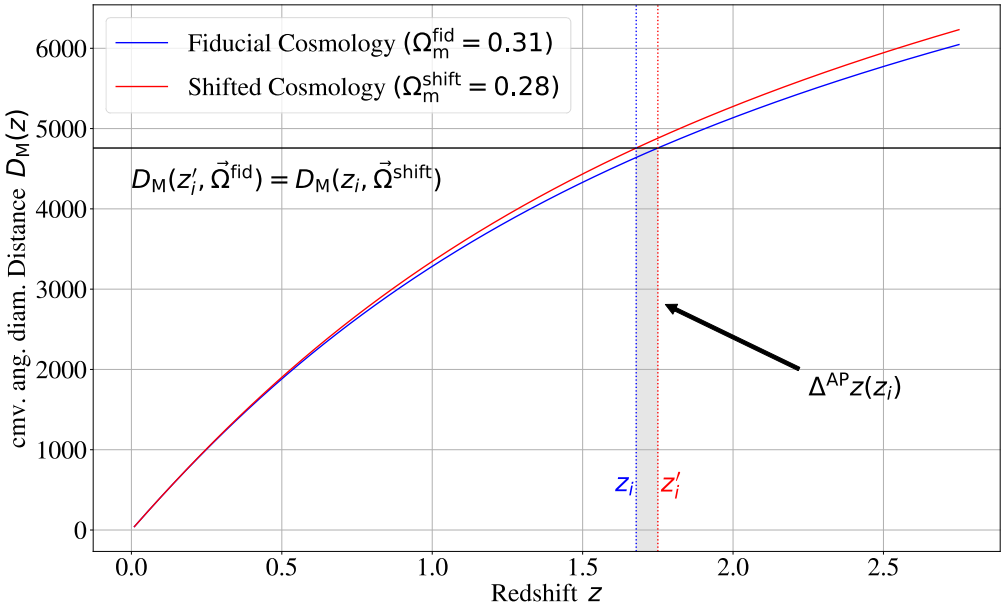


**Figure 2**. AP-like shift ingredient: determination of the shift $\Delta^{AP}z_i(z_i)$ (eq. (3.11)). In this illustration the shifted distance is obtained by a 10% decrease of the matter density $\Omega_m$. The blue line is the comoving angular diameter distance for the reference cosmology, the red line is the same quantity for a shifted cosmology where only the matter density parameter has been changed. The black horizontal line visualises where $D_M(z_i, \mathbf{\Omega}^{shift}) = D_M(z_i', \mathbf{\Omega}^{ref})$. See text for more details.

After shifting all galaxies individually, the effective redshift of a given galaxy sample, $z_*$, changes in a way that in general depends on the details of its initial redshift distribution $\bar{n}(z)$. For simplicity, we only consider the following two cases:

- *Shifted redshift cuts* (or fixed distance cuts): the redshift range of the blinded sample is changed according to the blinding scheme so that the selection of galaxies remains the same for the pre- and post-blinded catalog. As a consequence, we expect the effective redshift to be shifted according to

$$z_*' = z_* + \Delta z(z_*, \mathbf{\Omega}^{ref}, \mathbf{\Omega}^{shift}) \,. \tag{3.12}$$

- *Fixed redshift cuts* (or shifted distance cuts): the same redshift cuts are applied to the post-blinded catalog as to the pre-blinded one. In this way the effective redshifts of both catalogs remain nearly the same, because approximately as many galaxies enter the redshift bin of the sample as they leave it after blinding. This is only possible if the redshift cuts lay in regions where the galaxy density is comparable to the mean density $\bar{n}$. In this case we expect

$$z_*' \simeq z_* \,. \tag{3.13}$$

We anticipate that we test the validity of eqs. (3.12) and (3.13) in section 4.3, where we also motivate our recommendation to use shifted redshift cuts whenever possible.



JCAP09(2020)052

We can now derive an expression for the scaling parameters $\alpha'_\parallel$ and $\alpha'_\perp$ that would be measured from the blinded catalog. In general they can be written as:

$$\alpha'_\perp(z'_*) \equiv \frac{D'_M(z'_*)\, r_{\rm d}^{\rm ref}}{D_M^{\rm ref}(z'_*)\, r'_{\rm d}}\,, \qquad \alpha'_\parallel(z'_*) \equiv \frac{H^{\rm ref}(z'_*)\, r_{\rm d}^{\rm ref}}{H'(z'_*)\, r'_{\rm d}}\,, \tag{3.14}$$

but we need to express them as a function of $\mathbf{\Omega}^{\rm ref}$, $\mathbf{\Omega}^{\rm shift}$ and $\mathbf{\Omega}$. Since our blinding scheme does not change the early-time physics, the sound horizon at the baryon drag epoch is not affected by the blinding, therefore

$$r'_{\rm d} = r_{\rm d}\,. \tag{3.15}$$

Because the distances in eq. (3.14) were computed with the shifted cosmology, $\alpha'$ will depend on $D^{\rm shift}$. But in the blind analysis we assume they were obtained with the reference cosmology and use a power spectrum template computed from the reference cosmology. Hence, the perpendicular and parallel components $\alpha'_\perp$ and $\alpha'_\parallel$ are

$$\alpha'_\perp(z'_*) = \frac{D_M(z_*) r_{\rm d}^{\rm ref}}{D_M^{\rm shift}(z_*) r_{\rm d}}\,, \qquad \alpha'_\parallel(z'_*) = \frac{H^{\rm shift}(z_*)\, r_{\rm d}^{\rm ref}}{H(z_*)\, r_{\rm d}}\,. \tag{3.16}$$

Finally, the ratios of the scaling parameters we would measure from the blinded catalog with respect to the unblinded catalog can be obtained by combining eqs. (2.8) and (3.16)

$$\frac{\alpha'_\perp(z'_*)}{\alpha_\perp(z_*)} = \frac{D_M^{\rm ref}(z_*)}{D_M^{\rm shift}(z_*)}, \qquad \frac{\alpha'_\parallel(z'_*)}{\alpha_\parallel(z_*)} = \frac{H^{\rm shift}(z_*)}{H^{\rm ref}(z_*)}\,. \tag{3.17}$$

This final result eq. (3.17) is valid for both the fixed effective redshift from eq. (3.13) and the shifted effective redshift from eq. (3.12). The interpretation of the scaling parameters however is different in the two cases because $z'_*$ is different. In the case of shifted redshift cuts, the comoving distance measured from the blinded catalog is equal to the unblinded measurement, but interpreted at different redshift. If the measurements are applied to samples with the same effective redshifts, the blinded distance can be obtained from the underlying distance by multiplying it by the correction factor $\alpha'/\alpha$.

### 3.3 RSD-shift

Here we propose to use a similar machinery as the density-field reconstruction procedure to blind the catalog for the growth rate.[6] First of all, we use the reference cosmology to transform individual redshifts into distances to obtain the original redshift-space position $\mathbf{r}$ for each galaxy. Given that we do not know the underlying values of the galaxy bias and the growth rate in eq. (2.14) *a priori*, we choose reference values $b = b^{\rm ref}$ and $f = f^{\rm ref}$. Moreover, we need to adopt a method in order to obtain the smoothed density field. Here we choose to apply a gaussian filter with radius $R_{\rm sm}$ to the discrete galaxy field. With the reference values and smoothing scale as input, we solve eq. (2.14) iteratively in Fourier space, using the reconstruction code developed in ref. [47]. At this point, we diverge from the standard reconstruction procedure and use the estimated displacement field to add a RSD component that mimics a different growth rate $f^{\rm shift}$. In this way we transform the original redshift-space position $\mathbf{r}$ to the blinded redshift-space position $\mathbf{r}'$:

$$\mathbf{r}' = \mathbf{r} - f^{\rm ref}(\mathbf{\Psi}\cdot\hat{\mathbf{r}})\hat{\mathbf{r}} + f^{\rm shift}(\mathbf{\Psi}\cdot\hat{\mathbf{r}})\hat{\mathbf{r}}\,. \tag{3.18}$$

[6] Our numerical implementation is based on the reconstruction code used for eBOSS analysis, which is publicly available at https://github.com/julianbautista/eboss_clustering.



JCAP09(2020)052

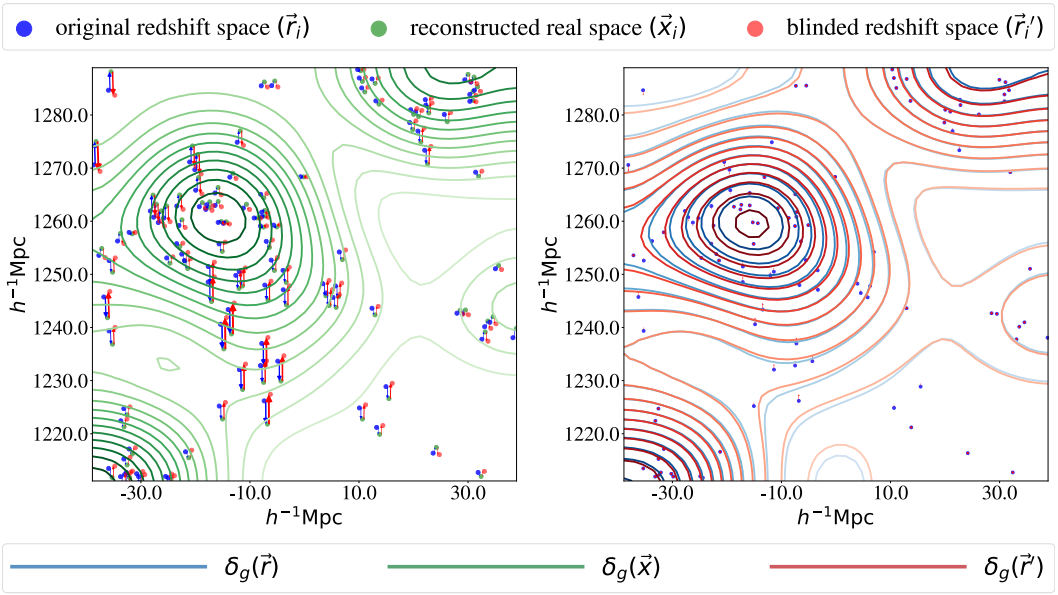


**Figure 3**. The two panels show the same slice with sidelength 77 $h^{-1}$ Mpc and depth 50 $h^{-1}$ Mpc of an original and blinded realisation of the CMASS North MD-Patchy mocks (see section 4.1 for more information). The observer is located at position $(0, 0)$, which is more than 1200 $h^{-1}$ Mpc distant from the slice shown here. We compare the blinded and the original galaxies in two different ways. Left panel: the green contours correspond to the solution of the real-space over-density field smoothed with a gaussian filter of radius $R_{\rm sm} = 10\ h^{-1}$ Mpc obtained with the iterative Fourier Space procedure. It is used to displace original galaxy positions (blue dots) along the line of sight (blue arrows) towards their reconstructed real-space positions (green dots) using the reference growth rate $f^{\rm ref} = 0.78$. From there, the galaxies are displaced back (red arrows) towards their blinded positions (red dots) using a different growth rate $f^{\rm shift} = 1.0$. To make the effect more visible the red and blue dots are slightly displaced horizontally. Right panel: the same slice, but here we show only the net displacement from the original positions (blue dots) towards the blinded positions (red arrows). Also shown are the original redshift-space over-density field (blue contours) and the blinded one (red contours). For illustrative purposes the shift considered is rather extreme, so the "squeezing" effect along the LOS can be appreciated "by eye".

Once we have obtained the blinded redshift-space position, we can obtain the blinded redshifts $z'$ using again the reference cosmology. Contrarily to $\Delta^{\rm AP} z$, the RSD-shifts are different for each galaxy, because they depend on the local matter density. Taking this into account, the RSD-shift for the $p$-th galaxy is $\Delta^{\rm RSD} z_p = z'_p - z_p$.

This procedure is equivalent to substitute redshift-space distortions from the underlying cosmology by those of the blinded. Hence, we expect the growth-rate measured from the blinded catalog $f'$ to differ from the underlying value $f$ by the difference between the reference and the shifted growth rates, so we write the *ansatz*

$$f' = f + f^{\rm shift} - f^{\rm\ ref}\,. \tag{3.19}$$

We test the validity of eq. (3.19) in section 4.4. The different steps of this procedure are visualised in the left panel of figure 3. Based on the pseudo-real-space displacement



JCAP09(2020)052

field $\Psi$ computed iteratively with $f^{\text{ref}}$, galaxies are shifted towards their (pseudo-)real-space position (blue arrows) and shifted back using the same displacement field, but $f^{\text{shift}}$ instead. For illustrative purposes, in this figure we show a rather extreme case ($f^{\text{ref}} = 0.78$, $f^{\text{shift}} = 1.0$) where $f^{\text{shift}}$ differs from $f^{\text{ref}}$ by $\sim 25\%$. Note that the shift is designed to be reversible: the blinded and original catalog would be exactly the same if $f^{\text{ref}} = f^{\text{shift}}$, which is also evident from eq. (3.19). The right panel shows the difference between the galaxy over-density fields of the blinded and the original catalog. Although we show a rather extreme case, the net squeezing of the central over-density along the $y$- direction can only be seen in nuances by eye.

For surveys being split in several redshift bins (or covering different galaxy samples which span different redshift ranges), the above procedure should be applied to each redshift bin of the survey. Hence, for each bin, different values for the input parameters ($b^{\text{ref}}, f^{\text{ref}}$) as well as the shifted growth rate $f^{\text{shift}}$ need to be chosen. It is possible to treat each bin independently, such that the overall growth history among samples cannot be modelled before unblinding. However, a more useful approach in practice is to blind coherently among samples by choosing a reasonable parameterisation of the redshift evolution of the growth rate as for example eq. (2.12).

## 4 Test on mocks

Having described the theory of our blinding scheme, we now validate it on the (mock) galaxy catalogs from BOSS. Their detailed specifications are described in section 4.1. We apply the individual blinding shifts $\Delta^{\text{AP}} z_i$, $\Delta^{\text{RSD}} z_i$ and their combination on the mock galaxy catalogs. We treat each of the blinded mock catalogs as if it were an actual blinded measurement and run the analysis pipeline described in section 2 with a fiducial configuration specified in section 4.2. Finally, we quantify the performance of the studied blinding schemes by comparing the physical parameters measured from the blinded catalog with their theoretical expectation given by eqs. (3.17) and (3.19).

Note that throughout this paper we work in Fourier space and do not extend our analysis to configuration space for simplicity. This is, because a correlation function analysis basically relies on the same information content as a power spectrum analysis and our blinding scheme affects both analysis types in the same way. We leave a detailed comparison of the blinding performance for different estimators for future work.

### 4.1 Original and blinded mock catalogs

Mock galaxy catalogs play an essential role in interpreting cosmological data. They are calibrated on N-body simulations at a given cosmological model and correspond to independent realisations of the galaxy distribution as observed by the galaxy survey. We use the MultiDark-Patchy BOSS DR12 (MD-Patchy) mocks provided by [48] and [49] which include a low redshift sample LOWZ ($z_* = 0.33$) with roughly 350,000 galaxies and a higher redshift sample CMASS ($z_* = 0.60$) with roughly 800,000 galaxies.[7] The cosmological parameters used to generate the initial conditions of the mocks, as well as the reference cosmology adopted to analyse the original and the blinded catalogs, are given in table 1. Note a difference of 0.1% on $r_{\text{d}}$ values predicted by these two cosmology models. This shift in the BAO

[7] The effective redshifts used in this work are different from the actual BOSS samples because the redshift cuts are different.



JCAP09(2020)052

| Cosmology | $\Omega_m$ | $\Omega_b h^2$ | $h$ | $\sigma_8$ | $n_s$ | $M_\nu$ [eV] | $r_\mathrm{d}$ [Mpc] |
|---|---|---|---|---|---|---|---|
| Reference | 0.31 | 0.022 | 0.676 | 0.8288 | 0.9611 | 0.06 | 147.78 |
| MD-Patchy | 0.307115 | 0.02214 | 0.6777 | 0.8288 | 0.9611 | 0 | 147.66 |

**Table 1**. Values of cosmological parameters and sound horizon at radiation drag for the reference and the MD-Patchy mocks cosmology. In both cases a flat-ΛCDM cosmology and GR are assumed, so $w = -1$ and $\gamma = 0.55$.

scale is reflected by the factor $(r_\mathrm{d}/r_\mathrm{d}^\mathrm{ref})$ in the scaling parameters, $\alpha_\parallel$ and $\alpha_\perp$, and it is not modified during the blinding procedure.

We employ the blinding scheme presented in section 3 to produce different sets of blinded catalogs. For one of the sets we only change the background evolution (AP only), for another we only apply the density-dependent shift (RSD only), and finally we combine the two (Combined). The values for the shifted physical parameters $\Omega^\mathrm{shift}$ as well as the expectation for the cosmological parameters $\mathbf{\Theta}$ at each of the two redshift bins LOWZ ($z_* = 0.33$) and CMASS ($z_* = 0.60$) are given in table 2. In addition, the parameter values of the blinded cosmology $\Omega'$, that we expect to infer from the blinded physical parameters, are also reported. Note that these cosmological parameters differ from the shifted cosmology used to generate the blinded catalog. As in our blinding scheme, the background parameters $\Omega_\mathrm{m}^\mathrm{shift}$ and $w^\mathrm{shift}$ are basically used to replace the reference cosmology, $\Omega_\mathrm{m}^\mathrm{ref}$ and $w^\mathrm{ref}$, so for those parameters we expect the deviation between $\mathbf{\Omega}'$ and $\mathbf{\Omega}^\mathrm{ref}$ to be the same as the one between $\mathbf{\Omega}^\mathrm{ref}$ and $\mathbf{\Omega}^\mathrm{shift}$, but in the opposite direction. Thus, for $\mathbf{\Omega}^\mathrm{shift} - \mathbf{\Omega}^\mathrm{ref} = \Delta\mathbf{\Omega}$ we expect $\mathbf{\Omega}' - \mathbf{\Omega}^\mathrm{ref} = -\Delta\mathbf{\Omega}$.

We apply relative shifts on $\Omega_\mathrm{m}$ and $w$ with respect to their reference values of order of 10%. We find that this corresponds approximately to $1\sigma$ deviation when fitting $w$ and $\Omega_\mathrm{m}$ to BAO LOWZ and CMASS data with a Planck prior on $\Omega_b h^2$. For the RSD-only blinding we perform a very extreme shift with $\gamma = 0$ or $f(z) = 1$ to fully exploit the capabilities of our method and to make the effect of RSD-blinding more visible. For the combined shift we choose a relatively moderate value.

In practice, the choice of how much the shifted values can deviate from the reference parameters should depend on the forecasted sensitivity of the data and probably not exceed deviations of $3\sigma$. Too large deviations can spoil the robustness of the analysis, because some of the usually made approximations, e.g. a fixed covariance matrix computed at the reference cosmology, might not hold.

### 4.2 Analysis on mocks: set up and approach

Here we present the fiducial setup of the BAO and RSD analyses. *A priori*, the blinded data should be treated as if it were the original data, or in other words, the analyses should not depend on the blinding. Therefore the methodology presented here is applied to the original and the blinded catalogs in the same way. The general procedure is already explained in section 2, but in the following we provide the numerical details.

For the conversion from redshifts to distances we always use the reference cosmology given in table 1. These cosmological parameters are also used to compute the linear matter power spectrum template with `CLASS` [26].

To estimate the original and the blinded power spectra we follow the steps explained in the paragraph Power spectrum estimator of section 2. Using the distance-redshift relation assuming the reference cosmology, we place the LOWZ and CMASS galaxies in boxes of length $L_\mathrm{box} = 2500\ h^{-1}\,\mathrm{Mpc}$ (LOWZ) and $L_\mathrm{box} = 3700\ h^{-1}\,\mathrm{Mpc}$ (CMASS) with $512^3$ grid



JCAP09(2020)052

| Cosmology/ Physical parameter at $z_*$ | | $\Omega_{\rm m}$ | $w$ | $\gamma$ | $\alpha_\parallel(z_*)$ | | $\alpha_\perp(z_*)$ | | $f(z_*)$ | |
|---|---|---|---|---|---|---|---|---|---|---|
| | | | | | 0.33 | 0.60 | 0.33 | 0.60 | 0.33 | 0.60 |
| Reference $\Omega_{\rm m}^{\rm ref}$ | | 0.31 | -1.0 | 0.55 | 1.000 | 1.001 | 0.999 | 1.000 | 0.69 | 0.78 |
| AP only | Shifted $\Omega_{\rm m}^{\rm shift}$ | 0.279 | -1.1 | 0.55 | 0.964 | 0.980 | 0.950 | 0.970 | 0.69 | 0.78 |
| | Blinded $\Omega'_{\rm m}$ | 0.341 | -0.9 | 0.55 | | | | | | |
| RSD only | Shifted $\Omega_{\rm m}^{\rm shift}$ | 0.31 | -1.0 | 0.0 | 1.002 | 1.002 | 1.003 | 1.002 | 1.0 | 1.0 |
| | Blinded $\Omega'_{\rm m}$ | 0.31 | -1.0 | 0.0 | | | | | | |
| Combined | Shifted $\Omega_{\rm m}^{\rm shift}$ | 0.279 | -1.1 | 0.825 | 0.964 | 0.980 | 0.950 | 0.970 | 0.58 | 0.70 |
| | Blinded $\Omega'_{\rm m}$ | 0.341 | -0.9 | 0.825 | | | | | | |

**Table 2**. In the first line of this table we provide the values of the reference cosmological parameters that we aim to blind for $\{\Omega_{\rm m}, w, \gamma\}$, together with the corresponding derived values $\{\alpha_\parallel, \alpha_\perp, f\}$ in each redshift bin. In the following lines the cosmological parameters and expected derived parameters are shown for each of the 3 blinding cases we investigate. The shifted cosmology is used to generate the blinded catalog, whereas the blinded cosmology is the one that we expect to measure.

cells each. We compute the multipole power spectra in Fourier space using the Yamamoto method [50, 51]. We interpolate galaxies on the grid by using the triangular-shaped-cloud scheme and obtain the monopole and quadrupole in the interval $0 < k\,[\,h\,{\rm Mpc}^{-1}] < 0.30$ for linearly binned wave vectors $k$ with $\Delta k = 0.01\ h\,{\rm Mpc}^{-1}$. For both the BAO anisotropic and the full-shape analysis we restrict our fits to $0.02 < k\,[\,h\,{\rm Mpc}^{-1}] < 0.20$.

We fit the BAO and RSD models described in paragraph BAO anisotropic power spectrum model and paragraph Full shape power spectrum model of section 2 to the original and blinded power spectra using Monte-Carlo Markov Chains (MCMCs). We use the standard Metropolis Hastings algorithm, where sequences (called chains) starting at different points sample parameter space so that the density of points sampled is proportional to the posterior. Convergence is assessed by the Gelman-Rubin criterion [52] and the stopping criterion adopted for the MCMC chains is $1 - R < 0.01$ for all parameters. For the full-shape RSD model we have 3 physical parameters and $(4N_j)$ nuisance parameters, where $N_j$ is the number of disconnected patches of the sky observed. For the BAO anisotropic model we have 2 physical parameters and $[1 + (1 + N_i N_\ell) N_j]$ nuisance parameters per redshift bin, where $N_\ell$ is the number of multipoles and $N_i$ the number of coefficients in the broadband polynomial. Regarding the dispersion scales $\Sigma_\parallel$ and $\Sigma_\perp$ of eq. (2.15), we fit the mean of 1000 mock catalog power spectra and find

$$\begin{aligned} \Sigma_\parallel^{\rm LOWZ} &= 13.85\ h^{-1}\,{\rm Mpc}\,, & \Sigma_\perp^{\rm LOWZ} &= 9.03\ h^{-1}\,{\rm Mpc}\,, \\ \Sigma_\parallel^{\rm CMASS} &= 12.18\ h^{-1}\,{\rm Mpc}\,, & \Sigma_\perp^{\rm CMASS} &= 7.31\ h^{-1}\,{\rm Mpc}\,. \end{aligned} \tag{4.1}$$

For both models we perform a joint monopole and quadrupole fit ($N_\ell = 2$) for the north and south galactic caps of LOWZ and CMASS ($N_j = 2$). For the polynomial broadband expansion we go up to order $N_i = 3$. Hence, we have 17 free parameters for the BAO anisotropic model and 11 for the full-shape RSD model per redshift bin. We refer to these parameters as $\boldsymbol{\theta} = \{\boldsymbol{\Theta}$, nuisance parameters$\}$. The prior ranges of all these parameters are given in table 3 and they are the same for all redshift bins.

The likelihood function for the parameters $\boldsymbol{\theta}$ is defined as

$$\mathcal{L}(\boldsymbol{\theta}) \propto e^{-\chi^2(\boldsymbol{\theta})/2}\,, \tag{4.2}$$



JCAP09(2020)052

| Parameter | Prior range |
|---|---|
| $\alpha_\parallel$ | $[0.6, 1.4]$ |
| $\alpha_\perp$ | $[0.6, 1.4]$ |
| $\beta$ | $[0, 30]$ |
| $B$ | $[0, 20]$ |
| $A_i$ $[10^3(\,h^{-1}\,\mathrm{Mpc})^{5-i}]$ | [-20, 20] |
| $f$ | $[0, 3]$ |
| $b_1$ | $[0, 10]$ |
| $b_2$ | [-10, 10] |
| $\sigma_P\,[\,h^{-1}\,\mathrm{Mpc}]$ | $[0, 20]$ |
| $A_{\mathrm{noise}}$ | [-5, 5] |

**Table 3**. Uniform prior ranges for parameters used in anisotropic BAO and FS analysis. The $\alpha$'s in the top section are used in both BAO and FS analyses, parameters in the second and third sections are used only in BAO and FS analysis, respectively. The $A_i$ are the three parameters to model the broadband.

where the $\chi^2$ is obtained by a matrix multiplication of the difference-vector between data and model with the inverse covariance:

$$\chi^2(\boldsymbol{\theta}) = \sum_{\ell,\ell'}^{\ell_{\max}} \sum_{k,k'}^{k_{\max}} \left(P^{(\ell)}_{\mathrm{model}}(k,\boldsymbol{\theta}) - P^{(\ell)}_{\mathrm{data}}(k)\right) C^{-1}_{(\ell k)(\ell' k')} \left(P^{(\ell')}_{\mathrm{model}}(k',\boldsymbol{\theta}) - P^{(\ell')}_{\mathrm{data}}(k')\right) . \quad (4.3)$$

Both data and model vectors contain $(k_{\max} - k_{\min})/\Delta k$ entries for monopole and quadrupole each. The covariance matrix $C$ is assumed to be fixed, and estimated from 1000 independent realisations per patch of the MD-Patchy mock catalogs without blinding. We do not modify the covariance matrix when analyzing blinded catalogs (e.g. by estimating it from 1000 blinded mocks), because the blinded data should be treated as if we did not know that it was blinded. When inverting $C$ we apply the Hartlap correction [53] to take into account the finite number of mock catalogs. The north and south galactic cap are assumed to be fully independent, and therefore, their likelihoods are multiplied to obtain the combined one, $\mathcal{L}_{\mathrm{NGC+SGC}} = \mathcal{L}_{\mathrm{NGC}} \times \mathcal{L}_{\mathrm{SGC}}$.

### 4.3 AP-like shift performance

We now focus on the performance of the geometrical blinding shift $\Delta^{\mathrm{AP}} z$ (section 3.2). We apply the methodology explained in section 4.2 to the set of blinded mocks characterised by the parameter values of row "AP only" in table 2. In this section, the blinding and the analysis are performed on pre-reconstruction catalogs i.e., on the original ones. Results relative to the combination of the two effects including reconstruction procedure are presented in section 4.5.

We use the shifted cosmology specified in row "AP only" of table 2 to convert the original catalog redshifts to distances, then transform them to blinded redshifts using the reference cosmology (yielding the blind catalog). This changes the number density distribution $\bar{n}(z)$, as shown in figure 4. The $\bar{n}(z)$ of the original catalog (blue histogram) is transformed to the shifted distribution (orange histogram). The overlap area appears in purple. The shifted



JCAP09(2020)052

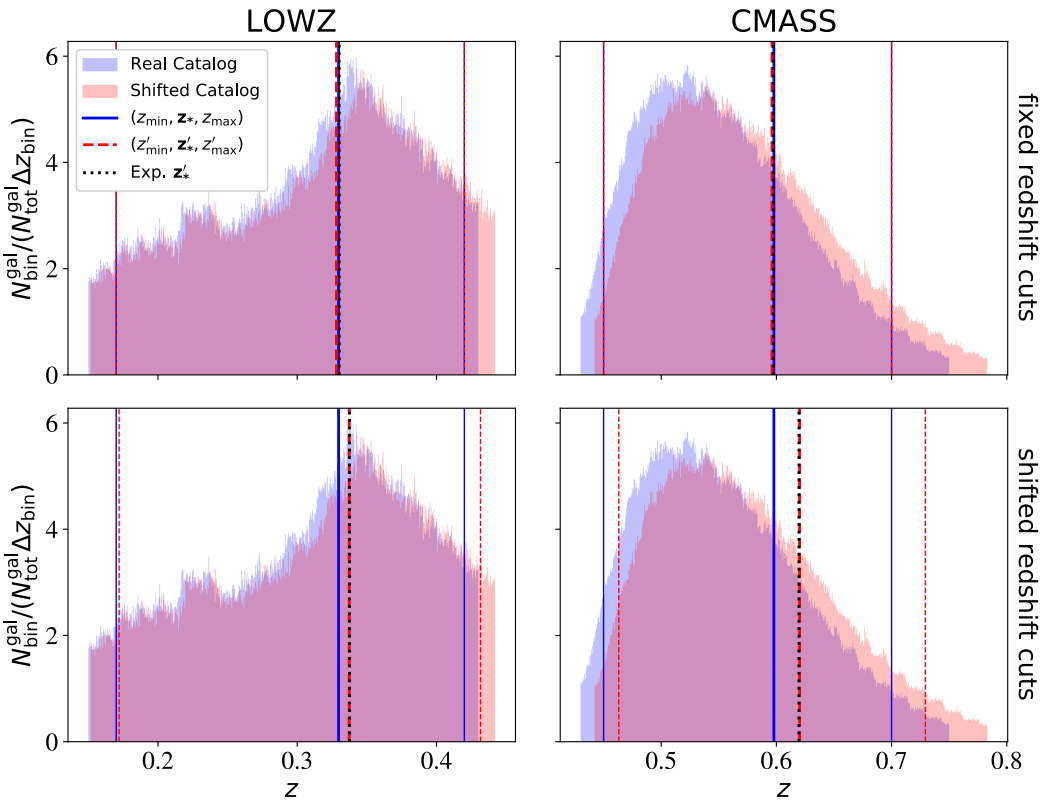


**Figure 4**. Normalised galaxy redshift distributions of LOWZ (left panels) and CMASS (right panels). The blue area represents the original catalog galaxies and the red area the blinded catalog of a scenario where $\Omega_{\rm m}$ and $w$ were reduced by 10%. Overlapping regions are shown in purple. The distribution of the upper and lower panels are the same, but with different cuts in redshift. If we keep the cuts fixed (upper panels), the effective redshift does not change significantly after blinding. By shifting the cuts according to the blinding scheme (lower panels) the effective redshift is shifted in the same way as expected.

parameters are lowered by 10% with respect to the reference ones, thus the (shifted) distances for individual galaxies are larger, and consequently the blinded redshifts are (slightly) increased by $\Delta^{\rm AP} z$.

This naturally leads to a shift of the effective redshift of the sample, whose implications for the analysis are discussed below.

The top panels of the figure 4 illustrate the "fixed redshift cuts" convention and the bottom panel the "shifted redshift cuts". In the "fixed redshift cuts" case, the cuts (thin dashed lines) are decided and fixed before blinding the catalog. If the cuts are not located at the edge of the distribution — i.e,. there is some padding — the effective redshift does not change considerably after blinding, because while some galaxies leave the selected region on one side, new galaxies enter the region from the other side. Here, we cut the original catalogs at $z = 0.17$ and $z = 0.42$ for LOWZ, and $z = 0.45$ and $z = 0.7$ for CMASS. In both redshift bins, after blinding, approximately 5% of galaxies leave the selected range at the top edge



JCAP09(2020)052

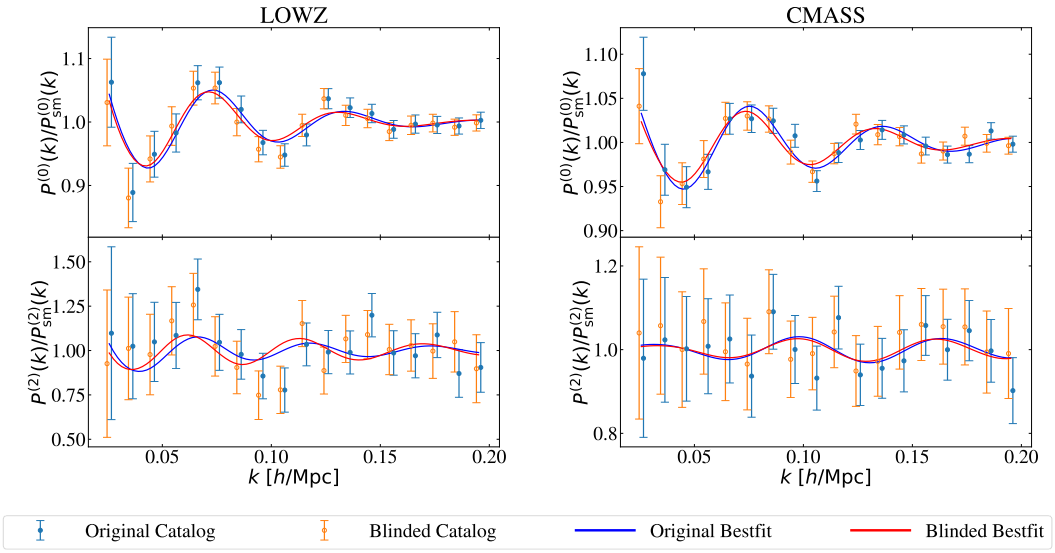


**Figure 5**. Measured power spectra of one LOWZ (left) and one CMASS (right) mock catalog (both original and blinded) with the best-fit anisotropic BAO model (blue) in comparison with its blinded counterpart (red) using the "shifted redshift cuts" convention. Data points are slightly displaced by $\Delta k = \pm 0.001\ h\,\mathrm{Mpc}^{-1}$ for better visibility. In all cases, both data and model prediction are divided by the corresponding best-fit prediction of the broadband.

and about 5% enter from the bottom edge. The effective redshifts of the original and blinded catalogs agree within 0.1%. However, the change of effective redshift highly depends on the details of the redshift distribution, as well as the position of the cuts, so the agreement we find between $z_*$ and $z'_*$ in the case of LOWZ and CMASS should not be generalised to other galaxy samples.

In the "shifted redshift cuts" case on the other hand, the selection cuts are made in such a way that the objects belonging to the sample are the same pre- and post-blinding. Hence, the cuts on the blinded catalog (thin red dashed lines) are displaced from the original cuts (thin blue continuous lines) according to $\Delta^{\rm AP}z$; the measured effective redshifts of the samples (thick lines) are also displaced, matching exactly the shift predicted by $\Delta^{\rm AP}z$ (black dotted line).

In the next step, we measure the monopole and quadrupole power spectra of the original and the blinded catalogs and fit to them our anisotropic BAO and full-shape RSD models as described in section 4.2. As an example, in figure 5 we show the power spectra together with the best-fit anisotropic BAO model for a pair of original and blinded mock with the "shifted redshift cuts" convention. We show the oscillatory part of the power spectrum only. After blinding, the oscillation peaks are shifted towards smaller $k$ leading to a decrease of the measured $\alpha_\parallel$ and $\alpha_\perp$ with respect to the original catalog. This is consistent with our expectation given in table 2.

In figure 6 we show a comparison between the scaling parameters corresponding to the best-fit anisotropic BAO model of figure 5 and the expected values given in table 2. We directly show the corresponding distances perpendicular (comoving angular diameter distance $D_M(z)$) and parallel (Hubble distance $D_H = c/H(z)$) to the LOS rescaled by $r_{\rm d}$. The left



JCAP09(2020)052

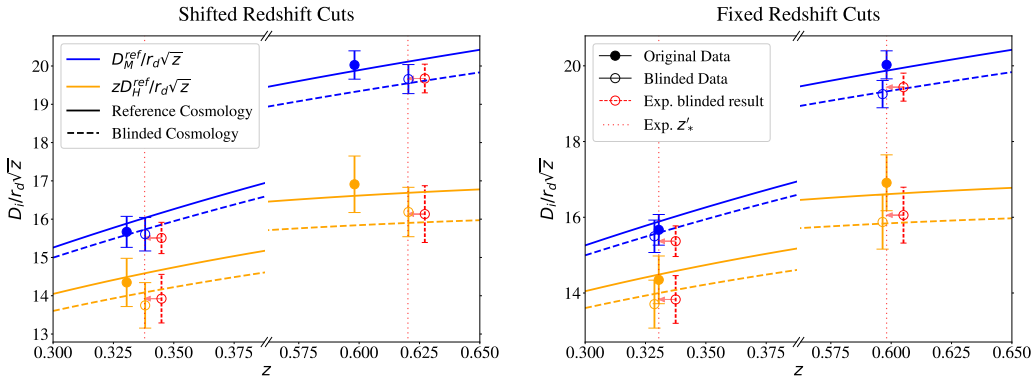


**Figure 6**. Comparison of the anisotropic distance measurement between one of the original mock realisations (filled dots) and its blinded counterpart (empty dots). The effective redshift positions are different in the case of shifted redshift cuts (left panel), while they are almost the same ($< 0.5\%$ difference) in the case of fixed redshift cuts (right panel). Red data points mark the expected blinded result obtained by applying eq. (3.17) to the original data. They are slightly displaced to avoid overlap; their true redshift positions are indicated by red arrows and vertical dotted lines. The rescaling factor $\sqrt{z}$ improves the visibility of the different data points and has no physical meaning.

panel shows the results using "shifted redshift cuts" convention, where blinding changes the effective redshift of the sample.

On the right panel the "fixed redshift cuts" convention is shown, where the effective redshift does not change. In both cases the expectation represented by the red points matches the blinded distance measurement very well. The error bars of the expected blinded result are chosen to have the same size as the original error bars. As we can see, their size is similar to the error bars obtained from the blinded data. In addition, figure 6 shows the distance-redshift relation of the reference cosmology $\boldsymbol{\Omega}^{\text{ref}}$, that is very close to the MD-Patchy mock underlying cosmology, and the blinded cosmology, which is the one that we would expect to measure.

We repeat this analysis for 100 realisations (both original and blinded) pairs of mock catalogs and test the agreement between measurement and expectation of the scaling parameters for each pair.[8]

The overall performance is summarised in figure 7. Each dot represents the measured values of a parameter from the blinded and original catalogs, shown in the $y$- and $x$-axis, respectively. The scatter of the mocks is visualised by the purple 68% and 95% confidence level contours, that were obtained by weighting each point with its corresponding uncertainties for each catalog. The spread of the points parallel to the diagonal $y = x$ indicates the intrinsic scatter of the mocks with respect to the given parameter; in case the original and the blinded catalog were the same, all points would be located along that diagonal. However, by using the shifted cosmology given in table 2 we expect the points to scatter around the dashed line described by the formula

$$y(x) = \frac{\alpha'_{\text{theo}}}{\alpha_{\text{theo}}}\, x\,, \tag{4.4}$$

[8]Note that for each mock catalog 6 MCMC are run in parallel (we refer to these as sets of chains). In total in this paper we are presenting the results of 2216 sets of MCMC chains.



JCAP09(2020)052

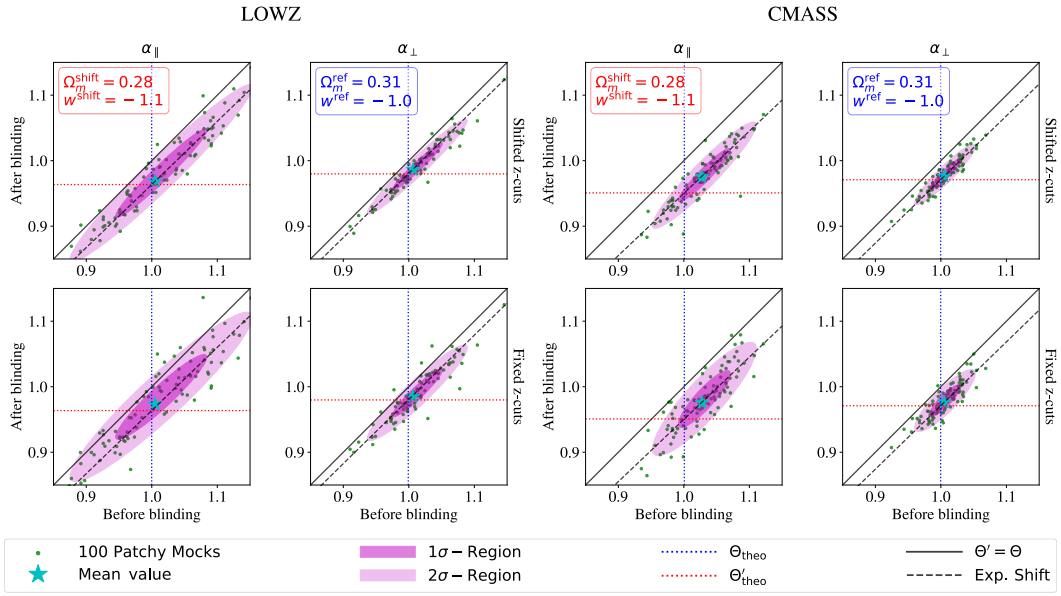


**Figure 7**. Effect of AP-only shifts blinding on pre-reconstruction BAO-only analysis. The panels show $\alpha_\parallel$ and $\alpha_\perp$ best-fitting results for the pre-reconstruction BAO-only analysis on 100 mock realisations (green dots) and their mean values (cyan stars) for the underlying cosmology and the blinded cosmology (using only AP-like shifts). Left (right) panels display the measurements from the LOWZ (CMASS) sample. Upper panels correspond to the "shifted redshift cuts" and lower panels to the "fixed redshift cuts" convention. Purple regions indicate the 68% and 95% confidence level regions. Dashed lines represent the expected shift of the mock distribution from the diagonal due to blinding. Blue dotted lines represent the underlying values corresponding to the MD-Patchy mocks cosmology, whereas red dotted lines show the "underlying" values of the blinded catalogs.

where $\alpha_{\rm theo}$ and $\alpha'_{\rm theo}$ correspond to the theoretical values given in table 2. The scatter of points perpendicular to the line parameterised by eq. (4.4) indicates how much the measurement of a single blinded mock catalog typically deviates from the expectation given the measurement of the original mock. This deviation is purely statistical, as the overall cloud scatters around the line predicted by eq. (4.4). For all cases there is a good agreement between the mock distribution and the prediction of the blinded result represented by eq. (4.4).

The mean values of the mocks (cyan stars) agree very well with the theoretical values of table 2 given by the coloured dotted lines in figure 7. Also, our results for the original mocks are in concordance with previous analysis as in [33].

From figure 7 we can clearly appreciate that for the fixed redshift cuts case (right panels) the scatter in direction perpendicular to the diagonal is slightly enhanced with respect to the shifted redshift cuts case (left panels). This is because in the former case the galaxy sample changes after blinding and thus the Fourier modes sampled, leading to a cosmic variance effect. This is avoided in the latter case, where the blinded catalog contains the same galaxies (and samples exactly the same modes) as the original catalog.

We conclude that the shifted redshift cuts case gives a blinding procedure that is a more accurate prediction of the behaviour of each individual mock catalog. For this reason we recommend whenever possible to adopt the "shifted redshift cuts" convention. In the



JCAP09(2020)052

following we always refer to the "shifted redshift cuts" convention unless explicitly mentioned otherwise.

### 4.4 RSD shift performance

Here we focus on the perturbation-level blinding shift $\Delta^{\rm RSD}z$ (section 3.3). Starting from the original catalogs, we generate the set blinded mocks using the parameter values of row "RSD only" in table 2 and a reference galaxy bias value of $b^{\rm ref} = 1.85$. Then we apply the methodology explained in section 4.2 to the set of blinded mocks.

The left panel of figure 8 shows the measurements obtained from 100 LOWZ mocks for three different cases. The blue (solid) lines correspond to the multipoles measured from the original catalogs. The green (dashed) lines correspond to the catalogs obtained after removing the redshift-space component as an intermediate step during the reconstruction procedure using the reference growth rate and galaxy bias. The quadrupole is almost zero, which demonstrates that reconstruction efficiently removes the RSD-induced anisotropy on large scales. As explained in section 3.3, for the blinding procedure we use the displacement field obtained from the reconstructed real space positions to add a new RSD contribution corresponding to the shifted growth rate. The multipoles measured from the blinded catalogs are shown in red (dotted) lines.

One important ingredient of the blinding procedure is the choice of the smoothing scale $R_{\rm sm}$ used to filter the discrete galaxy over-density field. For too-large value of $R_{\rm sm}$ the small scale perturbations are washed out, and thus ignored. On the other hand, for a too-small value of $R_{\rm sm}$, the obtained field is dominated by nonlinear velocities, which cannot be efficiently modelled. Hence, the choice of smoothing scale implies a trade-off between these effects.

The right panel of figure 8 shows the reconstructed real space power spectra obtained for three different smoothing scales. For $R_{\rm sm} = 15\ h^{-1}\,{\rm Mpc}$ we see a bump for $0.05 < k\,[\,h\,{\rm Mpc}^{-1}] < 0.20$ indicating that anisotropies due to RSD are not properly removed. In the same $k$-range, a smoothing scale of $R_{\rm sm} = 5\ h^{-1}\,{\rm Mpc}$ leads to a negative quadrupole, suggesting that it over-predicts the linear RSD anisotropies because of the superimposed nonlinear velocities. We find that a value of $R_{\rm sm} = 10\ h^{-1}\,{\rm Mpc}$ optimally reduces both effects (for LOWZ and CMASS); thus we adopt this choice for the rest of this work. This is also in agreement with previous findings as in ref. [32]. The choice of smoothing scale is further discussed in appendix A where we show that the procedure presented here is robust to the choice of the smoothing scale.

We apply the full shape model introduced in paragraph Full shape power spectrum model to the blinded mocks and estimate the relevant parameters. The results for the recovered parameters $\mathbf{\Theta} = \{\alpha_\parallel, \alpha_\perp, f\sigma_8\}$ for each individual mock are summarised in figure 9.

Since the AP-like shift is not included here, we expect no deviation due to blinding for $\{\alpha_\parallel, \alpha_\perp\}$. As we can see from the two left columns, on average this is indeed the case: statistically, the recovered parameters from the blinded mocks follow this expectation. This shows that RSD-like shifts along the LOS are not degenerate with the AP-like shifts: the induced change of $f$ due to blinding does not propagate into a systematic bias on $\alpha_\parallel$, $\alpha_\perp$.

The expected change due to blinding of $f\sigma_8$ (see right columns) is given by the dashed line parameterised as

$$y(x) = x + (f^{\rm shift} - f^{\rm\ ref})\sigma_8^{\rm ref}\,, \tag{4.5}$$



JCAP09(2020)052

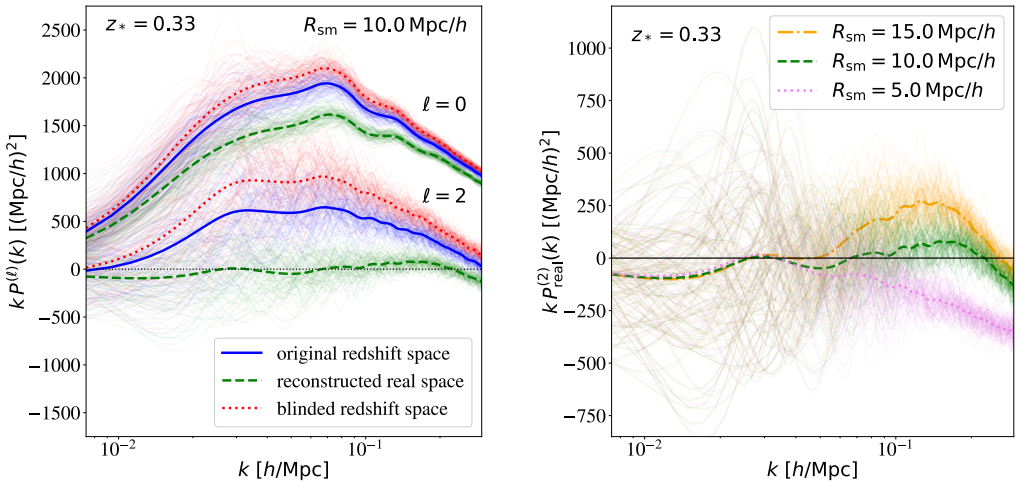


**Figure 8**. Left panel: measured monopole and quadrupole from 100 LOWZ SGC mocks. Thin lines correspond to individual measurements, thick lines to their mean. Right panel: reconstructed real-space quadrupoles for different choices of smoothing scales adopted in the RSD-blinding procedure.

corresponding to eq. (3.19) multiplied by the matter density fluctuation amplitude of the reference template $\sigma_8$.[9] This can be understood by considering that, in standard RSD analyses, $f$ and $\sigma_8$ are completely anti-correlated, and the measurements are thus sensitive to their product only. As stated in section 3.3 here we decide to blind for $f$ coherently following eq. (2.12), but this choice is not unique and could be replaced by a relation that also takes into account the different evolution of $\sigma_8$ with $\gamma^{\rm shift}$, e.g., by rescaling $f^{\rm shift}$ accordingly.

Note that here we have deliberately chosen to show a very extreme shift towards $\gamma^{\rm shift} = 0$. As presented in table 2, this corresponds to a 20% change of the growth rate parameter $f$ for CMASS and almost 50% for LOWZ galaxies (recall that effective redshifts are $z_* = 0.33$ for LOWZ and $z_* = 0.6$ for CMASS).

This consideration is key to understand the different behaviour of the mocks in figure 9. While the blind CMASS catalogue matches the expectation very accurately, the value of $(f\sigma_8)'$ is over predicted by $\sim 1\sigma$ for the LOWZ sample. The chosen value of $\gamma^{\rm shift} = 0$, and hence $\Delta\gamma = 0.55$ indicates the upper limit for an accurate prediction for the growth rate after blinding. This extreme case, while very illustrative, should not be applied if possible in any realistic blinding scenario. The resulting catalog would still be blind, but the condition to be able to "unblind parameter values without the need to rerun the analysis pipeline" would not be satisfied.

The predictability of the blinding procedure proposed here for shifted values deviating by up to 20% should be more than enough given the anticipated precision level of future galaxy surveys at all redshifts.

Another important observation from figure 9 is that even mocks that are distant from the dashed blue line follow eq. (4.5) very well. Therefore we conclude that even for mocks

[9] Note that the method presented here does not allow one to blind for the value of $\sigma_8$ itself, as we only shift radial and not angular positions.



JCAP09(2020)052

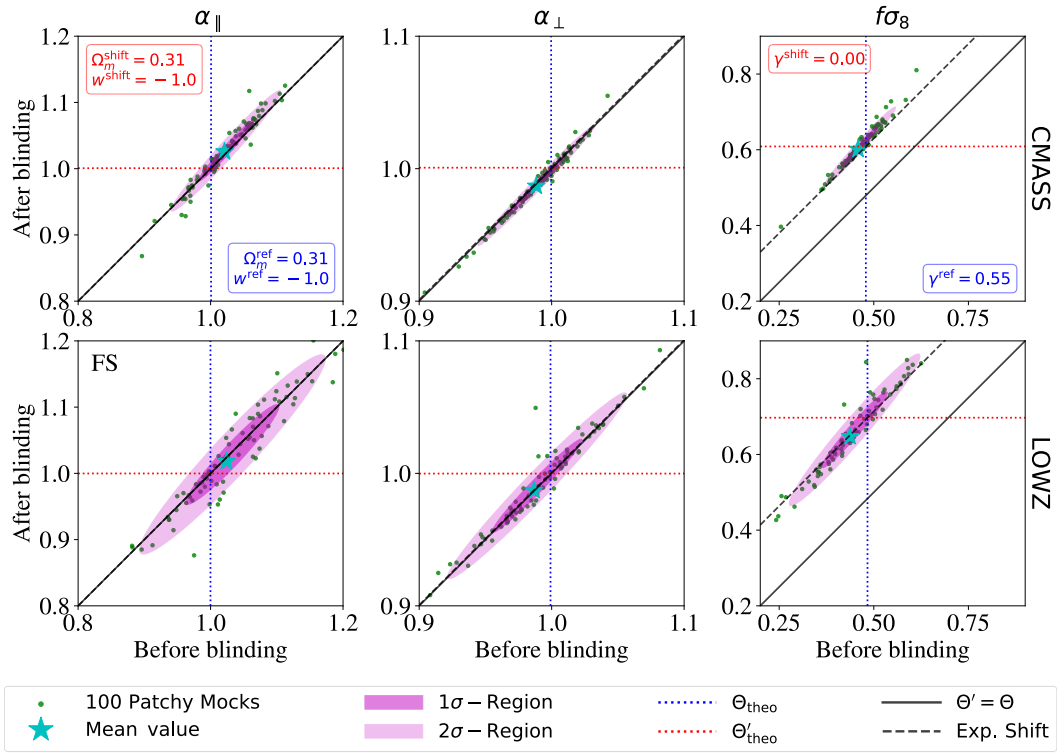


**Figure 9**. Effect of RSD-only shift blinding on full shape analysis results. Best-fit physical parameters $\alpha_\parallel$ (left panels), $\alpha_\perp$ (middle panels) and $f\sigma_8$ (right panel) from 100 mock realisations (green dots) and their mean values (cyan stars) for the underlying (reference) cosmology and the blinded cosmology. Upper panels show the measurements from the CMASS mocks, lower panels the LOWZ mocks and the purple regions give the $1-2\sigma$ spread of the mocks. The dashed line shows the expected shift of the mock distribution from the diagonal due to blinding. The blue dotted lines represent the underlying values corresponding to the MD-Patchy mocks cosmology, whereas red dotted lines show the "underlying" values of the blinded catalogs.

with different best fit parameters with respect to the reference ones, the blinding shift can be well predicted.

### 4.5 Combined shift performance

Having shown the performance of the AP-like and the RSD shift individually, here we investigate the performance when both shifts are combined. This provides a more realistic blinding scenario, closer to the way we envision it to be applied to real data.

The first question to be addressed is how both shifts shall be combined. While in principle the shifts can be applied in any order, in practice each operation on the catalog relies on different inputs, different assumptions and has different optimisation requirements, and thus the order does matter.

In particular, the AP-like shift $\Delta^{\rm AP}z$ is cosmology-independent, as it does not depend on $\mathbf{\Omega}^{\rm ref}$, but only on the input $\Delta\mathbf{\Omega}^{\rm shift}$ propagating directly into the $\alpha$-parameters which describe generically the expansion history. While for this application we have decided to



JCAP09(2020)052

adopt a $w$CDM-type expansion history, it could incorporate even more general models such as varying dark energy or modified gravity.

On the other hand the RSD shift $\Delta^{\rm RSD}z$ relies on additional assumptions. The RSD blinding algorithm requires, as input, reference values for $\{\Omega_{\rm m}^{\rm ref}, w^{\rm ref}\}$ to convert redshifts to comoving distances, and $\{f^{\rm ref}, b^{\rm ref}, R_{\rm sm}\}$ to find a solution for the reconstructed smoothed real-space over-density. Although the impact of an unphysical reference cosmology on the obtained blinded catalog is small, it is important to recognise this conceptual difference with respect to the AP-like shift, which is independent of $\mathbf{\Omega}^{\rm ref}$.

In this case, if we were to first apply to the catalogue $\Delta^{\rm AP}z$, followed by $\Delta^{\rm RSD}z$, the intended deviation from the reference cosmology induced by $\Delta^{\rm AP}z$ would propagate into the calculation of $\Delta^{\rm RSD}z$. We find that this leads to small but unnecessary biases contributing to the computation of the final blinded catalog. Therefore, a more natural and recommended choice consists in applying the shifts in reversed order. First, run the reconstruction-like algorithm with input parameters tuned to catalogs generated from a reference cosmology that match key properties of the sample. Second, take the RSD-blinded catalog and convert redshifts to distances using a shifted cosmology (AP-like shift). Any biases that might occur during the first step (RSD shift) do not propagate into the second step (AP-like shift), because the latter is purely geometrical, homogeneous and model-independent. Another point in favour of this order is, that it nicely matches the order of steps in which the BAO and RSD analyses is carried out. We *first* convert redshifts to distances using a reference cosmology and *then* measure the summary statistic of choice. The idea of our scheme is to carry out these steps "backwards" in order to mimic a different cosmology. Therefore, we advocate to use the order "RSD shift first, AP-like shift second" for the combined blinding shift and we adopt that strategy in what follows.

We blind the mocks according to the last entry of table 2. We carry out two different types of analysis: we fit the BAO anisotropic power spectrum model both to pre-reconstruction (BAO prerecon fit) and post-reconstruction (BAO postrecon fit) mocks to obtain constraints on the scaling parameters in section 4.5.1. In section 4.5.2 we show the results obtained for the Full shape power spectrum model which is used to jointly fit the scaling parameters and growth rate amplitude (FS fit).

### 4.5.1 BAO analysis results

Here we show the results of our BAO prerecon and postrecon fits. For reconstruction, we follow the procedure explained in paragraph Redshift-space distortions and reconstruction using an input growth rate $f^{\rm ref}(z)$ corresponding to $\Lambda$CDM ($\gamma^{\rm ref} = 0.55$), a galaxy bias of $b^{\rm ref} = 1.85$, and a smoothing scale of $R_{\rm sm} = 10\,h^{-1}\,$Mpc both for the blinded and the original mock catalogs. The impact of choosing the same growth rate in both cases is very small as shown in more detail in section 5.

All BAO fit results obtained from the original and the blinded mocks generated using the combined shift are shown in figure 10. For the prerecon case (left panels) we see that the agreement between the mock distribution and the prediction (dashed line) is as accurate as that obtained for the AP-only shift in figure 7. This suggests, that the prerecon BAO analysis results are stable against the additional RSD shift included in this section. In other words: modifying the RSD signal at the catalog level leaves unaltered the information extracted from the anisotropic BAO signal, confirming the discussion of the previous subsection. The right panels show that reconstruction reduces the intrinsic scatter along the diagonal (note that the x-axis and y-axis scales are the same for all subplots). This is expected, as recon-



JCAP09(2020)052

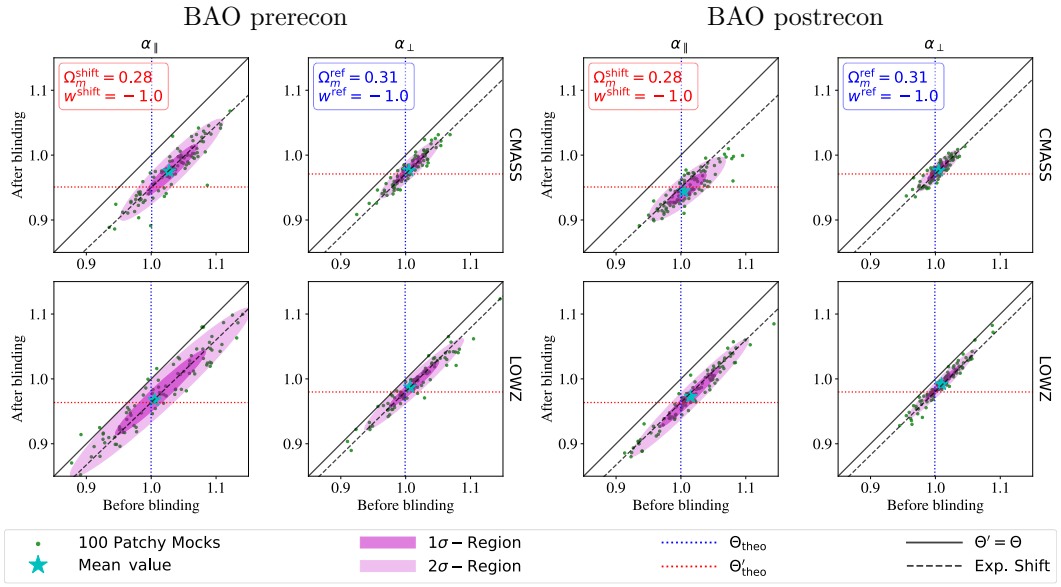


**Figure 10**. Effect of AP-like+RSD shift blinding on prerecon (left panels) and postrecon (right panels) BAO-only analyses. The panels show $\alpha_\parallel$ and $\alpha_\perp$ best-fit results for 100 mock realisations (green dots) and their mean values (cyan stars) for the underlying cosmology and the blinded cosmology (using AP only shifts). Upper (lower) panels display the measurements from the CMASS (LOWZ) sample. Purple regions indicate the 68% and 95% confidence level regions. Dashed lines represent the expected shift of the mock distribution from the diagonal due to blinding. Blue dotted lines represent the underlying values corresponding to the MD-Patchy mocks cosmology, whereas red dotted lines show the "underlying" values of the blinded catalogs.

struction enhances the BAO peak, which increases the signal-to-noise ratio. Furthermore, reconstruction brings the mean of the mocks (cyan star) closer to the theoretical prediction given by the blue and red lines, in particular for CMASS.

A potential worry with this procedure is that, as shown in ref. [54], using input parameters for the reconstruction procedure significantly different from the underlying ones, may lead to biases in postreconstruction BAO analyses. Here, we find that also in the BAO postrecon case the agreement between mock distribution and expectation is encouragingly good.

In addition to the best-fit results, we are particularly interested in whether the blinding scheme leads to a change of error bars, and hence the significance of the measurement. Therefore, we show in figure 11 the errors on the scaling parameters on a mock-to-mock basis with the same setup as in figure 10. Black lines indicate where the errors of blinded and original mocks coincide, whereas purple dashed lines show a linear regression to the mocks represented by green dots. Shaded contours show the $1\sigma$-region of the linear regression. The scatter of the error bars before and after blinding is consistent with the identity line. Only for the CMASS postrecon case we observe a small trend towards smaller errors after blinding. Again, this could be related to a suboptimal choice of input parameters for reconstruction as for example the galaxy bias. Also note that blind measurements make use of a covariance matrix obtained from unblind mocks, which could propagate into an over- or underestimation of the error bars, depending on the shifted cosmology used to generate the blinded data. But



JCAP09(2020)052

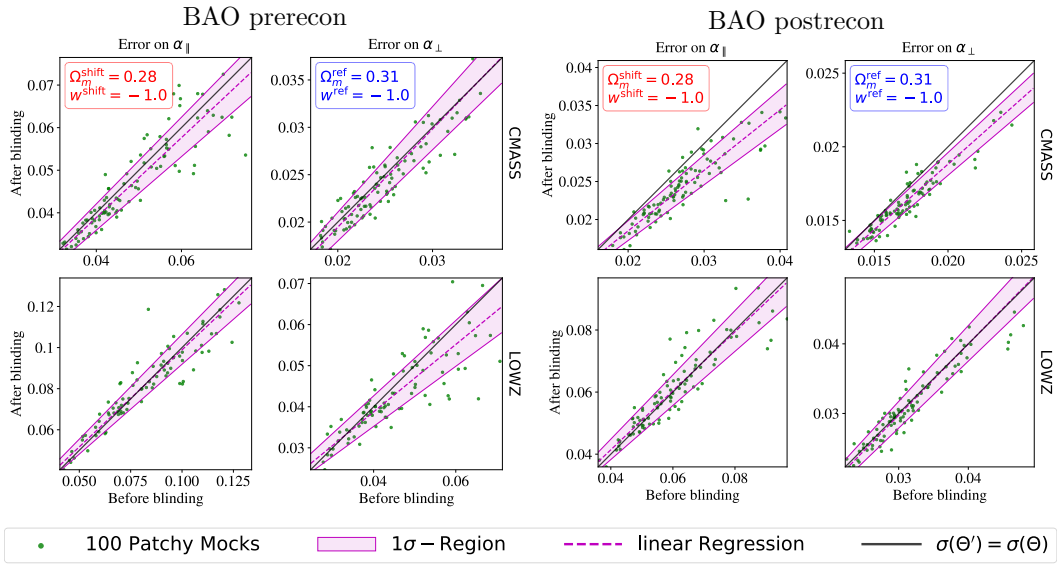


**Figure 11**. Effect of AP+RSD shift blinding on error-bars obtained from prerecon (left panels) and postrecon (right panels) BAO fits. The shaded regions describe the $1\sigma$-region when fitting a linear regression to the mock distribution.

as figure 11 suggests, this effect is very small. Therefore we argue that the overall agreement is promising and conclude that the blinding procedure does not lead to additional biases corrupting the significance of the blind measurements.

### 4.5.2 FS analysis results

The results for the FS fits are shown in figure 12. As in figure 10, the green points correspond to the different realisations and the cyan stars represent the mean of the mocks. It is possible to appreciate that the inferred parameters from the blinded mocks are nicely aligned with the dashed line, which is the expected "locus". The fact that the cyan star does not coincide with the intersection of the red and blue dotted line is not due to the blinding procedure (in fact the systematic affects both determinations before and after blinding); it is possibly caused by the modeling itself applied to "fast" mocks rather than full N-body and to the relatively small number of realisations used.

Here, we also quantify the effect of the combined blinding on the recovered parameters errors. This is illustrated in figure 13, for the same set up as in figure 12 (combined shifts, FS fit). Again, the black diagonal line indicates where errors before and after blinding coincide and the dashed purple line is a linear regression to the points with $1\sigma$ uncertainty given by the shaded region. Similarly to figure 11, the errors before and after blinding are centered around the diagonal indicating no systematic change. This demonstrates that blinding does not affect significantly the error-bars.

### 4.5.3 $\chi^2$ before and after blinding

Another important consistency check is the comparison of best fit $\chi^2$ before and after blinding. This is shown in figure 14 for all cases discussed in sections 4.5.1 and 4.5.2. Again, each pair



JCAP09(2020)052

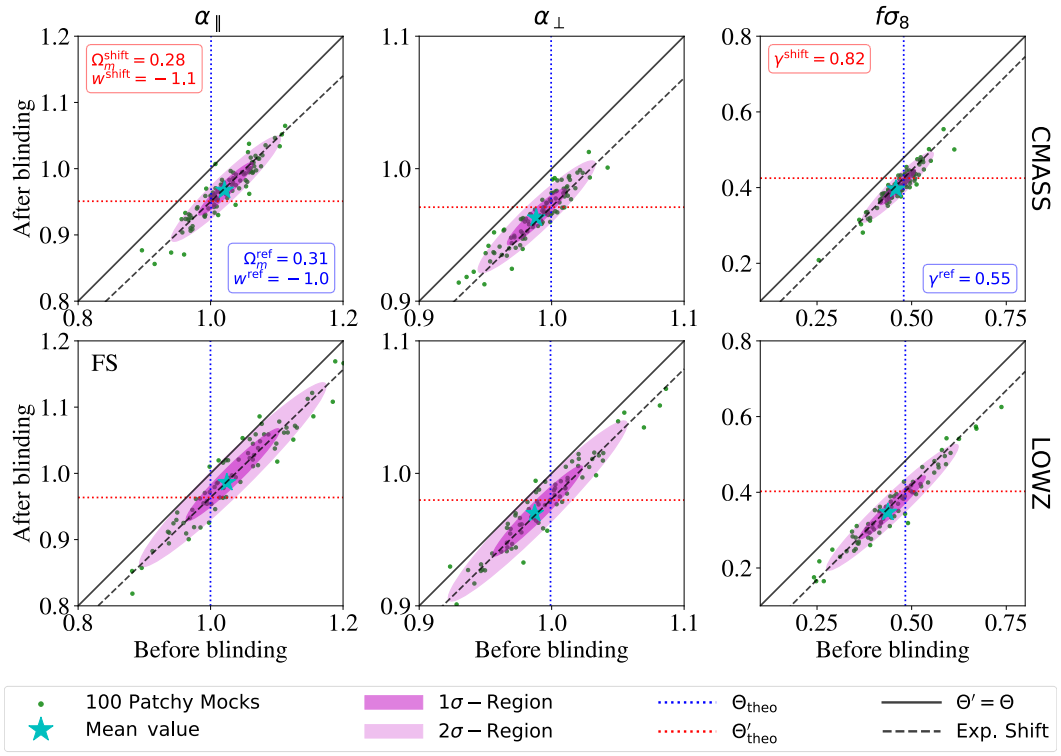


**Figure 12**. "Full shape" fits on mocks with combined shift blinding. Comparison of recovered values for $\alpha_\parallel$ (left panels), $\alpha_\perp$ (middle panels) and $f\sigma_8$ (right panel) from 100 mock realisations (green dots) and their mean values (cyan stars) for the underlying (reference) cosmology and the blinded cosmology. Upper panels show the measurements from the CMASS mocks, lower panels the LOWZ mocks and the purple regions give the $1-2\sigma$ spread of the mocks. The dashed line shows the expected shift of the mock distribution from the diagonal due to blinding. The blue dotted lines represent the underlying values corresponding to the MD-Patchy mocks cosmology, whereas red dotted lines show the 'underlying' values of the blinded catalogs.

of mocks is represented by a green dot and the black diagonal shows where the values before and after blinding coincide. We note that there is an intrinsic scatter of $\chi^2$ among the mocks in a range of about $0.6 < \chi^2/\mathrm{ndf} < 1.4$. In general we see that the mock distribution is aligned with the black diagonal, meaning that blinding does not systematically change the $\chi^2$. However, there is some scatter around the diagonal, meaning that the blinding shift can either improve or worsen the goodness of fit. Since this scatter is much smaller than the intrinsic scatter of mocks, we argue that it is not relevant. Overall, the alignment along the identity line of $\chi^2$ before and after blinding proves our blinding procedure to be stable enough to be applied to spectroscopic galaxy survey data.

## 5 Worked example: application to BOSS DR12 data

We use BOSS DR12 catalog [55] to present a practical example of applying the blinding procedure proposed in this paper to real data. The Baryon Oscillation Spectroscopic Survey



JCAP09(2020)052

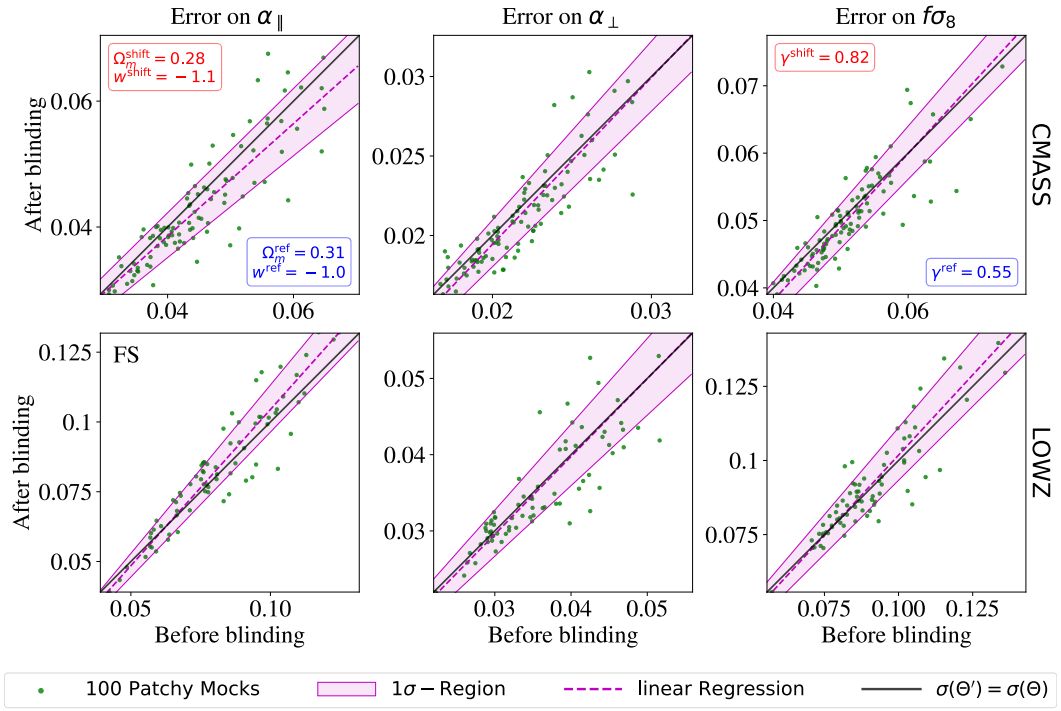


**Figure 13**. Effect of combined AP+RSD shifts blinding for full shape analysis on the errors-bars. Errors on $\alpha_\parallel$, $\alpha_\perp$ and $f\sigma_8$ from 100 mock realisations (green dots) for the underlying (reference) cosmology and the blinded cosmology (last entry of table 2). The errors before and after blinding are centred around the diagonal indicating no systematic change. The dashed purple line is a linear regression to the points and the shaded region its $1\sigma$ errors.

(BOSS) [56] is part of the Sloan Digital Sky Survey III [57]. BOSS measured spectroscopic redshifts [58, 59] for more than 1 million galaxies in an effective volume of $V_{\rm eff} = 7.4\,{\rm Gpc}^3$. The galaxy survey includes the LOWZ sample with 361 762 galaxies [60] covering the redshift range of $0.15 < z < 0.43$ and the CMASS sample, with 777 202 galaxies at $0.43 < z < 0.70$.

We proceed by applying all the steps presented in sections 3.2 and 3.3 to create a blinded catalog. We assume the same reference cosmology as given in table 1 and use the shifted cosmology of the "Combined" case given in table 2. We use the shifted redshift cuts convention explained in section 4.3. Hence, the blinded catalog contains 334 053 LOWZ galaxies in the redshift range $0.17 < z < 0.43$ and 746 889 CMASS galaxies in the range $0.46 < z < 0.73$; this corresponds to an effective redshift of 0.34 for LOWZ and 0.62 for CMASS. Once obtained the blinded catalog, we create a synthetic random catalog matching its number density distribution with redshift but with 50 times the number of objects. This random catalog is used to calculate the blinded survey window function. For the power spectrum measurement we proceed similarly to section 4.2 with the only difference being that we use a finer grid with $1024^3$ cells for the same volume.

The catalogs contain a certain set of weights to account for several observational effects: a redshift failure weight ($w_{\rm rf}$), a fibre collision weight ($w_{\rm fc}$) and a weight ($w_{\rm sys}$) incorporating angular systematics such as seeing conditions and stellar foreground [22]. These weights are



JCAP09(2020)052

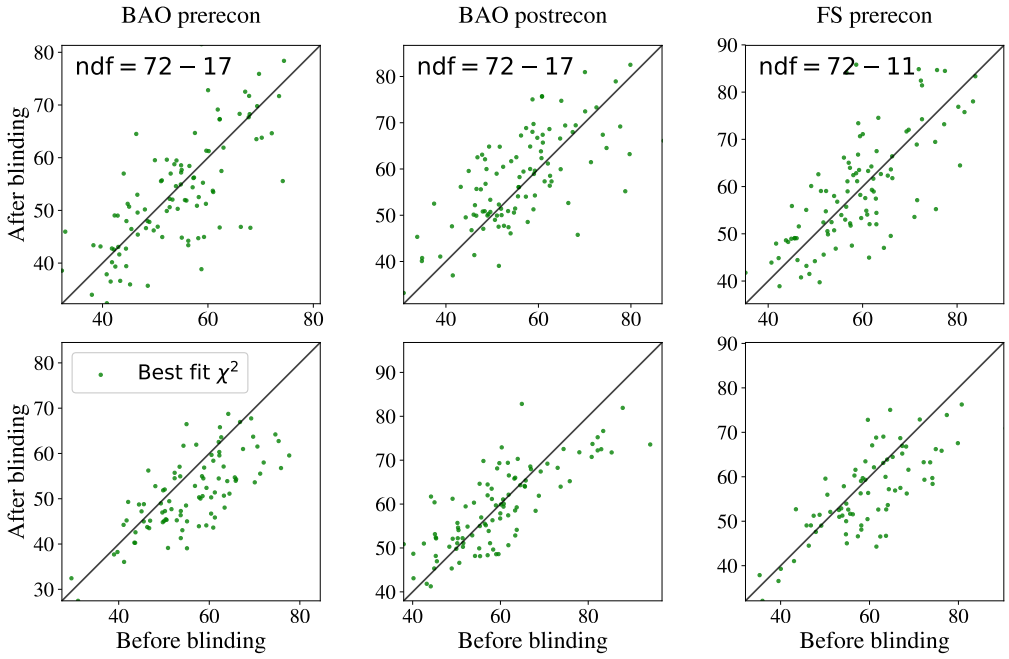


**Figure 14**. Effect of AP+RSD shift blinding on $\chi^2$ values from 100 mock realisations (green dots) for all types of analysis considered here. The left, middle and right panels show the best fit $\chi^2$ for BAO prerecon, BAO postrecon and FS respectively. The top row corresponds to CMASS and the bottom row to LOWZ fits.

common to the original and blinded catalogs. The combined weight for each individual target galaxy is given as

$$w_c = w_{\rm sys}(w_{\rm rf} + w_{\rm fc} - 1)\,. \tag{5.1}$$

For the power spectrum measurements we take the combined weight $w_c$ into account as described in paragraph Power spectrum estimator.

For the fits we use a wave number range of $0.02 < k\,[\,h\,{\rm Mpc}^{-1}] < 0.20$ for the monopole and $0.04 < k\,[\,h\,{\rm Mpc}^{-1}] < 0.20$ for the quadrupole. The cut on the largest scales is chosen to be more conservative than in the case of the MD-Patchy mocks due to the known presence of systematic effects in the quadrupole for scales larger than $k = 0.04\,h\,{\rm Mpc}^{-1}$ as shown in [61].

For the purpose of testing the effect of blinding on reconstruction we apply the reconstruction algorithm described in paragraph Redshift-space distortions and reconstruction on the blinded catalogs. We use the reference cosmology $\mathbf{\Omega}^{\rm ref}$ to convert redshifts to distances, a galaxy bias of $b^{\rm ref} = 1.85$, and a smoothing scale of $R_{\rm sm} = 10\,h^{-1}\,{\rm Mpc}$. We create two sets of reconstructed catalogs using two different reference cosmologies. In one set we use the reference value of the growth rate $f(z) = f^{\rm ref}(z)$ corresponding to $\gamma = 0.55$ while in the other set we use the shifted values (see table 2) corresponding to a growth history with $\gamma = 0.825$, which is that of our target blind cosmology. We expect the choice of the reference cosmology to deliver a more precise measurement on the reconstructed catalogs, as it would



JCAP09(2020)052

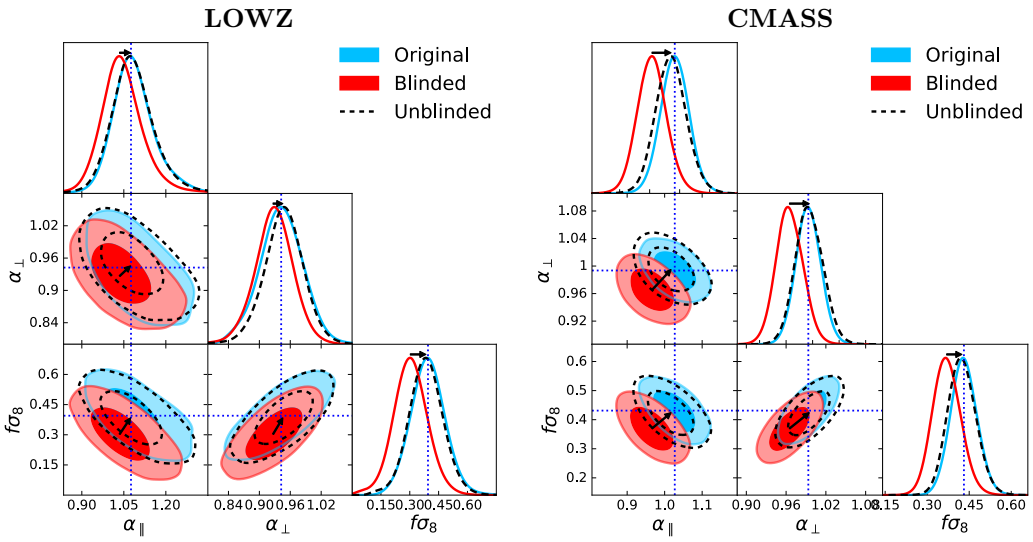


**Figure 15**. Full shape fit to the combined shift blinding applied to the BOSS DR12 data. 68% and 95% confidence level marginalised posteriors of the physical parameters $\alpha_\parallel$, $\alpha_\perp$ and $f\sigma_8$ obtained when fitting the FS model to the blinded (red contours) and the original catalog (blue contours) from LOWZ (left) and CMASS (right) galaxy samples. The dashed contours are obtained by correcting the blinded posteriors by eqs. (4.4) and (4.5) (fast unblinding) as indicated by the arrows. Blue dotted lines mark the best-fit parameters obtained after rerunning the FS analysis on the unblinded catalog.

correctly "undo" the RSD signal induced by blinding. To quantify the effect of a sub-optimal choice of $f$ we present results for these two representative values.

We proceed by fitting the FS model to the blinded catalogs and the BAO anisotropic model to the reconstructed blinded catalogs with the same parameters and prior ranges as given in table 3. Sometimes in the BOSS literature, these get referred to as "pre-recon" and "post-recon" analyses, respectively. We fit the BAO anisotropic model to the mean of 1000 reconstructed original mock realisations with varying nonlinear damping scales. As a result we find

$$\begin{aligned} \Sigma_\parallel^{\rm LOWZ} &= 8.6\ h^{-1}\,{\rm Mpc} \qquad & \Sigma_\perp^{\rm LOWZ} &= 5.8\ h^{-1}\,{\rm Mpc}\,, \\ \Sigma_\parallel^{\rm CMASS} &= 4.3\ h^{-1}\,{\rm Mpc} \qquad & \Sigma_\perp^{\rm CMASS} &= 4.3\ h^{-1}\,{\rm Mpc}\,. \end{aligned} \tag{5.2}$$

We keep these values fixed when analyzing the data, both for the blinded and the original catalogs. Again, this is to follow the good practice of treating the blinded data in the same way as if we would not know that it is blinded.

In figure 15 we present blinded two-dimensional marginalised constraints (red contours) from the FS analysis for model parameters $\alpha_\parallel$, $\alpha_\perp$ and $f\sigma_8$ for the LOWZ (left panel) and CMASS samples (right panel). In a similar fashion, we show the results for the BAO anisotropic model parameters $\alpha_\parallel$ and $\alpha_\perp$ fitted to reconstructed CMASS catalogs in figure 16. On the left we use the reference value of the growth rate $f^{\rm ref}$ and on the right the shifted value $f^{\rm shift}$ for reconstruction.



JCAP09(2020)052

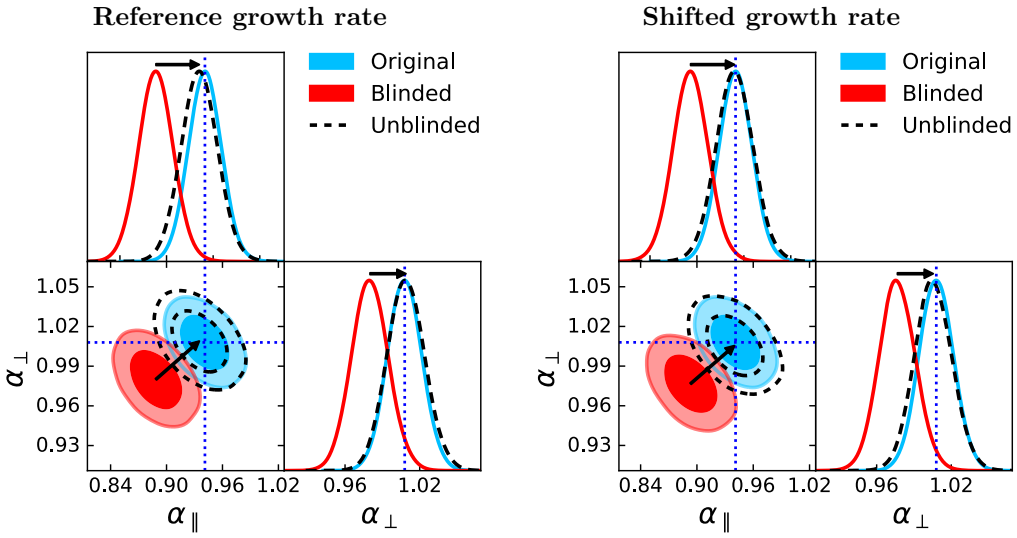


**Figure 16**. Post-reconstruction anisotropic BAO fit to the combined shift blinding applied to the BOSS DR12 data. The figure shows 68% and 95% confidence level marginalised posteriors of $\alpha_\parallel$ and $\alpha_\perp$ obtained when fitting the BAO anisotropic model to the blinded (red contours) and the original CMASS catalog (blue contours) post-reconstruction. In the left panel the same reference growth rate $f = 0.784$ was used, while in the right panel we performed reconstruction on the blinded catalog with $f = 0.695$ corresponding to the growth history we aimed to blind for. The dashed contours are obtained by correcting the blinded posteriors by eqs. (4.4) and (4.5) (fast unblinding) as indicated by the arrows. Blue dotted lines mark the best-fit parameters obtained after rerunning the BAO analysis on the unblinded catalog.

Next, we unblind in two steps as anticipated in figure 1. First, from our knowledge of $\Delta\boldsymbol{\Omega}$ we can directly use eqs. (3.17) and (3.19) to predict the expected underlying results:

$$\begin{aligned} \alpha_\perp(z_*) &= \frac{D_M^{\rm shift}(z_*)}{D_M^{\rm ref}(z_*)}\alpha'_\perp(z'_*)\,, \\ \alpha_\parallel(z_*) &= \frac{H^{\rm ref}(z_*)}{H^{\rm shift}(z_*)}\alpha'_\parallel(z'_*)\,, \\ f &= f' - f^{\rm shift} + f^{\rm\ ref}\,, \end{aligned} \tag{5.3}$$

where the primed quantities are measured from the blinded data. These shifts are indicated by the black arrows and yield the dashed contours in figures 15 and 16. Then we repeat the analysis on the unblinded (original) catalogs with the same settings as for the blinded catalogs. The results are represented by the blue contours in figures 15 and 16, where the position of the corresponding best fit parameters is represented by the vertical dotted blue lines.

LOWZ and CMASS samples have been blinded coherently, but LOWZ is at lower redshift and covers a smaller effective volume; as a result the blinding-induced shift is less significant in LOWZ than in CMASS.

Figure 15 shows an excellent agreement between the best-fit scaling parameters obtained from the full shape analysis of the original catalog and those obtained from the blinded catalog



JCAP09(2020)052

after correction of the estimated posterior. For $f\sigma_8$ we observe a larger difference between the measured and predicted, but this is a small fraction of a standard deviation, which in any case is consistent with the effect of sample variance, as observed in the mocks (see figure 12). The size and shape of the confidence regions is also well recovered by the blinded posterior after correction.

Figure 16 highlights the agreement of mean values and confidence regions of the scaling parameters obtained post reconstruction from the anisotropic BAO analysis of the original catalog and of the blinded catalog after correction. The mean values of scaling parameters are recovered particularly accurately after unblinding (keeping in mind that reconstruction step has been implemented on the blinded catalog). The figure also shows that the choice of the adopted value of the growth rate parameter for reconstruction is not important: the difference between the underlying and blinding values, $\Delta f \sim 0.09$ does not lead to a significant change for the mean values nor for the error bars. We do observe that the choice of the shifted growth rate delivers a slightly better match between the corrected and the original posteriors (especially regarding the shape and not so much the position of the peak), but this can be subject to statistical fluctuations.

The results of all fits described in this section are presented in table 4. As already shown in figures 15 and 16, the recovered mean values by applying the "correction" of eq. (5.3) to blinded catalogs agree very well with the actual measurements from the original catalogs. Furthermore, we see that they do not significantly change the error bars. We observe differences of the best-fit $\chi^2$ between blinded and original catalogs, but there is no preference towards increasing or decreasing it: for LOWZ it decreases after unblinding, while for CMASS it increases. We argue, that this is likely to be a statistical fluctuation, that we also observed for pairs of blinded/original mock catalogs (see for instance figure 14). All results obtained from the original catalogs are within $1-\sigma$ agreement with previous analyses such as [62]. Though, small difference sourced from the different choice of redshift cuts is expected.

Finally, table 4 as well as figures 15 and 16 demonstrate that the blinding procedure presented here is suitable to be applied to a real survey and it comfortably meets all the criteria we initially required for a good blinding scheme.

## 6 Conclusions and discussion

We have presented a novel catalog-level blinding scheme for galaxy redshift surveys. We have shown how it is possible to shift the position of galaxies in a redshift- and density-dependent way along the line of sight as to implement designed modifications to the measurements of expansion history and growth rate. In particular it is possible to modify in a fully controlled way, the physical parameters $\alpha_\parallel, \alpha_\perp, f\sigma_8$, where the first two (scaling parameters) describe the background expansion history and the latter the growth of perturbations. These parameters can be shifted coherently across redshift and galaxy samples according to a chosen cosmological model, but shifts can also be applied in a much more flexible way. By not altering the galaxies' angular positions, this approach avoids adding unnecessary complications into the treatment of angular systematics and makes accidental unblinding extremely unlikely. In addition, the blinding technique does not significantly affect the shape of the marginalised posterior distributions of the measured parameters when the covariance matrix appropriately describe the blinded statistics.

An executive summary of our blinding scheme is shown in figure 17. It can be understood as a zoom into the "blind box" of figure 1, that shows our proposal for how to embed blinding in standard clustering analyses.



JCAP09(2020)052

| Fit | Sample | Case | $\alpha_\parallel$ | $\alpha_\perp$ | $f\sigma_8$ | $\chi^2$/ndf |
|---|---|---|---|---|---|---|
| FS | LOWZ | blinded | $1.046 \pm 0.079$ | $0.927 \pm 0.042$ | $0.303 \pm 0.091$ | $45.3/(68-11)$ |
| | | unblinded | $1.085 \pm 0.082$ | $0.945 \pm 0.043$ | $0.383 \pm 0.091$ | $45.3/(68-11)$ |
| | | original | $1.086 \pm 0.077$ | $0.943 \pm 0.043$ | $0.398 \pm 0.092$ | $46.5/(68-11)$ |
| | CMASS | blinded | $0.966 \pm 0.040$ | $0.965 \pm 0.020$ | $0.370 \pm 0.050$ | $38.8/(68-11)$ |
| | | unblinded | $1.017 \pm 0.042$ | $0.995 \pm 0.021$ | $0.424 \pm 0.050$ | $38.8/(68-11)$ |
| | | original | $1.027 \pm 0.038$ | $0.994 \pm 0.019$ | $0.431 \pm 0.047$ | $57.8/(68-11)$ |
| BAO + post-recon ($f^{\text{ref}}$) | LOWZ | blinded | $0.977 \pm 0.042$ | $0.997 \pm 0.033$ | - | $61.3/(68-17)$ |
| | | unblinded | $1.014 \pm 0.047$ | $1.018 \pm 0.036$ | - | $61.3/(68-17)$ |
| | | original | $0.997 \pm 0.039$ | $1.036 \pm 0.032$ | - | $48.9/(68-17)$ |
| | CMASS | blinded | $0.889 \pm 0.019$ | $0.980 \pm 0.015$ | - | $45.2/(68-17)$ |
| | | unblinded | $0.935 \pm 0.021$ | $1.010 \pm 0.016$ | - | $45.2/(68-17)$ |
| | | original | $0.941 \pm 0.018$ | $1.008 \pm 0.014$ | - | $59.6/(68-17)$ |
| BAO + post-recon ($f^{\text{shift}}$) | LOWZ | blinded | $0.979 \pm 0.042$ | $0.995 \pm 0.033$ | - | $64.8/(68-17)$ |
| | | unblinded | $1.015 \pm 0.045$ | $1.015 \pm 0.034$ | - | $64.8/(68-17)$ |
| | | original | $0.997 \pm 0.039$ | $1.036 \pm 0.032$ | - | $48.9/(68-17)$ |
| | CMASS | blinded | $0.893 \pm 0.019$ | $0.977 \pm 0.015$ | - | $44.9/(68-17)$ |
| | | unblinded | $0.940 \pm 0.021$ | $1.007 \pm 0.016$ | - | $44.9/(68-17)$ |
| | | original | $0.941 \pm 0.018$ | $1.008 \pm 0.014$ | - | $59.6/(68-17)$ |

**Table 4**. Parameter results, errors and best-fit $\chi^2$ for all the fits on BOSS LOWZ and CMASS data presented in this section. The full chains, bestfit values and the blinded catalogs can be found at https://github.com/SamuelBrieden/BlindingCatalogs. The first rows correspond to the FS fits on the blinded, original and corrected catalogs. The second and third groups of rows refer to the correction given by eq. (5.3) and visualized in figures 15 and 16. The following rows represent the BAO anisotropic fits on reconstructed catalogs, where reconstruction of blinded catalogs was carried out either with the reference growth rate or the shifted growth rate. Note that for the original catalogs we always used the reference growth rate.

By applying the proposed blinding scheme to a suite of mock survey catalogs, we have shown (either explicitely or by construction) that it satisfies all the requirements for a good blinding procedure: *i)* the effect on observables and best-fit parameters can be predicted easily; *ii)* it is difficult to unblind accidentally; *iii)* it does not interfere with key analysis aspects (especially regarding systematics); *iv)* it does not change significantly the error bars; *v)* it is not too numerically intensive *vi)* it is easy to infer unblinded parameter constraints with enough accuracy prior to rerun the analysis pipeline again on the original catalog.

In particular, we have verified and quantified the robustness and accuracy of the proposed blinding scheme regarding points *iv)* and *vi)*; the parameters posterior obtained for the blind catalog can be shifted back analytically to recover to a good approximation the posterior for the original catalog. This can be done for example, directly from the output of MCMCs. In addition, the proposed blinding methodology fulfills points *i)* and *v)* by design. The most numerically intensive step is the RSD-blinding step which takes as much time as applying the reconstruction algorithm to the catalog. In our configuration using BOSS catalogs this takes 5-7 minutes on a dual core CPU depending on the Sample it is applied to. This is comparably mild given that the blinding code needs to be applied to the data once, and not to thousands of mock realisations.



JCAP09(2020)052

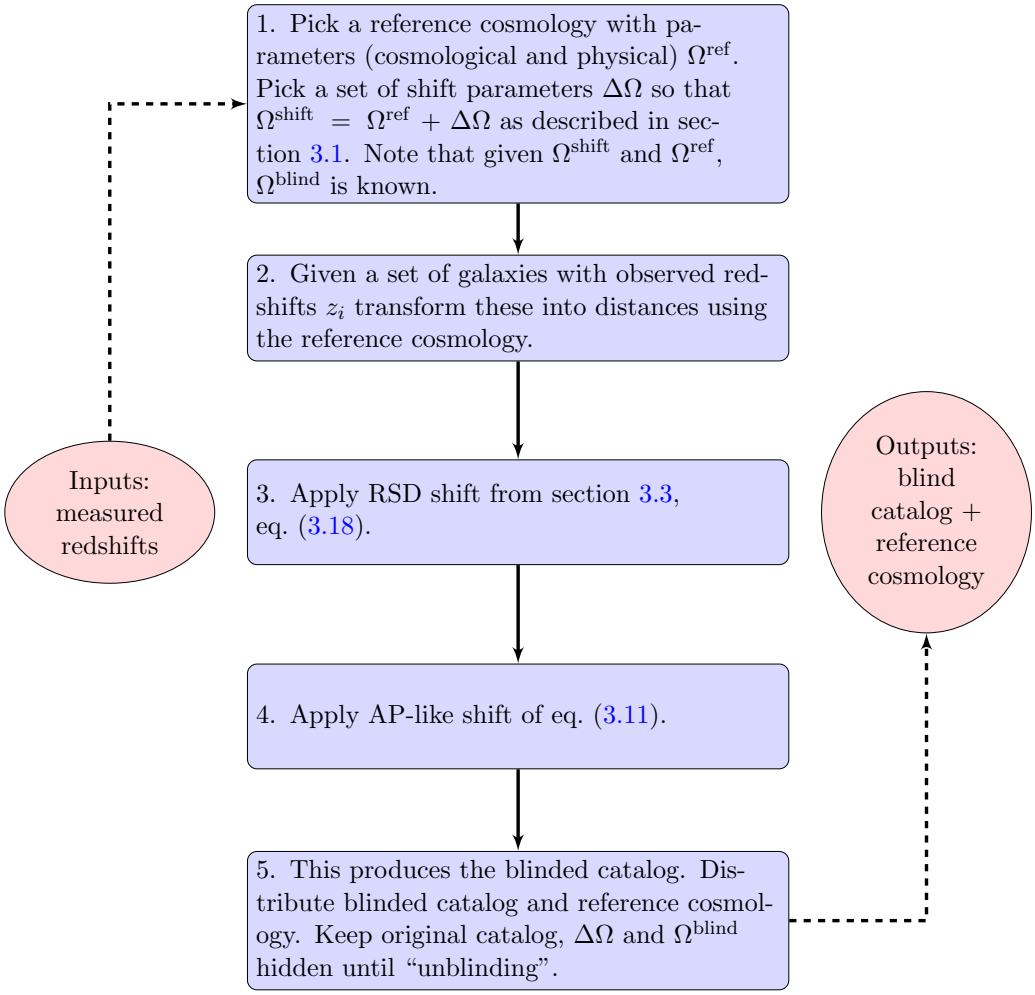


**Figure 17**. Summary of the proposed blinding procedure presented in this paper. In case that blinding for the growth rate is not necessary, step 3 can be skipped.

The optimal performance of the blinding (regarding points *iv)* and *vi)*) depends on the magnitude of the blinding shift applied: the larger the shift the less robust the approach becomes; too large deviations between the reference and the shifted cosmology can spoil the predictability of the blinding scheme, because some of the usually made approximations may fail (fixed covariance matrix, adoption of reference model etc.). The choice of how much the shifted values can deviate from the reference parameters should depend on the forecasted sensitivity of the data, and should probably not exceed deviations of $3\sigma$. We have demonstrated how a large shift leads to a (graceful) degradation of performance by shifting the growth rate parameter by 50%; even in this extreme case, only point *vi)* slightly looses accuracy.

To satisfy all the above criteria to a high level of fidelity (especially point *iv)*) the approach can be tuned (beyond setting reasonable shifts amplitudes). For example, the



JCAP09(2020)052

smoothing scale intrinsic to the reconstruction procedure may be adjusted to reduce noise, but a sub-optimal choice does not affect the recovered parameter values. Similarly, the choice of the linear bias parameter and the growth rate $f$ adopted for the reconstruction step, may affect the error-bars estimated from the (blinded or original) catalog, if they do not match the "underlying values". However, in this work we have found that the effect of the latter is very small.

Another point, also common to the traditional (non-blind) analyses, is the calibration of the mock survey catalogs used to estimate the covariance matrix. It is well known that to yield a correct estimate of the parameters errors, the amplitude of clustering in the mocks used to estimate the covariance must match the clustering amplitude of the data. But the clustering amplitude is not well known when the mocks are being created (before the data are taken and/or because the data are blind). Usually this calibration is done at the halo occupation distribution level and on small non-cosmological scales, and in this case one has the freedom to calibrate the mocks to the blinded data or to the original catalog. Should the mocks be calibrated on the blind catalog, one possibility is that, at the unblinding step, the galaxies positions in the mocks can be shifted "back" with a procedure similar to the blinding done on the data but in the opposite direction. In this way the mocks would match more closely the clustering properties of the original data.

Finally we have applied the procedure to the BOSS DR12 data release, which serves also as an illustrative example of how the whole process (from original data, to build catalog, analysis, unblinding procedure until final results) could be implemented in practice. Even for BOSS data, we have demonstrated that the blinding procedure recovers to high accuracy the official (original) results.

However, our idea laid out in figure 1 of how to implement the blinding procedure in the analysis pipeline can be further adapted depending on specific needs of the collaboration/survey. Other ways are possible: instead of creating a single blinded catalog only, one can create several ones to be analyzed by different subgroups of the collaboration or circulate the blinded catalogs together with the original catalog. We prioritize our proposal to create a single blind catalog to be used by all collaboration members, because this maintains the possibility to cross-check between subgroups. Also we prefer to leave the original catalog hidden until unblinding, because it makes blinding more robust avoiding potential accidental or willing unblinding.

For the magnitude of the blinding shift with respect to the anticipated (Fisher-forecasted) sensitivity we suggested to choose values up to $3\sigma$ to ensure that the assumption of a parameter-independent (fixed) covariance does still hold. Again, this number is not set in stone and should be chosen carefully depending both on the sensitivity of the experiment and the "state-of-the-art" knowledge of the parameters in question. We have worked here under the assumption that the covariance matrix is computed only once and is not changed with the blinding/unblinding procedure. However, if computationally feasible, the covariance matrix could be initially calibrated on the blinded catalogs and then re-calibrated on the unblinded one. This approach would support larger shifts.

We have not discussed the criteria for freezing the analysis pipeline and going ahead with unblinding because this may also be very experiment-specific. We have only commented here that any criteria based on the value of the best-fit $\chi^2$ (whether can be deemed acceptable or not) should take into consideration the spread in best-fit $\chi^2$ values observed in figure 14. The spread in best-fit $\chi^2$/ndf values for both the original catalog and the blinded one range from $\sim 0.5$ to $\sim 1.5$. The spread induced by blinding is a fraction of that scatter and there



JCAP09(2020)052

is no systematic trend: blinding does not statistically alter the best-fit $\chi^2$ values, but the criteria for defining an "acceptable" $\chi^2$ should be calibrated on a suite of survey mocks.

While we have only tested explicitly the full shape and anisotropic BAO analyses, there is no reason to believe that the proposed scheme would not work for non-template-based analysis methods such as EFTofLSS [63, 64]. Moreover, being only a line-of-sight shift, it is probably possible to generalise the scheme to other tracers such as Lyman-$\alpha$, quasars or line-intensity mapping.

To conclude, we have presented a fast, robust and reliable catalog-level blinding scheme for galaxy redshift catalogs. Although this work is motivated to be applied to spectroscopic surveys, we do not see any obvious limitation for it to be used in future photometric surveys as well. We envision that it will be of value to increase the robustness of cosmological results from forthcoming LSS surveys and making their cosmological implications free from possible confirmation bias and experimenter's bias. We make publicly available at https://github.com/SamuelBrieden/BlindingCatalogs the following products: BOSSDR12 data and 100 PatchyMock catalogs, that have all been blinded using the "Combined" case given in table 2 as well as associated power spectrum measurements, Monte Carlo Markov chains and bestfit values for the FS and BAO (pre- and postreconstruction) models.

## Acknowledgments

We acknowledge the DESI collaboration and the GC working group for motivating us to explore catalog-based blinding for galaxy redshift surveys, and we thank them for "keeping us real". We thank Hee-Jong Seo, Lado Samushia and Alexander Mead for useful comments on the draft. We thank Gaby Perez and the IT team at ICCUB for their support and dedication in keeping the computer clusters running despite the difficulties of the prolonged COVID19 lockdown. We thank an anonymous referee for useful comments that improved the quality of this paper. Funding for this work was partially provided by the Spanish MINECO under projects AYA2014-58747-P AEI/FEDER, UE, PGC2018-098866-B-I00,FEDER, UE, and MDM-2014-0369 of ICCUB (Unidad de Excelencia María de Maeztu). HGM and SB acknowledge the support from la Caixa Foundation (ID 100010434) which code LCF/BQ/PI18/11630024. LV acknowledges support by European Union's Horizon 2020 research and innovation programme ERC (BePreSySe, grant agreement 725327). JLB is supported by the Allan C. and Dorothy H. Davis Fellowship.

The massive production of all MultiDark-Patchy mocks for the BOSS Final Data Release has been performed at the BSC Marenostrum supercomputer, the Hydra cluster at the Instituto de Fisica Teorica UAM/CSIC, and NERSC at the Lawrence Berkeley National Laboratory. We acknowledge support from the Spanish MICINNs Consolider-Ingenio 2010 Programme under grant MultiDark CSD2009-00064, MINECO Centro de Excelencia Severo Ochoa Programme under grant SEV- 2012-0249, and grant AYA2014-60641-C2-1-P. The MultiDark-Patchy mocks was an effort led from the IFT UAM-CSIC by F. Prada's group (C.-H. Chuang, S. Rodriguez-Torres and C. Scoccola) in collaboration with C. Zhao (Tsinghua U.), F.-S. Kitaura (AIP), A. Klypin (NMSU), G. Yepes (UAM), and the BOSS galaxy clustering working group. Funding for SDSS-III has been provided by the Alfred P. Sloan Foundation, the Participating Institutions, the National Science Foundation, and the U.S. Department of Energy Office of Science. The SDSS-III web site is http://www.sdss3.org/.

SDSS-III is managed by the Astrophysical Research Consortium for the Participating Institutions of the SDSS-III Collaboration including the University of Arizona, the Brazilian



JCAP09(2020)052

Participation Group, Brookhaven National Laboratory, Carnegie Mellon University, University of Florida, the French Participation Group, the German Participation Group, Harvard University, the Instituto de Astrofisica de Canarias, the Michigan State/Notre Dame/JINA Participation Group, Johns Hopkins University, Lawrence Berkeley National Laboratory, Max Planck Institute for Astrophysics, Max Planck Institute for Extraterrestrial Physics, New Mexico State University, New York University, Ohio State University, Pennsylvania State University, University of Portsmouth, Princeton University, the Spanish Participation Group, University of Tokyo, University of Utah, Vanderbilt University, University of Virginia, University of Washington, and Yale University.

JCAP09(2020)052

## A Effect of choice of smoothing scale

Here we extend the discussion on the choice of smoothing scale which was touched upon in section 4.4. Figure 8 illustrates that adopting a too small smoothing scale produces a field dominated by nonlinear velocities, which are hard to model. A too large smoothing scale instead washes out small scale perturbations. Since the $f$ parameter is affected by blinding only at scales above the smoothing scale, choosing a smoothing scale that is too large compared to the smallest scales included in the analysis would yield an effective scale-dependent $f$ in the blinded catalog. When applying the RSD shift to a catalog different from BOSS, we envision that the choice of smoothing scale should be calibrated on specific survey mocks beforehand. However, we do not expect that using a suboptimal smoothing will have a significant impact on the results.

Figure 18 shows mean ($f\sigma_8$) values, errors and best-fit $\chi^2$ before and after blinding for different smoothing scales for LOWZ and CMASS mocks. We can see from the left column, that in all cases the mean values of ($f\sigma_8$) are nearly identical. Only in the case of $R_{\rm sm} = 15\ h^{-1}\,$Mpc the distribution is slightly broadened. This is also reflected by the error distribution presented in the middle column, showing a small increase of the errors after blinding. For smaller smoothing scales the error bars do not deviate from the original ones. From the right panels we see that there is a non-significant trend towards higher $\chi^2$ with decreasing smoothing scale. Note that the overall $\chi^2$ distribution is slightly offset from the diagonal. This is related to the fact, that we show here a very extreme blinding shift towards $\gamma = 1.0$. We do not observe a systematic discrepancy in $\chi^2$ before and after blinding for more realistic blinding scenarios, as shown in figure 14.

We conclude that the dependence of the performance of the blinding procedure the specific choice of the smoothing scale is small enough, so that it does not need to be included in the modeling when analysing blinded catalogs. However, we suggest to calibrate the smoothing scale on mocks beforehand in order to minimise mis-estimation of the error bars.

## B Impact of deviations from the reference cosmology

Here, we study whether the template used for the FS analysis has any impact on parameter constraints when applied to blinded catalogs. Other works ([44, 45, 65]) have shown that the model-independent template fit approach delivers robust BAO and RSD results independent of the choice of template. To validate that these findings also hold for galaxy catalogs, that have been modified using the blinding scheme presented here, we proceed as follows.

In addition to the reference template we generate two linear power spectra with a cosmology far away from the reference one, that we call Low-Om and High-Om. They have

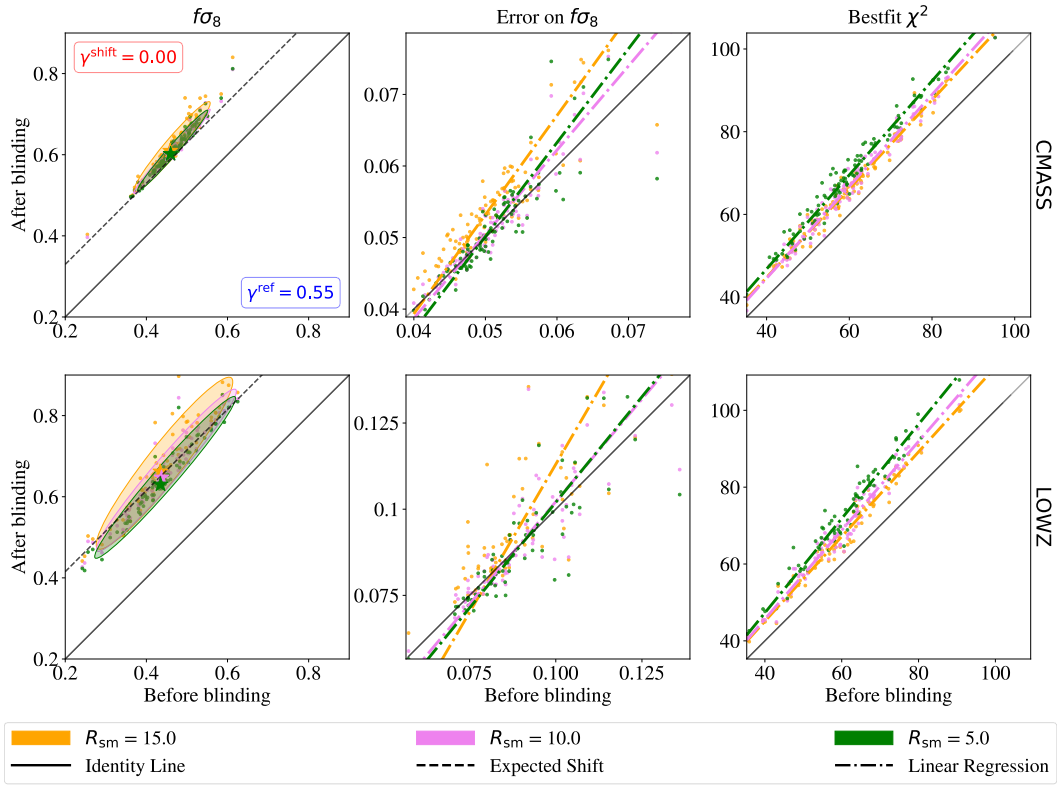


**Figure 18**. This figure shows FS fit results fo RSD-only blinding on $f\sigma_8$, $\sigma_{f\sigma_8}$ and best fit $\chi^2$ from 100 LOWZ and CMASS realizations. Each panel compares different values of smoothing scale used during the blinding process. The black dashed line in the left panels gives the theoretical expectation for the blinding shift. Colored dashed lines in the middle and right panels are linear regression fits to the mock distributions.

| Cosmology | $\Omega_m$ | $\Omega_b h^2$ | $h$ | $\sigma_8$ | $n_s$ | $M_\nu$ [eV] | $r_\mathrm{d}$ [Mpc] |
|---|---|---|---|---|---|---|---|
| MD-Patchy | 0.307115 | 0.02214 | 0.6777 | 0.8288 | 0.9611 | 0 | 147.66 |
| Ref | 0.31 | 0.022 | 0.676 | 0.8288 | 0.9611 | 0.06 | 147.78 |
| Low-Om | 0.286 | 0.023 | 0.7 | 0.82 | 0.96 | 0 | 147.15 |
| High-Om | 0.35 | 0.022 | 0.676 | 0.814 | 0.97 | 0.056 | 143.17 |

**Table 5**. Values of cosmological parameters and sound horizon at radiation drag for the MD-Patchy mocks cosmology and the cosmologies that were used to generate the different power spectrum templates for this analysis.

either a smaller value with respect to $\Omega_\mathrm{m}^\mathrm{ref}$ of $\Omega_\mathrm{m}^\mathrm{low} = 0.286$ or a higher value of $\Omega_\mathrm{m}^\mathrm{high} = 0.35$ and other differences are specified in table 5.

Next, we fit the FS model to the mean of 1000 original and blinded Patchy mock catalogs using the 3 different templates. We choose a wavevector range of $0.02\,h\,\mathrm{Mpc}^{-1} < k < 0.15\,h\,\mathrm{Mpc}^{-1}$. The mocks are blinded using the reference and shifted cosomology of the "Combined shift" case, specified in table 2.



JCAP09(2020)052

| Case | $\alpha'_\parallel/\alpha_\parallel$ | | $\alpha'_\perp/\alpha_\perp$ | | $f\sigma_8 - (f\sigma_8)'$ | |
|---|---|---|---|---|---|---|
| | $z = 0.33$ | $z = 0.60$ | $z = 0.33$ | $z = 0.60$ | $z = 0.33$ | $z = 0.60$ |
| Expectation | 0.9637 | 0.9502 | 0.9800 | 0.9702 | 0.0809 | 0.0541 |
| Ref | 0.960 ± 0.003 | 0.951 ± 0.002 | 0.982 ± 0.001 | 0.973 ± 0.001 | 0.091 ± 0.003 | 0.054 ± 0.002 |
| Low-Om | 0.965 ± 0.003 | 0.949 ± 0.002 | 0.981 ± 0.002 | 0.972 ± 0.001 | 0.078 ± 0.004 | 0.055 ± 0.003 |
| High-Om | 0.969 ± 0.003 | 0.956 ± 0.002 | 0.985 ± 0.002 | 0.978 ± 0.001 | 0.083 ± 0.004 | 0.058 ± 0.002 |

**Table 6**. The expected deviations in scaling parameters and $f\sigma_8$ between the original and blinded catalogs compared to the results from the fits on the mean of 1000 LOWZ and CMASS mocks for each template. We show ratios/differences instead of absolute values, because their expected values are independent of the template. All differences between expectation and prediction are below the 1% level, even for large deviations in cosmological parameters for the Low-Om and High-Om templates.

The performance of the different templates in reproducing the expected shift in the FS model parameters $\{\alpha_\parallel, \alpha_\perp, f\sigma_8\}$ due to blinding is shown in table 6. The expectation for the ratio of scaling parameters and difference in $f\sigma_8$ between original and blinded catalogs for LOWZ and CMASS is given by the first row. These values are independent of the choice of template, while the absolute values of the scaling parameters are not, because of their dependence on the fiducial cosmology. The subsequent rows show the results obtained from our MCMC fits to the mean of 1000 mocks using the different templates described by the cosmologies presented in table 5. We find a good agreement between theory and expectation for all three choices of template, despite the rather extreme differences among their cosmologies. This shows that galaxy clustering analyses based on a varying template approach can be applied without a problem to blinded catalogs.

## References


[1] DESI collaboration, *The DESI Experiment Part I: Science,Targeting, and Survey Design*, arXiv:1611.00036 [INSPIRE].

[2] EUCLID collaboration, *Euclid Definition Study Report*, arXiv:1110.3193 [INSPIRE].

[3] LSST collaboration, *Science-Driven Optimization of the LSST Observing Strategy*, arXiv:1708.04058 [INSPIRE].

[4] SKA collaboration, *Cosmology with Phase 1 of the Square Kilometre Array: Red Book 2018: Technical specifications and performance forecasts*, *Publ. Astron. Soc. Austral.* **37** (2020) e007 [arXiv:1811.02743] [INSPIRE].

[5] Planck collaboration, *Planck 2018 results. VI. Cosmological parameters*, *Astron. Astrophys.* **641** (2020) A6 [arXiv:1807.06209] [INSPIRE].

[6] K. Arisaka et al., *Improved upper limit on the branching ratio $B(K_L^0 \to mu^\pm e^\pm)$*, *Phys. Rev. Lett.* **70** (1993) 1049 [INSPIRE].

[7] J.R. Klein and A. Roodman, *Blind analysis in nuclear and particle physics*, *Annual Rev. Nucl. Part. Sci.* **55** (2005) 141.

[8] LIGO Scientific, VIRGO collaborations, *Search for Gravitational Waves from Compact Binary Coalescence in LIGO and Virgo Data from S5 and VSR1*, *Phys. Rev. D* **82** (2010) 102001 [arXiv:1005.4655] [INSPIRE].

[9] Supernova Cosmology Project collaboration, *Measurement of Omega(m), Omega(lambda) from a blind analysis of Type Ia supernovae with CMAGIC: Using color information to verify the acceleration of the Universe*, *Astrophys. J.* **644** (2006) 1 [astro-ph/0602411] [INSPIRE].




JCAP09(2020)052

[10] B.R. Zhang et al., *A blinded determination of $H_0$ from low-redshift Type Ia supernovae, calibrated by Cepheid variables*, *Mon. Not. Roy. Astron. Soc.* **471** (2017) 2254 [arXiv:1706.07573] [INSPIRE].

[11] DES collaboration, *Dark Energy Survey year 1 results: Cosmological constraints from galaxy clustering and weak lensing*, *Phys. Rev. D* **98** (2018) 043526 [arXiv:1708.01530] [INSPIRE].

[12] DES collaboration, *Blinding multiprobe cosmological experiments*, *Mon. Not. Roy. Astron. Soc.* **494** (2020) 4454 [arXiv:1911.05929] [INSPIRE].

[13] E. Sellentin, *A blinding solution for inference from astronomical data*, *Mon. Not. Roy. Astron. Soc.* **492** (2020) 3396 [arXiv:1910.08533] [INSPIRE].

[14] K. Kuijken et al., *Gravitational Lensing Analysis of the Kilo Degree Survey*, *Mon. Not. Roy. Astron. Soc.* **454** (2015) 3500 [arXiv:1507.00738] [INSPIRE].

[15] M. Asgari et al., *KiDS+VIKING-450 and DES-Y1 combined: Mitigating baryon feedback uncertainty with COSEBIs*, *Astron. Astrophys.* **634** (2020) A127 [arXiv:1910.05336] [INSPIRE].

[16] C. Blake and S. Bridle, *Cosmology with photometric redshift surveys*, *Mon. Not. Roy. Astron. Soc.* **363** (2005) 1329 [astro-ph/0411713] [INSPIRE].

[17] J. Asorey, M. Crocce, E. Gaztanaga and A. Lewis, *Recovering 3D clustering information with angular correlations*, *Mon. Not. Roy. Astron. Soc.* **427** (2012) 1891 [arXiv:1207.6487] [INSPIRE].

[18] C. Alcock and B. Paczynski, *An evolution free test for non-zero cosmological constant*, *Nature* **281** (1979) 358 [INSPIRE].

[19] N. Kaiser, *Clustering in real space and in redshift space*, *Mon. Not. Roy. Astron. Soc.* **227** (1987) 1.

[20] J.C. Jackson, *Fingers of God: A critique of Rees' theory of primoridal gravitational radiation*, *Mon. Not. Roy. Astron. Soc.* **156** (1972) 1P [arXiv:0810.3908] [INSPIRE].

[21] W.L.W. Sargent and E.L. Turner, *A statistical method for determining the cosmological density parameter from the redshifts of a complete sample of galaxies*, *Ap. J. L.* **212** (1977) L3.

[22] BOSS collaboration, *The clustering of galaxies in the SDSS-III Baryon Oscillation Spectroscopic Survey: Analysis of potential systematics*, *Mon. Not. Roy. Astron. Soc.* **424** (2012) 564 [arXiv:1203.6499] [INSPIRE].

[23] BOSS collaboration, *The clustering of galaxies in the SDSS-III Baryon Oscillation Spectroscopic Survey: baryon acoustic oscillations in the Data Releases 10 and 11 Galaxy samples*, *Mon. Not. Roy. Astron. Soc.* **441** (2014) 24 [arXiv:1312.4877] [INSPIRE].

[24] K.S. Dawson et al., *The SDSS-IV extended Baryon Oscillation Spectroscopic Survey: Overview and Early Data*, *Astron. J.* **151** (2016) 44 [arXiv:1508.04473] [INSPIRE].

[25] A. Lewis, A. Challinor and A. Lasenby, *Efficient computation of CMB anisotropies in closed FRW models*, *Astrophys. J.* **538** (2000) 473 [astro-ph/9911177] [INSPIRE].

[26] D. Blas, J. Lesgourgues and T. Tram, *The Cosmic Linear Anisotropy Solving System (CLASS) II: Approximation schemes*, *JCAP* **07** (2011) 034 [arXiv:1104.2933] [INSPIRE].

[27] H.A. Feldman, N. Kaiser and J.A. Peacock, *Power spectrum analysis of three-dimensional redshift surveys*, *Astrophys. J.* **426** (1994) 23 [astro-ph/9304022] [INSPIRE].

[28] E.V. Linder, *Cosmic growth history and expansion history*, *Phys. Rev. D* **72** (2005) 043529 [astro-ph/0507263] [INSPIRE].

[29] A. Nusser and M. Davis, *On the prediction of velocity fields from redshift space galaxy samples*, *Astrophys. J. Lett.* **421** (1994) L1 [astro-ph/9309009] [INSPIRE].



JCAP09(2020)052

[30] D.J. Eisenstein, H.-j. Seo and M.J. White, *On the Robustness of the Acoustic Scale in the Low-Redshift Clustering of Matter*, *Astrophys. J.* **664** (2007) 660 [astro-ph/0604361] [INSPIRE].

[31] N. Padmanabhan, M. White and J.D. Cohn, *Reconstructing Baryon Oscillations: A Lagrangian Theory Perspective*, *Phys. Rev. D* **79** (2009) 063523 [arXiv:0812.2905] [INSPIRE].

[32] A. Burden, W.J. Percival, M. Manera, A.J. Cuesta, M. Vargas Magaña and S. Ho, *Efficient Reconstruction of Linear Baryon Acoustic Oscillations in Galaxy Surveys*, *Mon. Not. Roy. Astron. Soc.* **445** (2014) 3152 [arXiv:1408.1348] [INSPIRE].

[33] BOSS collaboration, *The clustering of galaxies in the completed SDSS-III Baryon Oscillation Spectroscopic Survey: baryon acoustic oscillations in the Fourier space*, *Mon. Not. Roy. Astron. Soc.* **464** (2017) 3409 [arXiv:1607.03149] [INSPIRE].

[34] H.-J. Seo, F. Beutler, A.J. Ross and S. Saito, *Modeling the reconstructed BAO in Fourier space*, *Mon. Not. Roy. Astron. Soc.* **460** (2016) 2453 [arXiv:1511.00663] [INSPIRE].

[35] H. Gil-Marin, C. Wagner, L. Verde, C. Porciani and R. Jimenez, *Perturbation theory approach for the power spectrum: from dark matter in real space to haloes in redshift space*, *JCAP* **11** (2012) 029 [arXiv:1209.3771] [INSPIRE].

[36] P. McDonald and A. Roy, *Clustering of dark matter tracers: generalizing bias for the coming era of precision LSS*, *JCAP* **08** (2009) 020 [arXiv:0902.0991] [INSPIRE].

[37] T. Baldauf, U. Seljak, V. Desjacques and P. McDonald, *Evidence for Quadratic Tidal Tensor Bias from the Halo Bispectrum*, *Phys. Rev. D* **86** (2012) 083540 [arXiv:1201.4827] [INSPIRE].

[38] S. Saito, T. Baldauf, Z. Vlah, U. Seljak, T. Okumura and P. McDonald, *Understanding higher-order nonlocal halo bias at large scales by combining the power spectrum with the bispectrum*, *Phys. Rev. D* **90** (2014) 123522 [arXiv:1405.1447] [INSPIRE].

[39] H. Gil-Marín et al., *The power spectrum and bispectrum of SDSS DR11 BOSS galaxies –I. Bias and gravity*, *Mon. Not. Roy. Astron. Soc.* **451** (2015) 539 [arXiv:1407.5668] [INSPIRE].

[40] A. Taruya, T. Nishimichi and S. Saito, *Baryon Acoustic Oscillations in 2D: Modeling Redshift-space Power Spectrum from Perturbation Theory*, *Phys. Rev. D* **82** (2010) 063522 [arXiv:1006.0699] [INSPIRE].

[41] W.J. Percival and M. White, *Testing cosmological structure formation using redshift-space distortions*, *Mon. Not. Roy. Astron. Soc.* **393** (2009) 297 [arXiv:0808.0003] [INSPIRE].

[42] M.J. Wilson, J.A. Peacock, A.N. Taylor and S. de la Torre, *Rapid modelling of the redshift-space power spectrum multipoles for a masked density field*, *Mon. Not. Roy. Astron. Soc.* **464** (2017) 3121 [arXiv:1511.07799] [INSPIRE].

[43] BOSS collaboration, *The clustering of galaxies in the completed SDSS-III Baryon Oscillation Spectroscopic Survey: Anisotropic galaxy clustering in Fourier-space*, *Mon. Not. Roy. Astron. Soc.* **466** (2017) 2242 [arXiv:1607.03150] [INSPIRE].

[44] P. Carter, F. Beutler, W.J. Percival, J. DeRose, R.H. Wechsler and C. Zhao, *The impact of the fiducial cosmology assumption on BAO distance scale measurements*, *Mon. Not. Roy. Astron. Soc.* **494** (2020) 2076 [arXiv:1906.03035] [INSPIRE].

[45] J.L. Bernal, T.L. Smith, K.K. Boddy and M. Kamionkowski, *Robustness of baryon acoustic oscillations constraints to beyond-ΛCDM cosmologies*, arXiv:2004.07263 [INSPIRE].

[46] Brieden et al., *Blinding take 2*, in preparation.

[47] A. Burden, W.J. Percival and C. Howlett, *Reconstruction in Fourier space*, *Mon. Not. Roy. Astron. Soc.* **453** (2015) 456 [arXiv:1504.02591] [INSPIRE].

[48] F.-S. Kitaura et al., *The clustering of galaxies in the SDSS-III Baryon Oscillation Spectroscopic Survey: mock galaxy catalogues for the BOSS Final Data Release*, *Mon. Not. Roy. Astron. Soc.* **456** (2016) 4156 [arXiv:1509.06400] [INSPIRE].

JCAP09(2020)052

[49] S.A. Rodríguez-Torres et al., *The clustering of galaxies in the SDSS-III Baryon Oscillation Spectroscopic Survey: modelling the clustering and halo occupation distribution of BOSS CMASS galaxies in the Final Data Release*, *Mon. Not. Roy. Astron. Soc.* **460** (2016) 1173 [arXiv:1509.06404] [INSPIRE].

[50] K. Yamamoto, M. Nakamichi, A. Kamino, B.A. Bassett and H. Nishioka, *A Measurement of the quadrupole power spectrum in the clustering of the 2dF QSO Survey*, *Publ. Astron. Soc. Jap.* **58** (2006) 93 [astro-ph/0505115] [INSPIRE].

[51] D. Bianchi, H. Gil-Marín, R. Ruggeri and W.J. Percival, *Measuring line-of-sight dependent Fourier-space clustering using FFTs*, *Mon. Not. Roy. Astron. Soc.* **453** (2015) L11 [arXiv:1505.05341] [INSPIRE].

[52] A. Gelman and D.B. Rubin, *Inference from iterative simulation using multiple sequences*, *Stat. Sci.* **7** (1992) 457.

[53] J. Hartlap, P. Simon and P. Schneider, *Why your model parameter confidences might be too optimistic: Unbiased estimation of the inverse covariance matrix*, *Astron. Astrophys.* **464** (2007) 399 [astro-ph/0608064] [INSPIRE].

[54] B.D. Sherwin and M. White, *The Impact of Wrong Assumptions in BAO Reconstruction*, *JCAP* **02** (2019) 027 [arXiv:1808.04384] [INSPIRE].

[55] SDSS collaboration, *The Tenth Data Release of the Sloan Digital Sky Survey: First Spectroscopic Data from the SDSS-III Apache Point Observatory Galactic Evolution Experiment*, *Astrophys. J. Suppl.* **211** (2014) 17 [arXiv:1307.7735] [INSPIRE].

[56] BOSS collaboration, *The Baryon Oscillation Spectroscopic Survey of SDSS-III*, *Astron. J.* **145** (2013) 10 [arXiv:1208.0022] [INSPIRE].

[57] SDSS collaboration, *SDSS-III: Massive Spectroscopic Surveys of the Distant Universe, the Milky Way Galaxy, and Extra-Solar Planetary Systems*, *Astron. J.* **142** (2011) 72 [arXiv:1101.1529] [INSPIRE].

[58] Cutler Group, LP collaborations, *Spectral Classification and Redshift Measurement for the SDSS-III Baryon Oscillation Spectroscopic Survey*, *Astron. J.* **144** (2012) 144 [arXiv:1207.7326] [INSPIRE].

[59] S. Smee et al., *The Multi-Object, Fiber-Fed Spectrographs for SDSS and the Baryon Oscillation Spectroscopic Survey*, *Astron. J.* **146** (2013) 32 [arXiv:1208.2233] [INSPIRE].

[60] SDSS-III collaboration, *The Eleventh and Twelfth Data Releases of the Sloan Digital Sky Survey: Final Data from SDSS-III*, *Astrophys. J. Suppl.* **219** (2015) 12 [arXiv:1501.00963] [INSPIRE].

[61] H. Gil-Marín et al., *The clustering of galaxies in the SDSS-III Baryon Oscillation Spectroscopic Survey: BAO measurement from the LOS-dependent power spectrum of DR12 BOSS galaxies*, *Mon. Not. Roy. Astron. Soc.* **460** (2016) 4210 [arXiv:1509.06373] [INSPIRE].

[62] H. Gil-Marín et al., *The clustering of galaxies in the SDSS-III Baryon Oscillation Spectroscopic Survey: RSD measurement from the LOS-dependent power spectrum of DR12 BOSS galaxies*, *Mon. Not. Roy. Astron. Soc.* **460** (2016) 4188 [arXiv:1509.06386] [INSPIRE].

[63] G. D'Amico et al., *The Cosmological Analysis of the SDSS/BOSS data from the Effective Field Theory of Large-Scale Structure*, *JCAP* **05** (2020) 005 [arXiv:1909.05271] [INSPIRE].

[64] M.M. Ivanov, M. Simonović and M. Zaldarriaga, *Cosmological Parameters from the BOSS Galaxy Power Spectrum*, *JCAP* **05** (2020) 042 [arXiv:1909.05277] [INSPIRE].

[65] Gil-Marín et al., *The completed sdss-iv extended baryon oscillation spectroscopic survey: measurement of the bao and growth rate of structure of the luminous red galaxy sample from the anisotropic power spectrum between redshifts 0.6 and 1.0*, in preparation.

JCAP09(2020)052

# Part II

# SHAPEFIT

# 3

# EXTRACTING THE POWER SPECTRUM SHAPE

The second important pillar of the research presented in this thesis is the development of 'ShapeFit', as of now comprising four articles [2–5], three of them published. ShapeFit is a tool to extract information beyond BAO and RSD from galaxy maps. By adding a "shape" parameter to the standard BAO+RSD analysis pipeline and adapting the definition of the matter fluctuation amplitude, it is possible to capture most of the cosmological information in galaxy power spectra, that only the alternative direct model fits (or 'full modeling' (FM) fits) have been able to extract.

The first article [2] presented in this chapter exhibits not only the full derivation of the relevant ShapeFit equations (section three) but also an in-depth comparison with the alternative FM technique at the level of cosmology inference (sections 4 and 5). Furthermore, in section 2 it provides a deep understanding of the issue at hand, the difference between standard fixed template fits and FM fits, where table 2 and figures 2 and 3 are particularly relevant. Last but not least, in section 6 we propose a new method to correct at the data-level for the fact that the mode-averaged power spectrum measurements do not coincide with the naive bin-average usually applied within the theory model on large scales, we call it "geometrical effect". We run additional systematic tests (also in numerous appendices) on the Nseries LRG mocks before concluding in section 7. Additional systematic tests are carried out in several appendices, where especially the result of appendix B is interesting: it shows explicitely that ShapeFit reduces the residual template dependence of the standard RSD analysis.[1]

An overview of the ShapeFit method highlighting the modifications with respect to the standard RSD analysis is provided in figure 5.

1 In this publication the term "RSD analysis" is equal to the "FS" or "BAO+RSD analysis" as introduced in chapter 1.3. Note that, with the advent of FM analyses the pre-existing nomenclature became ambiguous and the community has not yet agreed on a single naming scheme. Hence, the analysis names are chosen depending on the context, where care is taken to provide the exact definitions of what kind of analysis is meant by each name.

Journal of Cosmology and Astroparticle Physics
An IOP and SISSA journal

# ShapeFit: extracting the power spectrum shape information in galaxy surveys beyond BAO and RSD

**Samuel Brieden,**[a,b] **Héctor Gil-Marín**[a] **and Licia Verde**[a,c]

[a]ICC, University of Barcelona,
IEEC-UB, Martí i Franquès, 1, E-08028 Barcelona, Spain
[b]Dept. de Física Quàntica i Astrofísica, Universitat de Barcelona,
Martí i Franquès 1, E-08028 Barcelona, Spain
[c]ICREA,
Pg. Lluís Companys 23, Barcelona, E-08010, Spain

E-mail: sbrieden@icc.ub.edu, hectorgil@icc.ub.edu, liciaverde@icc.ub.edu

Received June 22, 2021
Revised October 22, 2021
Accepted November 22, 2021
Published December 24, 2021

**Abstract.** In the standard (classic) approach, galaxy clustering measurements from spectroscopic surveys are compressed into baryon acoustic oscillations and redshift space distortions measurements, which in turn can be compared to cosmological models. Recent works have shown that avoiding this intermediate step and fitting directly the full power spectrum signal (full modelling) leads to much tighter constraints on cosmological parameters. Here we show where this extra information is coming from and extend the classic approach with one additional effective parameter, such that it captures, effectively, the same amount of information as the full modelling approach, but in a model-independent way. We validate this new method (*ShapeFit*) on mock catalogs, and compare its performance to the full modelling approach finding both to deliver equivalent results. The *ShapeFit* extension of the classic approach promotes the standard analyses at the level of full modelling ones in terms of information content, with the advantages of *i)* being more model independent; *ii)* offering an understanding of the origin of the extra cosmological information; *iii)* allowing a robust control on the impact of observational systematics.

**Keywords:** cosmological parameters from LSS, galaxy clusters, power spectrum, redshift surveys

**ArXiv ePrint:** 2106.07641


https://doi.org/10.1088/1475-7516/2021/12/054

JCAP12(2021)054

## Contents



JCAP12(2021)054

## 1 Introduction

Observations of the Cosmic Microwave Background (CMB, e.g., [1, 2]) radiation have been pivotal in establishing the standard cosmological model (the so-called ΛCDM model) and to open the doors to precision cosmology. The CMB has, however, the fundamental limitation of originating from a 2D surface at a given cosmic epoch. Observations of the Large Scale Structure (LSS) over large 3D volumes can yield a dramatic increase in the number of accessible modes and trace the evolution of clustering across cosmic times.

The three-dimensional clustering of galaxies is rapidly becoming one of the most promising avenue to study cosmology from the late-time Universe. Spectroscopic galaxy redshift surveys have witnessed a spectacular success covering increasing larger volumes: 2-degree Field (2dF, [3]), Sloan Digital Sky Survey II (SDSS-II, [4]), SDSS-III Baryon Oscillation spectroscopic Survey (BOSS, [5–7]), SDSS-IV extended BOSS (eBOSS, [8–10]); and this trend is set to continue: the on-going Dark Energy Spectroscopic Instrument (DESI, [11, 12]) and up-coming Euclid satellite mission [13], as just two examples.

Baryon Acoustic Oscillations (BAO) is an imprint in the power spectrum of sound waves in the pre-recombination Universe offering a "standard ruler" observable through galaxy clustering [14–21]. The standard approach to analyse galaxy redshift clustering, used extensively and part of official surveys' pipelines, has used the standard ruler signature in the galaxy power spectrum to obtain determinations of the distance-redshift relation at the effective redshift of the surveys' samples exploiting the Alcock-Paczynski effect [22]. The process of density-field reconstruction, e.g., [23], is widely adopted to reduce the information loss induced by non-linearities. In this approach, the geometric information extracted from the BAO peak position is largely model-independent: the physical quantity constrained is directly related to the expansion history and independent of the parametrization of the expansion history given by specific cosmological models. The reconstruction step induces some model-dependence but this has been shown to be very weak [24]. Redshift Space Distortions (RSD, pioneered by [25]) arise from the non-linear relation between cosmological distances — natural input to the theory modelling — and the (observed) redshifts. They enclose information about the velocity field and have been used to extract constraints on the amplitude of velocity fluctuations times the dark matter amplitude fluctuations, characterized by the parameter combination $f\sigma_8$.

BAO and RSD results and their cosmological interpretation for state-of-the-art surveys have been presented e.g., in [26], for the SDSS-III BOSS survey, and in [27], for the SDSS-IV eBOSS survey, and the success of this approach is behind much of the science case for forthcoming surveys. From now on we refer to this, now standard, approach as "classic"[1] The classic approach is conceptually different from the way, for example, CMB data are interpreted and from the analysis of LSS data pre-BAO era (see e.g., [28–31]). When the BAO detection in galaxy redshift surveys became of high enough signal to noise, it was quickly recognized that it carried most of the interesting signal, see e.g., [32, 33], and the community then adopted the, now classic, BAO and RSD approach. BAO and RSD analyses, with the help of a template of the power spectrum, compress the power spectrum data into few physical observables which are sensitive only to late-time physics, and it is these observables that are then interpreted in light of a cosmological model. CMB data analyses, on the other

[1] Classic in the Merriam Webster dictionary: serving as a standard of excellence, of recognized value. We use here the word classic as "of high quality standard in its respective genre based on judgement over a period of time" and "can be considered as standard".



JCAP12(2021)054

hand, compare directly the measured power spectrum to the model prediction, requiring the choice of a cosmological model to be done *ab initio*. Recently, the development of high performance codes based on the FFTLog algorithm [34] giving rise to fast model evaluations of, for instance, the so-called "Effective Field Theory of Large Scale Structure", e.g., [35–42], has prompted part of the community to analyse galaxy redshift clustering in a similar way as CMB and pre-BAO era LSS data (see e.g., [28–30] and references therein), by comparing directly the observed power spectrum, including the BAO signal, the RSD signal, as well as the full shape of the broadband power to the model's prediction. A full Markov Chain Monte Carlo (MCMC) exploration of the cosmological parameter space can then be performed obtaining cosmological constraints significantly tighter than in the standard analysis. For example [39, 40], imposing a Big Bang Nucleosynthesis (BBN) prior, obtain a 1.6% constraint on the Hubble constant, which is instead very mildly ($\sim 10\%$) constrained in the standard approach (see e.g., red contours in figure 5 of [27]). In what follows, we refer to this approach as "full modelling", to highlight the fact that while currently Effective Field Theory of Large Scale Structure is the theoretical modelling of choice for this approach, other choices are also possible.

The additional constraining power afforded by the second approach must arise, at least in part, from the broadband shape of the power spectrum, but a full physical interpretation of the origin of the extra constraining power is still lacking (but see e.g., [43] and refs. therein).

This paper serves three main objectives: 1) identify clearly where the additional information comes from and what physical processes it corresponds to, 2) bridge the classic and new analyses in a transparent way and 3) extend the classic analysis in a simple and effective manner to capture the bulk of this extra information. In passing, we also present a new definition and interpretation of the physical parameter describing amplitude of velocity fluctuations which further reduce the model-dependence of the traditional RSD analysis. We stress here that the theoretical models for the power spectra adopted by the published works of the "classic" and "full modelling" approaches are different. The main motivation of this paper is not to do a first principles comparison including all combinations of theoretical models and fitting methodologies. In this paper we stick to the theoretical models and fitting methodologies as adopted in the literature, using as much as possible codes made publicly available by the authors of the relevant papers. When extending the classic approach we will take care in introducing as minimal modifications as possible. The rest of the paper is organized as follows: in section 2 we review the known approaches for the cosmological interpretation of galaxy clustering. While this is background material it serves the purpose of highlighting differences and similarities across approaches and make explicit their dependence on (or independence of) assumptions about a cosmological model. Section 3 introduces the phenomenological extension of the classic approach, which we call *ShapeFit*, an executive summary of it in the form of a flowchart is presented in figure 5, and section 4 presents our setup for its application to mock catalogs. In section 5 we show a direct comparison between the different analysis approaches and perform additional systematic tests of the proposed *ShapeFit* in section 6. The conclusions are presented in section 7. The appendices present technical details and relevant systematic tests.

## 2 Theoretical background

In this section we provide an overview of the most common LSS analysis strategies to date. To understand how to compare them directly with each other, and how to interpret the resulting



JCAP12(2021)054

parameter constraints as done in section 2.4, it is important to spell out clearly what physical processes, what observational features and what model ingredients are relevant for each of the approaches. This background section serves for this purpose.

### 2.1 The ΛCDM model: notation and definitions

If not stated otherwise, we work in the flat ΛCDM model with the following parameter basis

$$\mathbf{\Omega} = \{\Omega_i\} = \{\omega_{\rm cdm}, \omega_{\rm b}, h, \sigma_8, n_s, M_\nu\} \,, \tag{2.1}$$

where $\omega_{\rm cdm}$ and $\omega_{\rm b}$ are the physical density parameters of the cold dark matter and baryons respectively. In addition, we use the subscript 'cb' to refer to the cold dark matter + baryon component, m for the total matter including non-relativistic neutrinos, and $\nu$ for neutrinos. When the dimensionless Hubble-Lemaître parameter, $h$, is introduced $H_0 = h \times 100$ km s$^{-1}$ Mpc$^{-1}$, they are related to the energy density fractions $\Omega_X$ for any species $X \in \{\rm b, cdm, m, r, \gamma, \nu, \Lambda, \dots\}$ for baryons, cold dark matter, matter, relativistic species, photons, neutrinos, cosmological constant, etc., as

$$\omega_X = \Omega_X h^2. \tag{2.2}$$

Within the flat ΛCDM model these quantities fulfill the budget equation

$$\underbrace{\Omega_\gamma + \Omega_{\nu,r}}_{\Omega_{\rm r}} + \underbrace{\Omega_{\rm cdm} + \Omega_{\rm b} + \Omega_{\nu,m}}_{\Omega_{\rm m}} + \Omega_\Lambda = 1 \tag{2.3}$$

at all times. The physical photon densiy $\omega_\gamma$ is effectively fixed by the precise COBE measurement of the CMB temperature $T_0 = 2.7255 \pm 0.0006$ [44], via

$$\omega_\gamma = \frac{8\pi^3 T_0^4}{45\,(H_0/h)^2\, M_P^2} = (2.472 \pm 0.002) \times 10^{-5} \,, \tag{2.4}$$

where $M_P$ is the Planck mass in natural units. This measurement of $\omega_\gamma$ is commonly used as a prior, and its central value is implicitly adopted within the term "flat ΛCDM". In the following we stick to this convention, although one could in principle allow $T_0$ to be a free parameter [45].

We also include the sum of the neutrino masses $M_\nu$ as a free parameter, where we choose 2 massless states (counted as radiation) and 1 massive state (counted as matter).

On the background level, assuming homogeneity and isotropy on large scales, the geometry of the universe is fully described by the Hubble expansion rate as function of redshift, $z$,

$$H(z) = H_0 \sqrt{(1+z)^4 \Omega_{\rm r} + (1+z)^3 \Omega_{\rm m} + \Omega_\Lambda} \,, \tag{2.5}$$

where the Hubble distance $D_H$ and the comoving angular distance $D_M$ are given as

$$D_H(z) = \frac{c}{H(z)} \,, \qquad D_M(z) = \int_0^z \frac{c dz'}{H(z')}. \tag{2.6}$$

Linear perturbations in the energy density of a given species $X$ from the homogeneous background are encoded in the power spectrum $P_X(k)$ describing the 2-point statistics as a function of wavevector $k$ in Fourier space. It is written as the product of the primordial



JCAP12(2021)054

| Cosmology | $\omega_{\rm cdm}$ | $\omega_{\rm b}$ | $h$ | $\sigma_8$ | $n_s$ | $M_\nu$ [eV] | $\Omega_{\rm m}$ | $r_{\rm d}$ [Mpc] |
|---|---|---|---|---|---|---|---|---|
| Planck | 0.1190 | 0.022 | 0.676 | 0.8288 | 0.9611 | 0.06 | 0.31 | 147.78 |

**Table 1**. Reference values of cosmological parameters for the ΛCDM base of eq. (2.1) and its derived parameters, the matter density parameter, $\Omega_{\rm m}$, and the sound horizon at radiation drag, $r_{\rm d}$. As it is customary, we report $r_{\rm d}$ in units Mpc, although we use $h^{-1}$Mpc units throughout the rest of this work. The reported parameter values are close to the Planck best-fit cosmology [2].

power spectrum $\mathcal{P}_\mathcal{R}(k)$ and the squared transfer function $\delta_X(k)$ obtained from solving the perturbed coupled Boltzmann equations for each species $X$,

$$P_X(k,z) = \frac{2\pi^2}{k^3}\mathcal{P}_\mathcal{R}(k)\delta_X^2(k,z) = \frac{2\pi^2}{k^3}A_s\left(\frac{k}{0.05\,\mathrm{Mpc}^{-1}}\right)^{n_s-1}\delta_X^2(k,z)\,, \tag{2.7}$$

where the standard inflationary model assumes the primordial power spectrum to be nearly scale-invariant, with global amplitude $A_s$ and scalar tilt $n_s$.

Since the global amplitude is modulated by the transfer function as well, it is common in LSS analyses to replace $A_s$ by the total amplitude $\sigma_8$ at redshift zero as a free parameter. In general the redshift-dependent $\sigma_8$ is defined as the matter density fluctuation at a given redshift $z$ smoothed on spheres of 8 Mpc/$h$,

$$\sigma_8^2(z) \equiv \int_0^\infty \mathrm{d}(\ln k)\, k^3 P_{\rm m}(k,z) W_{\rm TH}^2(k\cdot 8h^{-1}\mathrm{Mpc})\,, \tag{2.8}$$

where $W_{\rm TH}$ is the spherical top hat filter. The "amplitude parameters", $A_s$ and $\sigma_8$, are defined on different scales and at different epochs; in particular, while $A_s$ is a primordial quantity with direct interpretation in terms of early-time physics, $\sigma_8$ is a late-time quantity, with more direct interpretation from observations of LSS clustering. Also note that the primordial amplitude $A_s$ is defined with respect to a certain pivot scale given in Mpc units, while the scale of interest for $\sigma_8$ has $h^{-1}$Mpc units. Therefore, the wave-number $k$ in eq. (2.7) is given in Mpc$^{-1}$ units, while in eq. (2.8) and in what follows we write $k$ in units $h$Mpc$^{-1}$.

The reference cosmology $\mathbf{\Omega}^{\rm ref}$ used throughout this work, if not stated otherwise, is given in table 1 for the parameter base introduced in eq. (2.1) and other derived parameters. We refer to this set of parameters as "Planck".

### 2.2 Parameter dependence of the (real space) linear matter power spectrum

The main quantity needed to model the observable galaxy power spectrum multipoles is the real-space, linear matter power spectrum, $P_m(k)$. Here, we illustrate its dependence on key cosmological and physical parameters. Real world effects such as galaxy bias are discussed in section 2.3. As eq. (2.7) indicates, the primordial power spectrum is assumed to be a power law with an amplitude $A_s$ and a spectral slope $n_s$. These quantities are set by the mechanism that generated the initial conditions, but not by the subsequent evolution of the Universe. The late-time linear matter power spectrum is not a power law; this is encoded by the transfer function, which captures linear physics relevant after the end of inflation. As such, it depends on the content of the Universe, and its early-time expansion history.

The primordial power spectrum is always defined for $k$ in units of Mpc$^{-1}$. The LSS power spectrum on the other hand is usually defined for $k$ in units of $h$Mpc$^{-1}$. This is intimately related to the fact that observations measure angles and redshifts and not distances directly. Hence, distances are obtained assuming a specific theoretical model, with specific parameters



JCAP12(2021)054

values, as given by the reference model. The model-dependence of this step can be made more transparent by defining distances in units of a theoretical quantity (or "ruler") and then making explicit the scaling of the power spectrum and the wave vector with the theory ruler. The use of "little $h$" is the classic example, with $h = H_0/H_0^{\rm ref}$ where the reference model has $H_0^{\rm ref} = 100$ km s$^{-1}$ Mpc$^{-1}$. Moreover, as it will become clear below, it is useful to go beyond $h$ and also consider scaling of distances with respect to the BAO standard ruler, the sound horizon at radiation drag, $r_d$, yielding $s \equiv r_{\rm d}/r_{\rm d}^{\rm ref}$; $s$ enters the normalization of the power spectrum and the scaling of the wave vector in much the same way as $h$.

In the top panel of figure 1 we show the matter power spectrum for the "Planck" cosmology (solid black line), and the one corresponding to a universe without baryons, where all the matter consists of dark matter (dotted black line). The latter can be described by only one characteristic scale, the scale of matter-radiation equality,

$$k_{\rm eq} = a_{\rm eq} H_{\rm eq} = 7.46 \times 10^{-2} \, \frac{\omega_{\rm cb}}{h} \left( \frac{T_0}{2.7\,{\rm K}} \right)^{-2} , \tag{2.9}$$

which corresponds to the modes entering the Hubble horizon at the redshift of equality, $z_{\rm eq}$, which depends on the physical density $\omega_{\rm cb} = \omega_{\rm cdm} + \omega_{\rm b}$ comprising cold dark matter and baryons. The numerical calculation of the matter power spectrum is carried out with the Boltzmann code CLASS [48], which uses $\omega_{\rm cdm}$ as input parameter. However, for some applications it is more instructive to show the parameter $\omega_{\rm cb}$.

The effect of baryons on the matter power spectrum is characterized by an additional scale, the sound horizon at baryon radiation drag epoch,

$$r_{\rm d} = \int_{z_{\rm d}}^{\infty} d\tilde{z} \, \frac{c_s(\tilde{z})}{H(\tilde{z})} , \tag{2.10}$$

where $c_s(z)$ is the sound speed of the tightly coupled photon-baryon fluid, and $z_d$ the epoch of baryon drag. This is the maximum scale over which baryon pressure waves could have travelled from initial times until the baryon-photon decoupling. The sound horizon has two major effects on the power spectrum, which can be seen in figure 1 by comparing the dotted to the solid black line. First, it acts as a Jeans scale, damping the power spectrum for modes $k_{\rm damp} > 1/r_{\rm d}$ (green dashed line). Second, it introduces the BAO, whose peaks and troughs locations are given by the red and blue dotted lines. Interestingly, the slope of the baryon suppression reaches its maximum at the same scale that corresponds to the zero-crossing before the first BAO trough at $k_{\rm slope} = \pi/r_{\rm d}$ (green dotted line). This shows that the scale of the suppression and the BAO wiggle position are indeed directly linked to each other by $r_{\rm d}$. We anticipate here that we will make use of this important fact in section 3.3.

In the middle panel of figure 1 we show the normalized derivative of the matter power spectrum with respect to the base ΛCDM parameters introduced in section 2.1. The effect of varying $\sigma_8$ (black dashed line) and $n_s$ (orange dashed line) is trivial, they just change the power spectrum global amplitude and tilt respectively. The sum of neutrino masses $M_\nu$ (magenta dashed line) acts as a step-like suppression at the scales at which neutrino free streaming occurs $k \approx 0.01\,h^{-1}$Mpc. Note that the differential of each parameter $\partial\Omega_i$ is normalized by a factor $\Delta_i$ as to match the effect of $\sigma_8$ at large scales. While varying one parameter, all other parameters are fixed to their fiducial value in table 1. In effect, the normalized derivative with respect to each parameter is the same at the smallest wavevectors and the zero-crossing occurs at the same characteristic wavevector $k \approx 1/(8\,h^{-1}{\rm Mpc})$ for the cases where $\sigma_8$ is fixed.



JCAP12(2021)054

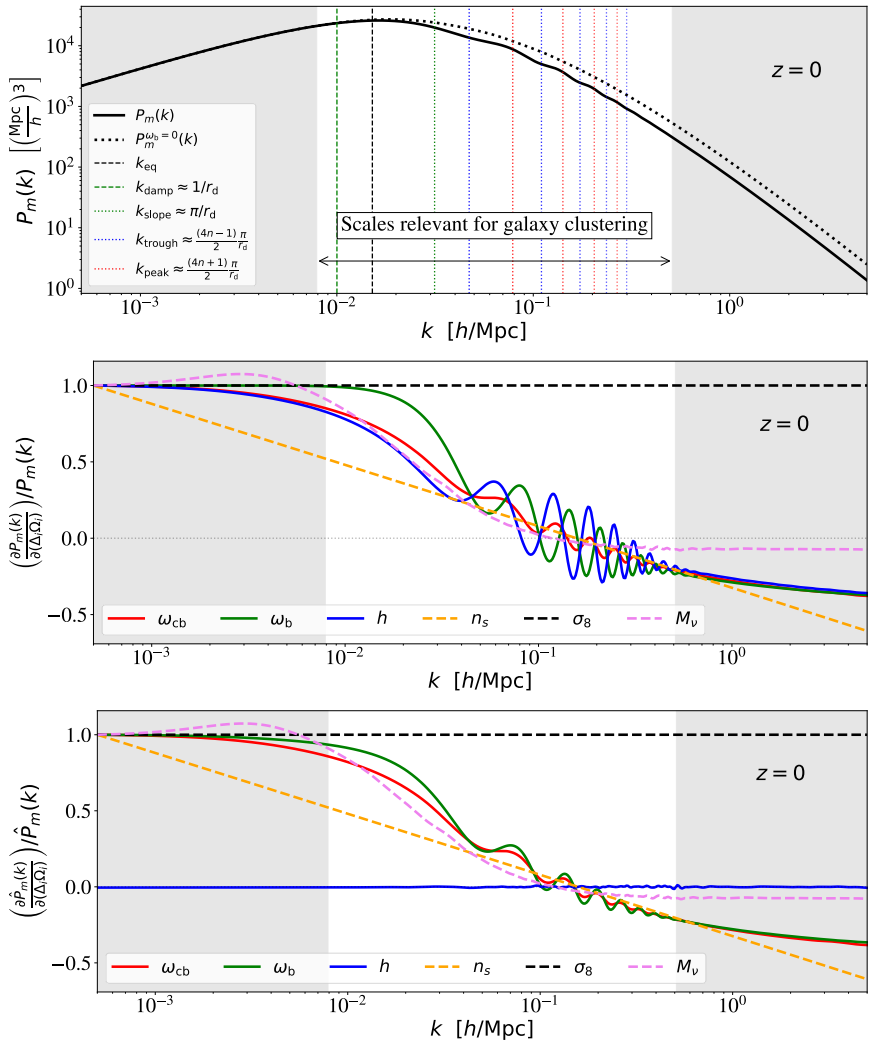


**Figure 1**. *Top panel:* linear matter (cold dark matter + baryons+ neutrinos) power spectrum $P_m(k)$ at $z = 0$ and its characteristic scales: the equality between matter and radiation $k_{\rm eq}$ (black dashed vertical line), the turn-around, which coincides with $k_{\rm eq}$, the BAO-peaks and -troughs (red and blue vertical dotted lines, respectively) estimated as function of $r_{\rm d}$, and the scale where the baryon suppression reaches its maximal slope, $k_{\rm slope} = \pi/r_{\rm d}$ (green dotted vertical line). To highlight the baryon suppression effect, the black dotted line shows $P_m(k)$ in the zero-baryon case for comparison. *Middle panel:* $z = 0$ $P_m(k)$ parameter dependence for varying $\Omega_i \in \{\omega_{\rm cb}, \omega_{\rm b}, h, n_s, \sigma_8, M_\nu\}$. The normalization factors $\Delta_i$ are chosen such that all parameters have the same impact on the power spectrum as $\sigma_8$ in the large scale limit. *Bottom panel:* same lines as in the middle panel, but after rescaling by $r_{\rm d}$ according to eq. (2.11), so that the BAO wiggle positions overlap. In all panels, the non-shaded $k$-range highlights the usual observed range for spectroscopic galaxy surveys, $0.008 \leq k\,[h{\rm Mpc}^{-1}] \leq 0.5$. This figure should remind the reader of the landmark works [20, 46, 47] and references therein.

JCAP12(2021)054

We can appreciate that the parameters $\{\omega_{\rm cb}, \omega_{\rm b}, h\}$ have the same effect on the small and large scale limit, but show differences at intermediate scales: the onset of suppression on scales $0.01 < k\,[h{\rm Mpc}^{-1}] < 0.05$ and the oscillation amplitude and position on scales $0.05 < k\,[h{\rm Mpc}^{-1}] < 0.5$. However, from the plot it is not clear whether different apparent amplitudes are related to a pure change in amplitude or to the shift of BAO position.

Therefore, in the bottom panel of figure 1 we show the same cases after rescaling by $s$, the shift in sound horizon corresponding to the shift in cosmological parameter, such that the BAO position overlaps for all the lines,

$$P_m(k) \longrightarrow \hat{P}_m(k) = \frac{1}{s^3} P_m\left(\frac{k}{s}\right), \qquad s = \frac{r_{\rm d}(\Omega_i + \partial\Delta_i\Omega_i)}{r_{\rm d}(\Omega_i)}\,. \tag{2.11}$$

Lines corresponding to a shift in parameters that leave $r_{\rm d}$ unchanged (dashed lines) are, of course, unaffected by the rescaling. For $\sigma_8$ this is not strictly correct, there is a residual dependence on the scale in the filter function (see eq. (2.8)), as $\sigma_8$ does change after the transformation (2.11). Here we actually used a redefinition of $\sigma_8$ introduced and motivated in section 3.1.

On the other hand, for the parameters that have an impact on $r_{\rm d}$ (solid lines), we observe a systematically different behaviour. First, the effect of the parameter $h$ is completely absorbed by the rescaling, because we express the sound horizon $r_{\rm d}$ in $h^{-1}$Mpc units. Second, $\omega_{\rm cb}$ and $\omega_{\rm b}$ have a nearly identical effect on the slope, with only a small offset coming from $k_{\rm eq}$. In fact, $k_{\rm eq}$ and $r_{\rm d}$ are closely related within standard ΛCDM, as the relevant physical effects leading to these scales occur at relatively adjacent times, not allowing for much freedom to change one without changing the other. Third, while their effect on the slope is qualitatively similar in the $k$-range of interest, $\omega_{\rm b}$ has a larger impact on the BAO wiggle amplitude than $\omega_{\rm cb}$. This is expected, as the amplitude depends on the ratio $\omega_{\rm b}/\omega_{\rm cb}$. Note that, to reduce the dynamic range to display in figure 1 (and to normalize their effect on large scales), $\Delta_{\omega_{\rm cb}}$ has a different sign than $\Delta_{\omega_{\rm b}}$. Although the effect of the parameters $\omega_{\rm cb}$, $\omega_{\rm b}$ and $n_s$ on the shape of the matter power spectrum is expected to be somewhat degenerate, the change in slope by $\omega_{\rm cb}$, $\omega_{\rm b}$ is scale-dependent, while for $n_s$ it is scale-independent by definition. We will come back to this point later.

Of course what the figure shows and the discussion refers to is the effect of the Γ parameter ($\Gamma \sim \Omega_m h$ in ΛCDM where however the $\sim$ sign is key as there is a rich dependence on early-time physics in the shape of the matter transfer function see e.g., [46, 47, 49] and the extensive discussion in [20]). These references, especially [20] as will be clear later, are key to offer a physical interpretation of the information provided by the power spectrum and transfer function shape.

From this purely theoretical investigation of the linear matter power spectrum we conclude that when trying to measure even the base ΛCDM parameters directly from clustering data, without external priors or data-sets, the resulting constraints are expected to be highly degenerate.

In particular, we have shown that the effect on the power spectrum slope of $\{\omega_{\rm cb}, \omega_{\rm b}, h, n_s\}$ (or of $\{\omega_{\rm cb}, \omega_{\rm b}, n_s\}$ when removing the $r_{\rm d}$ dependence) is qualitatively similar. The situation is further complicated by the fact that we observe galaxies, which are biased tracers of the cold dark matter + baryon power spectrum in redshift space, and with non-linear corrections playing an important role. It is well known that using the matter power spectrum or the cold dark matter + baryon power spectrum as an input for modelling the galaxy clustering in redshift space can make a difference in the constraints of the sum of neutrino masses [50–52].



JCAP12(2021)054

We refer the reader to these references for more details. This is, however, beyond the scope of this paper. In the following we stick to the convention and nomenclature of the CLASS code.

### 2.3 From dark matter in real space to galaxies in redshift space

We start by writing the density and velocity real space spectra for biased tracers at 1-loop standard perturbation theory (SPT) as in [53]:

$$\begin{aligned} P_{g,\delta\delta}(k) &= b_1^2 P_{m,\delta\delta}(k) + 2b_2 b_1 P_{m,b2\delta}(k) + 2b_{s2} b_1 P_{bs2,\delta}(k) + b_2^2 P_{m,b22}(k) + \\ &\quad 2b_2 b_{s2} P_{m,b2s2}(k) + b_{s2}^2 P_{bs22}(k) + 2b_1 b_{3\mathrm{nl}} \sigma_3^2(k) P_{\mathrm{m,lin}}(k) \\ P_{g,\delta\theta}(k) &= b_1 P_{m,\delta\theta}(k) + b_2 P_{m,b2\theta}(k) + b_{s2} P_{m,bs2\theta}(k) + b_{3\mathrm{nl}} \sigma_3^2(k) P_{\mathrm{m,lin}}(k) \\ P_{g,\theta\theta}(k) &= P_{\theta\theta}\,, \end{aligned} \tag{2.12}$$

where $P_{xy}$ with $x, y = \delta$ or $\theta$ are the auto and cross power spectra of non-linear density ($\delta$) and velocity ($\theta$) perturbations, $P_{m,\mathrm{lin}}$ denotes the linear matter power spectrum and $P_{b2,x} P_{bs2,x}$ represent 1-loop corrections to the linear bias expansion. The exact expressions for these terms and $\sigma_3$ can be found in eq. B2- B7 of [54]. Biasing is parametrized by four bias parameters, the first and second order biases $b_1, b_2$ [55], and the non-local biases $b_{s2}, b_{3\mathrm{nl}}$ [56]. Under the assumption of local Lagrangian conditions these two non-local biases can be written as a function of $(b_1 - 1)$ and are not independent parameters. Some studies have shown that in general this local condition holds for dark-matter haloes [57–59], but is not necessarily true for galaxies with an arbitrary halo occupation distribution e.g., [60]. We follow the usual assumption that, at the scales of interest, the galaxy velocity field is unbiased.

Going from real space to redshift space introduces an additional dependence on the angle $\vartheta$ of wavevectors with respect to the line-of-sight (LOS), which is usually parametrized by $\mu = \cos(\vartheta)$. It is widespread to adopt the redshift space formulation from [61] and extended by [62],

$$\begin{aligned} P_{\mathrm{RSD}}(k,\mu) = \left(1 + [k\mu\sigma_P]^2/2\right)^{-2} \Big[ & P_{g,\delta\delta}(k) + 2f\mu^2 P_{g,\delta\theta}(k) + f^2\mu^4 P_{g,\theta\theta}(k) + \\ & b_1^3 A^{\mathrm{TNS}}(k,\mu,f/b_1) + b_1^4 B^{\mathrm{TNS}}(k,\mu,f/b_1) \Big]\,, \end{aligned} \tag{2.13}$$

where the Lorentzian damping term in front incorporates the effect of non-linear RSD, also called Fingers-of-God effect. Here $\mu$ is the cosine of the angle to the LOS, $\sigma_P$ is a phenomenological incoherent velocity dispersion parameter, and $f$ denotes the linear growth rate $dD/d\ln a$ where $D$ is the linear growth factor and $a$ the scale factor. Eq. (2.13) describes the so-called TNS model (see the definition of the coefficients $A^{\mathrm{TNS}}, B^{\mathrm{TNS}}$ in [62]). We follow the usual approach of expanding the power spectrum $\mu$-dependence in the Legendre-polynomials orthonormal base. This procedure allows us to describe the LOS dependence through a series of multipoles. Although the multipole-expansion requires an infinite set of multipoles, in practice just the first 2 or 3 non-null multipoles are used.[2] The power spectrum multipoles are thus constructed by integrating $P_{\mathrm{RSD}}$ times the corresponding Legendre polynomials over $\mu$

$$P_{\mathrm{RSD}}^{(\ell)}(k) = (2\ell+1) \int_{-1}^{1} P_{\mathrm{RSD}}(k,\mu) \mathcal{L}_\ell(\mu)\, d\mu\,. \tag{2.14}$$

[2] In the same fashion an infinite $\mu$-binning is required to extract the full available information, but in practice signal-to-noise arguments limit this to just 2 or 3 bins in $\mu$ (see for e.g., [63]).



JCAP12(2021)054

Combining the signal from the monopole ($\ell = 0$) and quadrupole ($\ell = 2$) allows to break the usual large-scale degeneracy between linear bias and growth of structure. Adding the hexadecapole ($\ell = 4$) helps in breaking degeneracies between the AP effect and redshift space distortions. Although the non-linear terms $\{A, B\}^{\rm TNS}$ of eq. (2.13) include $\mu^6$ and $\mu^8$ contributions, the amount of information of these in the scales of interest is very small, and so, the information contained in the higher-order multipoles ($\ell > 4$). For this reason all the cosmological analysis up-to-date stop at the hexadecapole level. We do not consider the odd-multipoles such as the dipole ($\ell = 1$) and octopole ($\ell = 3$) in our standard cosmological analyses. These are, by definition, zero under the flat-sky approximation and in the absence of selection effects, and do not contain cosmological information. However, some recent studies have shown that these measurements may be useful for an accurate modelling of the window function at very large-scales (wide-angle effects) on real surveys [64].

### 2.4 Extracting cosmological information from the galaxy power spectrum: An overview of BAO, RSD and FM analyses

A spectroscopic galaxy survey measures the redshifts of a large number of targeted galaxies at a given angular position. The galaxies are grouped in redshift bins with different effective redshift. For each bin the summary statistics are measured, these are the 2-point correlation function and power spectrum; the 3-point correlation function and bispectrum, and even higher order moments if needed. These statistics may contain several spurious signals related to how the observations have been performed: the angular and radial selection function [65]; the effect of imaging observational systematics [9]; the effect of redshift failures or collisions [66, 67]; which need to be corrected either in the catalogue (usually by weighting the galaxies, or down-sampling the random catalogue) or by accounting them in the modelling part.

In a nutshell, the standard approach, (e.g., BAO and RSD analyses, which from now on we will refer to as "classic" approach) relies in compressing the data into physical observables that, *i*) represent the universe's late-time dynamics; *ii*) are as much as possible model-independent; and *iii*) can be in turn interpreted in light of the cosmological model of choice.

In the case of the classic BAO analysis the physical observable is the position of the BAO peak in the clustering signal along and across the LOS. Thus, in this approach a power spectrum or correlation function template (computed once for a reference cosmological model) is used to fit the data, that is separated into a wiggle or oscillatory component containing the BAO information, and a broadband component (also referred to as non-wiggle or smooth), which does not contain any BAO information. The smooth component is marginalized over and the BAO position is measured by rescaling the wiggle component[3] by the following free (physical) parameters,

$$\alpha_\perp(z) = \frac{D_M(z)\, r_{\rm d}^{\rm ref}}{D_M^{\rm ref}(z)\, r_{\rm d}}\,, \qquad \alpha_\parallel(z) = \frac{H^{\rm ref}(z)\, r_{\rm d}^{\rm ref}}{H(z)\, r_{\rm d}}\,. \tag{2.15}$$

These are used as rescaling variables and correspond to the ratios between the underlying and the reference distances[4] across and along the LOS in units of the sound horizon at baryon drag epoch defined in equation (2.10).

[3] The BAO amplitude is also damped in the wiggle component in order to account for the bulk-flow motions.

[4] The reference (sometimes referred to as "fiducial") distances depend on the chosen model used to convert redshifts into distances. On the other hand, the reference sound horizon is the theory prediction of the reference model (for fixed-template approaches). Although one could choose two different reference models, for the sound horizon and the distances, is of common practice to use the same, which is the approach we follow in this work.



JCAP12(2021)054

In practice, the combined scaling is applied to the model via a coordinate transformation of wavevector $k$ and cosine of angle with respect to the LOS $\mu$

$$k \longrightarrow \widetilde{k} = \frac{k}{\alpha_\perp}\left[1+\mu^2\left(\frac{\alpha_\perp^2}{\alpha_\parallel^2}-1\right)\right]^{1/2}, \tag{2.16}$$

$$\mu \longrightarrow \widetilde{\mu} = \mu\frac{\alpha_\perp}{\alpha_\parallel}\left[1+\mu^2\left(\frac{\alpha_\perp^2}{\alpha_\parallel^2}-1\right)\right]^{-1/2}. \tag{2.17}$$

Finally, the modeled power spectrum multipoles of eq. (2.14) can then be written in terms of the transformed coordinates as

$$P_{\rm RSD}^{(\ell)}(k) = \frac{(2\ell+1)}{2\alpha_\perp^2\alpha_\parallel}\int_{-1}^{1} P_{\rm model}(\widetilde{k}(k,\mu),\widetilde{\mu}(\mu))\mathcal{L}_\ell(\mu)\,d\mu\ . \tag{2.18}$$

Hence, the classic BAO analysis compresses the measured galaxy power spectrum multipoles in a given redshift bin, into $\alpha_\parallel$, $\alpha_\perp$, which are interpreted as the BAO peak position information, along and across the LOS, at that redshift. These quantities describe the geometry and expansion history of the Universe in a model-independent way. Under the umbrella of ΛCDM, they can be interpreted in terms of the $\Omega_{\rm m}$ and $H_0 r_{\rm d}$ variables. However, the scaling parameters do not capture the effect that $\Omega_{\rm m}$, $H_0$ and the matter-radiation equality scale have on the matter transfer function which contains extra, non-BAO-based, cosmological information [20, 43, 68].

A widely used approach to enhance the BAO signal and obtain more stringent constraints on cosmological parameters, is the reconstruction algorithm e.g., [23, 69, 70], that uses the measured overdensity field to sharpen the BAO peak by partially undoing non-linear evolution. Although it involves weak model assumptions (such as GR, linear bias, homogeneity, etc...), the bulk of information obtained after reconstruction is still purely geometric and model-independent. In a recent work, [24] show how some of these assumptions have a negligible impact on the final results.

In the case of the classic RSD analysis, the physical observable is not only the BAO position, but also the anisotropy signal generated by redshift space distortions, mainly at linear and quasi-linear scales. The analysis follows a similar strategy as the BAO analysis, with the difference that the scaling parameters are applied to the full $P^{(\ell)}(k)$ template (i.e., the $P^{(\ell)}(k)$ for a reference cosmological model) without any wiggle-broadband decomposition. Due to the inclusion of the broadband signal, the RSD analysis is sensitive to the monopole-to-quadrupole ratio which is parametrized by $f\sigma_8$.[5] The growth rate of structures $f$, is responsible for the large-scale bulk velocity component along the LOS, that induces an enhanced clustering signal in this direction. Unlike the anisotropic signal generated by the AP effect, the enhanced clustering caused by the RSD does not modify the BAO peak position: this makes it possible to disentangle the RSD from the AP effect, that otherwise would appear very degenerate. Note that, what we call "classic RSD analysis" has been called Full Shape analysis in earlier works, as it includes both the BAO and the broadband. However, this name is too easy to confuse with what we call "Full Modelling analysis". Hence the name RSD analysis, which can be thought of as an enhanced BAO (or 'BAO-plus' as in the SDSS-IV official release[6])

[5] To be precise, the ratio is only parametrized by $f$, while the absolute amplitude is given by $\sigma_8$, which is fixed by the template. In practice, both parameters are very degenerate and the combination $f\sigma_8$ is template-independent.

[6] https://svn.sdss.org/public/data/eboss/DR16cosmo/tags/v1_0_1/likelihoods/.



JCAP12(2021)054

analysis, that also includes the amplitude part of the broadband and its anisotropy, induced by RSD.

The classic RSD analysis compresses the power spectrum multipoles into $\alpha_\parallel$, $\alpha_\perp$, $f\sigma_8$, similarly to what the classic BAO analysis does, but with the additional growth of structures information. It is well known that in GR $f$ is determined by $\Omega_m$ (the growth history being completely determined by the expansion history).[7] The classic approach however, does not make this connection and treats $f\sigma_8$ as an independent quantity to be measured directly.

Therefore, in the case we assume a flat ΛCDM model and GR as the theory of gravity, $f\sigma_8$ is effectively a measurement of $\sigma_8$, as within ΛCDM $\Omega_{\rm m}(z)$ is obtained from $\alpha_\parallel$ and $\alpha_\perp$ and within GR the growth rate evolution $f(z)$ is completely fixed by $\Omega_{\rm m}(z)$. Crucially, the constraining power on $\sigma_8$ comes from the effect that $\Omega_{\rm m}(z)$ has on the background, not the effect of the matter density on the epoch of matter-radiation equality and thus on the shape of the transfer function. In summary, the classic RSD analysis is only sensitive to the effect that $\Omega_{\rm m}$, $H_0 r_{\rm d}$ and $\sigma_8$ have at the level of BAO peak position and the relative amplitude of the isotropic and anisotropic signals, but not on their effects on the matter transfer function itself. This is an important point to bear in mind: the shape of the matter transfer function is set by the physics of the early Universe ($z > 1000$); on the other hand, the expansion history and growth history probed by the "classic" BAO/RSD approach is only sensitive to late-time physics ($z \sim z_{\rm sample} \lesssim 1$ where $z_{\rm sample}$ denotes the typical redshift of the galaxy sample used to measure the power spectrum multipoles).

"Classic" BAO and RSD analyses have in common a key aspect: the attempt to compress, in a lossless way, the robust part of $P^{(\ell)}(k)$ signal into physical observables, that only depend on the late-time geometry and kinematic in a model-independent way, and not on other physics relevant to processes at play at a different epoch in the Universe evolution such as equality scale, sound horizon scale, primordial power spectrum or other quantities that enter in the matter transfer function.

In practice, this is achieved by fixing the power spectrum template: the information contained in the transfer function does not propagate into $\alpha_\parallel$, $\alpha_\perp$ and $f\sigma_8$. It can be demonstrated that this assumption actually holds by testing the universality of $f\sigma_8$ and the radial and angular distances in units of $r_d$,

$$\begin{aligned} \frac{D_M(z)}{r_{\rm d}} &= \alpha_\perp(z) \frac{D_M^{\rm ref}(z)}{r_{\rm d}^{\rm ref}} \\ \frac{D_H(z)}{r_d} \equiv \frac{c}{H(z) r_{\rm d}} &= \alpha_\parallel(z) \left[H^{\rm ref}(z) \cdot r_{\rm d}^{\rm ref}\right]^{-1} c \end{aligned} \tag{2.19}$$

when performing the fits with different power spectrum templates. In the case of BAO analysis, this universality has been demonstrated to hold impressively well even for exotic Early Dark Energy (EDE) and $\Delta N_{\rm eff}$ models [71]. The template independence for the RSD analysis has been studied for eBOSS [72] yielding reassuring results.[8]

While BAO fits are very mildly affected by non-linear corrections (the reconstruction step removes the bulk of the non-linear effects on the BAO signal and the small scales non-linear corrections are marginalized), for RSD fits it is important to model the $P^{(\ell)}(k)$ up to 1-loop or 2-loop order in Perturbation Theory (PT). In the classic approach these are usually computed

[7] For models where dark energy has an equation of state parameter different from $w = -1$, this parameter also appears with $\Omega_m$ in the expression for $f$ but introduces only small corrections.

[8] While the small residual template dependence has been small enough (a factor 5 smaller than the statistical errors) for eBOSS data, improvements might be needed for future data.



JCAP12(2021)054

once for the reference cosmology of the template, and scaled by $\alpha_\parallel$, $\alpha_\perp$ and $f\sigma_8$ accordingly during the fit. It has been shown that the PT kernels have a very weak dependence on cosmology [73], so that the amplitude parameters ($f$, $\sigma_8$) can just be a re-scaling and this is a valid assumption.

Recently, there have been a series of works following a fundamentally different route than the classic BAO and RSD analyses and very close to the way CMB data are analysed and interpreted.[9] This approach avoids the compression step and directly fits cosmological models to the $P^{(\ell)}(k)$ signal. We do not review the technical details of this approach here, we direct the reader to the references for that, but highlight important similarities and differences with the "classic" approach. As the parameter space is explored (usually via a MCMC), the likelihood evaluation involves calculating for every choice of cosmological parameter values the model prediction of the transfer function and the non-linear correction to the power spectrum corresponding to perturbation theory frameworks such as EFT e.g., [39, 42] or gRPT [76]. We call this approach the "Full modelling" (FM) analysis/fit in what follows. In this approach the parameter dependence of the transfer function and the geometry are not kept separated; in this way the information carried by the shape of the transfer function improves constraints on cosmological parameters that are usually interpreted as purely geometrical (e.g., $\Omega_m$, $h$).

This connection between early-time transfer function and late-time background dynamics in-built in the FM approach can be seen as an "*internal model prior*". The classic fixed template methods do not invoke a prior of that kind, as they do not establish this link. Such approaches are not taking advantage of a model prior and are thus recognized as "model-independent". While it is true that the template is fixed, it has been extensively demonstrated, that this choice does not introduce biases nor affect the error-bars. e.g., [71] and refs. therein. For this reason in the "classic" approach the choice of the cosmological model matters only at the stage of interpreting the constrains on the physical (compressed) parameters as constrains on cosmological parameters, with the physical (compressed) parameters being effectively model-independent. Of course this compression is not lossless, but, as extensively shown in the literature (see e.g. [77]), it captures fully the relevant information and there is conscious control on the information loss [33, 78–80]. In the FM approach on the other hand, the cosmological model must be chosen *ab initio*. Figure 7 of [39] drives this point home: in the FM approach for simple extensions of the ΛCDM that change late-time physics assumptions, the resulting error-bars increase to almost match those of the classic approach.

In practice, the FM approach must "undo" the effect of the reference model assumed to transform redshifts and angles into distances. This is achieved (see section 2.2. of [42]) by rescaling the modeled power spectrum multipoles from the model in consideration $\mathbf{\Omega}$ to the reference $\mathbf{\Omega}^{\rm ref}$. This is similar to eq. (2.18) with the only difference that the "$\alpha$ scaling parameters" are replaced by the so-called late-time scaling parameters defined as

$$\begin{aligned} q_\perp(z) &= \frac{D_M(z)}{D_M^{\rm ref}(z)}\,, & q_\parallel(z) &= \frac{D_H(z)}{D_H^{\rm ref}(z)}\,, \\ q_0(z) &= \left[q_\perp^2(z) q_\parallel(z)\right]^{1/3} = \frac{D_V(z)}{D_V^{\rm ref}(z)}\,, & D_V &= \left[D_M^2(z) D_H(z)\right]^{1/3}\,, \end{aligned} \tag{2.20}$$

and $q_0$ is the late-time scaling associated to the power spectrum monopole. It describes the volume-averaged, isotropic distance scaling and is of integral importance as we will

[9] As already mentioned, and for historical completeness, this is more a going back to the way galaxy surveys were analysed before circa 2010 rather than a radically new idea see e.g., [28–30, 63, 74, 75].



JCAP12(2021)054

| Fit type | Classic | | Full Modelling |
|---|---|---|---|
| | **BAO Fit** | **RSD Fit** | **FM fit** |
| **Information Source** | BAO Wiggles only | BAO + $P^{(\ell)}(k)$ amp. | Full $P^{(\ell)}(k)$ |
| $\mathbf{P_{lin}(k)}$ **template** | fixed | fixed | varies with model |
| **Non-linear correction** | marginalized over | computed once | varies with model |
| **Scaling parameters** | free $\alpha_\parallel$, $\alpha_\perp$ | free $\alpha_\parallel$, $\alpha_\perp$ | $\alpha_\parallel$, $\alpha_\perp$ derived by model |
| **Linear RSD** | marginalized over | free $f$ | $f$ derived by model |
| **Global amplitude** | marginalized over | $\sigma_8$ fixed or free | free $\sigma_8$ or $A_s$ |
| **Cosmological interpretation** | $\alpha_\parallel$, $\alpha_\perp$ can be compared to any model, sensitive to $\Omega_m, H_0 r_d$, | $\alpha_\parallel$, $\alpha_\perp$, $f\sigma_8$ can be compared to any model, sensitive to $\Omega_m, H_0 r_d$, $A_s$, $D(z)$ | done in a single step, but whole fit needs to be repeated for each model |

**Table 2**. Overview of the three main approaches to extract cosmological information from galaxy surveys to date.

discuss later. The main differences between the FM analysis and the classic BAO/RSD analyses are summarized in table 2.

### 2.5 BAO, RSD, and FM analyses: direct comparison on data

How do the differences between the FM and the classic approach described above translate into differences in cosmological parameter constraints? In the left panel of figure 2 we show the 1-$\sigma$ and 2-$\sigma$ confidence intervals in the $\omega_{\rm cdm} - h$ plane obtained from fitting the flat $\Lambda$CDM model to BOSS DR12 [82] data using the Boltzmann code CLASS [48] within the cosmological Sampler MontePython[10] [83] for three cases as follows. We fit the model to the compressed variables $\left\{\alpha_\parallel, \alpha_\perp, f\sigma_8\right\}$ obtained from the Fourier Space RSD fit [81] (grey contours) and from the consensus BAO (post-reconstruction) + RSD fit [26] (orange contours). Additionally, we show the constraints of the FM fit using the EFT approach and the publicly available code with the standard settings as in [39][11] (blue contours). Recall that, as in the baseline set up of [39] $h, A_s$ and $\omega_{\rm cdm}$ are varied with a flat uninformative prior, tight priors are imposed on $\omega_{\rm b}$ ($\omega_{\rm b} = 0.02268 \pm 0.00038$, Gaussian) and $M_\nu$ ($0.06\,{\rm eV} < M_\nu < 0.18{\rm eV}$, flat) and $n_s$ is fixed to its Planck 2018 base $\Lambda$CDM value. It is evident that the "internal model prior" of the FM fit leads to substantially more precise constraints than the classic method.

In past and present data releases of spectroscopic galaxy surveys, cosmological results are almost never presented for galaxy clustering data alone, but usually in combination with other datasets, especially with CMB data such as Planck [2]. This effectively fixes the sound horizon scale and the shape of the transfer function, so that the remaining galaxy clustering information beneficial for cosmological constraints is mostly captured by the geometrical information alone. In this particular case, as we see in the right panel of figure 2, the FM and RSD fits deliver effectively equivalent results. One may argue that the classic template-based fits have hence been designed to constrain cosmology in combination with Planck, which justifies fixing the template to Planck's cosmology in the first place. We stress here that this is not the case. Crucially, the agreement between the FM and classic fits is independent of the template used for the classic analysis, e.g., even for a template very different from the

[10]The code can be found at https://github.com/brinckmann/montepython_public.

[11]We use their publicly available code https://github.com/Michalychforever/CLASS-PT from [39] and its interface with MontePython https://github.com/Michalychforever/lss_montepython.



JCAP12(2021)054

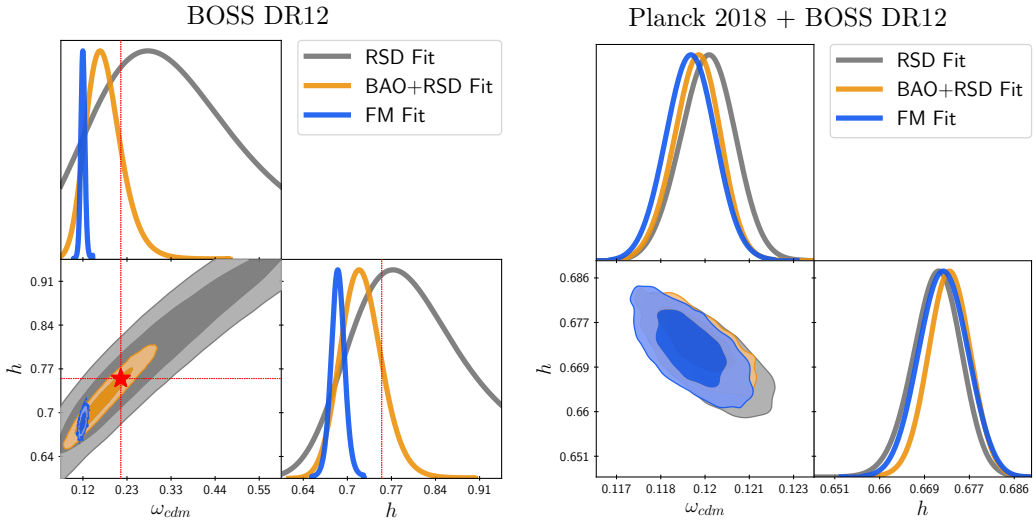


**Figure 2**. Posterior results of the base ΛCDM runs — where, following [39] $h, A_s$ and $\omega_{\rm cdm}$ are varied, tight Gaussian priors are imposed on $\omega_{\rm b}$ and $M_\nu$ and $n_s$ is fixed on BOSS DR12 data alone (left panel) and in combination with Planck (right panel) in the $(\omega_{\rm cdm} - h)$ plane. Grey contours correspond to the 68% and 95% confidence levels of the classic RSD-fit from [81], orange contours to the BOSS consensus result combining RSD and BAO analyses on pre- and post-reconstructed catalogues, respectively, [26] and blue contours to the FM-fit using the EFT approach from [39]. The red star corresponds to a trial model close to the RSD bestfit and still within 1-$\sigma$ of the BAO+RSD constraints, but completely excluded by the FM constraints.

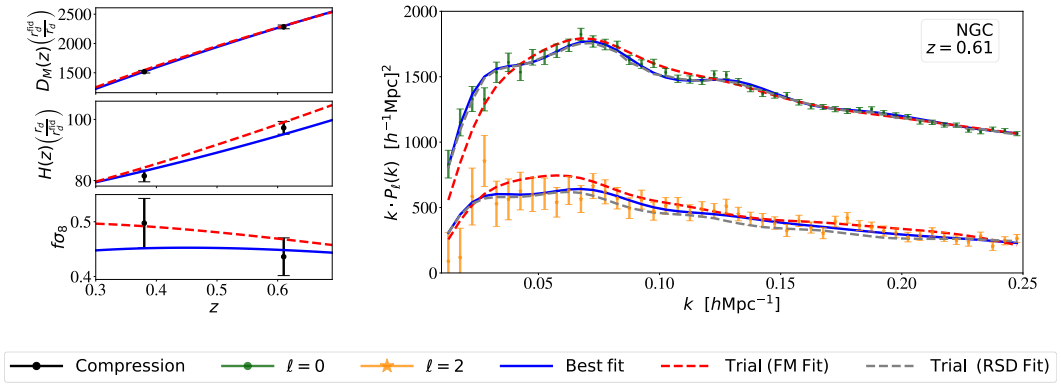


**Figure 3**. Left panel: the datapoints correspond to the BOSS DR12 BAO+RSD consensus results from [26]. The blue line is the model prediction from the FM bestfit, the red dashed line from the trial model (red star in figure 2). Right panel: here both models are compared to the monopole and quadrupole measurements from CMASS NGC. The grey dashed line corresponds to the trial model evaluated with the classic RSD method, while the red dashed line is computed with the FM method (with refitted nuisance in both cases).

JCAP12(2021)054

Planck cosmology, the obtained geometrical information would be the same. This is shown in appendix B, see also [72] for reference.

However, in this work we are especially interested in constraining cosmology with LSS data alone. In order to further understand, also visually, where the difference in constraining power between the fitting approaches arises, let us compare two suitably chosen models directly to the measurements.

From figure 2 (left panel) we select two models: the bestfit model from the FM fit located at the center of the blue contours, and a trial model displayed with the red star, selected such that it is still within the joint 1-$\sigma$ region in the $\omega_{cdm} - h$ plane of the BAO+RSD fit and close to the bestfit value of the RSD fit. In figure 3 we compare the FM-bestfit model (blue solid line) and the trial model (red dashed line) both evaluated within the EFT framework to the data. In the left panel they are compared to the compressed variables corresponding to the BOSS DR12 consensus values (corresponding to the orange contours in figure 2). None of the models seems to be a particularly better fit than the other. In fact, both reside at the $1-\sigma$ boundary of the orange contour in figure 2 within the same degeneracy direction between $\omega_{\rm cdm}$ and $h$. This is why they are basically indistinguishable in $D_M(z)/r_{\rm d}$. The right panel shows the two models in comparison with the measured $P^{(\ell)}(k)$ signal; for conciseness we only show the BOSS NGC sample at $z = 0.61$, as the picture does not change qualitatively for the other samples. Now it is possible to appreciate that the trial model (with refitted nuisance parameters) is a much worse fit, in fact it is completely excluded by the FM method. So why it is still a good fit within the classic method? The grey dashed line shows the trial model $P^{(\ell)}(k)$ evaluated within the RSD framework as follows. We use the values of $\left\{\alpha_{\parallel}, \alpha_{\perp}, f\sigma_8\right\}$ calculated from the trial model, apply them to the reference template and refit the nuisance parameters to the data. Since the transfer function is not altered during that process, the difference between the solid blue and the dashed grey line is purely geometrical (see left panel). This is why the trial model monopole is basically identical to the one of the bestfit model (the gray dashed line is indistinguishable from the blue line) and only the quadrupole shows some (small and statistically insignificant) residual differences due to the AP and RSD anisotropies.

It should be noted that the perturbation theory models implemented in this comparison are different between the FM and the classic RSD methods. Later we show, that the differences are unimportant in practice, as the agreement between the methods in the right panel of figure 2 indicates. To understand the meaning and relevance of the extra information that the FM fit captures, in the next section we show how to encode this extra information with a simple phenomenological extension of the classic fit which will enable one to bridge the two approaches in a transparent way.

## 3 Connecting FM analysis and classic RSD analysis: *ShapeFit*

We now proceed to present a way to connect the two "classic" and FM approaches which, for reasons which will become clear later, we call "*ShapeFit*". We will demonstrate that two ingredients are needed to bridge the two approaches: the correct definition, application and interpretation of the scaling parameters and the ability to model the signatures of early-time physics in the large-scales broadband shape of the real-space matter power spectrum.

### 3.1 Connection: scaling parameters interpretation

The "late-time scaling" used in the FM approach (described at the end of section 2.4) takes into account that the data is measured for a certain redshift-distance mapping corresponding



JCAP12(2021)054

to the reference model. Here, for purely pedagogical purpose, we review this late-time rescaling from a different point of view: what if, instead of scaling the model in consideration to the measured data, we correct the data in order to match the model at each step. For simplicity, we now focus on the real-space monopole data $P^{(0)}_{\rm data}$ (without loss of generality) and write conceptually[12] how to scale it from the reference $\mathbf{\Omega}^{\rm ref}$ to the model in consideration $\mathbf{\Omega}$,

$$P^{(0)}_{\rm data}(k,\mathbf{\Omega}) = q_0^3\, P^{(0)}_{\rm data}(q_0 k,\mathbf{\Omega}^{\rm ref})\ . \tag{3.1}$$

It is important to note that this operation involves the "average late-time scaling parameter" $q_0$ defined in (2.20) at two places: inside the argument of $P^{(0)}_{\rm data}$ and as an overall amplitude factor in units of volume. While this is a well known fact, we find it important to stress the dependence on the units here in order to motivate the next steps.

Crucially, in contrast to this "late-time scaling", we can identify an "early-time scaling" that takes into account that the linear power spectrum template is computed for the reference cosmology. The classic RSD analysis assumes[13] that all the early-time cosmology dependence is captured by the sound horizon scale $r_{\rm d}$ (defined in eq. (2.10)). We can apply this rescaling to the model in a similar fashion as to the data (see eq. (3.1)) by

$$P^{\rm lin}_{\rm model}(k,\mathbf{\Omega}) = s^3\, P^{\rm lin}_{\rm model}(sk,\mathbf{\Omega}^{\rm ref}) \quad \text{with} \quad s = \frac{r_{\rm d}}{r_{\rm d}^{\rm ref}}\,, \tag{3.2}$$

where, again, we need to introduce a volume rescaling $s^3$ taking into account that the power spectrum has units of volume. In this way the power spectrum amplitude is preserved when changing $s$. One can see, that the early-time rescaling on the model and the late-time rescaling on the data are very similar. The only difference is that the scaling with $s$ is purely isotropic and redshift independent, while a rescaling that involves $q_\parallel$ and $q_\perp$ allows for an additional anisotropic degree of freedom and redshift dependence. But the isotropic components of both scalings at a given redshift, $q_0$ and $s$, are indistinguishable in practice. This is the motivation for combining both scalings into the scaling parameters

$$\alpha_\perp(z) = \frac{q_\perp(z)}{s}\,, \qquad \alpha_\parallel(z) = \frac{q_\parallel(z)}{s}\,, \tag{3.3}$$

already introduced in eq. (2.15). Thus in the "classic" approach, instead of rescaling the data and the model separately, $\alpha_\perp$ and $\alpha_\parallel$ are applied to the model only, for reasons of practicality. This simply means that the data does not account for the arbitrary choice of a "fiducial" cosmology adopted to convert observed redshifts in distances to provide the input data-catalog, but the model is transformed into the "fiducial" coordinate system of the data instead. Although both ways of coordinate transformation are completely equivalent, we stress the difference in physical meaning here, as it is important later for the cosmological interpretation.

### 3.2 New scaling for the fluctuation amplitude

Having described the scaling parameters that change the modeled power spectra horizontally, in this section we look at the parameter that captures the "vertical" information, the matter

[12] Eq. (3.1) is presented only for illustrative purposes, in reality one needs to take into account the full angle dependence as done in eq. (2.18) for example.

[13] This is a very crude approximation as it just what is needed to shift the BAO bump to the equivalent location. So it is useful pedagogically but should not be applied as is.



JCAP12(2021)054

fluctuation amplitude smoothed on spheres with radius of $8\,h^{-1}$Mpc (see eq. (2.8)),

$$\begin{aligned}\sigma_8 &\equiv \sigma(R = 8h^{-1}\mathrm{Mpc}, \mathbf{\Omega})\,,\\ \sigma^2(R, \mathbf{\Omega}) &= \int \mathrm{d}(\ln k)\, k^3 P_{\mathrm{lin}}(k, \mathbf{\Omega}) W^2_{\mathrm{TH}}(kR)\,,\end{aligned} \tag{3.4}$$

where $W_{\mathrm{TH}}(kR)$ is the spherical top-hat filter. In the classic RSD analysis the amplitude of the matter fluctuations is usually fixed to the reference cosmology. The logic is that a change in $\sigma_8$ can be seen, in a very good approximation, as being completely absorbed into the scale-independent growth rate $f$ and the bias parameters. In this sense, it is possible to obtain template-independent quantities just by multiplying $f, b_1, b_2, \ldots$ by $\sigma_8$.

However, as explained in section 3.1, the classic RSD analysis implicitly assumes the "early-time rescaling", which induces a change in the interpretation of $\sigma_8$ via $\alpha_\parallel$ and $\alpha_\perp$. Therefore, $\sigma_8$ as defined in eq. (3.4) is actually *not* kept fixed while exploring parameter space during the RSD fit.

This can easily be accounted for by defining the fluctuation amplitude in such a way that it does not change during the fitting process, i.e., such that it is independent of changes in $s$:

$$\sigma_{s8} \equiv \sigma(R = s \cdot 8h^{-1}\mathrm{Mpc}, \mathbf{\Omega})\ . \tag{3.5}$$

We can show, that this quantity is indeed uniquely defined for a given reference template independent of the value of $s$ by plugging into the $\sigma(R)$ definition

$$\begin{aligned}\sigma^2_{s8}(\mathbf{\Omega}) &= \int_0^\infty \mathrm{d}(\ln k)\, k^3 P_{\mathrm{lin}}(k, \mathbf{\Omega}) W^2_{\mathrm{TH}}(ks \cdot 8h^{-1}\mathrm{Mpc}) && \Big| \mathbf{\Omega} \to \mathbf{\Omega}^{\mathrm{ref}}\\ &= \int_0^\infty \mathrm{d}(\ln k)\, k^3 s^3 P_{\mathrm{lin}}(sk, \mathbf{\Omega}^{\mathrm{ref}}) W^2_{\mathrm{TH}}(ks \cdot 8h^{-1}\mathrm{Mpc}) && \Big| k' = ks\\ &= \int_0^\infty \mathrm{d}(\ln k')\, k'^3 P_{\mathrm{lin}}(k', \mathbf{\Omega}^{\mathrm{ref}}) W^2_{\mathrm{TH}}(k' \cdot 8h^{-1}\mathrm{Mpc})\\ &= \sigma^2_8(\mathbf{\Omega}^{\mathrm{ref}})\ .\end{aligned} \tag{3.6}$$

To conclude, in the classic RSD analysis the fixed template fit allows for a dependence on early-time physics to be parametrized by $r_{\mathrm{d}}$. Therefore it does not actually measure the velocity fluctuation amplitude $f\sigma_8$ defined at an absolute smoothing scale, but the quantity $f\sigma_{s8}$, where the smoothing scale is defined relative to the sound horizon scale. This fact has been ignored in recent clustering data releases, mainly because cosmological constraints were presented in combination with Planck data, which implies $\sigma_{s8} = \sigma_8$. But for the scope of constraining cosmology from galaxy clustering alone, we emphasize that the following statement is of particular importance and an integral part of the *ShapeFit* presented in this work. The three physical parameters that the classic RSD analysis actually measures at a given redshift bin, $D_M/s$, $H \cdot s$, and $f\sigma(s \cdot 8h^{-1}\mathrm{Mpc})$ are *all* given in units of the sound horizon ratio $s$, whenever units of length are involved. This holds for cosmological distances and smoothing scales in particular. It should be noted that by using this convention the question whether to use length units of Mpc or $h^{-1}$Mpc (see [84]) does not need to be posed. For this reason we recommend to slightly modify the interpretation of the classic RSD parametrization of the perturbations amplitude, to use $\sigma_{s8}$ as a parameter and have $\sigma_8$ as a derived parameter instead. We stress here that our proposed redefinition of $f\sigma_8$ does not involve any changes on how to carry out the fit, but becomes important at the level of interpretation (see sections 3.4 and 3.5 for details).



JCAP12(2021)054

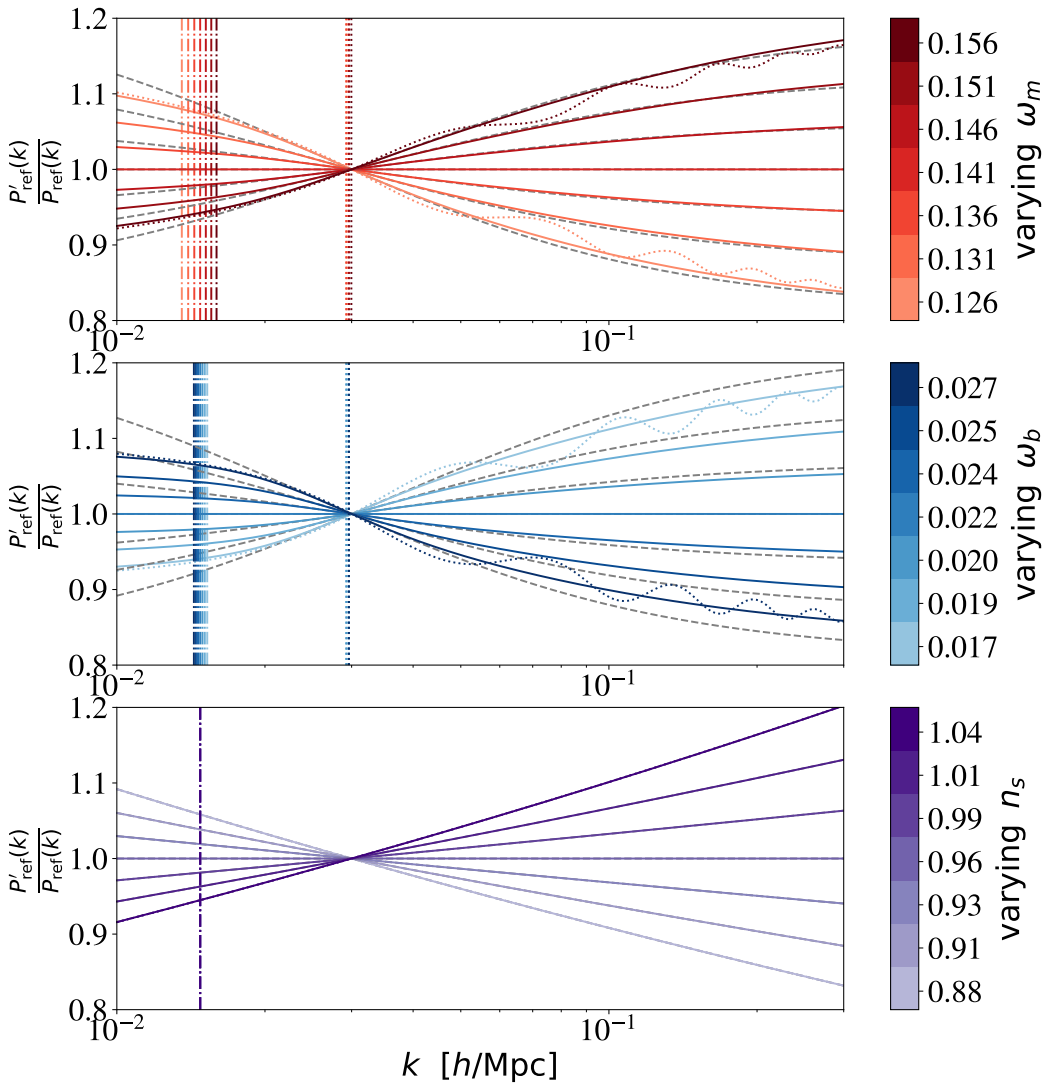


**Figure 4**. Rescaled EH98 prediction of the power spectrum shape (colored sold lines) comparison with the parameterization of eq. (3.7) for $a = 0.6, k_p = 0.03\,h\mathrm{Mpc}^{-1}$. This choice fits the response to $\omega_\mathrm{m}$ (upper panel) very well and to $\omega_\mathrm{b}$ (middle panel) less well but still sufficient for our purposes. Dashed-dotted vertical lines show the rescaled location of $k_\mathrm{eq}$ for each model and dotted vertical lines highlight the positions where the scale-dependent slope reaches a maximum. This position is constant with varying cosmological parameters and very close to the expectation $k_p = \pi/r_\mathrm{d}^\mathrm{ref} \approx 0.03\,h\mathrm{Mpc}^{-1}$. The scale independent slope fits the prediction of varying $n_s$ (bottom panel) perfectly by definition. For the most extreme shifts in parameters we also show in dotted lines the CLASS prediction, whose shape is matched very well by the EH98 formula.

JCAP12(2021)054

### 3.3 Modelling the linear power spectrum shape

The classic BAO and RSD approaches assume that all early-time physics is captured by the free parameter $r_{\rm d}$.[14] Yet, as discussed in section 2.2, there is additional early-time physics signal in the power spectrum. First, information on the primordial power spectrum independent of $r_{\rm d}$ is present about the primordial amplitude $A_s$ (which is completely absorbed by $\sigma_8$) and the primordial tilt $n_s$, which is not captured in any way within the classic approach. Moreover, the broadband is shaped by the transfer function encoding the evolution (scale and time dependence) of the initial fluctuations from inflation until the time of decoupling of the photon-baryon fluid, which in a ΛCDM model, depends on the physical baryon and matter densities $\omega_{\rm m}, \omega_{\rm b}$ and $h$ (see section 2.2 and the middle panel of figure 1). The bottom panel of this figure clearly shows that even after absorbing the dependence on $r_{\rm d}$ (and hence aligning the BAO wiggle position), there is an additional dependence mostly visible in the slope and the BAO wiggle amplitude.

This additional signal is ignored in classic BAO and RSD approaches for two main reasons. On one hand, the BAO wiggles are the most prominent feature in the power spectrum and their position provide the most robust standard ruler to infer the universe's expansion history. On the other hand, this approach decouples the early-time information from the late-time information, that encodes the dynamics of the universe during the matter and dark energy dominated epochs (without an internal model prior).

We present here a simple, phenomenological extension of the classic RSD fit that is able to capture the bulk of the information coming from the early-time transfer function. We propose to compress this additional signal into 1 or 2 effective parameters in such a way that early-time and late-time information is still decoupled, but can be easily and consistently combined at the interpretation stage when constraining cosmological parameters (i.e., the internal model prior can be imposed at the cosmological parameters inference step, but not before). Our goal is get the best of both approaches: on one hand to preserve the model-independent nature of the compressed physical variables of the classic approach; and on the other hand match the constraining power of the FM approach when interpreted within the cosmological model parametrization of choice.

As the bottom panel of figure 1 shows, the classic RSD fit already takes into account the change in the global amplitude due to $\sigma_8$ and $h$ through $f\sigma_{s8}$ and of course the BAO position through $r_{\rm d}$. As mentioned before, the additional degrees of freedom are the slope of the power spectrum (in a ΛCDM model depending on $\omega_{\rm m}, \omega_{\rm b}, n_s$) and the BAO wiggle amplitude depending on $\omega_{\rm b}, \omega_{\rm m}$. Within ΛCDM both effects are directly coupled, this is what we refer to as the internal model prior. As we aim to find a model-independent parametrization, we should keep both effects separate. Moreover, we focus only on the slope and do not model the BAO wiggle amplitude, keeping it to the prescription provided by the perturbation theory model at a given fixed template. We adopt this approach for two reasons. First, we expect the bulk of the additional signal to come from the variation of the slope, not the BAO amplitude. Second, the BAO amplitude signal is not as robust as its position. Some bias models for example can change the BAO amplitude (see e.g., [85]) and the amount of non-linear BAO damping is somewhat model-dependent [86].

Our *Ansatz* for modelling the slope of the linear power spectrum template is as follows. We assume that the logarithmic slope consists of two components: the overall scale-independent

[14] In fact, it is treated more as a unit rather than a free parameter at this step. However, when we interpret the unit in terms of cosmological parameters we actually constrain the parameter $r_{\rm d}$.



JCAP12(2021)054

slope $n$ (this is completely degenerate with $n_s$) and a scale-dependent slope $m$, that follows the transition of the linear power spectrum from the large scale to the small scale limit (in a $\Lambda$CDM model this is driven by the combined effect of $\omega_{\rm b} and \omega_{\rm m}$). To do so, we transform the reference power spectrum template, $P_{\rm ref}(k)$, into a new reference template, $P'_{\rm ref}(k)$, via a slope rescaling

$$\ln\left(\frac{P'_{\rm ref}(k)}{P_{\rm ref}(k)}\right) = \frac{m}{a}\tanh\left[a\ln\left(\frac{k}{k_p}\right)\right] + n\ln\left(\frac{k}{k_p}\right), \tag{3.7}$$

where the hyperbolic tangent is a generic sigmoid function reaching its maximum slope $m$ at the pivot scale $k_p$ and the amplitude $a$ controls how fast the large scale and small scale limits are reached. The pivot scale $k_p$ introduced here should not be confused with the "primordial pivot scale" $k_{\rm piv}$, that is usually chosen to be $k_{\rm piv} = 0.05\,{\rm Mpc}$ (see eq. (2.7)). In contrast, the pivot scale $k_p$ is chosen to coincide with $k_{\rm slope} = \pi/r_{\rm d}$ introduced in figure 1 corresponding to the location where the slope due to baryon suppression reaches its maximum.

We test this expectation numerically by comparing eq. (2.7) to the actual power spectrum shape (without BAO wiggles) obtained with the analytic EH98 [20] formula and its response to the parameters $\omega_{\rm m}$ and $\omega_{\rm b}$ after rescaling each curve by the corresponding value of $r_{\rm d}$. The latter is important, since the transformation displayed by eq. (3.7) is applied before rescaling the template, so that we need to rescale the cosmological prediction (here given by the EH98 formula) such that it matches the value of $r_{\rm d}^{\rm ref}$.

The comparison is shown in figure 4 for varying $\omega_{\rm m}$ (upper panel), $\omega_{\rm b}$ (middle panel) and $n_s$ (bottom panel). Colored solid lines are the EH98 no-wiggle power spectra ratios with color codes given by the adjacent color bars. The reference cosmology "Planck", to which they are compared, is given by table 1. We also show the position of $k_{\rm eq}$ after rescaling by $r_{\rm d}$ (dashed-dotted vertical lines). One can see that it is mildly affected by $\omega_{\rm b}$ (through the weak $\omega_{\rm b}$ dependence of $r_{\rm d}$) and by $\omega_{\rm m}$, since $k_{\rm eq}$ and $r_{\rm d}$ scale similarly with $\omega_{\rm m}$ as explained in section 2.2. For the most extreme parameter shifts, we also show the CLASS prediction (dotted lines), which agrees with the shape of the EH98 formula very well. The dashed grey curves correspond to the r.h.s. of eq. (3.7), where in the case of the $\omega_{\rm m}$ and $\omega_{\rm b}$ sub-panels the slope $m$ is given as the derivative of the colored curves at the pivot scale $k_p$ with $n = 0$; and vice versa for the $n_s$ sub-panel. For the latter, as we see from the bottom panel, the agreement between eq. (3.7) and the model is exact. This is simply because $n$ and $n_s$ are equivalent by definition, and this holds independent of the chosen pivot scale (as both describe a scale independent slope). In what follows, for simplicity, we will focus on the case where $n$ is fixed to 0, which is equivalent to impose a prior $n_s = n_s^{\rm ref}$.

We calibrate the remaining parameters $a$ and $k_p$ with the EH98 formula for varying $\omega_{\rm m}$ and find,

$$a \approx 0.6, \qquad k_p \approx 0.03\,h{\rm Mpc}^{-1} \approx \pi/r_{\rm d}^{\rm ref}, \tag{3.8}$$

matching the EH98 formula at 0.5% level precision on scales $0.02 < k\,[h^{-1}{\rm Mpc}] < 0.25$. The same choice of parameters also captures very well the $\omega_{\rm b}$-dependence, with at most 3% deviation in the same range of scales.

Now we have all the ingredients for the *ShapeFit*, where the transformation eq. (3.7) is applied before the rescaling by $\alpha_\perp$ and $\alpha_\parallel$. In this sense, the *ShapeFit* consists of applying the classic RSD fit to a reference template $P'_{\rm ref}(k)$, that is transformed at each step via (3.7) with free parameters $m$ (and $n$, if needed). In principle this transformation should be



JCAP12(2021)054

applied also to the reference power spectra that appear in the integrand of higher-order perturbation corrections. In our implementation, however, in order to avoid a re-evaluation of all perturbative terms at each step of the likelihood exploration, we apply this transformation as if it were independent of scale. In practice this means that we pre-compute all the loop corrections using the linear power spectrum given by $P_{\rm ref}$. During the likelihood evaluation we transform each of these terms using eq. (3.7), taking into account the power of the linear power spectrum used to compute them, which is a power of $N+1$ for the $N$-loop corrections. To be more precise, in the case of SPT we evaluate the 1-loop correction $P_{1-\rm loop} = P_{13} + P_{22}$ depending on the (new) reference linear template $P'_{\rm ref}$ and the corresponding kernels $F_i$ using the following approximations,

$$\begin{aligned} P_{13}(k) &= P'_{\rm ref}(k) \int_0^\infty d^3q\, P'_{\rm ref}(q) F_3(k,q,-q) \\ &\approx \left(\frac{P'_{\rm ref}(k)}{P_{\rm ref}(k)}\right)^2 P_{\rm ref}(k) \int_0^\infty d^3q\, P_{\rm ref}(q) F_3(k,q,-q), \\ P_{22}(k) &= \int_0^\infty d^3q\, P'_{\rm ref}(q) P'_{\rm ref}(|q-k|) F_2(k,q-k) \\ &\approx \left(\frac{P'_{\rm ref}(k)}{P_{\rm ref}(k)}\right)^2 \int_0^\infty d^3q\, P_{\rm ref}(q) P_{\rm ref}(|q-k|) F_2(k,q-k). \end{aligned} \tag{3.9}$$

We show in appendix D that this approximation is very good and more than sufficient for our purposes. With this, the computational time of *ShapeFit* is effectively indistinguishable from that of the classic RSD approach, except at the MCMC level, where the posterior sampling involves one (or two) extra parameters. It is of academic interest but still instructive to consider how the discussion of sections 3.1 and 3.2 would change if there were no BAO. In this case it would be misleading to interpret $s$ as the sound horizon ratio. Nevertheless, *ShapeFit* can be used in the case of zero baryons (or no-BAO) either by setting $s = 1$ (which is similar to the classic method where $s$ would be set to 1 inside the $\alpha$ terms), or by interpreting $s$ not as the sound horizon ratio, but rather as the ratio of "pivot scale" $k_p/k_p^{\rm ref}$ (see eqs. (3.6)–(3.9)). Generally speaking, the *ShapeFit* parameterization does not rely on BAO, but rather on the notion, that there is some early-time physics scale — a ruler — that mostly defines the power spectrum shape.

### 3.4 Cosmological interpretation

The *ShapeFit* constraints on the physical and phenomenological parameters, $\{\, \alpha_\parallel, \alpha_\perp, f\sigma_{s8}, m, n \,\}$ can be then interpreted in terms of cosmological parameters. This step is, naturally, very similar to the way standard RSD likelihoods are implemented already in the most common cosmological inference codes. In the classic RSD approach, results on $\left\{\alpha_\parallel, \alpha_\perp, f\sigma_8\right\}$ and their covariance for all redshift bins are used as input for cosmological parameters inference, where the $\chi^2$ (or log-likelihood) is computed for the theoretical prediction for each quantity given an input cosmological model and parameters values. For the *ShapeFit* the relevant aspects in this step are the calculation of the scaling parameters, fluctuation amplitude and growth rate, and the power spectrum slope (the only new ingredient).

**Scaling parameters.** The interpretation of $\left\{\alpha_\parallel, \alpha_\perp\right\}$ is exactly the same as in the classic RSD approach. Therefore, any existing likelihood computing these quantities using eq. (2.15) is left unchanged.



JCAP12(2021)054

**Fluctuation amplitude and growth.** The interpretation of $f\sigma_{s8}$ is nearly the same as in the classic RSD analysis with the only difference that we advocate the fluctuation amplitude to be defined as $\sigma_{s8}$ instead of $\sigma_8$, see eqs. (3.5) and (3.6) and section 3.2.

However, the slope rescaling (eq. (3.7) and section 3.3) changes $\sigma_{s8}$ for $m, n \neq 0$. Therefore, it is convenient to define the fluctuation amplitude $A_p$ at the pivot scale $k_p$

$$A_p^{\rm ref} = P^{\rm lin}_{\rm no-wiggle}\left(k_p, \mathbf{\Omega}^{\rm ref}\right) , \tag{3.10}$$

which does not change with slope by definition;[15] $A_p^{\rm ref}$ is defined for the reference template. As the analysis explores the posterior of the physical and phenomenological parameters, following section 3.3 it is possible to recognize that the amplitude parameter becomes, internally to the fit,

$$A_{sp} = \frac{1}{s^3} P^{\rm lin}_{\rm no-wiggle}\left(\frac{k_p}{s}, \mathbf{\Omega}\right) , \quad \text{with} \quad s = \frac{r_{\rm d}}{r_{\rm d}^{\rm ref}} . \tag{3.11}$$

This amplitude, $A_{sp}$, can be understood as the "late-time" counterpart of the amplitude of the primordial power spectrum $A_s$, but the two quantities should not be confused. The actual velocity fluctuation amplitude measurement is then given as $fA_{sp}^{1/2}$, and thus

$$f\sigma_{s8} = \frac{(f\sigma_{s8})^{\rm ref}}{(fA_{sp}^{1/2})^{\rm ref}} fA_{sp}^{1/2} . \tag{3.12}$$

Eq. (3.12) can be used in order to obtain the more frequently used $f\sigma_{s8}$ variable, although we advocate using $fA_{sp}^{1/2}$ for cosmological parameter inference. It should be clear (see also section 3.5) that we only propose a reinterpretation of the amplitude parameter not a change in the analysis or definitions.

**Power spectrum slope.** The new ingredient of the *ShapeFit* is given by the slope, parametrized by $m$, $n$ following eq. (3.7). The interpretation of the scale independent slope $n$ is trivial, as it can be directly related to the primordial scalar tilt $n_s$ via,

$$n = n_s - n_s^{\rm ref} . \tag{3.13}$$

The interpretation of the scale-dependent slope $m$ then becomes:

$$m = \frac{d}{dk}\left(\ln\left[\frac{P^{\rm lin}_{\rm no-wiggle}\left(\frac{k_p}{s}, \mathbf{\Omega}\right)/\mathcal{P}_{\mathcal{R}}\left(\frac{k_p}{s}, \mathbf{\Omega}\right)}{P^{\rm lin}_{\rm no-wiggle}\left(k_p, \mathbf{\Omega}^{\rm ref}\right)/\mathcal{P}_{\mathcal{R}}\left(k_p, \mathbf{\Omega}^{\rm ref}\right)}\right]\right)\Bigg|_{k=k_p} . \tag{3.14}$$

where $\mathcal{P}_{\mathcal{R}}\left(k, \mathbf{\Omega}\right)$ denotes the primordial density power spectrum. In case $n_s$ is varied during the cosmological fit, eq. (3.14) has to be applied to the power spectrum obtained when $n_s$ is fixed to the reference value. This ensures that a change in $n_s$ does not lead to a different prediction for $m$ but only for $n$ via eq. (3.13). In other words, $n$ is obtained from the primordial

[15] It should be noted, that the amplitude $A_{sp}$ needs to be obtained from the "no-wiggle" power spectrum (given by the EH98 formula for instance), to ensure that the BAO wiggles do not influence the amplitude. Normally, this is ensured by using $\sigma_8$ as the amplitude, a quantity, for which the BAO wiggles are integrated over. But since eq. (3.7) operates in Fourier Space, it is more convenient to define the amplitude in Fourier space as well.



JCAP12(2021)054

power spectrum, while $m$ is obtained from the transfer function squared (which is the power spectrum divided by the primordial power spectrum).

In practice, the no-wiggle linear power spectrum $P^{\rm lin}_{\rm no-wiggle}$ is computed using the EH98 formula. While being computationally much faster this formula matches the Boltzmann code output formally at the 5% level over a wide range of cosmologies. However, for the parameter range investigated here and since we are considering power spectrum ratios we find 1% level precision, suitable for this application. An implementation of the cosmological likelihood containing the interpretation of our *ShapeFit* BOSS DR12 results within MontePython is publicly available.[16]

### 3.5 *ShapeFit* implementation recipe

We summarize the changes to be done to the classic BAO+RSD analysis (and respective codes) to implement *ShapeFit* in the flowchart of figure 5. This chart can be seen as an executive summary of *ShapeFit* (upper dashed lines) from data acquisition to modelling and its cosmological interpretation (bottom dashed lines) including all pointers to relevant equations. In this flowchart the purple fields represent steps in the "classic" approach while orange fields represent the *ShapeFit* additions. Circles represent parameters, boxes in the top part of the diagram represent analyses steps, in the bottom part of the diagram represent products of theoretical calculations.

## 4 Application to mocks of SDSS-III BOSS survey data

We now describe our fiducial analysis setup which we use to compare the *ShapeFit* introduced in section 3 with the FM fit. The FM application is done following the EFT implementation by [39]. We first present the mocks in section 4.1 and describe the model choices in section 4.2.

### 4.1 Mock catalogs

We apply our analysis pipeline to the MultiDark-Patchy BOSS DR12 (Patchy) mocks created by [87, 88]. The fiducial ΛCDM parameters of the Multidark simulation are,

$$\Omega_{\rm m} = 0.307115, \quad \Omega_{\rm b} = 0.048206, \quad h = 0.6777, \quad \sigma_8 = 0.8288, \quad n_s = 0.9611\,. \tag{4.1}$$

The mock catalogs are designed to reproduce the angular and radial selection function and small scale clustering of BOSS DR12 data. These mocks have been used extensively in the development of the analysis of the BOSS survey, and provide many realizations, which is crucial for estimating covariance matrices and for stacking to reduce statistical errors. However it is important to keep in mind that these are not full N-body runs, but are based on Augmented Lagrangian Perturbation Theory and an exponential bias scheme. Small differences with N-body mocks are not unexpected. For this reason in section 6 we also consider independently generated Nseries mocks (see section 7.2 of [27] as well as section 2.2.2 of [72] for details) based on full N-body runs, populated using halo occupation distribution parameters that match Luminous Red Galaxies (LRG) observations and with the sky-geometry of BOSS DR12 CMASS northern galactic cap sample. In the remainder of this section we focus only on the (Patchy) mocks "ngc_z3" sample located at the north galactic cap and covering a redshift range of $0.5 < z < 0.75$ with effective redshift $z_{\rm eff} = 0.61$. We work with all 2048 realizations of the Patchy mocks, which are publicly available.[17]

[16] https://github.com/SamuelBrieden/shapefit_montepython_code.
[17] https://fbeutler.github.io/hub/boss_papers.html.



JCAP12(2021)054

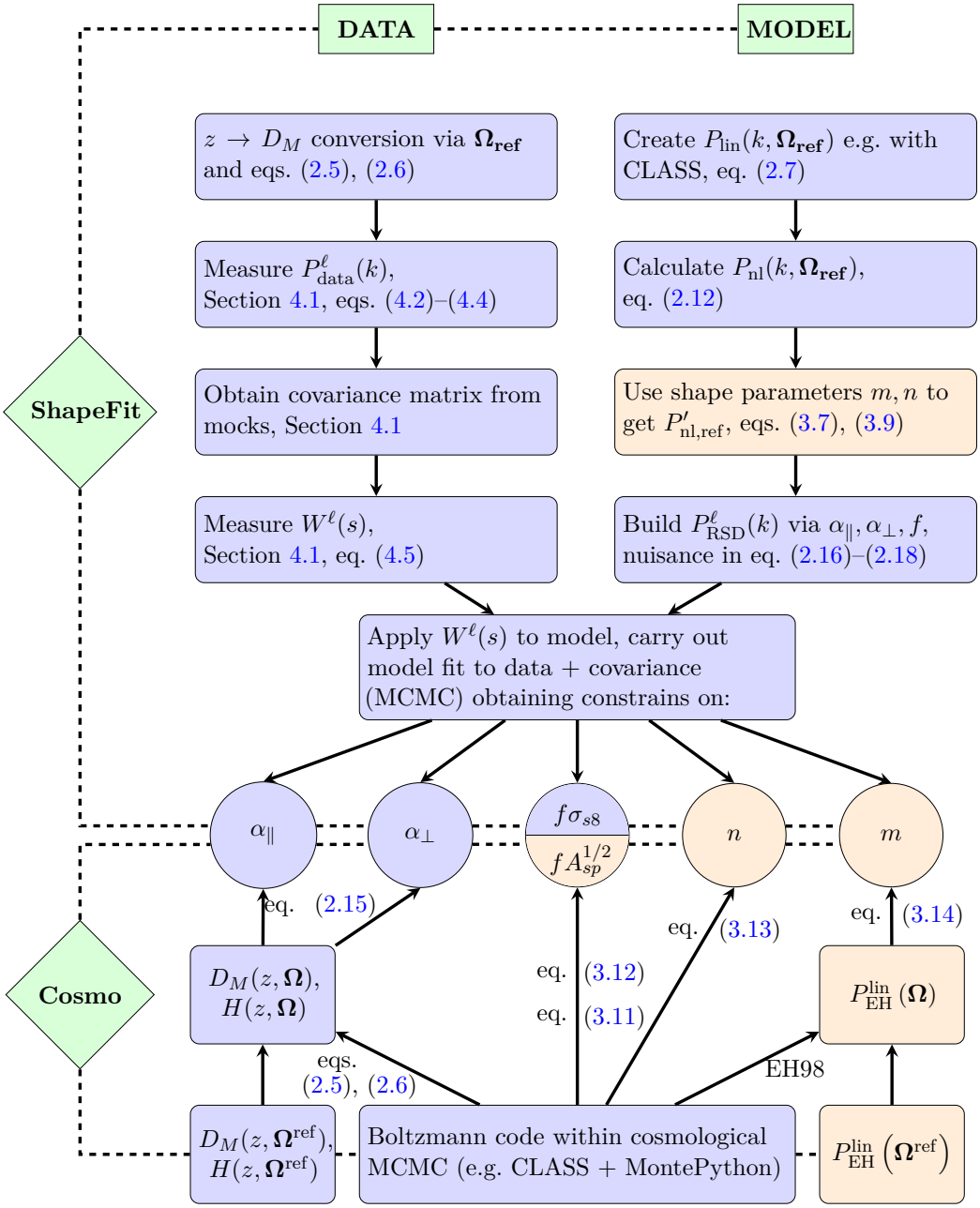


**Figure 5**. Executive summary of *ShapeFit* (upper dashed lines) from data acquisition ("DATA", see sections 2 and 4.1) to modelling ("MODEL") and its cosmological interpretation ("Cosmo") (bottom dashed lines, sections 2 and 3) including all relevant equations. The purple fields represent steps in the "classic" approach while orange fields represent the *ShapeFit* additions. Circles represent parameters, boxes in the top part of the diagram represent analyses steps, in the bottom part of the diagram represent products of theoretical calculations.

JCAP12(2021)054

In addition to angular positions and redshifts, the catalogs provide simulated close-pair weights $w_{\rm cp}$ to account for galaxy pairs neighboured closer than the instrument angular resolution (limited by the fiber size). Also, the catalogs contain the angle averaged number density $\bar{n}(z)$ for each galaxy, which allows one to construct the FKP weight $w_{\rm FKP}(z) = 1/(1+\bar{n}(z)P_0)$ [89]. This weight is used to minimize the power spectrum variance at $P_0 = 10,000\,[{\rm Mpc}h^{-1}]^3$, which corresponds to the galaxy power spectrum amplitude at $k \sim 0.1\,h{\rm Mpc}^{-1}$. We also use the random catalogs provided along with the mocks containing $\alpha_{\rm ran}^{-1} = 50$ times more objects than the individual mocks. They have the same selection function but no intrinsic clustering.

We measure the multipole power spectra of each individual mock catalog. Then, we take the mode-weighted power spectra average of all 2048 realizations, which is used as our dataset. The error bars (including correlations between different bins) are obtained from the covariance of the 2048 mocks. At the step of covariance matrix inversion, we apply the Hartlap correction [90] taking into account the small bias due to the finite number of mock catalogs. We fit the mean of the 2048 mocks and rescale the covariance matrix by a factor 0.01, which corresponds to the volume of 100 stacked mocks.[18] Finally, we compute the survey window function, which is needed in order to compare theoretical models to the mock data. Our procedure of the power spectrum estimation and the window function computation (which is standard) is described in more detail below.

**Power spectrum estimator.** We place the galaxies into a cubic box with length $L_{\rm box} = 3.6\,{\rm Gpc}h^{-1}$ using the reference cosmology of table 1 (with $\Omega_{\rm m} = 0.31$) to convert redshifts to distances. We assign galaxies and random objects to $512^3$ grids using the triangular shape cloud (TSC) grid assignment and using the interlacing technique to mitigate aliasing effects [91]. Using the obtained galaxy and random densities, $n(\mathbf{r})$ and $n_{\rm ran}(\mathbf{r})$, we follow standard practice and define the FKP function as [89],

$$F(\mathbf{r}) = \frac{w_{\rm FKP}(\mathbf{r})}{I_2^{1/2}}\left[w_{\rm cp}(\mathbf{r})n(\mathbf{r}) - \alpha_{\rm ran}n_{\rm ran}(\mathbf{r})\right]\,, \tag{4.2}$$

where the normalization factor $I_2$ is given as

$$I_2 = \int d^3\mathbf{r}\, w_{\rm FKP}(\mathbf{r})\,\langle w_{\rm cp}(\mathbf{r})n(\mathbf{r})\rangle^2\,\,. \tag{4.3}$$

We construct the power spectrum multipoles via Fourier transformations following the Yamamoto approximation [92, 93]

$$P^{(\ell)}(k) = \frac{(2\ell+1)}{2}\int\frac{d\Omega}{4\pi}\left[\int d\mathbf{r}_1\,F(\mathbf{r}_1)e^{i\mathbf{k}\cdot\mathbf{r}_1}\int d\mathbf{r}_2\,F(\mathbf{r}_2)e^{-i\mathbf{k}\cdot\mathbf{r}_2}\mathcal{L}_\ell(\hat{\mathbf{k}}\cdot\hat{\mathbf{r}}_2)\right] - P_{\rm sn}^{(\ell)}\,, \tag{4.4}$$

that assigns the varying LOS towards one of the galaxies of each pair. The Poisson shot noise term $P_{\rm sn}^{(\ell)}$ can be measured from the catalog and is subtracted from the monopole only, as for $\ell > 0$ it is zero. However, the amplitude of the shot noise term is treated as a free parameter in our analyses, as described in more detail in section 4.2. We measure the multipoles in bins of $\Delta k = 0.005\,h{\rm Mpc}^{-1}$ and make use of the scale-range $0.01 \le k\,[h{\rm Mpc}^{-1}] \le 0.15$ for the analyses in this paper.

[18] We do not rescale it to a volume of 2048 mocks, since this would decrease the error bars to a level much smaller than the model uncertainty (both of 1-loop SPT and of the semi-analytic models used to create the mocks). The corresponding effective volume of the 100 stacked mocks ($\approx 300\,{\rm Gpc}^3$ assuming the "Planck" cosmology) is still significantly larger than the effective volume of the next generation of galaxy redshift surveys.



JCAP12(2021)054

**Window function.** The resulting power spectrum of eq. (4.2) contains the effect of the survey selection function convolved with the actual galaxy power spectrum signal. In order to perform an unbiased analysis we need to include the effect of the survey selection in the theory model as well. We follow the formalism described in [65, 81] based on the Hankel transforms and implemented via FFT-log [34], which relies on multiplying the Hankel transform of the theory-predicted power spectra multipoles by the window function pair-counts functions performed on the random catalogue,

$$W_\ell(s) = \frac{(2\ell+1)}{I_2\alpha_{\rm ran}^{-2}} \sum_{j>i}^{N_{\rm ran}} \frac{w_{\rm cp}(\mathbf{r}_i) w_{\rm FKP}(\mathbf{r}_i) w_{\rm cp}(\mathbf{r}_j+\mathbf{s}) w_{\rm FKP}(\mathbf{r}_j+\mathbf{s})}{2\pi s^2 \Delta s} \mathcal{L}_\ell\left(\frac{\mathbf{x}_i\cdot\mathbf{s}}{x_i s}\right) . \tag{4.5}$$

The pair-count for each $s$-bin is normalized by the associated volume given by $2\pi s^2\Delta s$, where $\Delta s$ is the binning size of the $s$-count and the $j > i$ condition prevents double counting pairs. The window function is normalized by $I_2\alpha_{\rm ran}^{-2}$ in order to account for the difference in number density between the random and data catalogue and to ensure the very same normalization as the power spectrum computed from eq. (4.2). Normalizing both eqs. (4.2) and (4.5) by the same $I_2$ factor prevents spurious leakage of the small-scale fluctuations of the random catalogue into the cosmological parameters, such as $\sigma_8$ or $A_s$, that typically could yield to systematic shifts [94].

### 4.2 Priors and likelihoods

Here we present our analysis choices for the two methods we aim to compare, the *ShapeFit* and the FM fit. The *ShapeFit* is performed in two steps.[19] First, the physical parameters $\left\{\alpha_\parallel, \alpha_\perp, f, m, n\right\}$ are varied along with the nuisance parameters (compression step). Second, the results on physical parameters are treated as the new "input data" and compared to any cosmological model of choice (cosmology inference step) As it is customary, in the cosmology inference step the full covariance between the compressed variables is included in computing the likelihood and the resulting parameters posterior is sampled via MCMC. The FM fit consists of only one step, where the nuisance parameters are varied along with the cosmological parameters, while the physical parameters are not varied, since they are derived from the cosmological model. The fitting range in all presented runs is $0.01 \leq k\,[h\mathrm{Mpc}^{-1}] \leq 0.15$

In table 3 we show the model parameters and prior choices for both methods, where the model used for the *ShapeFit* is based on the 1-loop SPT +TNS model introduced in section 2.3 and the extensions described in section 3. As a representative model of the FM fit approach we choose the EFT implementation of [39], which is also based on 1-loop SPT, but with a few differences.

It is well known that the BAO amplitude is affected by non-linear coupling to large scale displacements (bulk flows), that are hard to model within Eulerian PT (at the base of 1-loop SPT, which is used in this work). In the FM approach this is done by implementing the so called "Infrared (IR) resummation" effect, that can be well described within Lagrangian PT, via a phenomenological damping of the BAO amplitude. Since there is no equivalent IR resummation correction in *ShapeFit* (at least not in this first implementation), and including this effect in the FM fit broadens the constraints, we perform the *ShapeFit* to FM comparison by not including IR resummation in the FM fit, but we return to this point in appendix A. It

[19] Actually the *ShapeFit* only consists of the first step, but the second step is needed in order to compare both analysis types.



JCAP12(2021)054

| Parameter | | Prior ranges | | | |
|---|---|---|---|---|---|
| type | name | SF min | SF max | FM min | FM max |
| Cosmological | $\omega_{\rm cdm}$ | [None, None] | | [None, None] | |
| | $h$ | [None, None] | | [None, None] | |
| | $\ln(10^{10}A_s)$ / $A^{1/2}$ | [None, None] | | [0.2, 2.0] | |
| Physical | $\alpha_\parallel$ | [0.5, 1.5] | | – | |
| | $\alpha_\perp$ | [0.5, 1.5] | | – | |
| | $f$ | [0, 3] | | – | |
| | $m$ | [−3, 3] | | – | |
| Nuisance | $b_1$ | [0, 10] | | [0, 10] | |
| | $b_2$ | [-10, 10] | | [-10, 10] | |
| | $b_{s2}$ | lag. | [-10, 10] | lag. | [-10, 10] |
| | $b_{\rm 3nl}$ | lag. | [-10, 10] | lag. | 0 |
| | $c_0\,[h^{-2}{\rm Mpc}^2]$ | – | | 0 | $(0 \pm 30)$ |
| | $c_2\,[h^{-2}{\rm Mpc}^2]$ | – | | $(0 \pm 30)$ | |
| | $c_4\,[h^{-4}{\rm Mpc}^4]$ | – | | $(500 \pm 500)$ | |
| | $\sigma_P\,[h^{-1}\,{\rm Mpc}]$ | [0, 10] | | – | |
| | $A_{\rm noise}$ / $\Delta P_{\rm noise}\,[h^{-3}{\rm Mpc}^3]$ | [-5, 5] | | $(0 \pm 5000)$ | |

**Table 3**. Prior ranges for parameters used for the *ShapeFit* and the FM fit. For each, we define a case with minimum ("min") and maximum ("max") freedom, where overlapping prior choices between the two choices are written in the center. Flat priors are given as [min, max], Gaussian priors are denoted as (mean ± std). Parameters separated by "/" correspond to different conventions used between *ShapeFit* and FM fit for the same physical effect, see text for details.

will become clear below that to see at a statistical significant level the effect of including or not the IR resummation for *ShapeFit* a survey volume of $\sim 300\,[{\rm Gpc}h^{-1}]^3$ would be needed.

The EFT model phenomenologically accounts for higher order non-linearities via the so called "counterterms" parametrized by $\{c_0, c_2, c_4\}$ (see [39] for the explicit equations). In summary, $c_0$ effectively corrects for dark matter behaving differently than a perfect fluid on small scales (monopole only) and $\{c_2, c_4\}$ take into account non-linear RSD (quadrupole only). While in the *ShapeFit* we use the non-linear RSD prescription of [62] (TNS model) in combination with a phenomenological Lorentzian damping parametrized by $\sigma_P$ (see eq. (2.13)), the counterterms $\{c_2, c_4\}$ are coefficients of a $2^{\rm nd}$ order Taylor expansion of the phenomenological damping describing the non-linear redshift space distortions. Hence, the EFT implementation of non-linear RSD is equivalent to our *ShapeFit* implementation, but with more freedom (2 parameters instead of 1).

Another difference is the interpretation of bias parameters, that in the *ShapeFit* incorporate an implicit scaling with $\sigma_{s8}$, while in the EFT fit they scale with the primordial fluctuation amplitude as $A^{1/2}$, where

$$A^{1/2} = (A_s/A_s^{\rm Planck})^{1/2}\,, \qquad A_s^{\rm Planck} = 2.0989 \times 10^{-9}\,. \tag{4.6}$$

Yet another difference concerning nuisance parameters is the convention for treating shot noise. While the EFT implementation uses a Gaussian prior on the difference between the shot noise with respect to Poisson shot noise $\Delta P_{\rm noise} = P_{\rm noise} - P_{\rm Poisson}$, we implement a flat prior on the fractional difference $A_{\rm noise}$, the amplitude of the Poisson-like, scale independent shot noise contribution. We have tested that this does not make any difference in the posterior distributions.



JCAP12(2021)054

Considering these differences in model assumptions between *ShapeFit* and FM fit we adopt two different nuisance parameter choices represented by a minimum freedom ("min") and a maximum freedom ("max") choice. The "min" convention is oriented towards the fiducial setup of most classic RSD analyses, where the non-local bias parameters are fixed by the local Lagrangian ("lag.") prediction [57, 58],

$$b_{s2} = -\frac{4}{7}(b_1 - 1), \qquad b_{3\mathrm{nl}} = \frac{32}{315}(b_1 - 1) \ . \tag{4.7}$$

In the maximum freedom case $b_{s2}$, $b_{3\mathrm{nl}}$ and $b_1$ are treated as independent parameters. We employ these relations also in the FM "min" case and also fix the counterterm $c_0$ to zero, in order to match the *ShapeFit* configuration. However we keep varying the counterterms $c_2, c_4$, as they are related to non-linear RSD, which in the *ShapeFit* is parametrized by $\sigma_P$ as described above. The "max" convention is oriented towards the fiducial setup of [39], where all counterterms are varied and the Lagrangian relations are relaxed. However, the third order non-local bias $b_{3\mathrm{nl}}$ is set to zero in the EFT implementation, because it is very degenerate with the monopole counterterm $c_0$. We do the same here, since we try to stick to the default configuration of [39] as close as possible. However, we vary $b_{3\mathrm{nl}}$ in the *ShapeFit*, in order to compensate for the fact, that $c_0$ is not an ingredient of our model. Further tests of the *ShapeFit* concerning modelling choices of non-local bias parameters are shown in sections 5.2, 6.2 and in appendix C.

Regarding the cosmological parameters, we choose a similar setup as in the baseline analysis of [39] for the PATCHY mocks varying the parameters given in the top rows of table 3. We fix the baryon density to the value of the simulation $\omega_\mathrm{b} = 0.02214$ and do not take into account a varying neutrino mass, since the PATCHY mocks were run with massless neutrinos. Concerning the primordial fluctuation amplitude $A_s$, for the FM fit we adopted the convention of [39] varying $A^{1/2}$ given in eq. (4.6). However, for the step of cosmological inference from the compressed *ShapeFit* results we adopted a flat prior on $\ln(10^{10} A_s)$. This different choice does not affect our cosmological results at all.

## 5 Results

The results of our fiducial analysis on the mocks described in section 4 is presented in two parts. First, we present the results of the parameter compression step comparing the *ShapeFit* with the classic RSD method (section 5.1). Afterwords, assuming a ΛCDM model, we compare the cosmological analysis of the compressed *ShapeFit* results to the model's parameter constraints obtained with the FM method (section 5.1). We also show extensions to our fiducial analysis by adding more cosmological parameters. In particular, we compare the performance of *ShapeFit* and FM fit when varying $\omega_\mathrm{b}$ and $n_s$ in sections 5.3 and 5.4 respectively.

For the mock "data" we always use the mean of 2048 PATCHY "ngc_z3" mocks, where we rescale the covariance to the volume 100 times one of these mocks. This represents a factor 10 times larger than most previous analyses, and significantly larger than the volume of any single tracer or sample of forthcoming surveys. As it will be clear below, by choosing to calibrate the covariance for such a large volume we will see systematic shifts in some parameters which would have gone otherwise unnoticed. These shifts highlight the limitations of the current modelling of non-linearities (see section 2.3), nevertheless, they are still below the $1\sigma$ expected statistical uncertainty for forthcoming surveys.



JCAP12(2021)054

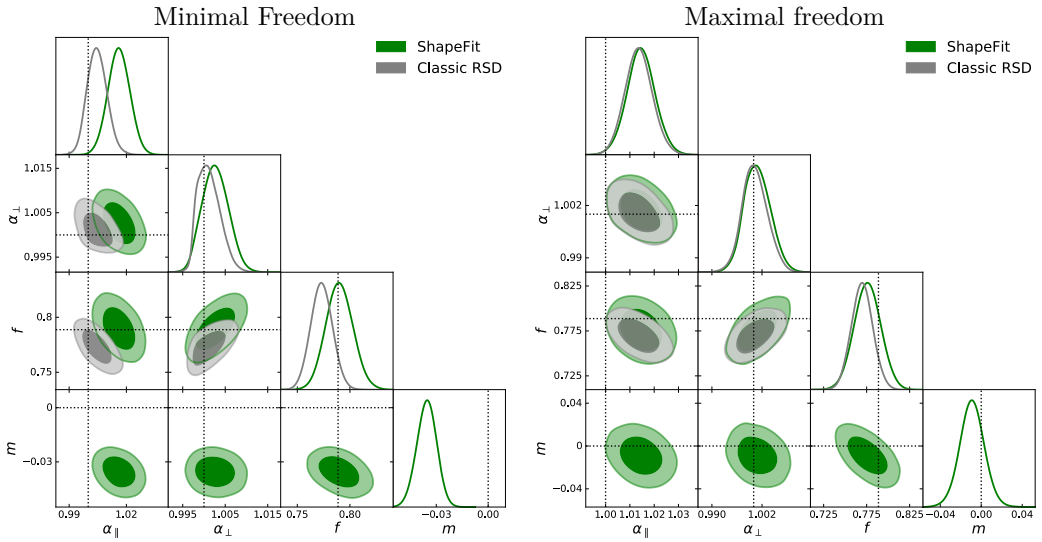


**Figure 6**. Results of the classic RSD fit (grey) and the *ShapeFit* (green) applied to the PATCHY "ngc_z3" sample, showing the "min" (minimal freedom, non-local bias parameters to follow the Lagrangian prediction) case on the left; and the "max" (maximal freedom, fully free non-local bias parameters) case on the right panel. For the "min" case we report a systematic deviation of the slope parameter from the expectation $m = 0$, indicating that assumptions about the biasing scheme may introduce systematic shifts even at very large and linear scales. To make explicit and quantify biases in recovered parameter estimates, the error-bars are relative to an effective volume of $300\,[h^{-1}\mathrm{Gpc}]^3$.

### 5.1 Parameter compression: classic RSD vs. *ShapeFit*

We fit the classic RSD and *ShapeFit* models to the mean of the PATCHY "ngc_z3" mocks using the physical and nuisance parameters of table 3. In both cases we use a template corresponding to the PATCHY cosmology of eq. (4.1), where the slope parameter $m$ is varied in the *ShapeFit* only, while it is fixed to $m = 0$ in the classic RSD fit by definition. We perform the fits for the "min" and the "max" conventions, where the non-local bias parameters $b_{s2}$ and $b_{3\mathrm{nl}}$ are either fixed to their Lagrangian prediction of eq. (4.7) or allowed to vary freely. The results for these cases are shown in figure 6 in the left and right panels, respectively, where grey contours correspond to the classic RSD Fit and green contours to the *ShapeFit*. The dashed lines indicate the underlying parameter values of the simulation.

The uncertainties on $\alpha_\parallel$ and $\alpha_\perp$ are very similar, almost indistinguishable, in the "classic" and *ShapeFit* approaches. On the other hand, *ShapeFit* recovers slightly larger errors on $f$ than the classic approach. This can be understood by considering that while $m$ shows no significant correlation with the $\alpha$ parameters, $m$ and $f$ are somewhat correlated at least for a sample with "ngc_z3" features. In the "min" case (see figure 6 left panel) we observe that the classic RSD constraints are closer to the theoretical prediction than the *ShapeFit* constraints. This is because when we enforce the non-local biases to follow the Lagrangian prediction, the constraint on $m$ experiences a systematic shift towards $m = -0.036 \pm 0.006$, hence being formally in $6\sigma$ tension with the expectation, $m = 0$. This shift in $m$ appears to be a much better fit to the data (bestfit $\chi^2_{m\neq 0} = 51$) than in the classic RSD case, where $m$ is forced to zero (bestfit $\chi^2_{m=0} = 95$). Once we allow the non-local bias parameters to vary freely ("max" case, right panel), we recover $m = 0$ and the constraints on the other physical parameters



JCAP12(2021)054

show very good agreement between classic RSD Fit and *ShapeFit*. Indeed, the bestfit $\chi^2$ for both types of fit is very similar in the max case ($\chi^2_{\rm max} \approx 44$) with a difference of only $\Delta\chi^2 = 0.02$ between classic RSD Fit and *ShapeFit*.

This indicates that even seemingly reasonable and well-motivated assumptions about bias can induce systematic errors in recovered cosmological parameters by affecting clustering even on very large, linear scales, and in particular when the slope $m$ is used for cosmological interpretation. This finding highlights the importance of having a modelling of bias as flexible as possible when interpreting the scale-dependence of clustering at all scales. We speculate that PATCHY mocks may have some bias signature not fully consistent with the local Lagrangian bias scheme. This signal was not evident in the classic RSD analyses, but when we allow $m$ to vary this becomes important. We anticipate not finding such behaviour in the N-body galaxy mocks describing a similar set of galaxies (as we will see in section 6.2).

In the "max" case, there are remaining biases on $\alpha_\parallel$ (of order $2\sigma$) and $f$ (of order $1\sigma$), for an effective survey volume of $300\,{\rm Gpc}^3$; such a large volume yields statistical errorbars with similar size as the model uncertainty. The modelling of non-linearities and redshift-space distortions will likely be improved before the on-going and future surveys are completed and ready for cosmological interpretation. Still, our results indicate that one must be careful with model assumptions, in particular about the galaxy bias model, as its choice can have a significant impact on the measured slope $m$. We perform more tests on different sets of N-body simulations and galaxy mock catalogs in section 6. Nevertheless the right panel of figure 6 demonstrates that *ShapeFit* recovers the standard "classic" compressed parameters with effectively the same uncertainties as the "classic" approach. The degradation of the constraints on $f$ introduced by the extra parameter $m$ (due to a small degeneracy between $f$ and $m$), is minimal, $\sim 20\%$ for a volume of $300\,[h^{-1}{\rm Gpc}]^3$, which is expected to decrease for smaller, more realistic survey volumes (for a DESI-like volume of $30\,[h^{-1}{\rm Gpc}]^3$ the degradation decreases to 5%).

### 5.2 Cosmological results: full modelling vs. *ShapeFit*

Figure 7 displays the cosmological results on $\omega_{\rm cdm}$, $h$ and the derived parameters, $\Omega_{\rm m}$, $\sigma_8$ obtained from interpreting the *ShapeFit* results within a $\Lambda$CDM model as explained in section 3.4, as well as from the direct FM fit (for comparison we added the classic RSD results (grey contours) as well, but also see [80]). In this case we keep $\omega_{\rm b}$ fixed at the mock expected value (see section 5.3 for results varying $\omega_{\rm b}$). Again, we explore the effect of local-Lagrangian bias assumption through the "min" and "max" cases defined in table 3. The FM fit results are displayed in blue ("max") and red ("min"), while the *ShapeFit* results are represented by the green ("max") and orange ("min") contours. We also present the results in table 4, where we added the case of a more realisic, DESI-like-survey volume of $30\,[h^{-1}{\rm Gpc}]^3$ by scaling the covariance of one PATCHY mock realisation by 10 (labeled ($V \times 10$)). As table 4 indicates, considering the latter covariance *ShapeFit* recovers the cosmological parameters very well in the "max" case (within $0.5\sigma$), while the results of the "min" case are clearly biased (by up to $2\sigma$). In the "max" case constraints are, unsurprisingly, weaker than in the "min" case. The same degradation in cosmological parameter constraints between the "min" and "max" cases is observed for the FM fit, albeit it shows larger biases in the recovered parameter values.

The reason why the FM fit results do not recover the PATCHY cosmology, is, at least in part, due to the systematic error in modelling the BAO wiggle amplitudes arising from neglecting IR effects.



JCAP12(2021)054

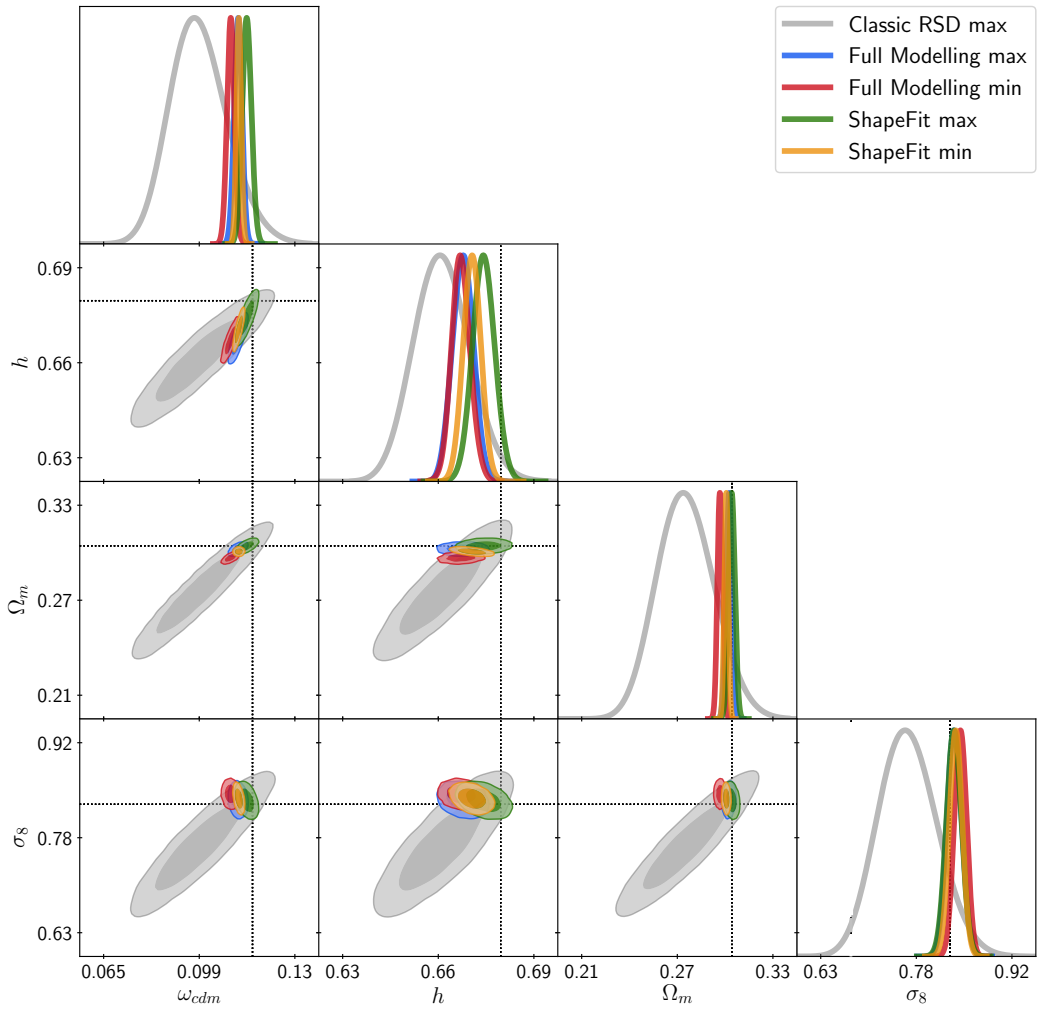


**Figure 7**. Results of the *ShapeFit* and FM fits to the PATCHY "ngc_z3" sample compared to the classic RSD "max" results for reference. The size of the constraints are very similar in the two cases, indicating that *ShapeFit* captures the bulk of cosmological information captured by FM. The systematic shifts associated to the FM contours are partly caused by neglecting the IR resummation correction, which modulates the BAO amplitude, but also broadens the constraints. *ShapeFit* does not use any BAO amplitude information, and therefore does not need to crucially account for any IR resummation correction (although it could be easily incorporated). The fact that the size of the constraints is very similar in the two cases indicates that the cosmological information enclosed in the BAO amplitude is subdominant to the one enclosed in the large-scale shape of the power spectrum.

From 1-loop Lagrangian PT it is well known that large scale bulk flows lead to a damping of the BAO amplitude. However, within Eulerian PT, which operates at the level of density field instead of displacement field, this effect is hard to model. The state-of-the-art attempt to model the large scale displacements within Eulerian PT, known as IR resummation, is to phenomenologically damp only the BAO wiggles, while leaving the broadband unchanged.



JCAP12(2021)054

| $\boldsymbol{\Omega}$ | Case | Fit | Mean | **Error,** $V = 3(\mathrm{Gpc}/h)^3$ | | **Bias/**$\sigma_{\boldsymbol{\Omega}}$**,** $V = 3(\mathrm{Gpc}/h)^3$ | |
|---|---|---|---|---|---|---|---|
| | | | | $(V \times 100)$ | $(V \times 10)$ | $(V \times 100)$ | $(V \times 10)$ |
| $\omega_{\mathrm{cdm}}$ | min | RSD | 0.1162 | 0.0110 | 0.0400 | −0.25 | −0.10 |
| | | SF | 0.1139 | 0.0009 | 0.0027 | −5.57 | −1.86 |
| | | FM | 0.1110 | 0.0014 | 0.0040 | −5.65 | −1.97 |
| | max | RSD | 0.0997 | 0.0105 | 0.0372 | −1.75 | −0.69 |
| | | SF | 0.1167 | 0.0017 | 0.0045 | −1.24 | −0.50 |
| | | FM | 0.1136 | 0.0015 | 0.0046 | −3.79 | −1.21 |
| $h$ | min | RSD | 0.6751 | 0.0079 | 0.0271 | −0.35 | −0.12 |
| | | SF | 0.6695 | 0.0026 | 0.0079 | −3.15 | −1.02 |
| | | FM | 0.6665 | 0.0027 | 0.0079 | −4.00 | −1.38 |
| | max | RSD | 0.6611 | 0.0079 | 0.0268 | −2.21 | −0.75 |
| | | SF | 0.6729 | 0.0032 | 0.0102 | −1.50 | −0.49 |
| | | FM | 0.6670 | 0.0031 | 0.0088 | −3.45 | −1.26 |
| $\Omega_{\mathrm{m}}$ | min | RSD | 0.3031 | 0.0174 | 0.0620 | −0.24 | −0.08 |
| | | SF | 0.3035 | 0.0012 | 0.0039 | −2.78 | −0.93 |
| | | FM | 0.2996 | 0.0017 | 0.0049 | −4.42 | −1.57 |
| | max | RSD | 0.2783 | 0.0178 | 0.0623 | −1.70 | −0.54 |
| | | SF | 0.3069 | 0.0021 | 0.0056 | −0.11 | −0.04 |
| | | FM | 0.3052 | 0.0019 | 0.0057 | −1.01 | −0.33 |
| $\sigma_8$ | min | RSD | 0.815 | 0.044 | 0.159 | −0.33 | −0.11 |
| | | SF | 0.838 | 0.010 | 0.029 | 0.88 | 0.30 |
| | | FM | 0.845 | 0.009 | 0.029 | 1.69 | 0.55 |
| | max | RSD | 0.765 | 0.044 | 0.153 | −1.48 | −0.53 |
| | | SF | 0.835 | 0.012 | 0.033 | 0.50 | 0.18 |
| | | FM | 0.836 | 0.012 | 0.032 | 0.57 | 0.21 |

**Table 4**. This table shows parameter constraints for $\boldsymbol{\Omega} = \{\omega_{\mathrm{cdm}}, h, \Omega_{\mathrm{m}}, \sigma_8\}$ given by the corresponding mean $\bar{\Omega}$, error $\sigma_\Omega$ and bias $(\bar{\Omega} - \Omega_{\mathrm{Patchy}})$ divided by $\sigma_\Omega$ with respect to the PATCHY cosmological parameters $\boldsymbol{\Omega}_{\mathbf{Patchy}} = \{0.118911, 0.6777, 0.301175, 0.8288\}$. For the different bias model cases "min" and "max" we compare the results of our RSD, *ShapeFit* (here abbreviated as SF) and FM fits. We carried out the fits using a covariance matrix corresponding to the volume of 100 stacked mocks $(V \times 100)$ and to 10 stacked mocks $(V \times 10)$, where $V = 3(h^{-1}\mathrm{Gpc})^3$. The mean values cited here are obtained from the $(V \times 100)$ runs, as these are more Gaussianly distributed. They do not necessarily coincide with the mean values of the $(V \times 10)$ runs due to non-Gaussianity, but we have checked that best-fits agree with each other. Also note that we present Gaussianized errors, although in fact they are slightly non-Gaussian, which is consistently taken into account for determining the bias.

The magnitude of this damping effect is inferred from theory and is, hence, highly model-dependent, which may lead to an underestimation of the error bars as shown in [86]. This is the reason why we designed the *ShapeFit* in such a way that it only extracts cosmological information from the BAO position, the overall power spectrum normalization, and the power spectrum slope; but not from the BAO amplitude. In order to have significant cosmological information on the amplitude of the BAO, we require a survey volume significantly larger than $300\,\mathrm{Gpc}^3$, and this is not expected to be available in the next decade. Nevertheless, one could extend the *ShapeFit* by an additional parameter governing the BAO amplitude; we leave this for future work.



JCAP12(2021)054

In appendix A we test the FM fit including the appropriate IR resummation correction finding that this helps to recover the expectation values of $\omega_{\rm cdm}, h$ and $\Omega_{\rm m}$ within 1-$\sigma$ and $\sigma_8$ within 2-$\sigma$, albeit broadening the resulting constraints. However it is important to recall that the PATCHY mocks are not N-body and simulate non-linearities in an approximate way. Hence, it is not guaranteed that the IR resummation scheme appropriately "describes" these mocks.

From table 4 we notice that the size of the posterior constraints on the relevant cosmological parameters are very similar: *ShapeFit* captures the same bulk of the cosmological information extracted by the FM fit. This shows that the extra information captured by FM compared to the classic approach is concentrated on large-linear scales and is indeed the early-time physics imprint left on the matter transfer function.

### 5.3 Impact of varying $\omega_{\rm b}$

In the previous sections we have fixed the $\omega_{\rm b}$ parameter to its PATCHY expected value, $\omega_{\rm b} = 0.02214$. This is motivated by the fact that usually the constrains from LSS alone on this parameter are not competitive with CMB or BBN ones. However, in some cases we may want to perform an analysis with no external prior constrains. In this section we present results obtained considering $\omega_{\rm b}$ as a parameter free to vary with a uniform prior in the range $[0.005, 0.04]$.

Figure 8 shows the *ShapeFit* (green) and FM fit (blue) results focusing on the "max" case only. Since the slope $m$ is degenerate with $\omega_{\rm b}$ and $\omega_{\rm cdm}$, *ShapeFit* does not constrain them individually, resulting in fully degenerate bands. Also the constrain on $h$ depends strongly on the $\omega_{\rm b}$-prior, as $h$ can only be measured from the BAO position once $\omega_{\rm cdm}$ is fixed by the slope. Therefore, for *ShapeFit* the parameters shown in the left panel $\omega_{\rm b}, \omega_{\rm cdm}$ and $h$ are effectively unconstrained. Instead, it constrains the (derived) parameters $\Omega_{\rm m}$, $\sigma_8$ and $D_V/r_{\rm d}$ shown in the right panel.

The additional constraining power of the FM fit comes from the BAO amplitude only, which breaks the degeneracy between $\omega_{\rm b}$ and $\omega_{\rm cdm}$. Once the prior on $\omega_{\rm b}$ is relaxed, the constraints on $\omega_{\rm b}$ are driven by the BAO amplitude, which depends linearly on $\omega_{\rm b}/\omega_{\rm cdm}$.

To show this explicitly, we consider the linear matter power spectrum obtained from parameter combinations that follow the $\omega_{\rm b} - \omega_{\rm cdm}$ degeneracy of *ShapeFit* in figure 8. If the power spectra obtained along this degeneracy show any difference, this means that there is some information loss induced by the *ShapeFit* compression, that needs to be investigated. Figure 9 displays the linear power spectra for different values of $\omega_{\rm b}$ (green lines), where all other cosmological parameters are read from the *ShapeFit* chain such as to represent the bestfits for each value of $\omega_{\rm b}$. As expected, nearly all curves share the same values of $\Omega_{\rm m}$, $h \times r_{\rm d}$ and hence also $D_V/r_{\rm d}$, such that their BAO wiggle positions overlap with each other. However, there is a remaining difference in tilt between the curves as can be seen from the EH98 (dotted) lines. This is, because the fitting formula introduced in eq. (3.7) is not optimized for varying $\omega_{\rm b}$. As shown in figure 4 our method reproduces the $\omega_{\rm b}$-behaviour with $\sim 5\%$ precision for the range $0.015 < \omega_{\rm b} < 0.03$ (which corresponds to a 40-$\sigma$ region considering the BBN measurement of $\omega_{\rm b}$).

Nevertheless, it is obvious from figure 9 that most of the differences between the green curves are encoded in the BAO amplitude. It is important to note that the BAO amplitude is an early-time physics imprint which, however, is heavily processed by late-time effects (e.g., non-linearities, mode-coupling, bias). This is the reason why the FM fit delivers biased results when these late-time effects are not taken properly into account (see the no-IR modelling case represented by blue contours). The effect of including the IR resummation correction in the



JCAP12(2021)054

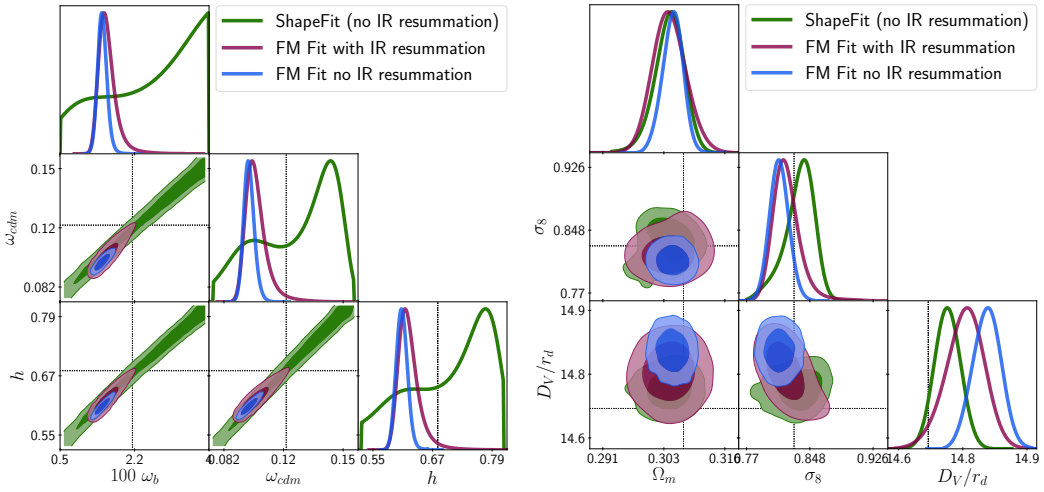


**Figure 8**. Results when analysing the PATCHY "ngc_z3" sample with free $\omega_{\rm b}$ within a flat prior range of $[0.005, 0.04]$. The green contours display the results from *ShapeFit*, whereas the blue and purple contours correspond to the FM fit case, with (purple) and without (blue) the IR resummation correction (see text for more details). Since *ShapeFit* does not compress any BAO amplitude feature, it is not able to break the degeneracies between $\omega_{\rm cdm}$, $\omega_b$, and $h$ (left panel), and in this case only credconstrains individually $\Omega_m$, $\sigma_8$ and $D_V/r_d$ (right panel). On the other hand, the FM fit does use the BAO amplitude and therefore is able to break such degeneracies. However, for both cases explored here, the inferred constraints result biased with respect to the expected values. This suggest that the BAO amplitude feature is not yet a reliable probe to be used in LSS analyses.

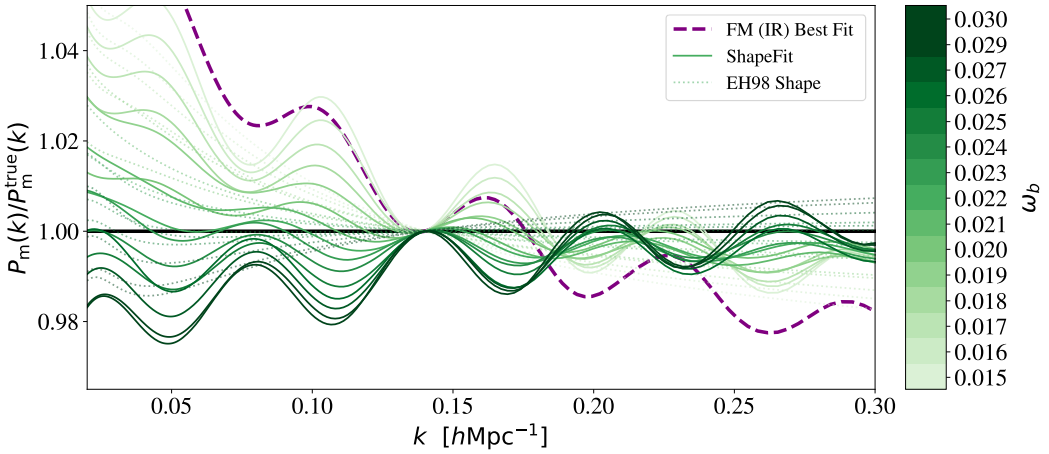


**Figure 9**. Linear matter power spectrum ratio $P_{\rm m}(k)/P_{\rm m}^{\rm true}(k)$ on scales $0.02 < k\,[h{\rm Mpc}^{-1}] < 0.3$ for different models: the dashed purple line corresponds to the FM bestfit (purple contours in figure 8), green lines are obtained from the green contours for different values of $\omega_{\rm b}$. Green dotted lines show the corresponding EH98 approximation. For improved visibility, the curves are rescaled in amplitude to match $\sigma_8$.

JCAP12(2021)054

FM fit (purple contours) is to broaden the posteriors, but not changing their peaks maxima. As a result the posteriors are still biased, but the broadening reduces the tension with the expected values at $2\sigma$. We also observe that the inclusion of IR resummation correction is to broaden the contours precisely along the degeneracy direction given by the green ones. Therefore, we conclude, constraints on $\omega_{\rm b}, \omega_{\rm cdm}$ and $h$ from FM alone, without any prior from early-time measurements, are not reliable at better than 25% for $\omega_{\rm b}$, 10% for $\omega_{\rm cdm}$ and 10% for $h$, when obtained with any of the state-of-the-art methods and modelling explored here.

### 5.4 Impact of varying $n_s$

The constraining power of *ShapeFit* when adding the scalar tilt $n_s$ as an additional free parameter in comparison with the FM fit is described here. In this case, *ShapeFit* needs to be run with both slope parameters, $m$ and $n$, introduced in section 3.3. Since the scale-independent and the scale-dependent slopes have a similar effect on the power spectrum, $m$ and $n$ are strongly anti-correlated. See the full parameter degeneracies when varying $m$ and $n$ in figure 18 of appendix C for the Nseries mocks for reference. Here, in the case of the PATCHY mocks, we do not show the *ShapeFit* results on physical parameters for conciseness and focus on the cosmological results.

The green contours of figure 10 display the posteriors derived from *ShapeFit* for the parameters of a flat-ΛCDM model. As in section 5.3, the results for the FM fit are shown for the cases where IR resummation correction is included (violet contours), and when it is not (blue contours). Both *ShapeFit* and FM + IR resummation approaches recover the PATCHY cosmology very well (marked with black dotted lines). On the other hand, the FM fit results without IR resummation are clearly biased, suggesting that the inclusion of IR resummation is crucial for the FM fit. This can be understood by considering that $n_s$ and $\omega_{\rm cdm}$ have similar effects on the power spectrum slope and thus for *ShapeFit* these two parameters are highly correlated. The FM fit uses the additional information provided by BAO-peak amplitude in order to break the degeneracy between $n_s$ and $\omega_{\rm cdm}$, hence the blue and violet contours are much narrower than the green contours. IR resummation affects the amplitude of the BAO signal, hence it is crucial to extract unbiased constraints from this signal. *ShapeFit* makes no use of the amplitude of the BAO and is hence insensitive to this.

Similar to the case when varying $\omega_{\rm b}$, we conclude that FM fit constraints on $n_s$ depend on the non-linear BAO damping model (late-time physics), while *ShapeFit* provides a conservative alternative, where the BAO amplitude is not used, such that the constrains on $\omega_{\rm cdm}$ and $n_s$ are purely driven by the slope (early-time physics). We note, that in this case we fixed $\omega_{\rm b}$ to its underlying value. If we allow to vary both $\omega_{\rm b}$ and $n_s$ for the FM fit, the bias in $\omega_{\rm b}$ observed in figure 8 propagates into a biased result on $n_s$, even when the IR resummation correction is applied.

## 6 Additional systematic tests on N-body catalogues

There is no perfect suite of mocks, all mocks are in some way an idealization of the survey and/or introduce some approximations. It is important to check whether results found on mocks are robust and not due to approximations introduced e.g., in the mock generation. PATCHY mocks explored in section 5 are not full N-body mocks, hence they are not appropriate for determining the systematic error budget of classic RSD analyses, and even less suited for the newly introduced shape parameter $m$. In other words, the number of available simulations and the total effective volume they cover, makes the PATCHY mocks an invaluable resource to



JCAP12(2021)054

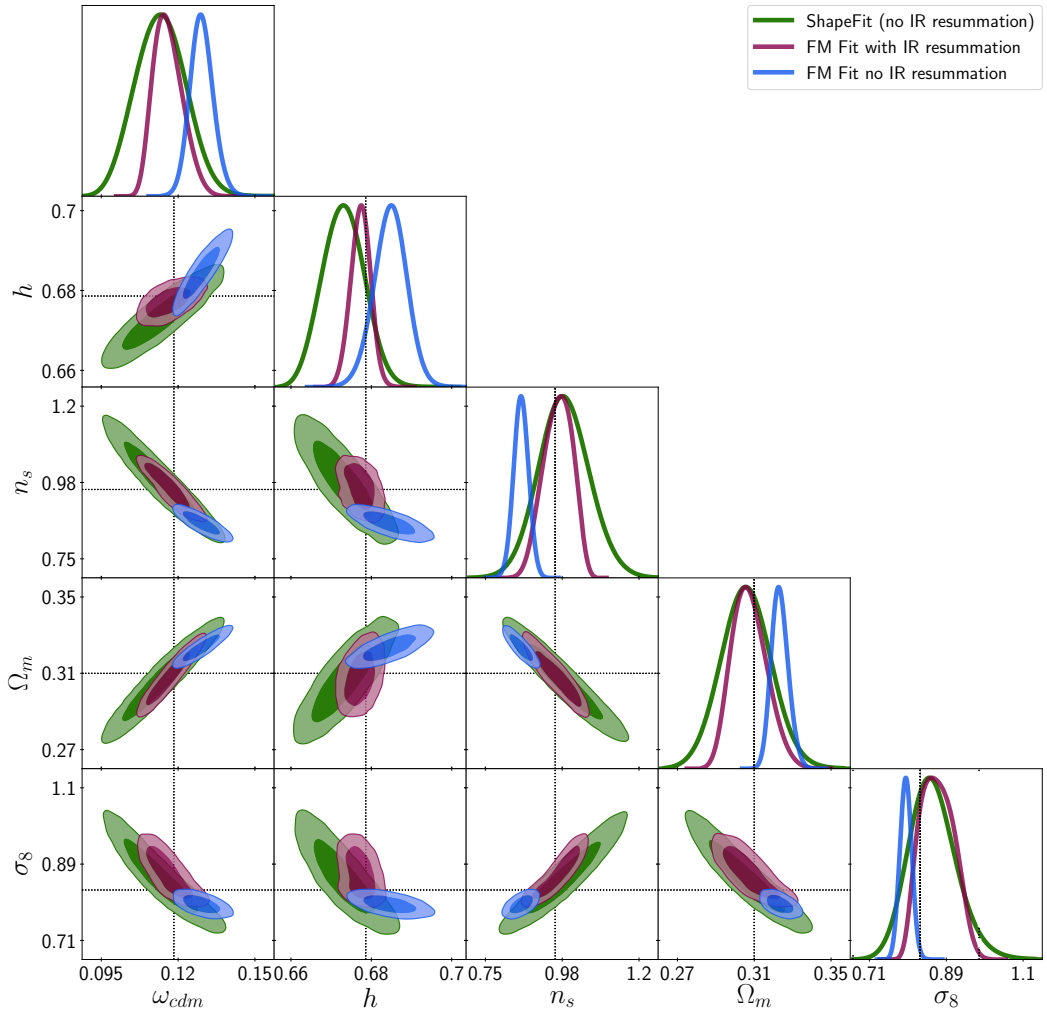


**Figure 10**. Derived posteriors for a flat-ΛCDM model (for a fixed $\omega_b$) for *ShapeFit* (green contours) and the FM fit to the PATCHY "ngc_z3" sample. The FM results are shown for the IR resummation correction turned on and off, in violet and blue contours, respectively. The differences between *ShapeFit* and FM posteriors are due to the extra constraining power from the BAO-peak amplitude (not implemented in *ShapeFit*) which helps to break degeneracies along $\omega_{cdm} - n_s$. The BAO-damping effect due to non-linear bulk flows, which IR resummation describes within FM, greatly reduces the BAO-amplitude-based constraining power, and hence broadens the $n_s$ posteriors.

estimate things like error-bars. However, to investigate potential residual systematics of the proposed *ShapeFit* implementation, we prefer to resort to N-body mocks.

In this section we present further tests of *ShapeFit* using two set of full N-body simulations. We want to investigate further the potential systematic errors on $m$, seen in the PATCHY mocks, in particular those under galaxy bias conditions such as local-Lagrangian assumptions (e.g., the left panel of figure 6).



JCAP12(2021)054

### 6.1 Systematic tests on dark matter particles in real space: geometric effects

We first focus on analysing the simplest possible case of a set of dark matter particles in real space without survey geometry or selection function. We use a N-body suite of 160 simulations with a flat ΛCDM cosmology consistent with the Wilkinson Microwave Anisotropy Probe bestfit cosmology (WMAP cosmology, [1]), with a box size $L = 2.4\,\mathrm{Gpc}h^{-1}$ and a total number of $N_p = 768^3$ particles. The initial conditions have been generated at $z = 49$ by displacing the particles according to the second-order Lagrangian PT from their initial grid points. We use the output at the three snapshots, $z = 0.5$, 1.0 and 1.5. Further details on these simulations can be found in section 3.1 and table 1 of [95]. Although we have the velocity information for each of the simulated particles, we do not apply in this case any redshift-space distortion displacement for simplicity.

We obtain the data-vector of each of these 160 realizations at each redshift bin, consisting of its monopole, quadrupole and hexadecapole signals between $0.02 \leq k\,[\mathrm{Mpc}h^{-1}] \leq 0.15$, sampled in bins of $\Delta k = 0.01\,h\mathrm{Mpc}^{-1}$ size, and with a total number of $13 \times 3$ elements. We take the average of the 160 data-vector realizations to form the mean data-vector to use as our dataset. The total associated volume of this data-vector corresponds to $6,448\,\mathrm{Gpc}^3$. We make use of the 160 realizations to estimate the covariance, following the same corrections as described in section 4.1. In this section, covariance (and errors on the figures) are rescaled to be those corresponding to the full effective volume available. In fact the goal is to explore small systematic shifts, which we want to uncover and quantify with the maximum precision afforded by the simulations available, independently, for now, of the statistical power of specific surveys. We fit the redshift-space distortion model of eqs. (2.12) and (2.13) with non-local bias parameters and with the local-Lagrangian conditions of (4.7). We set $n = 0$ for simplicity and only focus on exploring the posteriors of $\{\alpha_\parallel,\, \alpha_\perp,\, f,\, m\}$, when the rest of four nuisance parameters are also marginalized, $\{b_1,\, b_2,\, \sigma_P,\, A_{\rm noise}\}$. Note that since we are fitting the data-vector corresponding to dark matter particles in real space, and we will be using the reference template at the true own cosmology, we expect to recover $\alpha_{\parallel,\perp} = 1$, $f = 0$ and $m = 0$.

The dashed-empty contours of figure 11 show the posteriors of such analysis, for the 3 redshift bins in different colors, as labeled. We only show the difference between the measured and the expected value for the 4 relevant physical parameters, accordingly scaled as indicated by the legend for visualization purposes. We notice that even in this highly idealized, simple case systematic shifts are present: $\Delta^{\rm sys}_{\alpha_\parallel} \simeq 0.01\,(1\%)$, $\Delta^{\rm sys}_{\alpha_\perp} \simeq 0.005\,(0.5\%)$, $\Delta^{\rm sys}_{f} \simeq 0.003$ and $\Delta^{\rm sys}_{m} \simeq -0.04$. Being redshift-independent indicates that these shifts are not related to a theoretical limitation of the PT-model, or any biasing model assumption, but likely a geometric effect.

In fact, as it is standard procedure, for each $k_i$-bin (defining the power spectrum band-power), the model is evaluated at the effective $k$-vector of that $k$-bin, $P^{\rm model}(k_{i\,,\rm eff})$, where $k_{i\,,\rm eff} \equiv \langle \mathbf{k} \rangle_i$ is the ensemble average over all possible directions of the $\mathbf{k}$-vector within the $i$-bin. However, the data-vector is measured by taking the average of $P(\mathbf{k}_i)$ across all $\mathbf{k}$-directions, $P^{\rm data}(k_i) = \langle P^{\rm data}(\mathbf{k}) \rangle_i$. It is clear that $P^{\rm data}(k_i)$ and $P^{\rm model}(k_{i\,,\rm eff})$ are not representing the same quantity: $P(\langle k \rangle) \neq \langle P(k) \rangle$. It is mode discreteness that generates this effect. For a sufficiently large box the mode discreteness would be negligible, it is the survey geometry that introduces it and fully specifies it, hence the name "geometric effect".

Ignoring this effect can generate spurious signals, especially for the large-scale modes, where the number of modes per bin is small. Ideally we would like to evaluate the model's



JCAP12(2021)054

prediction for each $\mathbf{k}$ within the bin and take the average in the same way as when measuring the data-vector, $\langle P^{\rm model}(\mathbf{k}_i)\rangle$. However this is too computationally expensive to be adopted in a MCMC.

We propose here an approximation to account for this effect which is fast and sufficiently accurate for our purposes: we add the resulting "mean" effect to the data.

We construct a new data-vector, $P^{{\rm data},\,G^{-1}}$:

$$P^{{\rm data},\,G^{-1}}(k) = G^{-1}(k) \times P^{\rm data}(k), \tag{6.1}$$

where the geometric factor, $G$, is defined as

$$G(k) \equiv \frac{\langle P^{\rm model}(\mathbf{k})\rangle}{P^{\rm model}(\langle \mathbf{k}\rangle)}, \tag{6.2}$$

and where the ensemble average is taken over all directions of the $\mathbf{k}$-vector. Naturally $G(k)$ depends slightly on the parameters at which the model, $P^{\rm model}$ is evaluated,[20] so $G$ is obtained through several iterations, until we observe convergence (in practice one or two iterations suffice). We start by fitting the data-vector without any correction ($G(k) = 1$), evaluating $G(k)$ at the best fitting model (first trial correction), and first trial $P^{{\rm data},\,G^{-1}}(k)$. We repeat this process until we observe convergence in the derived posteriors. We have found convergence is reached by the second iteration.

Following this two-iteration process approach we produce the posteriors displayed in figure 11 in solid contours. We notice how the systematic offsets observed initially (empty-dashed contours i.e., $G(k) = 1$) are significantly reduced (by a factor 2 to 4 depending on the variable) when we account for the geometric correction: $\Delta^{\rm sys}_{\alpha_\parallel} \simeq 0.005\,(0.5\%)$, $\Delta^{\rm sys}_{\alpha_\perp} \simeq 0\,(0\%)$, $\Delta^{\rm sys}_f = 0.003$ and $\Delta^{\rm sys}_m = -0.01$. The geometric correction is particular important for $m$, neglecting it induces a systematic shift of $\Delta m \simeq -0.03$. The geometric effect is less important for $\alpha_{\parallel,\perp}$– neglecting it induces a systematic shift of 0.5%– and negligible for $f$. We estimate that the residual bias on $m$ after the proposed approximate geometric correction becomes comparable to the statistical error for an effective volume greater than $\sim 400{\rm Gpc}^3$. Without our proposed mean correction the bias would become comparable to the statistical error for volumes $\sim 25{\rm Gpc}^3$. Hence this correction is important and sufficient for on-going and forthcoming surveys. We conclude that such type of "geometric" corrections may be important when doing precision cosmology, especially for signals on large scales (i.e., $m$-derived quantities and the FM fit approach). It is important to keep in mind that the systematic shifts reported in figure 11 depend on the size of the chosen $k$-bin — the smaller the size of the bin, the smaller the required $G$-correction — as well as the size of the box in which the sample is embedded — the larger the box, the smaller the $G$-correction — (see next section). In general, these shifts only set a floor for the type of systematics we expect in real-life applications. Inaccuracies when modelling galaxy bias schemes and redshift space distortions, may increase the systematic errors reported in figure 11. We address these effects in the following sub-section.

[20] Note that one could also leave the data-vector intact and apply this inverse correction into the model: $P^{{\rm model},\,G} = G(k) \times P^{\rm model}(k)$ at each MCMC step, where $G$ would be pre-computed at a given fiducial model in order to save computational time. This approach may seem more physically motivated but is mathematically identical to what we follow.



JCAP12(2021)054

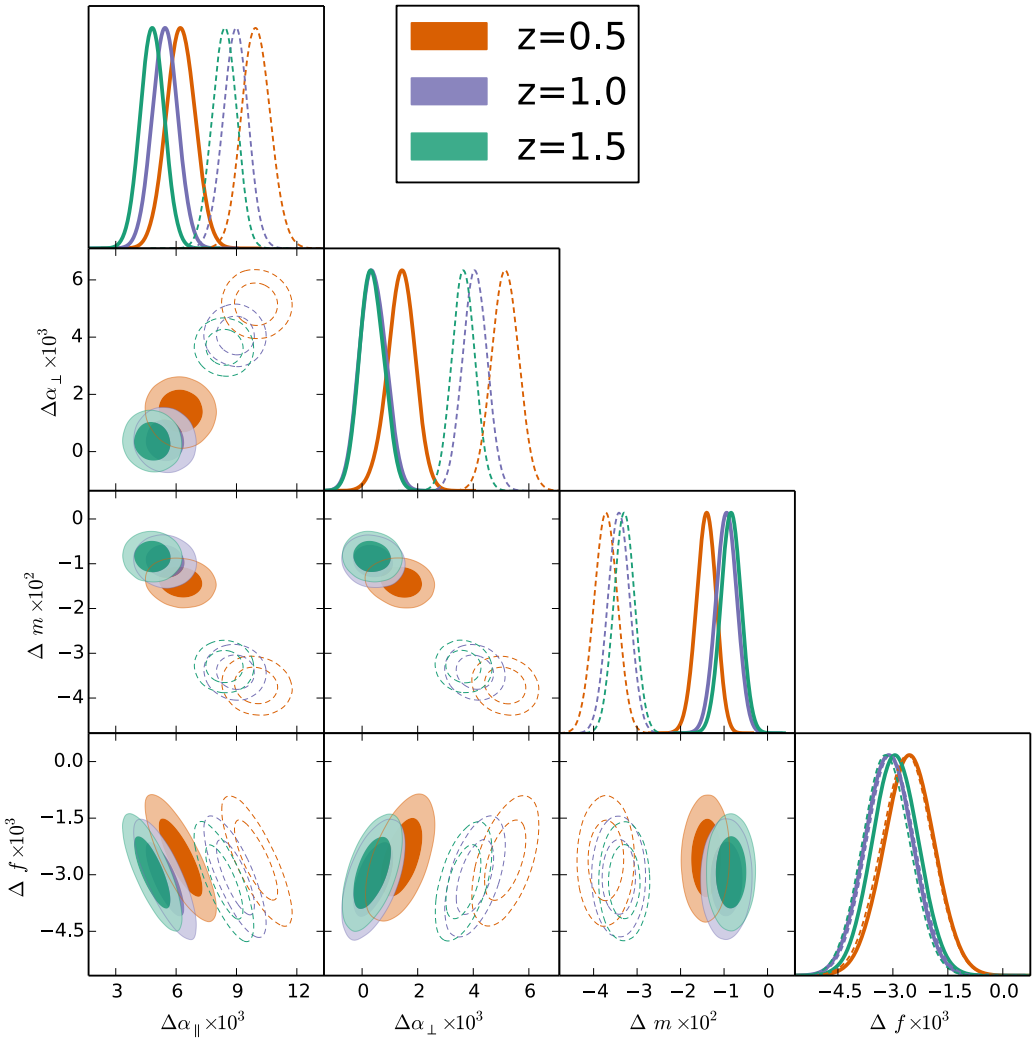


**Figure 11**. Posteriors derived when fitting the mean of 160 full N-body dark matter realization in real space. The covariance has been rescaled to correspond to an effective volume of 2200 $[h^{-1}\mathrm{Gpc}]^3$. We have used the model described in eqs. (2.12) and (2.13) and the local-Lagrangian bias scheme of eq. (4.7). In the plot we only show the physical parameters $\mathbf{p} = \{\alpha_\parallel, \alpha_\perp, f, m\}$, although the remaining four nuisance parameters are also varied (see text). The empty-dashed contours display the results of fitting the data-vector without any geometric correction (as usually done), whereas the filled contours account for the geometric correction through eq. (6.2). For all $\mathbf{p}$-variables the expected value is $\Delta\mathbf{p} = 0$. We observe that $m$ is especially sensitive to the geometric correction with a shift of about 0.03 towards positive values, for the specific set of geometric choices: $\Delta k = 0.01\,h\mathrm{Mpc}^{-1}$, size of the periodic box, $L = 2.4\,h^{-1}\mathrm{Gpc}$, and the $k$-range fitted, $0.02 \leq k\,[h\mathrm{Mpc}^{-1}] \leq 0.15$.

JCAP12(2021)054

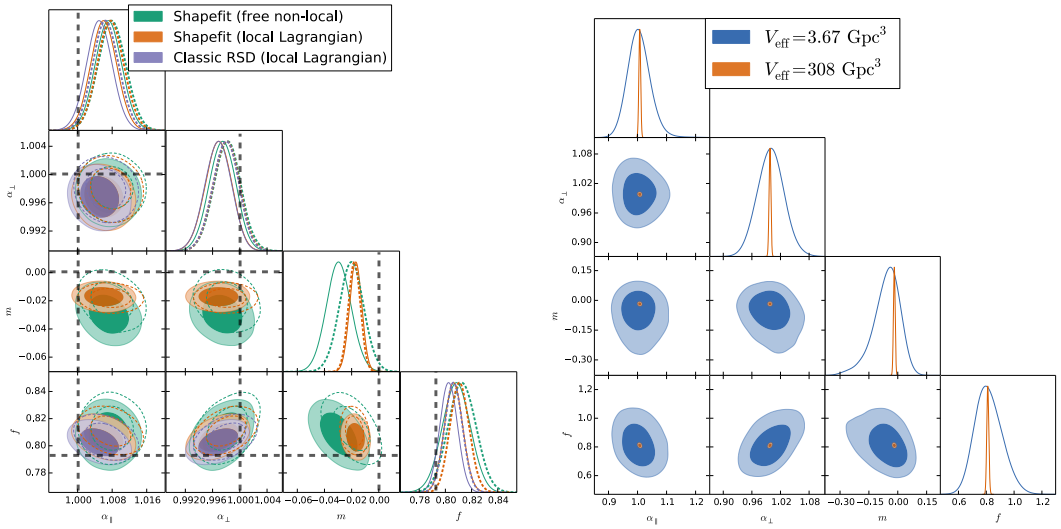


**Figure 12**. Posteriors from Nseries N-body mocks using $P^{(0,2,4)}$ at $0.02 \leq k\,[\mathrm{Mpc}h^{-1}] \leq 0.15$. In the left panel we display the comparison of classic RSD (purple) and *ShapeFit* (orange), both with local-Lagrangian bias parametrization of eq. (4.7), and *ShapeFit* with free non-local biases (green). All cases correspond to the fit of the mean power spectra of the 84 independent realizations with an associated effective volume of $V_{\rm eff} = 308\,\mathrm{Gpc}^3$). Horizontal black-dashed lines represent the true expected value for each compressed variable. The empty-dashed contours display the results without any geometric correction ($G = 1$) and the filled-solid contours with this correction included (see eq. (6.2) and text for details). The right panel displays the case of *ShapeFit* with the local-Lagrangian bias assumption when fitting the mean of the 84 realizations (orange, same to the left panel) and when fitting the averaged-posteriors of all 84 individual realizations (blue contours), which in this last case represents an effective volume similar to BOSS CMASS NGC, $3.67\,\mathrm{Gpc}^3$. We note how the small systematic errors detected in the left panel, are negligible compared to the real-life statistical errors derived when fitting the realistic case of BOSS CMASS with a volume of $3.67\,\mathrm{Gpc}^3$ shown in blue in the left panel.

### 6.2 Systematic tests on Nseries LRG mocks

We now explore how the compressed parametrization of *ShapeFit* performs when it is applied to full N-body galaxy mocks. We employ the Nseries galaxy mocks which have been used for determining the modelling systematic error budget in BOSS [26] and eBOSS [27] official RSD and BAO analyses.

The Nseries mocks have been generated out of 7 independent periodic boxes of $2.6\,h^{-1}$Gpc side, projected through 12 different orientations and cuts, to extract, in total, 84 pseudo-independent realizations with the sky geometry similar to the northern galactic cap of CMASS DR12 data, for $0.43 < z < 0.7$, resulting in an effective redshift of 0.56. The mass resolution is $1.5 \times 10^{11}\,M_\odot h^{-1}$, with $2048^3$ dark matter particles per box. The identified haloes are populated with galaxies following a halo occupation distribution model tuned to match the clustering of LRGs observed by BOSS. As in the standard procedure adopted by the BOSS collaboration, the covariance is estimated from the 2048 realizations of NGC CMASS DR12 PATCHY mocks catalogues. Additionally, we rescale all the estimated covariance terms by a 10% factor based on the ratio of particles, as the PATCHY mocks have 10% fewer particles than the Nseries mocks due to veto effects on the DR12 CMASS data. The underlying cosmology



JCAP12(2021)054

of the Nseries mocks is close to the WMAP one and they sample a total effective volume of $84 \times 3.67\,[\mathrm{Gpc}]^3$. Further information and details on the Nseries mocks can be found in section 7.2 of [27], as well as section 2.2.2 of [72].

Each of the Nseries mocks cover a larger physical volume than the dark matter simulation, so we have embedded them in a box of $4\,\mathrm{Gpc}h^{-1}$ side length. We use the same $k$-binning and data-vector entries as in section 6.1, but the larger box-size implies that the mode-sampling is much denser; this is expected to reduce the geometric effect seen in section 6.1.

The left panel of figure 12 displays the posteriors resulting from fitting the mean power spectrum multipoles from the 84 Nseries mock realizations. The dashed-empty contours show the posteriors drawn when fitting the data without any geometric-correction factor applied, whereas the solid-filled contours are when the $G$-factor is applied (see eq. (6.2) for reference). The different color schemes represent different types of fit or bias schemes, as labeled. The local-Lagrangian galaxy bias conditions of eq. (4.7) are applied to the classic RSD fit (purple contours) and to the *ShapeFit* (orange contours). Additionally, we also show the *ShapeFit* when the locality in Lagrangian space is relaxed (green contours). While only the physical parameters are shown, the nuisance parameters are included in the fit and marginalized over. For the *ShapeFit* parametrization we have set $n = 0$ for simplicity. The black-dashed lines indicate the expected values for the underlying cosmology of the Nseries mocks.

As expected, the geometric correction described in section 6.1 has a much smaller effect for the Nseries mocks.

This is due to a combination of two effects: the statistical errors for Nseries are larger than for the dark matter simulations, because of the smaller effective volume, $308\,\mathrm{Gpc}^3$ for Nseries and $6,448\,\mathrm{Gpc}^3$ for dark matter particles boxes. Moreover the larger size of the Nseries box, $L = 4\,\mathrm{Gpc}h^{-1}$, yield a finer sampling of $k$-modes than for the dark matter simulation, $L = 2.4\,\mathrm{Gpc}h^{-1}$, reducing the net effect.

We note that for the 3 studied cases, classic RSD with the local-Lagrangian bias assumption, and *ShapeFit* with and without the local-Lagrangian bias assumption, the expected parameters are recovered very well. We only detect a systematic shift on $m$ of order $0.01 - 0.02$, towards negative values, similar to the one reported in section 6.1. Note that for the Nseries mocks the recovered non-local bias parameters are very consistent with the local-Lagrangian prediction.

Additionally, letting $n$ and $m$ to be simultaneously free for the local-Lagrangian bias case, yields results very consistent with the $n = 0$ case (orange contours), and therefore with the expected value (see appendix C).

The right panel of figure 12 illustrates the effective volume-effect for the *ShapeFit* case with the non-local bias set to their local-Lagrangian prediction. The orange contour displays the fit to the mean of the 84 Nseries mocks (same as in the left panel), whose associated effective volume is $308\,\mathrm{Gpc}^3$. The blue contours are the resulting posterior from averaging the individual 84 posteriors, each of them with an associated effective volume of $3.67\,\mathrm{Gpc}^3$. For most of the parameters of interest the maxima of the posterior of the mean (orange) lies in the same position as the maxima of the mean of individual posteriors (blue). We observe a small displacement for $f$ and $m$, indicating some non-Gaussian behaviours on the tails of the distribution. We also note that the size of the systematic reported errors on the left plot, of order $\Delta_m^{\mathrm{sys}} \simeq 0.01 - 0.02$, are very sub-dominant with respect to the statistical errorbars of $m$ associated to a real-life volume, of $3.67\,\mathrm{Gpc}^3$, in the right panel in blue.

We conclude that for the *ShapeFit* analysis on Nseries mocks, with or without the local-Lagrangian bias assumption, the errors associated to modelling systematics are negligible



JCAP12(2021)054

for $\alpha_{\parallel,\perp}$ and $f$, and of 0.01–0.02 on $m$ towards negative values. We have not identified the source of such systematic shift, but we conclude that it does not have any significant impact when fitting actual datasets, whose statistical errorbars on $m$ tend to be of order of 5–10 times larger. We leave a more detailed study of such systematic effect and its mitigation in the next-generation of galaxy surveys for future work.

## 7 Conclusions

The standard (classic) approach to analyse galaxy redshift clustering, (that we refer to as BAO and RSD analyses), is conceptually different from the way, for example, CMB data are interpreted. With the help of a fiducial template of the power spectrum, the clustering data are compressed into few physical observables which are sensitive only to late-time physics, and it is these observables that are then interpreted in light of a cosmological model. There has been a renewed effort recently to analyse galaxy redshift clustering in a similar way as CMB data: by comparing directly the observed power spectrum, including the BAO signal, the RSD signal, as well as the full shape of the broadband power to the model's prediction. In this case, the model has to be chosen *ab initio*. We refer to this approach as full modelling (FM). The resulting posterior constraints on cosmological parameters of the ΛCDM model, or its simple extensions, are significantly tighter than in the classic analysis in a broad parameter space with no Planck constraints.

In this paper we have provided a full physical understanding of where the additional constraining power afforded by the second approach arises, and in doing so we have bridged the classic and new analyses in a transparent way.

The compressed physical variables of the classic approach represent the universe's late-time dynamics; they depend only on the geometry, expansion history and growth rate of the Universe in a model-independent way and they can be in turn interpreted in light of the cosmological model of choice. These variables do not capture and are insensitive to other physics relevant to processes at play at a different epoch in the Universe evolution such as equality scale, sound horizon scale, primordial power spectrum or other quantities that enter in the matter transfer function.

However, there is additional information in the clustering signal. Beside the primordial tilt, the broadband of the power spectrum is shaped by the matter transfer function encoding the evolution (scale and time dependence) of the initial fluctuations from inflation until the time of decoupling of the photon-baryon fluid, which in a ΛCDM model, depends on the physical baryon and matter densities $\omega_{\rm m}, \omega_{\rm b}$ and $h$. This, we have shown, is located mostly on large scales, and to a smaller extent in the amplitude of the BAO wiggles.

In the FM approach the parameter dependence of the transfer function and the geometry are not kept separated, in this way the information carried by the shape of the transfer function, improves constraints on cosmological parameters that are usually interpreted as purely geometrical. This can be seen as an "*internal model prior*". The classic fixed template methods do not invoke a prior of that kind, as they do not establish this link.

We have thus extended the classic analysis with a single additional phenomenological parameter, that captures the bulk of this extra information (section 3). We refer to this approach as *ShapeFit*. The physical understanding we provide is rooted on landmark works on the matter transfer function e.g., [20, 46, 49]. We are aware that a single parameter like $\Gamma \sim \Omega_m h$ is insufficient to correctly describe the data given the statistical power of state-of-the-art galaxy surveys [20]. *ShapeFit* introduces instead an effective parameter, $m$,



JCAP12(2021)054

the slope of the matter power spectrum at a specific pivot scale. The *ShapeFit* extension of the classic methodology captures the same broadband shape information as the FM fit by upgrading the classic RSD fit and at the same time retaining the power of compressing the two point statistics into well understood and model independent physical numbers that still disentangle early from late-time physics. The '*internal model prior*' is not needed until the very last step of interpreting the physical variable in light of a model.

In summary, *ShapeFit*:

- preserves the model-independent nature of the compressed physical variables of the classic approach,
- disentangles early-time from late-time physical information,
- matches the constraining power of the FM approach when interpreted within the cosmological model parametrization of choice (see figure 7),
- is a simple addition to the established "classic" codes and procedures with a simple physical interpretation,
- the computational time is effectively indistinguishable from that of the classic approach and $\sim 30$ times faster than the FM approach (at the level of cosmological inference),
- reduces the (already small) template-dependence of the classic approach.

In passing we have presented (section 3.2) a new definition and interpretation of the physical parameter describing amplitude of velocity fluctuations which further reduces the model-dependence of the traditional RSD analysis. We recommend adopting it in classic analyses even without *ShapeFit* extension.

*ShapeFit* does not include the additional information enclosed in the BAO amplitude for two reasons: *i)* this early-time information is relevant only if no CMB or BBN prior is adopted for $\omega_{\rm b}$, *ii)* even though the BAO amplitude is an early-time physics imprint it is however heavily processed by late-time effects (e.g., non-linearities, mode-coupling, bias) and therefore, we argue, not robust (see figure 8).

Given the level of sophistication and the systematic control of the classic approach, we have performed a battery of tests on mock surveys to quantify possible subtle systematic effects for *ShapeFit*. These are presented in section 6.2 and the appendices. We have highlighted a few systematic effects and proposed and tested mitigation strategies well suited to present and forthcoming surveys. The take-home message is that the power spectrum broadband shape is very sensitive to bias assumptions, even on large, linear scales. Therefore, we advocate to always allow maximal freedom for the bias and nuisance parameters in forthcoming data analyses, especially when FM and *ShapeFit* are used for cosmological interpretation.

We envision that the transparent physical interpretation offered by the simple extension of the classic approach proposed here will be useful in analysing and interpreting the clustering signal of current and forthcoming surveys in a robust way.

## Acknowledgments

We would like to thank Pauline Zarrouk, Andreu Font-Ribera and Jose Luis Bernal for their useful comments. We are also indebted to the anonymous referee for the help to significantly



JCAP12(2021)054

improve the manuscript. H.G-M. and S.B. acknowledges the support from 'la Caixa' Foundation (ID100010434) with code LCF/BQ/PI18/11630024. L.V. acknowledge support of European Unions Horizon 2020 research and innovation programme ERC (BePreSySe, grant agreement 725327). Funding for this work was partially provided by project PGC2018-098866-B-I00 MCIN/AEI/10.13039/501100011033 y FEDER "Una manera de hacer Europa", and the "Center of Excellence Maria de Maeztu 2020-2023" award to the ICCUB (CEX2019-000918- M funded by MCIN/AEI/10.13039/501100011033). The massive production of all MultiDark-Patchy mocks for the BOSS Final Data Release has been performed at the BSC Marenostrum supercomputer, the Hydra cluster at the Instituto de Fısica Teorica UAM/CSIC, and NERSC at the Lawrence Berkeley National Laboratory. We acknowledge support from the Spanish MICINNs Consolider-Ingenio 2010 Programme under grant MultiDark CSD2009-00064, MINECO Centro de Excelencia Severo Ochoa Programme under grant SEV- 2012-0249, and grant AYA2014-60641-C2-1-P. The MultiDark-Patchy mocks was an effort led from the IFT UAM-CSIC by F. Prada's group (C.-H. Chuang, S. Rodriguez-Torres and C. Scoccola) in collaboration with C. Zhao (Tsinghua U.), F.-S. Kitaura (AIP), A. Klypin (NMSU), G. Yepes (UAM), and the BOSS galaxy clustering working group.

JCAP12(2021)054

## A Impact of IR resummation on FM results

The Infrared (IR) resummation effects are not included in the baseline analysis shown in the main text. This is motivated by the fact that *ShapeFit* does not include this effect in the PT model used (in this case 1-loop SPT). The effect of IR resummation in the FM fit is to damp the amplitude of the BAO feature in the power spectrum model due to late-time physics effects (bulk flows), and therefore to broaden the likelihoods of those parameters sensitive to the amplitude of the BAO features. For this reason we opted for the non-IR option in FM fit as a baseline choice, for a fairer comparison between *ShapeFit* and FM fit likelihood's shapes.

However, since the IR resummation is an integral part of EFT power spectrum modelling, and therefore of FM fit, here we show how the likelihoods for these cases compare to each other when fitting the Patchy mocks, in the case of $\omega_b$ being fixed to its true value. Previously, in figure 8 we have already shown how they compare for the case of a uniform and wide prior on $\omega_b$.

Figure 13 is the analogous plot of figure 7, for the "max" case only (see text in section 4.2 for a full description of this choice), keeping the same color-code: blue for FM fit without IR resummation correction and green for *ShapeFit*. In purple we show the contours for FM fit with the IR resummation correction included. We remind the reader that *ShapeFit* does not use any BAO amplitude information, and therefore is, by construction, insensitive to IR resummation effects in $P(k)$.

Figure 13 shows how the inclusion of IR resummation correction help the contours of FM fit to shift towards the expected parameter values, at the expenses of broadening the contours. We stress that this shift only happens when the $\omega_b$ parameter is anchored to its true value. In the case $\omega_b$ is set to be free, the IR resummation correction does not produce the required shift towards the correct position, and only broadens the contours (see figure 8). The *ShapeFit* posteriors are naturally unaffected by ignoring the IR resummation correction and recover the expected parameters' values of the Patchy mocks cosmology.

In real-life applications (i.e., for effective survey volumes of $\lesssim 100\,\mathrm{Gpc}^3$) the IR resummation correction does not have a significant impact in the derived cosmological parameters. This is because the BAO amplitude information is dominated by other probes different to

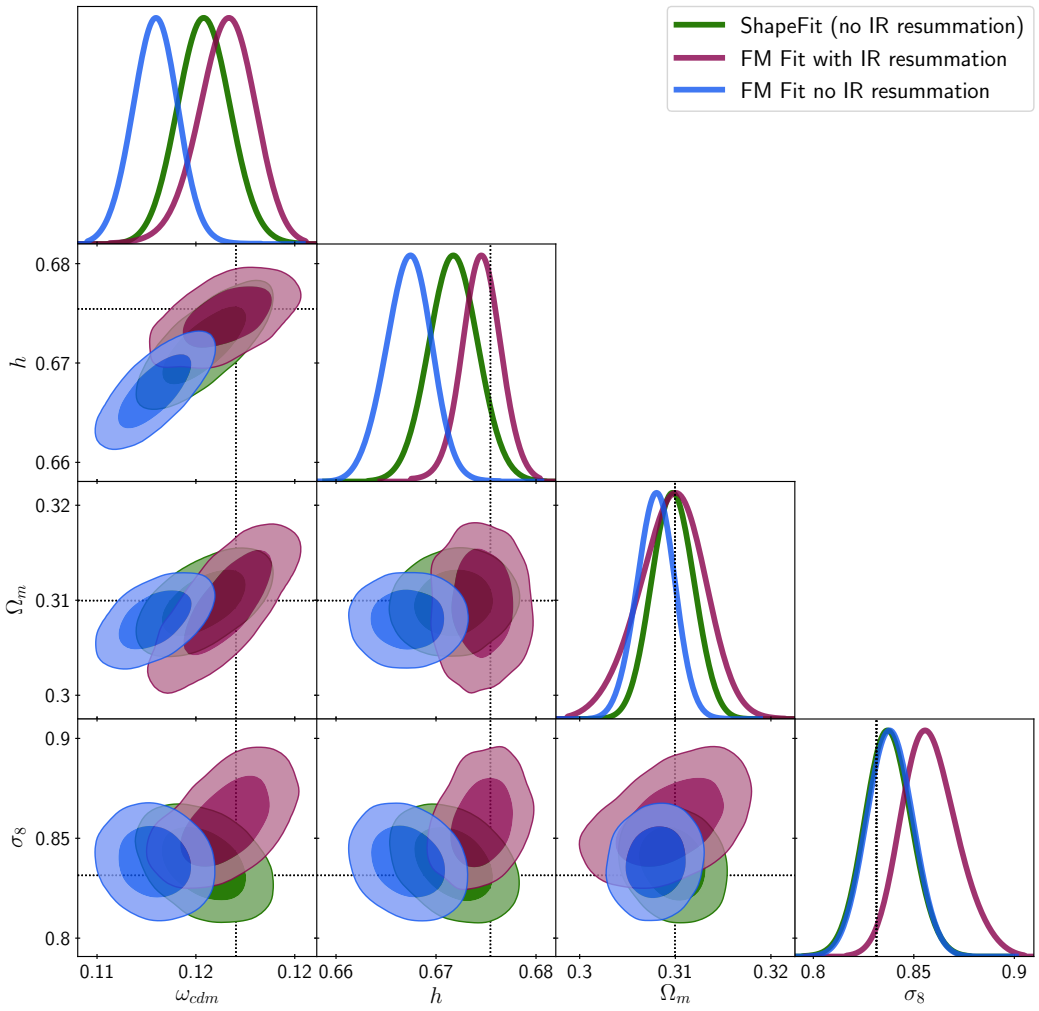


**Figure 13**. Posteriors resulting from fitting the mean of 2048 PATCHY "ngc_z3" mocks with a covariance corresponding to 100 times the size of one single realization, and with an associated effective volume of $\sim 300\,\mathrm{Gpc}^3$. For this case $\omega_b$ has been kept fixed to its true expected value (see figure 8 for the case where $\omega_b$ is kept as a free parameter) and the "max" choice been made for the Lagrangian bias treatment (see section 4.2). Blue and purple contours display the prediction from FM fit when IR resummation correction is ignored or accounted, respectively. The *ShapeFit* inferred contours are shown in green, where the BAO amplitude information is not used, and therefore the IR resummation correction has no effect.

LSS, such as CMB- or BBN-based analyses, and getting it right from the LSS does not add any significant information to the combined analysis. Also, for those studies doing an integral LSS-alone analysis, the amplitude of BAO is not yet a reliable feature we should be trusting. The reason is that the BAO damping is highly model dependent and involves non-linear physics (including galaxy formation) that we do not understand at the level required for precision cosmology today. A practical proof of that are the contours of figure 8, where when



JCAP12(2021)054

| Cosmology | $\omega_{\rm m}$ | $\omega_{\rm b}$ | $h$ | $\sigma_8$ | $n_s$ | $M_\nu$ [eV] | $N_{\rm eff}$ | $\Omega_{\rm m}$ | $r_{\rm d}$ [Mpc] |
|---|---|---|---|---|---|---|---|---|---|
| Planck | 0.1417 | 0.022 | 0.676 | 0.8288 | 0.9611 | 0.06 | 3.046 | 0.31 | 147.78 |
| PATCHY | 0.1411 | 0.022 | 0.678 | 0.8288 | 0.9611 | 0.0 | 3.046 | 0.307 | 147.64 |
| Nseries | 0.1401 | 0.023 | 0.700 | 0.82 | 0.96 | 0.06 | 3.046 | 0.286 | 147.15 |
| X | 0.1599 | 0.022 | 0.676 | 0.814 | 0.97 | 0.056 | 3.046 | 0.35 | 143.17 |
| Y | 0.1599 | 0.022 | 0.676 | 0.814 | 0.97 | 0.056 | 4.046 | 0.35 | 138.77 |
| Z | 0.2053 | 0.037 | 0.75 | 0.9484 | 0.96 | 0.0 | 3.046 | 0.365 | 123.97 |
| Om-high | 0.1417 | 0.022 | 0.595 | 0.7349 | 0.97 | 0.0 | 4.046 | 0.4 | 142.85 |
| Om-low | 0.1417 | 0.022 | 0.913 | 0.7983 | 0.97 | 0.0 | 4.046 | 0.17 | 142.85 |

**Table 5**. List of cosmological models for reference template potential dependence.

LSS data is analysed alone without any strong $\omega_b$ prior, even the IR resummation approach returns biased likelihoods for $\{h, \omega_b, \omega_{cdm}\}$.

## B Investigating the *ShapeFit* template dependence

Both the classic RSD Fit and the *ShapeFit* are template-based fitting methods: they measure physical parameters related to late-time dynamics of the universe given a fixed template set by early-time physics. Keeping the template fixed and only varying it according to late-time effects is an effective way to decouple the early-time dependence of cosmological parameters from the late-time observations. This degree of model-independence goes at the expense of introducing a certain "modelling systematic", coming from the fact that the template used for the analysis may not correspond to the underlying linear matter power spectrum of the universe.[21] It is therefore important to quantify this systematic by studying the impact of different templates on physical parameter results and this is what this appendix is dedicated to.

There are two questions we would like to address:

- How do the classic RSD Fit and the *ShapeFit* compare in terms of template independence for results on the traditional parameters $\alpha_\parallel, \alpha_\perp$ and $f\sigma_8$.
- What is the degree of template-dependence for the new *ShapeFit* parameter $m$.

To answer these questions we perform the classic RSD Fit and the *ShapeFit* for a set of 8 different template cosmologies presented in table 5. The "Planck" and "PATCHY" cosmologies are very similar (close to the cosmology preferred by Planck analysis) and have been introduced already in the main paper, as the "Nseries" parameters corresponding to the WMAP cosmology. We also use the "X", "Y", and "Z" templates, that correspond to $\omega_{\rm m}$-values extremely different from the "Planck" reference, and a different value of the effective number of neutrino species $N_{\rm eff}$ in the "Y" case. All these templates have also been used to study the template dependence of eBOSS results in [72]. In addition, we use templates generated from the "Om-high" and "Om-low" cosmology, that share the same value of $\omega_{\rm m}$ as "Planck", but extremely different Hubble parameters $h$, leading to a very high and a very low value of $\Omega_{\rm m}$ respectively.

[21] As a side-note, this modelling systematic given by the template dependence does not exist in the FM approach, where the template is varied consistently at each step given the model, by definition. However, avoiding this systematic goes at the expense of model dependence, as internal model priors need to be adopted.



JCAP12(2021)054

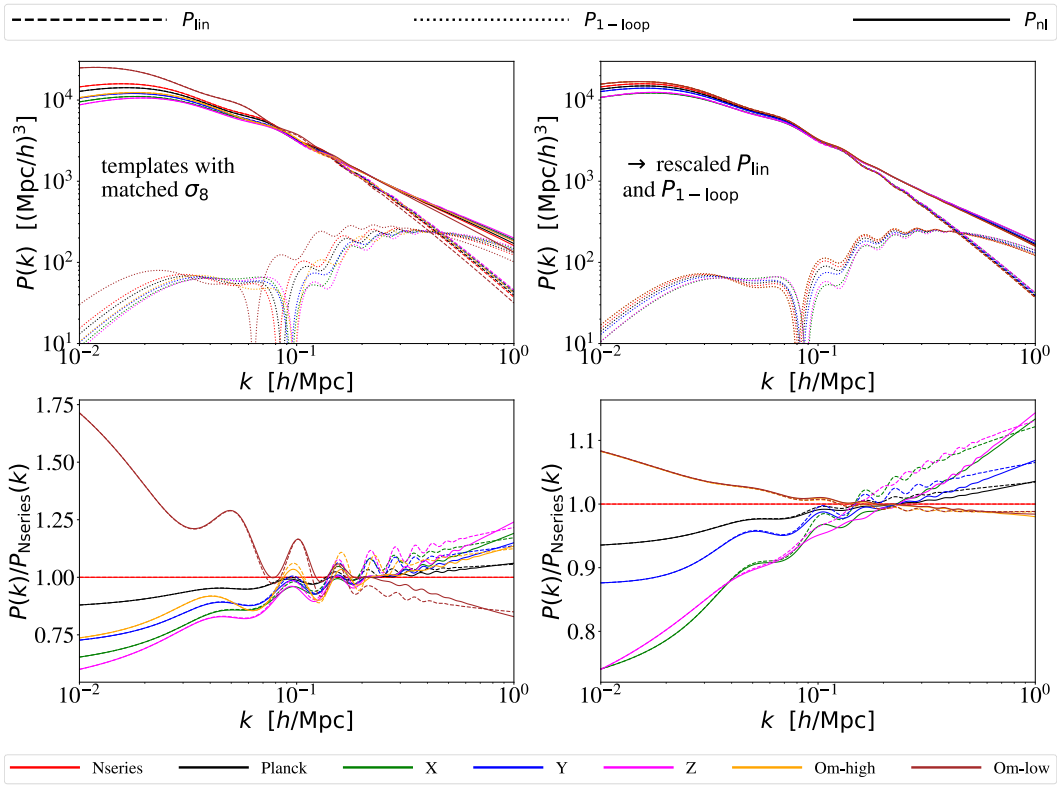


**Figure 14**. Power spectrum templates corresponding to the cosmologies of table 5 (without "Patchy" cosmology, as it is very similar to "Planck"). In the top row, we show the linear power spectra in dashed, the 1-loop corrections in dotted and their sum, the non-linear power spectra, in solid lines. The bottom row shows the power spectrum ratios with respect to the "Nseries" cosmology for either $P_{\rm lin}$ or $P_{\rm nl}$. Left panels show the spectra rescaled in amplitude by $\sigma_8$ for better visibility and for the right panels we applied the early-time rescaling (by the sound horizon ratio) to the spectra, such that their BAO positions match.

The linear power spectrum templates as well as the 1-loop corrections and the full non-linear templates are also shown in figure 14 for all cosmologies except for the "Patchy" cosmology, as it is very similar to "Planck". From the left panels one can see that the templates show deviations of up to 50% on large and 20% on small scales. After rescaling them via the early-time scaling given in eq. (3.2) to match the BAO positions (right panels), the deviations reduce to 25% and 10%, respectively. One can appreciate, even by eye, that the remaining disagreement between the templates after rescaling is well described by a slope. This is precisely the additional degree of freedom that *ShapeFit* delivers via the parameter $m$, which is missing in the classic RSD fit.

Figure 15 shows the posteriors for the northern "ngc_z3" PATCHY mocks analysed using *ShapeFit* (solid contours) and the classic RSD (dashed contours) using some of the different templates (displayed in different colours) listed in table 5 as the reference cosmology. In all cases we set $n = 0$ and we allow the non-local galaxy bias parameters to vary freely. For each case the data-vector has been constructed from the mean monopole and quadrupole signals of



JCAP12(2021)054

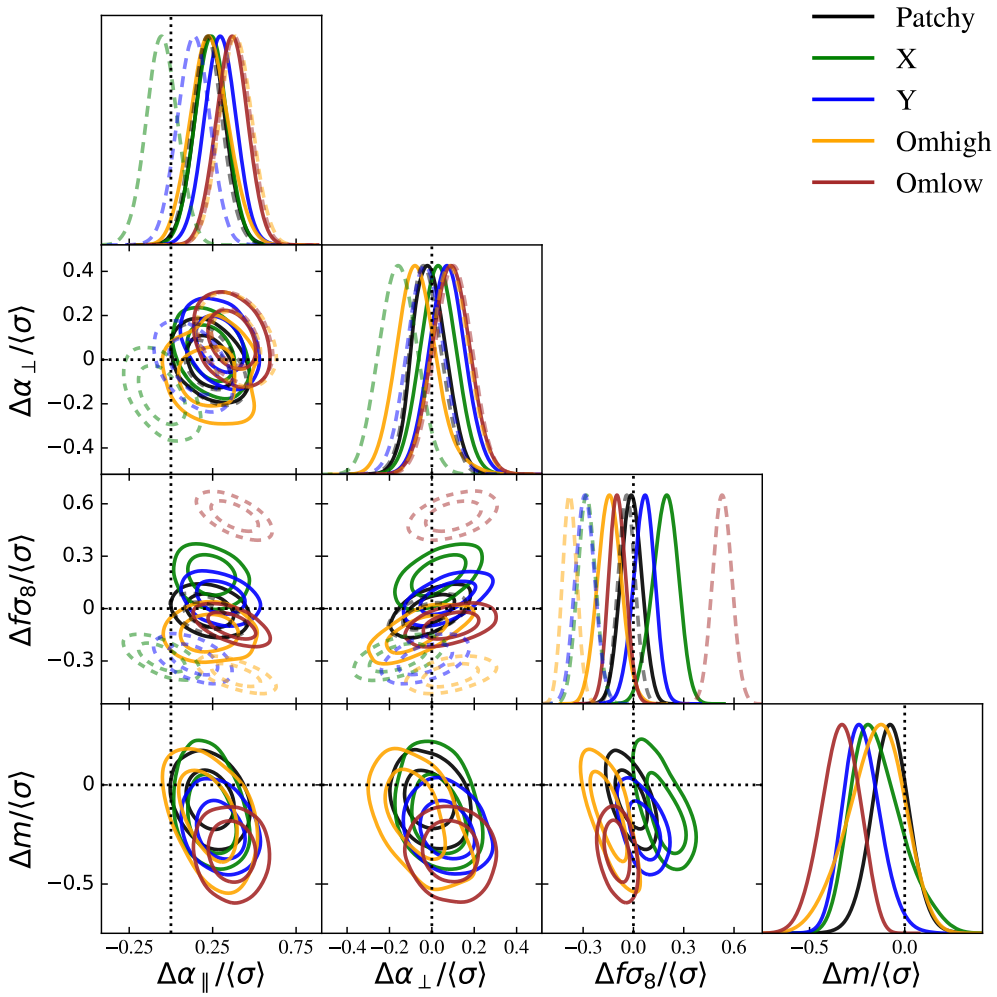


**Figure 15**. Comparison between templates used for the classic RSD Fit (dashed contours) and for the *ShapeFit* (solid contours) on the mean of 2048 PATCHY mocks with covariance for the volume of 100 realizations. We show posterior results for the physical parameters subtracted by the expectation, relative to the error normalized to the volume of a single PATCHY mock realization, $\sim 3\,\mathrm{Gpc}^3$. For all cases the non-local bias parameters are varied corresponding to the "max" case (see section 4.2 for details).

the 2048 realizations, and the associated covariance correspond to the volume of 100 PATCHY mocks. Each physical parameter, $p$, is displayed with its expected value, $p^{\rm exp}$ (different for each reference template) subtracted in such a way that the expected value coincides with 0, $\Delta p = p - p^{\rm exp}$. Additionally each $\Delta p$ is divided by the statistical error corresponding to one single realization of these mocks. As already discussed above, the choice of reporting the results for an effective volume of $\sim 3\mathrm{Gpc}^3$ is motivated by the fact that the PATCHY mocks' accuracy in reproducing the observed clustering properties is not guaranteed much beyond the limit afforded by the statistics of a single realization. Moreover we follow the procedure for template sensitivity presented in [72]. Using *ShapeFit* over the classic RSD method helps



JCAP12(2021)054

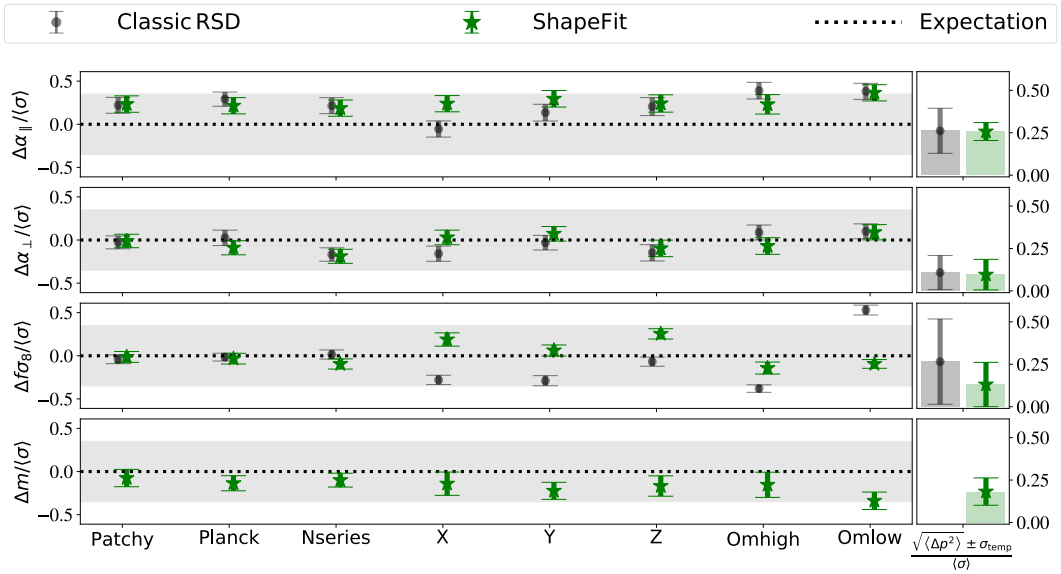


**Figure 16**. Results of compressed variables for all templates (see table 5) used for the classic RSD Fit and the *ShapeFit*, in both cases allowing non-local bias parameters to vary ("max" case in table 3). For each template we show the deviation $\Delta p$ from the expectation of $p$ for $\Delta p \in \{\Delta\alpha_\parallel, \Delta\alpha_\perp, \Delta f\sigma_8, \Delta m\}$ divided by the corresponding errors $\langle\sigma\rangle$ of each parameter when fitting the BOSS "ngc_z3" sample using the covariance of a single realization corresponding to a volume of $\sim 3\,\mathrm{Gpc}^3$. The classic RSD fit barely exceeds $0.5\,\langle\sigma\rangle$ while *ShapeFit* is bound below $0.35\,\langle\sigma\rangle$ deviations indicated by the grey band. The last column shows, again in units of $\langle\sigma\rangle$, the template-averaged deviation from the truth $\sqrt{\langle\Delta p^2\rangle}$ (represented by vertical histogram-bars) over-plotted with the intrinsic scatter among all templates $\sigma_{\mathrm{p,temp}}$ (represented by error bars) for each parameter $p$. It is important to note that the error bars do *not* indicate the error on the error, but the statistical spread, while the histogram bar represent the cumulative systematic bias. Hence, in case there is no systematic deviation, the error bar size is equal to the histogram height, (as it is the case for $\Delta\alpha_\perp$ and $\Delta f\sigma_8$.).

to bring the measured value of $\alpha_\parallel$ and $f\sigma_8$ close to the expected value ($\Delta p = 0$), removing a weak systematic residual associated with the reference template choice, which is present for the classic RSD analysis. $\alpha_\perp$ is unbiased for both classic RSD and *ShapeFit*. The new shape parameter $m$ does not show any significant bias neither. The deviation with respect to the expectation remains well below one half of the statistical error-bars expected for a volume of about $3\,\mathrm{Gpc}^3$ even for the extreme case of the templates 'X', 'Y' and 'Z'.

Figure 16 presents the displacement of the same physical variables shown in figure 15 in 1-dimensional panels, for the additional cosmologies of table 5, 'Planck', 'Nseries' and 'Z'.

In addition, the last column provides a "summary statistic" of all templates to facilitate evaluating the overall *ShapeFit* performance. The colored bars represent the "least squared" deviation $\sqrt{\langle\Delta p^2\rangle}$ from the truth, where we averaged over all $N^{\mathrm{temp}}$ templates

$$\left\langle \Delta p^2 \right\rangle = \frac{\sum_i^{N^{\mathrm{temp}}} \Delta p_i^2/\sigma_{p_i}^2}{\sum_i^{N^{\mathrm{temp}}} 1/\sigma_{p_i}^2}\,, \tag{B.1}$$

and the error bars show the intrinsic scatter of the bestfit values with template $\sigma_{\mathrm{temp}}$. We can see that the overall effect of *ShapeFit* on $\sqrt{\langle\Delta p^2\rangle}$ is rather mild for $\alpha_\parallel$ and $\alpha_\perp$, but very strong



JCAP12(2021)054

(factor 2 improvement) for $f\sigma_8$. On the other hand, *ShapeFit* shows significant improvement concerning the scatter $\sigma_{\rm temp}$ for $\alpha_\parallel$ and $f\sigma_8$, but not for $\alpha_\perp$. Ideally the cumulative systematic bias (histogram-bars) should not be larger than the statistical scatter (error-bars). Clearly for $\alpha_\parallel$ this is not the case, but is also not a problem with the adopted compression. We interpret it as an indication of insufficient accuracy in the adopted theoretical modelling at the level below or $\sim 0.25$ of one standard deviation. We can thus roughly estimate that, if the modelling is not improved, such bias may become a concern for volumes of the order of $\sim 40$ Gpc$^3$. Considering the individual templates we observe a similar trend as in figure 15: the visible bias of the classic RSD approach for $f\sigma_8$ in the X and Y cosmologies as well as the Om-high and Om-low cases, has puzzled and worried the experts for a while. *ShapeFit* helps to reduce the already small template dependence of the classic RSD analysis, even for extreme cosmologies (such as X, and Y), completely ruled out by CMB observations; even the parameter $m$ does not show a significant template dependence, although we note that the error on $m$ may increase for an inappropriate choice of template. We argue however, that this feature does not have a significant impact on future data analysis, as the extreme templates studied here are used for testing purposes only.

## C Full parameter-dependencies for *ShapeFit*

For clarity, the main text did not show the full posteriors including both physical and nuisance parameters. It is however important to study possible correlations between the shape parameter $m$ and the non-local biases: correlations between nuisance parameters and the physical parameters of interest may induce systematic biases in cosmological inference if the modelling of nuisance effects is incorrect or if unsuitable priors are imposed on the nuisance parameters. This is studied in this appendix.

In figure 17 we show the full correlations in all fitted parameters, both physical and nuisance, for the Nseries case with $m$ free, for the cases of local-Lagrangian ("min"case in orange contours) and free non-local biases ("max" case in green). For comparison we also show in purple the classic RSD case for local-Lagrangian.

On the other hand, in figure 18 we show the dependencies for the "min" case when both $m$ and $n$ are freely varied within *ShapeFit* (green contours). We note the high correlation between $m$ and $n$. This has to do with the intrinsic degeneracy between $\omega_{\rm b}$, $\omega_{\rm m}$ and $n_s$ through the slope, which can only be broken by modelling the BAO amplitude and imposing a strong prior on $\omega_{\rm b}$.

The full parameter degeneracies figures make a crucially important point (as already anticipated in section 6.2): the power spectrum broadband shape, and hence the slope $m$, is very sensitive to bias assumptions, even on large, linear scales. Therefore, we advocate to always allow maximal freedom for the bias and nuisance parameters in forthcoming data analyses, especially for FM fits and when the slope $m$ is used for cosmological interpretation. Of course, this slows down MCMC chains convergence, but *ShapeFit* has an advantage over the FM fit, as in the former the fit only needs to be done once, while for the latter it has to be repeated for any model of choice.

## D Impact of rescaling the non-linear template

We investigate the approximation of factorizing the parameter $m$ and $s$ outside the loop-integral corrections. This approximation is particularly useful because it allows us to pre-compute all loop-correction terms at a given reference cosmology, but varying the slope, $m$, and the



JCAP12(2021)054

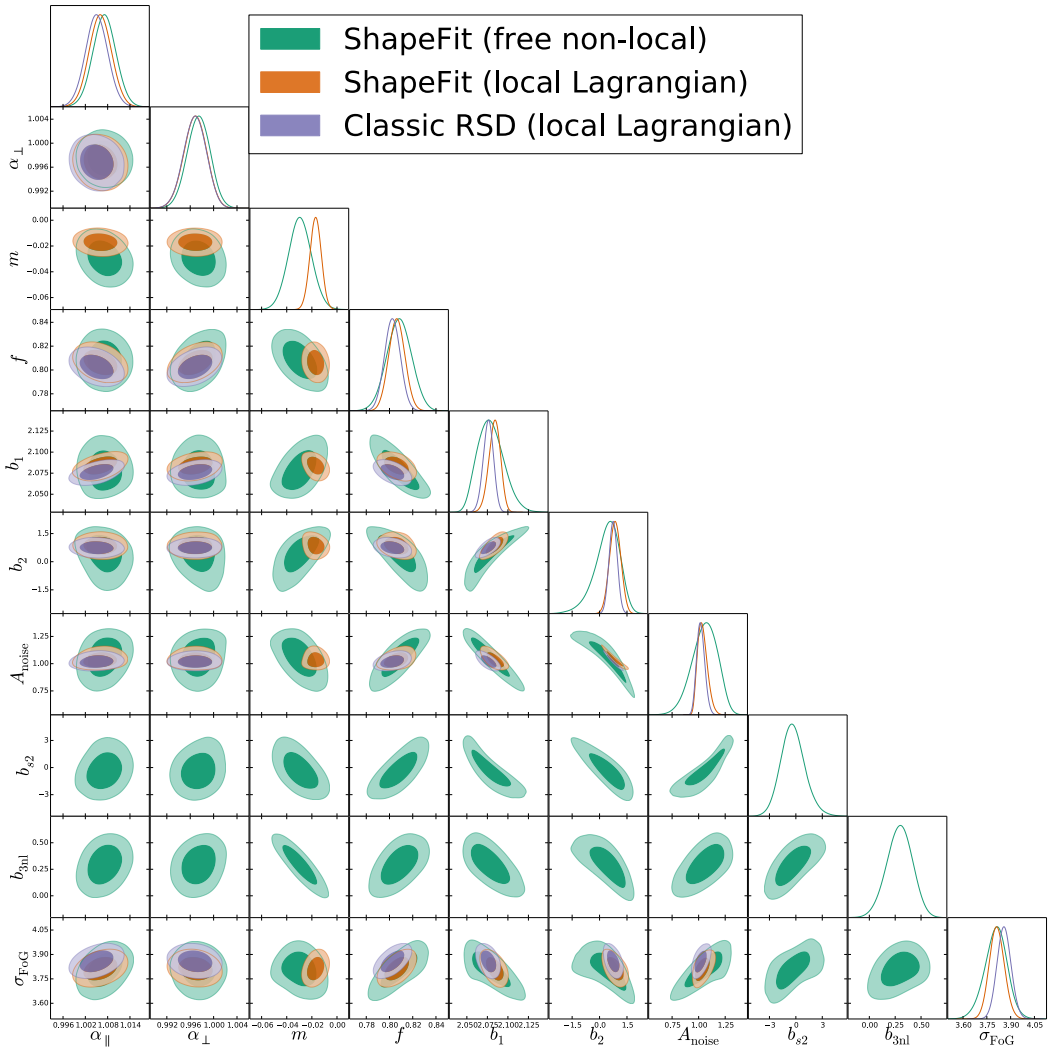


**Figure 17**. Posterior distribution for the mean of the Nseries mocks corresponding to what is shown in the left panel of figure 12, but in this case explicitly displaying the dependencies on nuisance parameters, including the non-local biases. Note the strong correlation between the shape parameter $m$ and the non-local biases $b_{s2}$ and $b_{3\rm nl}$.

BAO-template peak position, $s$, at each MCMC step. Note that the approximation involving $s$ has been extensively used in all the 'classic' RSD methods using the 'fixed-template' approach.

Figure 19 displays the difference between the non-linear 1-loop SPT (taking into account the non-linear bias and TNS terms corrections) exact evaluation of the power spectrum multipoles and the corresponding rescaling of a reference template evaluated at different values of $s$ ($\pm 0.05$, in blue) and $m$ ($\pm 0.1$, in purple), as it would be used in an actual MCMC run. Solid/dashed/dotted lines show the difference for the monopole/quadrupole/hexadecapole, relative to the amplitude of the monopole. The rest of nuisance parameters have been set to values close to the best-fitting case for the PATCHY and Nseries mocks. Of course marginalizing over the nuisance parameters will absorb some of these differences (see below).



JCAP12(2021)054

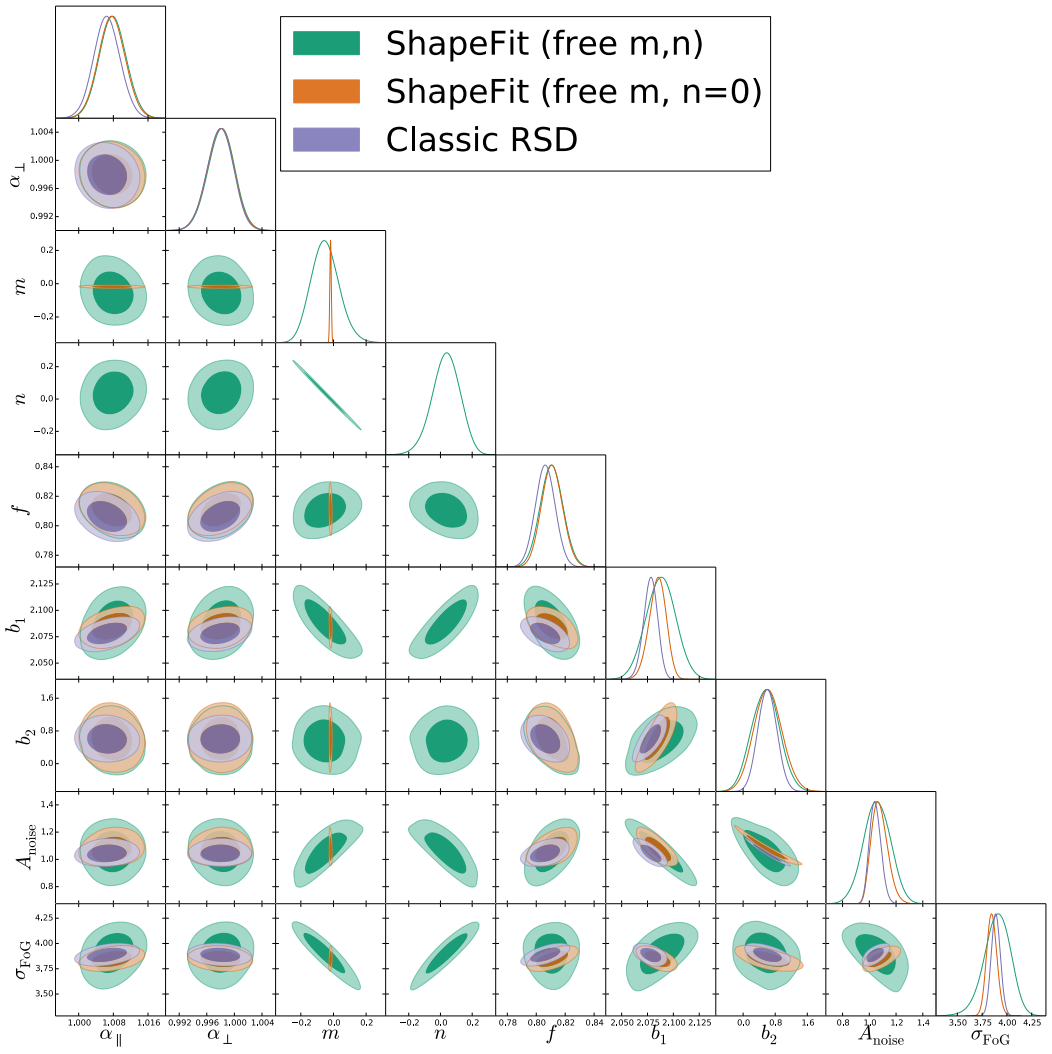


**Figure 18**. Posterior distribution for the mean of the Nseries mocks, corresponding to the "min" case shown in figure 12 (i.e., when locality in Lagrangian space is assumed), for *ShapeFit* with only $m$ varying (in orange contours), and when also $n$ is varied simultaneously to $m$ (green contours). For comparison, the classic RSD is also shown in purple contours. We note the strong correlation between $n$ and $m$ parameters.

We see that for both $m$ and $s$ the approximation is better than 2% for $k \leq 0.15\,h\mathrm{Mpc}^{-1}$, and 3% for $k \leq 0.20\,h\mathrm{Mpc}^{-1}$. These are actually comparable to the absolute typical errors of the model adopted in this paper (1-loop-SPT, TNS model, 1-loop bias corrections). The errors made by factorizing $m$ outside the loop integrals are of the same order as those introduced by the scaling of the BAO-template peak position, for shifts of $m \pm 0.1$ and $s \pm 0.05$, respectively. These small systematics errors are partially absorbed by nuisance parameters, such as $b_2$ and $\sigma_P$, and not affecting in any significant way the cosmological parameters inference, as it can be seen from appendix B.



JCAP12(2021)054

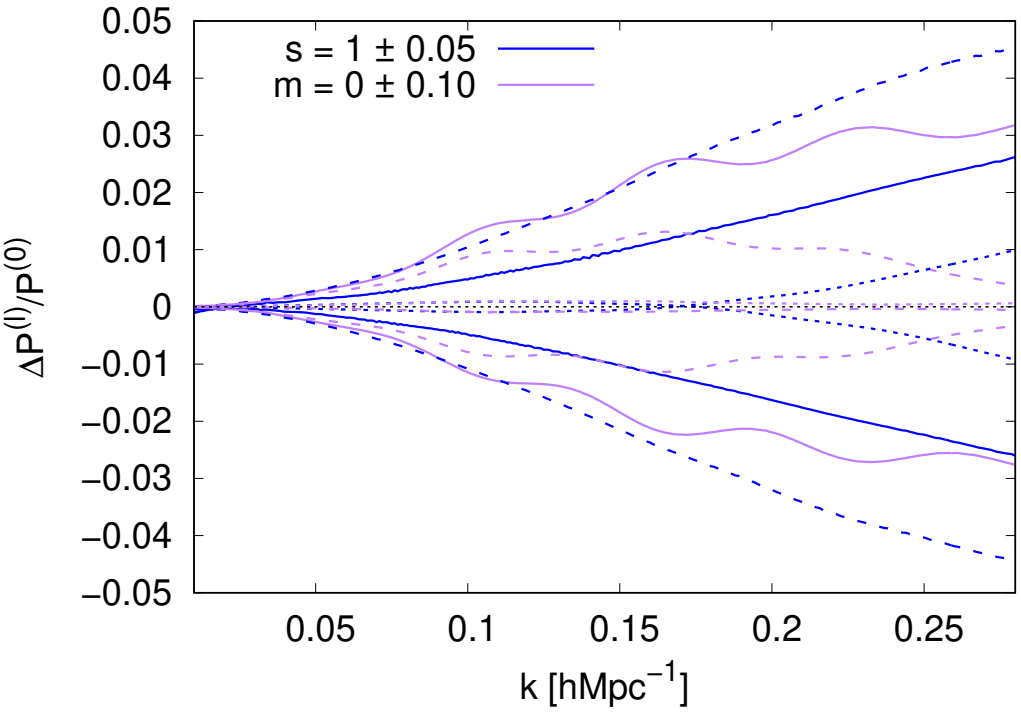


**Figure 19**. Systematic errors produced by rescaling the BAO-peak position $s$ and the shape parameter $m$ in the fixed-template implementation, $\Delta P^{(\ell)} \equiv P^{(\ell)}_{\rm rescaled} - P^{(\ell)}_{\rm exact}$, relative to the amplitude of the monopole, for reference. Blue lines display the effect of rescaling $s$ by $s = 1 \pm 0.05$ and purple lines for $m$ by $m = 0 \pm 0.1$. Solid, dashed and dotted lines display the effect for the monopole, quadrupole and hexadecapole, respectively. For the $k_{\rm max} = 0.15\,h{\rm Mpc}^{-1}$ used in this paper, the systematic error stays always below 2%.

We conclude that the 'fixed-template' implementation is a valid approach for both $s$- and $m$-rescaling, and produces systematic errors well within the current systematic error budget, as they are of the order of systematic errors associated to the theory model itself. Should the maximum $k$ be pushed so that more non-linear scales are (reliably) included and constraints shrink significantly compared to the cases considered in this paper, this approximation may need to be improved. We leave to future work how to do this without representing a computational bottleneck.

## References


[1] WMAP collaboration, *Nine-Year Wilkinson Microwave Anisotropy Probe (WMAP) Observations: Cosmological Parameter Results*, *Astrophys. J. Suppl.* **208** (2013) 19 [arXiv:1212.5226] [INSPIRE].

[2] PLANCK collaboration, *Planck 2018 results. VI. Cosmological parameters*, *Astron. Astrophys.* **641** (2020) A6 [*Erratum ibid.* **652** (2021) C4] [arXiv:1807.06209] [INSPIRE].

[3] C. Blake et al., *The 2-degree Field Lensing Survey: design and clustering measurements*, *Mon. Not. Roy. Astron. Soc.* **462** (2016) 4240 [arXiv:1608.02668] [INSPIRE].




JCAP12(2021)054

[4] SDSS collaboration, *The Sloan Digital Sky Survey: Technical Summary*, *Astron. J.* **120** (2000) 1579 [astro-ph/0006396] [INSPIRE].

[5] SDSS collaboration, *SDSS-III: Massive Spectroscopic Surveys of the Distant Universe, the Milky Way Galaxy, and Extra-Solar Planetary Systems*, *Astron. J.* **142** (2011) 72 [arXiv:1101.1529] [INSPIRE].

[6] BOSS collaboration, *The Baryon Oscillation Spectroscopic Survey of SDSS-III*, *Astron. J.* **145** (2013) 10 [arXiv:1208.0022] [INSPIRE].

[7] SDSS-III collaboration, *The Eleventh and Twelfth Data Releases of the Sloan Digital Sky Survey: Final Data from SDSS-III*, *Astrophys. J. Suppl.* **219** (2015) 12 [arXiv:1501.00963] [INSPIRE].

[8] A. Raichoor et al., *The completed SDSS-IV extended Baryon Oscillation Spectroscopic Survey: Large-scale Structure Catalogues and Measurement of the isotropic BAO between redshift 0.6 and 1.1 for the Emission Line Galaxy Sample*, *Mon. Not. Roy. Astron. Soc.* **500** (2020) 3254 [arXiv:2007.09007] [INSPIRE].

[9] A.J. Ross et al., *The Completed SDSS-IV extended Baryon Oscillation Spectroscopic Survey: Large-scale structure catalogues for cosmological analysis*, *Mon. Not. Roy. Astron. Soc.* **498** (2020) 2354 [arXiv:2007.09000] [INSPIRE].

[10] B.W. Lyke et al., *The Sloan Digital Sky Survey Quasar Catalog: Sixteenth Data Release*, *Astrophys. J. Suppl.* **250** (2020) 8 [arXiv:2007.09001] [INSPIRE].

[11] DESI collaboration, *The DESI Experiment Part I: Science,Targeting, and Survey Design*, arXiv:1611.00036 [INSPIRE].

[12] DESI collaboration, *The DESI Experiment Part II: Instrument Design*, arXiv:1611.00037 [INSPIRE].

[13] EUCLID collaboration, *Euclid Definition Study Report*, arXiv:1110.3193 [INSPIRE].

[14] SDSS collaboration, *Detection of the Baryon Acoustic Peak in the Large-Scale Correlation Function of SDSS Luminous Red Galaxies*, *Astrophys. J.* **633** (2005) 560 [astro-ph/0501171] [INSPIRE].

[15] 2DFGRS collaboration, *The 2dF Galaxy Redshift Survey: Power-spectrum analysis of the final dataset and cosmological implications*, *Mon. Not. Roy. Astron. Soc.* **362** (2005) 505 [astro-ph/0501174] [INSPIRE].

[16] P.J.E. Peebles and J.T. Yu, *Primeval adiabatic perturbation in an expanding universe*, *Astrophys. J.* **162** (1970) 815 [INSPIRE].

[17] J.R. Bond and G. Efstathiou, *Cosmic background radiation anisotropies in universes dominated by nonbaryonic dark matter*, *Astrophys. J. Lett.* **285** (1984) L45 [INSPIRE].

[18] J.A. Holtzman, *Microwave background anisotropies and large scale structure in universes with cold dark matter, baryons, radiation, and massive and massless neutrinos*, *Astrophys. J. Suppl.* **71** (1989) 1 [INSPIRE].

[19] W. Hu and N. Sugiyama, *Small scale cosmological perturbations: An analytic approach*, *Astrophys. J.* **471** (1996) 542 [astro-ph/9510117] [INSPIRE].

[20] D.J. Eisenstein and W. Hu, *Baryonic features in the matter transfer function*, *Astrophys. J.* **496** (1998) 605 [astro-ph/9709112] [INSPIRE].

[21] A. Heavens, R. Jimenez and L. Verde, *Standard rulers, candles, and clocks from the low-redshift Universe*, *Phys. Rev. Lett.* **113** (2014) 241302 [arXiv:1409.6217] [INSPIRE].

[22] C. Alcock and B. Paczynski, *An evolution free test for non-zero cosmological constant*, *Nature* **281** (1979) 358 [INSPIRE].

[23] D.J. Eisenstein, H.-j. Seo, E. Sirko and D. Spergel, *Improving Cosmological Distance Measurements by Reconstruction of the Baryon Acoustic Peak*, *Astrophys. J.* **664** (2007) 675 [astro-ph/0604362] [INSPIRE].

[24] P. Carter, F. Beutler, W.J. Percival, J. DeRose, R.H. Wechsler and C. Zhao, *The impact of the fiducial cosmology assumption on BAO distance scale measurements*, *Mon. Not. Roy. Astron. Soc.* **494** (2020) 2076 [arXiv:1906.03035] [INSPIRE].

[25] N. Kaiser, *Clustering in real space and in redshift space*, *Mon. Not. Roy. Astron. Soc.* **227** (1987) 1 [INSPIRE].

[26] BOSS collaboration, *The clustering of galaxies in the completed SDSS-III Baryon Oscillation Spectroscopic Survey: cosmological analysis of the DR12 galaxy sample*, *Mon. Not. Roy. Astron. Soc.* **470** (2017) 2617 [arXiv:1607.03155] [INSPIRE].

[27] EBOSS collaboration, *Completed SDSS-IV extended Baryon Oscillation Spectroscopic Survey: Cosmological implications from two decades of spectroscopic surveys at the Apache Point Observatory*, *Phys. Rev. D* **103** (2021) 083533 [arXiv:2007.08991] [INSPIRE].

[28] 2DFGRS collaboration, *The 2dF Galaxy Redshift Survey: The power spectrum and the matter content of the Universe*, *Mon. Not. Roy. Astron. Soc.* **327** (2001) 1297 [astro-ph/0105252] [INSPIRE].

[29] SDSS collaboration, *The 3-D power spectrum of galaxies from the SDSS*, *Astrophys. J.* **606** (2004) 702 [astro-ph/0310725] [INSPIRE].

[30] G. Efstathiou and S.J. Moody, *Maximum likelihood estimates of the two- and three-dimensional power spectra of the apm galaxy survey*, *Mon. Not. Roy. Astron. Soc.* **325** (2001) 1603 [astro-ph/0010478] [INSPIRE].

[31] WMAP collaboration, *First year Wilkinson Microwave Anisotropy Probe (WMAP) observations: Parameter estimation methodology*, *Astrophys. J. Suppl.* **148** (2003) 195 [astro-ph/0302218] [INSPIRE].

[32] J. Hamann, S. Hannestad, J. Lesgourgues, C. Rampf and Y.Y.Y. Wong, *Cosmological parameters from large scale structure — geometric versus shape information*, *JCAP* **07** (2010) 022 [arXiv:1003.3999] [INSPIRE].

[33] Y.-S. Song and W.J. Percival, *Reconstructing the history of structure formation using Redshift Distortions*, *JCAP* **10** (2009) 004 [arXiv:0807.0810] [INSPIRE].

[34] A.J.S. Hamilton, *Uncorrelated modes of the nonlinear power spectrum*, *Mon. Not. Roy. Astron. Soc.* **312** (2000) 257 [astro-ph/9905191] [INSPIRE].

[35] J.J.M. Carrasco, M.P. Hertzberg and L. Senatore, *The Effective Field Theory of Cosmological Large Scale Structures*, *JHEP* **09** (2012) 082 [arXiv:1206.2926] [INSPIRE].

[36] T. Nishimichi et al., *Blinded challenge for precision cosmology with large-scale structure: results from effective field theory for the redshift-space galaxy power spectrum*, *Phys. Rev. D* **102** (2020) 123541 [arXiv:2003.08277] [INSPIRE].

[37] A. Chudaykin, M.M. Ivanov, O.H.E. Philcox and M. Simonović, *Nonlinear perturbation theory extension of the Boltzmann code CLASS*, *Phys. Rev. D* **102** (2020) 063533 [arXiv:2004.10607] [INSPIRE].

[38] T. Colas, G. D'amico, L. Senatore, P. Zhang and F. Beutler, *Efficient Cosmological Analysis of the SDSS/BOSS data from the Effective Field Theory of Large-Scale Structure*, *JCAP* **06** (2020) 001 [arXiv:1909.07951] [INSPIRE].

[39] M.M. Ivanov, M. Simonović and M. Zaldarriaga, *Cosmological Parameters from the BOSS Galaxy Power Spectrum*, *JCAP* **05** (2020) 042 [arXiv:1909.05277] [INSPIRE].

[40] O.H.E. Philcox, M.M. Ivanov, M. Simonović and M. Zaldarriaga, *Combining Full-Shape and BAO Analyses of Galaxy Power Spectra: A 1.6% CMB-independent constraint on $H_0$*, *JCAP* **05** (2020) 032 [arXiv:2002.04035] [INSPIRE].



JCAP12(2021)054

[41] M. Lewandowski, L. Senatore, F. Prada, C. Zhao and C.-H. Chuang, *EFT of large scale structures in redshift space*, *Phys. Rev. D* **97** (2018) 063526 [arXiv:1512.06831] [INSPIRE].

[42] G. D'Amico et al., *The Cosmological Analysis of the SDSS/BOSS data from the Effective Field Theory of Large-Scale Structure*, *JCAP* **05** (2020) 005 [arXiv:1909.05271] [INSPIRE].

[43] O.H.E. Philcox, B.D. Sherwin, G.S. Farren and E.J. Baxter, *Determining the Hubble Constant without the Sound Horizon: Measurements from Galaxy Surveys*, *Phys. Rev. D* **103** (2021) 023538 [arXiv:2008.08084] [INSPIRE].

[44] D.J. Fixsen, E.S. Cheng, J.M. Gales, J.C. Mather, R.A. Shafer and E.L. Wright, *The Cosmic Microwave Background spectrum from the full COBE FIRAS data set*, *Astrophys. J.* **473** (1996) 576 [astro-ph/9605054] [INSPIRE].

[45] M.M. Ivanov, Y. Ali-Haïmoud and J. Lesgourgues, *H0 tension or T0 tension?*, *Phys. Rev. D* **102** (2020) 063515 [arXiv:2005.10656] [INSPIRE].

[46] J.M. Bardeen, J.R. Bond, N. Kaiser and A.S. Szalay, *The Statistics of Peaks of Gaussian Random Fields*, *Astrophys. J.* **304** (1986) 15 [INSPIRE].

[47] N. Sugiyama, *Cosmic background anistropies in CDM cosmology*, *Astrophys. J. Suppl.* **100** (1995) 281 [astro-ph/9412025] [INSPIRE].

[48] D. Blas, J. Lesgourgues and T. Tram, *The Cosmic Linear Anisotropy Solving System (CLASS) II: Approximation schemes*, *JCAP* **07** (2011) 034 [arXiv:1104.2933] [INSPIRE].

[49] J.R. Bond and A.S. Szalay, *The Collisionless Damping of Density Fluctuations in an Expanding Universe*, *Astrophys. J.* **274** (1983) 443 [INSPIRE].

[50] A. Raccanelli, L. Verde and F. Villaescusa-Navarro, *Biases from neutrino bias: to worry or not to worry?*, *Mon. Not. Roy. Astron. Soc.* **483** (2019) 734 [arXiv:1704.07837] [INSPIRE].

[51] S. Vagnozzi et al., *Bias due to neutrinos must not uncorrect'd go*, *JCAP* **09** (2018) 001 [arXiv:1807.04672] [INSPIRE].

[52] E. Castorina, E. Sefusatti, R.K. Sheth, F. Villaescusa-Navarro and M. Viel, *Cosmology with massive neutrinos II: on the universality of the halo mass function and bias*, *JCAP* **02** (2014) 049 [arXiv:1311.1212] [INSPIRE].

[53] BOSS collaboration, *The clustering of galaxies in the SDSS-III Baryon Oscillation Spectroscopic Survey: Testing gravity with redshift-space distortions using the power spectrum multipoles*, *Mon. Not. Roy. Astron. Soc.* **443** (2014) 1065 [arXiv:1312.4611] [INSPIRE].

[54] H. Gil-Marín et al., *The power spectrum and bispectrum of SDSS DR11 BOSS galaxies — I. Bias and gravity*, *Mon. Not. Roy. Astron. Soc.* **451** (2015) 539 [arXiv:1407.5668] [INSPIRE].

[55] J.N. Fry and E. Gaztanaga, *Biasing and hierarchical statistics in large scale structure*, *Astrophys. J.* **413** (1993) 447 [astro-ph/9302009] [INSPIRE].

[56] P. McDonald and A. Roy, *Clustering of dark matter tracers: generalizing bias for the coming era of precision LSS*, *JCAP* **08** (2009) 020 [arXiv:0902.0991] [INSPIRE].

[57] T. Baldauf, U. Seljak, V. Desjacques and P. McDonald, *Evidence for Quadratic Tidal Tensor Bias from the Halo Bispectrum*, *Phys. Rev. D* **86** (2012) 083540 [arXiv:1201.4827] [INSPIRE].

[58] S. Saito, T. Baldauf, Z. Vlah, U. Seljak, T. Okumura and P. McDonald, *Understanding higher-order nonlocal halo bias at large scales by combining the power spectrum with the bispectrum*, *Phys. Rev. D* **90** (2014) 123522 [arXiv:1405.1447] [INSPIRE].

[59] K.C. Chan, R. Scoccimarro and R.K. Sheth, *Gravity and Large-Scale Non-local Bias*, *Phys. Rev. D* **85** (2012) 083509 [arXiv:1201.3614] [INSPIRE].

[60] A. Barreira, T. Lazeyras and F. Schmidt, *Galaxy bias from forward models: linear and second-order bias of IllustrisTNG galaxies*, *JCAP* **08** (2021) 029 [arXiv:2105.02876] [INSPIRE].



JCAP12(2021)054

[61] R. Scoccimarro, *Redshift-space distortions, pairwise velocities and nonlinearities*, *Phys. Rev. D* **70** (2004) 083007 [astro-ph/0407214] [INSPIRE].

[62] A. Taruya, T. Nishimichi and S. Saito, *Baryon Acoustic Oscillations in 2D: Modeling Redshift-space Power Spectrum from Perturbation Theory*, *Phys. Rev. D* **82** (2010) 063522 [arXiv:1006.0699] [INSPIRE].

[63] A.G. Sanchez et al., *The clustering of galaxies in the SDSS-III Baryon Oscillation Spectroscopic Survey: cosmological constraints from the full shape of the clustering wedges*, *Mon. Not. Roy. Astron. Soc.* **433** (2013) 1202 [arXiv:1303.4396] [INSPIRE].

[64] F. Beutler, E. Castorina and P. Zhang, *Interpreting measurements of the anisotropic galaxy power spectrum*, *JCAP* **03** (2019) 040 [arXiv:1810.05051] [INSPIRE].

[65] M.J. Wilson, J.A. Peacock, A.N. Taylor and S. de la Torre, *Rapid modelling of the redshift-space power spectrum multipoles for a masked density field*, *Mon. Not. Roy. Astron. Soc.* **464** (2017) 3121 [arXiv:1511.07799] [INSPIRE].

[66] D. Bianchi and W.J. Percival, *Unbiased clustering estimation in the presence of missing observations*, *Mon. Not. Roy. Astron. Soc.* **472** (2017) 1106 [arXiv:1703.02070] [INSPIRE].

[67] F.G. Mohammad et al., *The Completed SDSS-IV extended Baryon Oscillation Spectroscopic Survey: Pairwise-Inverse-Probability and Angular Correction for Fibre Collisions in Clustering Measurements*, *Mon. Not. Roy. Astron. Soc.* **498** (2020) 128 [arXiv:2007.09005] [INSPIRE].

[68] F. Prada, A. Klypin, G. Yepes, S.E. Nuza and S. Gottloeber, *Measuring equality horizon with the zero-crossing of the galaxy correlation function*, arXiv:1111.2889 [INSPIRE].

[69] N. Padmanabhan, M. White and J.D. Cohn, *Reconstructing Baryon Oscillations: A Lagrangian Theory Perspective*, *Phys. Rev. D* **79** (2009) 063523 [arXiv:0812.2905] [INSPIRE].

[70] A. Burden, W.J. Percival, M. Manera, A.J. Cuesta, M. Vargas Magaña and S. Ho, *Efficient Reconstruction of Linear Baryon Acoustic Oscillations in Galaxy Surveys*, *Mon. Not. Roy. Astron. Soc.* **445** (2014) 3152 [arXiv:1408.1348] [INSPIRE].

[71] J.L. Bernal, T.L. Smith, K.K. Boddy and M. Kamionkowski, *Robustness of baryon acoustic oscillation constraints for early-Universe modifications of ΛCDM cosmology*, *Phys. Rev. D* **102** (2020) 123515 [arXiv:2004.07263] [INSPIRE].

[72] H. Gil-Marin et al., *The Completed SDSS-IV extended Baryon Oscillation Spectroscopic Survey: measurement of the BAO and growth rate of structure of the luminous red galaxy sample from the anisotropic power spectrum between redshifts 0.6 and 1.0*, *Mon. Not. Roy. Astron. Soc.* **498** (2020) 2492 [arXiv:2007.08994] [INSPIRE].

[73] P. Catelan, F. Lucchin, S. Matarrese and L. Moscardini, *Eulerian perturbation theory in nonflat universes: Second order approximation*, *Mon. Not. Roy. Astron. Soc.* **276** (1995) 39 [astro-ph/9411066] [INSPIRE].

[74] A.G. Sanchez et al., *Cosmological parameters from CMB measurements and the final 2dFGRS power spectrum*, *Mon. Not. Roy. Astron. Soc.* **366** (2006) 189 [astro-ph/0507583] [INSPIRE].

[75] B.A. Reid et al., *Cosmological Constraints from the Clustering of the Sloan Digital Sky Survey DR7 Luminous Red Galaxies*, *Mon. Not. Roy. Astron. Soc.* **404** (2010) 60 [arXiv:0907.1659] [INSPIRE].

[76] T. Tröster et al., *Cosmology from large-scale structure: Constraining ΛCDM with BOSS*, *Astron. Astrophys.* **633** (2020) L10 [arXiv:1909.11006] [INSPIRE].

[77] A.J. Ross, W.J. Percival and M. Manera, *The Information Content of Anisotropic Baryon Acoustic Oscillation Scale Measurements*, *Mon. Not. Roy. Astron. Soc.* **451** (2015) 1331 [arXiv:1501.05571] [INSPIRE].

[78] D.J. Eisenstein, H.-j. Seo and M.J. White, *On the Robustness of the Acoustic Scale in the Low-Redshift Clustering of Matter*, *Astrophys. J.* **664** (2007) 660 [astro-ph/0604361] [INSPIRE].



JCAP12(2021)054

[79] D.J. Eisenstein and M.J. White, *Theoretical uncertainty in baryon oscillations*, *Phys. Rev. D* **70** (2004) 103523 [astro-ph/0407539] [INSPIRE].

[80] S. Brieden, H. Gil-Marín and L. Verde, *Model-independent versus model-dependent interpretation of the SDSS-III BOSS power spectrum: Bridging the divide*, *Phys. Rev. D* **104** (2021) L121301, [2106.11931].

[81] BOSS collaboration, *The clustering of galaxies in the completed SDSS-III Baryon Oscillation Spectroscopic Survey: Anisotropic galaxy clustering in Fourier-space*, *Mon. Not. Roy. Astron. Soc.* **466** (2017) 2242 [arXiv:1607.03150] [INSPIRE].

[82] B. Reid et al., *SDSS-III Baryon Oscillation Spectroscopic Survey Data Release 12: galaxy target selection and large scale structure catalogues*, *Mon. Not. Roy. Astron. Soc.* **455** (2016) 1553 [arXiv:1509.06529] [INSPIRE].

[83] T. Brinckmann and J. Lesgourgues, *MontePython 3: boosted MCMC sampler and other features*, *Phys. Dark Univ.* **24** (2019) 100260 [arXiv:1804.07261] [INSPIRE].

[84] A.G. Sanchez, *Arguments against using $h^{-1}$Mpc units in observational cosmology*, *Phys. Rev. D* **102** (2020) 123511 [arXiv:2002.07829] [INSPIRE].

[85] L. Verde, R. Jimenez, F. Simpson, L. Álvarez-Gaumé, A. Heavens and S. Matarrese, *The bias of weighted dark matter haloes from peak theory*, *Mon. Not. Roy. Astron. Soc.* **443** (2014) 122 [arXiv:1404.2241] [INSPIRE].

[86] S.R. Hinton, C. Howlett and T.M. Davis, *Barry and the BAO Model Comparison*, *Mon. Not. Roy. Astron. Soc.* **493** (2020) 4078 [arXiv:1912.01175] [INSPIRE].

[87] F.-S. Kitaura et al., *The clustering of galaxies in the SDSS-III Baryon Oscillation Spectroscopic Survey: mock galaxy catalogues for the BOSS Final Data Release*, *Mon. Not. Roy. Astron. Soc.* **456** (2016) 4156 [arXiv:1509.06400] [INSPIRE].

[88] S.A. Rodríguez-Torres et al., *The clustering of galaxies in the SDSS-III Baryon Oscillation Spectroscopic Survey: modelling the clustering and halo occupation distribution of BOSS CMASS galaxies in the Final Data Release*, *Mon. Not. Roy. Astron. Soc.* **460** (2016) 1173 [arXiv:1509.06404] [INSPIRE].

[89] H.A. Feldman, N. Kaiser and J.A. Peacock, *Power spectrum analysis of three-dimensional redshift surveys*, *Astrophys. J.* **426** (1994) 23 [astro-ph/9304022] [INSPIRE].

[90] J. Hartlap, P. Simon and P. Schneider, *Why your model parameter confidences might be too optimistic: Unbiased estimation of the inverse covariance matrix*, *Astron. Astrophys.* **464** (2007) 399 [astro-ph/0608064] [INSPIRE].

[91] E. Sefusatti, M. Crocce, R. Scoccimarro and H. Couchman, *Accurate Estimators of Correlation Functions in Fourier Space*, *Mon. Not. Roy. Astron. Soc.* **460** (2016) 3624 [arXiv:1512.07295] [INSPIRE].

[92] K. Yamamoto, M. Nakamichi, A. Kamino, B.A. Bassett and H. Nishioka, *A measurement of the quadrupole power spectrum in the clustering of the 2dF QSO Survey*, *Publ. Astron. Soc. Jap.* **58** (2006) 93 [astro-ph/0505115] [INSPIRE].

[93] D. Bianchi, H. Gil-Marín, R. Ruggeri and W.J. Percival, *Measuring line-of-sight dependent Fourier-space clustering using FFTs*, *Mon. Not. Roy. Astron. Soc.* **453** (2015) L11 [arXiv:1505.05341] [INSPIRE].

[94] A. de Mattia and V. Ruhlmann-Kleider, *Integral constraints in spectroscopic surveys*, *JCAP* **08** (2019) 036 [arXiv:1904.08851] [INSPIRE].

[95] H. Gil-Marín, C. Wagner, J. Noreña, L. Verde and W. Percival, *Dark matter and halo bispectrum in redshift space: theory and applications*, *JCAP* **12** (2014) 029 [arXiv:1407.1836] [INSPIRE].

# 4

# BRIDGING THE DIVIDE

While the previous publication focused on galaxy mocks only, in the following published letter [3] we show the ShapeFit constraints on the observed BOSS DR12 LRG dataset. We show that the *shape* parameter is indeed sufficient to establish a bridge between the standard (or "classic") and the full-modeling types of analyses. We also provide a cosmological interpretation of the *shape* parameter $m$ in terms of the scale of equality between matter and radiation, proportional to the parameter combination $k_{\rm eq} \propto \Omega_{\rm m} h^2$ in units of $\mathrm{Mpc}^{-1}$ or $k_{\rm eq} \propto \Omega_{\rm m} h$ in units of $\mathrm{Mpc}^{-1} h$. Based on that, we also show a measurement of the Hubble parameter $h$, which is independent of the sound horizon $r_{\rm d}$.

Furthermore, this work explicitly shows that an erroneous treatment of observational systematics as well as signals due to unknown physics in the data (for example scale dependent bias due to primordial non-Gaussianity) result in biased parameter constrains in FM fits. On the other hand, 'ShapeFit' enables to flag such systematic uncertainties, as it disentangles the power spectrum shape (encoded in the new 'shape' parameter) from the geometrical information (encoded in the other physical parameters).

This is of particular importance for DESI, considering that especially during the data collection process (but also beyond) we need to understand exactly which part of the observed signal leads to which part of the cosmological constraints. By construction, ShapeFit can disentangle the different features, which is impossible for FM techniques. On top of that, by using ShapeFit it is sufficient to carry out a systematic analysis[1] only *once*, as the inferred systematic errors on compressed variables can be propagated easily to the cosmological models of choice. When using FM fits on the other hand, all systematic checks need to be performed for each cosmological model under investigation, resulting in a huge burden in terms of computational resources.

Having mentioned computational resources, it is worth noting that ShapeFit runs are 30 times faster than state-of-the-art FM fits, since ShapeFit is template based there is no need to reevaluate the higher order PT kernel inetgrals a each step, and the cosmological interpretation is based on linear PT only.

The letter [3] is structured as follows. In part I we shortly revisit the differences between fixed-template and FM methods and how

1 Examples for a thorough analysis of potential systematics can be found in the official BOSS and eBOSS collaboration papers of each tracer, e.g. [58, 68–72]. These works include careful studies on mocks of how a variety of analysis assumptions impact the results on compressed parameters.

ShapeFit can bridge the two. This is shown explicitlely on BOSS data in part II and figure 1, where the additional information coming from $m$ is displayed in part III and figure 2. Part III (in particular figures 3 and 4 therein) also features two examples where unknown observational or modeling systematics result in biased cosmological parameters for FM. But in case of ShapeFit these are purely absorbed by $m$, hence providing a robust diagnosis tool for detecting spurious yet unknown effects before reaching the step of model-interpretation. Conclusions and final remarks are provided in part IV.

Letter

# Model-independent versus model-dependent interpretation of the SDSS-III BOSS power spectrum: Bridging the divide

Samuel Brieden,[*] Héctor Gil-Marín,[†] and Licia Verde[‡]

*ICC, University of Barcelona, IEEC-UB, Martí i Franquès, 1, E-08028 Barcelona, Spain*

(Received 22 June 2021; accepted 2 November 2021; published 7 December 2021)

The traditional clustering analyses of galaxy redshift surveys compress the clustering data into a set of late-time physical variables in a model-independent way. This approach has recently been extended by an additional *shape variable* encoding early-time physics information. We apply this new technique, *ShapeFit*, to SDSS-III BOSS data and show that it matches the constraining power of alternative, model-dependent approaches, which directly constrain the model's parameters adopting a cosmological model *ab initio*. *ShapeFit* is ∼30 times faster, model independent, naturally splits early- and late-time variables, and enables a better control of observational systematics.

DOI: 10.1103/PhysRevD.104.L121301

## I. LARGE SCALE STRUCTURE CLUSTERING: INTERPRETATION

The traditional clustering analysis of large-scale structure (LSS) galaxy redshift surveys is done by compressing the power spectrum data products into physical variables in a largely model-independent way. These are the well-known Alcock-Paczynski (AP) scaling factors $\alpha_\perp$, $\alpha_\parallel$ [1] and the amplitude of velocity fluctuations, $f\sigma_8$ [2,3]. The AP scaling factors are obtained by observing the standard ruler provided by the baryon acoustic oscillation (BAO) feature. The amplitude of velocity fluctuations is obtained from the redshift space distortion (RSD) signal, which manifests itself as the modulation of clustering amplitude in redshift space as a function of the angle from the line of sight. This provides a powerful compression: from power spectrum multipoles as function of scale and redshift, to three quantities, the physical variables, per redshift bin. These are the physical variables that are then compared to theory predictions, within a given cosmological model, to constrain the numerical values of the model's parameters. The value of this classic approach lies in the fact that the model dependence is introduced only at the very end of the process, leaving most of the analysis as model independent as possible. In addition, this approach nicely disentangles information of the late-time universe from that of the early-time universe, which is particularly valuable for going beyond simple parameter fitting and pursuing ways to test the model and its underlying assumptions. It has a drawback, however: the compression is not lossless. Its target is robustness, but this comes at a cost.

This approach is conceptually different from the way in which, for example, cosmic microwave background (CMB) data are routinely analyzed. The CMB maps are compressed into angular power spectra (as done for galaxy clustering), but then these are directly used to constrain the values of the parameters of an adopted cosmological model. The so called "physical parameters" for the CMB were actually proposed in [4]. The original goal was to accelerate cosmological inference from CMB data, and some of these parameters are still employed to date for the computational speed-up they yield. But, in reality, the physical parameters capture phenomenological signatures of physical processes, and can then be interpreted *a posteriori* in terms of constraints on cosmological model parameters. The use of physical parameters in CMB analysis to produce model-independent constraints [5,6] and further compress CMB observations is not mainstream, at least in part, for two reasons. The CMB gives us a snapshot of the photon-baryon plasma at recombination, so is located at a single cosmic epoch; moreover, CMB photons must cross the entire Universe from the last scattering surface to $z = 0$, making it difficult to disentangle early-times physics signatures from late-times ones (but see [7,8]).

The galaxy power spectrum can also be interpreted in a way completely analogous to the way the CMB is analyzed. The development of relatively fast (significantly faster than N-body simulations) modeling techniques for the nonlinear galaxy power spectrum (e.g., effective field theory, EFT) has made this "full modeling" (FM) possible over the past

[*]sbrieden@icc.ub.edu
Also at Departament de Física Quàntica i Astrofísica, Universitat de Barcelona, Martí i Franquès 1, E-08028 Barcelona, Spain.
[†]hectorgil@icc.ub.edu
[‡]liciaverde@icc.ub.edu
Also at ICREA, Pg. Lluís Companys 23, Barcelona, E-08010, Spain.

 

couple of years ([9,10] and references therein). It became quickly apparent that this newer approach produces much tighter constraints on cosmological parameters than the classic (compressed-variables based) approach, if galaxy clustering is analyzed without external datasets, or strong external priors. On the other hand, in a joint CMB + LSS analysis (e.g., [11]) the two perform very similarly.

However, there is significant value in analyzing and interpreting galaxy clustering alone, especially not in combination with early-time probes. Separate analyses of observations of disparate epochs of the Universe are key to shed light on recent cosmological tensions (e.g., [12]), and propose explanations in terms of deviations from the standard cosmological model (e.g., [13]).

Until very recently, the extra signal responsible for the spectacular improvement provided by the FM approach was not well understood. However [14] showed that a simple, one (phenomenological) parameter extension of the classic approach, *ShapeFit*, can capture most of this extra signal and provides the same statistical power within a flat-ΛCDM model. The compression that *ShapeFit* provides is nearly lossless for models that are effectively described, or well approximated, by $w$CDM-like models or simple variations of the CDM model at horizon scales at early times. While the classic approach (and *ShapeFit*) relies on a template for compression, it has been extensively demonstrated that the choice of the cosmological model necessary to create the template is unimportant, does not constitute a model prior and does not produce any significant systematic shifts under the correct interpretation of their physical variables [14–16].

In the classic RSD fit, at a given redshift bin $z$, the full power spectrum multipoles, $P^{(\ell)}(k,z)$, are compressed in just three physical variables sensitive to late-time physics only. These are two background-level variables that describe the cosmic expansion in units of the standard ruler, $\alpha_{\parallel}(z)$ and $\alpha_{\perp}(z)$ (see Sec. 2.4 of [14]); and a perturbation-level variable that describes structures growth, $f\sigma_8(z)$. The extra information that the classic RSD neglects (and that the FM captures) is related to the shape of the transfer function. In addition to a more appropriate definition of velocity fluctuations $f\sigma_{s8}$, *ShapeFit* introduces a new variable $m$ [see Eqs. (3.5), (3.6) and (3.12) of [14] for definitions] which captures very well the bulk of the missing information. The physical interpretation of this $m$-variable is not any late-time physics phenomenon, but a series of early-time processes which modulate the broadband shape of the power spectrum (and the matter transfer function).

Hence, *ShapeFit* can be used to bridge the classic and FM approaches. The connection lies on making explicit and enforcing (or removing) a key "internal model prior" which ties together early- and late-time compressed variables (see [14]). While the compressed physical variables are model independent, the internal model prior connects the signature of early-time physics on the clustering signal on large scales, to the standard ruler signature constraining the late-time geometry and the redshift space signature of kinematics on the clustering.

## II. APPLICATION TO SDSS-III BOSS DATA

We employ the luminous red galaxy (LRG) samples of the SDSS-III BOSS survey [11], covering two nonoverlapping redshift ranges: $0.2 < z < 0.5$ (effective redshift 0.38), containing 604,001 galaxies; and $0.5 < z < 0.75$ (effective redshift 0.61) containing 594,003 galaxies. As done in BOSS official papers, we treat these two redshift samples as uncorrelated. The effective volume traced by these two samples is 3.7 and 4.1 $\mathrm{Gpc}^3$, respectively, for a total effective volume of 7.8 $\mathrm{Gpc}^3$.

This same dataset yields very different cosmological constraints when it is analyzed using the classic approach or the FM fit (see e.g., Fig. 2 of [14] gray contours for classic RSD alone, orange when BAO postreconstruction information is added, blue for FM fit). Both approaches yield very similar constraints when combined with a CMB prior (e.g., Planck; see the right panel of Fig. 2 in [14]), as this type of prior effectively fixes the early-time physics information enclosed in the broadband shape.

In what follows, parameter constraints are obtained with a standard Markov chain Monte Carlo (MCMC) posterior sampling [17]. The modeling of the clustering signal follows [9,14] and employs the Boltzmann solver [18] including the EFT extension from [19]. The left panel of Fig. 1 displays the constraints on the late-time universe physical variables $\{\alpha_{\parallel}, \alpha_{\perp}, f\sigma_8\}$ obtained by the classic RSD analysis (dashed black contours) and by *ShapeFit* analysis, with the extra early-time universe parameter $m$ (green contours), when both are applied to the high-redshift bin of BOSS.

The constraints on the three late-time universe physical parameters are not significantly modified by the addition of $m$ as a free extra variable, as $m$ is essentially uncorrelated with them. The small correlation between $m$ and, e.g., $f\sigma_8$ of $-0.3$ leads to only 5% increase in errors.

The posteriors of the left panel of Fig. 1 have been obtained without any strong model assumption [20], and hence are easily interpretable within a wide set of cosmological models. This model-interpretation process essentially places "internal model priors" among the physical variables, connecting them with the internal parameters of the assumed model. This is shown by the green contours of the right panel of Fig. 1. The *ShapeFit* contours of the left panel (and additionally another set of four parameters at the low-redshift bin, $z_{\mathrm{eff}} = 0.38$) are interpreted within a flat-ΛCDM model with a Gaussian big bang nucleosynthesis (BBN) prior $\omega_b = 0.02268 \pm 0.00038$ [9,21–23]; the resulting posteriors for $\{\omega_{cdm}, \Omega_m, h, \sigma_8\}$ are drawn. The constraints obtained by directly fitting the $P^{(\ell)}(k,z)$ shape on the same range of scales under the FM approach using EFT theory to describe the $P(k)$ modeling are shown in blue. Note the spectacular agreement between both

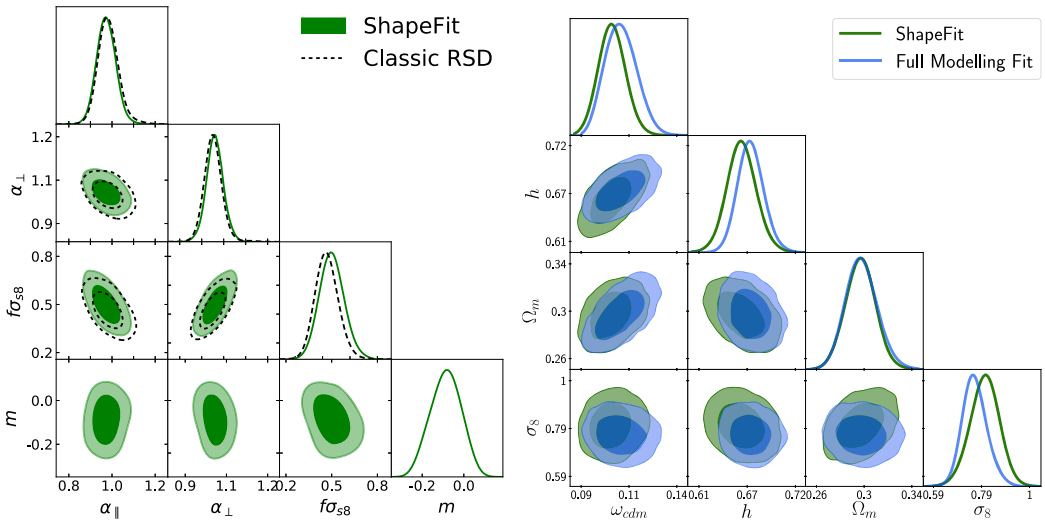


FIG. 1. Left panel: compressed physical parameter posteriors derived from power spectra measurements of the BOSS high-redshift sample, $z_{\rm eff} = 0.61$ (constraints from the low-redshift sample show a very similar behavior). Black dashed contours display the classic RSD results, while novel *ShapeFit* results are shown in green. In both cases the one-loop standard perturbation theory has been used to model the monopole and quadrupole signals for $0.01 \leq k[h\,\mathrm{Mpc}^{-1}] \leq 0.15$. Right panel: posteriors derived from low- and high-redshift samples of BOSS using the same scale cuts as in the left panel. The blue contours correspond to the FM approach when a flat-ΛCDM model (+BBN Gaussian prior on $\omega_b$) is directly fitted to the 224 power spectra multipoles bins, $P^{(\ell)}(k,z)$, using EFT to model the power spectrum. Conversely, green contours are drawn from the eight compressed physical variables of *ShapeFit*, interpreted under the same cosmological model as for the blue contours.

approaches, especially considering that the green contours are obtained from just eight variables (the four physical variables, $\{\alpha_\parallel, \alpha_\perp, f\sigma_8, m\}$ at two redshift bins), while blue contours are for 224 $P^{(\ell)}(k,z)$ measurements ($28k$-bins measurements for two multipoles, two redshift bins, and two galactic hemispheres). Another advantage of *ShapeFit* over the FM approach is computational time. Once the compressed variables are extracted (since this step is model independent it has to be done only once) the model fitting is very fast: one model evaluation on a single-core is 8 times faster than the FM run. As the cosmological interpretation of *ShapeFit* parameters is done without any nuisance parameters and due to the much simpler likelihood surface, an MCMC needs 5–10 times fewer sampled points than the FM method for the same level of convergence. *ShapeFit* yields an overall speed-up factor of 40–80.

## III. THE POWER OF THE SHAPE VARIABLE

Figure 2 shows the cosmological constraints for a standard flat-ΛCDM model, obtained from the low- and high-redshift BOSS samples using different sets of physical compressed variables. Gray contours arise from the classic RSD analysis using $\{\alpha_\parallel(z), \alpha_\perp(z), f\sigma_8(z)\}$, red contours from the *ShapeFit* analysis, but only using $m(z)$; green contours represent the *ShapeFit* analysis using the full combination of four physical variables per redshift bin (as for the right panel of Fig. 1). The transparent contours are for a broad uniform prior, $0.005 < \omega_b < 0.04$, the opaque contours for the Gaussian BBN prior. Note that relaxing the prior does not significantly affect the 1D posteriors measured by the classic RSD and $m$-only fit, but broadens the *ShapeFit* result on $\Omega_{\rm m}h$ by a factor ∼2.5.

The choice of parameters shown, $\{\Omega_m h, hr_s, \omega_{cdm}, \omega_b\}$, highlights the complementary between the late- and the early-time physical variables. The BAO signal naturally constrains $hr_s$ [24], while $m$ constrains $\Omega_m h$, as this variable is directly governing the shape of the matter transfer function via matter-radiation equality epoch. The relation between $m$ and $\Omega_m h$ is well approximated by the following fitting formula valid in the range $0.1 < \Omega_m h < 0.35$:

$$\frac{\Omega_m h}{\Omega_m^{\rm ref} h^{\rm ref}} = 0.13m^4 + 0.53m^3 + 0.86m^2 + m + 1. \quad (1)$$

Within a ΛCDM model, the purely late-time (uncalibrated) expansion history constrains the ratio $\alpha_\parallel/\alpha_\perp$ (also the relative isotropic signals among $z$ bins). This can be used to measure $\Omega_m$, which is particularly well constrained when low- and high-$z$ samples are combined (see Fig. 5 of [15]). In combination with the $\Omega_m h$ constraint provided by $m$, it is thus possible to produce a measurement of $H_0$. Note that, in spite of coming from galaxy clustering measurements, such measurement of $H_0$ *is not* arising only from

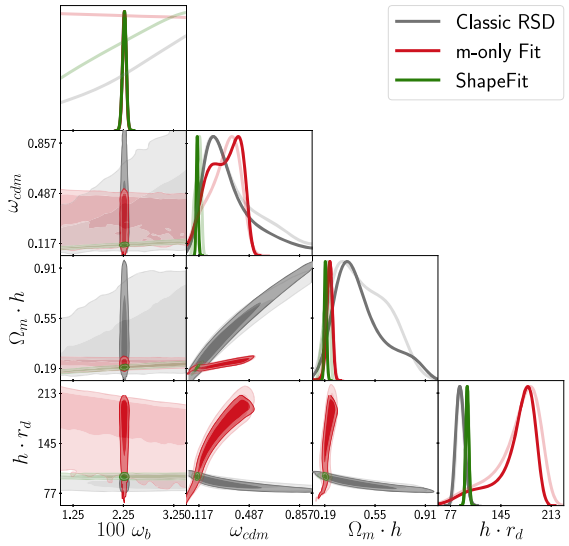


FIG. 2. Interpretation within a flat-ΛCDM model with a Gaussian BBN prior on $\omega_b$ (opaque contours) and without (transparent contours), of different physical variable constraints from the low- and high-redshift BOSS samples. Gray corresponds to classic RSD analysis based on late-time variables, $\{\alpha_\parallel(z), \alpha_\perp(z), f\sigma_8(z)\}$, red corresponds to the early-time shape variable $m(z)$ only, and their combination based on the ΛCDM internal model prior is shown in green.

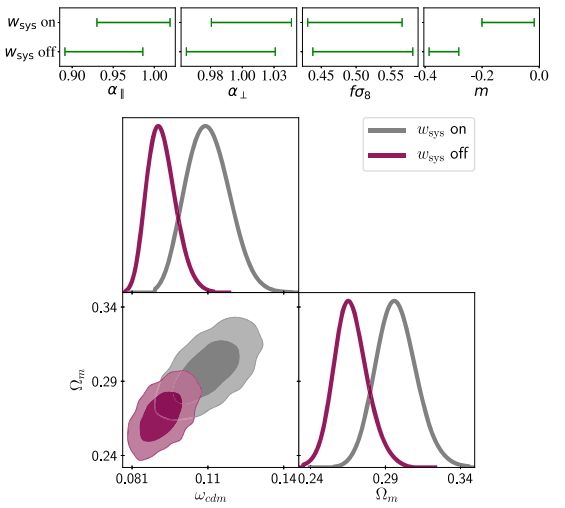


FIG. 3. Effect of turning on and off the imaging systematic weights of BOSS data: for *ShapeFit* in its compressed set of physical variables (upper panels); and for the FM fit in the $\Omega_m - \omega_{cdm}$ plane (lower panel). For *ShapeFit* $f\sigma_8$ and $\alpha_{\parallel,\perp}$ are barely affected by this correction, whereas $m$ absorbs most of the effect; for FM fit, $\omega_{cdm}$ and $\Omega_m$ are significantly biased.

late-time processes, but from a combination of early- and late-time universe physics. Following this procedure we use the $\Omega_m h$ measurement from the $m$-only analysis of BOSS LRGs data for $0.2 \le z \le 0.75$ (red contours of Fig. 2, $\Omega_m h = 0.220^{+0.029}_{-0.019}$, without the BBN prior on $\omega_b$), with the $\Omega_m$ constraint from the uncalibrated BAO of the full BOSS + eBOSS sample: $\Omega_m = 0.299 \pm 0.016$, see Table 4 of [15], which includes clustering measurements of low-redshift galaxies, LRGs, emission line galaxies, quasars and Lyman-$\alpha$ emission lines (or $\Omega_m = 0.330 \pm 0.037$ without Lyman-$\alpha$). The $\Omega_m h$ and $\Omega_m$ measurements are considered uncorrelated as they come from different physical effects and different scales ($m$ is almost uncorrelated with standard BAO variables, left panel in Fig. 1). We find $H_0 = 73.6^{+10.5}_{-7.5}$ (or $H_0 = 66.7^{+12.1}_{-10.1}$ without Lyman-$\alpha$, where the change is solely driven by the determination of $\Omega_{\rm m}$), independent of any prior on $\omega_b$, or the absolute length of the BAO standard ruler. We also report the value of $H_0$ obtained from applying *ShapeFit* to the LRG sample in combination of a BBN prior on $\omega_b$ (this is what is shown in the right panel of Fig. 1): $H_0 = 66.0^{+2.0}_{-1.7}$.

To quantify the impact of the known imaging systematics on cosmological constraints we repeat the above analysis by setting the systematic weights to unity in the BOSS catalogs (i.e., no correction for imaging systematic effects). As shown in Fig. 3 the scaling parameters and $f\sigma_8$ are left largely unchanged while $m$ is affected by a shift of about $2.4\sigma$. Not unsurprisingly, $m$ "absorbs" systematic effects such as seeing, completeness or extinction angular dependencies: late-time physics constraints from clustering measurements are significantly more robust than early-time physics constraints.

Finally, the advantage offered by a model-independent approach like *ShapeFit* can be appreciated by devising a situation where the internal consistency check fails.

It is well known that a primordial non-Gaussianity of the local type induces a scale-dependent bias in the clustering of biased tracers, which is important at very large scales [25,26]. This scale-dependent bias correction is proportional to the linear bias, the non-Gaussianity parameter $f_{\rm NL}$ and has a scale dependence $\sim 1/k^2$, hence a leakage of this signal into $m$ can be expected. We forecast the performance of *ShapeFit* and FM by generating mock power spectrum monopole and quadrupole signals according to two-loop resummed perturbation theory, and analyzing it as done for the BOSS NGC $0.5 \le z \le 0.75$ data with the same covariance matrix. For choices of bias parameters consistent with the bias of BOSS galaxies ($b \sim 2.2$), the effective redshift of BOSS and including only $k > 0.01h$ Mpc$^{-1}$, we find that a $f_{\rm NL} = \pm 60$ induces a change in $m$ of $\Delta m = \mp 0.08$ or, in general (linear response validated also for intermediate values), $\Delta m = -0.0013 f_{\rm NL}$, leaving all other physical parameters unaffected. This is shown in the left panel of Fig. 4: the presence of nonzero $f_{\rm NL}$ does not bias the recovery and cosmological interpretation of $\alpha_\parallel$, $\alpha_\perp$ and $f\sigma_8$.

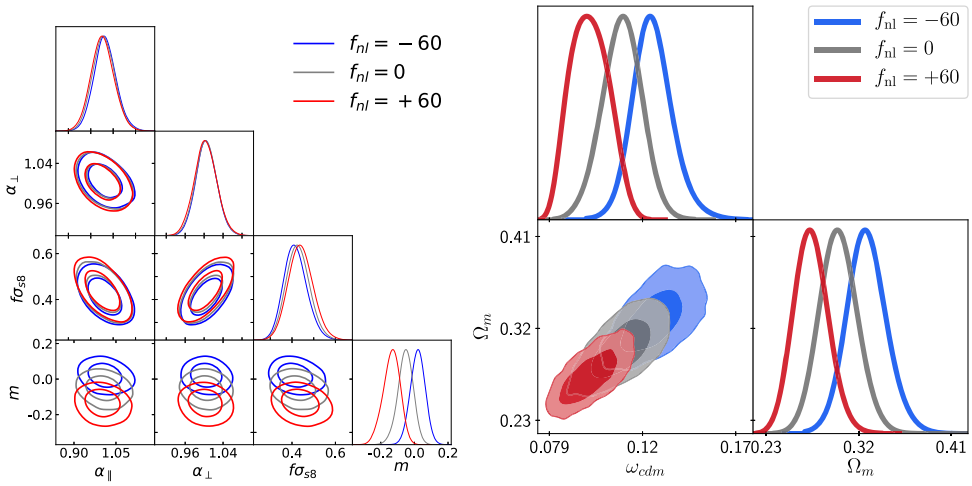


FIG. 4. Systematic bias caused by ignoring in the modeling a $f_{\rm NL}$ signal which is present in the data vector. In this case we have imprinted a mock $f_{\rm NL} = \pm 60$ signal, which is represented by red and blue contours. For *ShapeFit* (left panel) this systematic effect only impacts the shape parameter $m$ leaving $f\sigma_8$ and the scaling parameters unaffected. For the FM fit (right panel) it biases both $\Omega_m$ and $\omega_{cdm}$.

The right panel of Fig. 4 shows the effect on $\omega_{\rm cdm}$ and $\Omega_{\rm m}$ (other cosmological parameters are unaffected) of applying the FM pipeline to the same datasets containing a primordial non-Gaussian signal. Since the FM analysis avoids the compression step, the bias induced by $f_{\rm NL}$ directly propagates into model parameters, without the possibility to diagnose where the signal actually comes from, as it is the case in the *ShapeFit* approach. This indicates that in the presence of nonzero $f_{\rm NL}$, a FM analysis assuming Gaussian initial conditions would recover biased results for $\Omega_m$ and $\omega_{cdm}$. The difference in $\chi^2$ estimation between the fit for $f_{\rm NL} = 0$ and that for $f_{\rm NL} = 60$ is $\Delta\chi^2 = 5$ for FM (54 data points, ten parameters), indicating that a "goodness-of-fit" test relying on $\chi^2$ values would not be enough to signal any issue.

It is important to note that the scale-dependent bias effect of $f_{\rm NL}$ is usually considered negligible at scales $k > 0.03h\,{\rm Mpc}^{-1}$, hence the leakage of $f_{\rm NL}$ on $m$ for *ShapeFit* and the shift in $\omega_{cdm}$ and $\Omega_m$ for FM, is expected to become significantly more important for survey volumes that probe scales $k < 0.01h\,{\rm Mpc}^{-1}$ not included here.

## IV. CONCLUSIONS

For the BOSS dataset the shape parameter efficiently captures the extra information that FM approaches deliver. *ShapeFit*, by working in terms of the compressed variables, has essentially three main advantages over FM.

### A. Model independence and computing time

Once constraints on the physical variables are obtained they can be interpreted within multiple cosmological models at minimum computational cost. On the other hand, the full modeling approach requires to rerun the full analysis for each new choice of cosmology.

### B. Physical insight

The physical variables are naturally directly related to specific physical processes that happen in the Universe at different epochs. The scaling factors and the growth of perturbations are sensitive only to the late-time physics of the Universe. The shape parameter captures the shape of the power spectrum on large scales ($\sim$ to the horizon size at $z \gtrsim 1000$) which contains signatures of early-time physics. For a given cosmological model the early- and late-time effects are intrinsically related, which

(i) sets an internal model-prior implicit in the full model approach but made explicit in the *ShapeFit*;
(ii) the early- and late-time physical variables can be used to perform a powerful consistency test of the cosmological model.

### C. Systematics control

The *ShapeFit* analysis (as well as classic) naturally separates the cosmological information into variables which have very different systematic budgets. The BAO-inferred signal has been shown to be extremely robust to theoretical and observing systematics, with a conservative error budget for state-of-the-art measurements of $\lesssim 1\%$ [27]. The amplitude of velocity fluctuation can suffer from imaging and spectroscopic systematics if these are not exquisitely taken into account. The current estimate for this systematic budget is $\simeq 2\%$ [28]. The shape parameter can

severely suffer from observational large-scale systematics (e.g., extinction, seeing, completeness). For BOSS data we quantify that the known imaging systematic produces a $\sim 2.4\sigma$ shift in $m$ if not corrected. On the other hand, it absorbs nonstandard early-universe physics signals and prevents them to leak into and bias the determination of late-time parameters shaping the expansion/growth history.

We envision that the connection between the physical variables proposed by *ShapeFit* and the full modeling approach will provide a transparent bridge between model-independent and model-dependent interpretation of forthcoming galaxy redshift surveys and a direct physical understanding of their clustering results.

## ACKNOWLEDGMENTS

H. G-M. and S. B. acknowledge the support from la Caixa Foundation (ID100010434) with code LCF/BQ/PI18/11630024. L. V. acknowledges support of European Unions Horizon 2020 research and innovation program ERC (BePreSySe, Grant Agreement No. 725327). Funding for this work was partially provided by the Spanish MINECO under Project No. PGC2018-098866-B-I00 FEDER-EU. Funding for SDSS-III [29] has been provided by the Alfred P. Sloan Foundation, the Participating Institutions, the National Science Foundation, and the U.S. Department of Energy Office of Science.

[1] C. Alcock and B. Paczynski, An evolution free test for nonzero cosmological constant, Nature (London) **281**, 358 (1979).
[2] N. Kaiser, Clustering in real space and in redshift space, Mon. Not. R. Astron. Soc. **227**, 1 (1987).
[3] W. J. Percival and M. White, Testing cosmological structure formation using redshift-space distortions, Mon. Not. R. Astron. Soc. **393**, 297 (2009).
[4] A. Kosowsky, M. Milosavljevic, and R. Jimenez, Efficient cosmological parameter estimation from microwave background anisotropies, Phys. Rev. D **66**, 063007 (2002).
[5] Y. Wang and P. Mukherjee, Robust dark energy constraints from supernovae, galaxy clustering, and three-year Wilkinson microwave anisotropy probe observations, Astrophys. J. **650**, 1 (2006).
[6] Z. Zhai, C.-G. Park, Y. Wang, and B. Ratra, CMB distance priors revisited: Effects of dark energy dynamics, spatial curvature, primordial power spectrum, and neutrino parameters, J. Cosmol. Astropart. Phys. 07 (2020) 009.
[7] B. Audren, J. Lesgourgues, K. Benabed, and S. Prunet, Conservative constraints on early cosmology with MONTE PYTHON, J. Cosmol. Astropart. Phys. 02 (2013) 001.
[8] L. Verde, J. L. Bernal, A. F. Heavens, and R. Jimenez, The length of the low-redshift standard ruler, Mon. Not. R. Astron. Soc. **467**, 731 (2017).
[9] M. M. Ivanov, M. Simonovi, and M. Zaldarriaga, Cosmological parameters from the BOSS galaxy power spectrum, J. Cosmol. Astropart. Phys. 05 (2020) 042.
[10] G. D'Amico, J. Gleyzes, N. Kokron, K. Markovic, L. Senatore, P. Zhang, F. Beutler, and H. Gil-Marn, The cosmological analysis of the SDSS/BOSS data from the effective field theory of large-scale structure, J. Cosmol. Astropart. Phys. 05 (2020) 005.
[11] S. Alam *et al.* (BOSS Collaboration), The clustering of galaxies in the completed SDSS-III Baryon Oscillation Spectroscopic Survey: Cosmological analysis of the DR12 galaxy sample, Mon. Not. R. Astron. Soc. **470**, 2617 (2017).
[12] L. Verde, T. Treu, and A. G. Riess, Tensions between the rarly and the late Universe, in Nat. Astron. **3**, 891 (2019).
[13] E. Di Valentino, O. Mena, S. Pan, L. Visinelli, W. Yang, A. Melchiorri, D. F. Mota, A. G Riess, and J. Silk, In the realm of the Hubble tension—a review of solutions, Class. Quantum Grav. **38**, 153001 (2020).
[14] S. Brieden, H. Gil-Marín, and L. Verde, ShapeFit: Extracting the power spectrum shape information in galaxy surveys beyond BAO and RSD, J. Cosmol. Astropart. Phys. (2021).
[15] S. Alam *et al.* (eBOSS Collaboration), Completed SDSS-IV extended Baryon Oscillation Spectroscopic Survey: Cosmological implications from two decades of spectroscopic surveys at the Apache Point Observatory, Phys. Rev. D **103**, 083533 (2021).
[16] J. L. Bernal, T. L. Smith, K. K. Boddy, and M. Kamionkowski, Robustness of baryon acoustic oscillation constraints for early-Universe modifications of ΛCDM cosmology, Phys. Rev. D **102**, 123515 (2020).
[17] T. Brinckmann and J. Lesgourgues, MontePython 3: Boosted MCMC sampler and other features, Phys. Dark Universe **24**, 100260 (2019).
[18] D. Blas, J. Lesgourgues, and T. Tram, The cosmic linear anisotropy solving system (CLASS). Part II: Approximation schemes, J. Cosmol. Astropart. Phys. 07 (2011) 034.
[19] A. Chudaykin, M. M. Ivanov, O. H. E. Philcox, and M. Simonović, Nonlinear perturbation theory extension of the Boltzmann code CLASS, Phys. Rev. D **102**, 063533 (2020).
[20] Here, we mean model-assumptions other than homogeneity, isotropy, and scale-independent growth. The reconstruction step assumes that gravity at mildly nonlinear scales is well described by general relativity.
[21] E. G. Adelberger *et al.*, Solar fusion cross sections II: The pp chain and CNO cycles, Rev. Mod. Phys. **83**, 195 (2011).
[22] O. Pisanti, A. Cirillo, S. Esposito, F. Iocco, G. Mangano, G. Miele, and P. D. Serpico, PArthENoPE: Public algorithm evaluating the nucleosynthesis of primordial elements, Comput. Phys. Commun. **178**, 956 (2008).
[23] N. Schöneberg, J. Lesgourgues, and D. C. Hooper, The BAO + BBN take on the Hubble tension, J. Cosmol. Astropart. Phys. 10 (2019) 029.

[24] J. L. Bernal, L. Verde, and A. G. Riess, The trouble with H0, J. Cosmol. Astropart. Phys. 10 (2016) 019.

[25] N. Dalal, O. Dore, D. Huterer, and A. Shirokov, Imprints of primordial non-Gaussianities on large-scale structure: Scale dependent bias and abundance of virialized objects, Phys. Rev. D **77**, 123514 (2008).

[26] S. Matarrese and L. Verde, The effect of primordial non-Gaussianity on halo bias, Astrophys. J. Lett. **677**, L77 (2008).

[27] G. Merz *et al.*, The clustering of the SDSS-IV extended baryon oscillation spectroscopic survey quasar sample: Testing observational systematics on the baryon acoustic oscillation measurement, Mon. Not. R. Astron. Soc. **506**, 2503 (2021).

[28] A. Smith *et al.*, The completed SDSS-IV extended baryon oscillation spectroscopic survey: N-body mock challenge for the quasar sample, Mon. Not. R. Astron. Soc. **499**, 269 (2020).

[29] http://www.sdss3.org/.

# 5

# PT CHALLENGE: VALIDATION OF SHAPEFIT

In the publication of this chapter [4], we demonstrate the robustness of Shapefit by applying it to the blind PT challenge initiated by [83]. The challenge setup and our main cosmological results submitted blindly to the challenge initiator can be found at the website [88].

For our baseline result, labeled "SIM-like", we chose the same setup (prior knowledge on shotnoise, fitted $k$- and $\ell$- range, order in PT, number of free bias parameters) as the one chosen in the baseline FM analyses of [83]. And comparable to their case, we recover all the varied cosmological parameters $\{\Omega_m, h, \ln(10^{10} A_s)\}$ well within $2\sigma$, with identical[1] precision as for the other participants which used the FM technique. Note that, the statistical error bars are obtained from the covariance corresponding to the volume of the 10 stacked realizations, $566\,\mathrm{Gpc}h^{-1}$. This volume is 10-20 times larger than the volume probed by future galaxy surveys such as DESI.

In addition to this remarkable result, the work presented here contains another important lesson. It explicitely shows that systematics present in either the modeling or in the data may only be spotted at the model-agnostic compression step and remain largely unnoticed if the model (in this case ΛCDM) is chosen *a priori*. In this particular case, we show that the inclusion of the hexadecapole (cases labeled "DATA-like") leads to a bias of up to $4\sigma$ at the level of compressed variables, while showing apparently phenomenal $\sim 1\sigma$ agreement at the level of ΛCDM parameters.

Of course, in an ideal case (such as the PT challenge case), the systematic effect of the hexadecapole unveils itself also in the model-dependent analysis through the $\chi^2$ statistic. In fact, this issue was already discovered in [83], which is why the hexadecapole was not included in their baseline analysis in the first place. Nevertheless, we argue that for real data it might be dangerous if the only applicable diagnosis tool for unknown systematics consists of the $\chi^2$-test. This is, because the error bar estimation might not be optimal or even biased and hence obscure the $\chi^2$ estimation. The ShapeFit methodology, on the other hand, by construction allows for another layer of consistency check before the model-interpretation step. In this spirit, ShapeFit delivers a reliable basis for studying the impact of systematics.

Finally, we also provide a new type of analysis on mocks, where we split the different mock realisations over redshift, which allows for a

1 Of course there is some scatter in constraining power among the participants, but in general the ShapeFit error sizes match those in order of magnitude.

more realistic scenario, in which also actual the redshift evolution of real data is taken into account.

The publication is structured as follows. After introducing the PT challenge setup (section 2) and summarizing ShapeFit (section 3), we provide an overview of the methodology and different runs in section 4. We present the main result in section 5 and show additional tests including variations from the baseline in section 6. We introduce the split of realisations among redshift bins and present corresponding results in section 7 before we finally conclude in section 8.

All in all, this work is an important milestone on the road towards establishing ShapeFit as a robust tool for the DESI main analysis pipeline.

Journal of Cosmology and Astroparticle Physics
An IOP and SISSA journal

# PT challenge: validation of ShapeFit on large-volume, high-resolution mocks

**Samuel Brieden,**[a,b] **Héctor Gil-Marín**[a] **and Licia Verde**[a,c]

[a]ICC, University of Barcelona, IEEC-UB,
Martí i Franquès, 1, E-08028 Barcelona, Spain
[b]Dept. de Física Quàntica i Astrofísica, Universitat de Barcelona,
Martí i Franquès 1, E-08028 Barcelona, Spain
[c]ICREA,
Pg. Lluís Companys 23, Barcelona, E-08010, Spain

E-mail: sbrieden@icc.ub.edu, hectorgil@icc.ub.edu, liciaverde@icc.ub.edu

Received January 26, 2022
Accepted May 6, 2022
Published June 8, 2022

**Abstract.** The ShapeFit compression method has been shown to be a powerful tool to gain cosmological information from galaxy power spectra in an effective, model-independent way. Here we present its performance on the blind PT challenge mock products presented in [1]. Choosing a set-up similar to that of other participants to the blind challenge we obtained $\Delta \ln (10^{10} A_s) = -0.018 \pm 0.014$, $\Delta \Omega_{\rm m} = 0.0039 \pm 0.0021$ and $\Delta h = -0.0009 \pm 0.0034$, remaining below $2\sigma$ deviations for a volume of $566\,[h^{-1}{\rm Gpc}]^3$. This corresponds to a volume 10 times larger than the volume probed by future galaxy surveys. We also present an analysis of these mocks oriented towards an actual data analysis using the full redshift evolution, using all three redshift bins $z_1 = 0.38$, $z_2 = 0.51$, and $z_3 = 0.61$, and exploring different set-ups to quantify the impact of choices or assumptions on noise, bias, scale range, etc. We find consistency across reasonable changes in set-up and across redshifts and that, as expected, mapping the redshift evolution of clustering helps constraining cosmological parameters within a given model.

**Keywords:** cosmological parameters from LSS, cosmological simulations, galaxy surveys, power spectrum

**ArXiv ePrint:** 2201.08400


https://doi.org/10.1088/1475-7516/2022/06/005

JCAP06(2022)005

## Contents



## 1 Introduction

With the advent of precision cosmology, our lack of understanding of the nature of the dark components of the Universe (dark matter and dark energy) has been and continues to be the main science driver for galaxy redshift surveys of increasingly large cosmological volumes. The global effort of mapping the large scale structure (LSS) with high fidelity and over large cosmic volumes of the Universe continues to provide data sets of unprecedented statistical power, and ever more stringent constraints on cosmology [2, 3]. It is therefore of fundamental importance to have accurate theoretical modeling for the key summary statistics which can then be confronted to those measured from these surveys. As the statistical errors shrink with the larger cosmological volumes mapped, systematic errors introduced by the theoretical modeling should be kept under exquisite control. In this spirit, the authors of [1] launched the (blind) PT challenge, where PT stands for "perturbation theory". This is a N-body mock challenge, initially used to (blindly) test Effective Field Theory of Large Scale Structure (EFTofLSS); the — still blind — simulations outputs were subsequently made available to the community and several other groups have participated to the challenge with their own theoretical modeling approaches and implementations.

To date, all the entries to the challenge have adopted modeling methodologies that fall under the "full modeling" (FM) approach, in the terminology of [4]. This approach follows the same philosophy as the analyses of Cosmic Microwave Background (CMB) data: the



JCAP06(2022)005

maps are compressed into power spectrum summary statistics (a compression that is nearly lossless for CMB, and would be nearly lossless for LSS in the fully linear regime) and these quantities are directly compared to theory predictions for a given cosmological model to constrain the model's parameters.

But this is not the main way clustering analysis of LSS galaxy redshift surveys has been carried out for the past ∼15 years, which refs. [4, 5] refers to as "classic". In contrast to FM, the "classic" clustering analysis is done by first compressing the power spectrum data into physical variables — the Alcock-Paczynski (AP) scaling factors and the amplitude of velocity fluctuations — and then interpreting the physical variables in light of a model. The advantage of this "classic" approach is that the (cosmological) model-dependence is introduced at the very end of the process, at the interpretation stage, leaving most of the analysis as model-independent as possible. It also offers a simple way to disentangle late-time physics information from that coming from the early Universe. The compression aims at isolating the part of cosmological signal which information-content is least affected by systematics (see e.g., [6–9]), for this reason called BAO+RSD, where BAO stands for baryon acoustic oscillations and RSD by redshift space distortions. This, however comes at a cost: the compression is not lossless. By emphasising robustness and accuracy over precision, the "classic" compressed variables approach produces less stringent constraints on cosmological parameters than the FM approach, especially in the (minimal, flat) ΛCDM model.

Refs. [5] and [4] shed light on the origin, localization and physics of extra signal responsible for the spectacular improvement in cosmological parameters constraints provided by the FM over the "classic" approach. A simple, one-parameter phenomenological extension of the "classic" approach was hence proposed: ShapeFit. It has been shown that ShapeFit can capture most of the FM extra signal and that it provides virtually the same statistical power in terms of cosmological parameter constraints. In [4], ShapeFit was applied to the BOSS DR12 data and its performance compared to that of the FM approach of a specific implementation of the EFTofLSS by [10]. In this paper we present the application of ShapeFit to the PT challenge. While the application to real data presented in [4] offer a well-rounded test, because real survey data include a whole suite of real-world effects, the sheer combined volume of the PT challenge reduces the statistical errors to a point that they become negligible (its volume is an order of magnitude larger than that of the forthcoming galaxy redshift surveys [11]) and clearly surfaces any residual modeling systematics. This is the added value of the results presented in this paper.

The rest of the paper is organized as follows. In section 2 we give a brief overview of the PT challenge set-up. In section 3 we review the "classic" and FM approaches, motivating ShapeFit and its advantages over "classic" and FM; we briefly describe the ShapeFit compression and its cosmological interpretation. In any of these analyses several different choices are possible in terms of priors, freedom given to nuisance parameters, and various (simulated) data cuts. Section 4 presents the different choices (set-ups) we explored and motivates our two baseline set-up which results were submitted to the PT challenge. This section also includes an explanation on how to transform (cosmological) model-independent constraints on the physical variables to constraints on the value of the cosmological parameters of a specific model (e.g., ΛCDM). The main results are presented in section 5 where we also compare the performance of ShapeFit with that of FM in one implementation of EFTofLSS, while section 6 reports results for the other set-ups and serves to illustrate the sensitivity of the recovered constraints to various assumptions and modeling choices. Because the single redshift output set-up is highly idealized, in section 7 we present results for a more realistic scenario where different redshift bins are co-analyzed. Finally, we conclude in section 8.



JCAP06(2022)005

## 2 (Blind) PT challenge set-up

The blind PT challenge was designed by [1] with the aim to provide a controlled means of testing and benchmarking theoretical models for summary statistics of galaxy redshift surveys with a particular focus on each model's or approach's ability to recover and constrain cosmological parameter within ΛCDM. For that purpose, they carried out a suit of simulations consisting in 10 realizations (which we will later refer to as # 1,. . . , 10, each of these representing a different realization of the initial conditions at a given cosmology) in cubes of comoving side length 3840 $[h^{-1}\mathrm{Mpc}]$ with $3072^3$ particles, where the 3 input ΛCDM parameters, $\Omega_\mathrm{m}, A_s$ and $H_0$, were randomly selected from a Gaussian probability distribution centered at the Planck fiducial cosmology with a width of $4\sigma$ of the Planck experiment. These randomly drawn values (which are the same for the 10 simulations) were kept secret (blind) and not known to us or any of the participants. Other cosmological parameters such as the primordial tilt and the baryon-to-matter ratio were fixed to $\Omega_\mathrm{b}/\Omega_\mathrm{m} = 0.1571$ and $n_s = 0.9649$.

From the simulation output, galaxy mock catalogs were generated using the Rockstar halo finder [12] and a Halo Occupation Distribution (HOD) description roughly matching BOSS galaxy data. The mock catalogs of the 10 simulations were produced for three snapshots at redshifts $z_1 = 0.38$, $z_2 = 0.51$, $z_3 = 0.61$ each, all coming from the evolution of the same initial conditions and therefore, not independent.

Power spectra were measured from the actual galaxy positions in redshift space. The AP distortion is later included by re-defining the $k$-vectors and the line-of-sight (LOS, constant throughout the box) assuming a fiducial cosmology with $\Omega_\mathrm{m}^\mathrm{fid} = 0.3$ (see section III-C of [1] for details). The Poissonian shot noise term was measured and subtracted from the signal. The authors of ref. [1] made public the measured power spectra monopole, quadrupole and hexadecapole for each simulation and each snapshot and the corresponding covariance matrix [13]. The covariance matrices are provided for two different scenarios: one to match the volume and number density of BOSS data, and the other one corresponding to the simulation volume and density itself. In both cases the covariance was estimated analytically; the correlation between different multipoles $\ell$ at same wave-vector $k$ is nonzero, and the correlation between adjacent $k$-bins is ignored. Moreover, the covariance matrices are provided individually at each snapshot and do not include any correlation among redshift bins.

Several groups have already participated in this challenge and presented their — blindly obtained — results. Already in the initial paper by [1], results were presented by the so called "east coast" and "west coast" teams who validated their implementations of the Effective Theory of Large Scale Structure (EFTofLSS) based on their works [10] and [14], respectively. This was followed by [15] who used the PT challenge public material for testing their implementations of MONE, REPT and LPT [16]. Finally, [17] participated in the challenge using a halo-model based emulator. Participants have kept the challenge blind for the community by publishing their results (after unblinding) only as differences between input and derived parameters values.

## 3 ShapeFit

### 3.1 Motivation

The ShapeFit methodology provides a bridge between the classic BAO+RSD approach and the FM approach: by extending the classic fixed template fit with one extra effective parameter which captures most of the information that the classic BAO+RSD approach neglects;



JCAP06(2022)005

ShapeFit has been shown to match well the FM constraining power while retaining the advantages of a model-agnostic compression [4]. The advantages that the ShapeFit compression offers include being:

- easy to implement, because it relies on the standard BAO+RSD analysis requiring only minimal modifications to existing pipelines.
- easy to interpret, as the compressed parameters have an intuitive physical meaning, easy to access via analytical formulae and/or Boltzmann codes.
- very fast, because -as a fixed template method- it does not need calls to Boltzmann and PT codes at each evaluation step.
- computationally cheap, as it only requires a minimal set of runs for a given analysis, that do not need to be repeated for each cosmological model under investigation.
- conveniently practical due to the reduced number of degrees of freedom (four cosmology parameters per redshift bin) with respect to the full $n$-point statistics dataset ($\mathcal{O}(100)$). This eases massively the requirements on the number of mock catalogs needed to estimate correctly the inverse covariance matrix [18–20] in a combined pre- and post-reconstruction analysis of a real survey with overlapping redshift bins.
- robust, as it makes explicit how each physical observable correlates with systematic uncertainties.
- highly modular, as the cosmological implications of each observable can be studied independently.

In what follows, we summarize the most important ingredients of ShapeFit as applied to the blind PT challenge in two steps. First, we explain the compression step based on the fixed template (or standard ruler) method and second we explain how to interpret the compressed parameters in terms of cosmological models. For a more comprehensive description we refer to ref. [5], and in particular its figure 5 for a complete overview.

### 3.2 The ShapeFit compression

The first step in the ShapeFit pipeline consists of computing the non-linear galaxy power spectrum in redshift space for a fiducial cosmology. This process is standard to most previously employed BAO+RSD or "Full Shape" template fits. The linear power spectrum template is generated with the publicly available with CAMB [21] code using the CAMB parameter file provided at the PT challenge website [13]. Since this file does not contain information on the blinded parameters values, we choose $h^{\rm fid} = 0.676$, $A_s^{\rm fid} = 2.05 \times 10^{-9}$ and $\Omega_{\rm m}^{\rm fid} = 0.3$. The choice of $\Omega_{\rm m}^{\rm fid}$ is motivated by the fact that the same value is used by ref. [1] for the AP distortion, while our choices for $h^{\rm fid}$ and $A_s^{\rm fid}$ are arbitrary.

Next, we compute the perturbation theory (PT) kernels corresponding to the adopted linear template. In this work we test two PT models: one-loop Standard Perturbation Theory (1LSPT, see [22]) and two-loop Renormalized Perturbation Theory (2LRPT, see [23]). Both models incorporate four bias parameters describing the connection between dark matter and galaxy density fluctuations in real space: the first and second order biases, $b_1$ and $b_2$ [24], and the non-local biases, $b_{s2}$ and $b_{\rm 3nl}$ [25]. The latter are often assumed to follow the local Lagrangian relations [26–28], $b_{s2} = -4/7(b_1 - 1)$ and $b_{\rm 3nl} = 32/315(b_1 - 1)$, establishing a direct



JCAP06(2022)005

link between the non-local biases and $(b_1 - 1)$. But these relations are motivated by theoretical considerations on the dark matter to halo connection, which does not necessarily translate equivalently into the dark matter to galaxy connection. Therefore, we may later relax this assumption in certain occasions. Our adopted redshift space formulation is based on [29] and extended by the TNS model [30] including a Lorentzian Fingers-of-God (FoG) suppression term parametrized by $\sigma_{\rm FoG}$. In addition, our model allows for a shot noise term whose amplitude coefficient is $A_{\rm noise}$ (see [31] for details) providing a correction which captures possible deviations from Poissonian statistics. Since shot noise is well under control in this idealized application, we employ a tight Gaussian prior $A_{\rm noise} = 1.00 \pm 0.01$ by default, similar to [1]. In a practical application, however, it is common (and recommendable) to allow for deviations from Poissonian shot noise, which can lead to additional parameter degeneracies, which, if non-Gaussian in a high-dimensional parameter space, can appear as mild biases when marginalization effectively projects them in a lower-dimensional parameter space. Hence we also study the impact of relaxing this prior allowing for a width of up to 30%, $1.00 \pm 0.30$. To summarize, so far we introduced six parameters per redshift bin $\{b_1, b_2, b_{s2}, b_{3\rm nl}, \sigma_{\rm FoG}, A_{\rm noise}\}$ representing our nuisance parameters $\theta_{\rm nuis}$ (where different priors/relations between them are possible as explained above and as explicitly adopted later on).

As common to other standard BAO+RSD template fit pipelines, the precomputed non-linear galaxy power spectrum in redshift space (plus modifications due to $\theta_{\rm nuis}$) is in parallel modified by a set of physical parameters per redshift bin $\theta_{\rm phys} = \left\{\alpha_\parallel, \alpha_\perp, f, m\right\}$ defined in the following. The scaling parameters $\alpha_\parallel$ and $\alpha_\perp$ add the degree of freedom of a distance dilation along and across the line of sight respectively. The growth rate $f$ allows for a variation in anisotropy that enters our adopted RSD prescription. Finally, the slope $m$ -the new ShapeFit ingredient- is applied to the linear power spectrum *a posteriori* to effectively parametrize a slope variation at the pivot scale $k_p$, at which the slope between its large scale and small scale limits reaches its maximum. In practice, this is achieved by multiplying the fiducial linear power spectrum template with the exponential of a generic sigmoid function

$$P_{\rm lin}^{\rm fid\,\prime}(k, m) = \exp\left(\frac{m}{a}\tanh\left[a \ln\left(\frac{k}{k_p}\right)\right]\right) \cdot P_{\rm lin}^{\rm fid}(k) \tag{3.1}$$

and replace $P_{\rm lin}^{\rm fid}(k)$ by $P_{\rm lin}^{\rm fid\,\prime}(k)$ in each term that depends on the linear power spectrum.As in [5], we set $a = 0.6$ and $k_p = 0.03\,\left[h{\rm Mpc}^{-1}\right]$ motivated by the analytic Eisenstein and Hu, 1998 (EH98) formula [32, 33].

### 3.3 The cosmological interpretation

Let us now review the physical meaning and interpretation of the physical parameters $\theta_{\rm phys}$ to guide their interpretation in terms of cosmology.

It is important to keep in mind that, in the context of the fixed template approach, the scaling parameters $\alpha_\parallel, \alpha_\perp$ do not probe the absolute distance scale but rather the relative distance with respect to the standard ruler. This standard ruler is given by the sound horizon at radiation drag, $r_{\rm d}$, which sets the scale of the linear power spectrum template. The length of the standard ruler is set by early-time physics and can be constrained by early-time physics observations when interpreted within a cosmological model for the early Universe. From late-time observations, such as LSS, and without early-time physics assumptions, the length of the standard ruler is not known. Therefore, the scalings $\alpha_\parallel, \alpha_\perp$ are interpreted as the



JCAP06(2022)005

ratio between the underlying ("true") distances $D_\parallel, D_\perp$ and the fiducial distances $D_\parallel^{\rm fid}, D_\perp^{\rm fid}$ respectively in units of the standard ruler $r_{\rm d}$,

$$\alpha_\perp(z) = \frac{D_M(z)/r_{\rm d}}{D_M^{\rm fid}(z)/r_{\rm d}^{\rm fid}}\,, \qquad \alpha_\parallel(z) = \frac{D_H(z)/r_{\rm d}}{D_H^{\rm fid}(z)/r_{\rm d}^{\rm fid}}\,, \tag{3.2}$$

where the distance $D_\parallel$ along the LOS is the Hubble distance $D_H(z) = c/H(z)$, the distance $D_\perp$ across the LOS is the comoving angular diameter distance $D_M(z) = \int_0^z c/H(z')dz'$ and $H(z)$ is the Hubble expansion rate.

The growth rate $f$ is related to the logarithmic derivative of the growth factor $g(a)$ with respect to the scale factor $a$. In the context of the fixed template approach however, we need to be careful, since the fit is carried out with fixed overall amplitude. Therefore, we need to take into account that the estimated growth rate $\widetilde{f}$ -as well as the bias parameters- implicitly scales with the power spectrum amplitude. Although there are several ways to describe this, here we adopt the notation,

$$\widetilde{f}(z) = \frac{d\ln g(a)}{d\ln a} A_p(z)\,, \qquad A_p = \left( \frac{\left(\frac{r_{\rm d}^{\rm fid}}{r_{\rm d}}\right)^3 P_{\rm lin}\left(\left(\frac{r_{\rm d}^{\rm fid}}{r_{\rm d}}\right) k_p, z\right)}{P_{\rm lin}^{\rm fid}(k_p, z)} \right)^{1/2}\,, \tag{3.3}$$

where $A_p$ is the square root of the ratio between the amplitude of the underlying power spectrum, suitably rescaled by the choice of the fiducial sound horizon, to that of the power spectrum of the fiducial cosmology at the pivot scale $k_p = \pi/r_{\rm d}$. This convention is motivated in eqs. (3.7) and (3.8) of [5].

It is straightforward to convert $\widetilde{f}$ into the conventionally-used velocity fluctuation amplitude $f\sigma_8$. But within ShapeFit, it is convenient to define the amplitude as in eq. (3.3), because at the pivot scale $k_p$ -by construction- the amplitude remains constant when varying the slope $m$.

The slope $m$ is related to the smooth (no-wiggle) linear matter transfer function $T_{\rm nw}(k)$ which in practice we recompute at each model evaluation during posterior exploration with MCMC, and the fiducial one by

$$m = \frac{d}{dk}\left( \ln\left[ \frac{\left(\frac{r_{\rm d}^{\rm fid}}{r_{\rm d}}\right)^3 T_{\rm nw}^2\left(\left(\frac{r_{\rm d}^{\rm fid}}{r_{\rm d}}\right) k\right)}{T_{\rm nw}^{\rm fid\,2}(k)} \right] \right)\Bigg|_{k=k_p}\,. \tag{3.4}$$

where the derivative is taken at the pivot scale $k_p$.[1] Following ref. [5] prescription, we use the analytic Eisenstein & Hu 1998 (referred to as EH98) formula [32, 33] to calculate the no-wiggle transfer function, but other methods like a numerical separation of the transfer function into a wiggle and a no-wiggle part are also possible (see appendix D on [34]).

Given a cosmological model described by a set of cosmological parameters, the dependence of the physical parameters on the cosmological parameters is enclosed in $r_{\rm d}$, $D_M$, $D_H$, $g$, $P_{\rm lin}$ and $T_{\rm nw}$.

[1] The factor $(r_{\rm d}^{\rm fid}/r_{\rm d})^3$ in the numerator of eq. (3.4) was omitted in ref. [5] as it does not change the derivative. It is included here explicitly to make more transparent the connection to eq. (3.3).



JCAP06(2022)005

## 4 Methodology

We briefly describe our adopted set-up for the ShapeFit compression and its cosmological interpretation, as applied to the blind PT challenge data. We list several different set-up variations and motivate our baseline choice, adopted to represent our fiducial results which were submitted to the blind PT challenge coordinator. The extensive variations on the fiducial set-up serve to quantify the robustness of the results to these choices.

### 4.1 ShapeFit compression set-up

For our baseline analysis we take the average of the power spectra of all 10 realisations at a single redshift, in this particular case we chose $z_3 = 0.61$. We also analyzed the $z_1$ and $z_2$ redshift bins, finding equivalent results. The provided covariance, corresponding to the volume of a single realization, was rescaled to a volume of 566 $\left[h^{-1}\mathrm{Gpc}\right]$ (10 realisations).

As explained in section 3.2, we create a template using the blind PT challenge CAMB input file, adding $h^{\mathrm{fid}} = 0.676$, $A_s^{\mathrm{fid}} = 2.05 \times 10^{-9}$ and $\Omega_{\mathrm{m}}^{\mathrm{fid}} = 0.3$. We compute the first and second-order loop corrections using PTcool [35].The ShapeFit analysis is carried out by varying the four physical parameters, $\theta_{\mathrm{phys}}$, and several combinations of nuisance parameters. We consider different fitting configurations exploring combinations of nuisance parameters being varied, multipoles and range of scales considered, modelling of non-linearities, which are all listed in table 1.[2] Broadly, these set-ups can be split in two categories:

1. **SIM-like** (also labeled as initial letter "S"). These set-ups are tuned towards fitting a synthetic, simulated and thus idealized dataset, where the very large scales are under control and the shot noise is known. Therefore, we employ a narrow 1% prior on the shot noise amplitude $A_{\mathrm{noise}}$ and set $k_{\mathrm{min}} = 0.0$, not imposing any large scale cut. This is compatible with the analysis choices of other blind PT challenge participants. To be consistent with the choices of most of the other participants, we also set $k_{\mathrm{max}} = 0.12 \left[h\mathrm{Mpc}^{-1}\right]$, fit the monopole and quadrupole only, and choose 1LSPT as our baseline modeling for non-linearities.

2. **DATA-like** (also labeled as initial letter "D"). These cases are tuned towards an actual data analysis, similar to the methodologies employed in [2, 3], where large scales are affected by systematics and the shot noise value is unknown. Therefore, we allow for a broader prior on $A_{\mathrm{noise}}$ of up to 30% and set a large-scale cut at $k_{\mathrm{min}} = 0.02 \left[h\mathrm{Mpc}^{-1}\right]$. As in the data analyses of [2, 3] we set $k_{\mathrm{max}} = 0.15 \left[h\mathrm{Mpc}^{-1}\right]$, fit monopole, quadrupole and hexadecapole and choose the 2LRPT as baseline modeling for non-linearities for our template-fits.

As far as non-local bias parameters $b_{\mathrm{s}^2}$ and $b_{\mathrm{3nl}}$ are concerned, for the DATA-like cases we explore all possible combinations of setting them to their local Lagrangian prediction ("local" in the label) or varying them freely. For the SIM-like cases, we vary both parameters freely, to explore potential deviations from the local Lagrangian dark matter-halo connection and to enable a more direct comparison with previous analyses based on the EFT approach. For more details, see the section 4.2 of [5]. There it is shown that varying $b_{\mathrm{s}^2}$ and $b_{\mathrm{3nl}}$ (labeled

[2]Not all the cases presented in the table are discussed in details in the main text or shown in the figures, but are presented in the table for completeness. In the spirit of open science, readers interested in the outputs of specific runs can send a reasonable request to the authors.



JCAP06(2022)005

| Case | Bias | $\sigma_{A_{\rm noise}}$ | Model | $k$-range | Multipoles | Geo | Blind? |
|---|---|---|---|---|---|---|---|
| S008 | $b_{s^2}$, $b_{3nl}$ free | 1% | 1LSPT | $[0.00, 0.08]$ | $\ell = 0, 2$ | No | Yes |
| **SIM-like** | $\boldsymbol{b_{s^2}}$**,** $\boldsymbol{b_{3nl}}$ **free** | **1%** | **1LSPT** | $\mathbf{[0.00, 0.12]}$ | $\boldsymbol{\ell = 0, 2}$ | **Yes** | **Yes** |
| S1 | $b_{s^2}$, $b_{3nl}$ free | 1% | 1LSPT | $[0.00, 0.12]$ | $\ell = 0, 2$ | No | Yes |
| S2 | $b_{s^2}$, $b_{3nl}$ free | 1% | 2LRPT | $[0.00, 0.12]$ | $\ell = 0, 2$ | No | Yes |
| **DATA-like MAX** | $\boldsymbol{b_{s^2}}$**,** $\boldsymbol{b_{3nl}}$ **free** | **30%** | **2LRPT** | $\mathbf{[0.02, 0.15]}$ | $\boldsymbol{\ell = 0, 2, 4}$ | **No** | **Yes** |
| **" (geo)** | $\boldsymbol{b_{s^2}}$**,** $\boldsymbol{b_{3nl}}$ **free** | **30%** | **2LRPT** | $\mathbf{[0.02, 0.15]}$ | $\boldsymbol{\ell = 0, 2, 4}$ | **Yes** | **No** |
| Dbs2b3nl-20 | $b_{s^2}$, $b_{3nl}$ free | 20% | 2LRPT | $[0.02, 0.15]$ | $\ell = 0, 2, 4$ | No | Yes |
| Dbs2b3nl-15 | $b_{s^2}$, $b_{3nl}$ free | 15% | 2LRPT | $[0.02, 0.15]$ | $\ell = 0, 2, 4$ | No | Yes |
| Dbs2b3nl-5 | $b_{s^2}$, $b_{3nl}$ free | 5% | 2LRPT | $[0.02, 0.15]$ | $\ell = 0, 2, 4$ | No | Yes |
| Dbs2b3nl-1 | $b_{s^2}$, $b_{3nl}$ free | 1% | 2LRPT | $[0.02, 0.15]$ | $\ell = 0, 2, 4$ | No | Yes |
| Dbs2b3nl-1-geo | $b_{s^2}$, $b_{3nl}$ free | 1% | 2LRPT | $[0.02, 0.15]$ | $\ell = 0, 2, 4$ | Yes | Yes |
| Dbs2b3nl-1-12 | $b_{s^2}$, $b_{3nl}$ free | 1% | 2LRPT | $[0.02, 0.12]$ | $\ell = 0, 2, 4$ | No | Yes |
| Dbs2b3nl-1-20 | $b_{s^2}$, $b_{3nl}$ free | 1% | 2LRPT | $[0.02, 0.20]$ | $\ell = 0, 2, 4$ | No | Yes |
| Dbs2b3nl-1-25 | $b_{s^2}$, $b_{3nl}$ free | 1% | 2LRPT | $[0.02, 0.25]$ | $\ell = 0, 2, 4$ | No | Yes |
| Dbs2b3nl-1-12-geo | $b_{s^2}$, $b_{3nl}$ free | 1% | 2LRPT | $[0.02, 0.12]$ | $\ell = 0, 2, 4$ | Yes | No |
| Dbs2b3nl-1-20-geo | $b_{s^2}$, $b_{3nl}$ free | 1% | 2LRPT | $[0.02, 0.20]$ | $\ell = 0, 2, 4$ | Yes | No |
| Dbs2b3nl-1-25-geo | $b_{s^2}$, $b_{3nl}$ free | 1% | 2LRPT | $[0.02, 0.25]$ | $\ell = 0, 2, 4$ | Yes | No |
| Dbs2-30 | $b_{s^2}$ free | 30% | 2LRPT | $[0.02, 0.15]$ | $\ell = 0, 2, 4$ | No | Yes |
| Dbs2-30-geo | $b_{s^2}$ free | 30% | 2LRPT | $[0.02, 0.15]$ | $\ell = 0, 2, 4$ | Yes | No |
| Dbs2-20 | $b_{s^2}$ free | 20% | 2LRPT | $[0.02, 0.15]$ | $\ell = 0, 2, 4$ | No | Yes |
| Dbs2-15 | $b_{s^2}$ free | 15% | 2LRPT | $[0.02, 0.15]$ | $\ell = 0, 2, 4$ | No | Yes |
| Dbs2-5 | $b_{s^2}$ free | 5% | 2LRPT | $[0.02, 0.15]$ | $\ell = 0, 2, 4$ | No | Yes |
| Dbs2-1 | $b_{s^2}$ free | 1% | 2LRPT | $[0.02, 0.15]$ | $\ell = 0, 2, 4$ | No | Yes |
| Dbs2-1-geo | $b_{s^2}$ free | 1% | 2LRPT | $[0.02, 0.15]$ | $\ell = 0, 2, 4$ | Yes | Yes |
| Db3nl-30 | $b_{3nl}$ free | 30% | 2LRPT | $[0.02, 0.15]$ | $\ell = 0, 2, 4$ | No | Yes |
| Db3nl-30-geo | $b_{3nl}$ free | 30% | 2LRPT | $[0.02, 0.15]$ | $\ell = 0, 2, 4$ | Yes | No |
| Db3nl-20 | $b_{3nl}$ free | 20% | 2LRPT | $[0.02, 0.15]$ | $\ell = 0, 2, 4$ | No | Yes |
| Db3nl-15 | $b_{3nl}$ free | 15% | 2LRPT | $[0.02, 0.15]$ | $\ell = 0, 2, 4$ | No | Yes |
| Db3nl-5 | $b_{3nl}$ free | 5% | 2LRPT | $[0.02, 0.15]$ | $\ell = 0, 2, 4$ | No | Yes |
| Db3nl-1 | $b_{3nl}$ free | 1% | 2LRPT | $[0.02, 0.15]$ | $\ell = 0, 2, 4$ | No | Yes |
| Db3nl-1-geo | $b_{3nl}$ free | 1% | 2LRPT | $[0.02, 0.15]$ | $\ell = 0, 2, 4$ | Yes | Yes |
| **DATA-like MIN** | **all local** | **30%** | **2LRPT** | $\mathbf{[0.02, 0.15]}$ | $\boldsymbol{\ell = 0, 2, 4}$ | **No** | **Yes** |
| **" (geo)** | **all local** | **30%** | **2LRPT** | $\mathbf{[0.02, 0.15]}$ | $\boldsymbol{\ell = 0, 2, 4}$ | **Yes** | **No** |
| Dblocal-20 | all local | 20% | 2LRPT | $[0.02, 0.15]$ | $\ell = 0, 2, 4$ | No | Yes |
| Dblocal-15 | all local | 15% | 2LRPT | $[0.02, 0.15]$ | $\ell = 0, 2, 4$ | No | Yes |
| Dblocal-5 | all local | 5% | 2LRPT | $[0.02, 0.15]$ | $\ell = 0, 2, 4$ | No | Yes |
| Dblocal-1 | all local | 1% | 2LRPT | $[0.02, 0.15]$ | $\ell = 0, 2, 4$ | No | Yes |
| Dblocal-1-geo | all local | 1% | 2LRPT | $[0.02, 0.15]$ | $\ell = 0, 2, 4$ | Yes | Yes |

**Table 1**. Blind PT challenge set-up overview. Most fits were carried out before unblinding, but some of them (indicated by the final column) were updated after unblinding to take into account the geometric correction, see text for more details. Only the boldface cases were submitted to the blind PT challenge coordinator including the DATA-like runs corrected after unblinding. These are discussed in section 5. The other cases represent further tests of the different ingredients such as the bias option, the prior on shot noise, the PT model, the fitted scale range and the geometric correction (Geo) presented in section 6. Unless specified otherwise in the second column, each of the non-local bias parameters $b_{s^2}$, $b_{3nl}$ is set to the local Lagrangian prediction. In all cases we fit the mean of all 10 realizations at the highest redshift bin $z_3 = 0.61$ using the corresponding high-volume covariance matrix. Not all these cases are discussed in details in the main text or shown in the figures, but are presented here for completeness.

JCAP06(2022)005

"MAX" in [5]) is equivalent to the EFT case with varying $b_{s^2}$ and counterterm $c_0$. In fact, $c_0$ has been found to be very degenerate with $b_{3\mathrm{nl}}$ [1, 10], hence varying only one of the two parameters is equivalent to varying only the other (or varying both). In [2, 3] on the other hand, both bias parameters are set to their local Lagrangian predictions (labeled "MIN" in [5]). This choice has been shown to be valid for the BOSS and eBOSS analyses which focus on BAO scales, neglecting large-scales broadband shape information [31, 34]. As it is not clear yet whether this strategy remains valid for upcoming surveys, we submitted to the blind challenge both the freely varying (DATA-like MAX) and local Lagrangian (DATA-like MIN) cases. For the submitted SIM-like case, it is important to note, we employed the "geometric correction" introduced in section 6 of [5]. At the largest scales, where $k$-bins are broad and there are few modes per bin, mode-discreteness introduces a mismatch between the conventionally averaged and the mode-averaged model evaluated at each bin. The "geometric correction" is a fast way to account for this effect. As we show in figure 4, this correction is important when fitting the whole $k$-range, and even when applying a large-scale cut at $k_{\mathrm{min}} = 0.02\,\left[h\mathrm{Mpc}^{-1}\right]$.[3]

The adopted parameters priors for the fits are given in the second and third sections of table 2. The results of the three submitted fits (highlighted in boldface in table 1) are presented in section 5. The remaining, not highlighted, cases are presented in section 6, where further tests of the different configuration ingredients such as the bias option, the prior on shot noise, the PT choices in modeling of non-linearities, the fitted scale range and the geometric correction are discussed.

### 4.2 From physical parameters to cosmological parameters constraints (and back)

While for any set of values for the cosmological parameters of a given cosmological model it is always possible to derive the corresponding physical parameter values, the converse is not true. There can be regions of physical parameter space that do not correspond to any choice of cosmological parameters within the families of models under consideration. To convert the ShapeFit constraints on the physical parameters into constraints on cosmological parameters for a given cosmological model we proceed as described in section 3.3.

For the fiducial model we compute the quantities $r_{\mathrm{d}}^{\mathrm{fid}}, D_M^{\mathrm{fid}}(z), D_H^{\mathrm{fid}}(z), P_{\mathrm{lin}}^{\mathrm{fid}}(k_p, z)$ and the fiducial smooth EH98 power spectrum. In-line with the blind PT challenge recommendations, we vary $\{\omega_{\mathrm{b}}, \omega_{\mathrm{cdm}}, h, \ln(10^{10}A_s)\}$ while setting the neutrino mass to zero, fixing the scalar tilt $n_s = 0.9649$ and employing a tight Gaussian prior on the baryon to matter ratio $\omega_{\mathrm{b}}/\omega_{\mathrm{m}} = 0.1571 \pm 0.0001$. This prior basically fixes $\omega_{\mathrm{b}}$ for a given input value of $\omega_{\mathrm{cdm}}$, such that the degrees of freedom of our ΛCDM fit are $\{\omega_{\mathrm{cdm}}, h, \ln(10^{10}A_s)\}$. With these choices we are matching the set-up of the other blind PT challenge participants. For each choice of cosmological parameters, and with the pre-computed values of the fiducial quantities, we obtain model predictions for $\left\{\alpha_{\parallel}(z), \alpha_{\perp}(z), f(z)A_p(z), m\right\}$ which are then compared with the ShapeFit constraints obtained from a cosmological MCMC using MontePython[36–38]. But note that running additional chains is actually not necessary, as they can instead be easily obtained from the ShapeFit chains via importance sampling [39]. This way of proceeding effectively imposes a ΛCDM prior on the ShapeFit results. With this approach it is then possible to visualize what the ShapeFit physical parameters constraints would be in a ΛCDM model by recomputing the physical parameters as if they were derived parameters of the (ΛCDM) cosmological parameters.

[3] We realized this fact after unblinding as explained in the second paragraph of section 5.



JCAP06(2022)005

| Parameter | | Prior | |
|---|---|---|---|
| type | name | range | type |
| Cosmological (ΛCDM Fit) | $\omega_\mathrm{b}$ | $[0.005, 0.04]$ | flat |
| | $\omega_\mathrm{cdm}$ | $[0.01, 0.99]$ | flat |
| | $h$ | $[0.1, 3.0]$ | flat |
| | $\ln(10^{10} A_s)$ | $[0.1, 10]$ | flat |
| | $\omega_\mathrm{b}/(\omega_\mathrm{b}+\omega_\mathrm{cdm})$ | $(0.1571 \pm 0.0001)$ | Gaussian |
| | $n_s$ | 0.9649 | fixed |
| | $M_\nu$ [eV] | 0.0 | fixed |
| Physical (ShapeFit) | $\alpha_\parallel$ | $[0.5, 1.5]$ | flat |
| | $\alpha_\perp$ | $[0.5, 1.5]$ | flat |
| | $f$ | $[0, 3]$ | flat |
| | $m$ | $[-3, 3]$ | flat |
| Nuisance (ShapeFit) | $b_1$ | $[0, 20]$ | flat |
| | $b_2$ | [-20, 20] | flat |
| | $b_{s2}$ | lag. / [-20, 20] | derived / flat |
| | $b_{3\mathrm{nl}}$ | lag. / [-20, 20] | derived / flat |
| | $\sigma_P$ $[h^{-1}\mathrm{Mpc}]$ | $[0, 10]$ | flat |
| | $A_\mathrm{noise}$ | $(1 \pm \sigma_{A_\mathrm{noise}})$ | Gaussian |

**Table 2**. Prior ranges for parameters used for *ShapeFit* and the cosmological fit. Flat priors are given as $[\mathrm{min}, \mathrm{max}]$, Gaussian priors are denoted as $(\mathrm{mean} \pm \mathrm{std})$. The prior knowledge about the baryon fraction $\omega_\mathrm{b}/\omega_\mathrm{m} = 0.1571$ is implemented as a Gaussian prior with very small width, which is equivalent to treating the ratio as fixed.

A summary of all parameters and priors used for ShapeFit and for the cosmological ΛCDM fit is given by table 2.

## 5 Results submitted to the blind PT challenge and changes post-unblinding

The results initially presented in this section (but now slightly updated as described below) were submitted to the blind PT challenge coordinator. After submission, the organizer revealed to us the true underlying model values (unblinding). To keep the PT challenge blind for the rest of the community in all figures and tables throughout this work we only show our results as differences from the true values.

More specifically, for any measured parameter $\theta$ we show $\Delta\theta = \theta - \theta^\mathrm{true}$. This applies both to physical and cosmological parameter constraints. Results not submitted to the PT challenge coordinator (some computed before the unblinding, see table 1) are presented in section 6.

We initially estimated that the geometric correction would be unimportant if a minimum wavenumber $k$ cut was imposed. This is certainly true for current and forthcoming surveys, for the full PT challenge volume it is still not statistically significant — not applying the geometric correction induces small shifts in the recovered variables, less than 1-$\sigma$ — but the effect is visible under close inspection. The results initially submitted neglected the



JCAP06(2022)005

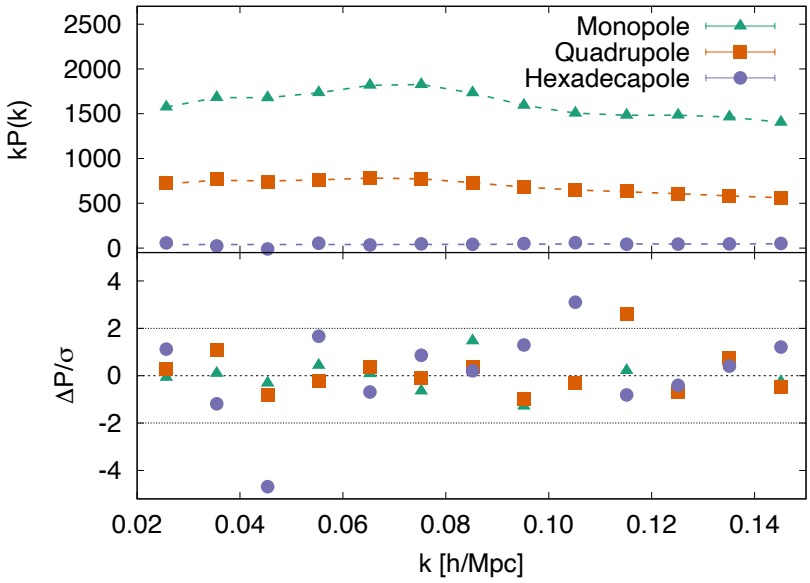


**Figure 1**. This figure shows the simulation data versus model comparison for the DATA-like MAX case. In the upper panel we show the multipole power spectra data and bestfit model and in the bottom panel their residuals in unit of the errors corresponding to a volume of 566 $\left[h^{-1}\mathrm{Gpc}\right]^3$. The monopole, quadrupole and hexadecapole data and bestfit are displayed as described in the legend.

geometric correction, which was then included subsequently. All the results presented here always include the geometric correction even with a minimum $k$ cut. As a consequence, these results are technically not blind (see table 1 for more details) but the changes compared to the blind version can only be appreciated upon very careful scrutiny.

The ShapeFit bestfit to the PT challenge multipoles is shown for one particular configuration (DATA-like MAX) in the top panel of figure 1. Since the error bars correspond to the mean of the realizations equivalent to 566 $\left[h^{-1}\mathrm{Gpc}\right]$ they are not visible by eye, but from the residuals in the lower panel it can be appreciated that the model delivers a good fit on the displayed wavevector range up to $k_{\mathrm{max}} = 0.15\ \left[h\mathrm{Mpc}^{-1}\right]$. The data points mostly remain within the $2\sigma$ band, but for the hexadecapole there is visibly a larger scatter, the most divergent ($4.5\sigma$) data point is at $k = 0.045\ \left[h\mathrm{Mpc}^{-1}\right]$. This hints towards a problem with the hexadecapole related to the inhomogeneous distribution of the directions of the $k$-vectors, that we will return to later.

The physical parameters constrained with ShapeFit are shown as dashed curves in the left panel of figure 2. The SIM-like constraints (see specifications in table 1) are displayed in green-dotted, the DATA-like MAX and MIN cases in orange and red-dotted, respectively. For all cases we recover the true values $\Delta\theta_{\mathrm{phys}} = 0$ (indicated by black dashed lines) well within $1.5\sigma$, except for $\alpha_{\parallel}$ in the DATA-like cases, where we find a bias of $4-5\sigma$. In the DATA-like cases there are four main changes compared to the SIM-like cases: use of 2LRPT instead of 1LSPT, the wider prior on the shot-noise amplitude, the higher $k_{\mathrm{max}}$ and the inclusion of



JCAP06(2022)005

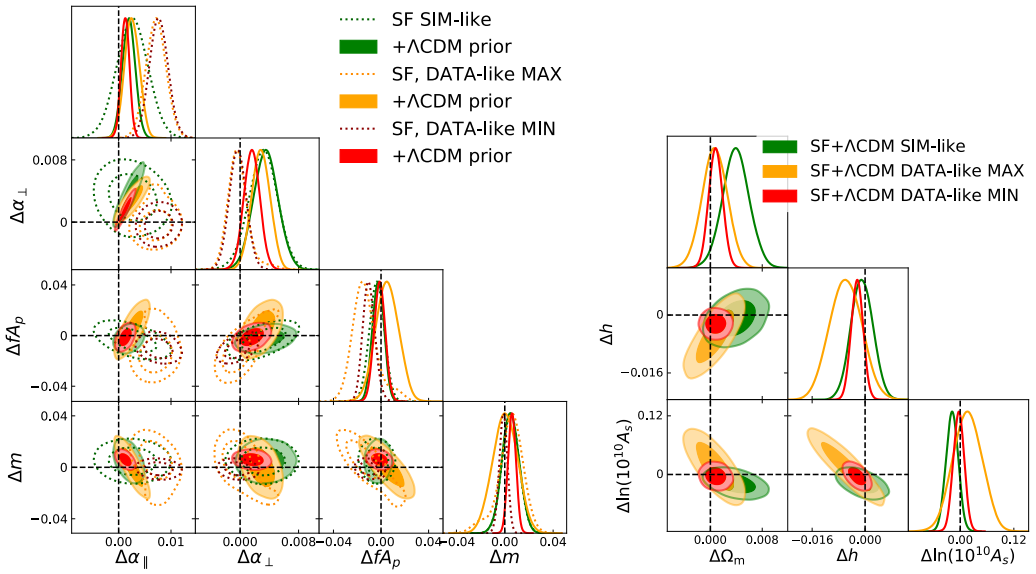


**Figure 2**. These represent our main results for the blinded physical parameters (left panel) and the blinded cosmological parameters $\{\Delta h, \Delta\Omega_{\rm m}, \Delta \ln(10^{10}A_s)\}$ (right panel). To ensure that the PT challenge remains blind for the rest of the community, results are visualized as differences from their true values. The dashed vertical and horizontal lines guide the eye to zero difference. Dotted, empty contours represent the ShapeFit (SF) results and continuous, filled contours the corresponding (cosmological parameters) results with a ΛCDM prior imposed. We show the SIM-like results in green, the DATA-like MAX case in orange and the DATA-like MIN case in red. The numerical results can also be found in table 3.

the hexadecapole. We verify in section 6 that the inclusion of the hexadecapole drives the systematic shift; in particular, it shifts $\alpha_\parallel$ by $\Delta_\alpha = 0.005$, which amounts to most[4] of the difference between the maximum of the green-dotted and range-dotted $\alpha_\parallel$ posteriors. The effect on the $\alpha$'s of the inclusion of the hexadecapole has not been explored thoroughly in the literature (but see [31] and footnote in sec B1 of [1]). The shift induced by the hexadecapole seen here is below the $2\sigma$ level for DESI-like survey and not significant for a BOSS/eBOSS-like survey. We leave this to further investigation in future work. Also, the higher $k_{\rm max}$ and the inclusion of the hexadecapole result in smaller error-bars for the $\alpha$s. The size of the error-bars on $m$ (and somewhat on $fA_p$) on the other hand is driven by the choice of prior on the nuisance bias parameters.

The ShapeFit results, which are (cosmological) model-independent, can be interpreted within the ΛCDM model as discussed in section 4.2. We refer to this as imposing a ΛCDM prior and this case is shown as filled contours in both panels of figure 2. It is easier to understand the filled contours in the left panel of figure 2 after considering the right figure panel, where the ShapeFit+ΛCDM prior constraints are shown for the cosmological parameters constrained by the analysis: $h$, $\ln(10^{10}A_s)$, $\Omega_m$. For all cases we find excellent agreement with the true cosmology with biases of at most $2\sigma$. Comparing the DATA-like MIN and MAX cases, we find that the local Lagrangian bias assumption leads to reduced error bars

[4]The remaining bit of $\Delta_\alpha = 0.003$ can be explained by the choice of maximum wavevector. See section 6 and figure 7 in particular.



JCAP06(2022)005

| Type | Parameter | SIM-like | DATA-like MAX | DATA-like MIN |
|---|---|---|---|---|
| Physical | $\Delta\alpha_\parallel$ | $0.0026 \pm 0.0030$ | $0.0071 \pm 0.0019$ | $0.0076 \pm 0.0018$ |
| | $\Delta\alpha_\perp$ | $0.0031 \pm 0.0020$ | $-0.0002 \pm 0.0015$ | $-0.0003 \pm 0.0012$ |
| | $\Delta f A_p$ | $-0.0035 \pm 0.0063$ | $-0.0131 \pm 0.0111$ | $-0.0101 \pm 0.0052$ |
| | $\Delta m$ | $0.0049 \pm 0.0071$ | $0.0042 \pm 0.0112$ | $-0.0012 \pm 0.0034$ |
| $\Lambda$CDM Cosmological | $\Delta\Omega_\mathrm{m}$ | $0.0039 \pm 0.0021$ | $0.0006 \pm 0.0020$ | $0.0008 \pm 0.0011$ |
| | $\Delta h$ | $-0.0009 \pm 0.0034$ | $-0.0059 \pm 0.0048$ | $-0.0025 \pm 0.0018$ |
| | $\Delta \ln(10^{10} A_s)$ | $-0.0182 \pm 0.0136$ | $0.0168 \pm 0.0325$ | $-0.0032 \pm 0.0121$ |
| $\Lambda$CDM Derived | $\Delta\alpha_\parallel$ | $0.0019 \pm 0.0012$ | $0.0025 \pm 0.0014$ | $0.0013 \pm 0.0008$ |
| | $\Delta\alpha_\perp$ | $0.0035 \pm 0.0017$ | $0.0028 \pm 0.0012$ | $0.0016 \pm 0.0011$ |
| | $\Delta f A_p$ | $-0.0024 \pm 0.0048$ | $0.0053 \pm 0.0097$ | $-0.0012 \pm 0.0046$ |
| | $\Delta m$ | $0.0048 \pm 0.0071$ | $-0.0084 \pm 0.0104$ | $-0.0026 \pm 0.0034$ |

**Table 3**. Here we show the mean values and their corresponding symmetrized errorbars of the constrained parameters for the SIM-like, DATA-like MAX and DATA-like MIN cases specified in table 1. Using the configuration of table 2, the physical parameters are constrained with ShapeFit and the cosmological parameters are obtained by fitting the $\Lambda$CDM model to the ShapeFit results. Finally, we show again the physical parameters but this time derived from the cosmological fits, hence with a $\Lambda$CDM prior. The results shown here correspond to the same results shown in figure 2.

but does not bias the cosmological results, even given the precision of the PT challenge suite of simulations. Recall that the error-bars reported here for the PT challenge are for a volume of $566\,\mathrm{Gpc}h^{-1}$ which is about 10 times bigger than the volume covered by forthcoming surveys. In section 6 we further investigate the various bias assumptions and discuss their relevance for the ongoing and future surveys.

The $\lesssim 2\sigma$ deviations of the DATA-like cases in the cosmological parameter space seem mild compared to the $4\sigma$ deviations seen in the physical parameter space. To understand this, in the left panel of figure 2 we show the physical parameters constraints corresponding to the $\Lambda$CDM parameter constraints of the right panel. The filled contours in the left panel are hence derived from the dashed, empty contours by imposing a $\Lambda$CDM prior.

In the SIM-like case (green contours) this prior does not affect much $\alpha_\perp$, $fA_p$ and $m$, but significantly tightens the $\alpha_\parallel$ posterior. The reason is that within $\Lambda$CDM there is a tight correlation between $\alpha_\parallel$ and $\alpha_\perp$. By construction they are related for any model, because the perpendicular distance is the integral of the parallel distance (see the definitions below eq. (3.2)). Within $\Lambda$CDM however, the redshift evolution of the Hubble expansion rate is completely determined by $\Omega_\mathrm{m}$, meaning that for a given $\Omega_\mathrm{m}$, $\alpha_\parallel$ and $\alpha_\perp$ are not independent. In the ShapeFit compression with a $\Lambda$CDM prior, $\Omega_\mathrm{m}$ is constrained by $m$, hence $\alpha_\parallel$ and $\alpha_\perp$ become directly linked.

Considering the DATA-like cases we notice that -under the umbrella of $\Lambda$CDM- their $\alpha_\parallel$ posteriors agree very well with the SIM-like case, even though the pure ShapeFit constraints show a $4\sigma$ deviation. The filled contours are markedly shifted towards the true parameter values compared to the dashed contours. This means that the bias in $\alpha_\parallel$ observed in the ShapeFit DATA-like cases displaces $\alpha_\parallel$ to a region which is excluded by (or unphysical in) $\Lambda$CDM. Hence, the $\Lambda$CDM prior drives $\alpha_\parallel$ towards its correct value, at the expense of creating a tension between the $\Lambda$CDM and the model-independent result for $\alpha_\parallel$. For the other physical parameters the shifts induced by imposing the $\Lambda$CDM are much less dramatic.



JCAP06(2022)005

As further explored in section 6, it is important to investigate the ShapeFit model ingredients, such as the bias assumption, the shot noise prior, and others which may be responsible for the $\alpha_\parallel$ systematic bias. Nevertheless the left panel of figure 2 highlights an important point: some systematic biases can only be seen at the model-independent parameter compression stage and would not be spotted in the context of direct, model-dependent fits (especially for minimal-ΛCDM type-models).

Our main results are also summarized in table 3, where we show the physical parameters constrained with ShapeFit, the cosmological results of the ΛCDM fits and again the physical parameters, but this time derived from the model (which is equivalent to imposing a ΛCDM prior). As discussed before, the agreement with the truth is very good, especially for the SIM-like case. In the DATA-like cases, there are notable biases in $\alpha_\parallel$, that vanish once they are interpreted in light of the ΛCDM model. Interestingly, upon this model interpretation all the error bars decrease significantly by up to 50%, only the error on $m$ remains stable. This also occurs in the SIM-like case.

To quantify the apparent bias, for the two DATA-like cases we compare the corresponding $\chi^2$-values divided by the number of degrees of freedom ndf $= (N_{\rm data} - N_{\rm params})$ at the model-independent ShapeFit bestfit (SF) and at the ΛCDM bestfit (SF+ΛCDM):

$$\begin{aligned} \text{DATAlike MAX}: \quad & \chi^2_{\rm SF}/\text{ndf} = 62.2/(39-10) \qquad \chi^2_{\rm SF+\Lambda CDM}/\text{ndf} = 80.7/(39-6) \\ \text{DATAlike MIN}: \quad & \chi^2_{\rm SF}/\text{ndf} = 63.5/(39-8) \qquad \chi^2_{\rm SF+\Lambda CDM}/\text{ndf} = 79.7/(39-4) \end{aligned} \tag{5.1}$$

Note that the number of free parameters $N_{\rm params}$ is reduced by 4 for the ΛCDM case, as we fix the four physical parameters to the model prediction when evaluating the corresponding $\chi^2$. As argued before and shown in section 6, these relatively poor $\chi^2$/ndf of order $\sim 2-2.5$ are mostly induced by the hexadecapole.

For comparison, for the SIMlike case (without hexadecapole) we find a value $\chi^2_{\rm SF}/\text{ndf} = 11.3/(24-10)$ of order $\sim 1$ similar to other PT challenge participants [1].

This indicates that indeed the ShapeFit best fit without the ΛCDM condition imposed is better than when imposing it. However the absolute value of the $\chi^2$ is not a good absolute indicator to be used to test cosmology, because the $\chi^2$ is heavily affected by inadequacies of the modeling of the signal, independently of cosmology- as seen in the hexadecapole behaviour.

Since the SIM-like case is oriented towards reproducing as much as possible the settings chosen by the teams participating in [1], here we also show a direct comparison to one of the EFT implementations. In particular, we choose the publicly available CLASS-PT implementation by [10] and run the EFT model[5] using the same cosmological parameters and priors as in table 2. For the EFT nuisance parameters (bias parameters and counterterms) we choose the default configuration of [10] but without shot noise correction (i.e., shot noise correction set to zero as shot noise is assumed to be fully under control and correctly subtracted).

The results are shown in figure 3, where the green contours are the same as the SIM-like case in figure 2. Again, we show the physical parameters -with (filled contours) and without (dashed, empty contours) the ΛCDM prior- in the left panel and the ΛCDM cosmological parameters in the right panel. As we can see, the SIM-like results are in excellent agreement with the EFT results (grey contours)- both in terms of mean parameters and errors. The ShapeFit SIM-like case errors are somewhat smaller than for EFT, especially for the amplitude parameter, which might be due to the exclusion of additional significant freedom in extra nuisance parameters, the so-called counterterms, in our model. This is further explored in an upcoming work [34].

[5] When running the EFT model the ShapeFit pipeline and results of the SIM-like configuration were frozen.



JCAP06(2022)005

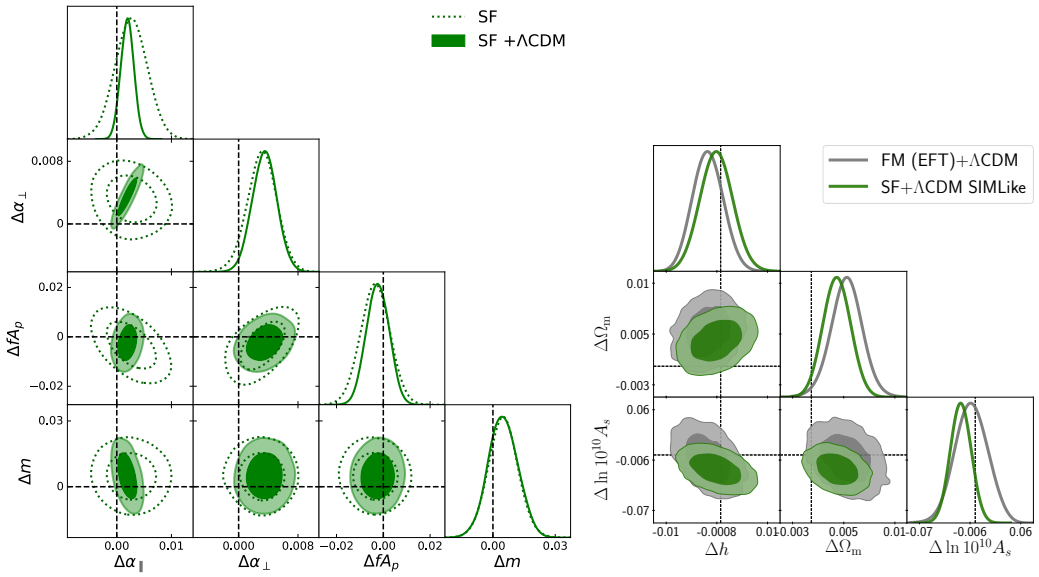


**Figure 3**. Comparison of our (ShapeFit) main results using the SIM-like convention (green contours, identical to the green contours of figure 2) with the FM case (grey contours) using the EFT implementation of [10]. In the left panel we show physical parameters constrained via the model-independent ShapeFit (dashed, empty contours) and combined with a ΛCDM prior (filled contours). The right panel displays the cosmological ΛCDM parameter space. See text for more discussion.

## 6 Additional tests

As anticipated in table 1 we perform a suite of tests to the blind PT challenge data to quantify the effect of our different model ingredients on the inferred parameters. These tests include the impact of i) the geometric correction, ii) including the second order loop correction, iii) dialing the allowed prior range on the shot noise amplitude, iv) choosing a certain bias prescription, v) varying the maximum wave-number used for the analysis, $k_{\rm max}$ and vi) including or not the hexadecapole. A few representative cases are illustrated in figures 4 to 7.

Figure 4 addresses points i) and ii); it shows that the effect of including second-order loop corrections is completely negligible, even for a large survey volume of 566 $\left[h^{-1}\mathrm{Gpc}\right]^3$. The central values for the parameters are affected at the sub-percent level and the error bars are unaffected. On the other hand, the effect of the geometric correction is very important, but only for $m$, which induces a shift in $m$ of $2\sigma$ when is not taken into account. As expected, the other parameters are relatively unaffected by this correction. This effect is driven by the largest scales: when excluding the large scales by increasing $k_{\rm min}$ to 0.02 $\left[h\mathrm{Mpc}^{-1}\right]$ we find that the effect of the geometric correction is reduced by a factor 5 (towards $\Delta m \sim \mathcal{O}(10^{-3})$), which is of same order of magnitude as the $1\sigma$ precision we find for $m$.

Figure 5 displays the impact of varying the amplitude of shot noise as a free parameter. Blue contours show the Poisson prediction with a Gaussian prior of 1% standard deviation, whereas for the orange contour this is increased up to 30%. When the shot noise prior is relaxed from 1% to 30% strong degeneracies appear with other bias parameters, mostly $b_{s^2}$ and $\sigma_{\rm FoG}$, which make the multi-dimensional posteriors highly non-Gaussian. As a consequence,



JCAP06(2022)005

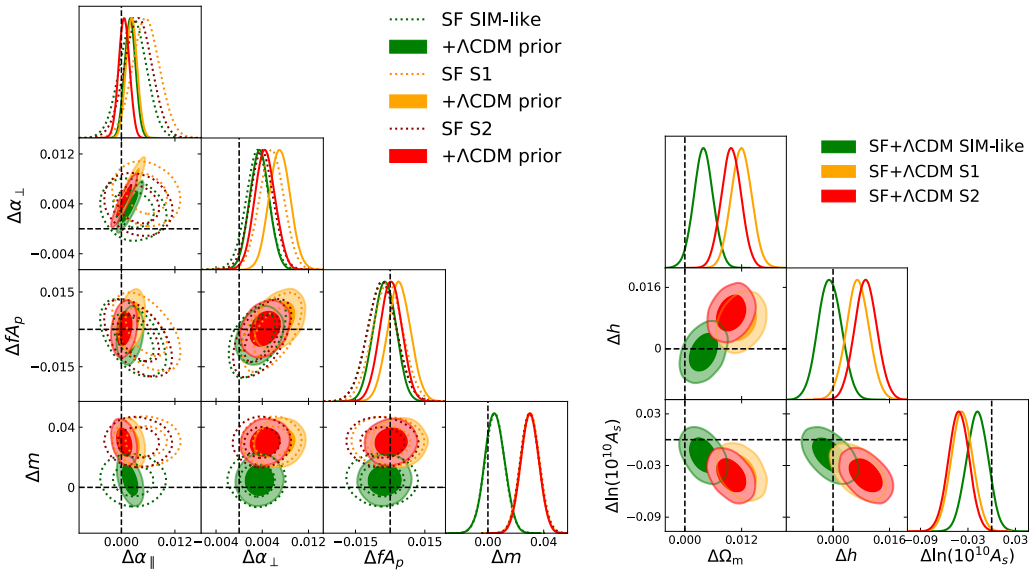


**Figure 4**. Left panel: comparison of the ShapeFit compressed variables either with (solid) or without (dotted) the ΛCDM prior between the baseline (SIM-like, green) and two analysis variations: in the first we do not apply the geometric correction (S1, orange) and in the second we omit the geometric correction *and* include the 2$^{\rm nd}$ order PT term. All cases have a maximum wave-vector of 0.12 $[h{\rm Mpc}^{-1}]$. Right panel: effect on the corresponding cosmological parameters within ΛCDM model.

the marginalized low-dimensional posteriors become moderately shifted, and the constraints on cosmological parameters degrade significantly, as shown. In terms of cosmology this degradation in statistical precision highly impacts $h$ and $A_s$, and mildly $\Omega_m$. Thus, we conclude that the choice of the prior around the shot noise amplitude may not severely impact the inferred means of cosmology, but their errors, which in addition tend to become less Gaussian.

The assumptions we make on the non-local bias parameters can highly impact the results on the compressed cosmological parameters. In particular, we find that the non-local bias parameter $b_{3\rm nl}$ is very degenerate with $m$, and therefore using an incorrect value (or functional form with $(b_1-1)$ may translate into a systematic shift on our inferred cosmology. When we enforce the local Lagrangian bias relation, $b_{3\rm nl} = 32/315(b_1-1)$ we find that $m$ is biased by $\sim 0.015\Delta m$ (corresponding to $\sim 1.3\sigma_m$ deviation) with respect to the best-fitting value when $b_{3\rm nl}$ is allowed to freely vary. We find that this is much less a problem for $b_{s^2}$ than for $b_{3\rm nl}$. Inevitably, when both biases are free to vary, the error bars on cosmological parameters increase by a factor $2-3$ due to correlations. This is illustrated in figure 6 for some representative cases. We conclude that for this particular sample, the non-local Lagrangian biases follow the halo local Lagrangian predictions well. Consequently, the main cosmological results are not systematically shifted when relaxing this assumption. However, the resulting error-bars do increase significantly. When the total volume of our sample is closer to that of forthcoming data (typically 10 to 100 times smaller than the PT challenge sample) this can become a problem, as relaxing both non-local bias parameters significantly weakens or, in the case of high noise samples, essentially erases the constrains on $m$ (as will be shown in a separate paper [34]). In these cases, using the local Lagrangian halo relation helps



JCAP06(2022)005

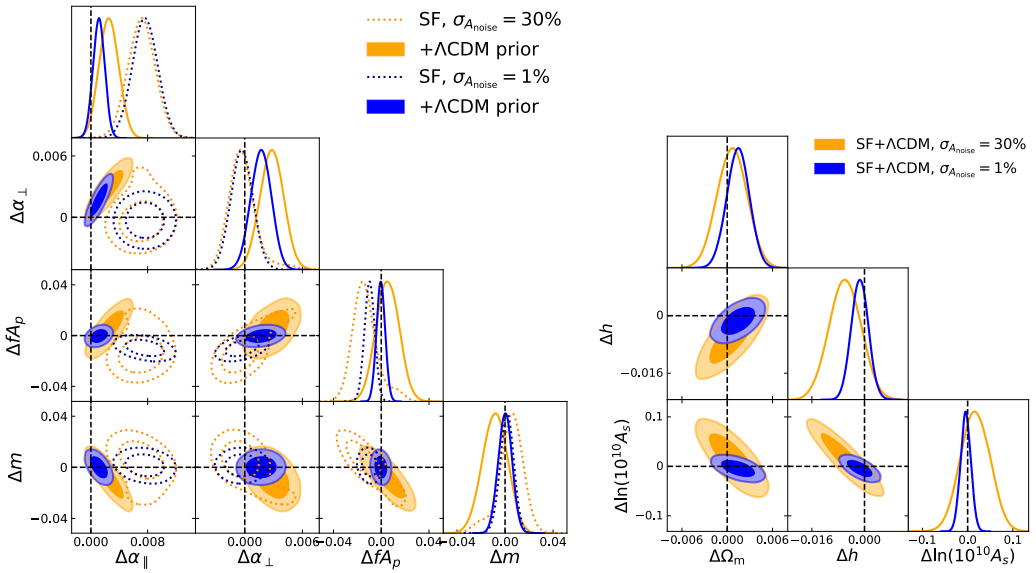


**Figure 5**. Impact of varying the shot noise term $A_{\rm noise}$ within 30% using a Gaussian prior (orange contours) versus effectively fixing it by employing a 1% prior (blue contours). In both cases we allow all bias parameters to vary freely and the fitted $k$-range is $[0.02, 0.15]$ using 2LRPT. Compressed variables or shown in the left and cosmological parameters in the right panel.

to constrain $m$, and hence use the shape of the power spectrum for cosmology constrains, but at the expenses of being more model-dependent. Alternatively one could impose strong Gaussian priors on higher order bias parameters, as done in most FM analyses, that would otherwise loose a lot of their constraining power. However, from the PT challenge simulations we do not find any strong reasons why to abandon the local Lagrangian assumption.

In addition, we compare the results obtained from different $k$ cuts at small scales. We select $k_{\rm max} \in \{0.12, 0.15, 0.20, 0.25\}\left[h{\rm Mpc}^{-1}\right]$, where in all cases we set the minimum wavenumber to $k_{\rm min} = 0.02\left[h{\rm Mpc}^{-1}\right]$, the model to 2LRPT, the bias parameters to follow the local Lagrangian prediction and the shot noise amplitude prior to 1%.

In the left panel of figure 7 we show the compressed parameter results for these different $k_{\rm max}$ cases. While for $k_{\rm max} = 0.12\left[h{\rm Mpc}^{-1}\right]$ and $k_{\rm max} = 0.15\left[h{\rm Mpc}^{-1}\right]$ only $\alpha_\parallel$ appears slightly biased, the fit degrades significantly and leads to large biases once higher wavenumbers are considered. We conclude that the 2LRPT+TNS fixed template approach with local bias assumption is not accurate enough for describing the non-linear scales of $k \geq 0.20\left[h{\rm Mpc}^{-1}\right]$ for the statistical precision of the PT challenge suite.

Finally, in the right panel of figure 7 we show the effect of including (or excluding) the hexadecapole signal ($\ell = 4$) from PT challenge data. We see that the hexadecapole biases $\alpha_\parallel$ by $\Delta\alpha_\parallel = 0.005$ and at the same time reduces the error bar by $\sim 50\%$. As anticipated in section 5, this effect together with the effect of increasing $k_{\rm max}$ from $0.12\left[h{\rm Mpc}^{-1}\right]$ to $0.15\left[h{\rm Mpc}^{-1}\right]$ (left panel of figure 7) drives the bias in $\alpha_\parallel$ observed in the "DATA-like" cases with respect to the "SIM-like" case.



JCAP06(2022)005

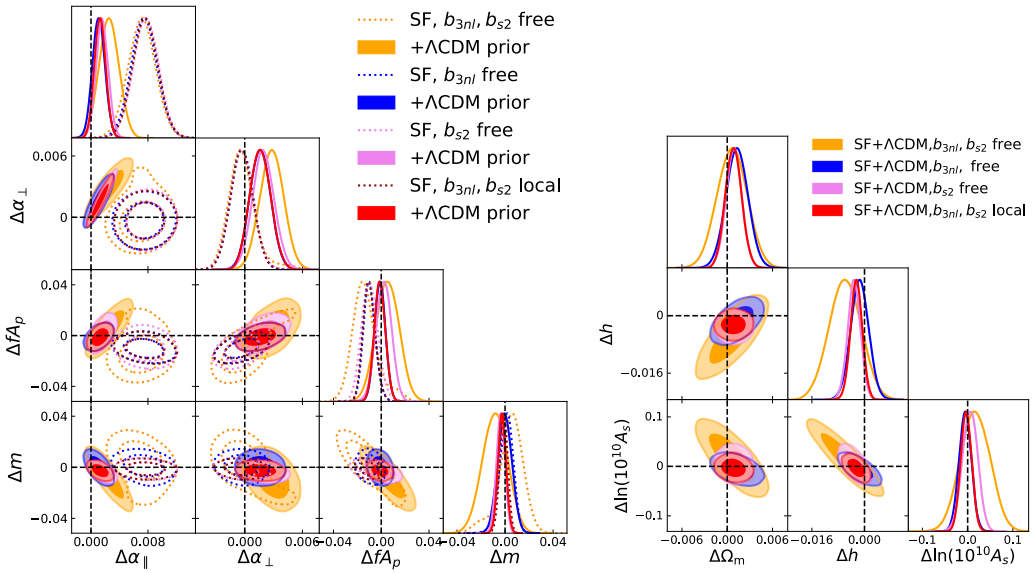


**Figure 6**. This figure shows the impact of varying the non-local bias parameters $b_{3\mathrm{nl}}$ and $b_{s^2}$ freely (orange contours) versus setting one of them ($b_{s2}$, blue contours; $b_{3nl}$, violet contours) or both (red contours) to their local Lagrangian prediction. In the left panel we show the compressed parameter constraints for the model-independent ShapeFit (empty, dotted contours) and for the ΛCDM prior (filled contours).

## 7 Combining all redshift bins: constructing a real data analysis scenario

So far, we have only considered cosmological analyses on individual redshift bins. In practice however, surveys observe dark matter tracers throughout a broad redshift range. It is customary to divide these tracers in several, and usually partially overlapping, redshift bins in order to capture cosmological information related to the evolution of cosmic structure across cosmic ages. In this section we analyze the PT challenge in a very similar way. In the FM approach the cosmological parameters are defined at $z = 0$ and therefore the redshift evolution is somewhat predetermined within the chosen model. In the classic (and ShapeFit) approach, the compressed variables are determined independently for each redshift bin, hence it is possible to track their time evolution in a model-independent way. The model dependence enters at the very end, when the compressed variables are interpreted in light of a model of choice.

As a preparatory step, we analyze the redshift outputs $z_1$ and $z_2$ in the same way as $z_3$ has been analyzed in section 5. In all cases considered here our baseline set-up is as follows: we fit the monopole, quadrupole, and hexadecapole data using 2LRPT on a wavevector range $0.02\left[h\mathrm{Mpc}^{-1}\right] < k < 0.15\left[h\mathrm{Mpc}^{-1}\right]$, where the non-local bias parameters are fixed to their local Lagrangian prediction and the shot noise term is varied within a 30% Gaussian prior. This corresponds to the set-up labeled "DATA-like MIN" in table 1.

Then, we take the following approach: we compute the average of realizations #1-3 evaluated at $z_1 = 0.38$, realizations # 4-7 at $z_2 = 0.51$, and realizations # 8-10 at $z_3 = 0.61$. In this way, we reproduce the behaviour of an actual lightcone, which would capture the full redshift range where the 3 redshift bins are independent from each other. This



JCAP06(2022)005

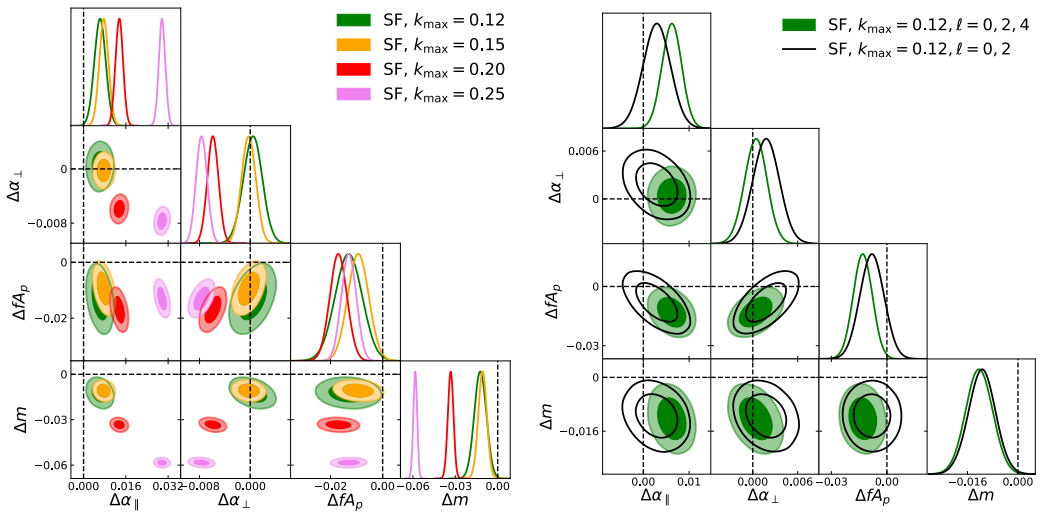


**Figure 7**. Left panel: comparison of the ShapeFit compressed variable constraints for different maximum scale cuts, including (in units $\left[h\mathrm{Mpc}^{-1}\right]$) $k_{\rm max} \in \{0.12, 0.15, 0.20, 0.25\}$ shown in (green, orange, red, violet) filled contours respectively. In all cases we set the minimum scale to $k_{\rm min} = 0.02$, the model to 2LRPT, the bias parameters to follow the local Lagrangian prediction and the shot noise amplitude prior to 1%. Due to the systematic bias for $k_{\rm max} \geq 0.20\,\left[h\mathrm{Mpc}^{-1}\right]$, we do not show the cosmological ΛCDM constraints here. Right panel: comparison of the compressed variables between including (filled, green contours) or not (empty, black contours) the hexadecapole ($\ell = 4$) from the fit. Regarding the remaining set-up, we choose the same as in the left panel, and set $k_{\rm max} = 0.12\,\left[h\mathrm{Mpc}^{-1}\right]$. Note that, therefore, the green contours are identical in both panels.

approach closely emulates a real survey catalogue, where different redshift-bins are treated as independent, as long as they are wide enough.[6] Also, we retain the same effective number of sampled modes (because we maintain the same volume) as for the single redshift analysis of section 5 and the preparatory step. While in a real world application, partially overlapping redshift bins would not be independent and would thus have a non-zero covariance, the set-up chosen here enables us to compare more directly the findings with the main results, and offers a more transparent interpretation.

In figure 8 we show the ShapeFit constraints on compressed variables (left panel) and the cosmological parameter constraints including the ΛCDM prior (right panel) obtained by analysing the data at different redshifts. On one hand we show the results when analyzing the mean of all 10 realizations evaluated at the same redshift (filled coloured contours). On the other hand, we show the cosmological constraints obtained from the ShapeFit results, for the case when the realizations are spread among the redshifts as described above, including the ΛCDM prior (empty black contours). Note that all these cases represent constraints based on the same comoving volume, in the coloured cases concentrated in a single redshift bin; and in the empty black contours spread among the 3 redshift bins.

We see that all redshift bins are consistent with each other within $0.5\sigma$, both in the compressed parameter and in the cosmological parameter space. The small deviations may

[6] This assumption is based on the Ergodic hypothesis, and it breaks down for scales comparable to the size of the bin. For this reason it is usual to split the survey in redshift bins which are overlapping and infer their correlation using mocks, as was done for BOSS DR12.



JCAP06(2022)005

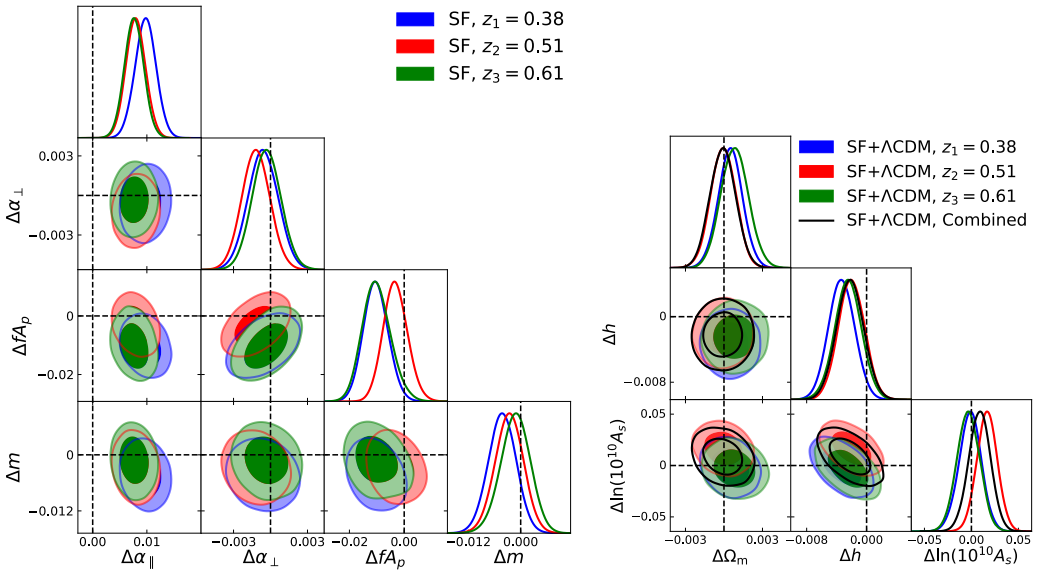


**Figure 8**. Compressed parameter blind constraints using ShapeFit (left panel) and the corresponding ΛCDM parameter constraints (right panel) obtained from analysing different redshift bins at $z_1 = 0.38$ (blue contours), $z_2 = 0.51$ (red contours) and $z_3 = 0.61$ (green contours). In addition, we show the cosmological parameter constraints for the case of combining the redshifts, but conserving the total volume, as described in the text (empty black contours). Dashed contours mark the theoretically expected values. The evident bias in $\alpha_\parallel$ is understood as discussed in section 5 and figure 2. In all cases we show the "DATA-like MIN" set-up, as customary for a real survey application.

arise due to i) differences in non linear structure formation (including non linear galaxy bias and RSD) at different redshifts, both in the N-body simulation and in the fiducial template, ii) different impact of shot noise in the different volumes, iii) and the degree of validity of the assumption of local Lagrangian bias may vary for the different HODs of the different redshift bins. As mentioned already in sections 5 and 6, the ShapeFit constraints on $\alpha_\parallel$ are biased in the "DATA-like MIN" case; this bias vanishes when applying the ΛCDM prior.

One might have expected the combined constraints (empty black contours) on cosmological parameters to be slightly tighter than the individual redshift constraints, although the effective number of sampled modes is the same. This is because in the framework of the LCDM model, having information at different epochs (or redshift bins) helps to break degeneracies among model parameters, more effectively than having more volume at a single redshift bin. This effect is seen very clearly, for example, in the $\Omega_m - h$ plane for the BAO cases when Ly-$\alpha$ measurements are combined with low galaxy measurements (see for e.g. figure 1 of [40]). Here the effect is not really appreciable because of the smaller redshift range explored.

## 8 Conclusions

We have applied for the first time the (model-independent) compressed variables analysis to the (blind) PT challenge simulations. All previous entries to the PT challenge used the full modeling approach instead. This work thus enables a more transparent comparison of these two complementary approaches to the cosmological analyses and interpretation of



JCAP06(2022)005

clustering of galaxy redshift surveys. In particular, for the compressed variables approach we implement ShapeFit [4, 5] which is fully equivalent to the "classic" approach for the AP and RSD parameters but includes in addition an extra effective parameter $m$ which captures the power spectrum broadband shape information.

Our chosen baseline (SIM-like) set-up in terms of range of scales, multipoles, shot noise and bias modeling assumptions, prescription for modeling non-linearities, nuisance parameters etc. was chosen to be as close as reasonably possible to the set-up of other PT challenge entries to facilitate comparison.

The volume of the PT challenge simulations is 10 times larger than that envisioned for future surveys, making it possible to uncover small systematic biases even below the level of statistical significance for foreseeable practical applications.

We find that, in general, ShapeFit recovers the input parameters well within $2\sigma$, and this accuracy level does not vary dramatically for reasonable changes from the baseline set-up (when changing the range of scales — within reason, — shot noise and bias modelling assumptions, prescription for modelling non-linearities, nuisance parameters etc.).

However, we find that the inclusion of the hexadecapole induces a significant systematic shift on the compressed variable $\alpha_{\parallel}$, when extracted in ShapeFit. This shift would be well below the $2\sigma$ level for future surveys, but clearly indicates that the modeling of the hexadecapole should be improved and the effect should be further investigated (for example, it is well-known that the hexadecapole is very sensitive to the inhomogeneous distribution of $k$-vector directions with respect to the line of sight, sec 5.1 of [41]). Nevertheless, it is important to note that this shift is only appreciable in the ShapeFit approach, and the constraints it produces on the model-independent compressed variables. There is no systematic offset in the FM approach within a ΛCDM model, or when interpreting the constraints on the compressed variables as constraints on the cosmological parameters for a ΛCDM model. This is because the systematic shift in $\alpha_{\parallel}$ happens to be in a direction that is not allowed by (or unphysical in) a ΛCDM model. This teaches us an important lesson: some systematic biases can be seen at the model-independent compressed variables stage, which would not be spotted in the context of direct, model-dependent fits (especially for minimal-ΛCDM type-models). More explicitly, it is not sufficient to calibrate and quantify the accuracy of a FM approach on a given family of models (say, ΛCDM-like models) and then extend it to a different family of models, especially if non-standard, non-trivial extensions of ΛCDM. Doing so might severely underestimate the predicted accuracy of the selected FM approach.

We find that the HOD adopted by the PT challenge produces a galaxy bias which is consistent with the local Lagrangian prescription. When analyzing real data, where we have very little control over bias, it may be of interest to sacrifice precision for accuracy and leave the bias parameters free; this would reduce potential biases at the expense of larger error-bars. However, depending on the survey specifications, leaving the bias parameters completely free might be too conservative, increasing the error-bars and reducing the signal-to-noise for interesting signatures (see [34]).

To conclude, looking at the performance of all the PT challenge entries so far (as in this site), the agreement is remarkable considering how different the approaches are and that the challenge is blind. Not only the statistical error bars are quite comparable — the statistical error-bars are not blind, but all approaches require some compression and compressing can be lossy — but that the systematic shifts (which are blind) are comparable and under control at least for forthcoming surveys. This agreement is particularly significant when comparing FM with compressed variable approaches given the fundamentally different nature of the



JCAP06(2022)005

two. A direct comparison is presented in figure 3: our results and constraints are in excellent agreement with the EFT results both in terms of mean parameters and errors. The small residual differences in the size of error-bars which may be due to the priors on specific nuisance parameters, will be explored elsewhere [34].

Because of its flexibility, speed, model-independence and, as demonstrated here, precision and accuracy, we envision that the compressed variables approach (including the ShapeFit extension) can offer a valuable contribution in improving the robustness of the analysis and interpretation of forthcoming galaxy redshift surveys.


## Acknowledgments

We would like to thank Takahiro Nishimichi for initiating and publishing the blind PT challenge and for useful correspondence regarding our questions about the challenge set-up. Also, we thank Diego Blas for helpful discussions on the IR resummation. H.G-M. and S.B. acknowledges the support from 'la Caixa' Foundation (ID100010434) with code LCF/BQ/PI18/11630024. L.V., H.G-M. and S.B. acknowledge support of European Unions Horizon 2020 research and innovation programme ERC (BePreSysE, grant agreement 725327). Funding for this work was partially provided by the Spanish MINECO under projects PGC2018-098866-B-I00 MCIN/AEI/10.13039/501100011033 y FEDER "Una manera de hacer Europa", and the "Center of Excellence Maria de Maeztu 2020-2023" award to the ICCUB (CEX2019-000918-M funded by MCIN/AEI/10.13039/501100011033)and MDM-2014-0369 of ICCUB (Unidad de Excelencia Maria de Maeztu). We acknowledge the IT team at ICCUB for the help with the Aganice and Hipatia clusters.


## A Impact of IR resummation correction on ShapeFit

Since for most FM applications to galaxy power spectra it is crucial to account for large scale bulk flows via the so-called Infrared (IR) resummation, we implement this strategy within our ShapeFit template fits as well and test its impact. Typically, the role of IR resummation is to damp the baryon acoustic oscillation amplitude by an exponential term depending on a certain damping scale $\Sigma(z)$ which depends on redshift. Formally, this damping scale depends on the cosmological model, which is why IR resummation is not usually implemented in the model-independent, "classic" template fits.

Here, we present an approximate scheme, where we ignore this weak cosmology dependence and fix $\Sigma = 3.91\,[h^{-1}\mathrm{Mpc}]$, which is the value we obtain for the fiducial template cosmology at $z = 0.61$. We adopt the implementation of IR resummation within 1LSPT given by eq. (7.4) of [42], where the corrected, IR resummed non-linear power spectrum is written as a function of the damping scale $\Sigma$, the growth factor $g(z)$ (called $D(z)$ in [42]) and the linear power spectrum decomposed into a smooth ($P_s$) and a wiggle ($P_w$) part. The impact of this correction is actually small in the BAO features compared to the standard (No IR) PT, as the exponential factor damping the wiggles gets compensated by the $(1 + k^2 g^2 \Sigma^2)$ factor within the $g^2$ term. Then, the effect of IR in the first loop correction, i.e., the $g^4$ term, is quite small. We do not consider the $g^6$ factor as it represent a small correction in the $k$'s of interest.

In the left panel of figure 9 we show the impact of including IR resummation (empty, dotted contours) with respect to the baseline (filled contours) on the ShapeFit compressed parameters for either $k_{\mathrm{max}} = 0.12\left[h\mathrm{Mpc}^{-1}\right]$ (green) or $k_{\mathrm{max}} = 0.15\left[h\mathrm{Mpc}^{-1}\right]$ (red). As expected, due to the very small correction of IR resummation on the BAO amplitude, the



JCAP06(2022)005

differences with respect to the baseline are mild. For $k_{\rm max} = 0.12$ (green contours) the filled and empty contours are nearly indistinguishable, while for $k_{\rm max} = 0.15$ (red contours) we see small differences below $0.2\sigma$ for $\alpha_\parallel, \alpha_\perp, fA_p$ and $1\sigma$ for $m$. However, this is a very mild deviation given the large volume of 566 $\left[h^{-1}\mathrm{Gpc}\right]^3$ considered here. In summary the inclusion of IR resummation corrections has no significant effects for the ShapeFit approach.

## B Impact of the baryon density prior choice

Since there might be some confusion in the literature about this, here we test the impact of the prior choice on the baryon density on cosmological constraints. In the case of the PT challenge, the baryon to matter density ratio is known *a priori*, motivated by the baseline ΛCDM Planck 2018 constraints:

$$\frac{\omega_{\rm b}}{\omega_{\rm m}} = 0.1571\,. \tag{B.1}$$

However, in most cases in the literature where late time quantities such as the BOSS DR12 and eBOSS DR16 data products are used to constrain cosmological parameters jointly with early time probes, priors on the baryon density today, $\omega_{\rm b}$, are adopted. These priors can be motivated either by CMB data, or by the observation of primordial Deuterium and Helium abundances in distant systems, often referred as "Big Bang Nucleosynthesis" (BBN) measurements.

Therefore, it is interesting to investigate to what degree our cosmological parameter constraints depend on the choice of prior information about the baryon density. For that purpose, we choose the bestfit value of $\omega_{\rm b}$ from our "SIM-like" run as a fiducial value. Then, we perform an additional cosmological fit to the "SIM-like" ShapeFit results but using a Gaussian prior centered around that fiducial $\omega_{\rm b}$ value with width $\Delta\omega_{\rm b} = 0.0001$ instead of imposing a prior on $\omega_{\rm b}/\omega_{\rm m}$ as done in our baseline analysis. The width of the prior is chosen such that $\omega_{\rm b}$ is effectively fixed to the same degree as $\omega_{\rm b}/\omega_{\rm m}$ has been fixed for the baseline (see table 2), such that there is no residual effect of the prior when carrying out the comparison.

The results are presented in the right panel of figure 9. The baseline "SIM-like" results with fixed baryon to matter density ratio are shown in green, while the additional run with fixed baryon density is shown in violet. Of course, both runs deliver the same mean results, as the prior on $\omega_{\rm b}$ chosen for the violet contours is given by the bestfit value of the green contours. While the errors on the matter density $\Omega_{\rm m}$ and the primordial fluctuation amplitude $A_s$ are insensitive to the type of baryon density prior, we see that the constraints on the Hubble parameter $h$ become tighter by a factor 2 once we employ a prior on $\omega_{\rm b}$ instead of $\omega_{\rm b}/\omega_{\rm m}$. This is in fact expected, as the former parameter contains information on $h$, while the latter does not.

From this we conclude that the constraints on $\Omega_{\rm m}$ and $A_s$ from LSS data are more robust and insensitive to the specific prior choice than constraints on $h$. Care has to be taken in particular when showing LSS results on $h$, that made use of an early-time physics assumption, as different, physically well motivated assumptions can lead to subtle differences in the posterior constraints.



JCAP06(2022)005

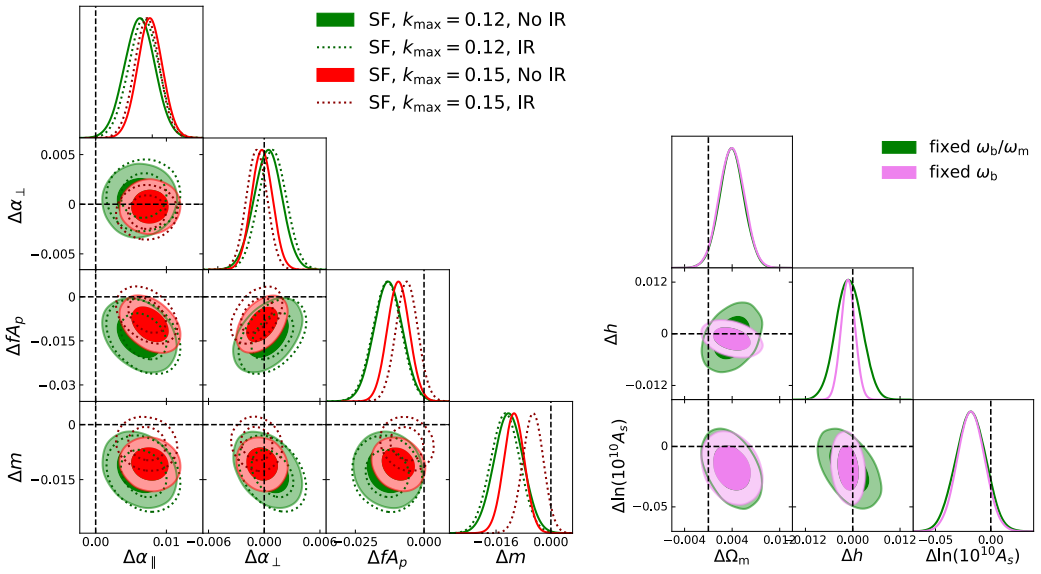


**Figure 9**. Left panel: impact on the ShapeFit compressed parameter constraints of including IR resummation (empty, dotted contours) or not (filled contours). The results are presented for two different choices of maximum wavevector, $k_{\rm max} = 0.12\,[h{\rm Mpc}^{-1}]$ (green) and $k_{\rm max} = 0.15\,[h{\rm Mpc}^{-1}]$ (red), where the bias parameters follow the local Lagrangian prediction and the shot noise correction prior is fixed to 1%. We find that including IR leads to very mild differences typically below $0.2\sigma$ reaching at maximum $1\sigma$ in $m$ for the $k_{\rm max} = 0.15\,[h{\rm Mpc}^{-1}]$ case. Right panel: blinded cosmological parameters obtained for the "SIM-like" set-up choosing two different implementations of baryon density $\omega_{\rm b}$ prior. In green, we show the baseline case for which we use our prior knowledge that the baryon to matter density ratio is set to $\omega_{\rm b}/\omega_{\rm m} = 0.1571$. In violet, we show the results for fixing the baryon density $\omega_{\rm b}$ to its best fit value found from the baseline run. The latter choice (motivated by BBN or CMB data) is more often used in the literature when constraining ΛCDM parameters using actual survey data. We find that the $\Omega_{\rm m}$ and $A_s$ constraints are insensitive to this prior choice, while constraints on $h$ broaden by a factor $\sim 2$ when choosing a prior on the baryon to matter density ratio rather than the baryon density itself.

## References


[1] T. Nishimichi et al., *Blinded challenge for precision cosmology with large-scale structure: results from effective field theory for the redshift-space galaxy power spectrum*, *Phys. Rev. D* **102** (2020) 123541 [arXiv:2003.08277] [INSPIRE].

[2] BOSS collaboration, *The clustering of galaxies in the completed SDSS-III Baryon Oscillation Spectroscopic Survey: cosmological analysis of the DR12 galaxy sample*, *Mon. Not. Roy. Astron. Soc.* **470** (2017) 2617 [arXiv:1607.03155] [INSPIRE].

[3] eBOSS collaboration, *Completed SDSS-IV extended Baryon Oscillation Spectroscopic Survey: cosmological implications from two decades of spectroscopic surveys at the Apache Point Observatory*, *Phys. Rev. D* **103** (2021) 083533 [arXiv:2007.08991] [INSPIRE].

[4] S. Brieden, H. Gil-Marín and L. Verde, *Model-independent versus model-dependent interpretation of the SDSS-III BOSS power spectrum: bridging the divide*, *Phys. Rev. D* **104** (2021) L121301 [arXiv:2106.11931] [INSPIRE].




JCAP06(2022)005

[5] S. Brieden, H. Gil-Marín and L. Verde, *ShapeFit: extracting the power spectrum shape information in galaxy surveys beyond BAO and RSD*, *JCAP* **12** (2021) 054 [arXiv:2106.07641] [INSPIRE].

[6] H.-J. Seo and D.J. Eisenstein, *Improved forecasts for the baryon acoustic oscillations and cosmological distance scale*, *Astrophys. J.* **665** (2007) 14 [astro-ph/0701079] [INSPIRE].

[7] D.J. Eisenstein, H.-J. Seo and M.J. White, *On the robustness of the acoustic scale in the low-redshift clustering of matter*, *Astrophys. J.* **664** (2007) 660 [astro-ph/0604361] [INSPIRE].

[8] D.J. Eisenstein and M.J. White, *Theoretical uncertainty in baryon oscillations*, *Phys. Rev. D* **70** (2004) 103523 [astro-ph/0407539] [INSPIRE].

[9] H.-J. Seo and D.J. Eisenstein, *Probing dark energy with baryonic acoustic oscillations from future large galaxy redshift surveys*, *Astrophys. J.* **598** (2003) 720 [astro-ph/0307460] [INSPIRE].

[10] M.M. Ivanov, M. Simonović and M. Zaldarriaga, *Cosmological parameters from the BOSS galaxy power spectrum*, *JCAP* **05** (2020) 042 [arXiv:1909.05277] [INSPIRE].

[11] DESI collaboration, *The DESI experiment part I: science, targeting, and survey design*, arXiv:1611.00036 [INSPIRE].

[12] P.S. Behroozi, R.H. Wechsler and H.-Y. Wu, *The ROCKSTAR phase-space temporal halo finder and the velocity offsets of cluster cores*, *Astrophys. J.* **762** (2013) 109 [arXiv:1110.4372] [INSPIRE].

[13] T. Nishimichi, *Multipole moment data for PT challenges*, https://www2.yukawa.kyoto-u.ac.jp/∼takahiro.nishimichi/data/PTchallenge/.

[14] G. D'Amico et al., *The cosmological analysis of the SDSS/BOSS data from the effective field theory of large-scale structure*, *JCAP* **05** (2020) 005 [arXiv:1909.05271] [INSPIRE].

[15] S.-F. Chen, Z. Vlah, E. Castorina and M. White, *Redshift-space distortions in Lagrangian perturbation theory*, *JCAP* **03** (2021) 100 [arXiv:2012.04636] [INSPIRE].

[16] S.-F. Chen, Z. Vlah and M. White, *Consistent modeling of velocity statistics and redshift-space distortions in one-loop perturbation theory*, *JCAP* **07** (2020) 062 [arXiv:2005.00523] [INSPIRE].

[17] Y. Kobayashi, T. Nishimichi, M. Takada, R. Takahashi and K. Osato, *Accurate emulator for the redshift-space power spectrum of dark matter halos and its application to galaxy power spectrum*, *Phys. Rev. D* **102** (2020) 063504 [arXiv:2005.06122] [INSPIRE].

[18] J. Hartlap, P. Simon and P. Schneider, *Why your model parameter confidences might be too optimistic: unbiased estimation of the inverse covariance matrix*, *Astron. Astrophys.* **464** (2007) 399 [astro-ph/0608064] [INSPIRE].

[19] E. Sellentin and A.F. Heavens, *Parameter inference with estimated covariance matrices*, *Mon. Not. Roy. Astron. Soc.* **456** (2016) L132 [arXiv:1511.05969] [INSPIRE].

[20] H. Gil-Marín and L. Verde, *How to optimally combine pre-reconstruction RSD and post-reconstruction BAO signals*, to appear.

[21] A. Lewis, A. Challinor and A. Lasenby, *Efficient computation of CMB anisotropies in closed FRW models*, *Astrophys. J.* **538** (2000) 473 [astro-ph/9911177] [INSPIRE].

[22] BOSS collaboration, *The clustering of galaxies in the SDSS-III Baryon Oscillation Spectroscopic Survey: testing gravity with redshift-space distortions using the power spectrum multipoles*, *Mon. Not. Roy. Astron. Soc.* **443** (2014) 1065 [arXiv:1312.4611] [INSPIRE].

[23] H. Gil-Marín et al., *The power spectrum and bispectrum of SDSS DR11 BOSS galaxies — I. Bias and gravity*, *Mon. Not. Roy. Astron. Soc.* **451** (2015) 539 [arXiv:1407.5668] [INSPIRE].



JCAP06(2022)005

[24] J.N. Fry and E. Gaztanaga, *Biasing and hierarchical statistics in large scale structure*, *Astrophys. J.* **413** (1993) 447 [astro-ph/9302009] [INSPIRE].

[25] P. McDonald and A. Roy, *Clustering of dark matter tracers: generalizing bias for the coming era of precision LSS*, *JCAP* **08** (2009) 020 [arXiv:0902.0991] [INSPIRE].

[26] T. Baldauf, U. Seljak, V. Desjacques and P. McDonald, *Evidence for quadratic tidal tensor bias from the halo bispectrum*, *Phys. Rev. D* **86** (2012) 083540 [arXiv:1201.4827] [INSPIRE].

[27] S. Saito, T. Baldauf, Z. Vlah, U. Seljak, T. Okumura and P. McDonald, *Understanding higher-order nonlocal halo bias at large scales by combining the power spectrum with the bispectrum*, *Phys. Rev. D* **90** (2014) 123522 [arXiv:1405.1447] [INSPIRE].

[28] K.C. Chan, R. Scoccimarro and R.K. Sheth, *Gravity and large-scale non-local bias*, *Phys. Rev. D* **85** (2012) 083509 [arXiv:1201.3614] [INSPIRE].

[29] R. Scoccimarro, *Redshift-space distortions, pairwise velocities and nonlinearities*, *Phys. Rev. D* **70** (2004) 083007 [astro-ph/0407214] [INSPIRE].

[30] A. Taruya, T. Nishimichi and S. Saito, *Baryon acoustic oscillations in* 2*D: modeling redshift-space power spectrum from perturbation theory*, *Phys. Rev. D* **82** (2010) 063522 [arXiv:1006.0699] [INSPIRE].

[31] H. Gil-Marín et al., *The completed SDSS-IV extended Baryon Oscillation Spectroscopic Survey: measurement of the BAO and growth rate of structure of the luminous red galaxy sample from the anisotropic power spectrum between redshifts* 0.6 *and* 1.0, *Mon. Not. Roy. Astron. Soc.* **498** (2020) 2492 [arXiv:2007.08994] [INSPIRE].

[32] D.J. Eisenstein and W. Hu, *Baryonic features in the matter transfer function*, *Astrophys. J.* **496** (1998) 605 [astro-ph/9709112] [INSPIRE].

[33] D.J. Eisenstein and W. Hu, *Power spectra for cold dark matter and its variants*, *Astrophys. J.* **511** (1997) 5 [astro-ph/9710252] [INSPIRE].

[34] S. Brieden, H. Gil-Marín and V. Licia, *Joint BAO, RSD and shape analysis and cosmological implications of BOSS and eBOSS samples over* 10 *billion years of cosmic evolution*, in preparation.

[35] H. Gil-Marín, *Ptcool*, https://github.com/hectorgil/PTcool.

[36] T. Brinckmann and J. Lesgourgues, *MontePython* 3*: boosted MCMC sampler and other features*, *Phys. Dark Univ.* **24** (2019) 100260 [arXiv:1804.07261] [INSPIRE].

[37] B. Audren, J. Lesgourgues, K. Benabed and S. Prunet, *Conservative constraints on early cosmology: an illustration of the Monte Python cosmological parameter inference code*, *JCAP* **02** (2013) 001 [arXiv:1210.7183] [INSPIRE].

[38] T. Brinckmann, *Montepython*, https://github.com/brinckmann/montepython_public.

[39] W.H. Press, S.A. Teukolsky, W.T. Vetterling and B.P. Flannery, *Section* 7.9.1 *importance sampling*, in *Numerical recipes: the art of scientific computing*, third edition, Cambridge University Press, New York, NY, U.S.A. (2007).

[40] A. Cuceu, J. Farr, P. Lemos and A. Font-Ribera, *Baryon acoustic oscillations and the Hubble constant: past, present and future*, *JCAP* **10** (2019) 044 [arXiv:1906.11628] [INSPIRE].

[41] BOSS collaboration, *The clustering of galaxies in the completed SDSS-III Baryon Oscillation Spectroscopic Survey: anisotropic galaxy clustering in Fourier-space*, *Mon. Not. Roy. Astron. Soc.* **466** (2017) 2242 [arXiv:1607.03150] [INSPIRE].

[42] D. Blas, M. Garny, M.M. Ivanov and S. Sibiryakov, *Time-sliced perturbation theory II: baryon acoustic oscillations and infrared resummation*, *JCAP* **07** (2016) 028 [arXiv:1605.02149] [INSPIRE].

JCAP06(2022)005

# 6

# MODEL-AGNOSTIC INTERPRETATION OF EBOSS DATA

This final chapter related to ShapeFit presents the article "Model-agnostic interpretation of 10 billion years of cosmic evolution traced by BOSS and eBOSS data" [5], currently under review for publication in JCAP.

In this article we apply ShapeFit, for the first time in combination with BAO reconstruction via the method of [89], to the BOSS+eBOSS LRGs spanning a redshift range from $0.2 \leq z \leq 1.0$ in three redshift bins and the eBOSS quasars spanning $0.8 \leq z \leq 2.2$. This represents the most constraining published specroscopic galaxy and quasar maps to date. Considering also the Lyman-$\alpha$ BAO data of [90] with $1.8 < z < 4.0$, we discuss the cosmological implications of this legacy dataset for a variety of models. This is done in a similar manner as for the official eBOSS analysis [36], but with addition of the measured shape parameter and further tests of the Shapefit methodology on high confidence mocks matching each tracer studied in the paper.

The article is structured as follows. Section 2 contains a brief summary of the different template-fit approaches that have been applied to data so far, from the philosophy of fixing the template in general to BAO types of analyses to RSD analysis and ShapeFit. In section 3 we present the datasets used throughout the work and provide in section 4 the constraints on the ShapeFit compressed physical parameters. These parameters are subsequently used as input to derive cosmological constraints on the standard flat $\Lambda$CDM parameters and single parameter extensions in section 5. This section also features a comparison between the individual tracers and a comparison with other approaches, either FM or classic. Then, we undergo a comprehensive study using mocks in section 6 to obtain the systematic error budget, and finally conclude with section 7. A suite of additional tests is provided in various appendices.

The implications of this work for galaxy clustering analyses and cosmology are manifold. By consistently combining ShapeFit with the post-reconstruction BAO signals of the LRG bins at the level of compressed variables and by considering a huge redshift range, we are able to provide the tightest constraints on the matter density today $\Omega_m$ to date from LSS alone under the assumption of standard flat $\Lambda$CDM. Generally, we see that the shape $m$ helps a lot when constraining models from LSS alone (see abstract and section 5.4 for exact numbers). However, once CMB data from Planck is included, the increase in constraining power with respect to the classic BAO+RSD

approach becomes vanishingly small. This is in line with (and justifies) previous BOSS and eBOSS cosmological results [35, 36], which were mostly obtained in combination with Planck.

Another interesting aspect of our work is that the influence of the shape on cosmological parameter constraints becomes less important the larger the considered redshift range. This is because for larger redshift ranges the geometrical and growth information captured by $D_M(z)/r_\mathrm{d}, H(z)r_\mathrm{d}, f\sigma_8(z)$ become pivotal in breaking parameter degeneracies, whereas the shape, supposed to be constant at all redshifts, does not gain much from extending the redshift range. In turn, a significant shift in shape with redshift could serve as a smoking gun for new physics (such as primordial non-Gaussianity) or -alternatively- point towards unaccounted systematics.

Prepared for submission to JCAP

# Model-agnostic interpretation of 10 billion years of cosmic evolution traced by BOSS and eBOSS data

**Samuel Brieden**[1,2] **Héctor Gil-Marín**[1] **Licia Verde**[1,3]

[1]ICC, University of Barcelona, IEEC-UB, Martí i Franquès, 1, E-08028 Barcelona, Spain
[2]Dept. de Física Quàntica i Astrofísica, Universitat de Barcelona, Martí i Franquès 1, E-08028 Barcelona, Spain
[3]ICREA, Pg. Lluís Companys 23, Barcelona, E-08010, Spain

E-mail: sbrieden@icc.ub.edu, hectorgil@icc.ub.edu, liciaverde@icc.ub.edu



**Abstract.** We present the first model-agnostic analysis of the complete set of Sloan Digital Sky Survey III (BOSS) and -IV (eBOSS) catalogues of luminous red galaxy and quasar clustering in the redshift range $0.2 \leq z \leq 2.2$ (10 billion years of cosmic evolution), which consistently includes the baryon acoustic oscillations (BAO), redshift space distortions (RSD) and the shape of the transfer function signatures, from pre- and post-reconstructed catalogues in Fourier space. This approach complements the standard analyses techniques which only focus on the BAO and RSD signatures, and the full-modeling approaches which assume a specific underlying cosmology model to perform the analysis. These model-independent results can then easily be interpreted in the context of the cosmological model of choice. In particular, when combined with $z > 2.1$ Ly-$\alpha$ BAO measurements, the clustering BAO, RSD and *Shape* parameters can be interpreted within a flat-ΛCDM model yielding $h = 0.6816 \pm 0.0067$, $\Omega_{\rm m} = 0.3001 \pm 0.0057$ and $10^9 \times A_s = 2.43 \pm 0.20$ (or $\sigma_8 = 0.858 \pm 0.036$) with a Big Bang Nucleosynthesis prior on the baryon density. Without any external dataset, the BOSS and eBOSS data alone imply $\Omega_{\rm m} = 0.2971 \pm 0.0061$ and $10^9 \times A_s = 2.39^{+0.24}_{-0.43}$ (or $\sigma_8 = 0.857 \pm 0.040$). For models beyond ΛCDM, eBOSS data alone (in combination with Planck) constrain the sum of neutrino mass to be $\Sigma m_\nu < 0.40$ eV with a BBN prior ($\Sigma m_\nu < 0.082$ eV) at 95% CL, the curvature energy density to $\Omega_{\rm k} = -0.022^{+0.032}_{-0.038}$ ($\Omega_{\rm k} = 0.0015 \pm 0.0016$) and the dark energy equation of state parameter to $w = -0.998^{+0.085}_{-0.073}$ ($w = -1.093^{+0.048}_{-0.044}$) at 68% CL without a BBN prior. These results are the product of a substantial improvement of the state-of-the-art methodologies and represent the most precise model-agnostic cosmological constrains using spectroscopic large-scale data alone.

## Contents

## 1 Introduction

Observations of the Cosmic Microwave Background (CMB, e.g., [1, 2]) have been pivotal in establishing the ΛCDM model as the standard model for cosmology. The interpretation of CMB observations is very sensitive to the (linear, and, within the standard cosmological model, simple and well understood) physics of the early Universe. However, one of the main puzzles of modern cosmology, the cosmic acceleration, is a late-time ($z \lesssim 1$) phenomenon, hence cosmological constraints from the late-time Universe observations are of crucial importance to study dark energy. Complementary to Supernovae observations, which first provided evidence for cosmic acceleration, the large-scale structure (LSS) of the Universe, provides a unique window into the evolution of the late-time Universe.

The development of massive spectroscopic surveys of galaxies and quasars over wide areas of the sky over the past two decades (e.g., [3–5]) has propelled the study of clustering of LSS into the realm of precision cosmology. The clustering of galaxies and other dark matter tracers (such as quasars or the Ly-$\alpha$ forest) provides precise measurements of the cosmic expansion history with baryon acoustic oscillations (BAO) and measurements of the rate of structure growth with redshift space distortions (RSD).

Perturbations in the photon-baryon fluid of the early Universe leave an imprint in the late-time clustering of cosmic structure as a feature (the BAO, [6]) observable in the LSS power spectrum and first detected by [4, 5]. The BAO feature offers a standard ruler whose length can be calibrated by early-time physics, but also, when observed in the late-time clustering, can be used to determine the expansion history of the Universe via the Alcock-Paczynski (AP) effect [7]. The tracer's power spectrum yields two scaling parameters – $\alpha_\parallel, \alpha_\perp$– respectively along and across the line-of-sight (LOS) direction. The information extracted is purely geometrical and model-independent, it is only mildly affected by non-linear physics, making the BAO one of the most robust probes of the late-time Universe. To reduce the potential bias on the BAO feature induced by non-linearities and to boost the BAO signal-to-noise, it is customary to apply the reconstruction technique [8, 9]. Reconstruction effectively generates an additional catalogue and thus additional 'post-recon' power spectra. These are highly correlated to the 'pre-recon' ones –hence their covariances must be carefully taken into account– but do add significant information and are used only for the BAO part of the analysis.

Furthermore, gravitationally-induced peculiar velocities give rise to deviations from the Hubble flow which imprint RSD on the three-dimensional map produced by redshift surveys. Pioneered by [10], RSD enclose information about the combination of the amplitude of velocity fluctuations with the dark matter amplitude perturbations. As such, they trace the growth history of cosmic structures, offering thus important insights into the nature of gravity.

Most analyses of state-of-the-art surveys, e.g., [11, 12], adopt what we refer to as the 'classic' approach in order to extract cosmological information from the tracers' clustering.

With the help of a template of the power spectrum, the clustering data are compressed into few (three per redshift interval considered corresponding to two scaling parameters and one growth rate parameter) physical observables, or compressed variables, which are only sensitive to late-time physics. The resulting constraints on these compressed variables can then be re-interpreted *a posteriori* as constraints on (cosmological) parameters for a given cosmological model (or family of models).

This 'classic' approach is conceptually different from the way, for example, the CMB power spectrum is analyzed, and from the analysis of LSS data pre-BAO era (see for e.g., [13–15]), which we refer to as 'full modeling' (or FM). After selecting a cosmological model *ab initio*, the measured power spectrum is compared directly to the model's prediction, and the model's parameters are then constrained by standard statistical inference. The procedure is repeated for every model under consideration.

If clustering is analyzed without external datasets or priors, the application of the FM approach to state-of-the-art redshift surveys (e.g., [16–18]) produces much tighter constraints on cosmological parameters than the classic approach. In a joint CMB+LSS analysis however the two perform very similarly.

In other words, the compression employed by the classic approach, disentangles the late-time physics from the early-time one, isolates the part of the cosmological signal least affected by systematics and makes the resulting constraints as model independent as possible (e.g., [19, 20] and refs. therein). But has the drawback that the compression is not lossless. Full modeling approaches are model-dependent, and computationally more demanding both in terms of analysis and of modeling of the signal, but –compared to the 'classic' approach– extract additional information mostly from the broadband shape of the power spectrum.

A simple one-parameter extension of the 'classic' approach, ShapeFit, was proposed by [21]. The ShapeFit phenomenological parameter $m$ is related to the shape of the power spectrum on very large scales and to the shape of the matter transfer function; it was designed to capture a series of early-time processes that affect the broadband power spectrum shape in the linear regime.

The application of ShapeFit to the large volume, high resolution, PT challenge [22] simulations suite [23] demonstrates that this approach is effectively unbiased even for a survey volume 10 times larger than that probed by future surveys. Ref. [24] presents the ShapeFit analysis of the Sloan Digital Sky Survey-III BOSS data and demonstrates that it matches the constraining power of FM approaches performed to date on the same data.

Here we consider the full BOSS and eBOSS observations campaigns [12] representing the final use of the Apache Point Observatory 2.5m Sloan Telescope for galaxy redshift surveys designed to measure cosmological parameters using BAO and RSD techniques. Four generations of Sloan Digital Sky Survey culminated with the eBOSS data release, which probes $\sim 10$ billion years of cosmic evolution through more than 2 million spectra. We apply the ShapeFit analysis on these data and present the resulting constraints on the physical parameters. We argue that ShapeFit extracts virtually all the robust and model-independent cosmological information carried by LSS clustering. The constraints on the physical parameters are then interpreted in light of a suite of popular cosmological models including the standard $\Lambda$CDM and its common one-parameter extensions.

It is worth highlighting that in producing the ShapeFit constraints on the physical parameters, no assumption is made about the underlying cosmological model. A Friedmann-Lemaitre-Robinson-Walker metric is assumed and thus statistical homogeneity and isotropy, although General Relativity (GR) is not assumed on large scales. However, Newtonian dy-

namics (hence GR) is assumed at small, mildly non-linear, scales when reconstruction is applied to boost the BAO signal. Within ShapeFit, no explicit scale-dependence of the growth rate is considered, hence the measured growth rate should be considered as effective, suitably weighted across the relevant scales. No assumption is made about early-time physics, the nature of dark energy, of dark matter or spatial curvature. However, unless otherwise stated, the interpretation of the constraints on the shape parameter $m$ assumes a power-law primordial power spectrum with fixed spectral slope; moreover a Big Bang nucleosynthesis (BBN) prior is adopted when converting the compressed variable constraints into cosmological parameters. Unless otherwise stated, galaxy bias is assumed to be local in Lagrangian space. This set of assumptions only affects the shape parameter constraints and not the other compressed variables.

The rest of the paper is organized as follows. In section 2 the theory and methodology are described. This section is mostly a review of material covered elsewhere in the literature, but its presentation is tuned to the current application. The data set used is presented in section 3 along with the simulated mock surveys which are employed to estimate the relevant covariance matrices. Model-independent results on the physical variables are presented in section 4 and their re-interpretation under the ΛCDM and a suite of extensions to this model are reported in section 5. Section 6 reports a suite of systematic checks performed on synthetic catalogues and estimates the overall systematic error budget. Finally we present the main conclusions of this work in section 7. The appendices quantify the impact on the final results of several assumptions ranging from the nature of tracer's bias, fiber collisions and prior choices.

## 2 Methodology, Theory and Data compression techniques

As mentioned in the introduction, there is more than a single way to perform a cosmological analysis to spectroscopic galaxy survey data. In this section we review and summarize approaches that are already in the literature, in particular [8, 9, 21, 25, 26] and references therein. This section however, also serves to highlight differences, similarities and connections among them. In this work, we focus on the fixed template approach, where the measured galaxy power spectra are compressed into physical variables $\boldsymbol{\Theta}_{\rm phys}$ at each redshift bin, which in turn can be interpreted in light of a cosmological model and its parameters $\boldsymbol{\Omega}$. Note that, within the compression step, the power spectra are fitted in a model-agnostic way, without imposing any of the ΛCDM-type of relations among (physical) parameters. In this way, (cosmological) model's assumptions are introduced only at the very late stages of the analyses. This has several advantages, for example, there is no need to re-do the fit if the cosmology paradigm changes, or when a novel model or class of models needs to be tested. This is one of the main reasons for adopting this philosophy of interpreting the spectroscopic data, rather than direct fits (or full modeling fits).

All model-agnostic fixed-template compression techniques rely on two fundamental steps. First, a fiducial cosmology $\boldsymbol{\Omega}^{\rm fid}$ is needed to generate a reference coordinate and unit system. The coordinate system depends on the distance-redshift relation and the unit system depends on the fiducial linear matter power spectrum template $P_{\rm lin}(k, \boldsymbol{\Omega}^{\rm fid})$ as function of wavenumber $k$. Second, the fiducial template is transformed as to be compared with the observable galaxy power spectrum multipoles in redshift space, $P^{(\ell)}_{\rm model}(k, \boldsymbol{\Theta}_{\rm model}|\boldsymbol{\Omega}^{\rm fid})$ given a certain model or compression type. Here the '|' sign indicates that the dependence of the fiducial cosmology is implicit rather than explicit. As we explain in more detail in section 3.3, the

final constraints on physical parameters do not depend on the template's choice.[1] The symbol $\boldsymbol{\Theta}_{\rm model}$ corresponds to a set of physical and nuisance parameters $\boldsymbol{\Theta}_{\rm model} = \boldsymbol{\Theta}^{\rm model}_{\rm phys} \cup \boldsymbol{\Theta}^{\rm model}_{\rm nuis}$ that is used to *i)* probe all late-time dynamics effects (geometry and/or growth) in the most generic, model-independent way, and *ii)* once the physical parameters are constrained at each redshift bin, use them to test cosmological models. This compression step is described for three different cases in section 2.2.

In particular, we review the 'classic' BAO and RSD analyses in addition to the recently introduced ShapeFit compression.

### 2.1 Fiducial cosmology

As anticipated above, the purpose of adopting a fiducial cosmology $\boldsymbol{\Omega}_{\rm fid}$ is twofold.

First, it is needed to generate a *coordinate system*. The galaxy positions provided by BOSS and eBOSS are measured in terms of angles and redshifts. These coordinates are transformed to distances based on a distance-redshift relation determined by the fiducial cosmology, in particular (within ΛCDM) by the matter density today $\Omega_{\rm m}$ and the Hubble expansion rate today (or 'little $h$') $H_0 = 100\,h\,{\rm km/s/Mpc}$. This coordinate transformation is essential to extract the full three-dimensional clustering statistics from galaxy catalogs, as different cosmological models affect the distances along and across the LOS differently.

Second, the fiducial cosmology is needed to generate a *unit system* for the distances (akin to interpreting the hatching of a ruler). This is provided by the fiducial matter power spectrum template $P_{\rm lin}(k, \boldsymbol{\Omega}^{\rm fid})$, whose shape is predominantly (but not solely) determined by the sound horizon at radiation drag epoch, $r_{\rm d}$, the so-called 'standard ruler'. In the template it manifests itself via the location of the wiggles on one hand (measured by the BAO analysis), and as a characteristic suppression scale on the other hand (measured by ShapeFit). The latter effect is somewhat degenerate (at the scales of interest for galaxy clustering) with the overall power spectrum slope determined by the scale of equality between matter and radiation, $k_{\rm eq}$, and the primordial tilt, $n_s$. But the power of ShapeFit is to measure the slope in a model-independent way.

In principle, one could adopt different fiducial cosmologies for the coordinate and the unit system. But, as it is customary, here we use the same fiducial cosmology for both tasks. For simplicity, we use the same fiducial cosmology $\boldsymbol{\Omega}_{\rm fid}$ employed in the official BOSS and eBOSS analyses, with parameter values listed in table 2.

Throughout this work we denote by 'fid' the quantities evaluated at that cosmology. The quantities without this notation denote the true underlying values of the sample we fit (either mock or actual data).

### 2.2 Modeling the power spectrum multipoles

In general, because the power spectrum of the observed galaxy map is constructed adopting a fiducial coordinate *and* unit system, the modeled power spectrum multipoles need to be rescaled to that system in order to be compared to the data. These coordinate and unit conversions (called late-time and early-time rescaling respectively in [21]) are almost perfectly degenerate, which is why they are often represented by the following scaling parameters,

[1] Previous studies have checked that there is a residual dependence which is very sub-dominant with respect to BOSS and eBOSS statistical errors, even for cases where this reference template is many standard deviations away from best-fit CMB anisotropy cosmologies. For detailed studies on how the arbitrary choice of the fixed template can impact the cosmological results, we refer the reader to Appendix B of [21].

$$\alpha_\parallel(z) \equiv \frac{D_H(z)/r_\mathrm{d}}{[D_H(z)/r_\mathrm{d}]^\mathrm{fid}}, \quad \alpha_\perp(z) \equiv \frac{D_M(z)/r_\mathrm{d}}{[D_M(z)/r_\mathrm{d}]^\mathrm{fid}} \ , \tag{2.1}$$

where $D_H(z) \equiv c/H(z)$ and $D_M(z) \equiv \int_0^z c/H(z')dz'$ are the distances along and across the LOS respectively, with Hubble expansion rate $H(z)$. These scaling-parameters are used to transform the power spectrum multipoles into the correct observable coordinates in units of the standard ruler and they are allowed to vary freely.

Note that the scaling parameters as defined in eq. (2.1) depend on the arbitrary choice of the template, but once they are converted to the physical distances in units of the BAO scale, $D_H/r_\mathrm{d}$ and $D_M/r_\mathrm{d}$, this dependence vanishes. Hence, we use both notations interchangeably, in particular we use $\{\alpha_\parallel, \alpha_\perp\}$ when referring to the template fits and $\{D_H/r_\mathrm{d}, D_M/r_\mathrm{d}\}$ when referring to their cosmological interpretation.

The modeled power spectrum multipoles for a given reference template based on the cosmology $\mathbf{\Omega}_\mathrm{fid}$ are usually written as,

$$P^{(\ell)}_\mathrm{model}(k) = \frac{(2\ell+1)}{2\alpha_\perp^2\alpha_\parallel} \int_{-1}^{1} P_\mathrm{model}(\widetilde{k}(k,\mu), \widetilde{\mu}(\mu), \mathbf{\Omega}_\mathrm{fid}, \mathbf{\Theta}_\mathrm{model}) \mathcal{L}_\ell(\mu)\, d\mu + g^{(\ell)}(\mathbf{X}_\mathrm{model}) \ , \tag{2.2}$$

where $\mathbf{\Theta}_\mathrm{model}$ includes physical and nuisance parameters of the compression method of choice, $g^{(\ell)}(\mathbf{X}_\mathrm{model})$ represents an arbitrary function accounting for the broadband signal which depends on multipole $\ell$ and extra free nuisance parameters, $\mathbf{X}_\mathrm{model}$, the coordinates $(k, \mu)$ are the wavevector in units $[\mathrm{Mpc}^{-1}h]$ and the cosine of the separation angle, $\mathcal{L}_\ell$ is the Legendre polynomial of order $\ell$ and the rescaled coordinates $(\widetilde{k}, \widetilde{\mu})$ are defined as,

$$\widetilde{k} = \frac{k}{\alpha_\perp}\left[1+\mu^2\left(\frac{\alpha_\perp^2}{\alpha_\parallel^2}-1\right)\right]^{1/2}, \quad \widetilde{\mu} = \mu\frac{\alpha_\perp}{\alpha_\parallel}\left[1+\mu^2\left(\frac{\alpha_\perp^2}{\alpha_\parallel^2}-1\right)\right]^{-1/2}. \tag{2.3}$$

The exact model implementation of $P_\mathrm{model}$ and the corresponding parameter-sets $\mathbf{\Theta}_\mathrm{model}$ and $\mathbf{X}_\mathrm{model}$ depend on the type of compression used to analyze the data. Different choices are summarized below.

### 2.2.1 BAO compression

For the BAO analysis, only the oscillatory feature within the power spectrum, at wavenumbers determined by the sound horizon at radiation drag $r_\mathrm{d}$, is of interest. Therefore it is customary to separate the fiducial linear power spectrum template into a no-wiggle ($P^\mathrm{fid}_\mathrm{nw} = P^\mathrm{fid}_\mathrm{lin} - P^\mathrm{fid}_\mathrm{wig}$) and a wiggle ($P^\mathrm{fid}_\mathrm{wig}$) part, such that the scaling only affects the oscillatory part $\mathcal{O}^\mathrm{fid}_\mathrm{lin} = P^\mathrm{fid}_\mathrm{lin}/P^\mathrm{fid}_\mathrm{nw}$, while the no-wiggle broadband shape is marginalized over. In practice, this is achieved by setting the following model power spectrum $P_\mathrm{model}$ into eq. (2.2) [27, 28]:

$$P_\mathrm{BAO}(k,\mu) = B^2(1+\beta\mu^2R)^2 P^\mathrm{fid}_\mathrm{nw}(k)\left[1+\left(\mathcal{O}^\mathrm{fid}_\mathrm{lin}(k)-1\right)e^{-\frac{1}{2}\left(\mu^2k^2\Sigma_\parallel^2+(1-\mu^2)k^2\Sigma_\perp^2\right)}\right], \tag{2.4}$$

where $B$ represents a global amplitude parameter, $\beta$ (defined as $\beta = f/b_1$)[2] incorporates linear (Kaiser) redshift space distortions, the damping terms $(\Sigma_\parallel, \Sigma_\perp)$ include the anisotropic, non-linear damping of the BAO-amplitude and $R$ is either the smoothing scale used in reconstruction (see section 2.3), or set to zero in case the BAO fit is performed on pre-reconstruction measurements.

[2]Within the BAO analysis we do not use this parameter to measure the growth rate $f$, but rather marginalize over it.

In addition, the broadband power spectrum is marginalized over by adding to each power spectrum multipole the following polynomial expansion of order $N = 5$ for BOSS LRGs and $N = 3$ for eBOSS LRGs:

$$g^{(\ell)}(\mathbf{X}_{\rm BAO}) = \sum_{i=1}^{N} A_i^{(\ell)} k^{2-i} \ . \tag{2.5}$$

Hence, our BAO-model is fully described by 2 physical parameters $\mathbf{\Theta}^{\rm BAO}_{\rm phys} = \left\{\alpha_\parallel, \alpha_\perp\right\}$ and 23 (15) nuisance parameters for BOSS (eBOSS) LRGs $\mathbf{\Theta}^{\rm BAO}_{\rm nuis} = \left\{\beta, B_{\rm N/S}, A^{(\ell)}_{i,N/S}\right\}$ per redshift bin, where subscripts 'N' and 'S' stand for the north and south galactic caps. The damping terms $(\Sigma_\parallel, \Sigma_\perp)$ are not varied freely but are set to fiducial values estimated from the mocks of each sample (see section 3.2).

### 2.2.2 RSD compression

In addition to the BAO analysis, where only the 'horizontal' information (coming from the wiggle position as a function of the angle to the LOS) is considered, the RSD analysis aims to gain cosmological insight also from the 'vertical' information (coming from the relative broadband amplitude as a function of the angle to the LOS).

Therefore, the first ingredient of the RSD compression are the scaling parameters $\left\{\alpha_\parallel, \alpha_\perp\right\}$ defined in eq. (2.1) which capture the AP-effect and are also sensitive to the absolute position of the BAO at drag epoch. Although strictly speaking the AP effect affects all scales (and not only the BAO scale) it has been shown (see appendix D of [21]) that the BAO signal greatly dominates over the rest of the scales, and therefore it is common practice in the literature to treat the BAO scale as fully degenerate with the scale dilation parameters (see also sections 2 and 3 of [21] for a further discussion on this topic).

The redshift space distortion effects on the other hand are sensitive to the following combination of parameters: the growth of structure $f$ times the amplitude of matter fluctuations at the scale of $8\,{\rm Mpc}\,h^{-1}$,

$$f(z) \times \sigma_8(z) \equiv f\sigma_8(z) = \Omega_{\rm m}^{\gamma}(z) \times \left[\int_0^\infty dq\, q^2 P_{\rm lin}(q;z) W_{\rm TH}(qR_8)\right]^{1/2} \tag{2.6}$$

where $\gamma = 6/11$ for General Relativity, $W_{\rm TH}$ is the top-hat function, which in this case smooths the fluctuations of the matter field in a scale of $R_8 \equiv 8\,{\rm Mpc}\,h^{-1}$ .

In practice, this is implemented within the fixed template fits as follows: the amplitude of matter fluctuations $\sigma_8$ is fixed by the template, which provides a 'standard amplitude' in a similar fashion to the standard ruler $r_{\rm d}$. The free parameter of the RSD compression is the growth rate $f$, which enters the galaxy power spectrum $P_g$ in redshift space following the TNS [29] model,

$$\begin{aligned} P_{\rm RSD}(k,\mu) = \left(1 + \left[k\mu\sigma_P\right]^2/2\right)^{-2} \big[\, & P_{g,\delta\delta}(k|\mathbf{\Omega}_{\rm fid}, \mathbf{b}) + 2f\mu^2 P_{g,\delta\theta}(k|\mathbf{\Omega}_{\rm fid}, \mathbf{b}) + f^2\mu^4 P_{g,\theta\theta}(k|\mathbf{\Omega}_{\rm fid}) \\ & + \ b_1^3 A^{\rm TNS}(k,\mu,f/b_1) + b_1^4 B^{\rm TNS}(k,\mu,f/b_1) \,\big] \ , \end{aligned} \tag{2.7}$$

where the density ('$\delta\delta$'), velocity ('$\theta\theta$') and cross ('$\delta\theta$') contributions to the galaxy power spectrum are obtained by applying two-loop Re-summed Perturbation Theory (2LRPT) to the fiducial power spectrum template as described in [28]. The power spectrum terms also depend on a set of bias parameters $\mathbf{b} = \{b_1, b_2, b_{s2}, b_{\rm 3nl}\}$ [30], where we assume the non-local bias parameters to follow the local Lagrangian prediction [31–33] of the co-evolution

model $b_{s2} = -4/7(b_1 - 1)$ and $b_{3\mathrm{nl}} = 32/315(b_1 - 1)$. We study the impact of relaxing these assumptions in Appendix A. The functions $A^{\mathrm{TNS}}, B^{\mathrm{TNS}}$ are provided by [29] and the Fingers of God effect (FoG, highly nonlinear RSD along the LOS on small scales, [34]) are modeled via the Lorentzian damping term in front of eq. (2.7) with free parameter $\sigma_P$.

Finally, we also take into account deviations from Poisson shot noise, $P_{\mathrm{Poisson}}$, in the monopole by setting into eq. (2.2)

$$g^{(\ell=0)}(\mathbf{X}_{\mathrm{RSD}}) = P_{\mathrm{Poisson}} \left[ \frac{A_{\mathrm{noise}}}{\alpha_\parallel \alpha_\perp^2} - 1 \right] , \tag{2.8}$$

where the $P_{\mathrm{Poisson}}$ values are provided by BOSS and eBOSS and $A_{\mathrm{noise}}$ is a free parameter for each redshift bin. Hence, the free parameters of the RSD compression consist of 3 physical parameters $\mathbf{\Theta}^{\mathrm{RSD}}_{\mathrm{phys}} = \{\alpha_\parallel, \alpha_\perp, f\sigma_8\}$ and 8 nuisance parameters $\mathbf{\Theta}^{\mathrm{RSD}}_{\mathrm{nuis}} = \left\{b_1^{\mathrm{N/S}}, b_2^{\mathrm{N/S}}, \sigma_P^{\mathrm{N/S}}, A_{\mathrm{noise}}^{\mathrm{N/S}}\right\}$ per redshift bin.

### 2.2.3 ShapeFit compression

The ShapeFit method is a simple, yet powerful, extension of the BAO+RSD compression, that has been developed and validated in [21], applied to BOSS DR12 data in [24] and successfully verified on high-volume N-body mocks [23] in the context of the blind PT challenge [22]. Below we briefly introduce the extra parameter of ShapeFit and the relevant cosmological interpretation.

First of all, it is important to stress that in the fixed template method what is fixed is actually not the amplitude $\sigma_8$ at a fixed scale $R_8$, but the amplitude $\sigma_{s8} = \sigma(R_{s8})$ at the scale

$$R_{s8} \equiv s \cdot 8\,\mathrm{Mpc}h^{-1}, \qquad s = \frac{r_{\mathrm{d}}}{r_{\mathrm{d}}^{\mathrm{fid}}} , \tag{2.9}$$

because all scales within the fixed template method can only be expressed in units of the standard ruler $r_{\mathrm{d}}$. Further explanation is provided in section 3.2 of [21] and eq. (3.6) therein.

Then, in addition to the RSD compression parameters from section 2.2.2, we include the shape parameter $m$ proposed in [21] (same parameterization and parameter values as eqs. (3.7) and (3.8) therein), which aims to capture information from the no-wiggle linear matter transfer function $T_{\mathrm{nw}}(k)$. Indeed, the shape of the transfer function for any model is predominantly determined by its slope in the transition region between the very large scales (where $T_{\mathrm{nw}}(k)$ is constant) and small scales (where it behaves like a power law). In particular, the scale-dependent slope reaches its maximum at the pivot scale $k_p = \pi/r_{\mathrm{d}} \sim 0.03\,h\mathrm{Mpc}^{-1}$, related to the standard ruler. In practice this scale is in a sweet spot: it is on large, linear scales where the scale dependence of the measured galaxy power spectrum is expected to be a faithful tracer of the transfer function shape and non-linearities are unimportant, yet it is a scale that is small enough to be sampled reasonably well by state-of-the-art and upcoming surveys.

Consequently, the measurement of $m$ can be interpreted within any model of choice as

$$m = \frac{d}{dk} \left( \ln \left[ \frac{\left(\frac{r_{\mathrm{d}}^{\mathrm{fid}}}{r_{\mathrm{d}}}\right)^3 \cdot T_{\mathrm{nw}}^2 \left( \left(\frac{r_{\mathrm{d}}^{\mathrm{fid}}}{r_{\mathrm{d}}}\right) \cdot k \right)}{T_{\mathrm{nw}}^{\mathrm{fid}\,2}(k)} \right] \right) \Bigg|_{k=k_p} . \tag{2.10}$$

Note that, within the ΛCDM model, $m$ does not depend on redshift, but a suite of physical processes might in principle introduce a (real or effective) redshift dependence [3]. Hence, when we fit the BOSS and eBOSS data, $m$ is recovered as a function of redshift. Only in the later stage, under the interpretation of $m$ within a specific model, redshift-independence is imposed.

Finally, our baseline ShapeFit parameter set for each redshift bin contains 4 physical and cosmologically interpretable parameters $\mathbf{\Theta}^{\rm ShapeFit}_{\rm phys} = \{\alpha_\parallel, \alpha_\perp, f\sigma_{s8}, m\}$ and the 8 nuisance parameters $\mathbf{\Theta}^{\rm ShapeFit}_{\rm nuis} = \left\{b_1^{\rm N/S}, b_2^{\rm N/S}, \sigma_P^{\rm N/S}, A_{\rm noise}^{\rm N/S}\right\}$ already introduced in section 2.2.2. The fits are carried out in the same fashion as described therein, so $P_{\rm ShapeFit}(k,\mu) = P_{\rm RSD}(k,\mu)$ where the linear no-wiggle transfer function is modified via the shape parameter $m$.

### 2.3 Reconstruction

It is customary to use the technique of reconstruction [8] to enhance the BAO peak detection within BAO fits.

The reconstructed catalogues are generated using the algorithm described by [9, 35] where the underlying dark matter density field is inferred from the actual galaxy field. This can be done efficiently only for tracers with sufficient high-density of objects, in our case the LRG samples. During the reconstruction process, each galaxy position is displaced to the position where this galaxy would reside if there were no bulk flows. This process successfully removes most of the non-linear effects from the BAO feature and enhances the detection of the BAO peak.

In this paper, as done in all similar SDSS analyses, we fit the reconstructed data with minimal information from the broadband clustering signal, attempting to isolate the signal of the BAO peak position along and across the LOS. This allows us to effectively constrain only $\alpha_\parallel$ and $\alpha_\perp$ from these catalogues.

The reconstruction process effectively produces a new catalogue of galaxies which we refer to as the post-reconstructed (or post-recon) catalogue. Conversely, the original catalogue takes the name of pre-reconstructed (pre-recon) catalogue. We treat the pair, reconstructed and pre-reconstructed catalogs as two separate but correlated catalogs; as such, the data-vectors derived from each can be combined using the appropriate correlation matrix, estimated from mock galaxy surveys as described in section 3.3.

### 2.4 Adopted naming convention for methodology and analysis approaches

In the rest of this paper we adopt the following naming conventions. We refer to BAO+RSD analyses as 'classic' approach and often use these two names interchangeably. This can be seen as a data compression that extracts the BAO and RSD signature into three purely late-time physical parameters, or physical variables, per redshift bin: $\{\alpha_\parallel, \alpha_\perp, f\sigma_{s8}\}$ [4]

The BAO signal is usually extracted from the reconstructed catalog. When this is not clear from the context we refer to this as BAO post-recon (as opposed to BAO pre-recon). The RSD analysis is always performed in the pre-recon catalogue. The BAO+RSD 'classic' analysis is extended by ShapeFit. We refer to this extended BAO+RSD+*Shape* as ShapeFit, interchangeably. In this case the full data set is compressed into four physical parameters per

[3] Effects of systematics or physics beyond the ΛCDM can leave signatures on $m$ see [24]

[4] The $f\sigma_{s8}$ convention was introduced by [21] only very recently, as it represents the quantity that the 'classic' fixed-template approach actually measures instead of $f\sigma_8$. As ref. [21] clearly explains, it is straightforward to convert between the two quantities at the cosmological interpretation step.

redshift bin, the forth being the shape parameter $m$, which is however not purely a late-time parameter. In the case that the shape parameter $m$ is varied during the template fit, but is *not* used for the cosmological interpretation, i.e., $m$ is marginalized but only the compressed variables representing BAO+RSD information are interpreted, we refer to that as 'classic' fit as well, because effectively the results are indistinguishable [21]. When the reconstructed catalogs are available, the full data set incorporates a stronger BAO signal by including a BAO post-recon analysis. This represents a further improvement to the original ShapeFit proposal and its applications to date [21, 23, 24], where the BAO signal was extracted exclusively from the pre-recon catalog.

## 3 Data

We use the publicly available data from the Sloan Digital Sky Survey-III [36, 37] and -IV [38, 39], corresponding to the respective observation campaigns, BOSS [40] and eBOSS [41]. Both campaigns make use of two multi-object spectrographs [42, 43] installed on the Apache Point Observatory 2.5-meter telescope located in New Mexico, USA [44] to carry out spectroscopic measurements from photometrically selected Luminous Red Galaxies (LRGs), Emission Line Galaxies (ELGs) and Quasar (QSO) samples, which have been used for both clustering and Ly-$\alpha$ studies.

In this paper we focus on re-analyzing only the LRG [45, 46] and quasar clustering [47] catalogues. For simplicity we do not re-analyse the Main Galaxy Sample (MGS) [48] and ELG samples [49], neither the Ly-$\alpha$ forest studies [50], which would require an effort beyond the scope of this paper.

However, in our cosmology fits later in section 5, we incorporate the eBOSS DR16 Lyman-$\alpha$ BAO-only compressed variable results of [50] obtained from their auto- (Ly$\alpha\times$Ly$\alpha$) and cross- (Ly$\alpha\times$QSO) spectra measurements at redshift $z_{\rm eff} = 2.33$. Collectively this data set probes the last 10 billion years of cosmic evolution through more than 2 million spectra.

To complement this 'late-time' data-sample for the purpose of cosmological interpretation in section 5, we include additional 'early-time' probes presented in section 3.4.

### 3.1 BOSS and eBOSS Data samples

We analyze the power spectrum multipoles –monopole, quadrupole and hexadecapole– of the catalogues listed in table 1, consisting of a total number of 1,723,267 unique objects, covering a redshift range of $0.2 < z < 2.2$. The goal is to perform a consistent BAO, RSD and ShapeFit-type of analysis which does not make *a priori* assumptions about the true underlying cosmological model or family of models, yet at the same time maximizes the amount of inferred cosmological information. These catalogues were originally analyzed by the BOSS and eBOSS team, with a strong focus on BAO and RSD features: [27, 51–56] analyzed the BOSS DR12 samples, [28, 57–59] analyzed the eBOSS DR16 samples. In addition, eBOSS also analyzed the ELG sample [49, 60, 61], which we do not use in this paper. Finally, these measurements were consistently combined by the BOSS and eBOSS collaboration in [62] and [12], respectively. Additionally to the standard RSD and BAO analyses, [63, 64] performed an analysis on BOSS data extracting also information on $\Omega_{\rm m}h^2$ from the shape of the power spectrum. Recently, further studies have been published focusing on analyzing BOSS and eBOSS data by fitting the full power spectrum to the prediction of a specific model (see for e.g., [16, 17, 65–68] just as few examples). Later in section 5.4.1 we compare our results to their findings.

| Catalogue | tracer | range | patch | objects | Ref |
|---|---|---|---|---|---|
| BOSS DR12 | LRG | $0.2 < z < 0.5$ | north | 429,182 | [45] |
| BOSS DR12 | LRG | $0.2 < z < 0.5$ | south | 174,819 | [45] |
| BOSS DR12 | LRG | $0.4 < z < 0.6$ | north | 500,872 | [45] |
| BOSS DR12 | LRG | $0.4 < z < 0.6$ | south | 185,498 | [45] |
| BOSS DR12 + eBOSS DR16 | LRG | $0.6 < z < 1.0$ | north | 255,741 | [46] |
| BOSS DR12 + eBOSS DR16 | LRG | $0.6 < z < 1.0$ | south | 121,717 | [46] |
| eBOSS DR16 | QSO | $0.8 < z < 2.2$ | north | 218,209 | [47] |
| eBOSS DR16 | QSO | $0.8 < z < 2.2$ | south | 125,499 | [47] |

**Table 1**. List of SDSS-III and -IV catalogues used in this paper and their number of objects. The total number of unique objects is 1,723,267, and the total effective volume is $2.82\,[\mathrm{Gpc}h^{-1}]^3$.

Throughout this paper we always assume that the northern and southern hemispheres are statistically independent, as it is the common practice. In the same fashion, we consider that the different redshift bins are independent, unless they are overlapping. This is the case for the BOSS DR12 redshift bins at $0.2 < z < 0.5$ and $0.4 < z < 0.6$, for which the covariance is inferred from a suite of mock galaxy surveys, as described in section 3.2. On the other hand the eBOSS DR16 LRG and quasar sample do overlap in the redshift range $0.8 < z < 1.0$, but their covariance can be neglected because of the low density of objects in this range (especially for quasars) as motivated in section 3.1 of [12].

The power spectra multipole measurements for the pre-recon LRGs and QSOs are displayed in figure 1 along with the BAO post-recon signal in the three LRG redshift bins as points with error-bars. Colored dashed lines are the best-fits of the model (see section 4). In the pre-recon panels the lower insets show residuals with respect to this model, whereas for the post-recon panel the two insets show the BAO feature in the monopole (isotropic BAO, upper inset) and in the $\mu^2$-moment (anisotropic BAO, bottom inset), defined as, $P^{(\mu^2)} \equiv P^{(0)} + 2/5P^{(2)}$. Black dotted lines in the bottom right panel display the best-fit 'mean' level for the broadband (no-wiggle) power. Note that the three LRG samples have been displaced vertically for visibility.

### 3.2 Galaxy mocks

Galaxy survey mocks are crucial to estimate the covariance matrices for the adopted data vectors. We employ a suite of galaxy mocks, matching the clustering properties and the sky-geometry of the data samples presented in table 1. These consist of $2 \times 2048$ realizations of the Multi-Dark Patchy mocks [69] for the northern and southern patches (hereafter Patchy mocks), for the two BOSS DR12 LRG samples. Additionally we consider $2 \times 1000$ realizations of the EZmocks [70] for the BOSS DR12 + eBOSS DR16 LRG sample, and for the eBOSS DR16 quasar sample, also for northern and southern patches. The EZmocks are generated from 5 different snapshots of large cubic periodic simulations based on the Zeldovich approximation [71], while the Patchy algorithm is based on 4 different snapshots of Augmented Lagrangian Perturbation Theory [72] and a bias scheme (hence the Patchy and EZmocks are often refereed to as fast mocks). Fast mocks are well suited for evaluating covariance matrices but their adoption to test or calibrate the accuracy of the adopted modeling of the signal require some care.

In total we have 12,192 mock realizations of the pre-reconstructed catalogues. Additionally, we run the reconstruction algorithm introduced in the previous section on the LRG

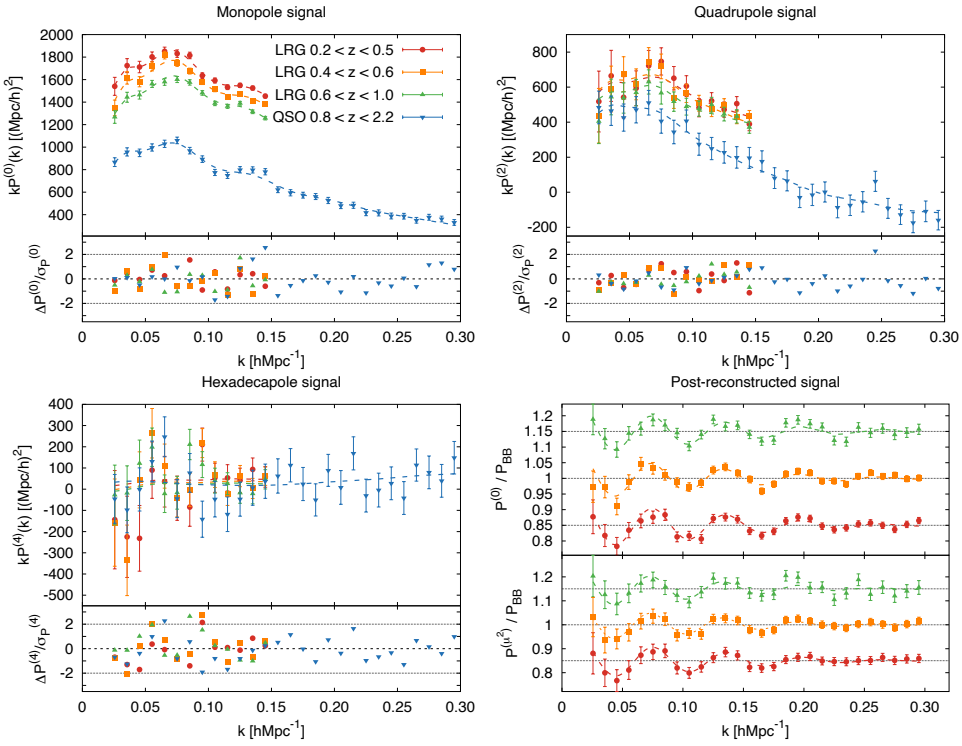


**Figure 1**. Measurements (points with error-bars) and best-fitting model (dashed lines with colors matching the data points). As labeled, the panels show the pre-reconstructed monopole (top-left), quadrupole (top-right) and hexadecapole (bottom-left) for the quasar sample and the three LRGs redshift bins. In each panel the bottom inset shows the residuals normalized by the *rms*. The bottom right panel shows the post-recon isotropic and anisotropic signals for the three LRGs redshift bins normalized by a smooth spectrum (broadband, BB) to highlight the BAO feature. Low (and high) LRG redshift bins are displaced vertically by $-(+)0.15$ for visibility.

| Cosmology | $\Omega_{\rm m}$ | $\Omega_{\rm b}$ | $h$ | $10 \times \Omega_\nu$ | $n_s$ | $A_s \times 10^9$ | $r_{\rm d}$ [Mpc] |
|---|---|---|---|---|---|---|---|
| Fiducial | 0.310 | 0.0481 | 0.676 | 1.400 | 0.97 | 2.040 | 147.78 |
| EZ | 0.307115 | 0.048206 | 0.6777 | 0 | 0.9611 | 2.1151 | 147.66 |
| Patchy | 0.307115 | 0.048206 | 0.6777 | 0 | 0.9611 | 2.1476 | 147.66 |

**Table 2**. List of cosmology models used in this paper: the reference or fiducial cosmology used for the fixed template (for convenience this is the same as the one used for the BOSS and eBOSS analyses in [11, 12]) and the true underlying cosmology of the two set of mocks used in this paper.

samples, obtaining an additional set of 10,192 realizations of the post-reconstructed mocks. Power spectrum multipoles are computed for each of these 22,384 mock realizations to extract a reliable power spectrum covariance, $C^{\ell,\ell'}_{k,k'}$, which allows us to individually fit each redshift-sample of both data catalogues and mock catalogues. The exact setup of these fits is described in section 3.3.

The true underlying cosmology of these mocks and the fiducial cosmology used to analyse them can be found in table 2. Additionally, in table 3 we list the mocks's true underlying

distance ratios, $D_H/r_{\rm d}$, $D_M/r_{\rm d}$, the expected values for the scaling parameters $\alpha_{\parallel,\perp}$, the true growth of structure parameter $f\sigma_{s8}$, and the expected shape parameter $m$ when these mocks are analyzed using the fiducial cosmology. Later in section 6 we will show how the actual analyses on the mocks perform and how close they are to their expected values.

| Redshift | $D_H/r_{\rm d}$ | $[\alpha_{\parallel}^{\rm exp}-1]\times 10^2$ | $D_M/r_{\rm d}$ | $[\alpha_{\perp}^{\rm exp}-1]\times 10^2$ | $f\sigma_{s8}$ | $m^{\rm exp}\times 10^2$ |
|---|---|---|---|---|---|---|
| 0.38 | 24.46 | −0.01 | 10.35 | −0.09 | 0.4736 | −1.15 |
| 0.51 | 22.64 | 0.03 | 13.41 | −0.07 | 0.4806 | −1.15 |
| 0.698 | 20.21 | 0.09 | 17.43 | −0.04 | 0.4659 | −1.15 |
| 1.48 | 12.92 | 0.21 | 30.11 | 0.04 | 0.3828 | −1.15 |

**Table 3**. True distances, expected dilations ($\alpha's$), growth rate and shape ($m$) when Patchy and EZ mocks are analyzed using the fiducial cosmology of table 2 as reference cosmology. Redshifts 0.38 and 0.51 correspond to the Patchy mocks true cosmology, whereas redshifts 0.698 and 1.48 to the EZmocks true cosmology. Note that the variables $D_H/r_{\rm d}$, $D_M/r_{\rm d}$ and $f\sigma_{s8}$ are not relative to the choice of the fixed-template used, and therefore do not have the index 'exp'.

### 3.3 Pre- and post-recon catalogue combination

The main results of this work (which are presented in section 4) are the constraints on the compressed physical variables $\mathbf{\Theta}_{\rm phys}^{\rm combined} = \{D_H/r_{\rm d}(z),\, D_M/r_{\rm d}(z),\, f\sigma_{s8}(z),\, m(z)\}^{\rm combined}$ obtained by consistently combining post-recon BAO and pre-recon ShapeFit results

$$\begin{aligned}&\mathbf{\Theta}_{\rm phys}^{\rm combined} = \mathbf{\Theta}_{\rm phys}^{\rm pre-recon} \cup \mathbf{\Theta}_{\rm phys}^{\rm post-recon} = \\ &\{D_H/r_{\rm d}(z),\, D_M/r_{\rm d}(z),\, f\sigma_{s8}(z), m(z)\}^{\rm pre-recon} \cup \{D_H/r_{\rm d}(z),\, D_M/r_{\rm d}(z)\}^{\rm post-recon}.\end{aligned} \tag{3.1}$$

For a combined post-recon BAO + pre-recon ShapeFit analysis it is crucial to correctly incorporate the covariance between the compressed variables from both types of fits. Especially the scaling parameters are expected to show a strong correlation for each pair of pre-recon and post-recon catalog. It is highly non-trivial to model this correlation analytically due to *i)* the non-linear nature of the reconstruction scheme and *ii)* the evident differences in the BAO and ShapeFit underlying models (especially the no-wiggle power spectrum decomposition).

One approach would be to infer the covariance matrix of the full combined data-vector $\langle P_\ell^{\rm pre-recon}(k,z) P_{\ell'}^{\rm post-recon}(k',z')\rangle$ and perform a simultaneous pre- and post-reconstruction fit directly from the multipoles. On the other hand, here we follow the approach taken by the BOSS and eBOSS team of combining the pre- and post-reconstruction results at the level of compressed variables: $\mathbf{\Theta}_{\rm phys}^{\rm pre-recon} \cup \mathbf{\Theta}_{\rm phys}^{\rm post-recon}$, which has the advantage of dealing with a smaller covariance matrix than the previous approach: $12\times 12$ elements for the BOSS LRG sample, and $6\times 6$ for the eBOSS LRG sample compared to $380\times 380$ and $190\times 190$ power spectrum elements, respectively. Recently, [73] showed how combining the pre- and post-recon information at the compressed variable stage only degrades the statistical precision on $5-10\%$ with respect to the simultaneous pre- and post-recon fits.

From the pre-recon catalogues, we extract a set of compressed elements, $\mathbf{\Theta}_{\rm phys}^{\rm pre-rec}(z)$ for each of the 12,192 pre-recon mock realizations; and from the post-recon catalogues a compressed set of elements $\mathbf{\Theta}_{\rm phys}^{\rm post-rec}(z)$ from the 10,192 realizations.

Using this information we are able to extract the block off-diagonal elements among different overlapping samples (for BOSS DR12 $0.2<z<0.5$ and $0.4<z<0.6$ samples), and among the pre- and post-reconstructed catalogues (for BOSS and eBOSS LRG samples).

All pre-recon ShapeFit fits to the mocks and the data are carried out with the parameter and prior settings stated in table 4. For the post-recon BAO fits we use the same priors on the scaling parameters and uninformative uniform priors on the nuisance parameters. For all fits we follow as close as possible the configuration chosen within the official eBOSS BAO and RSD analyses. In particular, we choose $k_{\rm max} = 0.15\,h{\rm Mpc}^{-1}$ for ShapeFit analyses of the LRG samples and $k_{\rm max} = 0.30\,h{\rm Mpc}^{-1}$ for the ShapeFit analysis of the QSO sample and the BAO analyses of LRGs. In all cases, we apply a maximum scale cut at $k_{\rm min} = 0.02\,h{\rm Mpc}^{-1}$ since larger scales are prone to observational systematics.

| Parameter (phys.) | Prior | Parameter (nuis.) | Prior |
|---|---|---|---|
| $\alpha_{\parallel}$ | $[0.5, 1.5]$ | $b_1$ | $[0, 20]$ |
| $\alpha_{\perp}$ | $[0.5, 1.5]$ | $b_2$ | [-20, 20] or $(5 \pm 2.5)$ |
| $f$ | $[0, 3]$ | $\sigma_P$ $[h^{-1}{\rm Mpc}]$ | $[0, 10]$ |
| $m$ | $[-3, 3]$ | $A_{\rm noise}$ | $(1 \pm 0.3)$ |

**Table 4**. Baseline prior ranges for the physical (left) and nuisance (right) parameters used for *ShapeFit*. Uniform priors are denoted as $[\min, \max]$, Gaussian priors as $(\text{mean} \pm \text{std})$. The non-local bias parameters $b_{s2}$ and $b_{\rm 3nl}$ are assumed to follow the local-Lagrangian prediction as function of $b_1$ as described in section 2.

### 3.4 Ancillary and external 'early time' data

Beside the large-scale structure datasets presented above we include the following complementary data, but only at the stage of interpreting the data in the light of cosmological models in section 5.

- **BBN:** By measuring the light elements' abundances of distant absorption systems – which serve as proxies for 'primordial' times and early-time physics– it is possible to infer the physical baryon energy density fraction $\omega_{\rm b}$ relying on our knowledge on nuclear reaction cross sections from solar observations, and our ability to correctly model the nuclear processes of Big Bang Nucleosynthesis (BBN) occurring only one second after the initial singularity. In this work we adopt the value $\omega_{\rm b} = 0.02235 \pm 0.00037$ from [12] (see also [74]) motivated by measurements of the relative deuterium to hydrogen abundance from [75] and solar fusion cross sections derived by [76].
- **Planck:** With its 2018 legacy data release [2] the Planck satellite mission provided the most detailed temperature and polarization maps of the cosmic microwave background (CMB) radiation ever observed. This relic radiation with mean temperature $T_{\rm CMB} = 2.7255K$ [77] was emitted when nuclei and electrons recombined $\approx$ 380,000 years after the Big Bang, at redshift $z_{\rm rec} = 1090$. We make use of the latest Planck data including the temperature and polarization auto and cross power spectra (TT, TE, EE, and lowE), as well as the Planck lensing measurements. CMB lensing measurements are certainly not early time, but this probe is used only in section 5 where model-dependence is re-introduced, so early-late separation is less important.

## 4 Model-Independent Results

Here we present the main results of this work, obtained from the ShapeFit analysis outlined in section 3.3. Our results are found in 4.1 and their comparison to the official eBOSS results is in section 4.2.

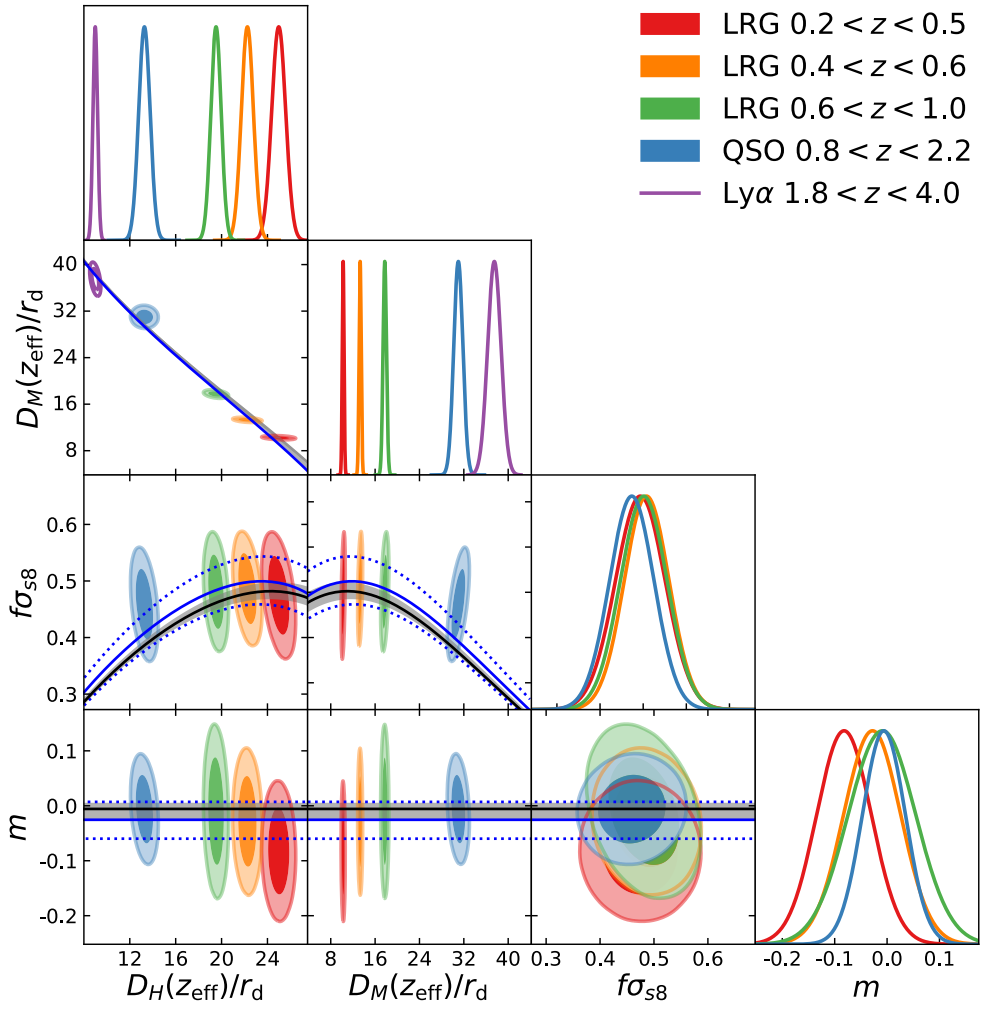


**Figure 2**. Main result of this paper: summary of the constraints on the compressed variables across all samples and redshifts. Filled, colored contours show the ShapeFit results. In the $D_H/r_{\rm d} - D_M/r_{\rm d}$ plane we also show the BAO-only result (empty, purple contour) obtained combining the Lyman-$\alpha$ auto- (Ly$\alpha\times$Ly$\alpha$) and cross- (Ly$\alpha\times$QSO) spectra measured at $z_{\rm eff} = 2.33$ by [50]. These constraints do not assume a $\Lambda$CDM model. For comparison, we highlight the prediction for the Planck $\Lambda$CDM best-fit and allowed $2\sigma$-range (black line, gray bands), and analogously the $\Lambda$CDM best-fit to the shown dataset including the corresponding $2\sigma$-range (blue line, blue dotted lines),

### 4.1 BAO, RSD and Shape evolution over 10 billion years of cosmic history

ShapeFit results on the compressed parameters $\{D_H/r_{\rm d}(z),\, D_M/r_{\rm d}(z),\, f\sigma_{s8}(z),\, m(z)\}$ are presented jointly for all analysed redshift bins as filled colored contours in figure 2. In addition, we show the BAO-only Lyman-$\alpha$ result of [50] (purple empty contour), which is included in our baseline dataset for cosmological interpretation in section 5. The strength of the presented compressed variables constraints relies on their model-independence. As inherent to the fixed

template fits described in section 2.2, throughout the fitting process no model assumptions or 'internal model priors' based on ΛCDM or any extensions to it are applied. And that is what makes this compressed dataset such a unique and powerful probe of the underlying nature of the Universe. Let us briefly specify the importance of model-independence for the different pieces of information represented by these compressed variables.

- **Geometry:** the geometrical information is traced via the AP anisotropy in units of the BAO scale, parameterized here by $D_H/r_{\rm d}(z)$ and $D_M/r_{\rm d}(z)$. Within any model, the parallel, $D_H(z)$, and perpendicular, $D_M(z)$, distances with respect to the LOS are directly linked to each other (see definition below eq. (2.1)). By allowing the parameters $D_H/r_{\rm d}(z)$ and $D_M/r_{\rm d}(z)$ to vary freely, without any imposed correlation, we are able to cross-check whether our fundamental assumptions (FLRW metric, homogeneous and isotropic expansion, etc.) hold.

- **Growth:** the information on the history of structure growth is traced via RSD, parameterized here by the rescaled velocity fluctuation amplitude $f\sigma_{s8}(z)$. Within Einstein's theory of General Relativity, the redshift evolution of this quantity is directly linked to the matter density $\Omega_{\rm m}$, which also determines the geometry of the universe. By allowing $f\sigma_{s8}(z)$ to vary freely, on one hand we decouple these model-interdependencies between geometry and growth, and on the other hand are able to verify the validity of Einstein's theory in the first place. Note that the RSD compression provides a unique dataset on (still not sufficiently explored) large scales, that may give rise to the detection (or ruling out) of certain modified gravity models.

- **Shape:** the *Shape* information, parameterized by $m(z)$, incorporates a number of physical effects already described before (see section 2.2.3). Most of these effects are of primordial, 'early-time', origin, and are not expected to leave an imprint on the *Shape* that varies with redshift, so $m(z) = m$. However, by constraining this parameter independently for each redshift bin, we may be able to find hints for models that have a redshift dependent impact on the *Shape*, for example due to a primordial non-Gaussianity signal $f_{\rm NL}$, or use it as a flag for possibly unaccounted observational systematics (see [24] for more details).

Having said that, we begin by comparing these model-independent constraints to the standard cosmological model, the flat ΛCDM model. In figure 2 we show the ΛCDM best-fit to our BOSS+eBOSS dataset as blue solid line, with the allowed $2\sigma$ region indicated via the blue dotted lines. We show the same (black line, grey bands) when considering Planck data only. See section 5 for the exact setup of our cosmology fits.

We can appreciate that the compressed constraints are in excellent agreement with the independent Planck-only ΛCDM best-fit. In particular, the model-independent BAO and AP constraints in the $D_H/r_{\rm d} - D_M/r_{\rm d}$ plane follow exactly the model prediction, which only allows a very tight relation. Therefore, there is no hint from this test of geometry that we would need to abandon our fundamental assumptions on the homogeneous and isotropic FLRW metric. The same holds for growth, for which the low redshift probes are in excellent agreement with the Planck ΛCDM prediction. However, as already noted by the eBOSS collaboration [12], we observe a small excess of clustering of $1.5\sigma$ for the QSO sample at $z = 1.48$. Although this is a rather mild anomaly (if any), we investigate the consistency between the LRG and QSO samples further in section 5.3. While our *Shape* measurements

are all consistent with Planck's ΛCDM prediction within $1\sigma$, we note a subtle tendency of decreasing $m$ with decreasing redshift.

In summary, the model-independent analysis of BOSS and eBOSS galaxies and Lyman-$\alpha$ delivers a unique cross-check of our fundamental assumptions and provides further powerful confirmation of the standard, flat ΛCDM model.

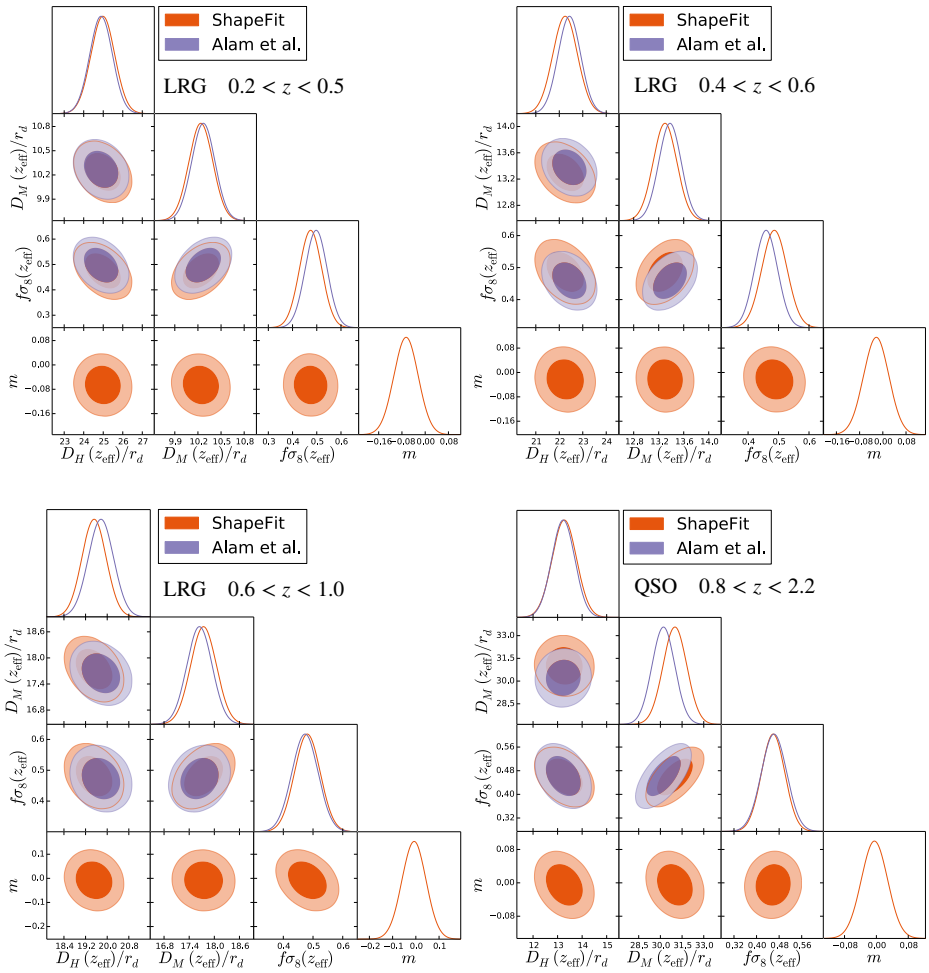


**Figure 3**. Comparison between the compressed variables inferred in this paper using ShapeFit (orange contours) and those from the official BOSS and eBOSS papers [11, 12] (purple contours) for all individual samples. ShapeFit constraints come from only using the Fourier space signal (the power spectrum), whereas the Alam et al. contours display the consensus between Fourier and configuration space. For the LRG panels both approaches (orange and purple contours) display the joint analysis of the full shape pre-recon and BAO post-recon signals. The numerical results are provided in table 5.

| Sample ($z_{\rm eff}$) | method. | $D_H/r_{\rm d}$ | $D_M/r_{\rm d}$ | $f\sigma_8$ | $m$ |
|---|---|---|---|---|---|
| LRG (0.38) | Alam et al. | $24.89 \pm 0.58$ | $10.27 \pm 0.15$ | $0.497 \pm 0.045$ | – |
| LRG (0.38) | *ShapeFit* | $24.98 \pm 0.61$ | $10.24 \pm 0.16$ | $0.462 \pm 0.045$ | $-0.066 \pm 0.042$ |
| LRG (0.51) | Alam et al. | $22.43 \pm 0.48$ | $13.38 \pm 0.18$ | $0.459 \pm 0.038$ | – |
| LRG (0.51) | *ShapeFit* | $22.26 \pm 0.53$ | $13.30 \pm 0.19$ | $0.482 \pm 0.041$ | $-0.023 \pm 0.044$ |
| LRG (0.698) | Alam et al. | $19.77 \pm 0.47$ | $17.65 \pm 0.30$ | $0.473 \pm 0.044$ | – |
| LRG (0.698) | *ShapeFit* | $19.54 \pm 0.45$ | $17.70 \pm 0.31$ | $0.478 \pm 0.043$ | $-0.008 \pm 0.052$ |
| QSO (1.48) | Alam et al. | $13.23 \pm 0.47$ | $30.21 \pm 0.79$ | $0.462 \pm 0.045$ | – |
| QSO (1.48) | *ShapeFit* | $13.27 \pm 0.50$ | $31.01 \pm 0.82$ | $0.458 \pm 0.041$ | $-0.005 \pm 0.033$ |

**Table 5**. Comparison of constraints on compression parameters quoted in Alam et al.[12] using the classic method, and the compression proposed by ShapeFit. For Alam et al. the results include both power spectrum and correlation function, whereas for ShapeFit only the power spectrum signal is used. In both cases the pre- and post-recon signals have been combined if available. Figure 3 displays the triangle plots for the same samples. Note that the LRG samples at $z_{\rm eff} = 0.38$ and 0.51 are correlated. The full covariance matrices for all these samples can be found in Appendix E.

### 4.2 Comparison with official BOSS and eBOSS results

As a next step we compare our ShapeFit constraints with the official BOSS and eBOSS results from [11, 12]. We compare to their consensus results obtained from Fourier and configuration space for pre-recon and post-recon catalogs where available, while our combined pre- and post-recon constraints are obtained from Fourier Space only.

The compressed variables constraints are shown in figure 3 and table 5 for each individual sample for ShapeFit (orange contours) and for the classic approach used by BOSS and eBOSS (purple contours). We find that both approaches are in excellent agreement only showing small deviations of order $0.2\sigma$ and at most $1\sigma$ in $D_M/r_{\rm d}$ for the quasars. We see that the shape parameter is nearly uncorrelated with the other parameters, therefore we expect its effect on their error bars to be negligible. The ShapeFit error bars are in very good agreement with the official reported errors, although these are constructed in different way as described above: for the official BOSS and eBOSS results there is an information gain coming from the correlation function signal, although this might be partially compensated by the inclusion of a systematic error contribution at the level of the compressed variables, which we do not consider here.[5] However, note that most of the systematic error budget arises from modeling the two-point statistics and the choice of fiducial cosmology (see for e.g., fig. 14 of [78]), which in ShapeFit is already accounted for via the shape parameter $m$.

We conclude that our ShapeFit constraints on $\{D_H/r_{\rm d}, D_M/r_{\rm d}, f\sigma_8\}$ are consistent with the official results and can be safely used for cosmological parameter estimation. In this work we are interested in using this set of parameters together with the shape $m$ for cosmological interpretation, see section 5. For further details on the ShapeFit systematic budget including the systematic error on $m$, see section 6.2.

## 5 Re-introducing model-dependence: Cosmology Interpretation

The advantage of parameter compression methods such as ShapeFit is that the whole power spectrum analysis presented before, from the performance on mocks towards the systematic budget determination, is performed only once, without the need to repeat it for every

[5] We explore the potential systematic error contribution of ShapeFit in section 6.

cosmological model in consideration. Therefore, once the three (four) compressed variables are obtained with the classic fit (ShapeFit), their cosmological interpretation is much more streamlined than for FM Fits.

In this section we are interested in the cosmological implication of the ShapeFit results for the BOSS and eBOSS LRGs and QSOs samples described before, with particular focus on the information gain provided by the new shape parameter $m$ with respect to the classic BAO+RSD approach.

The varied parameters and prior ranges for all the cosmological models considered are provided in table 6.

We start by considering the baseline ΛCDM model in section 5.1 and proceed with the extended cosmologies in section 5.2. We investigate the cosmological implications of the individual LSS tracers (LRGs, QSOs and Ly-$\alpha$) in section 5.3 and compare our results to other fitting approaches in section 5.4.

| Type | Parameter (phys.) | Prior | Usage |
|---|---|---|---|
| Baseline ΛCDM | $\omega_{\rm b}$ | $[0.005, 0.04]$ | Always |
| | $\omega_{\rm cdm}$ | $[0.001, 0.99]$ | Always |
| | $h$ | $[0.2, 2]$ | Always |
| | $\ln\left(10^{10} A_s\right)$ | $[0.1, 10]$ | Always |
| | $n_s$ | $[0.5, 1.5]$ | With Planck |
| | $\tau_{\rm reio}$ | $[0.004, 1.0]$ | With Planck |
| Extensions to ΛCDM | $\Sigma m_\nu$ (eV) | $[0.0, 1.0]$ | Section 5.2.1 |
| | $N_{\rm eff}$ | $[0.0, 9.0]$ | Section 5.2.2 |
| | $\Omega_{\rm k}$ | $[-0.8, 0.8]$ | Section 5.2.3, |
| | $w_0$ | $[-1.5, -0.0]$ | Section 5.2.4 |
| | $w_0 + w_a$ | $[-5.0, -0.0]$ | Section 5.2.4 |

**Table 6**. Prior ranges for the cosmological parameters. Whenever the extended parameters are not varied, they are fixed to $\Sigma m_\nu = 0.06\,\text{eV}$, $N_{\rm eff} = 3.046$, $\Omega_{\rm k} = 0$, $w_0 = -1$, $w_a = 0$. The reionisation optical depth $\tau_{\rm reio}$ and scalar tilt $n_s$ are only varied when Planck data is included in the chains, otherwise the scalar tilt is fixed to the fiducial value $n_s^{\rm fid} = 0.97$

### 5.1 Baseline ΛCDM

We show our baseline results for the classic fit (green), that includes the BAO+RSD information, and for ShapeFit (blue), which adds the *Shape* information, in figure 4. The cosmological constraints from the BOSS+eBOSS surveys alone are shown as empty, dotted contours, while the filled, continuous contours include the BBN-motivated Gaussian prior on $\omega_{\rm b}$ introduced in section 3.4. For comparison, we show the ΛCDM constraints from Planck alone (empty, black contours), which are in good agreement with the LSS ones.

The two panels of figure 4 correspond to the same cosmological runs, but for different parameter bases. On the left, we show the basis of varied parameters, while on the right we show those derived parameters that are more closely related to the physical parameters our LSS dataset is sensitive to, presented in section 4.1. Strikingly, the left panel parameters are quite unconstrained from LSS data alone. Both for the classic fit and for ShapeFit, there is a perfect degeneracy between $\omega_{\rm b}, \omega_{\rm cdm}$ and $h$ that can only be broken via the BBN prior or other early-time information. On the other hand, the right panel's parameters are almost insensitive to the BBN prior, which can be understood as follows.

The sound horizon scale in units of the Hubble constant today, $hr_{\rm d}$, is measured from the isotropic BAO information. Therefore, its constraints are nearly identical for the classic fit and ShapeFit. This is not the case for $\Omega_{\rm m}$, which is determined within the classic approach from the anisotropic BAO and AP effect alone, whereas for ShapeFit there is additional information coming from the shape $m$. As argued in [24] this parameter effectively constrains the combination $\Gamma_0 = \Omega_{\rm m} h$, which is also known as 'shape parameter' [6, 79, 80]. However, this parameter combination does not take into account the shape sensitivity to $\omega_{\rm b}$ due to the baryon suppression [81]. Therefore, in the right panel we show the more complex, scale-dependent 'effective shape parameter' $\Gamma_{\rm eff}(k)$ defined in eq. (30) of [6] evaluated at the pivot scale $k_p$ introduced in section 2.2.3. This parameter is constrained very well by ShapeFit, which propagates into an improvement of $\Omega_{\rm m}$ constraint with respect to the classic fit, even without imposing the BBN prior. Interestingly, we do not observe the same for the Hubble constant $h$, which for LSS data alone remains unconstrained even after adding $m$. Finally, the matter fluctuation amplitude $\sigma_8$ is well determined by both the classic fit and ShapeFit through our RSD measurement of the velocity fluctuation amplitude $f\sigma_{s8}$. Note that this constraint is completely independent of the BBN prior, whereas the constraint on the primordial fluctuation amplitude $A_s$ shows a certain $\omega_{\rm b}$-dependence. This is due to the fact that our LSS maps are sensitive to the total matter power spectrum amplitude and are not able to disentangle whether the amplitude is of primordial origin from inflation, from early time evolution of the transfer function (for example related to the baryon suppression at the time of photon decoupling) or attributed to the late-time growth of structures. Therefore, $\sigma_8$ is the natural variable to express the net clustering amplitude.

Another interesting aspect, related to the two parameter bases shown in the left and right panel of figure 4 respectively, is that for Planck alone the situation is inverted. While Planck constraints on physical densities $\omega_{\rm b}, \omega_{\rm cdm}$ and the Hubble parameter $h$ are much tighter than in the LSS case, they are of comparable size when considering the absolute matter density $\Omega_{\rm m}$ and the sound horizon in units of the Hubble constant $hr_{\rm d}$, which are strongly degenerate in the Planck case. It is interesting to note that the constraint on $\Omega_m$ from LSS alone (with a very weak $n_s$ prior, see appendix C) is more stringent than that from Planck, yet well in agreement. This demonstrates the complementary nature between the shown early-time and late-time datasets.

We conclude that the shape $m$ delivers a significant piece of information leading to a strong improvement in ΛCDM parameter constraints. This is related to the findings of [82] who obtain a constraint on $H_0$ from the galaxy power spectrum marginalizing over the sound horizon scale. Here, for example, for $\Omega_{\rm m}$ we find an improvement of factor 2 when including the *Shape*. A breakdown of the combined constraining power shown here into the contributions from individual tracers can be found in section 5.3. The exact numbers and how they compare to other approaches can be found in table 7 of section 5.4.

### 5.2 Extensions to the baseline ΛCDM model

We consider a variety of extensions to the baseline ΛCDM model in a similar way as presented in the official BOSS and eBOSS cosmology papers [12, 83]. Similar to those works, we focus on models that involve neutrino physics (sections 5.2.1 and 5.2.2) and models that change the geometry and growth history of the universe, such as curvature (section 5.2.3) and varying dark energy (section 5.2.4).

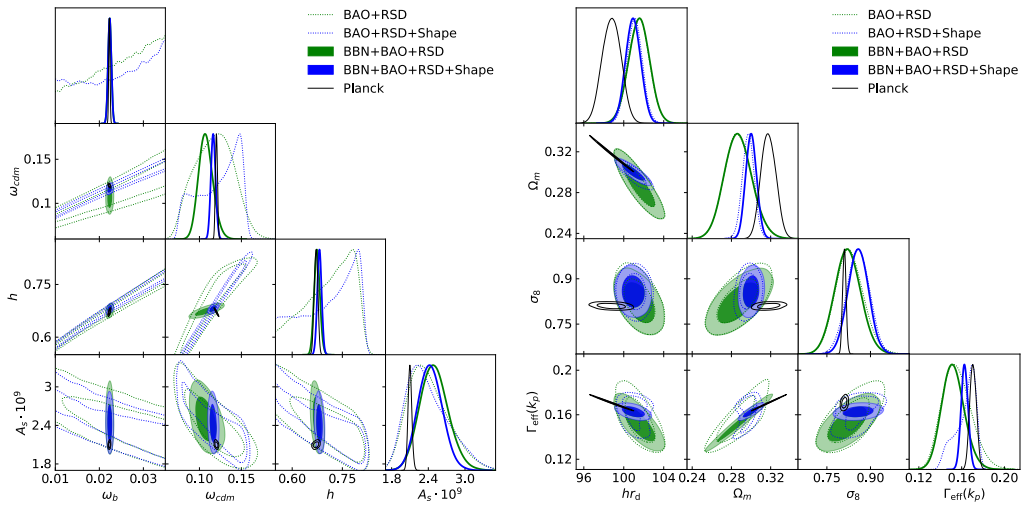


**Figure 4**. Baseline ΛCDM results for the classic fit (BAO+RSD information, green contours), ShapeFit (BAO+RSD+*Shape* information, blue contours) in comparison with Planck (black contours). The filled contours include a BBN-motivated Gaussian prior on $\omega_{\rm b}$, while the dotted contours span the full uniform prior range of the baryon density. The left panel shows the results in the basis of the varied parameters, while the right panel shows the derived cosmological parameters, that are more naturally constrained by our LSS dataset. As a result, the parameters on the right panel are (almost) insensitive to the BBN prior, which is not the case for those on the left panel.

### 5.2.1 Massive neutrinos

The measurement of the sum of neutrino masses $\Sigma m_\nu$ is of major interest for the scientific community and within reach for upcoming (and ongoing) cosmological surveys. The presence of massive neutrinos, or any relativistic, weakly-interacting particle species, that becomes non-relativistic once the temperature of the universe drops below its mass (also referred as 'warm dark matter') leaves a unique imprint on cosmological observables. If correctly modeled and verified for different probes, these features (described below in more detail) can lead towards the measurement of the sum of neutrino masses.

We know that neutrinos must possess a non-zero mass from neutrino oscillation experiments, that measure the mixing angle between neutrino flavours from different neutrinos sources, such as from solar and atmospheric [84], reactor [85] and accelerator [86] origins. The measured mixing angles can be translated into squared mass differences between the flavours. Although these measurements do not probe the absolute mass scale of neutrinos, they can be used to construct the minimal sum of neutrino masses allowed by the oscillation data given that the lightest neutrino has a mass of zero. Since the oscillation data is primarily sensitive to the *squared* mass differences (and not their sign), there are two possible mass hierarchies: either the smaller mass split occurs between the lightest and the second-to-lightest neutrino (normal hierarchy) or it occurs between the heaviest and the second-to-heaviest neutrino (inverted hierarchy). For the normal (inverted) hierarchy, the minimum neutrino mass sum consistent with the oscillation data is $\Sigma m_\nu > 0.0588\,\text{eV}$ ($\Sigma m_\nu > 0.0995\,\text{eV}$) [87].

While from particle physics experiments it is very challenging to measure the absolute neutrino mass scale -the strongest and most recent 95% upper limit of $\Sigma m_\nu < 2.4\,\text{eV}$ comes

from the KATRIN experiment [88]- cosmological surveys are currently beating this limit by a an order of magnitude. Intriguingly, the state-of-the-art 95% upper limit on the sum of neutrino masses coming from the combination of Planck with BOSS+eBOSS BAO and RSD data of $\Sigma m_\nu < 0.102\,\mathrm{eV}$ [12] is already very close to the lower limit predicted by neutrino oscillation experiments assuming the inverted hierarchy. Upcoming surveys will most probably either exclude the inverted hierarchy, detect a non-zero neutrino mass sum or even discriminate between neutrino masses of the individual flavours. However, any potential finding in this direction depends on the exact choice of underlying model. Therefore, it is crucial to verify the implications of non-zero neutrino masses for independent probes with robust control over any systematic effects that may arise from each probe. In this work, we introduce the shape of the power spectrum, parameterized through $m$, as an additional observable that may serve (among others) as a smoking gun towards a non-zero neutrino mass detection.

The implications of non-zero neutrino masses for cosmology are manifold and rather complex. Their subtle impact on cosmological observables has been reviewed in [89]. In a nutshell, there are three main effects. First, the transition of neutrinos from relativistic to non-relativistic species leads to a change in geometry. Depending on whether the total matter density today $\omega_\mathrm{m} = \omega_\mathrm{cdm} + \omega_\mathrm{b} + \omega_\nu$ or the cold dark matter + baryon density $\omega_\mathrm{cb} = \omega_\mathrm{cdm} + \omega_\mathrm{b}$ is kept fixed, either the early-time scale of equality between matter and radiation $k_\mathrm{eq}$ changes (in the former case) or the late-time distance ladder parameterised for example through the Hubble parameter $h$ changes (in the latter case). This effect can be measured by combining CMB with BAO data for example. Second, since the massive (but still very light) neutrinos have much higher thermal velocities than ordinary matter, they do not cluster on scales smaller than their free-streaming scale. As a consequence, they wash out small-scale perturbations and slow down the growth of structures. This has a measurable impact on the redshift dependence of the growth rate, assessed by RSD data. The third effect is related to the second one. Since massive neutrinos do not only change the redshift-dependence of the growth rate, but also its scale dependence, they induce a step-like suppression of the matter power spectrum at their free streaming scale. This has a measurable impact on the shape parameter $m$.

So far, this third effect has not been taken into account within the classic approach, for a number of reasons. As shown in figure 1 of [21], the step-like suppression induced by massive neutrinos is very degenerate with the other ΛCDM parameters, in particular combinations of $\omega_\mathrm{cdm}, n_s, \sigma_8$, at least within the restricted wavenumber range of $0.02 < k\,[h\mathrm{Mpc}^{-1}] < 0.15$ usually investigated in galaxy clustering. Moreover, the marginalization over bias parameters, the FoG effect, etc., make it even harder to extract robust neutrino mass information from the data. Finally, the BAO+RSD information is considered more robust than the *Shape* information, which is subject to systematic uncertainties of observational (see section 6) and modeling nature, such as unaccounted for scale dependent bias, relativistic effects or primordial non-gaussianity (see [24] for the latter case). Using the ShapeFit framework, where the shape $m$ is measured directly with nuisance parameters already marginalized out and the possibility to apply to it any custom systematic error budget, it is more convenient and intuitive to test the neutrino-mass-induced shape dependence of the power spectrum.

We assume three degenerate neutrinos with effective number of neutrino species $N_\mathrm{eff} = 3.046$, and with the mass split equally among them. As in the classic BAO+RSD approach by [12], we compare our $f\sigma_{s8}$ measurements to the model prediction of the 'cold' velocity fluctuation amplitude $f\sigma_8^\mathrm{cb}$, obtained from the cold dark matter + baryon power spectrum $P_\mathrm{cb}$

instead of the total matter power spectrum $P_{\rm m}$. This quantity has been shown to represent the galaxy clustering amplitude in a more universal way, since galaxies are tracers of the cold+baryon density field, that excludes the neutrino perturbations [90, 91]. Accordingly, we obtain theoretical predictions for the shape $m$ consistent with the 'cb' prescription by using the cold+baryon transfer function in the nominator of eq. (2.10).

We show our constraints on $\Sigma m_\nu$ and its correlation with $\Omega_{\rm m}$, $\sigma_8$, and the shape $m$ in figure 5. Again, green and blue contours represent the classic fit and ShapeFit respectively. Parameter constraints derived from Planck alone are shown in black. The left panel shows parameter constraints for LSS+BBN data, while in the right panel LSS data is combined with Planck.

From the left panel we see that the BBN+BAO+RSD data alone can not constrain neutrino mass, due to its degeneracy with fluctuation amplitude $\sigma_8$. However, this degeneracy is broken by the slope $m$. Hence, ShapeFit is able to provide an upper 95% confidence level bound on the neutrino mass of $\Sigma m_\nu < 0.40\,\text{eV}$, which is the tightest neutrino mass bound ever obtained from LSS data (in combination with the BBN prior). From Planck alone we find $\Sigma m_\nu < 0.24\,\text{eV}$, consistent with [2].

Note that the ShapeFit constraint relies on a fixed fiducial value of the primordial tilt $n_s$. Letting it vary freely would completely degrade the ShapeFit neutrino mass constraint, since the slope variation induced by $\Sigma m_\nu$ is degenerate with $n_s$ on the scales we consider here. Planck on the other hand provides the angular power spectrum shape on a huge range of scales, so that the scale-independent tilt can be inferred with high precision.

In the right panel we show the case where Planck data and the BOSS+eBOSS data are fitted jointly. In this case the neutrino mass constraints become much tighter due to the complementary information Planck provides with respect to the LSS surveys. For our Planck+BAO+RSD dataset we find $\Sigma m_\nu < 0.085\,\text{eV}$. Note that this is slightly smaller than the value reported in [12], we have verified that this is due to the fact that we exclude the MGS and ELG samples from our dataset.

Interestingly, this upper bound barely changes when adding the shape $m$, yielding $\Sigma m_\nu < 0.082\,\text{eV}$, as the additional information within the LSS shape is superseded by the Planck data. This can also be seen from figure 2 and has already been shown in figure 2 of [21]. We conclude that for this specific extension to the ΛCDM model the shape information from our BOSS+eBOSS dataset does not add much to the information that Planck provides. This also holds for all the other extended models analysed in this section. Therefore, in what follows, we focus on the cosmological constraints obtained from our dataset without Planck.

Nevertheless, $\Sigma m_\nu < 0.082\,\text{eV}$ at 95% C.L. implies that the minimum mass for the inverted hierarchy is excluded at 98% C.L. (assuming Gaussian errors).

### 5.2.2 Varying effective number of neutrino species

Another degree of freedom related to neutrinos is the effective number of neutrino species $N_{\rm eff}$. Given the standard model of particle physics and the measurement of Z-boson decay, we know that three neutrino species exist. However, we can not exclude that extra neutrino species (or other weakly interacting particles) existed in the early universe, when the temperature was higher than the energy range probed by laboratory experiments.

In this case the radiation density comprised of photons and neutrinos would change as

$$\omega_r = \omega_\gamma + \omega_\nu = \left[1 + \frac{7}{8}\left(\frac{4}{11}\right)^{4/3} N_{\rm eff}\right]\omega_\gamma \,. \tag{5.1}$$

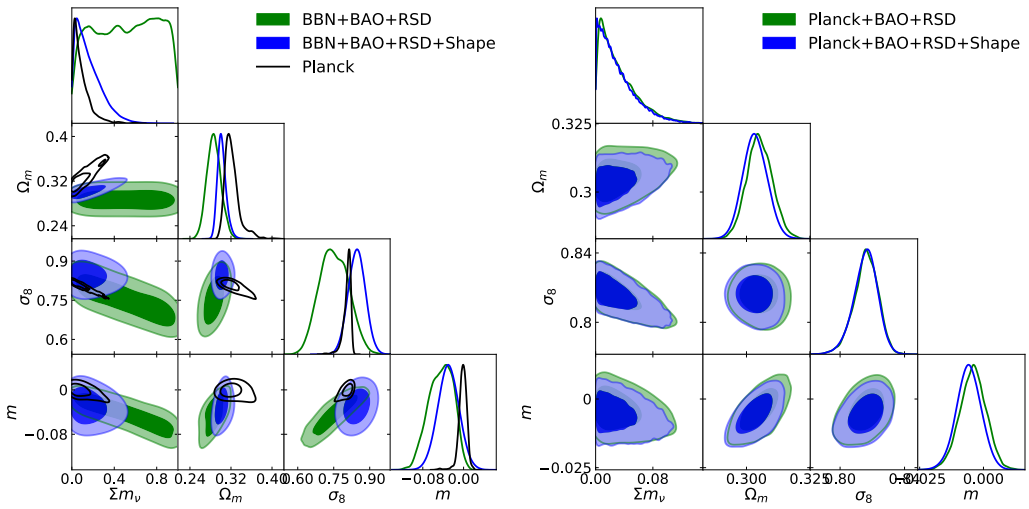


**Figure 5**. Neutrino mass,$\Sigma m_\nu$, bounds for different data combinations and $\Sigma m_\nu$ degeneracy with $\Omega_\mathrm{m}$, $\sigma_8$, and the power spectrum slope at the pivot scale, $m$. Results obtained with the classic BAO+RSD Fit are shown in green, while the ShapeFit results are shown in blue. In the left panel we compare both types of fit when combined with the BBN-motivated prior on $\omega_\mathrm{b}$ and with primordial tilt $n_s$ fixed to the reference value. For comparison, we also show the constraints obtained from Planck alone in black. In the right panel we show the results combined with Planck, allowing $\omega_\mathrm{b}$ and $n_s$ to vary freely.

Varying the parameter $N_\mathrm{eff}$ thus induces a change in the sound horizon $r_\mathrm{d}$ and the scale of matter and radiation equality $k_\mathrm{eq}$ while keeping the photon density (and therefore the CMB temperature fixed). At the background level, this effect is completely degenerate with the Hubble parameter $h$. Hence, extra relativistic degrees of freedom could help to reconcile the Hubble tension. However, this degeneracy is broken at the perturbation level, where $N_\mathrm{eff}$ has a variety of subtle effects. Current CMB observations from Planck strongly disfavor deviations from 3 neutrino species, from our Planck dataset we find $N_\mathrm{eff} = 2.941 \pm 0.45$ (95%) in agreement with [2].

We investigate whether ShapeFit is able to track the effect of $N_\mathrm{eff}$ on the matter power spectrum, which are *i)* a smooth tilt in the transition region between the small and the large scale limit and *ii)* a modulation of the BAO amplitude. ShapeFit is sensitive to effect *i)* through $m$, but not to effect *ii)*.

From the left panel of figure 6 we see that including $m$ reduces the cosmological parameter space allowed by LSS data. But neither the classic fit nor ShapeFit (both including the BBN-motivated prior on $\omega_\mathrm{b}$) are able to constrain $N_\mathrm{eff}$ due to its degeneracy with $h$. In fact, effect *i)* is a pure background effect coming from the shift in $k_\mathrm{eq}$. To capture effect *ii)* as well we would need to extract the BAO amplitude from the data with ShapeFit, which is a challenging task due to non-linear effects, such as the BAO wiggle suppression, that need to be modeled accurately and cross-checked to be free of observational systematic effects. Note that we do not consider here the dependence of the baryon density $\omega_\mathrm{b}$ and the Helium fraction $Y_\mathrm{He}$ on $N_\mathrm{eff}$ within the theoretical BBN prediction. We leave this, and a more complete fitting procedure including the BAO wiggle amplitude for future work.

When combining our LSS dataset with Planck we obtain $N_\mathrm{eff} = 3.16 \pm 0.41$ (95%) for

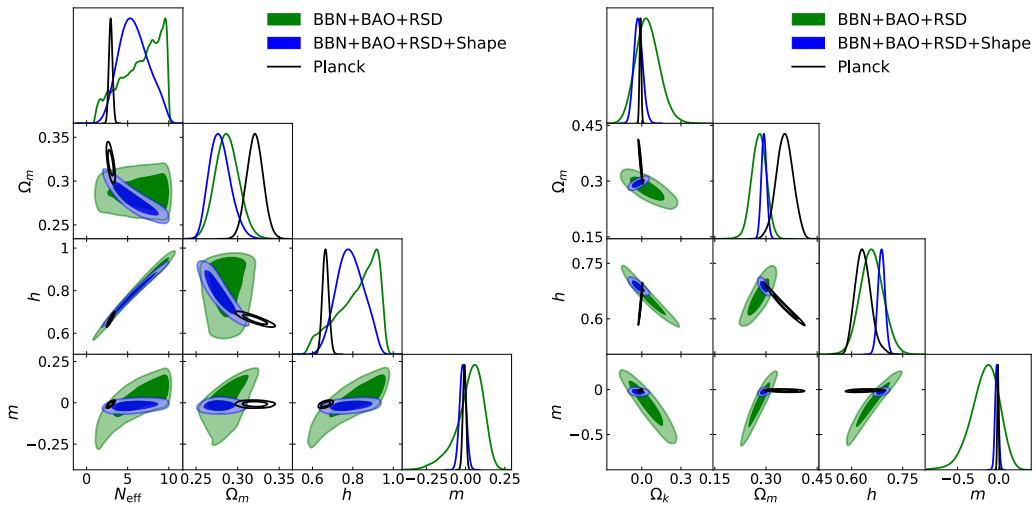


**Figure 6**. Left panel: Cosmological constraints in the case of allowing free number of effective degrees of freedom. Right panel: Cosmological constraints in the case of allowing for curvature.

the classic fit and $N_{\rm eff} = 3.12 \pm 0.38$ (95%) for ShapeFit, both consistent with the official Planck+BAO constraint $N_{\rm eff} = 2.99 \pm 0.33$ (95%) from [2].

### 5.2.3 Curvature

Spatial curvature is usually parameterised by the curvature energy density parameter $\Omega_k$ today entering the Friedmann equation and Hubble expansion rate with a redshift dependence proportional to $(1 + z)$. Also, non-zero curvature changes the geometry and as such the comoving angular diameter distance $D_M^{\Omega_k=0}$ (already defined in section 2.2 below eq. (2.1)) as

$$D_M^{\Omega_k} = \frac{c}{H_0} S_k\left(\frac{D_M^{\Omega_k=0}}{c/H_0}\right), \qquad S_k(x) = \begin{cases} \sin\left(\sqrt{-\Omega_k}x/\sqrt{-\Omega_k}\right) & \Omega_k < 0, \\ x & \Omega_k = 0, \\ \sinh\left(\sqrt{\Omega_k}x/\sqrt{\Omega_k}\right) & \Omega_k > 0\ . \end{cases} \tag{5.2}$$

While, when combining LSS data with Planck, the evidence for a flat universe with $\Omega_k = 0$ is striking [2, 12] (see also table 9), here we are particularly interested in the constraining power of our LSS data set on $\Omega_k$ and whether the shape $m$ helps to break its degeneracy with $\Omega_{\rm m}$ and $h$.

In the right panel of figure 6 we show the constraints on these cosmological parameters along with their degeneracy with $m$ for the classic fit (green), ShapeFit (blue) and Planck only (black). The latter provides the tightest constraint on curvature of $\Omega_k = -0.0104 \pm 0.0067$. Note that we also include the Planck lensing signal here, which is in agreement with a flat universe and strongly improves constraints with respect to considering the Planck temperature and polarization spectra only leading to $\Omega_k = -0.043 \pm 0.017$. For the classic fit we find $\Omega_k = 0.047^{+0.083}_{-0.099}$ and for ShapeFit $\Omega_k = -0.027^{+0.032}_{-0.037}$ delivering an improvement in constraining power of a factor $\sim 2.7$. As can be seen in the figure, this improvement comes from the measurement of the shape $m$.

All these results are consistent with zero curvature and their combination (either Planck+ Classic or Planck + ShapeFit) gives $\Omega_k = -0.0015 \pm 0.0016$. So, the Planck *Shape* information dominates over the LSS *Shape* constraint and the BAO+RSD measurements alone are sufficient due to their high degree of complementarity to Planck enabling to lift most of the parameter degeneracies.

Note that curvature only affects the geometry and growth of the universe, it does not leave any imprint on the galaxy power spectrum slope. Still, the slope measurement matters, due to its sensitivity to $\Omega_\mathrm{m}$, which breaks the degeneracy with $\Omega_k$. But once Planck is added, the shape $m$ does not further improve constraining power.

#### 5.2.4 Varying Dark Energy

The most important science driver behind any state-of-the-art spectroscopic survey is to unravel the nature of dark energy, which delivers the force behind the accelerated expansion of the universe observed by many disparate probes. Currently, this accelerated expansion is in accordance with the General Relativity prediction of Einstein's cosmological constant $\Lambda$, but a microscopic explanation for this constant term in the Friedman equation, leading to a constant expansion rate, does not exist yet.

The most general macroscopic description for this term relies in the assumption of a fluid called dark energy with negative equation of state paramter $w = p_\mathrm{DE}/\rho_\mathrm{DE}$ relating the dark energy pressure $p_\mathrm{DE}$ and density $\rho_\mathrm{DE}$. The dark energy equation of state parameter $w$ governs the evolution of the universe at late times. In general, the scale-factor dependence of the energy density of any fluid with constant equation of state is $\rho(a) \propto a^{-3(1+w)}$. For $w < -1/3$, it describes a fluid giving rise to accelerated expansion. For $w = -1$ in particular, the dark energy density $\rho_\mathrm{DE}$ remains constant yielding the same expansion rate as predicted by a cosmological constant $\Lambda$.

In this section we consider three cases for the evolution of the equation of state $w(a)$ with scale factor $a$,

$$w(a) = \begin{cases} -1 & (\Lambda\mathrm{CDM}), \\ w_0 & (w\mathrm{CDM}), \\ w_0 + w_a(1-a) & (w_0 w_a \mathrm{CDM}), \end{cases} \tag{5.3}$$

where the first case is consistent with $\Lambda$CDM, the second exhibits an equation of state constant with cosmic time and the third allows for a time dependence phenomenologically motivated by [92, 93].

We show the parameter constraints for the ($w$CDM) and ($w_0 w_a$CDM) cases in the left and right panel of figure 7, respectively. Again, we display the results of the classic fit in green, ShapeFit in blue and Planck in black, where for Planck we include the full temperature, polarization and lensing data, as described in section 3.4.

Our findings are analog to the case of allowing for curvature in section 5.2.3. Although varying the dark energy equation of state does not lead to a change in galaxy power spectrum shape,[6] the measurement of $m$ breaks the degeneracy of $w_0$ with $\Omega_\mathrm{m}$ and $h$. Hence, with LSS-only information, ShapeFit yields a constraint on the equation of state of $w_0 = -1.007^{+0.083}_{-0.073}$, is nearly as precise as that from the combination of Planck with the classic BAO and RSD ($w_0 = -1.090^{+0.050}_{-0.041}$), and a factor $\sim 1.5$ improvement with respect to the classic fit result of $w_0 = -0.81 \pm 0.12$.

[6] In fact, varying dark energy does change the shape of the power spectrum at the scale of equality between matter and dark energy. However this scale is of order $k \lesssim 10^{-3}\,h/\mathrm{Mpc}$ and is thus not observable.

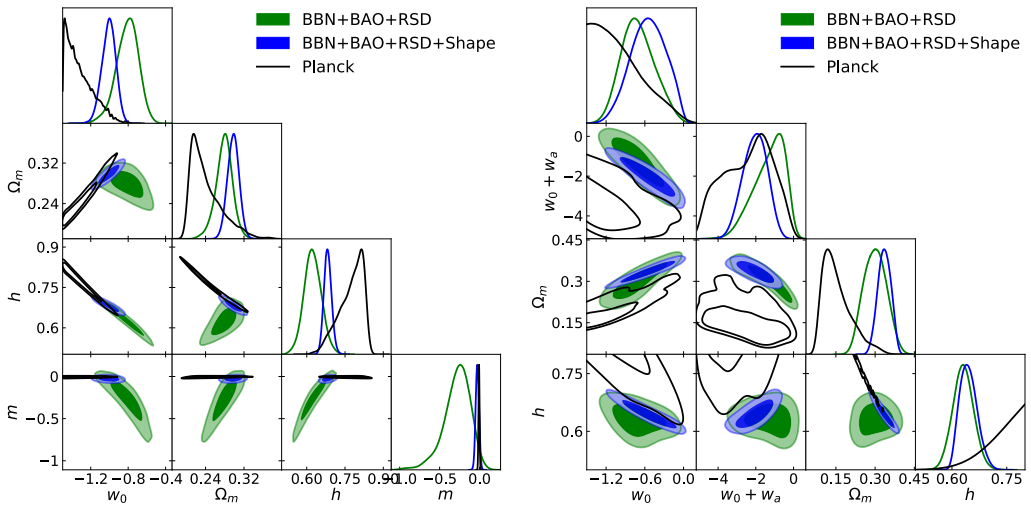


**Figure 7**. Left panel: Cosmological constraints within the $w_0$CDM model. Right panel: Cosmological constraints within the $w_0 w_a$CDM model.

The same observation holds for the ($w_0 w_a$CDM) case. The exact numbers are reported in table 9. There, we also show the results after combining Planck with our LSS dataset, finding that Planck dominates over the *Shape* constraints similar to the case of varying curvature. We conclude that, due to their high degree of complementarity to Planck, the information contained in BAO and RSD is sufficient to constrain cosmological parameters globally, i.e., by combining disparate probes of the universe.

Finally, we visualize the main conclusion of this section in figure 8, where we directly compare the most important extended models investigated in this section to the compressed data set and their ΛCDM predictions.

Each subpanel of figure 8 shows one of the compressed, physical parameters with respect to the Planck ΛCDM prediction displayed via the black dotted lines as a function of redshift. The measurements presented in section 3 and figure 2 are displayed as black data points and the blue continuous line represents the ΛCDM best-fit to the data set. Note that the information contained here so far is identical to figure 2. In addition, we show the theoretical predictions from three extensions to the baseline ΛCDM model, selected in the following way:

- ***ν*ΛCDM** (magenta, sparsely dashed lines): We show the model corresponding to a neutrino mass of $\Sigma m_\nu = 0.4\,\mathrm{eV}$, which is excluded by ShapeFit at the 95% confidence level. This corresponds to the $2\sigma$ edge of the blue contours in the left panel of figure 5.

- ***o*ΛCDM** (red, dashed lines): We show the best-fit model to the classic data set, consisting of BAO+RSD only, without the *Shape* information, when allowing $\Omega_k$ to vary freely. This corresponds to the best-fit of the green contours in the right panel of figure 6.

- ***w*CDM** (green, dash-dotted lines): Again, we show the best-fit model to the classic data set, but when allowing $w_0$ to vary freely. This corresponds to the best-fit of the green contours in the left panel of figure 7.

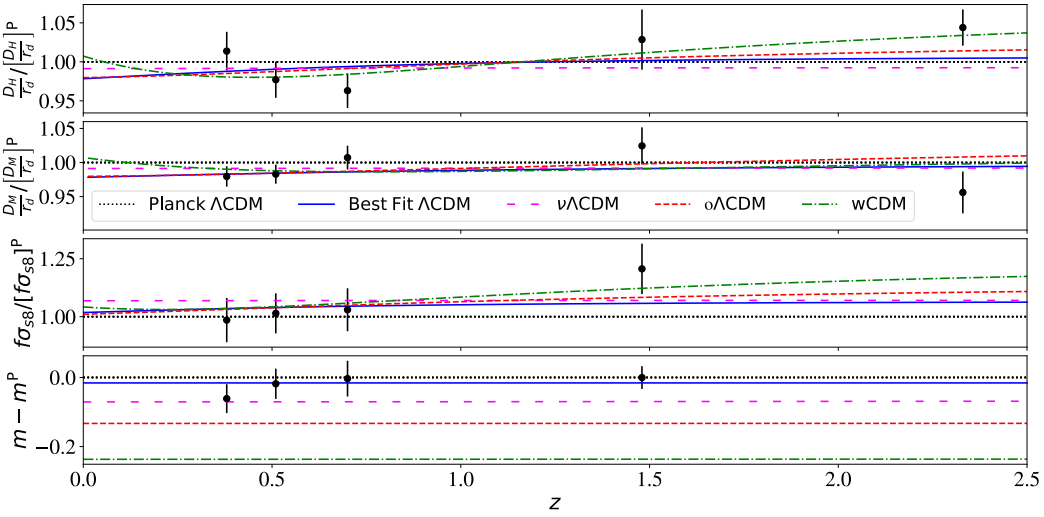


**Figure 8**. Comparison of several models with respect to the compressed dataset. Each panel shows the redshift dependence (colored lines) and measurements (black data points) of the compressed variables rescaled to the Planck (labeled 'P') ΛCDM prediction (black dotted lines). The blue, continuous lines represent the best-fit ΛCDM prediction to the ShapeFit dataset. The magenta, sparsely dashed lines correspond to a $\nu\Lambda$CDM model with $\Sigma m_\nu = 0.40\,\mathrm{eV}$ that is excluded by the ShapeFit dataset at $2\sigma$. Finally, we show the o$\Lambda$CDM (red, dashed lines) and wCDM (green, dash-dotted) models, that deliver the best-fit to the classic dataset, but are vastly excluded by the measurement of the shape $m$.

Figure 8 explicitly shows that -using LSS data alone- ShapeFit constrains models that leave in imprint on the power spectrum slope, such as in the $\nu\Lambda$CDM case. In addition, ShapeFit helps to constrain models by lifting parameter degeneracies, even if the parameter extensions themselves do not change the power spectrum slope, such as the $o\Lambda$CDM and $w\Lambda$CDM models. For these models in particular, by focusing on the red and green lines on figure 8, we can appreciate that the classic parameters are fitted equally well as the concordance ΛCDM, but these deviations from ΛCDM, deliver a *Shape* prediction in strong disagreement with the data. Therefore, the shape $m$ is a powerful probe when constraining models using LSS data alone.

Note that figure 8 is similar to figures 2 and 7 of the eBOSS cosmological results paper [12], but complementary in the parameter selection of the extended models shown. While their parameter choices are tuned to deliver a 'good fit' to Planck, but a 'bad fit' to their presented dataset, here we tune the parameters of $\Sigma m_\nu$, $\Omega_k$ and $w_0$ (and the remaining ΛCDM parameters) the other way around. As mentioned before, we select them such that the BAO and RSD compressed variables are fit well, but are in vast disagreement with our *Shape* measurement, (which is in agreement with Planck).

### 5.3 Consistency between individual tracers

We investigate the consistency between the different BOSS and eBOSS tracers (LRG's, QSO's, Ly$\alpha$) within the baseline ΛCDM model.

In figure 9 we show cosmological constraints from the three LRG samples at redshifts

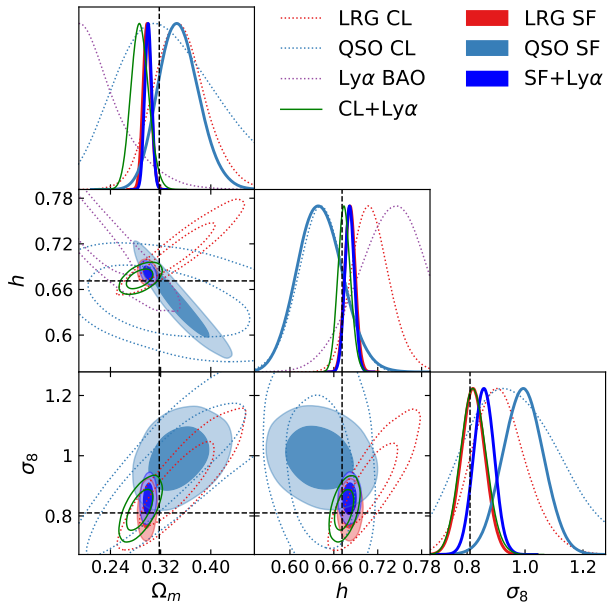


**Figure 9**. Comparison of cosmological constraints for different tracers. Empty contours show the classic (CL) analysis (BAO+RSD for galaxies, BAO for Lyman-$\alpha$) $\Lambda$CDM results for LRGs (red), QSOs (light blue), Ly-$\alpha$ (purple) and all combined (green). Filled contours show the corresponding ShapeFit (SF) $\Lambda$CDM results via the same color scheme, but with combined results shown in blue. Note that the green and blue contours here represent the same cases as in figure 4. In all cases a BBN prior on $\omega_{\rm b}$ is assumed. Dashed black lines indicate the Planck best-fit cosmology.

$0.2 < z < 1.0$ (red), the QSO sample at $0.8 < z < 2.2$ (light blue) and the Ly$\alpha$ forest at $1.8 < z < 4.0$ (purple) each, including a BBN prior. The results are shown both for the classic fit (empty dotted contours, labeled 'CL') and ShapeFit (filled contours, labeled 'SF') for comparison. Additionally, we show the cosmological constraints when combining all samples (green and dark blue contours) already presented in section 5.1. The best-fit Planck cosmology is indicated by black dashed lines.

We can appreciate the strong tightening of constraints due to the *Shape* for the LRG and QSO samples, especially in the $\Omega_{\rm m} - h$ plane. As expected, this effect is stronger for the individual samples than for the combined ones, because already in the classic case the individual samples are highly complementary in their cosmological parameter degeneracy directions. Thus the *Shape* becomes less important the larger the analysed redshift range is. Also note that the Ly$\alpha$ forest plays a crucial role breaking the degeneracies in the $\Omega_{\rm m} - h$ plane for the classic case. This is not the case for ShapeFit where the degeneracy is broken even across a smaller redshift baseline (see the consistency between red and dark blue contours).

In the $\Omega_{\rm m} - h$ plane the consistency between LRG's and QSO's for ShapeFit is remarkable. However, the $\sigma_8$ parameter recovered by ShapeFit LRG's and QSO's reveals a discrepancy of $2.1\sigma$. This should be compared to the $3.6\sigma$ tension between the same samples reported in Neveux et al. [68], who find,

$$\sigma_{8,z=0}^{\rm LRG} = 0.760 \pm 0.046 \qquad \sigma_{8,z=0}^{\rm QSO} = 1.12 \pm 0.10 \qquad \text{[Neveux et al.]} \,, \tag{5.4}$$

whereas (using the same Gaussian priors on $\omega_{\rm b}$ and $n_s$ as in [68]) we find,

$$\sigma_{8,z=0}^{\rm LRG} = 0.814 \pm 0.043 \qquad \sigma_{8,z=0}^{\rm QSO} = 0.993 \pm 0.071 \qquad \text{[this work]} \ . \tag{5.5}$$

While the LRG results of both methods can not be directly compared to each other, since [68] do not include the BOSS medium redshift sample at $z_{\rm eff} = 0.51$ and neither the BAO post-recon information, the $1\sigma$ discrepancy in $\sigma_8$ for QSO alone is surprising. We suggest that it is related to the differences between the FM approach of [68] and ShapeFit, coming from the lack of constraining power of the quasar sample alone. Nevertheless, after combining the samples and covering a larger redshift range, our results are well in agreement with [68], as shown in table 7.

### 5.4 Comparison with other approaches

In this section we compare the cosmological results presented in sections 5.1 and 5.2 to the official eBOSS collaboration results [12] and the results obtained by other, independent groups, who have used the same BOSS+eBOSS dataset (or a subset of it). As the initial motivation of ShapeFit has been to provide a bridge between fixed-template (classic) and varying-template (full modeling) approaches [24], how ShapeFit compares to each of these very different ways of interpreting spectroscopic galaxy surveys is of particular interest.

#### 5.4.1 Full modeling approaches

We compare our main results in light of the standard flat-ΛCDM model with three free parameters, $\{\Omega_{\rm m}, H_0, A_s\}$ with the most recent studies applied to the BOSS and eBOSS samples using different full modelling approaches. The first two rows of table 7 display the best-fitting $\Omega_{\rm m}$, $H_0$, $A_s$[7] values for the ShapeFit approach, with and without assuming a BBN prior on $\omega_{\rm b}$, and with a fixed value of $n_s$ to its reference value as described in table 6. This is followed by the results of full modelling studies, of which four have been applied to the BOSS DR12 LRG data, and two to the QSO and LRG eBOSS DR16 data (which contains the BOSS DR12 data). In addition, we also include the parameters derived from applying ShapeFit to these samples. We briefly describe below the main assumptions of these different analyses and compare them to our findings.

In D'Amico et al. [16] the authors employ the EFT [94, 95] approach to model the power spectrum monopole and quadrupole signals of the BOSS DR12 LRG sample split in two redshift bins: the so called LOWZ sample, $0.15 < z < 0.43$; $z_{\rm eff} = 0.32$ and the CMASS sample, $0.43 < z < 0.70$; $z_{\rm eff} = 0.57$, considering the scales $k \leq 0.20\,{\rm Mpc}^{-1}h$ for CMASS and $k \leq 0.18\,{\rm Mpc}^{-1}h$ for LOWZ. For CMASS, both northern and southern samples are considered, whereas for the LOWZ sample only the northern cap is analyzed. The $\omega_{\rm b}/\omega_{\rm m}$ ratio and $n_s$ index are assumed fixed at Planck's best-fit values.

Ivanov et al. [17] also use EFT to model the power spectrum monopole and quadrupole signals of BOSS DR12 applying the following redshift binning, $0.2 < z < 0.5$; $z_{\rm eff} = 0.38$ and $0.5 < z < 0.75$; $z_{\rm eff} = 0.61$; and considering the scales $k \leq 0.25\,{\rm Mpc}^{-1}h$, using both northern and southern galactic caps. An informative prior on $\omega_{\rm b}$ is employed motivated Planck observations, and $n_s$ is fixed to Planck's best-fit value. The neutrino mass is varied within the narrow range of (0.06-0.18) eV.

[7] The $\sigma_8$ is a derived parameter, obtained from the values of the $\{\Omega_{\rm m}, H_0, A_s\}$ parameters. However, since some authors choose to show it (instead of reporting $A_s$) we decide to display it as well.

| Sample | Priors | Method / Ref. | $\Omega_{\rm m}$ | $H_0\left[\frac{\rm km/s}{\rm Mpc}\right]$ | $A_s \cdot 10^9$ | $\sigma_8$ |
|---|---|---|---|---|---|---|
| Full | $n_s$ | **ShapeFit** | $0.2971 \pm 0.0061$ | – | $2.39^{+0.24}_{-0.43}$ | $0.857 \pm 0.040$ |
| | $\omega_{\rm b}, n_s$ | **ShapeFit** | $0.3001 \pm 0.0057$ | $68.16 \pm 0.67$ | $2.43 \pm 0.20$ | $0.858 \pm 0.036$ |
| LRG DR12 | $\frac{\omega_{\rm b}}{\omega_{\rm m}}, n_s$ | D'Amico [16] | $0.309 \pm 0.010$ | $68.5 \pm 2.2$ | $1.52 \pm 0.84$ | – |
| | $\omega_{\rm b}, n_s$ | Ivanov [17] | $0.295 \pm 0.010$ | $67.9 \pm 1.1$ | – | $0.721 \pm 0.043$ |
| | $\omega_{\rm b}, n_s$ | Philcox [65] | $0.2962^{+0.0082}_{-0.0080}$ | $67.81^{+0.68}_{-0.69}$ | – | $0.739^{+0.040}_{-0.041}$ |
| | $\omega_{\rm b}$ | Tröster [66] | $0.317^{+0.015}_{-0.019}$ | $70.4 \pm 2.4$ | – | $0.71 \pm 0.049$ |
| | $n_s$ | ShapeFit [24] | $0.295 \pm 0.014$ | – | $2.56 \pm 0.51$ | $0.806 \pm 0.065$ |
| LRG DR16 | $\omega_{\rm b}, n_s$ | Neveux [68] | $0.315 \pm 0.013$ | $66.9 \pm 1.9$ | – | $0.763 \pm 0.046$ |
| | $\omega_{\rm b}, n_s$ | **ShapeFit** | $0.2984 \pm 0.0066$ | $68.20 \pm 0.73$ | $2.24 \pm 0.24$ | $0.820 \pm 0.043$ |
| QSO DR16 | $\omega_{\rm b}, n_s$ | Neveux [68] | $0.321 \pm 0.016$ | $65.1 \pm 1.9$ | – | $1.12 \pm 0.10$ |
| | $\omega_{\rm b}, n_s$ | **ShapeFit** | $0.350 \pm 0.033$ | $64.1 \pm 3.1$ | $3.25 \pm 0.47$ | $0.993 \pm 0.072$ |
| LRG +QSO DR16 | $\omega_{\rm b}, \omega_{\rm cdm}, n_s$ | Semenaite [67] | $0.3037 \pm 0.0081$ | $68.55^{+0.84}_{-0.94}$ | – | $0.800 \pm 0.039$ |
| | $\omega_{\rm b}, n_s$ | Neveux [68] | $0.308 \pm 0.010$ | $66.4 \pm 1.4$ | – | $0.869 \pm 0.046$ |
| | $\omega_{\rm b}, n_s$ | **ShapeFit** | $0.3012 \pm 0.0057$ | $68.24 \pm 0.67$ | $2.42 \pm 0.20$ | $0.860 \pm 0.036$ |

**Table 7**. Comparison of ShapeFit results with other full modelling approaches when analyzing BOSS and eBOSS samples. The first column shows the used data sets in each approach, where 'Full' refers to the final release of the BOSS+eBOSS dataset shown in figure 2 (LRG+QSO+Ly$\alpha$); LRG DR12 refers to the BOSS LRG sample, $0.2 < z < 0.75$; LRG DR16 to the whole BOSS and eBOSS LRG samples, $0.2 < z < 1.0$; and QSO DR16 to the whole eBOSS quasar sample, $0.8 < z < 2.2$. The second column shows which parameters have either been fixed or varied within a Gaussian prior in each analysis (see text for details). The first two rows (and also those rows labeled in bold) display the best-fitting parameters of this work either with or without the prior on $\omega_{\rm b}$, motivated by BBN. Additionally, we display the results of other studies analyzing part of the BOSS and eBOSS data described here. All the quoted analyses assume a flat-ΛCDM model, but D'Amico et al, Ivanov et al. and Philcox et al. (along with our results) have fixed the $n_s$ parameter to Planck best-fit finding, and Tröster et al., Semenaite et al. and Neveux et al., allow $n_s$ to vary within a certain range (see text). This difference may considerably enlarge the error-bars on some of the ΛCDM parameters.

Compared to Ivanov et al. and D'Amico et al. results, our value for $A_s$ (or $\sigma_8$) is significantly larger. This is likely due to the fact that in their analysis the (necessary) re-normalization of the window function is ignored. We find, however, a very good agreement for $\Omega_{\rm m}$ as well as for $H_0$, which are less affected by this effect. Our analysis returns significantly smaller error-bars: a factor 1.8 smaller for $\Omega_{\rm m}$, a factor of 1.6 smaller for $H_0$ compared to Ivanov et al., a factor of 3.2 smaller for $H_0$ compared to D'Amico et al., because our analysis employs a larger sample, $0.2 < z < 4.0$, and it employs pre- and post-recon catalogues coherently, when available. The weaker constrain on $H_0$ from D'Amico et al. [16] with respect to Ivanov et al. [17] is due to the type of prior used: D'Amico et al. fix the $\omega_{\rm b}/\omega_{\rm m}$ ratio, whereas Ivanov et al. the baryon density $\omega_{\rm b}$ (see the effect of this prior choice in Appendix B of [23]).

Philcox et al. [65] use the same BOSS DR12 sample, and the same piors on $w_b$, $\Sigma m_\nu$ and $n_s$, as described in Ivanov et al., but additionally include the signal from the post-reconstructed catalogues which improves the BAO constraint. This allows them to better constrain $H_0$ and $\Omega_{\rm m}$ with respect to the corresponding pre-reconstructed study of Ivanov et al.. Compared to Philcox et al., ShapeFit with a BBN prior yields error-bars tighter by a factor of 1.4 for $\Omega_{\rm m}$, equal for $H_0$, and tighter by a factor of 1.1 for $\sigma_8$. As before the disagreement in the best-fit value for $\sigma_8$ is caused by the (non) re-normalization of the window in their analysis. In general the agreement with the obtained $\Omega_{\rm m}$ and $H_0$ best-fit values is very good.

Tröster et al. [66] use the same BOSS DR12 samples as in Ivanov et al., but instead of employing the power spectrum monopole and quadrupole signals they choose to model three LOS-wedges of the correlation function. They employ a perturbation theory model, gRPT, for describing the real-space statistics, combined with the TNS model from [29], and assume the usual local Lagrangian relations for the non-local biases. They use an informative but wider-than-usual prior on $\omega_{\rm b}$ (about 10 times wider than the usual BBN prior from [75]). This choice impacts the error-bars on $H_0$, which are much wider than the above studies. They also choose to use an uninformative wide prior on $n_s$ which also affects $H_0$, as well as $\Omega_{\rm m}$ and $\sigma_8$. Similarly to the above studies, Tröster et al. does not account for the necessary normalization of the window which impacts the recovered value of $\sigma_8$.

For completeness we also include the results derived from applying ShapeFit to the BOSS DR12 LRG sample, divided in two bins as in Ivanov et al, as described in [24]. Unlike the other studies, we do not apply any prior on $\omega_{\rm b}$ which only allow us to report constrains on $\Omega_{\rm m}$ and $A_s$. The difference in $\sigma_8$ is given by the normalization of the survey window, and the agreement for $\Omega_{\rm m}$ with the other studies is very good.

Neveux et al. [68] use the power spectrum monopole, quadrupole and hexadecapole signals of the BOSS DR12 LRG sample between $0.2 < z < 0.5$, the BOSS and eBOSS LRG samples between $0.6 < z < 1.0$ and the eBOSS quasar sample between $0.8 < z < 2.2$. Unlike our main result, they do not employ any reconstruction data, nor the Ly-$\alpha$ measurements. They describe the data using the perturbation theory implementation RegPT [96], along with the TNS model [29] under the assumption of local Lagrangian for the non-local biases. We choose to display their results with priors on $\omega_{\rm b}$ and $n_s$, to make the analysis setting closer to ours, and also display the results for the LRG sample and QSO sample alone. For comparison we also report our results on the same samples (see section 5.3 for a comparison of $\sigma_8$ under the same prior conditions).

For the whole LRG+QSO sample we find good consistency with our results on $\Omega_{\rm m}$ and $\sigma_8$. However, Neveux et al. reports a value for $H_0$ which is about $1\sigma$ smaller than our finding. This difference can be caused by the slightly different choice of priors, as well as the difference in the data-catalogue selection: we employ the post-reconstructed catalogues, as well as the galaxies between $0.5 < z < 0.6$. The impact of this can be more clearly seen on the size of the error-bars inferred from the LRG DR16 sample alone, where ours are significantly smaller. The most striking result arise when the QSO sample alone is considered, as the errorbars on $\Omega_{\rm m}$ and $H_0$ are substantially smaller in Neveux et al. compared to our approach: a factor of 2 and a factor of 1.6, respectively. On the other hand the value on $\sigma_8$ found by Neveux et al. is 1.4 times looser than ours. These differences deserve a more careful investigation we may address in future work.

Semenaite et al. [67] use the data from BOSS DR12 as in Ivanov et al, along with the eBOSS quasar sample between $0.8 < z < 2.2$. They do not use any post-reconstructed catalogue, nor eBOSS LRG data, nor Lyman-$\alpha$ data. They model three LOS-wedges of the correlation function using a perturbation theory implementation (Respresso [96, 97]), where the velocity power spectra are given by [98] and the redshift-space distortions are modelled according to the TNS model [29]. Instead of using the local Lagrangian bias relations they choose to use another approach motivated by the findings in [99]. We choose to display their results when Gaussian priors are used around $\omega_{\rm b}$, $\omega_c$ and $n_s$, as this is the closest choice to our type of analysis. We find consistent results on $\Omega_{\rm m}$ and $H_0$, but a $\sim 1\sigma$ discrepancy for $\sigma_8$. Their error-bars are larger than ours, partly because of not fixing $n_s$, but also because not employing the reconstructed catalogues, nor using the eBOSS LRG or Ly-$\alpha$ datasets.

### 5.4.2 Classic approaches

The comparison with other analyses that used the classic approach, and in particular the final cosmological analysis of eBOSS [12] serves two main purposes. We aim to *i)* show that interpreting our classic dataset (without the *Shape*) delivers the same cosmological results as in [12], *ii)* quantify the power of *Shape* in constraining cosmological models more in detail than done in sections 5.1 and 5.2 and *iii)* quantify the differences among the compression methods after combining with the Planck likelihood introduced in section 3.4.

All results of this paper are shown in comparison to the official BOSS+eBOSS counterpart (labeled '(e)BOSS') in table 8 for the ΛCDM model and 9 for ΛCDM extensions, in the same format as table 4 of [12]. Note that for the fits without Planck, [12] use only the BAO signal, while for our classic fits we always include the BAO and RSD signals. However, for the runs labeled 'Planck+(e)BOSS' we use publicly available fits from [12] labeled 'CMBLens+BAORSD' therein, which include both the BAO and RSD signals. Also, note that all results presented in this table do not rely on the BBN prior, which is the reason why $H_0$ remains unconstrained for all runs that do not include the Planck likelihood.

Concerning *i)*, we have already shown in section 4.2 that the agreement with [12] at the level of compressed variables is very good. However, we investigate whether the small residual differences leak into a measurable difference at the level of cosmological model parameters. Note that the dataset we use in this paper is slightly different from that in [12], where they also include isotropic BAO and RSD (assuming fixed BAO) measurements from the MGS sample and the anisotropic BAO+RSD measurement of the ELG sample at effective redshifts $z = 0.15$ and $z = 0.85$ respectively. We have monitored the effect of this deviation for the ΛCDM and $\nu$ΛCDM models. We find that by including the ELG and MGS data in our pipeline we recover exactly the same $\Omega_{\rm m}$ and $\Sigma m_\nu$ constraints as [12]. We therefore conclude that the main discrepancy between the official (e)BOSS and our classic results, which always remain well within $1\sigma$, are attributed to this slightly different choice.

| | $\Omega_{\rm m}$ | $H_0\left[\frac{\rm km/s}{\rm Mpc}\right]$ | $A_s \times 10^9$ | $\sigma_8$ |
|---|---|---|---|---|
| (e)BOSS BAO | $0.299 \pm 0.016$ | – | – | – |
| Classic [this work] | $0.287 \pm 0.014$ | – | $2.41^{+0.26}_{-0.41}$ | $0.828 \pm 0.048$ |
| ShapeFit [this work] | $0.2971 \pm 0.0061$ | – | $2.39^{+0.24}_{-0.43}$ | $0.857 \pm 0.040$ |
| BBN + (e)BOSS | $0.299 \pm 0.016$ | $67.35 \pm 0.97$ | – | – |
| BBN + Classic | $0.287 \pm 0.014$ | $67.42^{+0.84}_{-0.91}$ | $2.50^{+0.22}_{-0.25}$ | $0.822 \pm 0.044$ |
| BBN + ShapeFit | $0.3001 \pm 0.0057$ | $68.16 \pm 0.67$ | $2.43 \pm 0.20$ | $0.858 \pm 0.036$ |
| Planck | $0.3178 \pm 0.0079$ | $67.13 \pm 0.56$ | $2.1^{+0.028}_{-0.032}$ | $0.8101^{+0.0062}_{-0.0061}$ |
| Planck + (e)BOSS | $0.3109 \pm 0.0053$ | $67.68 \pm 0.40$ | – | – |
| Planck + Classic | $0.3081 \pm 0.0050$ | $67.83 \pm 0.38$ | $2.117^{+0.029}_{-0.033}$ | $0.8089^{+0.0060}_{-0.0064}$ |
| Planck + ShapeFit | $0.3067 \pm 0.0047$ | $67.94 \pm 0.36$ | $2.121^{+0.030}_{-0.033}$ | $0.8091^{+0.0057}_{-0.0065}$ |

**Table 8**. ΛCDM model: Comparison of our Classic and ShapeFit cosmological constraints with the official BOSS+eBOSS results that include the BAO only signal (labeled '(e)BOSS BAO') without Planck and the full BAO+RSD signals (labeled '(e)BOSS') combined with Planck. We present mean values with 68% C.L.

| | | $\Omega_{\rm m}$ | $H_0\left[\frac{\rm km/s}{\rm Mpc}\right]$ | $\Sigma m_\nu$ [eV] | $N_{\rm eff}$ | $\Omega_k$ | $w_0$ | $w_a$ |
|---|---|---|---|---|---|---|---|---|
| $\nu\Lambda$CDM | ShapeFit [this work] | $0.300^{+0.008}_{-0.011}$ | – | $< 0.54$ | – | – | – | – |
| | BBN + ShapeFit | $0.302^{+0.007}_{-0.010}$ | $68.03 \pm 0.68$ | $< 0.40$ | – | – | – | – |
| | Planck | $0.321^{+0.009}_{-0.015}$ | $66.95^{+1.1}_{-0.68}$ | $< 0.26$ | – | – | – | – |
| | Planck + (e)BOSS | $0.3089 \pm 0.0058$ | $67.87 \pm 0.45$ | $< 0.10$ | – | – | – | – |
| | Planck + Classic | $0.3052 \pm 0.0052$ | $68.14 \pm 0.40$ | $< 0.085$ | – | – | – | – |
| | Planck + ShapeFit | $0.3034 \pm 0.0049$ | $68.28 \pm 0.39$ | $< 0.082$ | – | – | – | – |
| $N_{\rm eff}\Lambda$CDM | Planck | $0.321 \pm 0.011$ | $66.5^{+1.4}_{-1.7}$ | – | $2.94^{+0.21}_{-0.24}$ | – | – | – |
| | Planck + Classic | $0.3066 \pm 0.0060$ | $68.5 \pm 1.3$ | – | $3.16 \pm 0.22$ | – | – | – |
| | Planck + ShapeFit | $0.3053 \pm 0.0056$ | $68.44 \pm 0.12$ | – | $3.12 \pm 0.19$ | – | – | – |
| o$\Lambda$CDM | (e)BOSS BAO | $0.285 \pm 0.023$ | – | – | – | $0.078^{+0.086}_{-0.099}$ | – | – |
| | Classic [this work] | $0.276^{+0.021}_{-0.019}$ | – | – | – | $0.054^{+0.079}_{-0.092}$ | – | – |
| | ShapeFit [this work] | $0.2943^{+0.0080}_{-0.0092}$ | – | – | – | $-0.022^{+0.032}_{-0.038}$ | – | – |
| | BBN + Classic | $0.279^{+0.023}_{-0.021}$ | $65.9 \pm 3.5$ | – | – | $0.047^{+0.083}_{-0.099}$ | – | – |
| | BBN + ShapeFit | $0.2942^{+0.0078}_{-0.0085}$ | $68.8 \pm 1.1$ | – | – | $-0.027^{+0.032}_{-0.037}$ | – | – |
| | Planck | $0.355 \pm 0.025$ | $63.4^{+2.6}_{-2.1}$ | – | – | $-0.0104 \pm 0.0067$ | – | – |
| | Planck + (e)BOSS | $0.3105 \pm 0.0056$ | $67.75 \pm 0.56$ | – | – | $0.0003 \pm 0.0017$ | – | – |
| | Planck + Classic | $0.3077 \pm 0.0052$ | $68.10 \pm 0.51$ | – | – | $0.0014 \pm 0.0017$ | – | – |
| | Planck + ShapeFit | $0.3058 \pm 0.0047$ | $68.25 \pm 0.49$ | – | – | $0.0015 \pm 0.0016$ | – | – |
| $w$CDM | (e)BOSS BAO | $0.271^{+0.038}_{-0.017}$ | – | – | – | – | $-0.69 \pm 0.15$ | – |
| | Classic [this work] | $0.279^{+0.018}_{-0.016}$ | – | – | – | – | $-0.81^{+0.13}_{-0.11}$ | – |
| | ShapeFit [this work] | $0.296 \pm 0.013$ | – | – | – | – | $-0.998^{+0.085}_{-0.073}$ | – |
| | BBN + ShapeFit | $0.298 \pm 0.013$ | $68.23 \pm 1.6$ | – | – | – | $-1.007^{+0.083}_{-0.073}$ | – |
| | Planck + (e)BOSS | $0.3039 \pm 0.0092$ | $68.6 \pm 1.0$ | – | – | – | $-1.037 \pm 0.039$ | – |
| | Planck + Classic | $0.2928 \pm 0.0093$ | $69.9 \pm 1.2$ | – | – | – | $-1.090^{+0.050}_{-0.041}$ | – |
| | Planck + ShapeFit | $0.2906 \pm 0.009$ | $70.1 \pm 1.2$ | – | – | – | $-1.093^{+0.048}_{-0.044}$ | – |
| $w_0w_a$CDM | BBN + Classic | $0.300^{+0.041}_{-0.051}$ | – | – | – | – | $-0.70^{+0.23}_{-0.31}$ | $-0.58^{+1.3}_{-0.76}$ |
| | BBN + ShapeFit | $0.335 \pm 0.027$ | – | – | – | – | $-0.55^{+0.30}_{-0.27}$ | $-1.50^{+0.96}_{-0.92}$ |
| | Planck + (e)BOSS | $0.329 \pm 0.017$ | $66.1 \pm 1.7$ | – | – | – | $-0.70 \pm 0.19$ | $-0.99^{+0.62}_{-0.52}$ |
| | Planck + Classic | $0.333 \pm 0.025$ | $65.7^{+2.2}_{-2.6}$ | – | – | – | $-0.63 \pm 0.26$ | $-1.29^{+0.79}_{-0.69}$ |
| | Planck + ShapeFit | $0.330 \pm 0.023$ | $66.0^{+2.2}_{-2.5}$ | – | – | – | $-0.64 \pm 0.25$ | $-1.27^{+0.78}_{-0.65}$ |

**Table 9**. ΛCDM extensions: Comparison of our Classic and ShapeFit cosmological constraints with the official BOSS+eBOSS results that include the BAO only signal (labeled '(e)BOSS BAO') without Planck and the full BAO+RSD signals (labeled '(e)BOSS') in the fits combined with Planck. We present mean values with 68% C. L., only in the case of $\Sigma m_\nu$ we present upper limits at 95% confidence level. We do not display the cases, for which the extended parameters are unconstrained.

About *ii)*, in general, we see that ShapeFit tends to yield slightly larger values of $\Omega_{\rm m}$ than the classic fit. Also, the constraining power improves significantly when adding the shape $m$, by a factor of about $2.5, 3, 1.5$ for $\Omega_{\rm m}$, $\Omega_{\rm k}$ and $w_0$, respectively. In this way, ShapeFit delivers competitive evidence for a flat universe ($\Omega_{\rm k} = 0$) and for a standard cosmological constant ($w_0 = -1$). In the case of $\nu\Lambda$CDM, ShapeFit has the ability to constrain the sum of neutrino masses, which the classic fit is not sensitive to.

Regarding *iii)*, when adding Planck data there is very good agreement between our classic and the officially-reported eBOSS results. We have verified that our own Planck-only constraints are in very good agreement with the official Planck results from [2]. As already anticipated, for the $\nu\Lambda$CDM case in the right panel of figure 5, the improvement of ShapeFit with respect to the classic fit is very modest once Planck is included because the shape information within Planck dominates over our constraint on $m$ from the LSS maps.

Still, this comparison indicates that for upcoming galaxy survey data, for example DESI [100], which will measure the *shape* more accurately, $m$ might play a significant role for constraining cosmology, even when including Planck.

## 6 Systematic checks and performance on synthetic catalogues

We aim to validate the robustness of the results presented in section 5 with respect to variations of the chosen baseline data pipeline, and to quantify the systematic error-budget of the used approach. As the results are insensitive to reasonable deviations from the adopted assumptions (see Appendix A), this section is likely of interest for experts, other readers may omit it at a first sitting.

For the specific performance of the perturbation theory model used we refer to the original ShapeFit paper [21] and PT challenge ShapeFit paper [23]. Both of them present the comparison of the model with respect to full N-body mocks, the Nseries mocks, and the PT challenge mocks, and both samples consist of haloes catalogues which have been populated with galaxies following a Halo Occupation Distribution (HOD) consistent with the LRG catalogues from BOSS data.

### 6.1 Galaxy fast-mocks

We start by running the same baseline setup used for the data on section 5, on the 2048 and 1000 realizations of the Patchy and EZmocks, respectively. These mocks were originally produced for inferring the covariance matrix of the power spectra of the data, the compressed-parameter matrix needed to combine pre- and post-recon parameters, and the correlation among the two overlapping redshift bins. However, we need to bear in mind that these mocks rely on approximate fast techniques and are not full N-body. Consequently, they do not require such high computational resources as a full N-body simulation, at the expense of not being fully accurate when describing the clustering. Therefore, they should not be used to determine the systematic error budget of our approach. Yet, we run the full data pipeline on them, rather than to validate the pipeline, to validate the mocks, as well as to check how consistent data and mocks are in terms of the inferred errorbars.

Figure 10 displays the triangle plot for the four physical parameters of interest, and for the four studied galaxy samples. The blue dots represent the result of the 2048 and 1000 realizations on the Patchy (for LRG $0.2 < z < 0.6$) and EZmocks (for LRG $0.6 < z < 1.0$ and QSO $0.8 < z < 2.2$), respectively. The red cross displays the performance of the data,

as presented in table 5. The horizontal and vertical dotted black lines display the expected values given the true cosmology of the mocks (see table 2).

We see that best-fit values of the data lie within the scatter cloud of the best-fitting values for the mocks. This is indeed expected as the mocks were designed to reproduce the clustering of the data. However, we do not necessarily expect that both data and mocks share the same cosmology, even within the statistical uncertainty of the samples. When comparing the performance of the mocks with their expected values (marked by the black dashed lines), we find that for the $D_H/r_{\rm d}$, $D_M/r_{\rm d}$ and $f\sigma_{s8}$ parameters, the agreement is excellent. Indeed, the mocks were designed with the aim of being able to reproduce both the BAO and the anisotropic clustering signal, as these are the two main scientific goals of the BOSS and eBOSS programs. Additionally, we find that the mocks tend to have a low value of the shape parameter, $m$, with respect to its expected value, with an offset of around $-0.05$ to $-0.10$, which corresponds to $1-2\sigma$ statistical of the BOSS/eBOSS data sample. We explore this particular feature more in detail in section 6.2, using full N-body mocks data (but see also Appendix A for the impact of the local bias assumption on the shape parameter for these mocks). In short, this observed behaviour corresponds to a limitation of the mocks (rather than to systematics of the model) due to the clustering of the mocks in the scale range of $0.05 < k\,[h{\rm Mpc}^{-1}] < 0.10$. In particular, pre-virialization terms (as for example those captured by 1-loop corrections) contribute to the clustering signal on the scales where $m$ is measured. But pre-virialization is not fully taken into account by the Zeldovich approximation, which these mocks rely on (see also Appendix A). As a result the model fitting procedure compensates by artificially lowering the best-fitting value of $m$.

This limitation has not been explicitly reported before because it did not impact how well the BAO and $f\sigma_{s8}$ parameters could be recovered from these mocks, as $m$ is very uncorrelated with them.

The panels of figure 11 display the $1\sigma$ errors corresponding to the best-fit values presented in figure 10. For the BOSS LRG samples for $0.2 < z < 0.6$ (top-left and top-right panels) the errors for the data (red cross) are very typical compared to those of the mocks (blue dots). The bottom sub-panels, corresponding to eBOSS LRG and QSO samples, indicate that in some cases, the error of the data is significantly smaller than the one reported on the mocks. This happens for the longitudinal BAO distance, $D_H/r_{\rm d}$, and shape parameter, $m$, in the LRG $0.6 < z < 1.0$ sample, and up to some degree for all the parameters in the QSO $0.8 < z < 2.2$ sample. This behaviour was already reported by the eBOSS team (see for e.g., the discussion in section 5.1 of [28] for the LRG sample; and section 3.2.2 of [59] for the QSO sample) and is caused by an excess of significance in the BAO detection of both quasars and LRGs, likely originated by noise fluctuations in the data, which were different from those in the mocks.

We aim to use the set of best-fit values (and their errors) of the mocks to perform quantitative tests: how their *rms* compares to the averaged errors, whether the distribution is Gaussian, as well as which are the typical deviations from their expected values. All this information is summarized in table 10, which displays the results for each of the four studied samples (each column), and for each of the four parameters of interest, $x = \alpha_{\parallel}$, $\alpha_{\perp}$, $f\sigma_{s8}$, $m$. For each of these parameters we display in rows the systematic offset between the best-fit of the mean of the mocks and its expected value, $\Delta x^{\rm av\cdot}$; the systematic offset between the mean of the best-fits of the individual mocks and its expected value, $\langle \Delta x \rangle$; the average of the error-bars of the best-fits, $\langle \sigma_x \rangle$, the *rms* among the best-fits, $S_x$; the mean of the $Z$-statistic, defined as $Z_{x_i} \equiv (x_i - \bar{x})/\sigma_{x_i}$, $\langle Z_x \rangle$; and the *rms* of $Z_{x_i}$, $S_{Z_x}$. All the $x$-variables of table 10 are

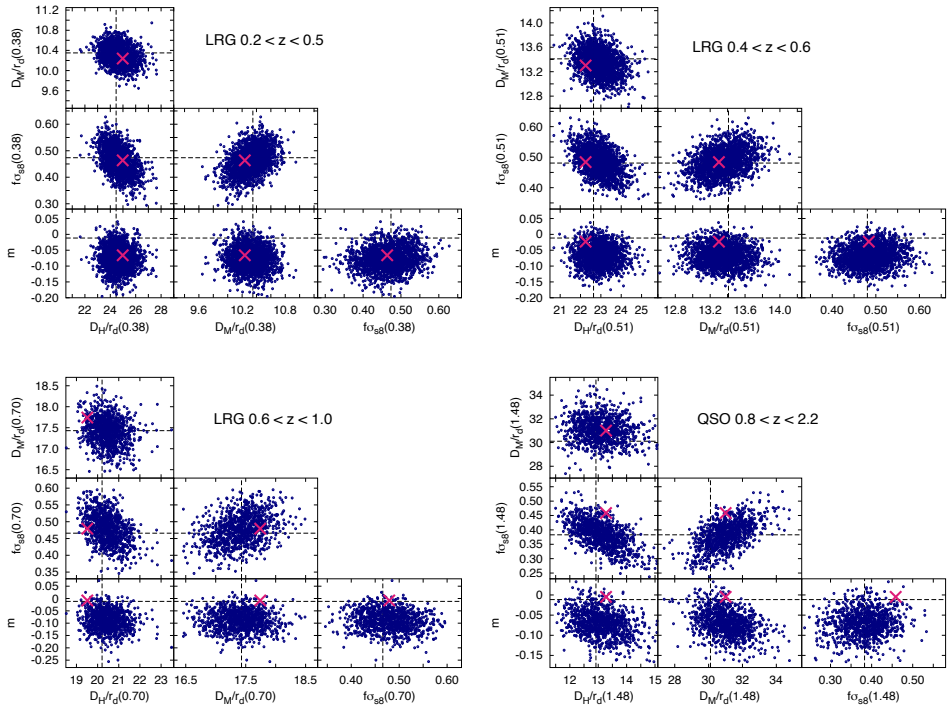


**Figure 10**. Triangle plots for the BOSS and eBOSS samples when the ShapeFit pipeline is applied. The four physical parameters of interest are shown in each panel: the BAO longitudinal and transverse distances, $D_H/r_\mathrm{d}$ and $D_M/r_\mathrm{d}$, respectively; the growth of structure $f$ times $\sigma_{s8}$; and the shape parameter $m$. Each panel displays one of the four studied BOSS/eBOSS samples, as indicated. The blue dots display the best-fits for these parameters in each of the mock realizations: 2048 for the Patchy mocks corresponding to the LRG samples $0.2 < z < 0.5$; ($z_\mathrm{eff} = 0.38$) and $0.4 < z < 0.6$; ($z_\mathrm{eff} = 0.51$); 1000 realizations for the EZmocks corresponding to LRG sample $0.6 < z < 1.0$; ($z_\mathrm{eff} = 0.70$), and the QSO sample $0.8 < z < 2.2$; ($z_\mathrm{eff} = 1.48$). The red cross represents the result for the actual data, as it is presented in table 5. The dotted black lines represent the expected values for the cosmology of the mocks (see table 2). All cases display the inferred parameters from both northern and southern patches. For the LRG samples, the pre-recon full shape information has been consistently combined with the post-recon catalogue BAO signal as described in section 3.3.

expressed in units of $10^3$ for better visualization. The statistics displayed in table 10 use all the available mock realizations, 2048 for the Patchy and 1000 for the EZmocks. The fits to the mean of the mocks offset-ed by the expected value, $\Delta x^{\mathrm{av}\cdot}$, correspond to the pre-reconstructed signal only, and its covariance (and error) correspond to 100 times the covariance (10 times the errors) of one single realization (including both northern and southern caps), and not the error of the mean of all used mocks. This ensures that the statistical errors are sufficiently small to clearly identify systematics relevant for the actual data sample. Unlike $\Delta x^{\mathrm{av}\cdot}$, the statistics related to the average of best-fits to individual mocks, $\langle \Delta x \rangle$, $\langle \sigma_x \rangle$, $S_x$, $Z_x$ and $S_{Z_x}$, contain both pre- and post-reconstruction information combined as described in section 3.3. All analyses are performed using the same pipeline employed to analyse the data and described in section 2.2.

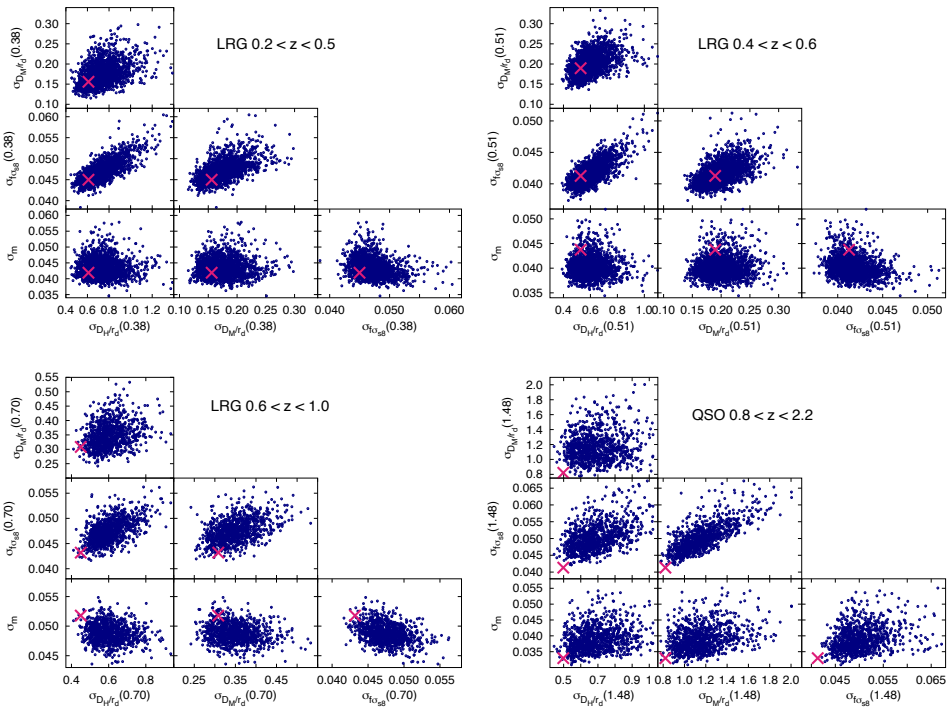


**Figure 11**. Same structure and notation as in figure 10, but displaying the $1\sigma$ error-bar for each parameter of interest.

The results regarding the offset between the expected value and the best-fit to the mean of the mocks, $\Delta x^{\rm av.}$, show a $1-2\%$ deviation for $\alpha_\parallel$; a $0-1.7\%$ deviation for $\alpha_\perp$; a $0-0.013$ deviation for $f\sigma_{s8}$; and a $-0.025$ deviation for $m$. Recall that the observed systematic offsets on the mocks should not be used to put constraints on the systematic error budget of the models, due to inaccuracies of the mocks when reproducing the actual clustering. However, we see a very good agreement with the expected value given the accuracy of the actual data, around 2% for $\alpha_\parallel$, 1.5% for $\alpha_\perp$, 0.040 for $f\sigma_{s8}$ and 0.040 for $m$.

In ideal Gaussian conditions[8] with sufficiently high signal-to-noise data (this is, large enough number of mock realizations) both $\langle\Delta x\rangle$ and $\Delta x^{\rm av.}$ should coincide. We indeed find a good agreement for $\alpha_\perp$ and $f\sigma_{s8}$, and reasonably good for $\alpha_\parallel$. On the other hand, $m$ shows significant differences, suggesting that the distribution of best-fitting values of $m$ is skewed towards negative values.

We now focus on the error-related quantities, $\langle\sigma_x\rangle$ and the *rms* of the best-fits, $S_x$. When the distribution is Gaussian and the covariance correctly modelled, these two error estimates should be very close. Indeed, we find a very good agreement among these two statistics for $\alpha_\parallel$, $\alpha_\perp$ and $f\sigma_{s8}$, indicating that not only the distribution for those variables is close to Gaussian, but also that there are no indications of covariance matrix-related issues. We do observe differences for $m$, but this is not a surprise, given the non-Gaussian signature

[8]When the distribution of best-fitting quantities is described by a Gaussian distribution, without any skewness or any anomalous kurtosis.

| Variable $\times 10^3$ | LRG(0.38) | LRG(0.51) | LRG(0.70) | QSO(1.48) |
|---|---|---|---|---|
| $\Delta\alpha_{\parallel}^{\rm av.}$ | $13.7 \pm 4.0$ | $20.4 \pm 3.6$ | $18.5 \pm 3.8$ | $-15.7 \pm 5.3$ |
| $\langle\Delta\alpha_{\parallel}\rangle$ | 7.4861 | 12.3344 | 14.6305 | 15.0770 |
| $\langle\sigma_{\alpha_{\parallel}}\rangle$ | 29.9673 | 26.5106 | 30.2284 | 53.8854 |
| $S_{\alpha_{\parallel}}$ | 33.4643 | 27.4981 | 31.4638 | 51.8706 |
| $\langle Z_{\alpha_{\parallel}}\rangle$ | $-0.0546$ | $-0.0406$ | $-0.0501$ | $-0.0851$ |
| $S_{Z_{\alpha_{\parallel}}}$ | 1.0723 | 1.0313 | 1.0055 | 0.9794 |
| $\Delta\alpha_{\perp}^{\rm av.}$ | $-2.4 \pm 2.4$ | $-6.2 \pm 2.2$ | $-6.8 \pm 2.6$ | $17.0 \pm 3.9$ |
| $\langle\Delta\alpha_{\perp}\rangle$ | $-2.3970$ | $-4.5816$ | $-3.3037$ | 32.3815 |
| $\langle\sigma_{\alpha_{\perp}}\rangle$ | 16.9014 | 14.9603 | 19.9959 | 38.9782 |
| $S_{\alpha_{\perp}}$ | 17.5587 | 14.6142 | 19.3600 | 35.6125 |
| $\langle Z_{\alpha_{\perp}}\rangle$ | 0.0043 | 0.0006 | $-0.0050$ | $-0.0344$ |
| $S_{Z_{\alpha_{\perp}}}$ | 1.0351 | 0.9744 | 0.9672 | 0.9215 |
| $\Delta f\sigma_{s8}^{\rm av.}$ | $3.9 \pm 5.7$ | $7.9 \pm 5.0$ | $12.7 \pm 6.0$ | $2.1 \pm 4.7$ |
| $\langle\Delta f\sigma_{s8}\rangle$ | 5.8290 | 11.6461 | 14.5541 | 7.8721 |
| $\langle\sigma_{f\sigma_{s8}}\rangle$ | 48.2098 | 41.9628 | 47.7991 | 51.4069 |
| $S_{f\sigma_{s8}}$ | 48.4473 | 40.6968 | 45.6538 | 49.9718 |
| $\langle Z_{f\sigma_{s8}}\rangle$ | 0.0032 | 0.0018 | $-0.0040$ | 0.0141 |
| $S_{Z_{f\sigma_{s8}}}$ | 1.0051 | 0.9670 | 0.9539 | 0.9600 |
| $\Delta m^{\rm av.}$ | $-25.0 \pm 5.2$ | $-26.0 \pm 5.0$ | $-27.2 \pm 5.5$ | $-19.0 \pm 3.9$ |
| $\langle\Delta m\rangle$ | $-65.3894$ | $-56.1880$ | $-77.3976$ | $-58.9662$ |
| $\langle\sigma_m\rangle$ | 43.3229 | 40.1828 | 48.8380 | 39.0732 |
| $S_m$ | 34.1271 | 31.2587 | 40.9830 | 31.6964 |
| $\langle Z_m\rangle$ | $-0.0199$ | $-0.0126$ | $-0.0111$ | $-0.0178$ |
| $S_{Z_m}$ | 0.7819 | 0.7709 | 0.8451 | 0.8216 |

**Table 10**. Statistics derived from the 2048 realizations of the Patchy mocks (for the LRG(0.38) and LRG(0.51) samples) and from the 1000 realizations of the EZmocks (LRG(0.70) and QSO(1.48) samples), for the four physical variables of interests, the BAO scales along and across the line of sight, $\alpha_{\parallel}$, $\alpha_{\perp}$, the growth of structure $f$ times $\sigma_{s8}$, and the shape parameter $m$. For each of these variables ($x = \alpha_{\parallel}$, $\alpha_{\perp}$ $f\sigma_{s8}$, $m$) we display the fit to the mean of the mocks minus its expected value, $\Delta x^{\rm av.}$; the average of individual fits minus its expected value, $\langle\Delta x\rangle$; the average of errors of the individual fits, $\langle\sigma_x\rangle$; the *rms* of all best-fits, $S_x$, the average of the $Z$-statistic (see text), $\langle Z_x\rangle$ and its *rms*, $S_{Z_x}$. The expected values for each of the samples can be found in table 3.

presented when comparing the best-fit of the mean to the average of individual best-fits. Another way to quantify the agreement between $S_x$ and $\langle\sigma_x\rangle$ is through the variable $Z_x$, which for Gaussian distributions should return a mean value of 0 and a *rms* of 1. Indeed we find a very good agreement of $Z = 0 \pm 1$ for $\alpha_{\parallel}$, $\alpha_{\perp}$ and $f\sigma_{s8}$. In particular, we find that $S_{Z_x}$ tend to be slightly above or below unity by just 5% for $\alpha_{\parallel}$, $\alpha_{\perp}$ and $f\sigma_{s8}$, which gives an order of magnitude on the accuracy of the errors reported on the analysis of the actual data. For the variable $m$ we find an offset on $Z$ of around $-0.015$ and a $S_{Z_m} \sim 0.8$ because of the non-Gaussian behaviour already described.

We conclude that the mocks describe well the expected clustering for the BAO variables, $\alpha_{\parallel}$ and $\alpha_{\perp}$, as well as for the anisotropic clustering, $f\sigma_{s8}$. They fail to reproduce accurately the signal of the shape parameter $m$, under-estimating its value by about $-0.025$, which corresponds to 1/2 to 2/3 of $1\sigma$ error for the data. We explain this effect as due to the

inaccuracy of fast techniques implemented in the production of the mocks. Both Patchy and EZmocks are based on the Zeldovich approximation that does not fully account for the effect of pre-virialization, which slightly boosts the amplitude of the shape of the power spectrum at the scales where $m$ is sensitive, $0.05 < k\,[h\mathrm{Mpc}^{-1}] < 0.10$.

The statistics of the errors for $\alpha_{\parallel}$, $\alpha_{\perp}$ and $f\sigma_{s8}$ show a very good agreement with the Gaussian statistics and confirm that the errors of the data are accurate at 5% level. For the variable $m$ we report a non-Gaussian distribution which tend to skew the distribution towards negative values.

### 6.2 Systematic error budget

In the previous section we have reported how the pipeline used for the data performed on the EZ and Patchy mocks. However, these mocks are based on fast methods, such as the Zeldovich approximation, and they do not describe the power spectrum clustering at the precision level required for setting the systematic error budget. For this reason we aim to test the performance of the pipeline on full N-body mocks. We focus on two sets, the Nseries mocks and the PT challenge mocks, which we briefly describe below.

The Nseries mocks[9] consist of 84 pseudo-independent realizations of the BOSS CMASS northern geometry within redshifts $0.43 < z < 0.70$; ($z_{\rm eff} = 0.56$), which were used by the BOSS team to set the official systematic error budget of the BAO and RSD measurements in the final cosmology paper [11]. The Nseries mocks have been generated out of 7 fully independent periodic boxes of $2.6\,h^{-1}$Gpc box side. For each of these cubic boxes 4 different orientations of the CMASS northern geometry are fitted, and each of these fitted orientations are applied on 3 pre-rotation positions of the box, where the 3 Cartesian positions and velocities are swapped, to extract all $7 \times 4 \times 3 = 84$ pseudo-independent realizations with BOSS northern geometry. The mass resolution is $1.5 \times 10^{11}\,M_{\odot}h^{-1}$, with $2048^3$ dark matter particles per box. The identified haloes are populated with galaxies following a HOD model tuned to match the clustering of LRGs observed by BOSS. These mocks are analyzed using the covariance matrix extracted from the Patchy mocks with the same sky geometry as these Nseries mocks. The matrix elements of this covariance are rescaled by 10% in order to account for the difference in particles between the Patchy mocks. This difference arises from veto mask effects which are not implemented in the Nseries mocks. The underlying cosmology of these mocks is consistent with the Wilkinson Microwave Anisotropy Probe (WMAP, [1]) best-fitting cosmology, $h = 0.7$, $\Omega_{\rm m} = 0.286$, $n_s = 0.96$, $\Omega_{\rm b} = 0.047$, $\sigma_8 = 0.820$. In total, these 84 pseudo-independent mocks have an associated effective volume of $106\,\mathrm{Gpc}^3h^{-3}$. Many previous works [18, 28, 53, 55–57, 102–106] make use of these 84 realizations, as if they were independent, to test their pipelines. This is only a good approximation when we exclusively focus on RSD- and BAO-related quantities. When we also want to test for the shape of the power spectrum, the additional realizations coming from the pre-rotations and the inherent real-space volume overlap among cuts, end up producing a severe under-estimation of the errors of parameters sensitive to the real space power spectrum on large scales, such as $m$. For this reason, we opt to carefully select a subset of these 84 skycuts to reduce the overlapping effect. In order to do so, we compute the cross power among the 12 different skycut orientations (including the pre-rotations) for each of the 7 boxes ($12 \times 11/2 = 66$ cross-power combinations for each box), and average each of these 66 cross spectra among the 7 independent realizations. We then select those 6 orientations per box whose $k$-mode-weighted added cross-power-spectrum-squared $k$-bins is closer to 0. This is motivated by the

[9] The Nseries mocks are publicly available in [101] .

fact that partially overlapping samples should have cross-power signal different than 0. We refer to this subset of $6 \times 7 = 42$ realizations as the Nseries-$\mathcal{Z}$[10], with a effective volume of $53\,\mathrm{Gpc}^3h^{-3}$. Additionally, we consider the 7 fully independent Nseries cubic boxes, with a total effective volume of $80\,\mathrm{Gpc}^3h^{-3}$.

The PT challenge mocks [22, 107] consist of 10 independent realizations in periodic boxes whose comoving side length is $3840\,[h^{-1}\mathrm{Mpc}]$ with $3072^3$ particles, where the 3 input $\Lambda$CDM parameters, $\Omega_\mathrm{m}$, $A_s$ and $H_0$, were randomly selected from a Gaussian probability distribution centered at the Planck fiducial cosmology.[11] Halo catalogues are identified by using ROCKSTAR halo finder [108]. Additionally, these haloes are populated using a HOD description roughly matching BOSS LRG galaxy data. Here we only focus on the snapshot produced at $z = 0.61$. The mocks are analyzed using an analytically estimated covariance (also provided by the PT-Challenge team), where the correlation between different multipoles at the same wave-vector $k$ is non-zero, and the correlation between adjacent $k$-bins is ignored. In total, these mocks have an associated effective volume of $566\,\mathrm{Gpc}^3h^{-3}$.

| $\Delta x \pm 2\sigma$ | Nseries-$\mathcal{Z}$ Sky | Nseries Box | PT challenge | $1\sigma$ error of data |
|---|---|---|---|---|
| $\alpha_\parallel$ | $0.0066 \pm 0.0088$ | $0.0082 \pm 0.0076$ | $0.0077 \pm 0.0036$ | $[0.022 - 0.038]$ |
| $\alpha_\perp$ | $-0.0038 \pm 0.0054$ | $-0.0021 \pm 0.0043$ | $-0.0003 \pm 0.0024$ | $[0.014 - 0.028]$ |
| $f\sigma_{s8}$ | $-0.0056 \pm 0.0115$ | $-0.007 \pm 0.010$ | $-0.0039 \pm 0.0049$ | $[0.041 - 0.045]$ |
| $m$ | $-0.014 \pm 0.013$ | $-0.009 \pm 0.012$ | $-0.0012 \pm 0.0068$ | $[0.033 - 0.052]$ |
| $\Omega_\mathrm{m}$ | $-0.0048 \pm 0.0050$ | $-0.0026 \pm 0.0043$ | $0.0008 \pm 0.0022$ | 0.0057 |
| $H_0$ | $-0.10 \pm 0.75$ | $-0.16 \pm 0.70$ | $-0.24 \pm 0.36$ | 0.67 |
| $A_s \times 10^9$ | $0.033 \pm 0.103$ | $0.008 \pm 0.093$ | $-0.007 \pm 0.053$ | 0.20 |

**Table 11**. Systematic offsets found when fitting the mean of the 42 Nseries-$\mathcal{Z}$ skycut mocks ($z_\mathrm{eff} = 0.56$; $V_\mathrm{eff} = 53\,[\mathrm{Gpc}h^{-1}]^3$), the Nseries cubic mocks ($z_\mathrm{eff} = 0.50$; $V_\mathrm{eff} = 80\,[\mathrm{Gpc}h^{-1}]^3$), and the PT challenge mocks ($z_\mathrm{eff} = 0.61$; $V_\mathrm{eff} = 566\,[\mathrm{Gpc}h^{-1}]^3$]), for the four compressed physical variables of interest, $x = \alpha_\parallel$, $\alpha_\perp$, $f\sigma_{s8}$ and $m$; as well as for the three cosmology variables, $x = \Omega_\mathrm{m}$, $H_0$ and $A_s$, derived from the interpretation of the physical variables within a $\Lambda$CDM model. For both Nseries and PT challenge mocks, the error-bars represent the 95% confidence level ($2\sigma$). For reference we also quote the $1\sigma$ statistical error for the full data sample, which spans along four LRG and QSO sub-samples within $0.2 < z < 2.2$, and therefore we just display the interval set by the largest and smallest error (see table 5 for the statistical error for each of the samples). The errors of the cosmology variables have the $2.1 > z$ Ly-$\alpha$ contribution and the BBN prior, as described in section 3.4. The analysis of data and mocks is done using the same pipeline assumptions as described in section 3. Unlike the LRG samples of the data, the Nseries or PT challenge mock data do not include the reconstruction signal.

Table 11 summarizes the observed offsets for these two sets of N-body mocks. The Nseries results are displayed for the power spectrum average of the 42 realizations of the 'Nseries-$\mathcal{Z}$ Sky' sample, and for the power spectrum average of the 7 cubic boxes, 'Nseries Box'. For reference the results from the average of the power spectra of the full 84 Nseries skycut mocks can be found in the panels of figure 12 of Ref. [21] in orange contours. On the other hand, the PT challenge results correspond to the DATA-like MIN in table 3 and red contours in fig. 2 of Ref. [23]. For each variable, we report the difference between the

[10] The indices for these realizations are $\{3, 6, 7, 8, 9, 12\} + 12i$, for $i = 0, \ldots, 6$.

[11] These randomly drawn values were kept secret (blind) and not publicly known. Other cosmological parameters such as the primordial tilt and the baryon-to-matter ratio were fixed to $\Omega_\mathrm{b}/\Omega_\mathrm{m} = 0.1571$ and $n_s = 0.9649$.

measured parameter and the expected quantity given the known cosmology of each set of mocks. The errors represent the 95% confidence level (i.e., they represent the $2\sigma$ contours) and correspond to the error of the mean. In order to set the systematic error budget we follow a similar criterion to the eBOSS team analysis: for each variable, when the observed offset on the mean of the mocks is within the $2\sigma$ confidence interval, the precision of the mocks' effective volume is not sufficiently high to resolve potential systematics deviations. When a systematic offset detected on the mocks (at $> 95\%$ confidence level, given the mocks statistics) represents a significant fraction of the $1\sigma$ statistical error of the data, we add this contribution in quadrature to the $1\sigma$ statistical error of the data to account for the systematic error[12]. For reference, we display the $1\sigma$ statistical error inferred from the data in the last column of table 11. For the physical variables we display the interval between the smallest and largest error found for the four redshift bins, whereas for the cosmology variables we simply quote the errors when all the samples (including Ly-$\alpha$) are considered, along with the BBN prior, as described in section 4 and 5. Note that, unlike the PT- and Nseries mocks, the analysis of the data combines measurements at different redshifts, which allows to break degeneracies in the $\Lambda$CDM variables and greatly reduce the error bars. For this reason the data, with an effective volume of the galaxy sample corresponding to $2.82\,[\mathrm{Gpc}h^{-1}]^3$ has errorbars on $\{\Omega_\mathrm{m},\, H_0,\, A_s\}$ comparable to the ones of the mock samples with much larger effective volumes.

Among the physical variables, we find that the Nseries-$\mathcal{Z}$ result for $m$ is off by $\sim 2\sigma$, which represent a $1/2$ to $1/4$ contribution to the statistical $1\sigma$ error of the data. This discrepancy vanishes when $m$ is inferred from the Nseries boxes ($m$ is well within the $2\sigma$ expected deviation), and it also not present for the PT challenge mocks (well within $1\sigma$ expected deviation). Unlike the PT challenge mocks, the Nseries skycut realizations are not fully independent. When considering the full 84 realizations we find $\Delta m \pm 2\sigma = -0.0172 \pm 0.0093$, a $3.8\sigma$ deviation from its expected value (see orange contours of fig. 12 of Ref. [21]), which is off by $1.5\sigma$ from the Nseries box results. Since both Nseries Sky and Nseries Box contain almost the same objects, this result is highly inconsistent. This discrepancy between skycuts and boxes motivated us to investigate effect of the overlap among the full 84 Nseries sky realizations. Indeed, because certain patches of the boxes are repeated among the 84 realizations, the parameter errors estimated from the mean of the 84 Nseries sky mocks is under-estimated, and in particular, this under-estimate is expected to be more severe at large scales, where the shape parameter $m$ is measured. By selecting those 42 realizations with less cross power among the realizations coming from the same box, we choose those realizations that are more independent (or less correlated), which helps to bring together the results from the Nseries Sky and boxes. We conclude that there may be still some residual overlap in the Nseries-$\mathcal{Z}$ sample, which slightly drives the deviation of $m$ away from the Nseries Box results, slightly outside the $2\sigma$ confidence interval. Since no relevant deviation is observed in the cases where the samples are fully independent, we do not consider necessary to add any systematic contribution to $m$.

We find $\alpha_\parallel$ is biased by $4.2\sigma$ in the PT challenge, as well as $2.1\sigma$ on the Nseries Box mocks, in both cases the systematic shift is of similar magnitude, $+0.0077$ and $+0.0082$, respectively. This represents a $1/3$ to $1/5$ of the statistical error of the data. As explained in Ref. [23], the origin of this systematic is related to the hexadecapole signal. Certainly, when repeating the fit on the mean using only the monopole and quadrupole signals we find an offset

[12]The eBOSS team followed the conservative approach of adding the $2\sigma$ interval as a systematic error, when no-systematic error could be determined. We do not follow this approach in this paper and add no error budget when the deviation is found to be within $2\sigma$ of the mean of the mocks.

of $-0.003 \pm 0.011$ for the Nseries Boxes; and $0.0040 \pm 0.054$[13] for the PT challenge mocks, both cases perfectly compatible with the expected result within the $2\sigma$ interval. However, the impact of this systematic error on the cosmology variables is non-existent. This may seem paradoxical at first sight, but is related to the effect of the model-prior. As discussed in Ref. [23], both $\alpha_{\parallel}$ and $\alpha_{\perp}$ variables are related via geometrical arguments within the ΛCDM model (as well as many other cosmology models). This tight relation in the parameter space of the $\alpha$'s forbids the region where the systematic on $\alpha_{\parallel}$ extends (and also limits the constraining power of the hexadecapole when the geometrical relation between $\alpha_{\parallel} - \alpha_{\perp}$ is imposed by the model). This can be seen in the left panel of fig. 2 of Ref. [23] (see red contours corresponding to the pipeline choices used in this paper), where the dashed empty contours display the parameter space allowed by the ΛCDM model, and the solid filled contours are those directly inferred from the model-agnostic analysis.

Focusing on the systematics of the ΛCDM parameters, we find that, from the PT challenge, Nseries-$\mathcal{Z}$ and Nseries Box mocks, all the three parameters are within the 95% confidence level drawn from the set of mocks, showing no hint of systematics. Because of the large effective volume of $V_{\rm eff} = 566\,[{\rm Gpc}h^{-1}]^3$ of the PT challenge mocks, the shift associated to the 95% is also considerably smaller than the size of the $1\sigma$ statistical error-bar –3 times smaller for $\Omega_{\rm m}$, 2 times smaller for $H_0$ and 4 times smaller for $A_s$– demonstrating that the total effective volume of these mocks is sufficiently high to limit the potential systematics on the data below a threshold which is significantly smaller than the statistical errors. Therefore we conclude that 1) we do not detect significant modeling systematics to be added to the cosmology variables, and 2) the precision in determining such systematics is small enough to make them negligible for the current BOSS+eBOSS combined catalogues.

## 7 Discussion and Conclusions

We make use of the final BOSS and eBOSS catalogues, product of four generations of Sloan Digital Sky Survey, representing a two decades long effort. BOSS and eBOSS probe over 10 billion years of cosmic evolution through more than 2 million spectra and represents the state-of-the art three-dimensional map of LSS to date. It will remain unrivaled until the next generation surveys [100, 109, 110] release their catalogues. The LSS clustering in BOSS and eBOSS catalogues has been analyzed by the SDSS collaboration using what we refer to as the 'classic' approach, where the clustering information is compressed into three physical parameters as a function of redshift: the line-of-sight and plane-of-the-sky apparent shift of the location of the standard ruler BAO feature in Fourier space which yields geometrical information on the expansion history and the amplitude of the redshift space distortions on linear scales which yields information on the linear growth rate of perturbations. But LSS clustering encloses extra cosmologically-relevant signal, most of which can be extracted from the large-scales *Shape* of the power spectrum. This is what the proposed ShapeFit [21] approach does. We extend the original ShapeFit formulation to include the post-recon BAO information, correctly accounting for the pre-recon and post-recon compressed variables covariance.

Then we apply the ShapeFit analysis on the BOSS and eBOSS data and present the resulting constraints on the physical parameters, which are summarized in Fig. 2. These can subsequently be interpreted in terms of a variety of cosmological models, to produce

[13] As in table 11, the errors correspond to the 95% confidence level.

constraints on each model's parameters. The standard ΛCDM model, with parameters calibrated from CMB observations, provides a good fit to the recovered compressed parameters which were derived independently of the model, offering a powerful consistency check for the underlying model's assumptions.

For the extensions to the ΛCDM model considered here (models with spatial curvature, dark energy equation of state parameter not equal to -1, both constant and varying in redshift according to the $w_0 - w_a$ parameterization, non-zero neutrino masses, and extra effective neutrino species), we find that the *Shape* improves the determination of the matter density parameter $\Omega_{\rm m}$, further helping to break parameter degeneracies. This additional information comes from the signature of physical processes around matter-radiation equality and is thus a late-time probe of early-time physics. This information is highly complementary to that captured by BAO and RSD signals. When BOSS and eBOSS data are analyzed in combination with CMB data, the additional constraining power of the *Shape* compared to BAO+RSD is unimportant. It is worth mentioning, however, that ShapeFit -assuming a power law power spectrum with fixed spectral index and a BBN prior on the physical baryon density- provides from late-time observations alone a bound on the sum of neutrino masses of $\Sigma m_\nu < 0.4$ eV (95% confidence), consistent with $\Sigma m_\nu < 0.24$ eV provided by CMB alone including lensing. ShapeFit in combination with Planck data yields $\Sigma m_\nu < 0.082$ eV, the tightest bound on the sum of neutrino masses from cosmology to date. The spatial curvature constraints from LSS alone improves by a factor 2.7 from the measurement of the *Shape*.

For dark energy models with constant equation of state parameter and $w_0 - w_a$ parameterization, the ShapeFit approach produces constraints on cosmological parameters comparable to those obtained by the combination of CMB+BAO+RSD. In other words, ShapeFit provides a late-time probe that can, in some cases, substitute the use of CMB data and yet achieve comparable statistical power.

It is important to stress that the compressed variables approach has several advantages compared to the alternative, full modeling (FM) approach where power spectra are directly compared to theory predictions for a given cosmological model to constrain the model's parameter. In the FM approach, the model needs to be chosen *ab inito*, hence the full analysis must be repeated to explore different models or families of models. As table 7 summarizes, the compressed variables can be translated very quickly and at low computational cost into cosmological parameters for any cosmological model of choice. Section 5.4.1 and Ref. [24] further show that this compression is effectively lossless at least for ΛCDM.

The compression aims at isolating the part of the signal whose information content is least affected by systematics. The compressed variables approach is model-agnostic; the model-dependence is introduced only at the interpretation stage, at the very end of the process. The physical parameters, capturing the effect on clustering of the physical processes at play, offer a simple way to disentangle late-time physics information from imprints of early-Universe physics. This is of value for going beyond simple parameter-fitting and for pursuing ways to test the model and its underlying assumptions. For a given cosmological model, constraints on the model's parameters come from a variety of signatures of disparate physical processing acting at different cosmic epochs; early-and late- time effects are intrinsically related. However, by measuring them separately as in the compressed variable approach, the early- and late-time physical variables provide a powerful consistency test of the cosmological model. The establishment of the ΛCDM model as the standard cosmological model, along with the avalanche of data in the first decade of the 2000', has transformed cosmology into a precision science. In precision cosmology the parameters of a given model (especially

the ΛCDM model and simple, one-parameter extensions) are measured incredibly precisely. But precision is meaningless without accuracy: the standard cosmological model is likely an effective model, as a first-principle physical understanding of dark matter and dark energy is still lacking. To move beyond precision cosmology, it is important to devise analyses and approaches that are as much as possible model-independent or model agnostic, and that make possible to test (some of) the model's underlying assumptions. ShapeFit represents an effort in this direction.

## A Impact of the non-local Lagrangian bias in the shape parameter

Here we explore the correlations arising between the shape parameter $m$ and the non-local bias parameters when we drop the local-Lagrangian bias assumption.

We start by fitting the mean of the EZ mocks under different assumptions for $m$, $b_{3\rm nl}$ and $b_{\rm s2}$. In order to avoid any interference with the survey geometry, or with the intrinsic redshift evolution within light-cone of the mock, we fit the averaged power spectrum of the 479 independent realizations of the EZmocks periodic cubic boxes. These boxes, whose length size is $L = 5\,{\rm Gpc}h^{-1}$ and output redshift $z = 0.675$, are one of the 5 snapshots used to construct the full EZ light-cone mocks, which are utilized to derive the covariance of the data. The covariance matrix for this specific analysis is derived from the 479 independent realizations of the boxes. As a data vector, we consider the mean of the 479 realizations, but use the scaled covariance corresponding to just one of the cubic boxes, which has around 100 times the number of galaxies of the full north and southern light-cones combined from $0.6 < z < 1.0$. This ensures that the statistical errors are sufficiently small for identifying systematics relevant for the actual data sample.

| Model | Baseline cosmology | Expected value $m^{\rm exp} \times 10^3$ | Recovered value $m \times 10^3$ | $\chi^2$/d.o.f. |
|---|---|---|---|---|
| Local, $m$ free | Fiducial | $-11.5$ | $-36.7 \pm 7.4$ | $46.0/(39-8)$ |
| Local, $m$ free | EZ (true) | 0 | $-29.5 \pm 7.2$ | $46.0/(39-8)$ |
| Local, $m \equiv 0$ | EZ (true) | 0 | 0 | $68.2/(39-7)$ |
| $b_{3\rm nl}$ free, $m$ free | EZ (true) | 0 | $16 \pm 11$ | $38.1/(39-9)$ |
| $b_{3\rm nl}$ free, $m \equiv 0$ | EZ (true) | 0 | 0 | $38.5/(39-8)$ |
| $b_{\rm s2}$ free, $m$ free | EZ (true) | 0 | $-28 \pm 11$ | $44.5/(39-9)$ |
| $b_{\rm s2}$ free, $m \equiv 0$ | EZ (true) | 0 | 0 | $55.1/(39-8)$ |

**Table 12**. Constraints derived from the mean of 479 independent EZmock realizations of periodic cubic boxes at $z = 0.675$. We display the expected and measured values of $m$ and the minimum $\chi^2$ value for different setups and baseline cosmologies. 'Local' stands for the fiducial setup used for the main analysis of the paper, in short this is $\ell = 0, 2, 4$ and $0.02 < k\,[h{\rm Mpc}^{-1} < 0.15$ and assuming for $b_{s2}$ and $b_{3\rm nl}$ the local Lagrangian relations. Variations of this Local set up model are: $m \equiv 0$ i.e., fixing the $m$ parameter to 0, and/or allowing $b_{3\rm nl}$ and $b_{\rm s2}$ to float free. The associated error corresponds to just one of the boxes, which has around 100 times the number of galaxies of NGC+SGC $0.6 < z < 1.0$ LRG sample. When $b_{3\rm nl}$ is set to be local, it takes the value of $\sim 0.11$ (given by the value of $b_1 \sim 2.1$). When it is set to be free it is constrained to be $b_{3\rm nl} = -0.44 \pm 0.12$ when $m$ is set to 0; and $b_{3\rm nl} = -0.54 \pm 0.13$ when $m$ is free (in this case $b_{3\rm nl}$ and $m$ have a cross-correlation factor of $-0.6$). Similarly, when letting $b_{s2}$ free we find $b_{s2} = 2.45 \pm 0.92$ for $m \equiv 0$, and $b_{s2} = 1.3 \pm 1.6$ when $m$ is free to vary. For the local Lagrangian bias case we find $b_{s2} \sim -0.64$ given the value of $b_1 \sim 2.1$.

Table 12 reports the results of fitting the signal from the EZmocks cubic boxes. For conciseness we show the best-fit values of $m$ and the minimum $\chi^2$ obtained for different pipeline choices: 'Local' is the fiducial pipeline used in the main analysis of this paper where the non-local biases are kept fixed to their local Lagrangian predictions; $m$ can be freely varied (along the rest of parameters as described in section 2.2.2) or can be fixed to $m \equiv 0$ when doing the fit. In addition, we show the results for the baseline cosmology set to the fiducial case (used through the main text of this paper) and the own true cosmology of the EZmocks (see table 2 for the details on these two baseline cosmologies). Note that this baseline cosmology is used exclusively for computing the template of our model.[14][15] For reference, we add the expected value of $m$, which by definition is 0 when the own true cosmology of the mocks is used as a baseline cosmology model. Under this simplistic approach we see how the recovered $m$ value is shifted away from its expected value when the 'Local' set up with $m$ freely varied is used. For both fiducial and EZ cosmologies we find that $m$ moves towards negative values by about $0.025 - 0.030$. This result is in line what found in figure 10 when the individual light-cone Patchy and EZmocks were analyzed, and thus excludes that spurious effects of the modelling of the window, or the intrinsic redshift evolution for the light-cone mocks can be the cause for this mismatch when recovering $m$. When we force $m$ to be 0 we find that the value of best-fitting $\chi^2$ significantly increases, just confirming that $m = 0$ is not a desired solution for the EZmocks. We then consider two follow up variations of this set up, allowing $b_{3\rm nl}$ and $b_{s2}$ to freely vary, with and without setting $m = 0$. We find that allowing $b_{s2}$ to be free, does not help significantly to recover the expected $m$. On the other hand, we find that when $b_{3\rm nl}$ is freely varied, we recover a more consistent $m$, at the same time that the best-fitting $\chi^2$ reduces significantly. For this specific case we find that the best-fit value for $b_{3\rm nl}$ is $b_{3\rm nl}(m \equiv 0) = -0.44 \pm 0.12$ and $b_{3\rm nl}(m\,\text{free}) = -0.54 \pm 0.13$; whereas for the local case $b_{3\rm nl}(\text{local}) \sim 0.11$. We discuss below the physical interpretation of these results.

Figure 12 shows the performance of four representative models described in table 12: (top panel) red lines correspond to the models with $m \equiv m^{\rm exp} = 0$; blue lines to the models with $m$ as a free parameter; solid lines to models with $b_{3\rm nl}$ set to its local Lagrangian prediction; dashed lines to the models where $b_{3\rm nl}$ is free; for all cases $b_{s2}$ is set to is local Lagrangian prediction. Black dots with errorbars correspond to the measured signal from the cubic EZ mocks. As in table 12, the error-bars correspond to $1\sigma$ of the volume of a single cubic realization. The bottom sub-panel display the ratio between the mocks measurement and the model best-fit, using the same color scheme. We see how floating $m$ free with local $b_{3\rm nl}$ (solid blue line) produces a power spectrum similar to that obtained by setting $m = 0$ and floating $b_{3\rm nl}$ free (red dashed line), illustrating the degeneracy between $m$ and $b_{3\rm nl}$. We also see very clearly how the signal (or feature in the power spectrum) responsible for obtaining a $m \neq m^{\rm exp}$ when $b_{3\rm nl}$ is local, is localized mainly at $k \simeq 0.045\,h{\rm Mpc}^{-1}$ (solid red squares deviating from the horizontal black dotted line in the bottom sub-panel). As we have commented in Sec 6.2 this behaviour is a spurious signal caused by the method adopted to produce the fast EZmocks. The EZmocks rely on the Zeldovic approximation thus miss to include key pre-virialization terms which slightly affect the amplitude of the power spectrum at large scales.

[14] Since the signal is measured from the Cartesian positions of galaxies in the periodic boxes, we do not require any cosmology for transforming redshifts into comoving distances, and therefore no Alcock-Paczysnki effect is induced.

[15] In all the fits we include the grid correction for which $P(\langle\mathbf{k}\rangle) \neq \langle P(\mathbf{k})\rangle$ as described in eq. 6.1-6.2 of [21], although for such large box it turns out to be a minor correction on $m$ for the $k$ range considered, $0.02 < k\,[{\rm Mpc}^{-1}h] < 0.15$, which shifts 4 units of $m \times 10^3$ towards positive values.

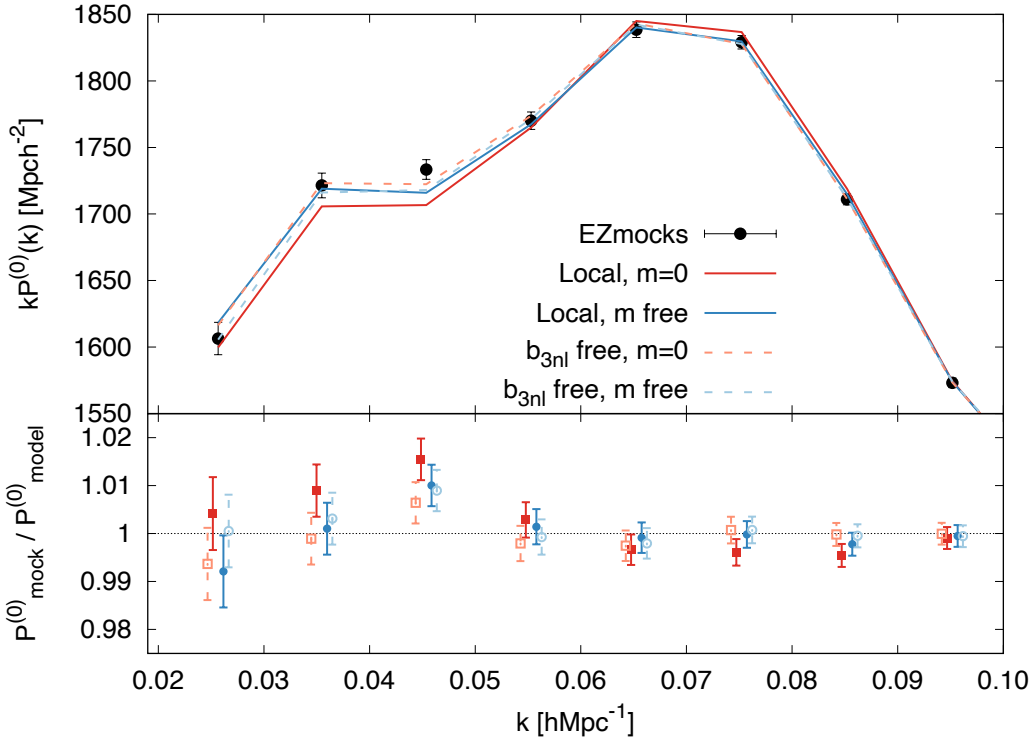


**Figure 12**. Performance of some of the models listed on table 12 (lines with colours) on the average of the 479 realizations of the periodic cubic EZmocks (black dots with error-bars). Red colour represents models where $m$ has been set to be 0 (its expected value), blue colour represents models with $m$ freely varied; solid lines represents models with Local Lagrangian conditions for $b_{3\rm nl}$, and dashed where $b_{3\rm nl}$ is freely varied. In all cases the models employ the true base-line template from the EZmocks. Although only the monopole is shown, we simultaneously fit the three relevant multipoles within the range $0.02 < k\,[h{\rm Mpc}^{-1}] < 0.15$, as for the data. The best-fitting values for $m$, $b_{3\rm nl}$ and minimum $\chi^2$ are displayed in table 12.

These missing negative terms, are responsible for an excess of power in the EZmocks at large scales, mimicking the effect of a non-local bias, and thus pushing the recovered $m$ to negative values under the local Lagrangian bias assumption for $b_{3\rm nl}$ (or pushing $b_{3\rm nl}$ away from its local prediction for $m = 0$). This is supported by the results obtained when fitting $m$ on N-body mocks, such as the PT challenge mocks (see [23] and section 6.2) where for a similar HOD we find results consistent with $m = 0$, as well as for the local Lagrangian prediction on $b_{3\rm nl}$ and $b_{s2}$.

The choice of assuming the local Lagrangian prediction on our main pipeline analysis applied for the data is hence well justified: when analyzing N-body mocks populated by galaxies following realistic HOD models, we find no sign of departure from locality. However, we want to test the impact of relaxing this assumption on the data, to quantify how much our results would change. This is displayed in figure 13 for the LRG $0.2 < z < 0.5$ sample: the $b_{3\rm nl}(b_{s2})$ bias parameter is allowed to depart from its local prediction in the left(right)

panel. For each type of bias we show 3 cases: its local case (purple contours), the case where its value is set to 0 (orange contours) and the case where we float this parameter free with a tight Gaussian prior around the value preferred by the EZmocks. Although we know that the best-fit value of $b_{3\rm nl}$ and $b_{\rm s2}$ for the EZmocks is an unphysical artifact of the fast techniques employed to generate these mocks, we assume those best-fitting non-local bias results as extreme cases if, mistakenly, the non-local parameters of the data were fixed by the signal of the EZmocks. In addition, table 13 reports the best-fit values of $m$ for the 4 data samples when $b_{3\rm nl}$ is kept to be local[16], when it is set to 0, and when is freely varied with a tight Gaussian prior around the preferred value when fitting the EZmocks.

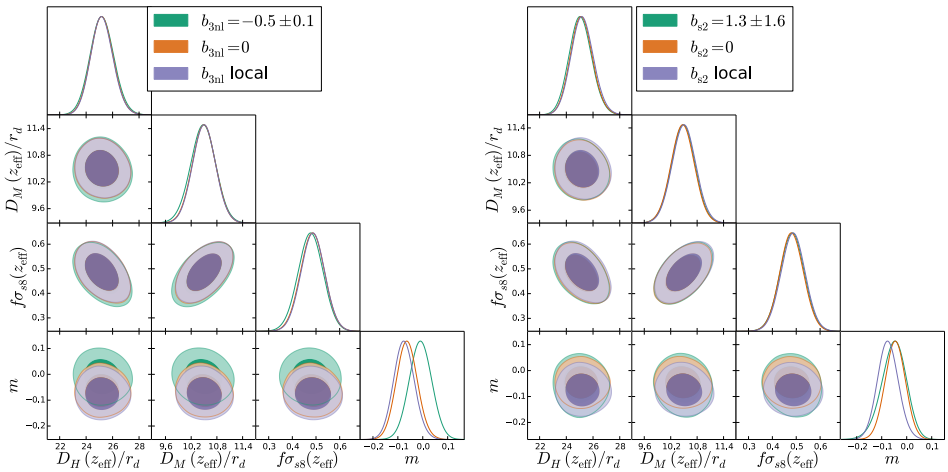


**Figure 13**. Impact of the assumptions for the non-local biases, $b_{3\rm nl}$ (left panel) and $b_{s2}$ (right panel) on the cosmology parameters for the LRG sample $0.2 < z < 0.5$ data sample for the pre-reconstruction catalogue only. The colours represent different choices on these bias parameters, as indicated in the legend. The green contours display the results with the written Gaussian prior on these non-local bias parameters (motivated by the value preferred by the EZmocks), the orange contours the results when setting these biases to 0; the purple contours the results of setting them to the local Lagrangian prediction (fiducial pipeline choice for these work). See table 13 for the numerical values of the left panel, along with the results when fitting the other data samples.

From the right panel of figure 13 we see that the impact of the choosing $b_{\rm s2}$ to be local, 0, or to be set around the value preferred for the EZmocks, has a very minor impact on $m$, and no impact at all on the rest of physical parameters. From the left panel we conclude that, if $b_{3\rm nl}$ departs from locality, fixing it to $b_{3\rm nl} = 0$ has no impact on the physical parameters, but setting it around the best-fit value preferred by the mocks, shift $m$ by $1.5\sigma$.

Table 13 displays the effect of changing the assumption on the locality of $b_{3\rm nl}$ for the four studied samples. As seen in the left panel of figure 13 for the LRG $0.2 < z < 0.5$ sample, only when $b_{3\rm nl}$ departs from locality and it is set around the preferred value for the EZmocks, the locality assumption has a noticeable impact on the best-fit $m$, yet no impact on the rest of the physical parameters. This shift in $m$ oscillates between $0.5\sigma$ and $1.5\sigma$ with respect to the local case, always towards positive values.

[16]Note that the values of $m$ for the $b_{3\rm nl}$ local cases of the LRG samples are slightly different from those reported by table 5, as in this case we only use the pre-reconstruction catalogues for simplicity.

| Sample | $b_{3\mathrm{nl}}$ local | $b_{3\mathrm{nl}} = 0$ | $b_{3\mathrm{nl}} = -0.5 \pm 0.1$ |
|---|---|---|---|
| LRG $0.2 < z < 0.5$ | $-0.075 \pm 0.042$ | $-0.063 \pm 0.042$ | $-0.009 \pm 0.045$ |
| LRG $0.4 < z < 0.6$ | $-0.033 \pm 0.044$ | $-0.021 \pm 0.044$ | $0.041 \pm 0.047$ |
| LRG $0.6 < z < 1.0$ | $-0.019 \pm 0.052$ | $-0.012 \pm 0.053$ | $0.017 \pm 0.055$ |
| QSO $0.8 < z < 2.2$ | $-0.005 \pm 0.033$ | $0.002 \pm 0.033$ | $0.028 \pm 0.035$ |

**Table 13**. Best-fit $m$ values under different assumptions on $b_{3\mathrm{nl}}$ for the four different data samples (pre-reconstruction only). $b_{s2}$ is assumed local Lagrangian.

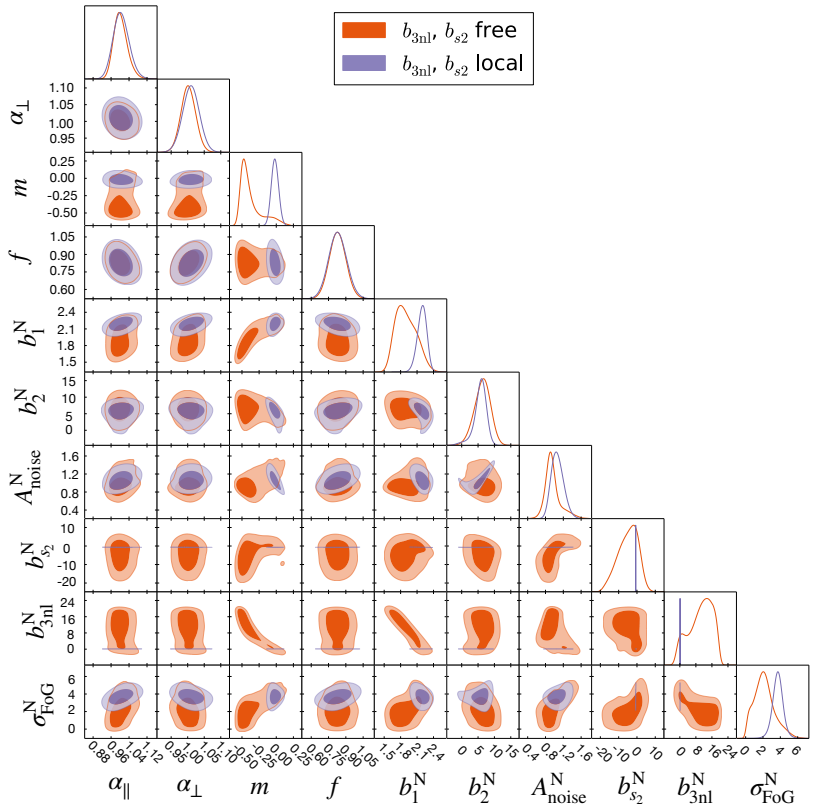


**Figure 14**. Posteriors for the pre-recon only BOSS+eBOSS LRG sample $0.6 < z < 1.0$. For clarity only the nuisance parameters of the NGC are shown (although the SGC is simultaneously constraint). The purple contours display the results when both $b_{3\mathrm{nl}}$ and $b_{s2}$ are set to their local Lagrangian predictions; the orange contours when they are freely varied with a wide uniform prior of $0 \pm 20$.

We conclude that the effect of $b_{s2}$ being local, or being set to the two explored non-local options has no impact at all on the physical parameters given the statistical precision of the data. The effect of $b_{3\mathrm{nl}}$ is more important, as anticipated at the beginning of this appendix. Although the local and $b_{3\mathrm{nl}} = 0$ choices show no significant difference among them given the size of statistical errors of the data, setting it to $-0.5 \pm 0.1$ significantly shifts the $m$ best-fit values, by around $1.5\sigma$. Although there is no strong evidence that the observed galaxies have such strong non-local behaviour (such extreme $b_{3\mathrm{nl}}$ values), the strong correlation found

between $b_{3\rm nl}$ and $m$ indicates that - for present and forthcoming surveys - the interpretation of the shape $m$ as a cosmology observable, regardless whether is done via the ShapeFit compression or via direct fits to the full $P(k)$ shape, relies on certain assumptions about the bias properties of the studied sample of galaxies. The other compressed parameters (and thus the cosmology extracted from them) are insensitive to these assumptions.

Finally, in figure 14 we display the full triangle plot of the pre-recon posteriors for the LRG eBOSS $0.6 < z < 1.0$ NGC sample, for the case where both $b_{s2}$ and $b_{3\rm nl}$ are set to their local Lagrangian prediction (purple contours) and where they are floated free with a wide uniform prior between $0 \pm 20$. We see how in the case the two non-local parameters are allowed to float free the constrains on $m$ largely degrade, returning essentially no-information from the shape. In addition, we see that both $b_{s2}$ and $b_{3\rm nl}$ hit the conservative prior limits, again indicating that the shape of the power spectrum is unable to simultaneously constrain $b_{s2}$, $b_{3\rm nl}$ and $m$ from power spectrum data alone. Because of this we do not report any preference of the data for non-local bias values. The inclusion of higher-order statistics in future data analysis may help to mitigate these large degeneration directions observed among $\{b_{3\rm nl}, b_{s2}, m\}$.

## B Fiber collision effect in the quasar sample

We aim to account for one of the main observational systematic effect of the eBOSS quasar samples, the fiber collisions. This effect is caused by the physical size of the optical fibers, which cannot be placed in the BOSS and eBOSS plates sufficiently close to each other to collect the spectra of imaging targets closer than a limiting angular size of 62", which for the quasar sample represents a physical distance of $\sim 0.9\,{\rm Mpc}h^{-1}$. Imaging targets closer than this minimum angular separation will have spectroscopic redshifts only if they lie in regions of the sky that have observed by more than one plate.

Thus, the eBOSS quasar catalogues tends to miss the redshift information of objects in regions where the density of objects is high. Not correcting by the effect of fiber collisions induces a change in the 3D clustering of the quasars (especially along the LOS), which can potentially bias the physical parameters we measure.

The fiber collision effect is imprinted in the EZmock quasar sample, and therefore by computing the physical parameters with and without the correction we can quantify the effect and validate the correction technique. We follow the approach proposed by [111] which accounts for the effect of fibre collisions in the modelling part (i.e., it does not correct the data catalogues, but the fitted model), which is also followed by the eBOSS quasar team analysis in Fourier space [59], as well as in configuration space [58].

In short, we modify the measured power spectrum by the following scale-dependent correction, $P_\ell^{\rm true}(k) = P_\ell^{\rm meas.}(k) - \Delta P_\ell(k)$, where $\Delta P_\ell(k)$ has two additive components, the uncorrelated and correlated,

$$\Delta P_\ell^{\rm uncorr}(k) = -f_s(2\ell+1)\mathcal{L}_\ell(0)\frac{(\pi D_{\rm fc})^2}{k})W_{\rm 2D}(kD_{\rm fc}), \tag{B.1}$$

$$\Delta P_\ell^{\rm corr}(k) = -\frac{(2\ell+1)f_s D_{\rm fc}^2}{4}\sum_{\ell'=0}^{\ell'_{\rm max}}\int_{k_{\rm min}}^{k_{\rm max}} qdq\, P_{\ell'}(q)\int_{\max(-1,-q/k)}^{\min(1,q/k)} d\mu \mathcal{L}_\ell(\mu) \times \mathcal{L}_{\ell'}(k\mu/q)W_{\rm 2D}(qD_{\rm fc}), \tag{B.2}$$

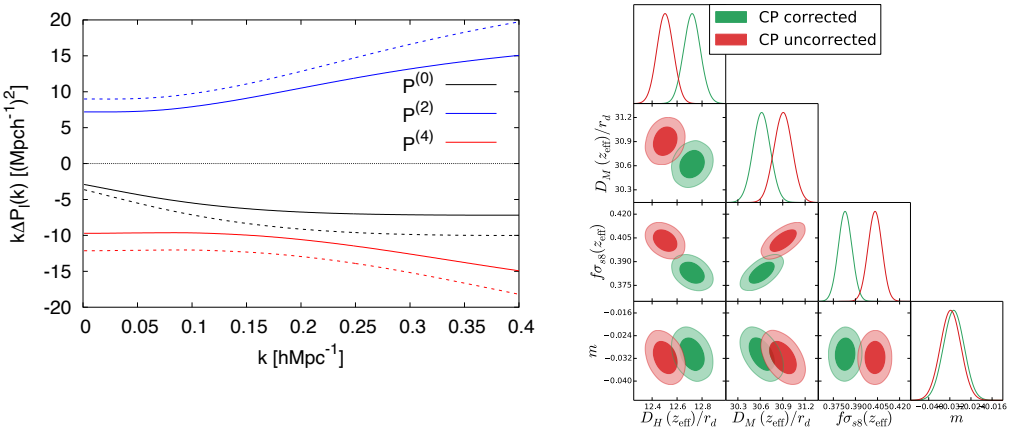


**Figure 15**. Left panel presents the close pair (CP in the figure legend) correction proposed by [111] implemented for the quasar sample according to eqs. (B.1)-(B.2). The solid/dashed lines display the total $\Delta P_\ell(k)$ correction for the northern/southern galactic cap, and the colors correspond to different $\ell$-multipoles, as displayed. The right panel displays the impact that ignoring the close pair correction has in physical parameters inferred from the mean power spectra of the 1000 realizations of quasar EZmocks: the fiber collision effect has been simulated in the EZmocks catalogues, and the (red) green contours show the analysis (not) correcting for them. The size of the contours correspond to a volume 100 times the volume of the data. Although not shown, the minimum $\chi^2$ improves when correcting for the close pairs from $202.7/(168-12)$ down to $132.1/(168-12)$, mainly due to the shift in the hexadecapole signal at all scales.

where, $W_{\rm 2D}(x) \equiv 2J_1(x)/x$ is the top-hat function in 2D, and $J_1$ is a Bessel function of the first kind and of order 1. The total effect of these collisions is $\Delta P_\ell(k) = \Delta P_\ell^{\rm uncorr}(k) + \Delta P_\ell^{\rm corr}(k)$. As suggested in [59] we take $f_c^{\rm NGC,SGC} = 0.36, 0.45$ (the fraction of objects affected by the fiber collisions in the northern and southern caps) and $D_{\rm fc} = 0.9\,{\rm Mpc}h^{-1}$ (the collision radius at the effective redshift of the quasars, $z = 1.48$). Although $\ell'_{\rm max}$ and $k_{\rm max}$ should extend to infinity, and $k_{\rm min}$ to 0, for practical reasons we choose $\ell'_{\rm max} = 8$, $k_{\rm min} = 10^{-3}\,h{\rm Mpc}^{-1}$ and $k_{\rm max} = 0.4\,h{\rm Mpc}^{-1}$. As discussed in [111] the effect of truncating $k_{\rm max}$ only affects the amplitude of the correction of the monopole, which is in any case re-absorbed by the free parameter which regulates the amplitude of shot noise. With these numbers, [59] determined that for the eBOSS quasars only 5% of the collisions were correlated (being actually groups of quasars physically close to each other), which implies that the dominant part of the $\Delta P_\ell(k)$ shift is $P_\ell^{\rm uncorr}(k)$, which is independent of the underlying true clustering of the quasars.

The left panel of figure 15 displays the total shift $\Delta P_\ell(k)$, for the northern (solid) and southern (dashed) patches, where the different colors stands for the different $\ell$-multipole contributions as indicated. Our analysis is insensitive to an overall scale-independent shift in $P^{(0)}$ as we are marginalizing over the amplitude of the shot noise.

Relative to the statistical error-bar of the quasar sample, the largest effect turns out to be in the hexadecapole, as is the multipole less affected by the bias parameters, which can also in part absorb part of the fiber collision effects. We find results very consistent with those shown in fig. 8 of [59].

The right panel of figure 15 displays how the best-fit physical parameters shift when the

mocks with the effect of fiber collisions imprinted are (not) corrected according to eqs. (B.1)-(B.2) in (red) green contours. We fit the mean of the 1000 realizations of the EZmocks (northern and southern caps), although the plotted errors correspond to 10 times of the statistical error of one realization. We report a change on $D_M/r_{\rm d}$, $D_H/r_{\rm d}$ and $f\sigma_{s8}$, which shifts the uncorrected mocks best-fitting values towards the expected values according to table 3. On the other hand, $m$ is barely affected by the fiber collision. This behaviour is expected, as most of the signal of $m$ comes from the derivative of $P^{(0)}$ at scales of $k \sim 0.05\,{\rm Mpc}^{-1}h$, which are barely affected by fiber collisions. Overall, the reported shift on the mocks represents a fairly small fraction of the error of the data, which is typically 10 times larger than the errors displayed by the plot.

| | $D_H/r_{\rm d}$ | $D_M/r_{\rm d}$ | $f\sigma_{s8}$ | $m$ | $\chi^2_{\rm min}$ |
|---|---|---|---|---|---|
| CP corr. | $13.27 \pm 0.50$ | $31.01 \pm 0.82$ | $0.468 \pm 0.042$ | $-0.005 \pm 0.033$ | 117.0 |
| CP uncorr. | $13.11 \pm 0.49$ | $31.23 \pm 0.82$ | $0.482 \pm 0.042$ | $-0.009 \pm 0.034$ | 117.5 |

**Table 14**. Effect of the fiber collisions on the best-fitting physical parameters of actual quasar data sample. CP corr. stands for the results when the fitted model accounts for the close pairs corrections via eqs. (B.1)-(B.2); CP uncorr. display the best-fits when this correction is ignored. Along with the best-fitting values we also report the valaue of the minimum $\chi^2$ with 168-12 degrees of freedom.

Table 14 presents the results of performing the fit of the actual quasar data taking into account the close pair correction of eqs. (B.1)-(B.2) (CP corr.), or ignoring it (CP uncorr.). We observe a fairly small shift, which cannot be distinguished from the intrinsic cosmic variance noise. However, as for the mocks, we see that $D_H/r_{\rm d}$ tends to increase by $1/3\sigma$, $D_M/r_{\rm d}$ and $f\sigma_{s8}$ tend to decrease by $1/4\sigma$ and $1/3\sigma$, respectively. On the other hand, $m$ is barely affected ($\sim 1/10\sigma$). We also report a slight improvement of the minimum $\chi^2_{\rm min}$ value of the fit, mainly due to an increase of the hexadecapole signal.

In summary, we see that the close pairs correction has a measurable effect only when the effective volume of the sample is about $\times 100$ the effective volume of the actual eBOSS data quasar sample, which shifts the posteriors of the BAO distances and $f\sigma_{s8}$ by a magnitude of $\lesssim 2\sigma$, whereas the shape parameter $m$ is unaffected. Nevertheless, for correctness, we do include this correction in our main analysis of the data, but we do not expect that inaccuracies on the exact free parameters of this model, such as the values of $f_c$ have any significant effect on the final results of this paper.

## C Impact of the prior assumptions

We discuss the motivations for and the effects of including certain priors in the analysis presented in the main text. We divide this appendix in two sections, the first one about the priors on nuisance parameters for the model-agnostic fit to the measured power spectra, and the second about the priors set during the interpretation of the compressed physical variables within a certain cosmology model.

### C.1 Prior assumptions on the model-agnostic analysis

In section 2.2.2 we have described the parametrization of the galaxy/quasar $P^{(\ell)}(k)$ model, with a set of physical and nuisance parameters. Among the nuisance parameters, the amplitude of shot noise $A_{\rm noise}$ and the second order bias $b_2$, are not particularly well constrained by power spectrum data alone, especially when the signal-to-noise ratio is not very high. As

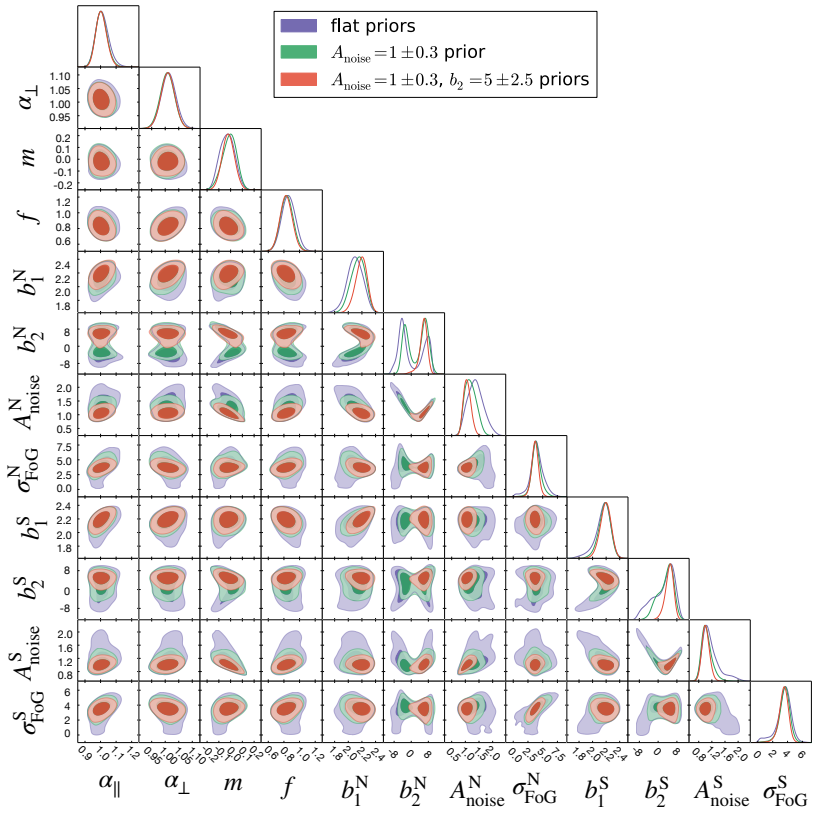


**Figure 16**. Posteriors for the pre-recon only BOSS+eBOSS LRG sample $0.6 < z < 1.0$. In purple the constraints using uniform wide priors for $A_{\rm noise}$ and $b_2$; in green when a Gaussian prior of $1 \pm 0.3$ is set for $A_{\rm noise}$; and in dark orange when additionally a Gaussian prior of $5 \pm 2.5$ is also set for $b_2$. For the rest of parameters uniform wide priors are used as presented in table 4.

shown in table 4 for all the samples we have set a Gaussian prior around the Poissonian noise prediction for the amplitude of shot noise, allowing a 30% deviation at $1\sigma$. This is a Gaussian prior of $A_{\rm noise} = 1 \pm 0.3$, for both northern and southern sample parameters. We know that halo-exclusion and the intrinsic clustering signal of the galaxy and quasar samples can induce some deviations from the pure Poissonian case, $A_{\rm noise} = 1$, but having this noise deviating by more than $\sim 0.6$ ($2\sigma$ of our Gaussian prior) is actually extremely unphysical. Nevertheless, we display in figure 16 the effect of this Gaussian 30% prior in green contours compared to the case with uniform wide priors on $A_{\rm noise}$ in purple contours, for the LRG $0.6 < z < 1.0$ sample. Although setting this Gaussian prior has some impact in some of the nuisance parameters, it barely has any impact on the physical variables, such as the BAO scaling distances, the growth, or the *Shape*.

In addition to the prior on $A_{\rm noise}$ we include a wide Gaussian prior around $b_2$ when analyzing the LRG $0.6 < z < 1.0$ sample. This choice is motivated by the multi-modal posterior this sample presents in the absence of this prior, and the strong degeneracy between the amplitude of shot noise and $b_2$ (see again purple and green in figure 16 for $b_2$). In particular, we find that $b_2$ prefers either $b_2 \sim 5$ with $A_{\rm noise} \sim 1$, or $b_2 \sim -5$ with $A_{\rm noise} \sim 1.5$.

This long degeneracy could be also restricted by imposing a tighter prior on $A_{\rm noise}$, but we decide that setting an additional Gaussian prior on $b_2$ around 5, with a wide $\pm 2.5$ deviation at $1\sigma$ amplitude is a cleaner approach to remove this spurious result. This feature only appears for the LRG sample at $0.6 < z < 1.0$, but not at the other two LRG samples due to the larger effective volume. We show in dark orange contours of figure 16 the effect of the combination of both Gaussian priors on $A_{\rm noise}$ and $b_2$.

In summary, the inclusion of the Gaussian priors on $A_{\rm noise}$ (in all the samples) and of $b_2$ (in the LRG $0.6 < z < 1.0$ sample) help to increase the convergence of the Monte Carlo Markov Chains and barely affects the posteriors of the physical parameters. For both parameters, having this priors help to exclude the unphysical results where the amplitude of shot noise significantly departs from its Poissonian prediction.

### C.2 Prior assumptions within a specific cosmology model

To extract tight cosmological constraints from LSS data alone, in particular from the BOSS and eBOSS maps presented here, it is necessary to impose physical Gaussian priors on some parameters to break degeneracies.

One of these parameters is the baryon density $\omega_{\rm b}$, which is well measured by BBN and the CMB, so it is instructive to adopt this measurement within the cosmological analysis. The impact of this prior assumption is already discussed in depth in section 5.1, $\omega_{\rm b}$ is very degenerate with $h$ and $\omega_{\rm cdm}$, but it does not affect the constraints on $\Omega_{\rm m}$ and $\sigma_8$ (see figure 4).

Another parameter that we do not vary freely in our baseline analysis is the spectral tilt $n_s$. Instead, we keep it fixed to the fiducial value $n_s^{\rm fid} = 0.97$. The reasoning is that the limited range of scales we consider for galaxy clustering are not sufficient to determine the scale-independent tilt with high accuracy, while the Planck temperature and polarization power spectra cover significantly larger, linear scales, that enable a precise determination of $n_s$. Due to its degeneracy with the shape $m$, allowing it to vary freely in the cosmological ShapeFit analysis would significantly degrade the constraining power of $m$. As shown in [21], it is possible to measure both $m$ and $n_s$ from the galaxy power spectra independently, but in this work we rely on the well measured knowledge on the scale independent tilt from the CMB and infer cosmological constraints from $m$ only.

In the left panel of figure 17 we show the impact of relaxing the prior $n_s = n_s^{\rm fid}$ (blue contours) by allowing to vary $n_s$ within a Gaussian prior probability distribution centered at the value $n_s^{\rm Planck} = 0.9649$ measured by Planck, with a width of $\Delta n_s = 0.02$, which is $5\times$ larger than the Planck measured standard deviation (red contours). We can see that this has no impact on $h$ and $\sigma_8$, but slightly degrades our $\Omega_{\rm m}$ constraints. While our baseline analysis returns $\Omega_{\rm m} = 0.3001 \pm 0.0057$, here we find $\Omega_{\rm m} = 0.2987 \pm 0.0073$.

We hence conclude that our baseline $\Lambda$CDM results are robust even under systematic deviations of $n_s$ from the Planck measured value.

## D Smoothing the BAO wiggles

To obtain the shape $m$ prediction for any combination of cosmological parameters we need to infer the matter transfer function 'no-wiggle' shape $T_{\rm nw}$ (or power spectrum shape $P_{\rm nw}$), entering eq. (2.10). However, this quantity with removed BAO signal is not a direct output of Boltzmann codes, and must hence be inferred in an additional step.

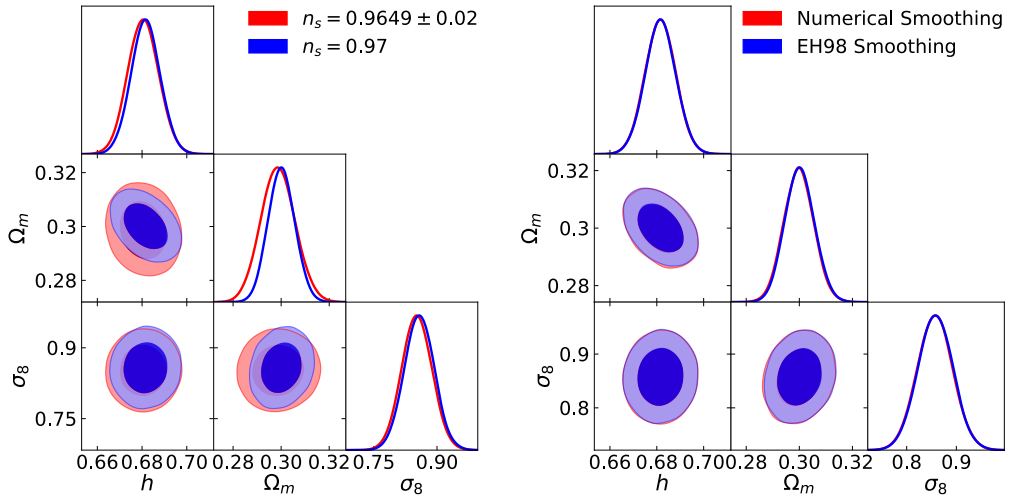


**Figure 17**. Left panel: Comparison between cosmological ΛCDM parameter constraints when varying the spectral index $n_s$ under a Gaussian prior (red contours) with respect to our baseline of fixing it to the fiducial value (blue contours). Right panel: Comparison of constraints for different BAO smoothing methods to determine the shape parameter $m$. We use either a numerical method to remove the BAO feature from the linear power spectrum (red contours) or the EH98 fitting function (blue contours).

Several numerical methods exist to extract the BAO signal from a fiducial power spectrum template, for example, in our BAO analysis we use the method from [112]. However, this method involves a polynomial fitting routine, which does not return stable results for all cosmological parameter combinations. Even for methods that rely on simple numerical functions such as fast Fourier transforms or interpolation (see for instance [113]) it is a non-trivial task to obtain stable results across cosmological parameter space. As argued extensively in appendix A of [114], this is because the BAO are a relatively minor signal compared to the broadband. Finding a universal numerical BAO extraction method is further complicated by the fact that other features in the linear power spectrum -determined by the matter-radiation equality turnover and baryon suppression scales- show a rich cosmology dependence. Any numerical method relying on a set of hyperparameters, such as the one presented in [115], must therefore be validated to deliver standardizable results against that cosmology dependence. Since such a validated method does not yet exist in the literature, in this work we use the analytic EH98 formula [6] to obtain our *Shape* predictions.

The drawbacks of the EH98 formula are its inaccuracy of up to 5% and its lack of validity beyond ΛCDM and simple parameter extensions of varying neutrino mass $\Sigma m_\nu$, effective number of neutrino species $N_{\rm eff}$, curvature $\Omega_{\rm k}$ or dark energy equation of state $w$. While the EH98 formula is still sufficient for the range of models explored in this paper, an alternative numerical method would be beneficial for future applications.

Here, we present a new numerical method as such an alternative and compare its performance with respect to the baseline EH98 formalism. The building block of this numerical smoothing is given by the following `scipy` (and `numpy`) functions:

*i)* We use the `find_peaks` function from `scipy.interpolate` to find the minima and

maxima of the gradient (using `numpy.gradient`) of the input spectrum. The scales at which these minima and maxima are found represent the nodes, that we require the output smooth function to cross. We start looking for peaks at a certain scale $k_{\rm start}$, which is our first hyperparameter. By default, we set $k_{\rm start} = 0.02\,[h{\rm Mpc}^{-1}]$

*ii)* We use the `interp1d` function from `scipy.signal` to interpolate two smooth functions crossing all minima (maxima) identified with the help of the peak finder in *i)* and combine both curves into the final output by computing their average. The order $j$ of the spline interpolation is our second hyperparameter. By default we perform quadratic interpolation, i.e. we set $j = 2$.

As argued before, we aim to establish a "standardizable" method, which delivers results independent of the hyperparameters.[17] To achieve this goal we proceed as follows:

1. We start with our fiducial linear matter power spectrum $P_{\rm lin}^{\rm fid}$ obtained from the Boltzmann code CLASS using the fiducial values of table 2 and calculate the corresponding smooth EH98 power spectrum $P_{\rm EH98}^{\rm fid}$.

2. We calculate the ratio $P_{\rm lin}^{\rm fid}/P_{\rm EH98}^{\rm fid}$ to divide out the power spectrum dependence on the turnover scale $k_{\rm eq}$, which is excellently modeled via the EH98 formula.

3. We apply the numerical smoothing (steps *i)* and *ii)*) with that ratio as input.

4. We multiply the de-wiggled output with $P_{\rm EH98}^{\rm fid}$ to obtain $P_{\rm num}^{\rm fid}$.

5. Given a cosmology $\mathbf{\Omega}$ different from the fiducial cosmology $\mathbf{\Omega}^{\rm fid}$, we compute the ratio $P_{\rm lin}/P_{\rm EH98}$ for that cosmology after rescaling them by the sound horizon ratio $s = r_{\rm d}/r_{\rm d}^{\rm fid}$ (as for the nominator of eq. (2.10)).

6. We "standardize" that ratio by dividing it by the pre-computed ratio for the fiducial cosmology, i.e. we compute $(P_{\rm lin}/P_{\rm EH98})/(P_{\rm lin}^{\rm fid}/P_{\rm EH98}^{\rm fid})$.

7. We use this "standardized" ratio as input for the numerical smoothing, steps *i)* and *ii)*.

8. We multiply the de-wiggled output with $P_{\rm EH98}\cdot(P_{\rm lin}^{\rm fid}/P_{\rm EH98}^{\rm fid})$ to obtain the final numerically smoothed power spectrum $P_{\rm num}$.

Note that steps 1.-4. are carried out only once to generate the fiducial templates, while steps 5.-8. need to be performed at each step in cosmlogical parameter space. From our tests using MCMC's we found that the "double standardization" procedure described here is sufficient to deliver stable results. In this way we can get rid of the dependence on $k_{\rm eq}$ (through the division by the EH98 formula) and the baryon suppression and onset of oscillation (through the division by the fiducial template ratio). If not taken into account, both of these effects can lead to artificial discontinuities in the determination of the shape $m$.

We explain this procedure visually and compare it to the pure EH98 smoothing method in figure 18. The top panel shows the ratio of $s^{i/j}$-rescaled power spectra $P_x(\mathbf{\Omega}^i)/P_y(\mathbf{\Omega}^j)$, where the subscripts $x, y$ either stand for the linear power spectrum ('lin') or for the no-wiggle linear power spectrum obtained via the analytic ('EH98') formula or the numerical method

[17] While we leave the demonstration of its independence from the hyperparameters for future work, here we argue why our method is well suited to be "standardizable": because we cancel out the standard ruler $r_{\rm d}$ and turnover scale $k_{\rm eq}$ power spectrum dependence.

('num') described here. The superscripts $i, j$ either stand for the fiducial cosmology ('fid') of table 2 or a cosmology (empty superscript) with displaced matter density $\Delta\omega_{\rm m} = -0.02$. In most cases the denominator is given by $P^{\rm fid}_{\rm num} = P_{\rm num}(k, \mathbf{\Omega}^{\rm fid})$ as reference, but also other cases are displayed for comparison. The exact values of the sub- and superscripts are specified in the legend, where the dependencies $P(\dots)$ are not written out for simplicity.

From the top panel of figure 18 we can appreciate the difference in *Shape* between the $s$-rescaled power spectrum of the displaced cosmology (purple line) and the fiducial power spectrum (black line). Their ratio (red, dotted line) still shows some residual wiggles due to the difference in BAO amplitude between the two cosmologies. Its residual with respect to the EH98 function (red, dotted line of bottom panel) is used as input for our numerical smoothing function (step 6). The advantage of using the residual power spectrum ratio as input is that the numerical method is more precise (and in particular more independent of the hyperparameters) the smaller the BAO amplitude. This is simply because with smaller amplitude there is less room left for possible numerical smoothing solutions. In fact, if the residual BAO amplitude is zero, all numerical smoothing operations would deliver identical results. The final numerically smoothed spectrum $P_{\rm num}/P^{\rm fid}_{\rm num}$ (red, dashed lines) can be compared to the baseline EH98 result $P_{\rm EH98}/P^{\rm fid}_{\rm EH98}$ (blue, dashed lines) in both panels. We see that they are in nearly perfect agreement for $k < 0.05\,[h{\rm Mpc}^{-1}]$ and reach at most a 2% discrepancy at $k = 0.1\,[h{\rm Mpc}^{-1}]$. Since we measure the slope at pivot scale $k_p = 0.03\,[h{\rm Mpc}^{-1}]$ (black, dotted lines), both methods deliver the exact same cosmological constraints, as demonstrated for our baseline ΛCDM model in the right panel of figure 17. However, to achieve this result it is very important to use for each cosmology the same BAO wiggle removal procedure as for the fiducial power spectrum template. This is because, in absolute terms, the EH98 prediction (blue, dotted lines) is quite different from the numerical calculation, in this case up to 5% and even up to 2% at $k_p$.

## E Full data-vectors and covariances

We list the full covariances and data-vectors corresponding to the compressed set of variables of the samples used in this paper. These results correspond to those listed in table 5, but explicitly displaying the cross correlation among parameters. Unlike in table 5 we display the $f\sigma_{s8}$ parameter (see section 2.2.3 for its definition), which is slightly different from the usual $f\sigma_8$ parameter which has been reported before.

The two BOSS LRG overlaping samples at $0.2 < z < 0.5$; $z_{\rm eff} = 0.38$ and $0.4 < z < 0.6$; $z_{\rm eff} = 0.51$ correspond to,

$$D^{\rm LRG}(0.38, 0.51) = \begin{pmatrix} D_H/r_{\rm d}(0.38) \\ D_M/r_{\rm d}(0.38) \\ f\sigma_{s8}(0.38) \\ m(0.38) \\ D_H/r_{\rm d}(0.51) \\ D_M/r_{\rm d}(0.51) \\ f\sigma_{s8}(0.51) \\ m(0.51) \end{pmatrix} = \begin{pmatrix} 24.979 \\ 10.239 \\ 0.47323 \\ -0.066479 \\ 22.256 \\ 13.302 \\ 0.48109 \\ -0.022856 \end{pmatrix}, \tag{E.1}$$

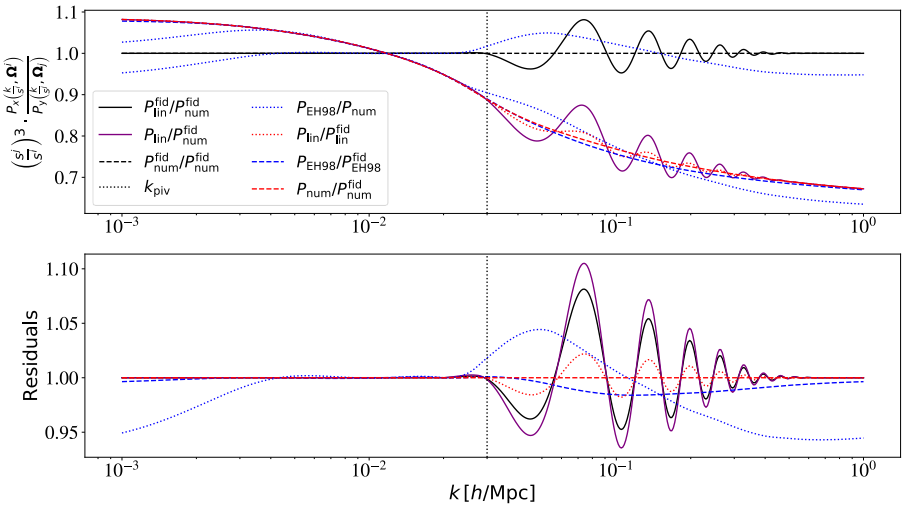


**Figure 18**. Comparison between the different BAO smoothing methods, the baseline EH98 method (blue, labeled 'EH98') and the numerical method (red, labeled 'num'), where the final results relevant for ShapeFit are represented by the dashed lines and the dotted lines display intermediate steps. In the top panel we show the fiducial power spectrum in black and the $s$-rescaled spectrum of a different cosmology with reduced matter density $\Delta\omega_{\rm m} = -0.02$ in purple. Both are divided by the numerically smoothed fiducial power spectrum $P^{\rm fid}_{\rm num}$ to visualize their difference in *Shape*. The ratio of both spectra, which serves as input for our numerical smoothing method (step 6 in text, where here we exclude the EH98 factors in the top panel, but include them in the bottom panel) is given by the red dotted line. The blue dotted lines show the ratio of the EH98 method with respect to the numerical method, which deviate from each other by up to 5%. Note, however, that ShapeFit relies on the relative shift in *Shape* with respect to the fiducial, which does not show any difference between methods at the pivot scale $k_p$ (black, dotted lines).

with covariance

$$C^{\rm LRG}\ (0.38; 0.51) = 10^{-3} \cdot \tag{E.2}$$

$$\begin{pmatrix} 370.75 & -29.539 & -11.436 & -1.3729 & 108.63 & -8.6873 & -3.2297 & -0.87764 \\ & 24.259 & 2.9207 & -0.52414 & -8.0277 & -4.2352 & 1.0342 & -0.25930 \\ & & 2.1106 & -0.073861 & -3.1726 & -0.29013 & 0.70911 & 0.071011 \\ & & & 1.7474 & -0.94588 & -0.58482 & 0.097818 & 0.74692 \\ & & & & 277.21 & -34.533 & -7.9761 & -1.5555 \\ & & & & & 35.805 & 2.8011 & -0.36639 \\ & & & & & & 1.6569 & -0.18942 \\ & & & & & & & 1.9244 \end{pmatrix}.$$

The BOSS and eBOSS LRG sample, $0.6 < z < 1.0$; $z_{\rm eff} = 0.698$ has,

$$D^{\rm LRG}(0.698) = \begin{pmatrix} D_H/r_{\rm d} \\ D_M/r_{\rm d} \\ f\sigma_{s8} \\ m \end{pmatrix} = \begin{pmatrix} 19.542 \\ 17.700 \\ 0.47947 \\ -0.008019 \end{pmatrix}, \tag{E.3}$$

and the following covariance,

$$C^{\rm LRG}(0.698) = 10^{-3}\begin{pmatrix} 201.75 & -46.049 & -5.4088 & -2.7122 \\ & 93.889 & 5.0808 & -0.51303 \\ & & 1.8683 & -0.70222 \\ & & & 2.6965 \end{pmatrix}. \tag{E.4}$$

Finally, the quasar sample at $0.8 < z < 2.2$; $z_{\rm eff} = 1.48$ has,

$$D^{\rm QSO}(1.48) = \begin{pmatrix} D_H/r_{\rm d} \\ D_M/r_{\rm d} \\ f\sigma_{s8} \\ m \end{pmatrix} = \begin{pmatrix} 13.274 \\ 31.007 \\ 0.46773 \\ -0.005327 \end{pmatrix}, \tag{E.5}$$

and covariance,

$$C^{\rm QSO}(1.48) = 10^{-3}\begin{pmatrix} 245.99 & -16.412 & -7.8840 & -4.4936 \\ & 669.76 & 20.710 & -5.9721 \\ & & 1.7861 & 0.086278 \\ & & & 1.0934 \end{pmatrix}. \tag{E.6}$$

We provide these compressed parameter covariances, the power spectra measurements, power spectrum covariances and window matrices employed in this analysis in [116].

## Acknowledgments

We thank Davide Gualdi for providing the building block of our numerical BAO smoothing function. This work makes use of the FFTW and GSL libraries, `scipy` and `numpy` `python` packages and plots were generated using `getdist` and `gnuplot`. We also thank the developers of CLASS and MontePython. H.G-M. and S.B. acknowledges the support from 'la Caixa' Foundation (ID100010434) with code LCF/BQ/PI18/11630024. L.V., H.G-M. and S.B. acknowledge support of European Union's Horizon 2020 research and innovation programme ERC (BePreSySe, grant agreement 725327). Funding for this work was partially provided by the Spanish MINECO under project PGC2018-098866-B-I00 MCIN/AEI/10.13039/501100011033 y FEDER "Una manera de hacer Europa", and the "Center of Excellence Maria de Maeztu 2020-2023" award to the ICCUB (CEX2019-000918-M funded by MCIN/AEI/10.13039/501100011033).

The MultiDark-Patchy mocks was an effort led from the IFT UAM-CSIC by F. Prada's group (C.-H. Chuang, S. Rodriguez-Torres and C. Scoccola) in collaboration with C. Zhao (Tsinghua U.), F.-S. Kitaura (AIP), A. Klypin (NMSU), G. Yepes (UAM), and the BOSS galaxy clustering working group.

We thank Cheng Zhao for providing the EZmock periodic cubic boxes for the quasar sample, as well as for the effort of providing the whole set of EZmocks light-cones for the eBOSS samples. We also thank Jeremy Tinker for leading the Nseries mocks production within the BOSS team effort.

We thank the whole BOSS and eBOSS teams for their valuable effort in creating the BOSS and eBOSS catalogues and making it publicly available for the community.

We acknowledge the IT team at ICCUB for the help with the Aganice and Hipatia clusters where all the calculations presented in this paper where done.

## References


[1] G. Hinshaw, D. Larson, E. Komatsu, D. N. Spergel, C. L. Bennett, J. Dunkley et al., *Nine-year Wilkinson Microwave Anisotropy Probe (WMAP) Observations: Cosmological Parameter Results*, *ApJS* **208** (Oct., 2013) 19, [1212.5226].

[2] Planck Collaboration, N. Aghanim, Y. Akrami, M. Ashdown, J. Aumont, C. Baccigalupi et al., *Planck 2018 results. VI. Cosmological parameters*, *A&A* **641** (Sept., 2020) A6, [1807.06209].

[3] C. Blake, S. Brough, M. Colless, C. Contreras, W. Couch, S. Croom et al., *The WiggleZ Dark Energy Survey: joint measurements of the expansion and growth history at $z < 1$*, *MNRAS* **425** (Sept., 2012) 405–414, [1204.3674].

[4] D. J. Eisenstein, I. Zehavi, D. W. Hogg, R. Scoccimarro, M. R. Blanton, R. C. Nichol et al., *Detection of the Baryon Acoustic Peak in the Large-Scale Correlation Function of SDSS Luminous Red Galaxies*, *ApJ* **633** (Nov., 2005) 560–574, [astro-ph/0501171].

[5] S. Cole, W. J. Percival, J. A. Peacock, P. Norberg, C. M. Baugh, C. S. Frenk et al., *The 2dF Galaxy Redshift Survey: power-spectrum analysis of the final data set and cosmological implications*, *MNRAS* **362** (Sept., 2005) 505–534, [astro-ph/0501174].

[6] D. J. Eisenstein and W. Hu, *Baryonic Features in the Matter Transfer Function*, *ApJ* **496** (Mar., 1998) 605–614, [astro-ph/9709112].

[7] C. Alcock and B. Paczynski, *An evolution free test for non-zero cosmological constant*, *Nature* **281** (Oct., 1979) 358.

[8] D. J. Eisenstein, H.-J. Seo, E. Sirko and D. N. Spergel, *Improving Cosmological Distance Measurements by Reconstruction of the Baryon Acoustic Peak*, *ApJ* **664** (Aug., 2007) 675–679, [astro-ph/0604362].

[9] A. Burden, W. J. Percival and C. Howlett, *Reconstruction in Fourier space*, *Monthly Notices of the Royal Astronomical Society* **453** (Oct., 2015) 456–468.

[10] N. Kaiser, *Clustering in real space and in redshift space*, *Monthly Notices of the Royal Astronomical Society* **227** (July, 1987) 1–21.

[11] S. Alam, M. Ata, S. Bailey, F. Beutler, D. Bizyaev, J. A. Blazek et al., *The clustering of galaxies in the completed SDSS-III Baryon Oscillation Spectroscopic Survey: cosmological analysis of the DR12 galaxy sample*, *Monthly Notices of the Royal Astronomical Society* **470** (Sept., 2017) 2617–2652.

[12] S. Alam, M. Aubert, S. Avila, C. Balland, J. E. Bautista, M. A. Bershady et al., *Completed SDSS-IV extended Baryon Oscillation Spectroscopic Survey: Cosmological implications from two decades of spectroscopic surveys at the Apache Point Observatory*, *Phys. Rev. D* **103** (Apr., 2021) 083533, [2007.08991].

[13] G. Efstathiou and S. J. Moody, *Maximum likelihood estimates of the two- and three-dimensional power spectra of the apm galaxy survey*, *Mon. Not. Roy. Astron. Soc.* **325** (2001) 1603, [astro-ph/0010478].

[14] 2dFGRS collaboration, W. J. Percival et al., *The 2dF Galaxy Redshift Survey: The Power spectrum and the matter content of the Universe*, *Mon. Not. Roy. Astron. Soc.* **327** (2001) 1297, [astro-ph/0105252].

[15] M. Tegmark, M. R. Blanton, M. A. Strauss, F. Hoyle, D. Schlegel, R. Scoccimarro et al., *The Three-Dimensional Power Spectrum of Galaxies from the Sloan Digital Sky Survey*, *ApJ* **606** (May, 2004) 702–740, [astro-ph/0310725].

[16] G. D'Amico, J. Gleyzes, N. Kokron, D. Markovic, L. Senatore, P. Zhang et al., *The*

*Cosmological Analysis of the SDSS/BOSS data from the Effective Field Theory of Large-Scale Structure*, *JCAP* **05** (2020) 005, [1909.05271].

[17] M. M. Ivanov, M. Simonović and M. Zaldarriaga, *Cosmological Parameters from the BOSS Galaxy Power Spectrum*, *JCAP* **05** (2020) 042, [1909.05277].

[18] O. H. E. Philcox and M. M. Ivanov, *BOSS DR12 full-shape cosmology: $\Lambda$ CDM constraints from the large-scale galaxy power spectrum and bispectrum monopole*, *Phys. Rev. D* **105** (Feb., 2022) 043517, [2112.04515].

[19] D. J. Eisenstein, H.-j. Seo and M. White, *On the Robustness of the Acoustic Scale in the Low-Redshift Clustering of Matter*, *The Astrophysical Journal* **664** (Aug., 2007) 660–674.

[20] H.-J. Seo and D. J. Eisenstein, *Baryonic Acoustic Oscillations in Simulated Galaxy Redshift Surveys*, *The Astrophysical Journal* **633** (Nov., 2005) 575–588.

[21] S. Brieden, H. Gil-Marín and L. Verde, *ShapeFit: extracting the power spectrum shape information in galaxy surveys beyond BAO and RSD*, *J. Cosmology Astropart. Phys.* **2021** (Dec., 2021) 054, [2106.07641].

[22] T. Nishimichi, G. D'Amico, M. M. Ivanov, L. Senatore, M. Simonović, M. Takada et al., *Blinded challenge for precision cosmology with large-scale structure: Results from effective field theory for the redshift-space galaxy power spectrum*, *Phys. Rev. D* **102** (Dec., 2020) 123541, [2003.08277].

[23] S. Brieden, H. Gil-Marín and L. Verde, *PT challenge: Validation of ShapeFit on large-volume, high-resolution mocks*, *arXiv e-prints* (Jan., 2022) arXiv:2201.08400, [2201.08400].

[24] S. Brieden, H. Gil-Marín and L. Verde, *Model-independent versus model-dependent interpretation of the SDSS-III BOSS power spectrum: Bridging the divide*, *Phys. Rev. D* **104** (Dec., 2021) L121301, [2106.11931].

[25] A. J. Ross, W. J. Percival and M. Manera, *The information content of anisotropic Baryon Acoustic Oscillation scale measurements*, *Monthly Notices of the Royal Astronomical Society* **451** (Aug., 2015) 1331.

[26] W. J. Percival and M. White, *Testing cosmological structure formation using redshift-space distortions*, *Mon. Not. Roy. Astron. Soc.* **393** (2009) 297, [0808.0003].

[27] BOSS collaboration, F. Beutler et al., *The clustering of galaxies in the completed SDSS-III Baryon Oscillation Spectroscopic Survey: baryon acoustic oscillations in the Fourier space*, *Mon. Not. Roy. Astron. Soc.* **464** (2017) 3409–3430, [1607.03149].

[28] H. Gil-Marín, J. E. Bautista, R. Paviot, M. Vargas-Magaña, S. de la Torre, S. Fromenteau et al., *The Completed SDSS-IV extended Baryon Oscillation Spectroscopic Survey: measurement of the BAO and growth rate of structure of the luminous red galaxy sample from the anisotropic power spectrum between redshifts 0.6 and 1.0*, *MNRAS* **498** (Oct., 2020) 2492–2531, [2007.08994].

[29] A. Taruya, T. Nishimichi and S. Saito, *Baryon Acoustic Oscillations in 2D: Modeling Redshift-space Power Spectrum from Perturbation Theory*, *Phys. Rev.* **D82** (2010) 063522, [1006.0699].

[30] BOSS collaboration, F. Beutler et al., *The clustering of galaxies in the SDSS-III Baryon Oscillation Spectroscopic Survey: Testing gravity with redshift-space distortions using the power spectrum multipoles*, *Mon. Not. Roy. Astron. Soc.* **443** (2014) 1065–1089, [1312.4611].

[31] T. Baldauf, U. Seljak, V. Desjacques and P. McDonald, *Evidence for quadratic tidal tensor bias from the halo bispectrum*, *Physical Review D* **86** (Oct, 2012) .

[32] S. Saito, T. Baldauf, Z. Vlah, U. Seljak, T. Okumura and P. McDonald, *Understanding higher-order nonlocal halo bias at large scales by combining the power spectrum with the bispectrum*, *Phys. Rev.* **D90** (2014) 123522, [1405.1447].

[33] K. C. Chan, R. Scoccimarro and R. K. Sheth, *Gravity and large-scale nonlocal bias*, *Phys. Rev. D* **85** (Apr., 2012) 083509, [1201.3614].

[34] J. C. Jackson, *A Critique of Rees's Theory of Primordial Gravitational Radiation*, *Monthly Notices of the Royal Astronomical Society* **156** (02, 1972) 1P–5P, [0810.3908].

[35] A. Burden, W. J. Percival, M. Manera, A. J. Cuesta, M. V. Magaña and S. Ho, *Efficient Reconstruction of Linear Baryon Acoustic Oscillations in Galaxy Surveys*, *Monthly Notices of the Royal Astronomical Society* **445** (Dec., 2014) 3152–3168.

[36] D. J. Eisenstein, D. H. Weinberg, E. Agol, H. Aihara, C. Allende Prieto, S. F. Anderson et al., *SDSS-III: Massive Spectroscopic Surveys of the Distant Universe, the Milky Way, and Extra-Solar Planetary Systems*, *AJ* **142** (Sept., 2011) 72, [1101.1529].

[37] BOSS Collaboration, "BOSS galaxy clustering catalogues." https://data.sdss.org/sas/dr12/boss/lss/.

[38] M. R. Blanton, M. A. Bershady, B. Abolfathi, F. D. Albareti, C. Allende Prieto, A. Almeida et al., *Sloan Digital Sky Survey IV: Mapping the Milky Way, Nearby Galaxies, and the Distant Universe*, *AJ* **154** (July, 2017) 28, [1703.00052].

[39] eBOSS Collaboration, "eBOSS galaxy and quasar clustering catalogues." https://data.sdss.org/sas/dr16/eboss/lss/catalogs/DR16/.

[40] K. S. Dawson, D. J. Schlegel, C. P. Ahn, S. F. Anderson, É. Aubourg, S. Bailey et al., *The Baryon Oscillation Spectroscopic Survey of SDSS-III*, *AJ* **145** (Jan., 2013) 10, [1208.0022].

[41] K. S. Dawson, J.-P. Kneib, W. J. Percival, S. Alam, F. D. Albareti, S. F. Anderson et al., *The SDSS-IV Extended Baryon Oscillation Spectroscopic Survey: Overview and Early Data*, *AJ* **151** (Feb., 2016) 44, [1508.04473].

[42] A. S. Bolton, D. J. Schlegel, É. Aubourg, S. Bailey, V. Bhardwaj, J. R. Brownstein et al., *Spectral Classification and Redshift Measurement for the SDSS-III Baryon Oscillation Spectroscopic Survey*, *AJ* **144** (Nov., 2012) 144, [1207.7326].

[43] S. A. Smee, J. E. Gunn, A. Uomoto, N. Roe, D. Schlegel, C. M. Rockosi et al., *The Multi-object, Fiber-fed Spectrographs for the Sloan Digital Sky Survey and the Baryon Oscillation Spectroscopic Survey*, *AJ* **146** (Aug., 2013) 32, [1208.2233].

[44] J. E. Gunn, W. A. Siegmund, E. J. Mannery, R. E. Owen, C. L. Hull, R. F. Leger et al., *The 2.5 m Telescope of the Sloan Digital Sky Survey*, *AJ* **131** (Apr., 2006) 2332–2359, [astro-ph/0602326].

[45] B. Reid et al., *SDSS-III Baryon Oscillation Spectroscopic Survey Data Release 12: galaxy target selection and large scale structure catalogues*, *Mon. Not. Roy. Astron. Soc.* **455** (2016) 1553–1573, [1509.06529].

[46] A. J. Ross, J. Bautista, R. Tojeiro, S. Alam, S. Bailey, E. Burtin et al., *The Completed SDSS-IV extended Baryon Oscillation Spectroscopic Survey: Large-scale structure catalogues for cosmological analysis*, *MNRAS* **498** (Oct., 2020) 2354–2371, [2007.09000].

[47] B. W. Lyke, A. N. Higley, J. N. McLane, D. P. Schurhammer, A. D. Myers, A. J. Ross et al., *The Sloan Digital Sky Survey Quasar Catalog: Sixteenth Data Release*, *ApJS* **250** (Sept., 2020) 8, [2007.09001].

[48] K. N. Abazajian, J. K. Adelman-McCarthy, M. A. Agüeros, S. S. Allam, C. Allende Prieto, D. An et al., *The Seventh Data Release of the Sloan Digital Sky Survey*, *ApJS* **182** (June, 2009) 543–558, [0812.0649].

[49] A. Raichoor, A. de Mattia, A. J. Ross, C. Zhao, S. Alam, S. Avila et al., *The completed SDSS-IV extended Baryon Oscillation Spectroscopic Survey: large-scale structure catalogues and measurement of the isotropic BAO between redshift 0.6 and 1.1 for the Emission Line Galaxy Sample*, *MNRAS* **500** (Jan., 2021) 3254–3274, [2007.09007].

[50] H. du Mas des Bourboux, J.-M. Le Goff, M. Blomqvist, N. G. Busca, J. Guy, J. Rich et al., *Baryon acoustic oscillations from the complete SDSS-III Lyα-quasar cross-correlation function at z = 2.4*, *A&A* **608** (Dec., 2017) A130, [1708.02225].

[51] A. G. Sánchez, E. A. Kazin, F. Beutler, C.-H. Chuang, A. J. Cuesta, D. J. Eisenstein et al., *The clustering of galaxies in the SDSS-III Baryon Oscillation Spectroscopic Survey: cosmological constraints from the full shape of the clustering wedges*, *MNRAS* **433** (Aug., 2013) 1202–1222, [1303.4396].

[52] A. J. Ross, W. J. Percival, A. G. Sánchez, L. Samushia, S. Ho, E. Kazin et al., *The clustering of galaxies in the SDSS-III Baryon Oscillation Spectroscopic Survey: analysis of potential systematics*, *Monthly Notices of the Royal Astronomical Society* **424** (Jul, 2012) 564–590, [1203.6499].

[53] F. Beutler, H.-J. Seo, S. Saito, C.-H. Chuang, A. J. Cuesta, D. J. Eisenstein et al., *The clustering of galaxies in the completed SDSS-III Baryon Oscillation Spectroscopic Survey: anisotropic galaxy clustering in Fourier space*, *MNRAS* **466** (Apr., 2017) 2242–2260, [1607.03150].

[54] M. Vargas-Magaña, S. Ho, A. J. Cuesta, R. O'Connell, A. J. Ross, D. J. Eisenstein et al., *The clustering of galaxies in the completed SDSS-III Baryon Oscillation Spectroscopic Survey: theoretical systematics and Baryon Acoustic Oscillations in the galaxy correlation function*, *MNRAS* **477** (June, 2018) 1153–1188, [1610.03506].

[55] S. Satpathy, S. Alam, S. Ho, M. White, N. A. Bahcall, F. Beutler et al., *The clustering of galaxies in the completed SDSS-III Baryon Oscillation Spectroscopic Survey: on the measurement of growth rate using galaxy correlation functions*, *MNRAS* **469** (Aug., 2017) 1369–1382, [1607.03148].

[56] J. N. Grieb, A. G. Sánchez, S. Salazar-Albornoz, R. Scoccimarro, M. Crocce, C. Dalla Vecchia et al., *The clustering of galaxies in the completed SDSS-III Baryon Oscillation Spectroscopic Survey: Cosmological implications of the Fourier space wedges of the final sample*, *MNRAS* **467** (May, 2017) 2085–2112, [1607.03143].

[57] J. E. Bautista, R. Paviot, M. Vargas Magaña, S. de la Torre, S. Fromenteau, H. Gil-Marín et al., *The completed SDSS-IV extended Baryon Oscillation Spectroscopic Survey: measurement of the BAO and growth rate of structure of the luminous red galaxy sample from the anisotropic correlation function between redshifts 0.6 and 1*, *MNRAS* **500** (Jan., 2021) 736–762, [2007.08993].

[58] J. Hou, A. G. Sánchez, A. J. Ross, A. Smith, R. Neveux, J. Bautista et al., *The completed SDSS-IV extended Baryon Oscillation Spectroscopic Survey: BAO and RSD measurements from anisotropic clustering analysis of the quasar sample in configuration space between redshift 0.8 and 2.2*, *MNRAS* **500** (Jan., 2021) 1201–1221, [2007.08998].

[59] R. Neveux, E. Burtin, A. de Mattia, A. Smith, A. J. Ross, J. Hou et al., *The completed SDSS-IV extended Baryon Oscillation Spectroscopic Survey: BAO and RSD measurements from the anisotropic power spectrum of the quasar sample between redshift 0.8 and 2.2*, *MNRAS* **499** (Nov., 2020) 210–229, [2007.08999].

[60] A. Tamone, A. Raichoor, C. Zhao, A. de Mattia, C. Gorgoni, E. Burtin et al., *The completed SDSS-IV extended baryon oscillation spectroscopic survey: growth rate of structure measurement from anisotropic clustering analysis in configuration space between redshift 0.6 and 1.1 for the emission-line galaxy sample*, *MNRAS* **499** (Dec., 2020) 5527–5546, [2007.09009].

[61] A. de Mattia, V. Ruhlmann-Kleider, A. Raichoor, A. J. Ross, A. Tamone, C. Zhao et al., *The completed SDSS-IV extended Baryon Oscillation Spectroscopic Survey: measurement of the BAO and growth rate of structure of the emission line galaxy sample from the anisotropic*

*power spectrum between redshift 0.6 and 1.1*, *MNRAS* **501** (Mar., 2021) 5616–5645, [2007.09008].

[62] S. Alam, F. D. Albareti, C. Allende Prieto, F. Anders, S. F. Anderson, T. Anderton et al., *The Eleventh and Twelfth Data Releases of the Sloan Digital Sky Survey: Final Data from SDSS-III*, *ApJS* **219** (July, 2015) 12, [1501.00963].

[63] C.-H. Chuang, F. Prada, M. Pellejero-Ibanez, F. Beutler, A. J. Cuesta, D. J. Eisenstein et al., *The clustering of galaxies in the SDSS-III Baryon Oscillation Spectroscopic Survey: single-probe measurements from CMASS anisotropic galaxy clustering*, *MNRAS* **461** (Oct., 2016) 3781–3793, [1312.4889].

[64] M. Pellejero-Ibanez, C.-H. Chuang, J. A. Rubiño-Martín, A. J. Cuesta, Y. Wang, G. Zhao et al., *The clustering of galaxies in the completed SDSS-III Baryon Oscillation Spectroscopic Survey: towards a computationally efficient analysis without informative priors*, *MNRAS* **468** (July, 2017) 4116–4133.

[65] O. H. E. Philcox, M. M. Ivanov, M. Simonović and M. Zaldarriaga, *Combining full-shape and BAO analyses of galaxy power spectra: a 1.6% CMB-independent constraint on $H_0$*, *J. Cosmology Astropart. Phys.* **2020** (May, 2020) 032, [2002.04035].

[66] T. Tröster, A. G. Sánchez, M. Asgari, C. Blake, M. Crocce, C. Heymans et al., *Cosmology from large-scale structure. Constraining ΛCDM with BOSS*, *A&A* **633** (Jan., 2020) L10, [1909.11006].

[67] A. Semenaite, A. G. Sánchez, A. Pezzotta, J. Hou, R. Scoccimarro, A. Eggemeier et al., *Cosmological implications of the full shape of anisotropic clustering measurements in BOSS and eBOSS*, *arXiv e-prints* (Nov., 2021) arXiv:2111.03156, [2111.03156].

[68] R. Neveux, E. Burtin, V. Ruhlmann-Kleider, A. de Mattia, A. Semenaite, K. S. Dawson et al., *Combined full shape analysis of BOSS galaxies and eBOSS quasars using an iterative emulator*, *arXiv e-prints* (Jan., 2022) arXiv:2201.04679, [2201.04679].

[69] F.-S. Kitaura, S. Rodríguez-Torres, C.-H. Chuang, C. Zhao, F. Prada, H. Gil-Marín et al., *The clustering of galaxies in the SDSS-III Baryon Oscillation Spectroscopic Survey: mock galaxy catalogues for the BOSS Final Data Release*, *Monthly Notices of the Royal Astronomical Society* **456** (Mar., 2016) 4156.

[70] C. Zhao, C.-H. Chuang, J. Bautista, A. de Mattia, A. Raichoor, A. J. Ross et al., *The completed SDSS-IV extended Baryon Oscillation Spectroscopic Survey: 1000 multi-tracer mock catalogues with redshift evolution and systematics for galaxies and quasars of the final data release*, *MNRAS* **503** (May, 2021) 1149–1173, [2007.08997].

[71] C.-H. Chuang, F.-S. Kitaura, F. Prada, C. Zhao and G. Yepes, *EZmocks: extending the Zel'dovich approximation to generate mock galaxy catalogues with accurate clustering statistics*, *MNRAS* **446** (Jan., 2015) 2621–2628, [1409.1124].

[72] F. S. Kitaura, G. Yepes and F. Prada, *Modelling baryon acoustic oscillations with perturbation theory and stochastic halo biasing.*, *MNRAS* **439** (Mar., 2014) L21–L25, [1307.3285].

[73] H. Gil-Marín, *How to optimally combine pre-reconstruction full shape and post-reconstruction BAO signals*, *arXiv e-prints* (Mar., 2022) arXiv:2203.05581, [2203.05581].

[74] A. Cuceu, J. Farr, P. Lemos and A. Font-Ribera, *Baryon Acoustic Oscillations and the Hubble constant: past, present and future*, *J. Cosmology Astropart. Phys.* **2019** (Oct., 2019) 044, [1906.11628].

[75] R. J. Cooke, M. Pettini and C. C. Steidel, *One Percent Determination of the Primordial Deuterium Abundance*, *ApJ* **855** (Mar., 2018) 102, [1710.11129].

[76] E. G. Adelberger et al., *Solar fusion cross sections II: the pp chain and CNO cycles*, *Rev. Mod. Phys.* **83** (2011) 195, [1004.2318].

[77] D. J. Fixsen, *The Temperature of the Cosmic Microwave Background*, *ApJ* **707** (Dec., 2009) 916–920, [0911.1955].

[78] A. Smith, E. Burtin, J. Hou, R. Neveux, A. J. Ross, S. Alam et al., *The completed SDSS-IV extended Baryon Oscillation Spectroscopic Survey: N-body mock challenge for the quasar sample*, *MNRAS* **499** (Nov., 2020) 269–291, [2007.09003].

[79] J. M. Bardeen, J. R. Bond, N. Kaiser and A. S. Szalay, *The Statistics of Peaks of Gaussian Random Fields*, *ApJ* **304** (May, 1986) 15.

[80] J. R. Bond and A. S. Szalay, *The collisionless damping of density fluctuations in an expanding universe*, *ApJ* **274** (Nov., 1983) 443–468.

[81] N. Sugiyama, *Cosmic Background Anisotropies in Cold Dark Matter Cosmology*, *ApJS* **100** (Oct., 1995) 281, [astro-ph/9412025].

[82] O. H. E. Philcox, B. D. Sherwin, G. S. Farren and E. J. Baxter, *Determining the Hubble constant without the sound horizon: Measurements from galaxy surveys*, *Phys. Rev. D* **103** (Jan., 2021) 023538, [2008.08084].

[83] C. P. Ahn, R. Alexandroff, C. Allende Prieto, F. Anders, S. F. Anderson, T. Anderton et al., *The Tenth Data Release of the Sloan Digital Sky Survey: First Spectroscopic Data from the SDSS-III Apache Point Observatory Galactic Evolution Experiment*, *ApJS* **211** (Apr., 2014) 17, [1307.7735].

[84] Super-Kamiokande Collaboration collaboration, Y. Fukuda, T. Hayakawa, E. Ichihara, K. Inoue, K. Ishihara, H. Ishino et al., *Evidence for oscillation of atmospheric neutrinos*, *Phys. Rev. Lett.* **81** (Aug, 1998) 1562–1567.

[85] Double Chooz Collaboration collaboration, Y. Abe, C. Aberle, J. C. dos Anjos, J. C. Barriere, M. Bergevin, A. Bernstein et al., *Reactor $\overline{\nu}_e$ disappearance in the double chooz experiment*, *Phys. Rev. D* **86** (Sep, 2012) 052008.

[86] T2K Collaboration collaboration, K. Abe, J. Adam, H. Aihara, T. Akiri, C. Andreopoulos, S. Aoki et al., *Observation of electron neutrino appearance in a muon neutrino beam*, *Phys. Rev. Lett.* **112** (Feb, 2014) 061802.

[87] I. Esteban, M. C. Gonzalez-Garcia, A. Hernandez-Cabezudo, M. Maltoni and T. Schwetz, *Global analysis of three-flavour neutrino oscillations: synergies and tensions in the determination of $\theta_{23}$, $\delta_{CP}$, and the mass ordering*, *Journal of High Energy Physics* **2019** (Jan., 2019) 106, [1811.05487].

[88] Katrin Collaboration, M. Aker, A. Beglarian, J. Behrens, A. Berlev, U. Besserer et al., *Direct neutrino-mass measurement with sub-electronvolt sensitivity*, *Nature Physics* **18** (Feb., 2022) 160–166.

[89] J. Lesgourgues and S. Pastor, *Massive neutrinos and cosmology*, *Phys. Rept.* **429** (2006) 307–379, [astro-ph/0603494].

[90] A. Raccanelli, L. Verde and F. Villaescusa-Navarro, *Biases from neutrino bias: to worry or not to worry?*, *Mon. Not. Roy. Astron. Soc.* **483** (2019) 734–743, [1704.07837].

[91] S. Vagnozzi, T. Brinckmann, M. Archidiacono, K. Freese, M. Gerbino, J. Lesgourgues et al., *Bias due to neutrinos must not uncorrect'd go*, *JCAP* **09** (2018) 001, [1807.04672].

[92] M. Chevallier and D. Polarski, *Accelerating Universes with Scaling Dark Matter*, *International Journal of Modern Physics D* **10** (Jan., 2001) 213–223, [gr-qc/0009008].

[93] E. V. Linder, *Exploring the Expansion History of the Universe*, *Phys. Rev. Lett.* **90** (Mar., 2003) 091301, [astro-ph/0208512].

[94] D. Baumann, A. Nicolis, L. Senatore and M. Zaldarriaga, *Cosmological non-linearities as an effective fluid*, *J. Cosmology Astropart. Phys.* **2012** (July, 2012) 051, [1004.2488].

[95] J. J. M. Carrasco, M. P. Hertzberg and L. Senatore, *The effective field theory of cosmological large scale structures*, *Journal of High Energy Physics* **2012** (Sept., 2012) 82, [1206.2926].

[96] A. Taruya, F. Bernardeau, T. Nishimichi and S. Codis, *Direct and fast calculation of regularized cosmological power spectrum at two-loop order*, *Phys. Rev. D* **86** (Nov., 2012) 103528, [1208.1191].

[97] T. Nishimichi, F. Bernardeau and A. Taruya, *Moving around the cosmological parameter space: A nonlinear power spectrum reconstruction based on high-resolution cosmic responses*, *Phys. Rev. D* **96** (Dec., 2017) 123515, [1708.08946].

[98] J. Bel, A. Pezzotta, C. Carbone, E. Sefusatti and L. Guzzo, *Accurate fitting functions for peculiar velocity spectra in standard and massive-neutrino cosmologies*, *A&A* **622** (Feb., 2019) A109, [1809.09338].

[99] R. K. Sheth, K. C. Chan and R. Scoccimarro, *Nonlocal Lagrangian bias*, *Phys. Rev. D* **87** (Apr., 2013) 083002, [1207.7117].

[100] A. Aghamousa, J. Aguilar, S. Ahlen, S. Alam, L. E. Allen, C. Allende Prieto et al., *The DESI Experiment Part I: Science,Targeting, and Survey Design*, .

[101] J. Tinker, "Nseries Nbody mocks catalogues for the BOSS CMASS NGC sample." https://www.ub.edu/bispectrum/page12.html.

[102] H. Gil-Marín, W. J. Percival, A. J. Cuesta, J. R. Brownstein, C.-H. Chuang, S. Ho et al., *The clustering of galaxies in the SDSS-III Baryon Oscillation Spectroscopic Survey: BAO measurement from the LOS-dependent power spectrum of DR12 BOSS galaxies*, *Monthly Notices of the Royal Astronomical Society* **460** (Aug., 2016) 4210.

[103] G. D'Amico, M. Lewandowski, L. Senatore and P. Zhang, *Limits on primordial non-Gaussianities from BOSS galaxy-clustering data*, *arXiv e-prints* (Jan., 2022) arXiv:2201.11518, [2201.11518].

[104] A. de Mattia and V. Ruhlmann-Kleider, *Integral constraints in spectroscopic surveys*, *JCAP* **08** (2019) 036, [1904.08851].

[105] M. Icaza-Lizaola, M. Vargas-Magaña, S. Fromenteau, S. Alam, B. Camacho, H. Gil-Marin et al., *The clustering of the SDSS-IV extended Baryon Oscillation Spectroscopic Survey DR14 LRG sample: structure growth rate measurement from the anisotropic LRG correlation function in the redshift range $0.6 < z < 1.0$*, *MNRAS* **492** (Mar., 2020) 4189–4215, [1909.07742].

[106] N. Hand, U. Seljak, F. Beutler and Z. Vlah, *Extending the modeling of the anisotropic galaxy power spectrum to $k = 0.4$ hMpc$^{-1}$*, *J. Cosmology Astropart. Phys.* **2017** (Oct., 2017) 009, [1706.02362].

[107] T. Nishimichi, "Multipole moment data for PT challenges." https://www2.yukawa.kyoto-u.ac.jp/~takahiro.nishimichi/data/PTchallenge/.

[108] P. S. Behroozi, R. H. Wechsler and H.-Y. Wu, *The ROCKSTAR Phase-space Temporal Halo Finder and the Velocity Offsets of Cluster Cores*, *ApJ* **762** (Jan., 2013) 109, [1110.4372].

[109] A. Aghamousa, J. Aguilar, S. Ahlen, S. Alam, L. E. Allen, C. Allende Prieto et al., *The DESI Experiment Part II: Instrument Design*, .

[110] R. Laureijs, J. Amiaux, S. Arduini, J.-L. Augueres, J. Brinchmann, R. Cole et al., *Euclid Definition Study Report*, *arXiv:1110.3193 [astro-ph]* (Oct., 2011) .

[111] C. Hahn, R. Scoccimarro, M. R. Blanton, J. L. Tinker and S. A. Rodríguez-Torres, *The Effect of Fiber Collisions on the Galaxy Power Spectrum Multipoles*, *MNRAS* **467** (May, 2017) 1940–1956, [1609.01714].

[112] D. Kirkby, D. Margala, A. Slosar, S. Bailey, N. G. Busca, T. Delubac et al., *Fitting methods for baryon acoustic oscillations in the Lyman-α forest fluctuations in BOSS data release 9*, *J. Cosmology Astropart. Phys.* **2013** (Mar., 2013) 024, [1301.3456].

[113] J. Hamann, S. Hannestad, J. Lesgourgues, C. Rampf and Y. Y. Y. Wong, *Cosmological parameters from large scale structure - geometric versus shape information*, *J. Cosmology Astropart. Phys.* **2010** (July, 2010) 022, [1003.3999].

[114] S. Hinton, *Extraction of Cosmological Information from WiggleZ*, 1604.01830.

[115] S. R. Hinton, C. Howlett and T. M. Davis, *Barry and the BAO Model Comparison*, *Mon. Not. Roy. Astron. Soc.* **493** (2020) 4078–4093, [1912.01175].

[116] S. Brieden, H. Gil-Marín and L. Verde, "BOSS and eBOSS data-vectors and covariances for ShapeFit." https://ub.edu/bispectrum/sdss_shapefit.html.

# Part III

# SUMMARY OF RESULTS AND FUTURE PROSPECTS

# 7

# SUMMARY OF RESULTS AND FUTURE PROSPECTS

Thanks to overwhelming technological and observational advancements over the past three decades, cosmology has become a precision science. This is mainly based on three grounds. First, observations of the CMB, from its monopole temperature with COBE in the 90's until mapping its tiny fluctuations with Planck in the recent years, brought to us deep understanding of the early-time processes of the universe. Secondly, direct measurements of the cosmic acceleration through SN and BAO have extended our understanding towards the late-time dynamics of the universe. Finally, this is accompanied by further insight from measurements of the growth rate of cosmic structures through weak lensing and RSD.

Instead of separating between early-time and late-time physics, these recent developments can also be categorized as model-dependent versus model-independent. The former category is represented by CMB and lensing observations while the latter is represented by SN observations on one hand and on the other hand by the BAO and RSD signals of galaxy clustering, the main topic studied in this thesis.

To put it in a nutshell, the common theme of the work presented in this thesis is a model-agnostic analysis of galaxy clustering observations extracting as much information as possible but maximizing the robustness at the same time. In this spirit, part ii, "ShapeFit", provides an improved tool to compress in a model-independent way galaxy power spectra into physical parameters, which are easily interpretable for a wide family of cosmological models. Part i, "Blinding", presents a way to blind galaxy catalogs, such that their analysis is not influenced by any model expectations. By putting the model interpretation at the very last step in the analysis pipeline, also ShapeFit contributes towards avoiding confirmation bias during the analysis. Hence, both of these research pillars go hand in hand, and being of major interest for spectroscopic surveys, both are expected to play an important role at the interface between observational data and theoretical models.

We now summarize the most important findings and discuss the future prospects for each of these pillars.

## 7.1 BLINDING

The publication [1] within chapter 2 presented the first method to blind spectroscopic galaxy catalogs, such that their inferred summary statistics coherently mimick a different expansion history, parameterised by the model-independent, distance scaling parameters $\alpha_\perp(z)$ and $\alpha_\parallel(z)$

across and along the line-of-sight (LOS), and a different growth rate history parameterised by the velocity fluctuation amplitude $f\sigma_8$. While the expansion law blinding leads to a coherent, redshift-dependent blinding-shift on galaxy LOS positions (redshifts), the growth-rate blinding is obtained by calculating the gradient of the overdensity field of the galaxies, meaning that the blinding shift in galaxy LOS position (redshift) involve a local dependence. This makes it impossible to accidentally unblind the blinded catalogs obtained with our method. The reason why we only blind the galaxy positions along the LOS and do not modify their angular positions is that they are targeted based on pre-determined photometric catalogs. Since these are already publicly known, and modifying the angular positions would lead to uncontrolled implications concerning angular systematics, we decided to only blind for the new spectroscopic infomation, which are the precise redshifts.

By blinding 400 realizations of the mock galaxy catalogs for extreme shifts in target blind parameters, we show that our catalog-level blinding scheme returns robust results compared to the analytic prediction, with a statistical fluctuation below 5% of the intrinsic RMS scatter of the mocks and a negligibly small systematic deviation. Also the inferred parameter errors and $\chi^2$ values remain stable between fitting the pre- and post- blinding data. While the demonstrated analytical predictability is encouraging and stresses the robustnesss of our method, we note that in a real analysis we suggest the collaboration pipeline to rerun on the full datavector after unblinding, in addition to a simple analytic transformation of the blinded results. Both results can finally be compared for consistency, as done in figures 15 and 16 of [1], also see figure 1 therein for the global set-up.

While the presented blinding scheme operating along the LOS as presented in [1] is already part of the official DESI analysis pipeline,[1] due to its high applicability we envision it to be applied to other galaxy surveys such as Euclid or Rubin as well. Beyond that, it could be easily applied to other tracers such as Lyman-$\alpha$, quasars or line-intensity mapping. As a next step, we attempt to extend our blinding scheme towards other cosmological signals such as primordial non-Gaussianity and massive neutrinos. Since these signals do not only imply an anisotropy along the LOS but also manifest themselves as isotropic scale-dependent shifts in the summary statistics, and since we do not aim to modify the angular galaxy positions, we need to blind the weights attributed to each galaxy. This method is currently under investigation and could also be used to blind for the *Shape* signal introduced in our work on ShapeFit.

1 Indeed, its validation on early DESI data is subject to an ongoing project of the author of this thesis.

## 7.2 SHAPEFIT

ShapeFit is an extension of the standard BAO+RSD template fits incorporating one or two additional parameters capturing the broadband shape of the matter power spectrum. Its full derivation and application to fast mocks is presented in the publication [2] within chapter 3 and its first application to actual data, in this case to BOSS DR12, in the letter [3] within chapter 4. We validated our method on high precision and high volume N-body simulations within the context of the blind PT challenge in the publication [4] within chapter 5 and apply it to the BOSS+eBOSS legacy LRG and QSO catalogs in the submitted article [5] presented in chapter 6.

In chapter 3, we show that our fixed-template method is capable of reproducing the results of more complex FM techniques, both in terms of mean values and standard deviations of cosmological parameters when adopting the standard ΛCDM model with conventional priors on the CMB temperature (from FIRAS), the baryon density (from BBN), and the spectral tilt (from CMB). But we see that once the baryon density prior and/or the spectral tilt prior is relaxed, the ShapeFit results are more conservative than for the FM technique, because in these cases parts of the signal that ShapeFit does not include (such as the BAO amplitude) become important to break parameter degeneracies. However, we have shown that on the other the ShapeFit constraints are more robust in these cases than the FM constraints, which depend on the exact implementation of non-linear corrections to the BAO amplitude for example. An important advantage of ShapeFit is its capability to separate the information in the data coming from purely late-time dynamics (such as expansion rate evolution and growth rate evolution) from the physics at play at early times, from inflation until the time of decoupling of the photon-baryon fluid. Within FM approaches however, the cosmological parameters that govern the early-time physics are influencing at the same time the late-time dynamics of the universe, what makes it impossible to disentangle the two. This is what in our work we refer to as the *internal model prior*, which is purposely broken within our ShapeFit parameter compression. Other advantages of ShapeFit encompass its speed and its physical intuition provided by the compression of $\mathcal{O}(10^2)$ datapoints into just four numbers per redshift bin.

In chapter 4, we show that when applied to BOSS DR12 data, again, we can reproduce the FM results from other works with ShapeFit. Furthermore, we show that the interpretation of the *shape* parameter $m$ in combination with a prior on the matter density $\Omega_m = 0.299 \pm 0.016$ from Table 4 of [36] provides a constraint on the Hubble constant of $h = 0.736^{+0.105}_{-0.075}$ without a prior on $\omega_b$ from BBN. This is of particular relevance in context of the still unresolved Hubble tension, as ShapeFit naturally incorporates a method to measure $h$ independently of the

sound horizon $r_{\rm d}$. In this way, ShapeFit offers a model-independent route for such a constraint, which since then has only been obained via a modification of the model-dependent FM analysis [91]. Our publication [3] within chapter 4 also directly shows the cosmological implications of the *internal model prior* assumed in FM types of analyses. We show that $m$ is subject to systematic shifts in case that the observational systematics are not properly taken into account or in presence of primordial non-Gaussianity, while these effects do not bias the other, late-time, physical parameters. While ShapeFit allows to disentangle the different physics at play, the naive FM fit does not distinguish between the early-time and late-time signals resulting in a bias of cosmological parameters without the diagnosis step of parameter compression in between. This is one of the major reasons (among other advantages already specified) why we advocate ShapeFit for the cosmological analysis of LSS surveys instead of FM techniques.

In chapter 5 we validate the ShapeFit compression method by participating in the blind PT challenge launched by [83]. For our baseline set-up labeled 'SIM-like' we obtain the following constraints on the (blinded) cosmological parameters: $\Delta \ln \left(10^{10} A_s\right) = -0.018 \pm 0.014$, $\Delta\Omega_{\rm m} = 0.0039 \pm 0.0021$ and $\Delta h = -0.0009 \pm 0.0034$, remaining below $2\sigma$ deviations for a volume of $566 \left[h^{-1}{\rm Gpc}\right]^3$, which is 10-20 times larger than the volume probed by future galaxy surveys. For the same set-up, we find that also our compressed parameter constraints on $\left\{\alpha_{\parallel}, \alpha_{\perp}, f, m\right\}$ are unbiased. For certain deviations from our baseline set-up, i.e. different modeling choices on galaxy bias and shotnoise amplitude and choosing different redshift bins, we do not find any significant deviation from our baseline set-up. However, when icreasing the scale range beyond $k_{\rm max} = 0.15\, h{\rm Mpc}^{-1}$, our constraints become biased due to neglecting higher order terms in PT becoming relevant given the small covariance of the PT challenge simulation. We also observe a bias in $\alpha_{\parallel}$ of $4\sigma$ when including the hexadecapole signal, where the origin for that bias is still under investigation. Interestingly, this bias does not occur in the cosmological parameter space, since the direction of the bias in the $\alpha_{\parallel} - \alpha_{\perp}$ is excluded by the $\Lambda$CDM model *a priori*. This serves as an explicit example why direct model fits (or FM fits) are not practical for systematic analyses, since the conclusions would always depend on the exact model assumptions of choice. Therefore, we recommend to use the ShapeFit methodology for such systematic tests, as it is *i)* generic enough to find and explore all possible effects of systematics and *ii)* precise enough to capture nearly the same information content as other FM techniques.

Finally, in chapter 6 we apply ShapeFit to the full BOSS+eBOSS LRG and quasar maps and infer the cosmological implications of this legacy dataset when combined with the Lyman-$\alpha$ tracer. Comparing with our ShapeFit results the standard flat-$\Lambda$CDM model we obtain, without any external dataset, $\Omega_{\rm m} = 0.2971 \pm 0.0061$ and $10^9 \times A_s = 2.39^{+0.24}_{-0.43}$

(or $\sigma_8 = 0.857 \pm 0.040$). For models beyond ΛCDM, BOSS+eBOSS data alone constrain the sum of neutrino mass to be $\Sigma m_\nu < 0.40$ eV with a BBN prior at 95% CL, the curvature energy density to $\Omega_k = -0.022^{+0.032}_{-0.038}$ and the dark energy equation of state parameter to $w = -0.998^{+0.085}_{-0.073}$ at 68% CL without a BBN prior. For the latter two parameters the newly added *shape* parameter helps to shrink the error bars with respect to the corresponding reported values in [36] by factors $\sim 3$ and $\sim 2$ respectively. However, we find that in combination with the most recent CMB data from Planck [25] the *shape* does not deliver any extra information. We also find that for standard ΛCDM type of models the gain from the *shape* decreases the larger the redshift range of the considered LSS dataset.[2] This result is of particular relevance for the DESI collaboration, which aims to report cosmological results obtained from the combination of all its tracers combined, covering a redshift range of $0.1 < z < 4.0$. Note, that most of the FM techniques proclaiming spectacular improvement in cosmological constraints of factors 10-20 have been obtained from individual tracers, but shrank to factors 2-3 once obtained from the full redshift range, in line with our findings. Concerning our systematic tests on mocks, we find that fast mocks that rely on certain approximations such as the Patchy mocks [92] and EZmocks [93] are well suited to reproduce the expected BAO and RSD variables but fail when it comes to the *shape*. In fact, these kind of fast mocks are not intended for precision analyses, their original purpose is providing covariance matrices. Hence, we carried out systematic checks using the full N-body Nseries mocks on top of the previously analysed PT challenge mocks finding no relevant systematic biases given the precision of the analysed dataset. Therefore, we conclude that ShapeFit is a robust method o extract cosmological information from galaxy surveys.

## 7.3 CONCLUDING REMARKS

To conclude this thesis, we would like to evaluate the impact of this work on the scientific community. The two research pillars presented here resulted in two important methodologies that are now part of the key cosmological analysis of DESI. This campaign is currently in the state of data collection and has already surpassed the number of galaxy spectra measured from all previous spectroscopic galaxy surveys combined. Its Year 1 analysis will have probed five times the effective volume of its preceding BOSS+eBOSS experiment. The author of this thesis is highly involved in this effort, which will remain unrivaled for the next decade. The synergies, however, with soon to be launched LSS surveys such as Rubin and Euclid will be immense.

2 However, models predicting an effective change of the slope as a function of redshift and tracer, should benefit of such type of analysis.

Beyond this contribution of the practical implementation of these methods into the DESI pipeline, the fundamental value of the two research pillars presented in this thesis rely in their philosophy of model-agnosticism.

In fundamental physics, there is a constant interplay between theoretical and experimental physics; the former relying on *deduction*, i.e., going from the general to the specific, the latter on *induction*, i.e., going from the specific to the general.

In fundamental cosmology, it is impossible to carry out experiments; there is only one single "experiment", the universe, in which we reside. Of course, there are different windows, through which we can observe the universe, but in the end all these observations probe just a single "experiment".

For that reason, cosmology tends to rely heavily on *deductions* starting from given models, and as cosmologists we tend to trust the -apparently- established models. Blinding and ShapeFit provide layers of protection against such unconscious confirmation bias. Despite all the recent successes of the standard ΛCDM model, emerged during the proclaimed "precision era of cosmology", it is important to bear in mind that it is an effective model, for which 95% of its ingredients are still unknown. Therefore, it is of fundamental importance to treat new incoming data with the least amount of prior assumptions, relaxing even established model relations, such that we are allowed to learn what the data tells us (*induction*), rather than to reproduce what the models tell us (*deduction*).

By putting the weight more into the *induction* side, we hope that the effort of this thesis will prove useful for the transition from the "precision era" to the "accuracy era" of cosmology.

# BIBLIOGRAPHY


[1] Samuel Brieden, Héctor Gil-Marín, Licia Verde, and José Luis Bernal. "Blind Observers of the Sky." In: *JCAP* 09 (2020), p. 052. DOI: 10.1088/1475-7516/2020/09/052. arXiv: 2006.10857 [astro-ph.CO].

[2] Samuel Brieden, Héctor Gil-Marín, and Licia Verde. "ShapeFit: extracting the power spectrum shape information in galaxy surveys beyond BAO and RSD." In: *JCAP* 2021.12, 054 (Dec. 2021), p. 054. DOI: 10.1088/1475-7516/2021/12/054. arXiv: 2106.07641 [astro-ph.CO].

[3] Samuel Brieden, Héctor Gil-Marín, and Licia Verde. "Model-independent versus model-dependent interpretation of the SDSS-III BOSS power spectrum: Bridging the divide." In: *Phys. Rev. D* 104.12, L121301 (Dec. 2021), p. L121301. DOI: 10.1103/PhysRevD.104.L121301. arXiv: 2106.11931 [astro-ph.CO].

[4] Samuel Brieden, Héctor Gil-Marín, and Licia Verde. "PT challenge: Validation of ShapeFit on large-volume, high-resolution mocks." In: (Jan. 2022). arXiv: 2201.08400 [astro-ph.CO].

[5] Samuel Brieden, Héctor Gil-Marín, and Licia Verde. "Model-agnostic interpretation of 10 billion years of cosmic evolution traced by BOSS and eBOSS data." In: (Apr. 2022). arXiv: 2204.11868 [astro-ph.CO].

[6] B. Abareshi et al. "Overview of the Instrumentation for the Dark Energy Spectroscopic Instrument." In: (May 2022). arXiv: 2205.10939 [astro-ph.IM].

[7] Albert Einstein. "The Foundation of the General Theory of Relativity." In: *Annalen Phys.* 49.7 (1916). Ed. by Jong-Ping Hsu and D. Fine, pp. 769–822. DOI: 10.1002/andp.200590044.

[8] Sir Isaac Newton. Translated by I. Bernard Cohen and Anne Whitman. *The Principia: Mathematical Principles of Natural Philosophy*. University of California Press, 1999. ISBN: 978-0-520-08816-0, 978-520-08817-7.

[9] Edwin Hubble. "A relation between distance and radial velocity among extra-galactic nebulae." In: *Proc. Nat. Acad. Sci.* 15 (1929), pp. 168–173. DOI: 10.1073/pnas.15.3.168.

[10] F. Zwicky. "Die Rotverschiebung von extragalaktischen Nebeln." In: *Helv. Phys. Acta* 6 (1933), pp. 110–127. DOI: 10.1007/s10714-008-0707-4.

[11] Yoshiaki Sofue and Vera Rubin. "Rotation curves of spiral galaxies." In: *Ann. Rev. Astron. Astrophys.* 39 (2001), pp. 137–174. DOI: 10.1146/annurev.astro.39.1.137. arXiv: astro-ph/0010594.

[12] Douglas Clowe et al. "A direct empirical proof of the existence of dark matter." In: *Astrophys. J. Lett.* 648 (2006), pp. L109–L113. DOI: 10.1086/508162. arXiv: astro-ph/0608407.

[13] Y. Fukuda et al. "Evidence for Oscillation of Atmospheric Neutrinos." In: *Phys. Rev. Lett.* 81 (8 1998), pp. 1562–1567. DOI: 10.1103/PhysRevLett.81.1562. URL: https://link.aps.org/doi/10.1103/PhysRevLett.81.1562.

[14] Y. Abe et al. "Reactor $\overline{\nu}_e$ disappearance in the Double Chooz experiment." In: *Phys. Rev. D* 86 (5 2012), p. 052008. DOI: 10.1103/PhysRevD.86.052008. URL: https://link.aps.org/doi/10.1103/PhysRevD.86.052008.

[15] K. Abe et al. "Observation of Electron Neutrino Appearance in a Muon Neutrino Beam." In: *Phys. Rev. Lett.* 112 (6 2014), p. 061802. DOI: 10.1103/PhysRevLett.112.061802. URL: https://link.aps.org/doi/10.1103/PhysRevLett.112.061802.

[16] Alan H. Guth. "The Inflationary Universe: A Possible Solution to the Horizon and Flatness Problems." In: *Phys. Rev. D* 23 (1981). Ed. by Li-Zhi Fang and R. Ruffini, pp. 347–356. DOI: 10.1103/PhysRevD.23.347.

[17] Andrei D. Linde. "A New Inflationary Universe Scenario: A Possible Solution of the Horizon, Flatness, Homogeneity, Isotropy and Primordial Monopole Problems." In: *Phys. Lett. B* 108 (1982). Ed. by Li-Zhi Fang and R. Ruffini, pp. 389–393. DOI: 10.1016/0370-2693(82)91219-9.

[18] K. Sato. "First Order Phase Transition of a Vacuum and Expansion of the Universe." In: *Mon. Not. Roy. Astron. Soc.* 195 (1981), pp. 467–479.

[19] Alexei A. Starobinsky. "Dynamics of Phase Transition in the New Inflationary Universe Scenario and Generation of Perturbations." In: *Phys. Lett. B* 117 (1982), pp. 175–178. DOI: 10.1016/0370-2693(82)90541-X.

[20] Ryan J. Cooke, Max Pettini, and Charles C. Steidel. "One Percent Determination of the Primordial Deuterium Abundance." In: *ApJ* 855.2, 102 (Mar. 2018), p. 102. DOI: 10.3847/1538-4357/aaab53. arXiv: 1710.11129 [astro-ph.CO].

[21] S. Gariazzo, P. F. de Salas, O. Pisanti, and R. Consiglio. "PArthENoPE revolutions." In: *Computer Physics Communications* 271, 108205 (Feb. 2022), p. 108205. DOI: 10.1016/j.cpc.2021.108205. arXiv: 2103.05027 [astro-ph.IM].

[22] D. J. Fixsen et al. "The Cosmic Microwave Background Spectrum from the Full COBE FIRAS Data Set." In: *ApJ* 473 (Dec. 1996), p. 576. DOI: 10.1086/178173. arXiv: astro-ph/9605054 [astro-ph].

[23] D. J. Fixsen. "The Temperature of the Cosmic Microwave Background." In: *ApJ* 707.2 (Dec. 2009), pp. 916–920. DOI: 10.1088/0004-637X/707/2/916. arXiv: 0911.1955 [astro-ph.CO].

[24] G. Hinshaw et al. "Nine-year Wilkinson Microwave Anisotropy Probe (WMAP) Observations: Cosmological Parameter Results." In: *ApJS* 208.2, 19 (Oct. 2013), p. 19. DOI: 10.1088/0067-0049/208/2/19. arXiv: 1212.5226 [astro-ph.CO].

[25] Planck Collaboration et al. "Planck 2018 results. VI. Cosmological parameters." In: *A&A* 641, A6 (Sept. 2020), A6. DOI: 10.1051/0004-6361/201833910. arXiv: 1807.06209 [astro-ph.CO].

[26] Simone Aiola et al. "The Atacama Cosmology Telescope: DR4 Maps and Cosmological Parameters." In: *JCAP* 12 (2020), p. 047. DOI: 10.1088/1475-7516/2020/12/047. arXiv: 2007.07288 [astro-ph.CO].

[27] D. Dutcher et al. "Measurements of the E-mode polarization and temperature-E-mode correlation of the CMB from SPT-3G 2018 data." In: *Phys. Rev. D* 104.2 (2021), p. 022003. DOI: 10.1103/PhysRevD.104.022003. arXiv: 2101.01684 [astro-ph.CO].

[28] Antony Lewis, Anthony Challinor, and Anthony Lasenby. "Efficient computation of CMB anisotropies in closed FRW models." In: *Astrophys. J.* 538 (2000), pp. 473–476. DOI: 10.1086/309179. arXiv: astro-ph/9911177 [astro-ph].

[29] Diego Blas, Julien Lesgourgues, and Thomas Tram. "The Cosmic Linear Anisotropy Solving System (CLASS). Part II: Approximation schemes." In: *Journal of Cosmology and Astro-Particle Physics* 2011.7, 034 (2011), p. 034. DOI: 10.1088/1475-7516/2011/07/034. arXiv: 1104.2933 [astro-ph.CO].

[30] Robert E. Williams et al. "The Hubble Deep Field: Observations, data reduction, and galaxy photometry." In: *Astron. J.* 112 (1996), p. 1335. DOI: 10.1086/118105. arXiv: astro-ph/9607174.

[31] S. Perlmutter et al. "Measurements of Ω and Λ from 42 high redshift supernovae." In: *Astrophys. J.* 517 (1999), pp. 565–586. DOI: 10.1086/307221. arXiv: astro-ph/9812133.

[32] Adam G. Riess et al. "Observational evidence from supernovae for an accelerating universe and a cosmological constant." In: *Astron. J.* 116 (1998), pp. 1009–1038. DOI: 10.1086/300499. arXiv: astro-ph/9805201.

[33] Shaun Cole et al. "The 2dF Galaxy Redshift Survey: Power-spectrum analysis of the final dataset and cosmological implications." In: *Mon. Not. Roy. Astron. Soc.* 362 (2005), pp. 505–534. DOI: 10.1111/j.1365-2966.2005.09318.x. arXiv: astro-ph/0501174.

[34] Daniel J. Eisenstein et al. "Detection of the Baryon Acoustic Peak in the Large-Scale Correlation Function of SDSS Luminous Red Galaxies." In: *Astrophys. J.* 633 (2005), pp. 560–574. DOI: 10.1086/466512. arXiv: astro-ph/0501171.

[35] Shadab Alam et al. "The Eleventh and Twelfth Data Releases of the Sloan Digital Sky Survey: Final Data from SDSS-III." In: *ApJS* 219.1, 12 (July 2015), p. 12. DOI: 10.1088/0067-0049/219/1/12. arXiv: 1501.00963 [astro-ph.IM].

[36] Shadab Alam et al. "Completed SDSS-IV extended Baryon Oscillation Spectroscopic Survey: Cosmological implications from two decades of spectroscopic surveys at the Apache Point Observatory." In: *Phys. Rev. D* 103.8, 083533 (Apr. 2021), p. 083533. DOI: 10.1103/PhysRevD.103.083533. arXiv: 2007.08991 [astro-ph.CO].

[37] Nick Kaiser. "Clustering in real space and in redshift space." In: *Monthly Notices of the Royal Astronomical Society* 227 (July 1987), pp. 1–21. ISSN: 0035-8711. DOI: 10.1093/mnras/227.1.1. URL: http://adsabs.harvard.edu/abs/1987MNRAS.227....1K (visited on 12/13/2018).

[38] J. C. Jackson. "Fingers of God: A critique of Rees' theory of primoridal gravitational radiation." In: *Mon. Not. Roy. Astron. Soc.* 156 (1972), 1P–5P. DOI: 10.1093/mnras/156.1.1P. arXiv: 0810.3908 [astro-ph].

[39] Leanne D Duffy and Karl van Bibber. "Axions as dark matter particles." In: *New Journal of Physics* 11.10 (2009), p. 105008. DOI: 10.1088/1367-2630/11/10/105008. URL: https://doi.org/10.1088/1367-2630/11/10/105008.

[40] *Particle Dark Matter: Observations, Models and Searches*. Cambridge University Press, 2010. DOI: 10.1017/CBO9780511770739.

[41] José Luis Bernal, Nicola Bellomo, Alvise Raccanelli, and Licia Verde. "Cosmological implications of Primordial Black Holes." In: *JCAP* 10 (2017), p. 052. DOI: 10.1088/1475-7516/2017/10/052. arXiv: 1709.07465 [astro-ph.CO].

[42] Uroš Seljak and Matias Zaldarriaga. "Signature of Gravity Waves in the Polarization of the Microwave Background." In: *Phys. Rev. Lett.* 78.11 (Mar. 1997), pp. 2054–2057. DOI: 10.1103/PhysRevLett.78.2054. arXiv: astro-ph/9609169 [astro-ph].

[43] Pau Amaro-Seoane et al. "Laser Interferometer Space Antenna." In: *arXiv e-prints*, arXiv:1702.00786 (Feb. 2017), arXiv:1702.00786. arXiv: 1702.00786 [astro-ph.IM].

[44] José Luis Bernal, Patrick C. Breysse, Héctor Gil-Marín, and Ely D. Kovetz. "User's guide to extracting cosmological information from line-intensity maps." In: *Phys. Rev. D* 100.12 (2019), p. 123522. DOI: 10.1103/PhysRevD.100.123522. arXiv: 1907.10067 [astro-ph.CO].

[45] Adam G. Riess et al. "A Comprehensive Measurement of the Local Value of the Hubble Constant with 1 km/s/Mpc Uncertainty from the Hubble Space Telescope and the SHoES Team." In: (Dec. 2021). arXiv: 2112.04510 [astro-ph.CO].

[46] Jose Luis Bernal, Licia Verde, and Adam G. Riess. "The trouble with $H_0$." In: *JCAP* 10 (2016), p. 019. DOI: 10.1088/1475-7516/2016/10/019. arXiv: 1607.05617 [astro-ph.CO].

[47] L. Verde, T. Treu, and A. G. Riess. "Tensions between the Early and the Late Universe." In: *Nature Astron.* 3 (July 2019), p. 891. DOI: 10.1038/s41550-019-0902-0. arXiv: 1907.10625 [astro-ph.CO].

[48] Nils Schöneberg et al. "The $H_0$ Olympics: A fair ranking of proposed models." In: (July 2021). arXiv: 2107.10291 [astro-ph.CO].

[49] A. Amon et al. "Dark Energy Survey Year 3 results: Cosmology from cosmic shear and robustness to data calibration." In: *Phys. Rev. D* 105.2 (2022), p. 023514. DOI: 10.1103/PhysRevD.105.023514. arXiv: 2105.13543 [astro-ph.CO].

[50] Ž. Ivezić et al. "LSST: From Science Drivers to Reference Design and Anticipated Data Products." In: *ApJ* 873, 111 (Mar. 2019), p. 111. DOI: 10.3847/1538-4357/ab042c. arXiv: 0805.2366.

[51] R. Laureijs et al. "Euclid Definition Study Report." In: *arXiv:1110.3193 [astro-ph]* (Oct. 2011). arXiv: 1110.3193. URL: http://arxiv.org/abs/1110.3193 (visited on 01/13/2018).

[52] Amir Aghamousa et al. "The DESI Experiment Part II: Instrument Design." In: (2016).

[53] Amir Aghamousa et al. "The DESI Experiment Part I: Science,Targeting, and Survey Design." In: (2016).

[54] Will J. Percival. "Large Scale Structure Observations." In: *186th Course of International School of Physics 'Enrico Fermi': New Horizons for Observational Cosmology*. Vol. 186. 2014, pp. 101–135. DOI: 10.3254/978-1-61499-476-3-101. arXiv: 1312.5490 [astro-ph.CO].

[55] Will J. Percival. "Recent Developments in the Analysis of Galaxy Surveys." In: *Proc. Int. Sch. Phys. Fermi* 200 (2020). Ed. by E. Coccia, J. Silk, and N. Vittorio, pp. 311–330. DOI: 10.3254/ENFI200013. arXiv: 1810.04263 [astro-ph.CO].

[56] Arnaud de Mattia and Vanina Ruhlmann-Kleider. "Integral constraints in spectroscopic surveys." In: *JCAP* 08 (2019), p. 036. DOI: 10.1088/1475-7516/2019/08/036. arXiv: 1904.08851 [astro-ph.CO].

[57] Hume A. Feldman, Nick Kaiser, and John A. Peacock. "Power-Spectrum Analysis of Three-dimensional Redshift Surveys." In: *Astrophysical Journal* 426 (1994), p. 23. DOI: 10.1086/174036. arXiv: astro-ph/9304022 [astro-ph].

[58] Héctor Gil-Marín et al. "The Completed SDSS-IV extended Baryon Oscillation Spectroscopic Survey: measurement of the BAO and growth rate of structure of the luminous red galaxy sample from the anisotropic power spectrum between redshifts 0.6 and 1.0." In: *MNRAS* 498.2 (Oct. 2020), pp. 2492–2531. DOI: 10.1093/mnras/staa2455. arXiv: 2007.08994 [astro-ph.CO].

[59] Florian Beutler and Patrick McDonald. "Unified galaxy power spectrum measurements from 6dFGS, BOSS, and eBOSS." In: *JCAP* 11 (2021), p. 031. DOI: 10.1088/1475-7516/2021/11/031. arXiv: 2106.06324 [astro-ph.CO].

[60] Ashley J. Ross et al. "The Completed SDSS-IV extended Baryon Oscillation Spectroscopic Survey: Large-scale structure catalogues for cosmological analysis." In: *MNRAS* 498.2 (Oct. 2020), pp. 2354–2371. DOI: 10.1093/mnras/staa2416. arXiv: 2007.09000 [astro-ph.CO].

[61] Kazuhiro Yamamoto et al. "A Measurement of the quadrupole power spectrum in the clustering of the 2dF QSO Survey." In: *Publ. Astron. Soc. Jap.* 58 (2006), pp. 93–102. DOI: 10.1093/pasj/58.1.93. arXiv: astro-ph/0505115 [astro-ph].

[62] Davide Bianchi, Héctor Gil-Marín, Rossana Ruggeri, and Will J. Percival. "Measuring line-of-sight-dependent Fourier-space clustering using FFTs." en. In: *Monthly Notices of the Royal Astronomical Society* 453.1 (Oct. 2015), p. L11. ISSN: 0035-8711. DOI: 10.1093/mnrasl/slv090. URL: https://ui.adsabs.harvard.edu/abs/2015MNRAS.453L..11B/abstract (visited on 11/19/2019).

[63] Florian Beutler, Emanuele Castorina, and Pierre Zhang. "Interpreting measurements of the anisotropic galaxy power spectrum." In: *JCAP* 03 (2019), p. 040. DOI: 10.1088/1475-7516/2019/03/040. arXiv: 1810.05051 [astro-ph.CO].

[64] Ashley J. Ross et al. "The Completed SDSS-IV extended Baryon Oscillation Spectroscopic Survey: Large-scale structure catalogues for cosmological analysis." In: *MNRAS* 498.2 (Oct. 2020), pp. 2354–2371. DOI: 10.1093/mnras/staa2416. arXiv: 2007.09000 [astro-ph.CO].

[65] Anand Raichoor et al. "The completed SDSS-IV extended Baryon Oscillation Spectroscopic Survey: large-scale structure catalogues and measurement of the isotropic BAO between redshift 0.6 and 1.1 for the Emission Line Galaxy Sample." In: *MNRAS* 500.3 (Jan. 2021), pp. 3254–3274. DOI: 10.1093/mnras/staa3336. arXiv: 2007.09007 [astro-ph.CO].

[66] Brad W. Lyke et al. "The Sloan Digital Sky Survey Quasar Catalog: Sixteenth Data Release." In: *ApJS* 250.1, 8 (Sept. 2020), p. 8. DOI: 10.3847/1538-4365/aba623. arXiv: 2007.09001 [astro-ph.GA].

[67] eBOSS Collaboration. *eBOSS galaxy and quasar clustering catalogues*. https://data.sdss.org/sas/dr16/eboss/lss/catalogs/DR16/.

[68] Arnaud de Mattia et al. "The completed SDSS-IV extended Baryon Oscillation Spectroscopic Survey: measurement of the BAO and growth rate of structure of the emission line galaxy sample from the anisotropic power spectrum between redshift 0.6 and 1.1." In: *MNRAS* 501.4 (Mar. 2021), pp. 5616–5645. DOI: 10.1093/mnras/staa3891. arXiv: 2007.09008 [astro-ph.CO].

[69] Richard Neveux et al. "The completed SDSS-IV extended Baryon Oscillation Spectroscopic Survey: BAO and RSD measurements from the anisotropic power spectrum of the quasar sample between redshift 0.8 and 2.2." In: *MNRAS* 499.1 (Nov. 2020), pp. 210–229. DOI: 10.1093/mnras/staa2780. arXiv: 2007.08999 [astro-ph.CO].

[70] Julian E. Bautista et al. "The completed SDSS-IV extended Baryon Oscillation Spectroscopic Survey: measurement of the BAO and growth rate of structure of the luminous red galaxy sample from the anisotropic correlation function between redshifts 0.6 and 1." In: *MNRAS* 500.1 (Jan. 2021), pp. 736–762. DOI: 10.1093/mnras/staa2800. arXiv: 2007.08993 [astro-ph.CO].

[71] Amélie Tamone et al. "The completed SDSS-IV extended baryon oscillation spectroscopic survey: growth rate of structure measurement from anisotropic clustering analysis in configuration space between redshift 0.6 and 1.1 for the emission-line galaxy sample." In: *MNRAS* 499.4 (Dec. 2020), pp. 5527–5546. DOI: 10.1093/mnras/staa3050. arXiv: 2007.09009 [astro-ph.CO].

[72] Jiamin Hou et al. "The completed SDSS-IV extended Baryon Oscillation Spectroscopic Survey: BAO and RSD measurements from anisotropic clustering analysis of the quasar sample in configuration space between redshift 0.8 and 2.2." In: *MNRAS* 500.1 (Jan. 2021), pp. 1201–1221. DOI: 10.1093/mnras/staa3234. arXiv: 2007.08998 [astro-ph.CO].

[73] Paul Carter et al. "The impact of the fiducial cosmology assumption on BAO distance scale measurements." In: *MNRAS* 494.2 (May 2020), pp. 2076–2089. DOI: 10.1093/mnras/staa761. arXiv: 1906.03035 [astro-ph.CO].

[74] José Luis Bernal, Tristan L. Smith, Kimberly K. Boddy, and Marc Kamionkowski. "Robustness of baryon acoustic oscillation constraints for early-Universe modifications of Λ CDM cosmology." In: *Phys. Rev. D* 102.12, 123515 (Dec. 2020), p. 123515. DOI: 10.1103/PhysRevD.102.123515. arXiv: 2004.07263 [astro-ph.CO].

[75] Max Tegmark et al. "Cosmological Constraints from the SDSS Luminous Red Galaxies." In: *Phys. Rev. D* 74 (2006), p. 123507. DOI: 10.1103/PhysRevD.74.123507. arXiv: astro-ph/0608632.

[76] Will J. Percival et al. "The shape of the SDSS DR5 galaxy power spectrum." In: *Astrophys. J.* 657 (2007), pp. 645–663. DOI: 10.1086/510615. arXiv: astro-ph/0608636.

[77] Beth A. Reid et al. "Cosmological constraints from the clustering of the Sloan Digital Sky Survey DR7 luminous red galaxies." In: *MNRAS* 404.1 (May 2010), pp. 60–85. DOI: 10.1111/j.1365-2966.2010.16276.x. arXiv: 0907.1659 [astro-ph.CO].

[78] Mikhail M. Ivanov, Marko Simonović, and Matias Zaldarriaga. "Cosmological Parameters from the BOSS Galaxy Power Spectrum." In: *JCAP* 05 (2020), p. 042. DOI: 10.1088/1475-7516/2020/05/042. arXiv: 1909.05277 [astro-ph.CO].

[79] Guido D'Amico et al. "The Cosmological Analysis of the SDSS/-BOSS data from the Effective Field Theory of Large-Scale Structure." In: *JCAP* 05 (2020), p. 005. DOI: 10.1088/1475-7516/2020/05/005. arXiv: 1909.05271 [astro-ph.CO].

[80] Tilman Tröster et al. "Cosmology from large-scale structure. Constraining ΛCDM with BOSS." In: *A&A* 633, L10 (Jan. 2020), p. L10. DOI: 10.1051/0004-6361/201936772. arXiv: 1909.11006 [astro-ph.CO].

[81] A. J. S. Hamilton. "Uncorrelated modes of the non-linear power spectrum." In: *MNRAS* 312.2 (Feb. 2000), pp. 257–284. DOI: 10.1046/j.1365-8711.2000.03071.x. arXiv: astro-ph/9905191 [astro-ph].

[82] Marko Simonović et al. "Cosmological perturbation theory using the FFTLog: formalism and connection to QFT loop integrals." In: *JCAP* 04 (2018), p. 030. DOI: 10.1088/1475-7516/2018/04/030. arXiv: 1708.08130 [astro-ph.CO].

[83] Takahiro Nishimichi et al. "Blinded challenge for precision cosmology with large-scale structure: Results from effective field theory for the redshift-space galaxy power spectrum." In: *Phys. Rev. D* 102.12, 123541 (Dec. 2020), p. 123541. DOI: 10.1103/PhysRevD.102.123541. arXiv: 2003.08277 [astro-ph.CO].

[84] Hendrik Hildebrandt. "Cosmological results from the Kilo Degree Survey." In: *PoS* EPS-HEP2017 (2017). Ed. by Paolo Checchia et al., p. 039. DOI: 10.22323/1.314.0039.

[85] H. Hildebrandt et al. "KiDS+VIKING-450: Cosmic shear tomography with optical and infrared data." In: *Astron. Astrophys.* 633 (2020), A69. DOI: 10.1051/0004-6361/201834878. arXiv: 1812.06076 [astro-ph.CO].

[86] J. Muir et al. "Blinding multi-probe cosmological experiments." In: *arXiv:1911.05929 [astro-ph]* (Nov. 2019). arXiv: 1911.05929. URL: http://arxiv.org/abs/1911.05929 (visited on 11/15/2019).

[87] Elena Sellentin. "A blinding solution for inference from astronomical data." In: *arXiv:1910.08533 [astro-ph, physics:gr-qc, physics:physics]* (Oct. 2019). arXiv: 1910.08533. URL: http://arxiv.org/abs/1910.08533 (visited on 11/01/2019).

[88] Takahiro Nishimichi. *Multipole moment data for* PT *challenges*. https://www2.yukawa.kyoto-u.ac.jp/~takahiro.nishimichi/data/PTchallenge/.

[89] Héctor Gil-Marín. "How to optimally combine pre-reconstruction full shape and post-reconstruction BAO signals." In: *arXiv e-prints*, arXiv:2203.05581 (Mar. 2022), arXiv:2203.05581. arXiv: 2203.05581 [astro-ph.CO].

[90] Hélion du Mas des Bourboux et al. "Baryon acoustic oscillations from the complete SDSS-III Ly$\alpha$-quasar cross-correlation function at z = 2.4." In: *A&A* 608, A130 (Dec. 2017), A130. DOI: 10.1051/0004-6361/201731731. arXiv: 1708.02225 [astro-ph.CO].

[91] Oliver H. E. Philcox, Blake D. Sherwin, Gerrit S. Farren, and Eric J. Baxter. "Determining the Hubble constant without the sound horizon: Measurements from galaxy surveys." In: *Phys. Rev. D* 103.2, 023538 (Jan. 2021), p. 023538. DOI: 10.1103/PhysRevD.103.023538. arXiv: 2008.08084 [astro-ph.CO].

[92] F. S. Kitaura, G. Yepes, and F. Prada. "Modelling baryon acoustic oscillations with perturbation theory and stochastic halo biasing." In: *MNRAS* 439 (Mar. 2014), pp. L21–L25. DOI: 10.1093/mnrasl/slt172. arXiv: 1307.3285 [astro-ph.CO].

[93] Chia-Hsun Chuang et al. "EZmocks: extending the Zel'dovich approximation to generate mock galaxy catalogues with accurate clustering statistics." In: *MNRAS* 446.3 (Jan. 2015), pp. 2621–2628. DOI: 10.1093/mnras/stu2301. arXiv: 1409.1124 [astro-ph.CO].

The bibliography printed above refers to citations in the Introduction, in individual chapter introductions and in Summary of Results, Discussions and Conclusions. Citations in each individual publication can be found listed within the corresponding publication.

## COLOPHON

This document was typeset using the typographical look-and-feel `classicthesis` developed by André Miede and Ivo Pletikosić. The style was inspired by Robert Bringhurst's seminal book on typography "*The Elements of Typographic Style*". `classicthesis` is available for both LaTeX and LyX:

https://bitbucket.org/amiede/classicthesis/

Happy users of `classicthesis` usually send a real postcard to the author, a collection of postcards received so far is featured here:

http://postcards.miede.de/

Thank you very much for your feedback and contribution.

*Final Version* as of July 12, 2022 (classicthesis v4.6).